10º SEED MOL

Química Teórica para a Vida!

SIMPÓSIO DE ESTRUTURA ELETRÔNICA & DINÂMICA MOLECULAR

Pirenópolis - GO

4 a 8 de Novembro de 2024

BRASIL

LIVRO DE RESUMOS

Universidade de Brasília
Instituto de Química

SIMPÓSIO DE ESTRUTURA ELETRÔNICA E DINÂMICA MOLECULAR

LIVRO DE RESUMOS
10º SeedMol

Coordenador: João Batista Lopes Martins



UnB

Brasília-DF
2025

©2025 SEEDMOL

[1ª edição]

A responsabilidade pelos direitos autorais de textos e imagens dessa obra é **dos autores.**

Elaboração e informações
Universidade de Brasília
Instituto de Química
Campus Universitário Darcy Ribeiro, Instituto de Química, CEP 70904900 Brasília - DF, Brasil
Contato: (61)3107-3886 Site: www.seedmol.unb.br E-mail: seedmol@gmail.com

Dados Internacionais de Catalogação na Publicação (CIP)
(Biblioteca Central da Universidade de Brasília – BCE/UNB)

S612l Simpósio de Estrutura Eletrônica e Dinâmica Molecular (10. : 2025 : Brasília).
Livro de resumos [recurso eletrônico] : 10° SeedMol / coordenador, João Batista Lopes Martins. – Brasília : Universidade de Brasília, Instituto de Química, 2025.
362 p. : il.

Inclui bibliografia e índice.
Textos em português e inglês.
ISBN 978-65-999119-2-7.

1. Estrutura eletrônica - Congressos. 2. Dinâmica molecular - Congressos. 3. Simpósio de Estrutura Eletrônica e Dinâmica Molecular (10. : 2025 : Brasília). I. Martins, João B. L. (coord.). II. Título.

CDU 54.022

Fernanda Cordeiro de Carvalho – Bibliotecária – CRB 1/2339

PREFÁCIO

Esta é a décima edição do Simpósio de Estrutura Eletrônica e Dinâmica Molecular

10º SeedMol.

O 10º SeedMol ocorreu de 04-08 de novembro de 2024, no Campus UEG Pirenópolis, Goiás. É uma edição comemorativa de dez anos do evento, caracterizada pelo objetivo de fortalecer a pesquisa no Centro-Oeste e no país, além de promover um valioso espaço para o desenvolvimento de novas colaborações, para a discussão ampla da área, e para a construção e formação do conhecimento dos estudantes, com excelente profissionais e pesquisadores. Tendo em vista, a necessidade de formação de novos profissionais com uma visão multidisciplinar, com enfoque em metodologias de modelagem e simulação computacional também é um objetivo do evento.

A área do evento é bastante ampla, partindo da Química Teórica e Computacional, da Estrutura Eletrônica, Física Atômica e Molecular, Química Medicinal, e Modelagem e Simulação Molecular, dentre outros. É um evento que trata temas atuais e de ponta, necessários para o desenvolvimento da sociedade. Daí se tornou um evento consolidado no cenário nacional, com uma expressiva repercussão dentre os participantes, atingindo um excelente grau de satisfação com relação à divulgação científica.

O caminho até a realização do evento foi longo, com variados contratempos, a grande maioria devido a diminuição de recursos para a pesquisa e desenvolvimento, apesar dos recentes avanços. Foram necessárias algumas mudanças no evento, para adequar aos recursos obtidos, prezando a qualidade. O evento contou com 176 inscritos, dos quais 18% eram alunos de graduação, 28% eram alunos de mestrado, 29% eram alunos de doutorado, 5% bolsistas de pós-doutorado e 20% de profissionais e professores de ensino médio. Quanto ao gênero, houve a participação de 75% de homens e 24% de mulheres e 1% não binário. Quanto a distribuição geográfica, foram atendidos 17 Estados e Distrito Federal, contando com 56 municípios. A maior parte do DF, GO e SP. Tivemos participantes estrangeiros: Uruguai, Estados Unidos, Espanha, Alemanha e Bélgica. O evento recebeu diversos elogios dos participantes estrangeiros e nacionais. Os estudantes e pesquisadores puderam aproveitar o momento, um ambiente profícuo para debates e desenvolvimento das áreas correlatas ao evento.

O evento também conta com uma publicação de artigos originais no Topical Collections “10th Symposium on Electronic Structure and Molecular Dynamics – 10th SeedMol” do Journal of Molecular Modeling (Qualis A4). O 10º. SeedMol obteve mais de 512 seguidores nos canais do Instagram e Facebook do evento. Houve a participação de estudantes de ensino médio, que também apresentaram pôster, esses estudantes são do programa de Iniciação Científica de Ensino Médio.

PREFÁCIO

Organizador:

Dr. João B. L. Martins (IQ/UnB, Chair), ORCID: 0000-0001-8677-3239

Comitê Organizador e Científico:

Dra. Adelia Aquino (TTU, Texas)
Dra. Alessandra Albernaz (IF/UnB)
Dr. Alexandre Amaral Leitão (UFJF)
Dr. Alexandre Cavalheiro Dias (UnB)
Dra. Andréia Luisa da Rosa (UFG)
Dr. Benedito Jose Costa Cabral (Universidade de Lisboa)
Dr. Breno Rodrigues Lamaghere (CEFET-MG)
Dr. Daniel Francisco Scalabrini Machado (UnB)
Dr. Davi Alexsandro Cardoso Ferreira (UnB)
Dr. Demétrio Antônio da Silva Filho (IF/UnB)
Dra. Elaine Fontes Ferreira da Cunha (UFAL)
Dr. Elton Anderson Santos de Castro (UEG)
Dra. Edna da Silva Machado Rodrigues (UnB)
Dra. Érica Cristina Moreno Nascimento (IQ/UnB)
Dr. Geraldo Magela e Silva (UnB)
Dr. Gerd Bruno da Rocha (DQ, UFPB)
Dr. Giovanni Finoto Caramori (UFSC)
Dr. Guilherme Duarte Ramos Matos (UnB)
Dr. Guilherme Colherinhas (UFG)
Dr. Herbert De Castro Georg (UFG)
Dr. Hélio Anderson Duarte (UFMG)
Dr. Itamar Borges Junior (IME)
Dr. Jeronimo Lameira Silva (UFPA)
Dr. Jose Diogo Lisboa Dutra (UFS)
Dr. José R. dos Santos Politi (IQ/UnB)
Dr. Julio Cosme Santos da Silva (UFAL)
Dr. Julio Ricardo Sambrano (UNESP)
Dr. Lenoardo Baptista (UERJ)
Dr. Luciano Ribeiro (UEG)
Dr. Luiz Antonio Ribeiro Junior (UnB)
Dr. Luiz Fernando Roncaratti Junior (UnB)
Dr. Miguel San Miguel (Unicamp)
Dr. Nailton Martins Rodrigues (UFMA)
Dr. Nelson Henrique Morgon (Unicamp)
Dr. Nivan Bezerra da Costa Júnior (UFS)
Dra. Patricia R P Barreto (INPE)
Dra. Paula Homem de Mello (UFABC)
Dr. Paulo Augusto Netz (UFGRS)
Dr. Pedro Henrique De Oliveira Neto (UnB)
Dr. Ricardo Gargano (IF/UnB, Chair)
Dr. Sergio Antonio De Souza Farias (UFOPA)
Dr. Sergio Emanuel Galembeck (FFCLRP, USP)
Dr. Tertius Lima da Fonseca (IF/UFG)
Dr. Valter Henrique Carvalho Silva (UEG)
Dra. Vivian Vanessa França (UNESP)
Dr. Werner Treptow (UnB)

www.seedmol.com.br

04-08 de novembro de 2024

Livro de Resumos 10^o SeedMol

SEEDMOL

4-8 de novembro de 2024

Sumário

1 Palestras **3**

2 Minicursos **25**

3 Resumos **33**

Índice Remissivo **360**

1 Palestras



Investigating properties and applications of intercalation materials using DFT

Alexandre A. Leitão
Grupo de Físico-Química de Sólidos e Interfaces - GFQSI
Departamento de Química/Department of Chemistry
Universidade Federal de Juiz de Fora - UFJF

Abstract

Beyond a great swelling ability, layered silicates also allow the functionalization of their layers and intercalation of cations and molecules in their interlayer region to form various robust green materials that are used as CO2 adsorbents, drug carriers, or catalysts. One of these compounds, magadiite, despite the research on its applications for decades, had its structure elucidated only in 2021 by a combination of 3D electron diffraction and DFT calculations. The calcining process of sodium magadiite was also studied using a combination of DFT calculations and statistical thermodynamics. Intermediate structures produced by thermal treatment were revealed. We also report a detailed study of the Na-, K-, Mg-, and Ca-magadiites including the structure of the layers formed by water molecules coordinated to the cations and interacting with silicate layers. Finally, the interactions of Au, Ag, Pd, Pt single atoms with H-magadiite and H-[Al]-magadiite surfaces were calculated and the best sites for stabilization and migration energies were compared.

10º SIMPÓSIO DE ESTRUTURA ELETRÔNICA & DINÂMICA MOLECULAR
SEEDMOL 4 a 8 novembro | 2024 Pirenópolis, Goiás

Unveiling PROTACS: Insights into Structure and Dynamics through 2DIR spectroscopy

Ana V. Cunha[1]
[1]STRUCCHEM, Departement of Chemistry, Groenenborgerlaan 171, 2020 Antwerp, Belgium
ana.cunha@uantwerpen.be

Keywords: Molecular Dynamics, Proteolysis targeting chimeras, structural chemistry, IR spectroscopy, 2DIR spectroscopy.

Abstract

Proteolysis-targeting chimeras (PROTACs) a 'cute chemical curiosity' [1] that paved the way for the next generation of molecular inhibitors. PROTACs, first reported in 2001 by Sakamoto et al. [2], are heterobifunctional molecules that specifically bind to a target protein and induce its degradation by acting on a specific E3 ligase [3]. Thus, they present an alternative solution for the lack of "drugability" of some biological targets [4, 5]. PROTACs consist of two connected ligands:
(1) that binds to the protein of interest, known as POI, and (2) another that binds to the E3 ubiquitin ligase. They function by binding the E3 ligase with the POI, thereby inducing a proximity that results in the ubiquitination of the POI, and its subsequent proteasomal degradation [5]. In this study we use linear and two-Dimensional InfraRed spectroscopy (2DIR) to retrieve structural information from a VHL-recruiting PROTAC complexed with the bromodomain of human SMARCA2. The protein structure (pdb code:7Z6L) is shown in figure 1.

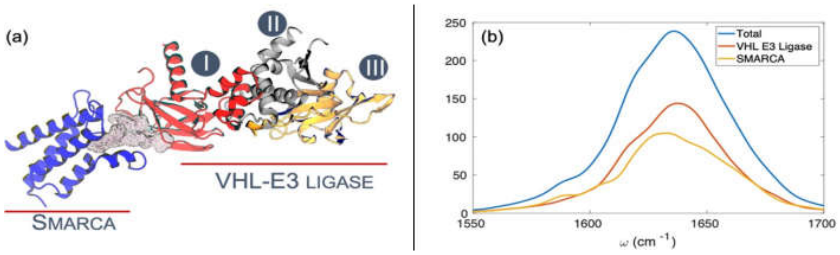


***Figure 1**: (a) PROTAC, pink wireframe representation, bound to SMARCA unit, blue, and the VHL E3 ligase domain, red, and yellow . (b) FTIR spectra of the different protein units: total, blue line; VHL E3 ligase, red line; SMARCA orange line.*

[1] Bekes, M.; Langley, D. R.; Crews, C. M., Nat. Rev. Drug Discov, *PROTAC targeted protein degraders: the past is prologue*, 2022, 21, 181– 200.
[2] Sakamoto, K.; Kim, K.; Kumagai, A.; Mercurio, F.; Crews, C.; Deshaies, R., PNAS, *Protacs: Chimeric molecules that target proteins to the Skp1–Cullin–F box complex for ubiquitination and degradation*, **2001**, **98, 8554–8559.**
[3] Hopkins, A.; Groom, C. Nat. Rev. Drug Discov, *The druggable genome*, **2002**, 1, 727–730.
[4] Furihata, H.; Yamanaka, S.; Honda, T.; Miyauchi, Y.; Asano, A.; Shibata, N.; Tanokura, M.; Sawasaki, T.; Miyakawa, T., Nat. Commun, *Structural bases of IMiD selectivity that emerges by 5-hydroxythalidomide*, **2020**, 11.
[5] Buckley, D. L.; Van Molle, I.; Gareiss, P. C.; Tae, H. S.; Michel, J.; Noblin, D. J.; Jorgensen, W. L.; Ciulli, A.; Crews, C. M. J. Am. Chem. Soc., *Targeting the von Hippel-Lindau E3 ubiquitin ligase using small molecules to disrupt the VHL/HIF-1α interaction*, **2012**, 134, 4465–4468.

10º SIMPÓSIO DE ESTRUTURA ELETRÔNICA & DINÂMICA MOLECULAR
SEEDMOL 4 a 8 novembro | 2024 Pirenópolis, Goiás

Electronic and optical properties of low-dimensional phosphorene

Andréia Luísa da Rosa[1]
[1]Universidade Federal de Goiás Instituto de Física Quantum Computational Materials Science Group Campus Samambaia, Goiânia - GO, Brazil

Abstract
Phosphorene is a recently developed two-dimensional (2D) material that has attracted tremendous attention because of its unique anisotropic optical properties and quasi-one-dimensional (1D) excitons. We use first-principles calculations combined with the maximally localized Wannier function tight binding Hamiltonian (MLWF-TB) and Bethe-Salpeter equation (BSE) formalism to investigate quasi-particle effects of 2D and quasi-1D blue and black phosphorene nanoribbons. Our electronic structure calculations show that both blue and black phosphorene monolayers are semiconductors. On the other hand black phosphorene zig-zag nanoribbons are metallic. Similar behavior is found in very thin blue phosphorene zig-zag and armchair nanoribbons. As a general behavior, the exciton binding energy decreases as the ribbon width increases, which highlights the role of quantum confinement effects. The solution of the BSE shows that blue phosphorene monolayer has an exciton binding energy four times higher than that of their black phosphorene counterpart. Furthermore, both monolayers show a different linear optical response with respect to light polarization, as black phosphorene is highly anisotropic. We find a similar, but less pronounced, optical anisotropy for blue phosphorene monolayer, caused exclusively by the quasi-particle effects, thus revealing exciting features of these nanoribbons and providing important advances in the understanding of quasi-one dimensional phosphorus-based materials.
]

Explainable Chemical Artificial Intelligence: Machine Learning of Real-Space Chemical Descriptors.

Miguel Gallegos[1], Valentín Vassilev-Galindo[2], Igor Poltavsky[3], Alexandre Tkatchenko[3], Ángel Martín Pendás[1].
[1]Departamento de Química Física y Analítica. Universidad de Oviedo. 33006 Oviedo, Spain.
[2]IMDEA Materials Institute, C/Eric Kandel 2, 28906 Getafe, Madrid, Spain.
[3]Department of Physics and Materials Science, University of Luxembourg, L-1511 Luxembourg City, Luxembourg.
ampendas@uniovi.es.

Keywords: Machine Learning; Real-space descriptors; Quantum Theory of Atoms in Molecules..

Abstract
In the modern chemical narrative, there is a constant drive for more accurate outcomes, driven by the unparalleled ability of Artificial Intelligence (AI) to estimate chemical properties with unprecedented accuracies. This has resulted in the proliferation of black boxes, extremely accurate but of elusive interpretation. While valuable, these tools are prone to suffer from the Clever Hans effect, which ultimately hinders our understanding of chemical phenomena. Transcending beyond mere numerical accuracy, recent endeavors have been made in the quest for the sought-after interpretability, leading to the field of Explainable AI (XAI). However, the exploration of this discipline in chemistry is still in its infancy, with limited progress. To bridge this gap, we show how Explainable Chemical AI (XCAI) can emerge from integrating physically rigorous theories, such as the Atoms in Molecules framework, [1] with cutting-edge AI kernels. Encompassing a modified version of the SchNet architecture, [2] our approach (SchNet4AIM) can estimate local (atomic and pairwise) quantities with remarkable accuracy while ensuring the precise reconstruction of the corresponding molecular properties. Additionally, intrinsic explainability is showcased through the study of a supramolecular binding phenomenon, where SchNet4AIM provides quantum chemically consistent insights into the driving forces behind complexation and discerns the most dominant contributions to the latter. Overall, this approach goes beyond numerical precision by offering chemically interpretable insights, broadening the range of applicability of computationally demanding theoretical tools to previously unexplored domains. [3]

References

1. Bader, R. F. W. Atoms in Molecules: A Quantum Theory. (Clarendon Press, Oxford, 1990).
2. Schütt, K. T.; Sauceda, H. E., Kindermans, P.-J.; Tkatchenko, A. & Müller, K.-R; J. Chem. Phys. 2018, 148, 241722.
3. Gallegos, M; Vassilev-Galindo, V.; Poltavsky, I.; Martín Pendás, A.; Tkatchenko, A.; Nat. Commun. 2024, 4345.

Computational electrocatalysis: search for catalysts for the CO_2 reduction and hydrogen evolution reactions using the computational hydrogen electrode model.

Breno R. L. Galvão[1].
[1]Centro Federal de Educação Tecnológica de Minas Gerais, CEFET-MG,
Av. Amazonas 5253, 30421-169 Belo Horizonte, Minas Gerais, Brazil.
brenogalvao@gmail.com
Keywords: electrocatalysis; data mining; CO2 reduction;

Abstract

In this work, we first present a protocol to reveal the underlying mechanisms for nanoalloy stabilization, based on data-mining techniques (t-SNE, k-means and correlation analysis). After that, we present new results on computational electrocatalysis using the computational hydrogen electrode model. Possible catalysts studied include doped and non-doped copper nanoparticles, single-atom-doped silver surfaces, and metal atoms loaded on fullerenes.

Many chemical reactions that are crucial to our society can be made faster and cheaper by the development of more active or selective heterogeneous catalysts. Such catalysts benefit from the presence of imperfections such as kinks and dopants, which can be presented by nanoparticles or high-Miller-index surfaces.

In this work, we first review a protocol that has been developed and improved in our group to reveal the underlying mechanisms for nanoalloy stabilization, based on data-mining techniques (such as t-SNE, k-means and correlation analysis).[1,2]

After that, we present new results on computational electrocatalysis using the computational hydrogen electrode model. We have searched for new catalysts for important reactions involved in the energetic transition, such as the CO_2 reduction reaction, hydrogen evolution reaction (HER), oxygen reduction reaction (ORR), and the oxygen evolution reaction (OER). Possible catalysts studied analysed here were doped and non-doped copper nanoparticles, single-atom-doped silver surfaces,[3] and metal atoms loaded on fullerenes.

Acknowledgements

This work is supported by Fundação de Amparo à Pesquisa do estado de Minas Gerais (FAPEMIG), grants APQ-00597-22 and APQ-03705-23, and Conselho Nacional de Desenvolvimento Científico e Tecnológico (CNPq), grant 311508-2021-9.

References

1. L. B. Pena, L. R. Da Silva, J. L. F. Da Silva, B. R. L. Galvão, J. Phys. Chem., v. 159, 244310, 2023, https://doi.org/10.1063/5.0180906

2. T. M. Souza, L. B. Pena, J. L. F. Da Silva, B. R. L. Galvão, Phys. Chem. Chem. Phys., v. 26, 15877, 2024 https://doi.org/10.1039/D4CP00672K

3. M. M. C. B. Neto, L. G. Verga, J. L. F. Da Silva, B. R. L. Galvão, J. Phys. Chem., v. 160, 094706, 2024, https://doi.org/10.1063/5.0192055

Towards the digitalization of Theory and Experiments

Celso Ricardo Caldeira Rêgo
Karlsruhe Institute of Technology

The ScienceAI project aims to combine predictive and generative AI into a single tool, connecting experimental and theoretical science. This approach allows researchers from different domains to use AI-driven solutions without needing deep expertise in specific subfields. ScienceAI is designed to be versatile and applicable across various disciplines such as Chemistry, Physics, Material Science, Engineering, Agriculture, and more. The project is powered by the Llama family model, an advanced open-weight Large Language Model (LLM) tailored to scientific needs. A key feature is its self-constructed vector store, built from a vast body of scientific literature and refined using advanced topic modeling techniques. This significantly improves the model's ability to generate accurate, data-driven insights with scientific precision.
Additionally, ScienceAI introduces a new paradigm of scientific workflows. These workflows generate simulation protocols that can be easily transformed into digital workflows using the SimStack framework or similar tools. This innovation bridges the gap between complex computational tasks and researchers with limited computational expertise, making advanced simulation tools more accessible and democratizing their use across scientific communities.

Impact of the Polymorphism and Relativistic Effects on the Electronic Properties of Inorganic Metal Halide Perovskites

Diego Guedes-Sobrinho[1]
[1]Quantum Chemistry and Thermodynamic Materials group (Q^2M), Chemistry Department, Federal University of Paraná, Curitiba-PR, Brazil.
guedessobrinho@ufpr.br.
Keywords: Perovskites, Bulk Rashba, Polymorphism, Density Functional Theory.

Metal halide perovskites (MHPs) have been in the spotlight given their high power conversion efficiencies surpassed 26% for $CH(NH_3)_2PbI_3$ single-junction devices. However, the journey for the development of a commercial optoelectronic device in solar cells requires overcoming some limitations, such as: *i*) instability issues related to the organic cations; *ii*) presence of toxic Pb; *iii*) the comprehension of the polymorphic effects on the optoelectronic properties in detriment of *Pm3m* structure. [1,2,3] We have investigated all those effects on the ABX_3 MHPs, where A = CH_3NH_3 (MA), Cs, whereas B = Ge, Sn, Pb, and X = Cl, Br, I. For instance, it is not fully clarified how bulk Rashba effect (i.e., spin degeneracy breaking on the band edges) correlates with the optoelectronic performance of those materials when polymorphic motifs are considered.

Our protocol accounts for the spin-orbit coupling effects combined with the Density Functional Theory by including relativistic quasiparticle corrections. Therefore, our findings are summarized as the following:

a) the strong spin-orbit coupling (SOC) and metal-off centering in the octaedrons are *sine qua non* conditions for bulk Rashba splitting in $MAPbI_3$ in all crystalline phases (cubic, tetragonal, and orthorhombic). The MA dipoles suppression can reduce the $MAPbI_3$ gap energy by promoting a degeneracy breaking in the electronic states from the PbI_3 framework.[2,3]

b) we revealed the important role of the spin−orbit coupling (SOC) by the stability improvement throughout the B = Ge → Sn → Pb sequence for $CsB(Cl,Br,\text{ or }I)_3$ all-inorganic MHPS, taking a set of local motif contributions based on distortions on the octahedrons, relative tiltings, Cs displacement, and metal off-centering networks.[4]

c) the lack of permanent dipole moment in Cs results in $CsPbI_3$ polymorphs with a pronounced Pb on-centering-like feature, which causes suppression in their respective bulk Rashba effect.[3]

d) statistical models of MHP-alloys showed that the efficiency of solar cells can be improved, for instance, in $CsPb_{1-x}Sn_xI_3$ and $(MA_{1-x}Cs_x)PbI_3$ alloys, providing some perspective of design.[5,6]

Acknowledgements

The authors thank the Ogun Computer at CIMATEC SENAI (Salvador – BA) and "Laboratório Central de Processamento de Alto Desempenho" (LCPAD) financed by FINEP through CT-INFRA/UFPR projects, both in Brazil for the support to perform the electronic structure calculations. The authors gratefully acknowledge the Santos Dumont /LNCC for super computer resources.

References

1. Guedes-Sobrinho, D.; Rego, C. R. C. Sci. Rep. 13, 4446, 2023.
2. Araujo, L. O.; Guedes-Sobrinho, D. J. Phys. Chem. Lett. 12, 7245, 2021.
3. Araujo, L. O.; Guedes-Sobrinho, D. J Comput Chem. 44:1395, 2023.
4. Araujo, L. O.; Guedes-Sobrinho D. J. Phys. Chem. C 126, 2131, 2022.
5. Araujo, L. O.; Guedes-Sobrinho, D. npj Computational Materials 10, 146, 2024.
6. Araujo, L. O.; Guedes-Sobrinho, D., J. Alloys Comp. 992, 174485, 2024

Efeitos relativísticos no estudo computacional de complexos de metais de transição

Diego Fernando da Silva Paschoal[1]

[1]Núcleo de Química Teórica e Computacional de Macaé, Polo Ajuda, Instituto Multidisciplinar de Química, Centro Multidisciplinar UFRJ-Macaé, Universidade Federal do Rio de Janeiro, Macaé, RJ, Brasil.

e-mail: diegopaschoal01@gmail.com; diegofspaschoal@macae.ufrj.br

Existe um grande interesse na Química de metais de transição devido à sua ampla gama de aplicações, como no desenvolvimento de materiais tecnológicos e de fármacos com potencial biológico. No entanto, estudos computacionais desses complexos de metais de transição são custosos e de difícil resolução, principalmente devido a necessidade de inclusão dos efeitos relativísticos. Os efeitos relativísticos podem influenciar propriedades eletrônicas, geométricas e espectroscópicas dos complexos, impactando diretamente na previsão de suas reatividades e comportamentos. Nesta palestra, serão discutidas a previsão computacional de parâmetros de RMN, cinética e eletroquímica de complexos de metais de transição, com foco na inclusão dos efeitos relativísticos. Abordagens visando a previsão das propriedades de interesse empregando potenciais de caroço efetivo, aproximações ZORA, DKH e X2C, e cálculos relativísticos de quatro componentes serão discutidas.

Theoretical prediction of a novel class of electrides for applications in redox catalysis and quantum computing

Evangelos Miliordos[1], Andrei Evdokimov[1], Benjamin Jackson[2]
[1]Auburn University, Auburn, AL, USA
[2] Pacific Northwest National Laboratory, Richland, WA, USA.
emiliord@auburn.edu
Materials; Solvated electrons; Transition metals

Abstract
This high-level quantum chemical study reveals that metal complexes can accommodate bound diffuse electrons in their periphery making species, which mimic hydrogenic atoms. These complexes (called solvated electron precursors or SEPs) are present in concentrated metal ammonia solutions, where solvated electrons orbit around the positively charged metal ammonia skeleton. A typical example is $Li(NH_3)_4$, which has a $Li(NH_3)_4^+$ core and one peripheral electron populating a hydrogenic shell model but with the nuclear or jellium shell energy order: 1s, 1p, 1d, 2s, 2p, 1f, 2d. We demonstrate that transition metal ammonia complexes retain electrons in both their inner-d shell and the peripheral orbitals. In addition, two such complexes can bind together (like two hydrogen atoms producing molecular hydrogen) and form σ, σ*, π, π* orbitals identical to traditional diatomic molecules. The formation of dimers and polymers is confirmed experimentally in saturated lithium ammonia solutions, which create the so-called liquid or expanded metals. For the first time, we propose the bridging of two SEPs by replacing ammonia ligands with diamines or hydrocarbon chains. For small chains the two diffuse electrons couple into a closed-shell singlet, but for longer chains the two electrons prefer a triplet spin configuration. The spin coupling can be adjusted by the chain length and by decorating the chain with functional groups. We demonstrate that SEPs can capture, reduce, and convert CO_2 to industrial platform chemicals and that the spin of the diffuse electrons can be used as a qubit. Based on these results, we proposed the existence of novel 2d- and 3d-materials composed of linked-SEPs, which can serve both as redox catalysts and quantum computing materials.

Acknowledgements
The authors are indebted to Auburn University for financial support and especially the James E. Land endowment. This work was completed with resources provided by the Auburn University Easley Cluster. This material is based upon work supported by the U.S. National Science Foundation under Grant No. CHE-1940456.

References
1. Jackson, B. A.; Khan, S. N.; Miliordos, E.; Chem. Comm. 2023, 59, 10572.
2. Hartweg, S.; Barnes, J.; Yoder, B. L.; Garcia, G. A.; Nahon, L.; Miliordos, E.; Signorell, R.; Science 2023, 380, 1161.

Vibrational Signatures of Hydrogen Bonding and Halogen Bonding

Gregory S. Tschumper

Department of Chemistry, Missouri University of Science and Technology
Rolla, Missouri 65409 USA

The subjects of solvation, molecular recognition and supramolecular self-assembly provide some of the motivation and impetus for the work that is the focus of the talk. Convergent approaches to quantum mechanical (QM) *ab initio* electronic structure calculations have provided tremendous insight into the structures, energetics and spectroscopic signatures of molecular clusters held together by relatively weak, non-covalent interactions (London dispersion forces, hydrogen bonding, halogen bonding, π-stacking, etc.) [1-3]. Unfortunately, the computational demands associated with the most accurate and reliable QM methods often prohibit their application to large molecular systems. Part of this talk will focus on strategies that systematically converge toward exact numerical solutions of the electronic Schrödinger equation via methodical application of correlated wave function methods and Gaussian atomic orbital basis sets. That will set the stage for an overview of computational techniques for non-covalent clusters that take advantage of the many-body expansion (MBE) of the total energy. A layered, ONIOM-like approach [4] to the MBE is one such technique that we have been using to extend demanding QM electronic structure computations, such as the CCSD(T) method, to larger systems [5]. If time permits, some recent applications of our 2-layer *N*-body:Many-body QM:QM method will also be discussed [6].

[1] "Reliable Electronic Structure Computations for Weak Noncovalent Interactions," G.S. Tschumper in *Reviews in Computational Chemistry*; K.B. Lipkowitz and T.R. Cundari, Eds; Wiley: Hoboken, **26**, 39–90 (2009). http://dx.doi.org/10.1002/9780470399545.ch2

[2] "Getting down to the Fundamentals of Hydrogen Bonding: Anharmonic Vibrational Frequencies of $(HF)_2$ and $(H_2O)_2$ from *Ab Initio* Electronic Structure Computations," J.C. Howard, J.L. Gray, A.J. Hardwick, L.T. Nguyen and G.S. Tschumper, *J. Chem. Theory Comput.*, **10**, 5426–5435 (2014). http://dx.doi.org/10.1021/ct500860v

[3] "Observation of the Low-Frequency Spectrum of the Water Trimer as a Sensitive Test of the Water-Trimer Potential and the Dipole-Moment Surface," R. Schwan, C. Qu, D. Mani, N. Pal, G. Schwaab, J.M. Bowman, G.S. Tschumper and M. Havenith, em Angew. Chem. Int. Ed., **59**, 11399–11407 (2020). http://dx.doi.org/10.1002/anie.202003851

[4] "The ONIOM Method and Its Applications," L.W. Chung, W.M.C. Sameera, R. Ramozzi, A.J. Page, M. Hatanaka, G.P. Petrova, T.V. Harris, X. Li, Z. Ke, F. Liu, H.-B. Li, L. Ding, and K. Morokuma *Chem. Rev.*, **115**, 5678–5796 (2015). http://dx.doi.org/10.1021/cr5004419

[5] "Benchmark Structures and Harmonic Vibrational Frequencies Near the CCSD(T) Complete Basis Set Limit for Small Water Clusters: $(H_2O)_{n=2,3,4,5,6}$," J.C. Howard and G.S. Tschumper, *J. Chem. Theory Comput.*, **11**, 2126–2136 (2015). http://dx.doi.org/10.1021/acs.jctc.5b00225

[6] "Competition Between Solvent/Solvent and Solvent/Solute Interactions in the Microhydration of the Tetrafluoroborate Anion, BF_4^- $(H_2O)_{n=1,2,3,4}$" L.N. Olive, E.V. Dornshuld, H.F. Schaefer and G.S. Tschumper, *J. Phys. Chem. A*, **127**, 8806–8820 (2023). http://dx.doi.org/10.1021/acs.jpca.3c04014

Unveiling new aspects of nonlocal correlations in 1D quantum phase transitions

Isaac Martins Carvalho[1]
[1]Institute of Chemistry, Sao Paulo State University, 14800-090, Araraquara, São Paulo, Brazil.

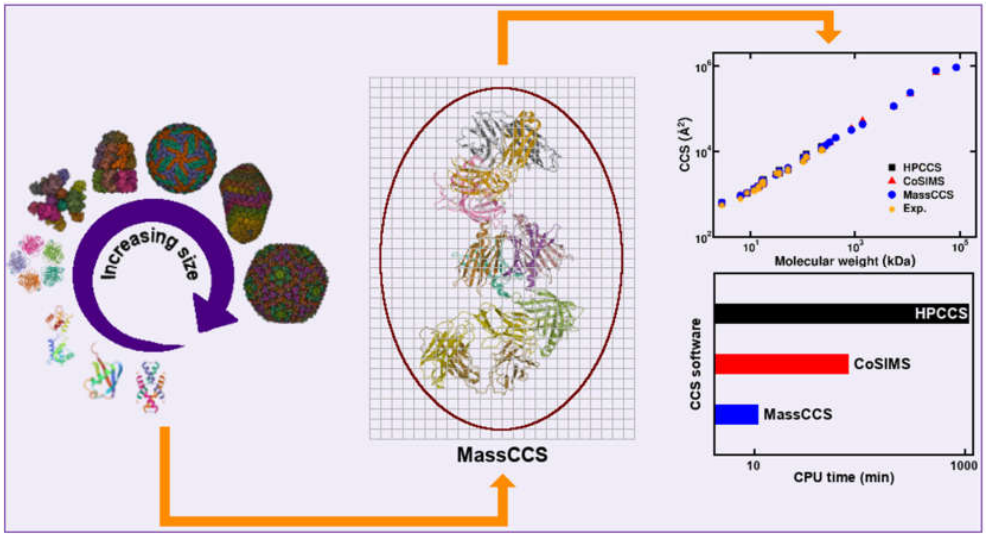
Abstract

Accurately predicting the electronic structure of nanostructures remains a formidable challenge. In this context, Density Functional Theory (DFT) and Density Matrix Renormalization Group (DMRG) have emerged as powerful computational tools for addressing electronic correlation effects. We provide a brief overview of the fingerprints of entanglement in disordered systems, address issues in Density Functional Theory (DFT) for Hubbard models, and examine the impact of electric fields on one-dimensional fermionic systems. We will discuss in particular the $Ba_{2-x}Sr_xCuO_{3+\delta}$ cuprate chain within the framework of the extended Hubbard model resolved by using DMRG, highlighting how nonlocal correlations are related to charge fluctuations during the superconducting phase transition.

MassCCS: Collision-Cross Section Calculations for Macromolecular Assemblies

Samuel Cajahuaringa[1], Daniel Caetano[1], Leandro Zanotto[1], Guido Araujo[2] and Munir Skaf*[1]
[1]Institute of Chemistry and Center for Computing in Engineering and Sciences, University of Campinas – UNICAMP, Campinas, SP
[2]Institute of Computing and Center for Computing in Engineering and Sciences, University of Campinas – UNICAMP, Campinas, SP
Email of the corresponding author: *skaf@unicamp.br*
Keywords: ion-mobility; mass-spectrometry; collision-cross-section; molecular modeling.

Abstract
Ion Mobility Mass Spectrometry (IM-MS) is a highly accurate technique for analyte characterization and a valuable tool for the structural characterization of biomolecular systems. The interpretation of IM-MS data is still a challenge and depends on accurate theoretical estimates of collision cross section (CCS) of the molecular target against the buffer gas. In this talk, I present MassCCS, a highly efficient and accurate new software for computing orientationally averaged CCS for ion-mobility mass-spectrometry ranging from small organic molecules to large macromolecular assemblies containing millions of atoms. MassCCS combines the Trajectory Method and the linked-cell algorithm to achieve orders of magnitude speed-ups with respect to the fastest codes currently available for CCS calculations using the Trajectory Method.



Acknowledgements
The authors thank Fapesp (grant # 2103/08293-7) for supporting this work.

References
1. Christofi, E.; Barran, P. *Chem. Rev.* 2023, *123*, 2902.
2. Cajahuaringa, S.; Caetano, D. L. Z.; Zanotto, L. N.; Araujo, G.; Skaf, M. S. *J. Chem. Inf. Mod.* 2023, *63*, 3557.

10º SIMPÓSIO DE ESTRUTURA ELETRÔNICA & DINÂMICA MOLECULAR
SEEDMOL 4 a 8 novembro | 2024 Pirenópolis, Goiás

Theoretical investigation of new methods to enhance the chemical reactivity of graphene

Pablo A. Denis[1,*], Nicolas F. Martins[2], J.A.S. Laranjeira,[2] J.R. Sambrano[2]
[1]*Computational Nanotechnology, DETEMA, Facultad de Química, UDELAR, CC 1157, 11800 Montevideo, Uruguay.*
[2]List all distinct addresses in the same ways [Times New Roman, 12]
andrees_1975@hotmail.com
Keywords: graphene; covalent functionalization; density functional theory

Abstract

In this study, we use first principles calculations to introduce three methods for enhancing the chemical reactivity of graphene. Our results show that introducing free radicals, incorporating heteroatom doping, and using specific substrates can significantly increase the reaction energies during the covalent functionalization of graphene.

Introduction

Although graphene can be easily transformed into graphene oxide, fluorographene, or graphane, its chemical reactivity is limited. For example, Diels-Alder cycloaddition reactions onto perfect graphene [1] are endergonic with its addition possible only at the edges or defect sites. For example the addition of 2,3-dimethoxy-1,3 butadiene (DMBD) is not favorable by 50 kcal/mol. Analysis of the latter process revealed that one of the major causes of such inertness is the huge energetic cost required to alter the planar sp^2 framework of graphene. For example, when a C_6H_4 is added to graphene via a [4+2] cycloaddition, 74.8 kcal/mol are necessary to deform the sheet to the structure that it has in the product. The situation is somewhat similar when other dienes or dienophiles are considered. Therefore, it is essential to develop methods that can help to cover such large energy costs. To that end, we propose three approaches that can help the sp^2 carbon atoms adopt a sp^3 hybridization without incurring a huge energetic penalty. These processes involve: b) the introduction of free radicals on selected positions [2] a) heteroatom doping with *3p* elements [3] , and c) the use of adequate substrates [4].

Methodology

We performed M06-L periodic density functional calculations over a 5×5 unit cell. This size of lattice parameters prevents any lateral interactions between the functional groups attached. For comparative purposes, we also performed calculations using a circumcoronene model, which is large enough to mimic graphene. The basis set employed was Pople´s 6-31G*.

In addition to the latter calculations, we also carried out VDW-DF calculations as implemented in SIESTA. We used the double-zeta basis set with polarization functions and fixed the orbital confining cut-off to 0.01 Ry. The split norm utilized was 0.15. The DFT implementation in SIESTA can be prone to significant basis set superposition error (BSSE), even with a relatively low degree of radial confinement. To avoid this problem, we used the counterpoise correction suggested by Boys and Bernardi.

Results and Discussion

In Figure 1, we show the structure of the graphene sheet functionalized with a C_6H_4 following a [4+2] route. In is clear that to facilitate the reaction, the atoms near the addition site need to be altered to make the reaction more favorable

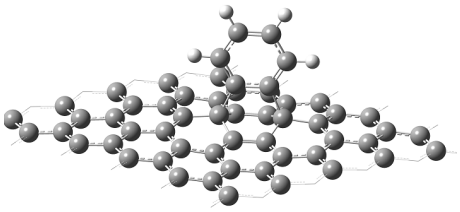


Figure 1. Optimized structure for the addition to C_6H_4 to graphene following a [4+2] path.

In first place we considered the addition of six fluorine atoms to the opposite side of the sheet that the C_6H_4 is being added, as shown in Figure 2.

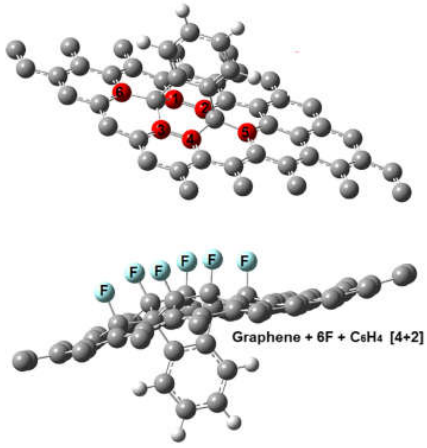


Figure 2: Optimized structure for the addition to C_6H_4 to graphene partially fluorinated with six F atoms, following a [4+2] path.

Starting from a reaction energy of -9.6 kcal/mol for the pristine sheet, it is possible to obtain a reaction energy of -183.4 kcal/mol when the reaction is carried out on the graphene sheet bearing six fluorine atoms at the positions highlighted in red in Figure 2. We note that although the most negative RE is obtained when six fluorine atoms are present, here is a gradual decrease of the reaction energies with the number of fluorine atoms present as shown in Figure 3.

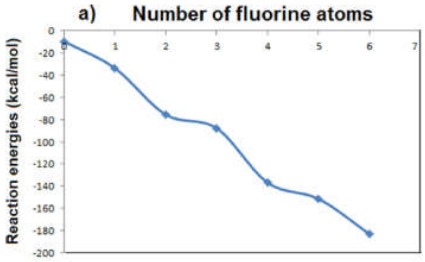


Figure 3. Reaction energies computed for the addition of C6H4 to fluorinated graphene with respect to the number of F atoms present.

The second possible approach is the use of heteroatoms, based on the fact that *3p* dopants protrude out of the graphene plane when incorporated to the graphene framework. The cycloadditions reaction can be performed over these two atoms as shown in Figure 4. Following this approach the reaction energies are as low as -112.5 kcal/mol. It is important to stress that it is crucial to use silicon. If phosphorus is utilized the reaction energies are improved but less negative, about -48.6 kcal/mol

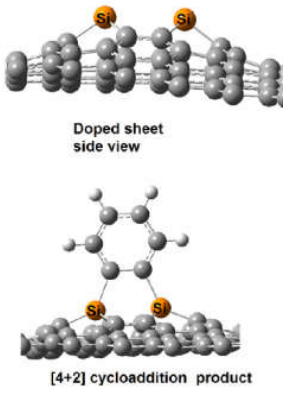


Figure 4: Optimized structure for the addition to C_6H_4 to graphene sheet doped with two Si atoms in para position.

In the third and final method, we considered the reaction onto graphene grown over silicon carbide. In this case, the role of the

fluorine atoms discussed above is played by the silicon atoms of the substrate. It is important to recall that when graphene is grown over SiC a particular structure is obtained where the Clar Sextets are maximized and for a 32 atoms graphene unit cell, only eight of them form covalent bonds with the substrate, as shown in Figure 5.

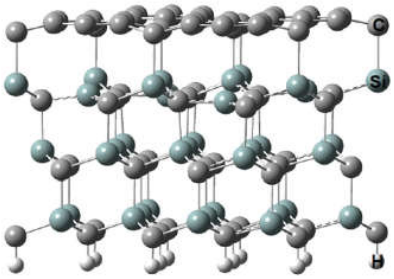


Figure 5: Optimized unit cell for a graphene sheet grown over SiC.

As observed in the previous cases the reaction energies become significantly more negative when the reaction occurs on the supported sheet. For example, in the case of the [4+2] cycloadditions the reaction energy becomes -71.6 kcal/mol, a significant increase with respect to the value computed for the pristine sheet. Nevertheless, the structure of the carbon buffer layer makes possible another reaction different that the [4+2] or the [2+2]. In that case The C_6H_4 unit is added to two carbon atoms in meta disposition, with a reaction energy of -81.3 kcal/mol, as shown in Figure 6. Therefore, the approach selected not only improves the reaction energies but also changes the structure of the product making possible the synthesis of structures that without support are unstable.

Conclusion s

In summary, by means of first-principles calculations, we have shown that it is possible to significantly increase the chemical reactivity of graphene, by two employing heteroatom doping, addition of free radicals or selection of the adequate substrate. Now the efforts should be directed to elaborate methods that can dope graphene with a specific disposition of the dopants, functionalize graphene at specific positions with free radicals or finding the adequate substrate that can bind to graphene at specific positions.

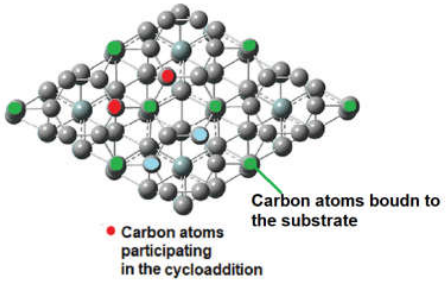


Figure 6. Carbon atoms participating in the rare cycloadditions of C_6H_4 to the buffer layer of epitaxial graphene.

Acknowledgements

The authors thank PEDECIBA Quimica, CSIC, ANII, Uruguay and Brazilian funding agencies FAPESP (2022/03959-6), CAPES (88887.467334/2019-00), and CNPq (307213/2021-8). The computational facilities were supported by resources supplied by the Molecular Simulations Laboratory (São Paulo State University, Bauru, Brazil). The authors thank the reviewers for useful comments that contributed to improving the manuscript.

References

1. P.A. Denis, Chem. Eur. J. 2013, 19, 15719-15725.
2. P.A. Denis, Chem. Phys. Lett. 2017, 684, 79-85.
3. P.A. Denis, ChemistrySelect 2016, 1, 5497-5600
4. P.A. Denis, New J. Chem. 43, 2019, 11251-11257.

Viriális: A Web-based Software to Calculates the Second Virial Coefficient

Patricia RP Barreto[1], Alberto Seleto de Soza[2], Joao Pedro Marretto Helmeister[3], João Pedro Ribeiro Azevedo[4], Alessandra Ferreira Albernaz[4],
[1]Laboratório Associado de Plasma, Instituto Nacional de Pesquisas Espaciais, CP515, São José dos Campos – SP – Brasil,
[2]Departamento de Engenharia de Materiais, Escola de Engenharia de Lorena da USP - Área II - Lorena – SP,
[3]Universidade Estadual de Campinas, Faculdade de Ciências Aplicadas, Limeira, SP CEP 13484-350, Brazil,
[4]Instituto de Física, Universidade Brasília, CP04455, Brasília, DF CEP 70919-970, Brazil.
Email of the corresponding author: *patricia.barreto@inpe.br*

Keywords: Monte Carlo Integration, Potential Energy Surface, Second Virial Coefficient, Interactive web based program, rate constant, transition state theory.

Abstract

In this talk, we are going to show de newer version of APUAMA and VIRIALIS code. Both code were writing in Python and are web-based. APUAMA is a code to calculate the reaction rate and thermodynamics properties, based in the transition state theory. The new version can get all-necessary data from the Gaussian output directly and shows the results in function of temperature, as well as, the Arrhenius parameters. The VIRIALIS calculates the second virial coefficient of AB diatomic molecules as well as A_2-B_2 polyatomic molecules. It performs a nonlinear fitting, generating a potential energy surface according to the generalized fifth-degree Rydberg function and the Pirani potential. Thus, VIRIALIS returns the second virial coefficient in terms of temperature. The APUAMA and VIRIALIS, show the results, in the code web-page as table or figures, and they can be downloaded.

10º SIMPÓSIO DE ESTRUTURA ELETRÔNICA & DINÂMICA MOLECULAR
SEED MOL
4 a 8 novembro | 2024
Pirenópolis, Goiás

Electronic Structure of [2,2]Cyclophanes

Sérgio Emanuel Galembeck

Departamento de Química, FFCLRP, Universidade de São Paulo, 14040-901, Ribeirão Preto – SP, Brasil

Cyclophanes are cyclic systems composed by rings containing the maximum number of non-cumulative conjugated double bonds. These compounds exhibit a wide range of applications, including synthetic chemistry, catalysis, polymer chemistry, and selective molecular recognition of several classes of molecules. In analytical chemistry, they have been proposed for use in chiral stationary phases. Additionally, cyclophanes have found applications in nanotechnology, such as in molecular wires, nonlinear optics, and quantum dots.

For several years, our research group has been investigating the electronic structure of [2,2]cyclophanes (Figure 1). Our initial studies focused on the electronic structure, aromaticity, and the effects of fluorine substitution on aromatic hydrogens. These investigations have provided valuable insights into the intra- and intermolecular interactions of these compounds. However, the relative importance of through-space interactions between the aromatic rings and through-bond interactions through the aliphatic bridges remained unclear. Recent studies have demonstrated that electron density transmission primarily occurs through the aliphatic bridges, via the through-bond mechanism. In parallel with these studies, we have also explored the effects of exocyclic complexation of [2,2]paracyclophanes with the $[Ru(NH_3)_6]^{2+}$ group and endocyclic complexation with various neutral atoms and ions.

Furthermore, this review will discuss other ongoing research projects in our laboratory, including the study of complexes containing the RuNO group and the characterization of N-O and P-O bonds in organic compounds.

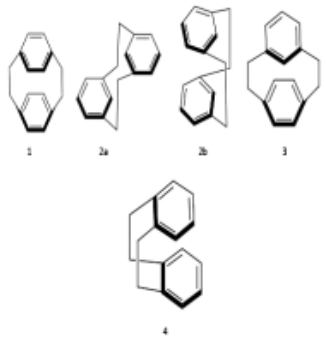


Figure 1 – [2,2]cyclophanes

(FAPESP, CNPq, CAPES)

The Mysteries of Chirality, Solvation, and Optical Activity

T. Daniel Crawford[1,2]
[1]Department of Chemistry, Virginia Tech, Blacksburg, Virginia, U.S.A.
[2]Molecular Sciences Software Institute, Blacksburg, Virginia, U.S.A.
crawdad@vt.edu
Keywords: chirality; quantum chemistry; coupled cluster theory; response theory

Abstract
The determination of the "handedness" of chiral compounds remains a fascinating and critical challenge in which theory and computation play a vital role. In the effort to assign the absolute stereochemical configurations of chiral isolates, quantum chemical models have the potential to provide experimentalists with robust predictions of the requisite spectroscopic signatures, such as specific rotation, circular dichroism rotatory strengths, Raman scattering circular intensity differences, and more. However, such properties are among the most challenging to simulate because of their delicate dependence on a variety of intrinsic and extrinsic factors. Solvent effects, for example, not only dramatically expand the complexity of the simulation, but can sometimes even alter the sign of the chiral response. In this lecture, I will discuss recent efforts in my group toward the goal of developing reliable theoretical predictions of chiroptical properties, including the exploration of reduced-scaling methods, a variety of implicit and explicit solvation models, and explicitly time-dependent quantum dynamics.

Is It Possible to Start a Business Based on Theoretical Chemistry?

Valter Henrique Carvalho-Silva[1*], F. O. Sanches-Neto[2], and Bruno M. D'Abadia[3]

[1]Lab for Modeling of Physical and Chemical Transformations, Research and Graduate Center, Goiás State University, Anápolis, Brazil;
[2]Instituto Federal de Educação, Ciência e Tecnologia de Goiás, Valparaíso de Goiás, GO, Brasil
[3]Câmara dos Deputados Federais - Palácio do Congresso Nacional, Câmara dos Deputados, Praça dos Três Poderes, Brasília - DF, Brasil

**fatioleg@ueg.br*
Keywords: Entrepreneurship in theoretical chemistry; pharmaceutical innovation; molecular modeling; artificial intelligence in industry.

Abstract.

Theoretical chemistry, historically seen as an academic field distant from the private sector, has shown growing potential for entrepreneurship, especially when applied to practical challenges faced by industry. This lecture explores how knowledge of physicochemical phenomena can be transformed into innovative business opportunities, with a focus on the pharmaceutical market in the state of Goiás, the second-largest pharmaceutical hub in Brazil. Goiás, with its robust pharmaceutical industry, faces constant challenges related to drug stability, compound degradation, and process optimization. Through tools based on molecular modeling, artificial intelligence, and advanced statistical analysis, it is possible to assist companies in the rapid identification of degradation pathways, impurity analysis, and process optimization, resulting in greater efficiency and cost reduction. The lecture will address the initial perspectives and challenges faced in entrepreneurship within theoretical chemistry, highlighting the role of partnerships between academia and the industrial sector. MInPro will be presented as a case study, demonstrating that the fusion between scientific rigor and market demands can result in ventures with synergistic impact for both academia and the private sector. The creation of the startup MInPro, founded on a solid academic background in theoretical chemistry, exemplifies how this area can be applied to create advanced technological solutions for the private sector. In a scenario where innovation is increasingly crucial, entrepreneurship based on theoretical chemistry emerges as a promising strategy to drive economic and technological growth in the state of Goiás.

[1] F. Sanches-Neto, N. Coutinho, V. Aquilanti, W. Silva, and V. Carvalho-Silva, J Braz Chem Soc (2023).
[2] F. O. Sanches-Neto, J. R. Dias-Silva, L. H. Keng Queiroz Junior, and V. H. Carvalho-Silva, Environ Sci Technol **55**, 12437 (2021).
[3] V. H. Carvalho-Silva, H. B. Napolitano, B. M. D'Abadia, and K. C. Mundim, Revista Processos Químicos **17**, 76 (2023).

Allosteric Modulation of Membrane Proteins by Small Low-Affinity Ligands.

Werner Treptow[1]
[1]Laboratório de Biologia Teórica e Computacional (LBTC), Universidade de Brasília DF, Brasil

treptow@unb.br

Keywords: membrane proteins | low-affinity ligands | allosteric modulation | binding free energy

Abstract
Under an applied external stimulus (*eg.* voltage, surface tension or chemical potentials), membrane proteins may respond to a variety of ligands, including weak-affinity small-molecule solutes accounting for functional effects in the mM concentration range. Such weak-affinity molecules may interact with multiple sites of a membrane protein in a highly degenerate manner to a degree that it's better conceived as a partition phenomenon, hard to be characterized at the molecular interface of the protein. Based on a recent concentration-dependent thermodynamic analysis of that partition process,[1] we elaborate a novel and detailed theoretical description of the allosteric mechanism of membrane proteins in presence of weak-affinity solutes and external stimulus. Free-energy stability of the partition process and its energetic impact on the protein coupling with the external stimulus are quantified and the outcome is a simple formulation that allows equilibrium shifts between two conformational states of the protein to be described in terms of the grand-canonical partition function of the ligand at dilute concentrations.[2] Model's predictions of the spatial distribution and response probability shifts across a variety of solute concentrations and thermodynamic conjugates can be directly compared to measurements, making it especially useful to interpret experimental data at the atomic resolution.

Acknowledgements
The work was supported by National Council for Scientific and Technological Development CNPq [grant number 302089/2019-5 and 200114/2020-4], Coordenação de Aperfeiçoamento de Pessoal de Nível Superior CAPES [grant number 23038.010052/2013-95], and Fundação de Apoio a Pesquisa do Distrito Federal FAPDF [grant number 193.001.202/2016].

References
1. Cirqueira L, Stock L and Treptow W; *Comput Struct Biotechnol J* 2022, 20, 4885-4891.
2. Treptow W; *J Chem Inf and Model* 2023, 63, 2047-2057.

2 Minicursos



MINICURSO: Definição de protocolos computacionais em cálculos de química quântica,

Diego Fernando da Silva Paschoal[1]

[1]Núcleo de Química Teórica e Computacional de Macaé, Polo Ajuda, Instituto Multidisciplinar de Química, Centro Multidisciplinar UFRJ-Macaé, Universidade Federal do Rio de Janeiro, Macaé, RJ, Brasil.

e-mail: diegopaschoal01@gmail.com; diegofspaschoal@macae.ufrj.br

A definição de um protocolo computacional para a realização de cálculos de química quântica é crucial para a determinação de propriedades moleculares. Um protocolo adequado deve ser preciso, eficiente e reprodutível. A definição de um protocolo computacional envolve a escolha do método teórico e do conjunto de funções de base, avaliação do papel do solvente e dos efeitos relativísticos, definição do software de simulação e dos parâmetros de cálculo, tratamento dos dados e validação. Assim, o presente minicurso visa uma abordagem teórico-prática dos aspectos envolvidos no desenvolvimento de um protocolo computacional para cálculos de química quântica com ênfase na descrição das propriedades de ressonância magnética nuclear e reatividade de compostos de metais de transição. Os participantes aprenderão a definir e implementar protocolos computacionais para cálculos de química quântica, desde os conceitos teóricos fundamentais até a execução de simulações em softwares como ORCA, ReSpect etc.

Minicurso: Modelando sistemas biológicos com métodos de química quântica

Prof. Gerd Bruno Rocha
Departamento de Química – Pós-graduação em Química – Universidade Federal da Paraíba
gbr@academico.ufpb.br; www.quantum-chem.pro.br

Em química, um dos grandes desafios na área de modelagem molecular é o tratamento químico-quântico completo de sistemas de alta complexidade, tais como: biomoléculas, materiais, superfícies, polímeros, soluções, etc[1]. Quando se usa técnicas de escalonamento linear nos computadores de hoje já é possível a modelagem de grandes moléculas com cerca de 1 milhão de átomos usando DFT[2] e 2 milhões usando métodos semiempíricos[3]. Estas técnicas também reduzem o tempo de computação de propriedades específicas em estudos sistemáticos de grandes conjuntos de moléculas de tamanho médio[4,5,6]. Ainda nessa perspectiva, métodos de estrutura eletrônica que escalonam linearmente podem ser combinados com dinâmica molecular[7] produzindo estratégias computacionais altamente eficientes para simulação de sistemas moleculares complexos. Estes fatos criam a real possibilidade de estudarmos e apresentarmos novos entendimentos de importantes fenômenos em bioquímica, biofísica, biotecnologia e nanotecnologia. Algo nesse sentido tem sido feito no nosso grupo de pesquisa[8,9,10,11] a partir do software PRIMoRDiA[12], que é de domínio público (https://github.com/igorChem/PRIMoRDiA1.0v).

Neste minicurso teórico/prático serão abordados aspectos teóricos de métodos semiempíricos de química quântica e realizadas atividades computacionais envolvendo: (i) enovelamento de proteínas, (ii) termodinâmica de complexos enzima-ligante, (iii) interações intermoleculares de complexos enzima-ligante e (iv) reatividade em catálise enzimática.

Os requisitos para acompanhar esse minicurso é ter conta na Google e entender minimamente de Python. Usaremos a plataforma Google Colab (https://colab.research.google.com/) para as nossas modelagens e simulações. Deixo um repositório público onde algum material pode ser consultado: https://github.com/RochaGerd/Chemistry_with_Python.

1. Clary DC. Quantum chemistry of complex systems. *Science (80-)*. 2006;314(5797):265-266. doi:10.1126/science.1133434
2. VandeVondele J, Borštnik U, Hutter J. Linear Scaling Self-Consistent Field Calculations with Millions of Atoms in the Condensed Phase. *J Chem Theory Comput*. 2012;8(10):3565-3573. doi:10.1021/ct200897x
3. Anisimov VM, Bliznyuk AA. Charge transfer effects in the GroEL-GroES chaperonin tetramer in solution. *J Phys Chem B*. 2012;116(22):6261-6268. doi:10.1021/jp211385e
4. Urquiza-Carvalho GA, Fragoso WD, Rocha GB. Assessment of semiempirical enthalpy of formation in solution as an effective energy function to discriminate native-like structures in protein decoy sets. *J Comput Chem*. 2016;37(21):1962-1972. doi:10.1002/jcc.24415
5. Fukushima K, Wada M, Sakurai M. An insight into the general relationship between the three dimensional structures of enzymes and their electronic wave functions: Implication for the prediction of functional sites of enzymes. *Proteins Struct Funct Bioinforma*. 2008;71(4):1940-1954. doi:10.1002/prot.21865
6. Stewart JJP. Application of the PM6 method to modeling proteins. *J Mol Model*. 2009;15(7):765-805. doi:10.1007/s00894-008-0420-y
7. Melo MCR, Bernardi RC, Rudack T, et al. NAMD goes quantum: an integrative suite for hybrid simulations. *Nat Methods*. 2018;15(5):351-354. doi:10.1038/nmeth.4638
8. Grillo IB, Urquiza-Carvalho GA, Rocha GB. Quantum chemical descriptors based on semiempirical methods for large biomolecules. *J Chem Phys*. 2023;158(20). doi:10.1063/5.0132687
9. Rocha-Santos A, Chaves EJF, Grillo IB, de Freitas AS, Araújo DAM, Rocha GB. Thermochemical and Quantum Descriptor Calculations for Gaining Insight into Ricin Toxin A (RTA) Inhibitors. *ACS Omega*. 2021;6(13):8764-8777. doi:10.1021/acsomega.0c02588
10. Grillo IB, Urquiza-Carvalho GA, Bachega JFR, Rocha GB. Elucidating Enzymatic Catalysis Using Fast Quantum Chemical Descriptors. *J Chem Inf Model*. 2020;60(2):578-591. doi:10.1021/acs.jcim.9b00860
11. Grillo IB, Urquiza-Carvalho GA, Chaves EJF, Rocha GB. Semiempirical methods do Fukui functions: Unlocking a modeling framework for biosystems. *J Comput Chem*. January 2020:jcc.26148. doi:10.1002/jcc.26148
12. Grillo IB, Urquiza-Carvalho GA, Rocha GB. PRIMoRDiA: A Software to Explore Reactivity and Electronic Structure in Large Biomolecules. *J Chem Inf Model*. 2020;60(12):5885-5890. doi:10.1021/acs.jcim.0c00655

Refinamento *de novo* de ligantes de alvos biológicos usando o software DOCK6 e preparação de cálculos alquímicos de energia livre relativa

Objetiva-se apresentar de forma simples e introdutória como usar o software DOCK6, desenvolvido em colaboração com a SUNY Stony Brook e a UC San Francisco, para explorar o espaço químico de potenciais ligantes em receptores biológicos conhecidos. A partir dessa prática, também será discutida a preparação de cálculos de energia livres relativas para avaliar a estabilidade relativa dos ligantes propostos em relação ao original. Presume-se familiaridade com UNIX/LINUX e a posse de um computador pessoal. Conhecimentos básicos em Python são recomendados.

Ministrante: Guilherme D. R. Matos

Modelagem Tri dimensional da Estrutura de Proteínas pelo Modeller,

Dr. Kauê Santana (UFOPA)

https://orcid.org/0000-0002-2735-8016

Este minicurso tem como objetivo introduzir os participantes às técnicas de modelagem comparativa de proteínas, utilizando duas ferramentas amplamente reconhecidas: Modeller e o plugin EasyModeller no PyMOL. A modelagem comparativa é uma abordagem essencial em bioinformática que permite prever a estrutura tridimensional de proteínas com base em estruturas de proteínas previamente elucidadas .

Durante as aulas, os participantes aprenderão os fundamentos da modelagem de proteínas, incluindo:

1. Fundamentos da Modelagem Comparativa: Compreensão dos princípios básicos e a importância da homologia na predição estrutural.

2. Utilização do Modeller: Passo a passo na utilização do Modeller para construir modelos tridimensionais, incluindo a busca por estruturas de homólogos e a geração das coordenadas atômicas.

3. Integração com PyMOL: Trabalhando com o plugin EasyModeller, os participantes abordarão como integrar e visualizar modelos gerados de forma intuitiva, além de aprender a refinar e avaliar a qualidade dos modelos obtidos.

4. Estudo de Casos Práticos: Exercícios práticos focados em diferentes proteínas, para aplicar o conhecimento adquirido e aprofundar-se na análise de resultados.

Serão usados os seguintes programas: Modeller, PyMol, UCSF Chimera, Servidor Swiss-Model

Ao final do minicurso, os participantes estarão aptos a realizar modelagem comparativa de proteínas, utilizando Modeller e PyMOL como ferramentas principais, ampliando suas habilidades na área de bioinformática e contribuindo para pesquisas em biologia molecular.

Minicurso: A construção de funções de onda apropriadas para a descrição de sistemas polieletrônicos e a utilização dessas funções para o estudo de diferentes propriedades, atômicas e moleculares, e da ligação química

Dr. Marco Antonio Chaer do Nascimento

UFRJ

Neste minicurso vamos, inicialmente, estabelecer as condições necessárias para que uma função de onda possa descrever um sistema polieletrônico, átomo ou molécula, e como construir funções de onda que satisfazem essas condições. Em seguida, mostraremos que o uso de funções de onda que não levam em consideração todas as condições necessárias para a descrição de um sistema polieletrônico, pode levar a falsos conceitos, interpretações errôneas e aproximações não justificáveis. Em particular, mostraremos como a dupla ocupação de orbitais atômicos ou moleculares, a interpretação usual da integral de troca, de parte da energia de correlação, e a chamada “energia de correlação não dinâmica”, decorrem do uso de funções de onda inapropriadas para a descrição de sistemas polieletrônicos. Na segunda parte do minicurso, faremos uso de funções de onda com a forma apropriada para descrever diferentes propriedades, atômicas e moleculares, e para estudar a natureza da ligação química.

Minicurso: Simulação computacional da adsorção de moléculas em MOFs

Nailton Martins Rodrigues

UFMA

A classe de polímeros de coordenação conhecida como MOFs (*Metal Organic Frameworks*), são compostas por estruturas que se destacam devido a sua porosidade regular, alta estabilidade térmica, grande volume de poros e área superficial. Tais características viabilizam uma vasta gama de aplicações, que se estendem desde o uso como carreadores de fármacos [1, 2], na captura de pesticidas [3, 4] e de gases poluentes [5, 6] bem como no armazenamento de gás combustível [7], entre outros. As aplicações citadas exploram a adsorção de moléculas no poro e superfície de MOFs, adsorção essa que pode ser química ou física, sendo esta última a mais estudada, seja por viés experimental ou teórico.

Para gases, um dado muito relevante em estudos nesse tema é a isoterma de adsorção, que pode ser obtida utilizando métodos clássicos como o de Monte Carlo Grã Canônico (MCGC) e a isoterma gerada pelo método ser condizente com dados experimentais. O MCGC descreve bem interações fracas com as de van der Walls pela utilização de parâmetros de Lennard-Jones, e interações fortes de caráter eletrostático utilizando o potencial de Coulomb. Devido a sua simplicidade ao utilizar um modelo clássico para descrever as estruturas, o MCGC passa a ter baixo custo computacional, que o torna viável para estudar sistemas com centenas ou até milhares de átomos.

Neste viés, o minicurso irá abordar os conceitos e as equações necessária para a construção de um modelo clássico, que descreva bem uma MOF, um ou mais gases, e as possíveis interações entre esses. Com isso, o modelo será utilizado em simulações de MCGC para obter isotermas de adsorção em diferentes temperaturas, distribuição radial, mapa de distribuição, bem como outros dados capazes de caracterizar as interações não-ligantes.

[1] Z. Ma, B. Moulton, Coordination Chemistry Reviews, 255 (2011) 1623-1641.
[2] I.B. Vasconcelos, T.G.d. Silva, G.C.G. Militão, T.A. Soares, N.M. Rodrigues, M.O. Rodrigues, N.B.d. Costa, R.O. Freire, S.A. Junior, RSC Advances, 2 (2012) 9437.
[3] K. Vikrant, D.C.W. Tsang, N. Raza, B.S. Giri, D. Kukkar, K.H. Kim, ACS applied materials & interfaces, 10 (2018) 8797-8817.
[4] N.M. Rodrigues, M.F. de Souza, J.R. Dos Santos Politi, J.B.L. Martins, J Mol Model, 28 (2022) 316.
[5] Z. Li, G. Xiao, Q. Yang, Y. Xiao, C. Zhong, Chemical Engineering Science, 120 (2014) 59-66.
[6] N.M. Rodrigues, L.J. Dos Santos, E.S.M. Rodrigues, J.B.L. Martins, J Mol Model, 27 (2021) 240.
[7] L. Xia, Q. Liu, Computational Materials Science, 126 (2017) 176-181.

3 Resumos



Ethanethiol dimers: MP2 study

Airan F. S. Brito[1], Adelia J. A. Aquino[2], José Roberto dos Santos Politi[1], João B. L. Martins[1]
1 University of Brasilia, Institute of Chemistry, Computational Chemistry Laboratory, Brasilia, DF, Brazil, 70910-900
2 Department of Mechanical Engineering, Texas Tech University, Lubbock, TX 79409-1021 USA

Keywords: ethanethiol, ethanethiol dimers, thiols mp2 optimization,

Abstract
This study investigates the most stable configurations of ethanethiol dimers. Using the second order Moller-Plesset perturbation theory (MP2), we found a difference between the dimer conformations, where the most stable was found with the trans-gauche configuration.

Introdução

Nas últimas décadas, tem sido estudada a presença de diversas espécies química em ambientes espaciais[1–4]. A presença de tióis em gelos interestelares tem sido largamente explorada na literatura [1–4]. O estudo focou-se na análise das interações intermoleculares do etanotiol em suas conformações, considerando que o composto possui duas conformações anti e gauche, foram analisadas as interações entre as possibilidades consideradas anti-anti, anti-gauche e gauche-gauche.
Diferentemente das interações covalentes, nas interações intermoleculares as forças são fracas, requerendo métodos de química computacional de maior acurácia, os quais em geral demandam um maior tempo e esforço computacional. Tanto teórico quanto experimentalmente, a espectroscopia tem sido uma ferramenta útil para o estudo destas interações.
O meio interestelar apresenta baixa densidade. Praticamente consistindo de gás (acima de 99%) e poeira interestelar, dos quais 74% é hidrogênio e 24% hélio. A abundância de enxofre em meio interestelar é um objeto de recorrente estudo, sendo presente em cerca de 0,04% no meio interestelar[10].
Enxofre e compostos de enxofre apresentam importância tanto no meio interestelar como em questões ambientais e relativas a biogênica. Assim, o espectro vibracional e eletrônico destas espécies torna-se de grande relevância. Dentre as moléculas mais comuns encontradas no meio interestelar estão o H_2S, SO_2 e OCS. Mas também, gelos de tióis têm sido estudados experimentalmente e computacionalmente [11–14].
O objetivo deste trabalho é estudar as interações do etanotiol entre seus monômeros tanto anti quanto gauche, suas formas mais estáveis, geometrias e interações intermoleculares. O conhecimento das suas formas mais estáveis é importante para estudos em gelos espaciais, e na área da biogênica, podendo complementar trabalhos de astroquímica.

Materiais e Métodos

Tendo como objetivo verificar as interações entre dímeros, sobretudo a ligação de hidrogênio, foram efetuados cálculos computacionais para determinar as interações destes dímeros. Para tanto, foi utilizado o programa de estrutura eletrônica GAUSSIAN16.
Buscando balancear custo computacional e qualidade de representação, foram aplicados diferentes níveis de cálculos como: a teoria de perturbação de Møller-

Presset (MP2). Foram aplicadas uma série de funções de bases, as bases utilizadas foram aug-cc-pVTZ, aug-cc-pVQZ e def2-TZV. Para uma melhor precisão foi considerado criticamente o erro de superposição de bases BSSE, para observa-lo foram utilizados os cálculos de correção Counterpoise (CP) a partir dos dímeros otimizados pelos métodos mencionados. Para análise de propriedades relacionadas, as interações não covalentes (NCI), foi utilizado o programa MultiWFN para os cálculos aliado ao VMD para visualização das interações.

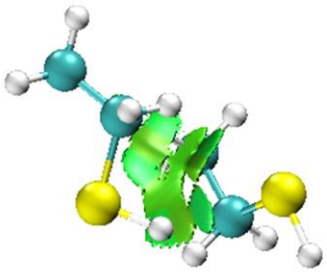
Resultados

Com a otimização dos dímeros, encontramos oito conformações estáveis possíveis, duas com moléculas anti-anti, três gauche-gauche e três anti-gauche.
Selecionamos o dímero mais estável de cada conformação para a análise:

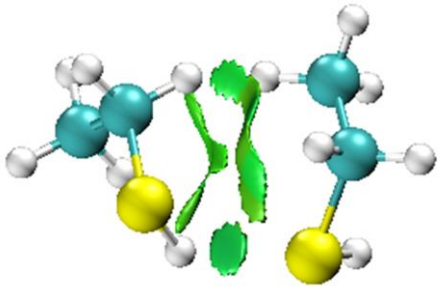
	Anti-Gauche	Gauche-Gauche	Anti-Anti
Distância S...S	3,83395	3,8540	3,8493
Energia de Interação Com CP (kcal/mol)	-4.16	-3,89	-3,92
Frequência SH	2757,09	2750	2736
Distancia S...H	1,77781	2,7060	3,0577
ΔH (kJ/mol)	16,51	16,42	14,91
ΔG(kJ/mol)	-19,65	-21,31	-20,12

Obtendo a visualização das interações não covalentes (NCI), da conformação mais estável, através do Multiwfn/VMD, é possível perceber que há uma área de interação considerável (em verde/van der Waals). Mostrando diversas interações fracas que corroboram a interação do dímero do etanotiol na mesma faixa de dímeros conhecidos como o da molécula de água ou o do homólogo, o dímero do etanol.

Anti-anti



Gauche-gauche



Anti-Gauche

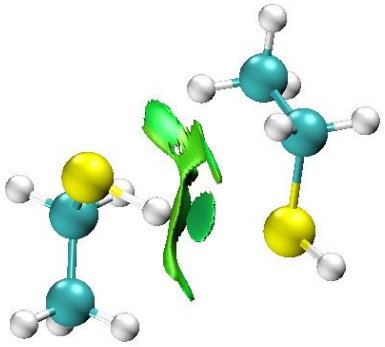


Figura 1 – NCI dos dímeros mais estáveis MP2/aug-cc-pVTZ.

Conclusões

A interação entre dímeros do etanotiol é mais estável entre uma molécula anti e outra gauche, quando o posicionamento destas moléculas favorece as interações S-H. Porém, a diferença entre as energias de interação não é tão considerável. O que mostra que mesmo que haja a predominância da interação anti-gauche, será possível encontrar aglomerados da molécula nas duas outras conformações.
Não obstante, a interação gauche-gauche mostrou-se a menos favorecida, indicando

que possivelmente aglomerados de etanotiol teriam em minoria esta interação.
Outrossim, é notável que a interação S...H é mais decisiva na estabilidade da interação que a repulsão S...S, já que em todos as interações mais estáveis, tanto anti-anti, anti-gauche e gauche-gauche, a estabilidade é mais favorecida quando as moléculas de enxofre estão próximas, do que quando estão separadas.

References

[1] V. Barone, M. Biczysko, C. Puzzarini, Acc. Chem. Res.2015, 48, 1413–1422.
[2] E. L. Graef, J. B. L. Martins, J. Mol. Model.2019, 25, 183.
[3] C. Barrales-Martínez, D. Cortés-Arriagada, S. Gutiérrez-Oliva, Molecular Hydrogen Formation in the Interstellar Medium: The Role of Polycyclic Aromatic Hydrocarbons Analysed by the Reaction Force and Activation Strain Model, 2018.
[4] F. Salama, G. A. Galazutdinov, J. Krellowski, L. Biennier, Y. Beletsky, I. O. Song, Astrophys. J.2011, 728, DOI 10.1088/0004-637X/728/2/154.
[5] A. H. T. Li, S. D. Chao, J. Mol. Struct.2009, 897, 90–94.
[6] P. Lipkowski, S. J. Grabowski, T. L. Robinson, J. Leszczynski, J. Phys. Chem. A2004, 108, 10865–10872.
[7] K. Hermansson, J. Phys. Chem. A2002, 106, 4695–4702.
[8] S. Tsuzuki, A. Fujii, Phys. Chem. Chem. Phys.2008, 10, 2584–2594.
[9] S. Pramanik, D. Chopra, J. Indian Inst. Sci.2020, 100, 43–59.
[10] D. V Mifsud, Z. Kaňuchová, P. Herczku, S. Ioppolo, Z. Juhász, S. T. S. Kovács, N. J. Mason, R. W. McCullough, B. Sulik, Space Sci. Rev.2021, 217, 14.
[11] R. L. Hudson, P. A. Gerakines, Astrophys. J.2018, 867, 138.
[12] D. Plant, D. S. Tarbell, C. Whiteman, J. Am. Chem. Soc.1955, 77, 1572–1575.
[13] R. G. Bhuin, B. Sivaraman, J.-I. Lo, B. N. R. Sekhar, B.-M. Cheng, T. Pradeep, N. J. Mason, J. Chem. Phys.2014, 141, 231101.
[14] A. Mielcarek, A. Dołęga, J. Mol. Struct.2016, 1103, 217–223

10º SIMPÓSIO DE ESTRUTURA ELETRÔNICA & DINÂMICA MOLECULAR
SEEDMOL 4 a 8 novembro | 2024 Pirenópolis, Goiás

Performance Evaluation of Density Functional Theory in Describing Molecular Interactions of Ozone-Depleting Substances and Environmentally Relevant Molecules

Alessandra F. Albernaz[1.]
[1]Instituto de Física, Universidade Brasília, Brasília, DF CEP 70919-970, Brazil.
albernaz@unb.br
Keywords: Density Functional Theory; Ozone-Depleting Substances; Atmospheric Chemistry; Molecular Interactions; Computational Modeling.

Abstract
This study assesses the effectiveness of Density Functional Theory (DFT) in modeling molecular interactions of ozone-depleting substances (ODS) and key atmospheric molecules like CO, CO_2, O_2, and CH_4. By comparing DFT results with experimental data and other theoretical methods, we identify the strengths and limitations of DFT in these contexts, aiming to improve the accuracy of environmental modeling.

Introduction

The depletion of the ozone layer remains a critical environmental concern due to its essential role in shielding terrestrial life from harmful ultraviolet (UV) radiation. Substances such as chlorofluorocarbons (CFCs) and halons have been identified as major contributors to ozone degradation through complex molecular interactions in the stratosphere.[1] Understanding the molecular interactions of these substances is critical for developing effective mitigation and replacement strategies. The stratospheric ozone layer functions as a vital protective barrier, absorbing and attenuating the majority of the Sun's harmful UV radiation.

In addition to ODS, molecules such as carbon monoxide (CO), carbon dioxide (CO_2), oxygen (O_2), and methane (CH_4) are integral to atmospheric processes, including oxidative reactions and greenhouse gas dynamics. Precise modeling of their interactions contributes to a comprehensive understanding of atmospheric chemistry and aids in addressing broader issues related to air quality and global climate change.

Methodology

This work focuses on conducting extensive Density Functional Theory (DFT) calculations using various exchange-correlation functionals to model the interactions between selected ozone-depleting substances (ODS) and environmentally relevant molecules. The goal is to rigorously compare the computational results against empirical, data and results obtained from other high-level ab initio methods, such as Coupled Cluster and Møller-Plesset perturbation theories.

A diverse set of widely used and emerging DFT functionals will be selected to cover a broad spectrum of approximation levels. Computational modeling will be performed, including geometry opti-mizations and energy calculations, followed by an analysis of interaction potentials and reaction pathways, that are essential for under-standing the behavior of the molecular systems at a detailed level. The computational results will be compared with experimental measurements, such as bond lengths, interaction energies, and spectroscopic data.

Additionally, the results will be evaluated against other theoretical methods to ensure the robustness of the DFT models. Through this process, the study aims to identify and quantify any discrepancies, thereby understanding the limitations of specific functionals and the conditions under which they perform optimally.

Results

Among the systems studied, we present selected results for the CO-CO system. To describe the interaction energy for the CO…CO complex we conveniently use the well-known body-fixed Jacobi coordinate system, illustrated in Figure 1.

The first parameter is *R*, the distance between the centers of mass of each monomer. To reduce the computational complexity we resort to the rigid rotor approach. The bond length of each monomer was optimized using the *Gaussian16* program[2] calculated at the aug-cc-pVQZ basis set and several DFTs and, with counterpoise correction (CP) to basis set superposition error (BSSE)[3].

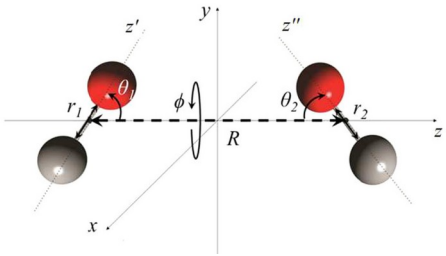


Figure 1: The coordinate reference system for CO-CO.

In Figure 2 we display all leading configurations (LC) used for the calculations. Figure 3 shows cuts along *R* through the PESs for Z_1 angular configuration, calculated with several functionals.

The literature ab initio results for the global minima of the PES, V_{Z1}=-120 cm^{-1} and the equilibrium distance is ca. 4.2 Å.[4] When evaluating DFT functionals against the ab initio literature, the energies and equilibrium distances of the global minima on the potential energy surface (PES) serve as critical benchmarks for accuracy.

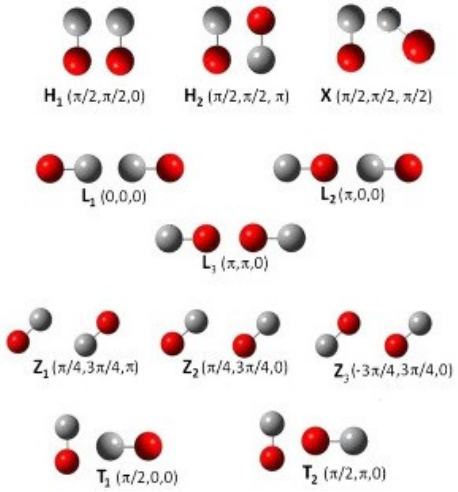


Figure 2: The eleven leading configurations of the CO-CO system.

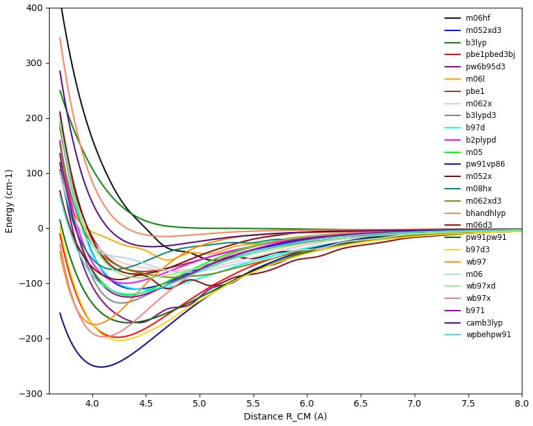


Figure 3: Intermolecular potential energies of each LC configuration of CO...CO system calculated with several functionals.

According to the reference, the ab initio results indicate a global minimum energy of approximately -120 cm^{-1} and an equilibrium distance of around 4.2 Å.

Among the tested functionals, WPBEhPW91, M05, and B971 stand out

for their close agreement with these reference values. The WPBEhPW91 functional, with an energy of -119.3 cm^{-1} and an equilibrium distance of 4.3 Å, shows excellent concordance with the ab initio results, particularly in energy, where it deviates by only 0.7 cm^{-1} from the reference value. The slight difference in the equilibrium distance (0.1 Å) also suggests a highly accurate modeling of the molecular interaction.

The M05 functional produced an energy of -121.46 cm^{-1} and an equilibrium distance of 4.3 Å. While the energy is slightly further from the reference value, with a difference of 1.46 cm^{-1}, the equilibrium distance is identical to that of WPBEhPW91, indicating that despite the slightly lower energy, M05 can model the geometry with high precision.

Finally, the B971 functional, with an energy of -124.78 cm^{-1} and an equilibrium distance of 4.3 Å, presents the largest discrepancy from the reference energy, with a difference of 4.78 cm^{-1}. However, the equilibrium distance remains consistent with the other functionals, suggesting that despite predicting a lower energy, B971 still accurately models the molecule's geometric configuration.

In summary, all three functionals proved effective in modeling the equilibrium distances, with WPBEhPW91 being the closest to the reference energy value. The minor differences observed can be attributed to the specific characteristics of each functional in describing molecular interactions, but overall, they all show good agreement with the available ab initio results from the literature.

Acknowledgements

This work was financially supported by the FAPDF – nº 31167.146.32883.19042022.

References

[1] United Nations Environment Programme, The Montreal Protocol on Substances that Deplete the Ozone Layer. http://www.unep.org/ozone/pdf/Montreal-Protocol2000.pdf, 2000.
[2] M. J. Frisch, *et. al*. Gaussian16, Revision C.01, 2016. http://www.gaussian.com/.
[3] S. F. Boys, F. Bernardi, Mol. Phys. 2002, 100, 65–73.
[4] P.R.P. Barreto et al., J. Mol. Spectroscopy 337 (2017) 163–177.

10º SIMPÓSIO DE ESTRUTURA ELETRÔNICA & DINÂMICA MOLECULAR
SEEDMOL 4 a 8 novembro | 2024 Pirenópolis, Goiás

Interpretação da Cinética *Super*-Arrhenius em Processos Biológicos: Incorporação da Relação de Stokes-Einstein-Kramers

Alex Bispo Gama [1], Valter Henrique Carvalho Silva [2.]
abg@aluno.ueg.br
Palavras-chave: *Super*-Arrhenius; transitividade; constante cinética.

Abstract

A química cinética é crucial em várias áreas científicas, mas entender como as constantes cinéticas variam com a temperatura em condições extremas é complicado devido a desvios do comportamento clássico previsto pela lei de Arrhenius. Esses comportamentos, conhecidos como não-Arrhenius, estão sendo cada vez mais estudados, especialmente por suas aplicações nas indústrias farmacêutica e alimentícia. Este trabalho explora o comportamento super-Arrhenius em processos biológicos, onde as constantes cinéticas variam de forma não linear com a temperatura, desafiando a lei de Arrhenius. O modelo de transitividade proposto integra as teorias de Kramers e Stokes-Einstein com o formalismo de Aquilanti-Mundim, permitindo descrever desvios do comportamento clássico de Arrhenius e interpretando a transitividade como o tempo de visitação dos estados energéticos. O modelo sugere que a descontinuidade observada nos diagramas de Arrhenius pode ser arbitrária, defendendo uma descrição contínua dos processos biológicos e eliminando a necessidade do conceito de temperatura de quebra (ABT). A abordagem fornece um ajuste preciso para dados empíricos e oferece uma interpretação físico-química significativa para parâmetros energéticos, contribuindo para a compreensão dos fenômenos não-Arrhenius em nível celular.

Introdução

Dentre os comportamentos não-lineares no diagrama de Arrhenius, $\ln k \; vs \; 1/T$, o *super-Arrhenius* (convexo) – onde os fenômenos de transporte aceleram os processos à medida que a temperatura aumenta – é encontrado em um conjunto amplo de fenômenos, especialmente em processos biológicos: catálise enzimática ou heterogênea, processos mediados por membrana e naqueles controlados por difusão ou por transporte em geral (SILVA et al., 2013; TRUHLAR; KOHEN, 2001).

Aqui incorporamos alguns modelos previstos na literatura que podem descrever esses desvios: i) Teoria de Kramers (POLLAK; TALKNER, 2005), baseada empiricamente em constantes cinéticas de reação escaladas com o inverso da viscosidade η do solvente, $k \propto \eta^{-1}$, sendo a viscosidade representada pela formulação de Stokes-Einstein, ii) o modelo de Aquilanti-Mundim (AQUILANTI et al., 2010), inspirado na termodinâmica não-extensiva de Tsallis, capaz de descrever esses desvios a partir do parâmetro d e definida como, $k(\beta) = A(1 - d\varepsilon^{\ddagger}\beta)^{1/d}$ e iii) mais recentemente, nosso grupo propôs o diagrama baseado na função Transitividade (MACHADO et al., 2019). A Transitividade é definida em termos do inverso da derivada logaritma da constante cinética k em função de β, interpretada como o tempo de visitação dos estados energéticos envolvidos no processo dinâmico. A proposição do formalismo de Aquilanti-Mundim e a relação de Stokes-Einstein-Kramers, nos permite comprovar as condições em que existe descontinuidade real nos sistemas estudados e serão utilizados como norteadores para a proposição de novos modelos cinéticos em processos biológicos bem como possibilitarão a interpretação dos fenômenos que estariam envolvidos no comportamento não-Arrhenius a nível celular.

Metodologia

Utilizando as ferramentas computacionais *Transitivity 1.0.3* (MACHADO et al., 2019) e

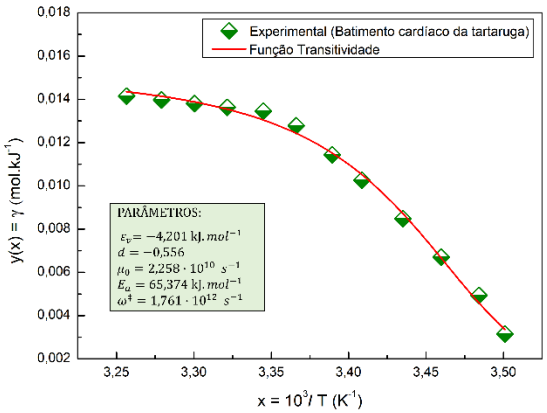
OriginPro, foram catalogados e ajustados, através do nosso modelo da transitividade, os dados experimentais de vários sistemas biológicos: batimento cardíaco, morte celular, movimento biológico, permeação de membrana, respiração, entre outros (SILVA et al., 2013; TRUHLAR; KOHEN, 2001). Suas transitividades experimentais foram calculadas através de derivadas numéricas, utilizando técnicas de processamento de dados, *smoothing*, quando necessário. Também foram feitas representações gráficas da transitividade (γ) em função de beta ($\beta = 1/T$) que exprimem a dependência da energia de ativação com a temperatura. A partir disso, será proposto aos modelos ajustados um significado físico-químico, analisando a possibilidade de parâmetros energéticos estarem conectados com parâmetros termodinâmicos, e se existe uma temperatura na qual o sistema cessa quando $d > 0$.

Resultados

O modelo fenomenológico para transitividade foi desenvolvido incorporando o formalismo de Aquilanti-Mundim e a relação de Stokes-Einstein-Kramers e é expresso como:

$$\gamma\,(\beta) = \frac{1}{E}\left(1 - \frac{\mu_0(1-d\varepsilon_v\beta)^{\frac{1}{d}-1}\,\varepsilon_v}{\sqrt{{\mu_0}^2(1-d\varepsilon_v\beta)^{\frac{2}{d}} + 4\omega^{\ddagger 2}}}\right)^{-1}$$

onde μ_0 é a fricção, definida por $\mu = 6\pi\eta R/M$, ε_v e E_a são parâmetros energéticos da barreira de ativação, onde ε_v pode estar conectado com parâmetros termodinâmicos, ω é a frequência imaginária do estado de transição e $d \equiv RT^{\dagger}/\varepsilon_v$ é o parâmetro de deformação, onde para os casos *super*-Arrhenius, ${\varepsilon_v}^{\dagger} = RT^{\dagger}$ marca a mínima energia para o sistema ser "ativo".
O modelo da Transitividade, quando tende a valores limites, converge para modelos convencionais: A lei de Arrhenius é recuperada nos limites em que (i) $\beta \to 0$ e (ii) $\beta \to 1/d\varepsilon_v$, em regimes de alta e baixa fricção. Nota-se que β não tende ao infinito, pois o sistema cessa antes à uma temperatura mínima, a temperatura de "morte" ($T^{\dagger}$). Ao invés disso, $\beta \to 1/d\varepsilon_v$.
As formulações baseadas no conceito de Transitividade foram aplicadas à descrição de diversos fenômenos sobre a dependência da temperatura de processos de constantes cinéticas além de Arrhenius e Eyring (SILVA, et al., 2019). Na Figura abaixo está representado o diagrama da Transitividade, $\gamma\ vs\ 1/T$, de um resultado inicial para o batimento cardíaco da tartaruga (MARTIN, 1904) onde nosso modelo da Transitividade pode ser adequado.



Fonte: Elaborada pelo autor (2022).

Diversos processos biológicos são convencionalmente descritos a partir de uma temperatura de ABT (temperatura de quebra), ou seja, o sistema alcança uma temperatura de transição onde o sistema muda de um regime para outro e a reação varia drasticamente, decaindo sempre linearmente. Entretanto, a aplicação do modelo da Transitividade nos dá um indicativo de que a descrição convencional é arbitrária podendo ser descrita por uma função contínua e sem descontinuidades.

Discussão

Observa-se que os dados experimentais exprimem um comportamento *super*-Arrhenius, onde a adequação do modelo da transitividade aos dados da dependência da temperatura do processo pode ser um indicativo de que o sistema pode ser descrito por uma função contínua e sem quebra. Dessa forma, o nosso modelo generaliza o problema de ABT, dando um indicativo da inexistência de uma descontinuidade para o processo estudado.
Para correlacionar parâmetros de fricção e frequência imaginária do sistema estudado com estados de transição específicos ou bandas do infravermelho, as unidades foram convertidas

para cm^{-1}, respectivamente, $\mu_0 = 7{,}5315 \cdot 10^{-1}\ cm^{-1}$ e $\omega^{\ddagger} = 58{,}7\ cm^{-1}$. A ocorrência de

frequências mais baixas em sistemas no estado de transição geralmente indica uma reorganização interna do sistema, como movimentos de rotação ou translação de moléculas, sem transferência de partículas. Nos processos biológicos, como o batimento cardíaco, isso sugere um efeito coletivo onde a reorganização interna do sistema resulta nessas frequências mais baixas.

Conclusões

Para lidar com a cinética de processos onde a lei de Arrhenius não é obedecida em baixas temperaturas, o modelo da transitividade para a formulação proposta neste trabalho nos guia para uma abordagem consistente e relevante na produção de percepção física e na sua adequação aos sistemas estudados. O modelo fornece um bom ajuste dos dados empíricos para uma ampla variedade de taxas biológicas, dando uma interpretação satisfatória para os fenômenos envolvidos no comportamento não-Arrhenius a nível celular e admitindo em quais condições a descontinuidade no diagrama de Arrhenius é real nos sistemas biológicos estudados, excluindo, portanto, a necessidade de se introduzir o conceito de ABT. A função transitividade não somente revela-se como uma excelente ferramenta capaz de computar parâmetros energéticos relacionados aos sistemas biológicos, como também pode fornecer uma interpretação física para esses parâmetros.

Agradecimentos

Agradeço à Universidade Estadual de Goiás e ao meu orientador Valter Henrique Carvalho Silva por todo suporte dado na elaboração deste trabalho.

Referências

1. AQUILANTI, V.; MUNDIM, K. C. et al.; Chem. Phys. Lett. 2010, 498, 209.
2. MACHADO, H. G.; NETO, F. O. S. et al.; Molecules, 2019, 24, 20.
3. MARTIN, E. G.; AJP Content, 1904, 11, 370-393.
4. POLLAK, E.; TALKNER, P.; Chaos, 2005, 15, 1–11.

5. SILVA, V. H. C. et al.; Chemical Physics Letters, 2013, 590, 201–207.
6. SILVA, V. H. C.; COUTINHO, N. D. et al.; Front. Chem. 2019, 7, 1.
7. TRUHLAR, D. G.; KOHEN, A.; Proc. Natl. Acad. Sci. 2001, 98, 848.

Desenvolvimento de uma Metodologia de Otimização de Funcionais RSH Fisicamente Inspirada no Princípio da Mínima Polarizabilidade

Ana Carolina Felisberto Araujo[1], Pedro Henrique Ferreira Matias[1], Mateus R. Barbosa[1], Heibbe Cristhian Benedito de Oliveira[1], Daniel Francisco Scalabrini Machado[2].
[1]Universidade Federal de Goiás (UFG), Instituto de Química (IQ), Laboratório de Estrutura Eletrônica e Dinâmica Molecular (LEEDMOL), Goiânia, Brasil.
[2]Universidade de Brasília (UnB), Instituto de Química, Brasília, Brasil.
carol.felisberto@discente.ufg.br.
Palavras-chave: RSH, Polarizabilidade, Polímeros Orgânicos.

Abstract

A new protocol for optimizing the range-separation parameter (ω) of RSH functionals founded on the minimum polarizability principle (MPP), which ensures that the natural evolution of a given system moves toward minimum polarizability. This new protocol presents a lower computational cost, improving the prediction of optoelectronic properties directly dependent on linear polarizability (α), such as Refractive Index (n) and ABBE Number (ν). The protocol proposed showed promising initial results for functional optimization scheme in polymeric systems.

Introdução

Polímeros orgânicos exercem um papel essencial na ciência de materiais, tendo potencial para compor dispositivos ópticos como sensores e fotocatalisadores.[1,2,3] A polarizabilidade (α) é a resposta linear da disposição eletrônica de uma molécula sob exposição a um campo elétrico externo.[4] O princípio da mínima polarizabilidade indica que todo sistema tende à menor polarizabilidade e, por isso, materiais ópticos podem ter suas propriedades optoeletrônicas aprimoradas seguindo este princípio.[5]

Existe uma grande demanda em protocolos para correção de descrições de propriedades de caráter local obtidas pela Teoria do Funcional de Densidade (DFT), destacando-se a otimização do parâmetro ômega (ω).[6] Os protocolos convencionais como, por exemplo, a varredura do parâmetro ω dentro do esquema Jgap[2,6], requer dados a respeito da estrutura eletrônica dos sistemas neutros, catiônicos e aniônicos, totalizando um número grande de cálculos. Uma alternativa para minimizar o valor de ω em funcionais RSH pode ser fisicamente inspirada no princípio da mínima polarizabilidade, à medida que, esta requer apenas informações sobre a polarizabilidade linear (α) do estado fundamental e, por conseguinte, é capaz de reduzir o número de cálculos necessários em três vezes quando comparada aos demais métodos.[6,7]

Logo, espera-se que a otimização do parâmetro ω a partir da minimização de α acarrete em uma melhora sensível de suas propriedades.[5,7,8]

Metodologia

A otimização do parâmetro ω fisicamente inspirada no princípio da mínima polarizabilidade foi realizada para o funcional LC-BLYP[8] em polímeros orgânicos, variando em ordem crescente o número de unidades monoméricas da cadeia. Após a otimização, os valores de α encontrados foram comparados com valores de referência teóricos[9,10,11].

Todos os cálculos foram realizados pelo programa de química computacional Gaussian 16[12] e todas as implementações foram escritas em linguagem de programação *python3.x*. O protocolo de otimização proposto faz uso do algoritmo de busca *Golden Proportion* reduzindo ainda mais o número de cálculos

necessários. A Figura I traz um esquema do protocolo proposto.

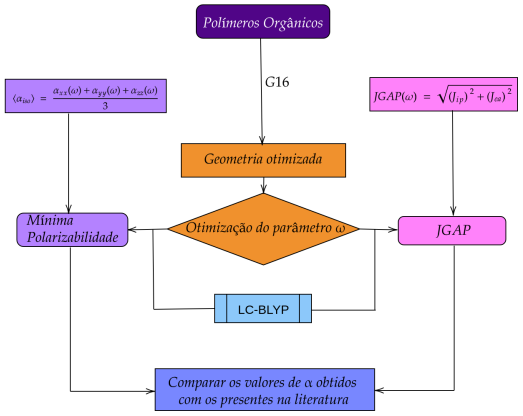


Figura I. Fluxograma sequência dos cálculos.

Resultados e Discussão

A otimização do parâmetro ω resultou nos seguintes valores de polarizabilidade (α):

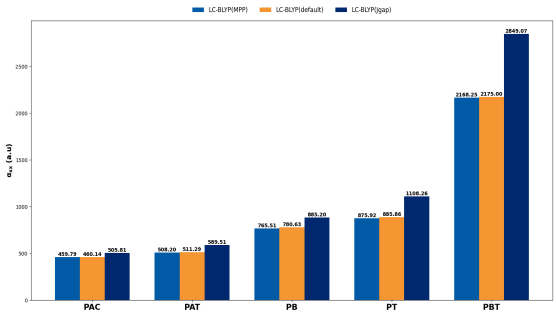
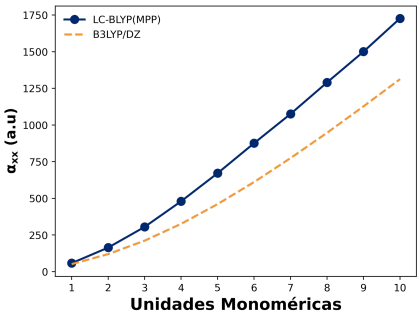


Figura II. Polarizabilidade longitudinal (a.u.) obtida para polímeros de 6 unidades monoméricas. Onde cis-poliacetileno (PAC), trans-poliacetileno (PAT), Poli(1,4-fenileno) (PB), Politiofeno (PT), e Polibutatrieno (PBT) foram otimizados utilizando o funcional LC-BLYP (MPP) (azul), LC-BLYP (*default*) (amarelo) e LC-BLYP (*Jgap*) (azul escuro), respectivamente.

Conforme observado na Figura II, a implementação do algoritmo de busca para otimização do funcional LC-BLYP baseando-se na mínima polarizabilidade forneceu resultados satisfatórios em relação ao cálculo *default* e a otimização via Jgap. Os valores de ω encontrados para o método proposto são iguais a 0.50 (PAC), 0.57 (PAT), 0.86 (PB), 0.62 (PT) e 0.52 (PBT).
Os valores de Polarizabilidade Linear calculados se aproximam dos valores teóricos existentes na literatura. Isso pode ser observado na Figura III.

A)



B)

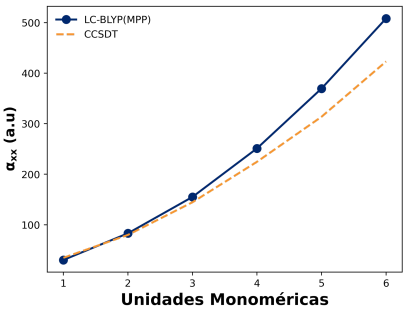


Figura III: Polarizabilidade longitudinal em relação ao tamanho da cadeia do polímero A) PT e B) PAT. Estão representados os valores de α calculados através da otimização do funcional LC-BLYP (azul) e os valores teóricos encontrados na literatura (amarelo).

Como mostrado na Figura III, há uma concordância na tendência de aumento da polarizabilidade com o tamanho da cadeia, em relação à referência.

Conclusão

A proposta metodológica forneceu resultados satisfatórios, com valores mínimos para ômega e polarizabilidade linear. Foram obtidos valores de "α" menores em nossa metodologia, quando comparados à varredura do parâmetro ômega via esquema Jgap, uma vez que este resultou em valores mais elevados até mesmo em referência à "α" obtida por meio do funcional convencional. Além disso, foi possível constatar a influência do tamanho da cadeia no valor da polarizabilidade, que

resulta em uma crescente. Os valores encontrados estão em concordância com o valor teórico e experimental esperado.

Agradecimentos
CNPq, CAPES, FAPEG, LAMCAD, PPGQ-UFG, IQ-UFG, LMSC-IQ-UNB, LEEDMOL-IQ-UFG.

Referências

1. Badi N., Lutz J. Chemical Society Reviews, (2009), 3383-3390, 38 (12).
2. Brédas J.,Beljonne D., Coropceanu V., et al. Chemical Reviews, (2004), 4971-5003, 104(11).
3. Wang, T.-X., Liang, H.-P., Anito, D. A., Ding, X., & Han, B.-H. (2020). Journal of Materials Chemistry A.
4. Park, S. S., Lee, S., Bae, J. Y., & Hagelberg, F. (2011). Chemical Physics Letters, 511(4-6), 466–470.
5. Machado, D.F.S. 2017. Tese (Doutorado) - Universidade de Brasília, Brasília, 2017.
6. Neto, A. P.; Machado, D. F. S.; Lopes, T. O.; Camargo, A. J.; de Oliveira, H. C. The Journal of Physical Chemistry B 2018, 122, 8439–8450.
7. Maekawa, S.; Moorthi, K. The Journal of Physical Chemistry B 2016, 120, 2507–2516.
8. Chai, J.-D., & Head-Gordon, M. (2008). The Journal of Chemical Physics, 128(8), 084106.
9. Afzal M., Hachmann J.. Physical Chemistry Chemical Physics, (2019), 4452-4460, 21(8).
10. Limacher, Peter A., Kurt V. Mikkelsen, and Hans Peter Lüthi. The Journal of chemical physics 130.19 (2009).
11. Oviedo, M. Belén, Niranjan V. Ilawe, and Bryan M. Wong. Journal of chemical theory and computation 12.8 (2016): 3593-3602.
12. Frisch, M. J. et al. Gaussian 16 Revision C.01. 2016; Gaussian Inc. Wallingford CT.

Modeling the atomic-scale structure and morphological transformation of $BiVO_4$ with Low and High-Index facet

Ana Cristina Mora Tello[1*] and Katherine Paredes-Gil[2]
[1]Instituto de Química de São Carlos, Universidade de São Paulo, P.O. Box 780, São Carlos, São Paulo 13566-590, Brazil.
[2]Departamento de Química, Facultad de Ciencias Naturales, Matemática y del Medio Ambiente, Universidad Tecnológica Metropolitana, 8940577, Santiago, Chile.
*anacmora@gmail.com

Keywords: $BiVO_4$; Energy surfaces; Wulff construction, crystal facets.

Abstract

$BiVO_4$ is a promising material for photocatalytic applications, and understanding its surface characteristics is crucial for optimizing its performance. This study explores the structure and electronic properties of the surfaces of $BiVO_4$. We employ density functional theory (DFT) to calculate the surface energies of various low-index planes of $BiVO_4$, providing detailed insights into the anisotropy of surface and was found that can exist four, five, six, and sevenfold-coordinated Bi atoms while the V atoms are two and three-fold-coordinated. Using calculated surface energy data, we construct morphologies through the Wulff construction method, which predicts the equilibrium shape of $BiVO_4$ crystals. Our findings reveal the predominant facets in the $BiVO_4$ ideal morphology of are (010), (110), (011), and (101) surfaces. By comparing theoretical predictions with experimental data from the literature, we validate the accuracy of the Wulff construction for $BiVO_4$ and enhance our understanding of its crystal growth behavior.

Introduction

$BiVO_4$ has emerged as a promising photocatalytic material due to its non-toxic, low-cost, photo-stable, favorable band-edge positions and eco-friendly features.[1-3] The catalytic performance in terms of activity, selectivity, and stability properties strongly depend on the crystal form and the surface atomic arrangement. Low-index facets generally have a more ordered and regular atomic arrangement, which can lead to different reactivity compared to high-index facets, which have a more disordered or less densely packed surface structure and often have higher surface energy, making them more reactive and influencing how well the material interacts with reactants or how it participates in catalytic processes.[4] Therefore, study of surface-structure has attracted increasing interest, ranging from well-defined single-crystal planes to nanoscale facets on nanomaterials for both metals and metal oxides. In this work, we are interested in providing a deeper insight into the high-index facets of $BiVO_4$ and rationalizing the geometry and structure local to the high-index of $BiVO_4$ surfaces

Methodology

To delve into the relationship between the structure and morphology of the $BiVO_4$, density functional theory calculations as implemented in Crystal17 code have been applied to the bulk and surfaces of the $BiVO_4$ (*I2/a*). Bi atom was described by using the effective core potential (ECP) Bi_60MFD_s4411p411d411_Heifets_2013. [3] In contrast, the V and O atoms are defined for the Gaussian-type-functions basis sets

pob_TZVP_2012. To account for the exchange and correlation effect, the B3LYP functional with 5% of Hartree-Fock exchange was employed in all *ab-initio* calculations. Series of Coulomb and exchange integrals were truncated to 10 8, 10^{-8}, 10^{-8}, 10^{-8}, and 10^{-16}. The shrinking factor (Pack-Monkhorstad Gilatnet) was set to 8. The 010), (011), (110), (101), (121), (123), (132) and (321) surfaces of $BiVO_4$, were represented by using a slab model repeated periodically. The slabs were constructed by using the lattice parameter optimized for the bulk. For the slab calculations, the convergence energy tests regarding stickness were done. The terminations with the lowest surface energy are considered thermodynamically more stable. The values of the surface energies (E_{surf}) are calculated by using Eq. (1):

$$E_{surf} = \frac{E_{slab} - nE_{bulk}}{2A} \qquad (Eq.1)$$

where E_{slab} is the total slab energy, n is the number of bulk units in the slab, E_{bulk} is the bulk energy, and A is the area of the slab. From the E_{surf} calculated values, the equilibrium morphology of the crystal is determined by using the Wulff constructions, which minimize the total surface free energy at the fixed volume.

Results

Analysis of the environmental chemistry of the models used to describe the surfaces was realized to explore the chemical and physical properties of $BiVO_4$ once these are responsible for the properties of the materials.

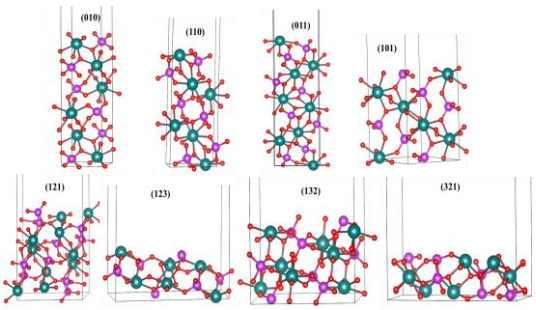


Figure 1. Surfaces models of (010), (110), (011), (101), (121), (123), (132) and (321) for $BiVO_4$. Green. pink and red balls represent Bi, V and O atoms, respectively.

Figure 1, reveals that can exist four, five, six, and sevenfold-coordinated Bi atoms while the V atoms are two and three-fold-coordinated.

Table 1 lists the calculated Area (Å), Bi and V coordination number, surface energy (E_{surf}), and bandgap (E_{gap}^{surf}) for the surfaces of $mBiVO_4$. The results were obtained after the optimization process and thickness convergence for slab models consisting of 20, 30, 40, 48, 24, 40, and 48 layers were used to describe the (010), (011), (110), (101), (121), (123), (132) and (321) surfaces, respectively.

Table 1. Area (Å), Bi and V coordination number in the top surface, surface energy (E_{surf}), and bandgap E_{gap}^{surf} for the surfaces of $mBiVO_4$ (*I2/a*).

Surface	Area	Sites	E_{surf}	E_{gap}^{surf}
(010)	26.6	Bi_{6c}	0.46	2.60
(110)	33.2	Bi_{6c}	0.56	2.87
(011)	33.2	Bi_{5c}	0.62	2.67
(101)	42.6	Bi_{6c}	0.78	2.37
(121)	50.8	Bi_{6c}; Vi_{3c}	1.05	2.43
(123)	100.5	Bi_{5c}; Bi_{6c}; Bi_{7c}; Vi_{2c}	1.35	2.20
(132)	79.2	Bi_{5c}; Bi_{6c}; Vi_{2c}	0.98	2.15
(321)	100.5	(2)Bi_{5c}; Vi_{3c}	1.15	2.25

According to the E_{surf} found in Table 1, the calculated stability order of the surfaces was (010) > (110) > (011) > (101) > (132) > (121) > (321) > (123). It should be noted that the similar E_{surf} values between (110) and (011), surfaces, are a result of the atomic distribution on the surface.

In the case of surfaces (010), (011) and (110) it was observed that show bandgap values (Table 1) close to the bulk (2.61 eV). The decrease in the bandgap value of the (121), (321) and (123) surfaces can be attributed to the undercoordination $[VO_3 \cdot V_O^x]$ clusters present on the surfaces, which induce

the formation of intra-band gap states of the bulk due to the localization of the excess electron in V 3d valence orbitals.

Theoretical morphology in equilibrium condition was estimated by means of simple Wulff methodology using the calculated surfaces energies. The obtained Wulff crystal of the ideal structure presented an orthorhombic morphology described for (010), (110), (011), and (101) surfaces, in accordance with reported studies found in the literature that show this morphology is one of the most common for this system.[5] By assuming the ideal morphology as a starting point (see Figure 2), it was possible to create the experimental morphology, by varying the surface energies. The experimental morphology take into account the (010), (101), (121), (123), and (321) surfaces.

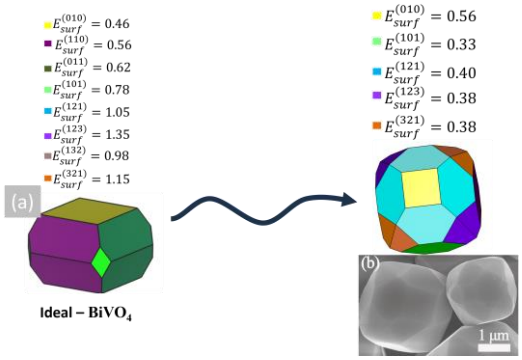


Figure 2. Calculation of available experimental morphologies of $BiVO_4$ with high index surface by using the Wulff construction. The values of surface energy are in J/m2. The experimental morphology can be seen in the inset, where FE-SEM image was inserted for comparison purposes.[4]

Conclusions

In this study, a comprehensive analysis was conducted to investigatethe structure of the surfaces of $BiVO_4$. Furthermore, the surface energy of brookite $BiVO_4$was evaluated using Wulff construction method. The morphology of brookite $BiVO_4$ in vacuum Wulff structure simulation shows that the main exposed surfaces of $BiVO_4$ in vacuum are (010), (011), (110) and (101) and both These studies are helpful to understand how to achieve morphology control by adjusting the surface energy values of different $BiVO_4$ crystal surfaces including low and high-index facets.

Acknowledgements

Financial support from the Brazilian funding agency CNPq and the São Carlos Chemistry Institute are gratefully acknowledged.

References

1. Rodrigues, M. H. M.; and *et al*. Mater. Chem. Phys. 2023, 296, 127198. Li, P.; Cheng, X.; He, H.; Zhou, Y.; Zou, Z. Adv. Mater. 2017, 30, 1, 1703119.
2. Gaikwad, M. A.; Suryawanshi, U. P.; Ghorpade, U. V.; Jang, J. S.; Suryawanshi, M. P.; Kim, J. H. Small. 2022, 18, 2105084.
3. Rather, R. A.; Mehta, A.; Lu, Y.; Valant, M.; Fang, M.; Liu, W. nt. J. Hydrogen Energy. 2021, 2355510182.
4. Li, P.; Cheng, X.; He, H.; Zhou, Y.; Zou, Z. Adv. Mater. 2017, 30, 1, 1703119.
5. Yang, J.; Wang, D.; Zhou, X.; Li, C. Chemistry. 2013, 19, 4, 1320.

Impacto da Solvatação Aquosa nos Parâmetros Geométricos e Eletrônicos da Caramboxina por Dinâmica Molecular Car-Parrinello

Oliveira, Ana Paula de Oliveira[1], Luciano Ribeiro[1]
[1] Grupo de Química Teórica e Estrutural de Anápolis, Câmpus Central, Universidade Estadual de Goiás (UEG), Anápolis – GO – Brasil
apooliver750@hotmail.com

Keywords: Star fruit, Natural Products, Molecular modeling

Abstract

The carambola (*Averrhoa carambola L.*), an exotic fruit introduced to Brazil in the 18th century, belongs to the Oxalidaceae family and originates from tropical regions in Asia. Caramboxin (CBX), a neurotoxin found in carambola, has a chemical structure analogous to an amino acid. In patients with chronic kidney disease, CBX is not properly excreted, leading to symptoms ranging from uncontrollable hiccups and dizziness to potentially fatal conditions. This study aims to analyze the electronic and geometric properties of the CBX molecule using Car-Parrinello molecular dynamics in a water-solvated system. Additionally, we performed radial distribution function analyses for the interactions between O2-H and O4-H, providing insights into the hydrogen bonding behavior of the solvated CBX molecule.

Introdução

A caramboxina (Figura 1), 2-(2-amino-2-carboxietil)-6-hidroxi-4-metoxi-ácido benzóico, é uma substância recém caracterizada, é um análogo do aminoácido não protéico semelhante à fenilalanina, apresenta formula molecular $C_{11}H_{13}NO_6$, encontrada na carambola, e seu metabolismo ocorre com a subsequente excreção pelos rins[1,3].

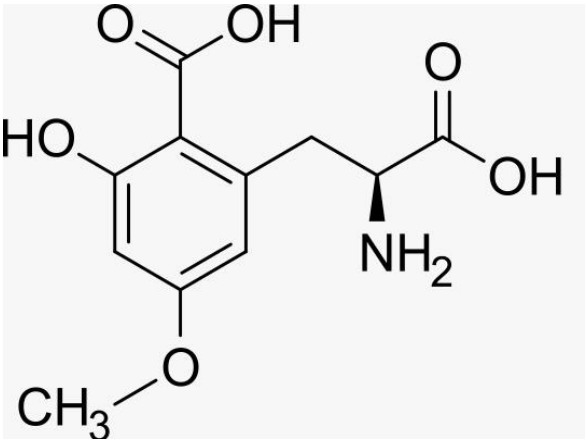


Figura 01. Fórmula estrutural 2D da Caramboxina

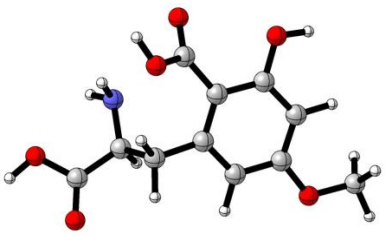


Figura 02: Fórmula estrutural otimizada por DFT b3lyp/6.31g da caramboxina.

O objetivo principal do presente trabalho é estudar os efeitos geométricos e eletrônicos na molécula de Caramboxina solvatada em água, sendo realizado por meio de dinâmica molecular de Car-Parrinello.

Metodologia

Para analisar as propriedades geométricas e eletrônicas do sistema, foram gerados "ensembles" da caramboxina solvatada em 105 moléculas de água, em uma caixa ortorrômbica com dimensões de 13,4 x 16,4 x 20,4 Å, escolhida após algumas simulações que verificaram o melhor encaixe às dimensões da molécula. Os protocolos para a minimização das funções de onda e a evolução da dinâmica seguiram os procedimentos adotados na literatura especializada. A análise dos dados para determinação dos comprimentos de ligação, ângulos, função de distribuição radial de pares, tempo médio de residência, entre outros, será feita utilizando o *software* GQTEA, tal programa gqtea é uma rotina computacional desenvolvida pelo grupo de Química Teórica e Estrutural de Anápolis – QTEA. Tal programa é capaz de converter a trajetória gerada no Quantum Espresso em coordenadas cartesianas para visualização no VMD, calcular comprimento de ligação, ângulo interatômico, ângulo diedral, distribuição radial de pares, coeficiente de difusão, tempo médio de residência, análise de ligações de hidrogênio e algumas propriedades eletrônicas.

Resultados

Foram realizados cálculos de energia acompanhando a adiabaticidade, fator extremamente importante para garantir a coerência dos resultados.

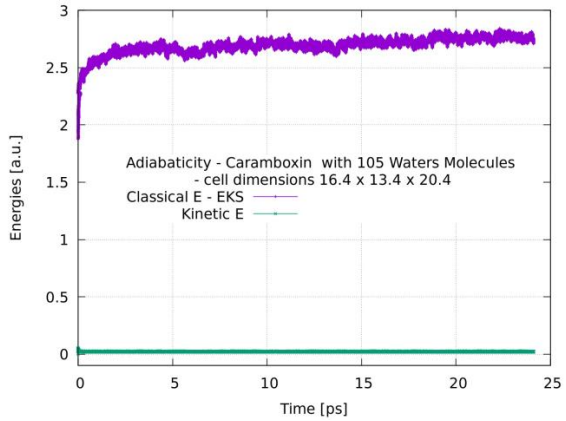


Figura 03. Energias cinéticas e eletrônicas em função do tempo de simulação

Como podemos observar na Figura 03, o controle de adiabaticidade para a molécula solvatada com 105 moléculas de água está em 23 ps, e a intenção é controlá-lo até 40 ps. Até o presente momento, a adiabaticidade do sistema está mantida, conforme apresentado na Figura 3.

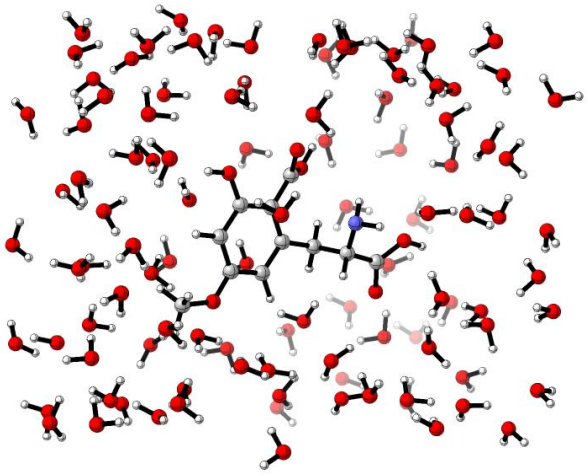


Figura 04. Caixa contendo a caramboxina solvatada em 105 moléculas de água após o processo de otimização.

Na Figura 04, podemos observar as interações por ligações de hidrogênio entre a molécula de água e a molécula de caramboxina, principalmente na região do grupamento amino, carboxila e hidroxilas

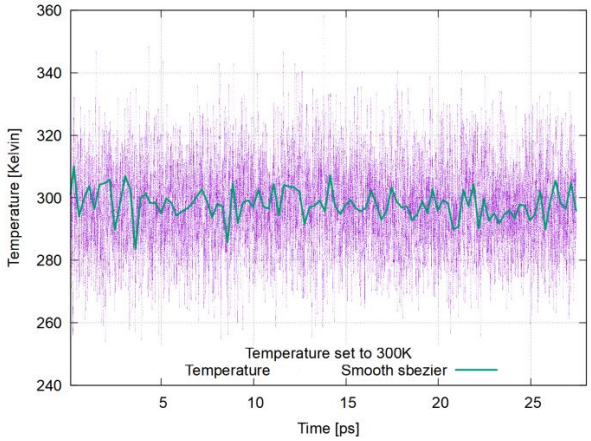


Figura 05. Monitoramento do controle de temperatura durante a simulação com o uso de termostato Nose-Hoover.

Na Figura 05, demonstramos o controle de temperatura durante a simulação de Car-Parrinello. Termostatos Nose-Hoover foram utilizados na dinâmica. Os sítios de maior polaridade da molécula de caramboxina interagem com as moléculas de água na caixa contendo 105 moléculas.

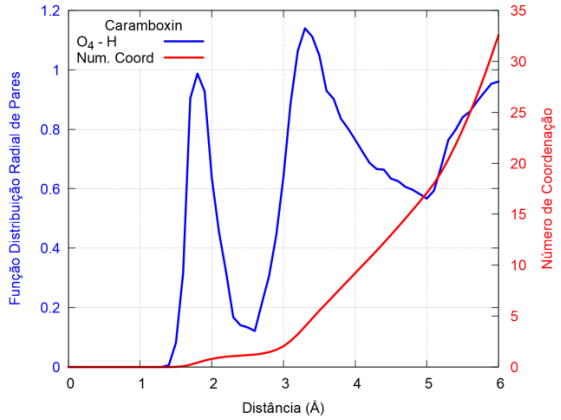


Figura 06. Função de distribuição radial e número de coordenação para o oxigênio da carbonila (O_4) da caramboxina interagindo com os hidrogênios das moléculas de água.

Na Figura 06, um pico em 1,8 Å indica a formação de fortes ligações de hidrogênio entre o oxigênio da carbonila e os hidrogênios da água. O número de coordenação aumenta rapidamente após esse pico, atingindo 30 a 35 entre 4 e 5 Å, sugerindo que a caramboxina está densamente solvatada por moléculas de água.

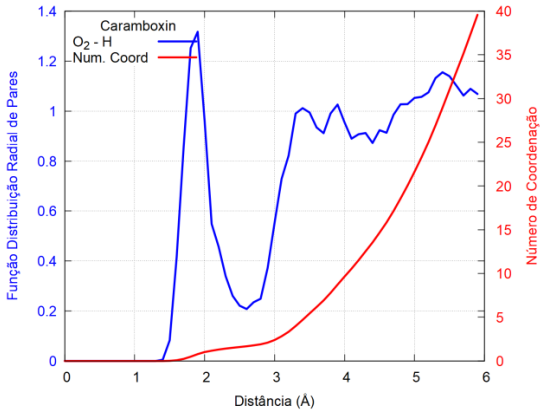


Figura 07. Função de distribuição radial e número de coordenação para o oxigênio duplamente ligado ao carbono quiral (O_2) da caramboxina.

Na Figura 07, o primeiro pico em torno de 1,8 Å indica a formação de ligações de hidrogênio entre o oxigênio duplamente ligado e os hidrogênios da água, embora menos intensas do que no caso do oxigênio da carbonila. O número de coordenação também cresce, atingindo 30 a 35 em 5 Å, sugerindo uma boa solvatação do O_2, mas com interações potencialmente menos dominantes.

Conclusão

As análises realizadas até o momento demonstram que a caramboxina está densamente solvatada por moléculas de água, com fortes interações de ligação de hidrogênio especialmente em torno do oxigênio da carbonila (O_4), evidenciado por picos significativos na função de distribuição radial em aproximadamente 1,8 Å. O oxigênio duplamente ligado ao carbono quiral (O_2) também mostra boa solvatação, embora com interações de hidrogênio menos intensas comparadas a O_4. A dinâmica de solvatação continua sendo realizada para tempos de simulação superiores a 50 ps, com o objetivo de obter uma compreensão mais profunda e detalhada.

Agradecimentos

References

1. **Garcia-Cairasco, N.; Moyses-Neto, M.; Del Vecchio, F.; Oliveira, J. A. C.; Dos Santos, F. L.; Castro, O. W.; Arisi, G. M.; Dantas, M.; Carolino, R. O. G.; Coutinho-Netto, J.;** *Elucidating the Neurotoxicity of the Star Fruit.* Angew. Chem., 2013, 125, 49, 13305-13308. Wiley. DOI:

2. **Ghani, A.;** *Medicinal Plants of Bangladesh with Chemical Constituents and Uses.* 2nd ed., Dhaka, Asiatic Society of Bangladesh, 2003, 10. ISBN: 9789845123488.

3. Neto, M. M. et al.; *Intoxication by Star Fruit (Averrhoa carambola) in 32 Uraemic Patients: Treatment and Outcome.* Nephrol. Dial. Transplant., 2003, 18, 1, 120-125.

4. Pichieri, F.; *Molecular Structure and Conformations of Caramboxin, a Natural Neurotoxin from the Star Fruit: A Computational Study.*

DFT study of a heterodimer of the tuberculostatic drug isoniazid with malic acid, coformer occurring in a solid dispersion of the drug

Silva, A. P.[1], Moura, A. C.[1], Lima A. D. S. G.[1], Ribeiro, P. R. S.[1], Lage, M. R.[1]
[1]Programa de Pós-Graduação em Ciência dos Materiais (PPGCM), Centro de Ciências de Imperatriz (CCIM), Universidade Federal do Maranhão (UFMA), Imperatriz, Maranhão, 65.900-410, Brazil.
anderson.ps@discente.ufma.br
Keywords: Isoniazid; Malic Acid; Intermolecular Interaction; DFT; Solid Dispersion.

Abstract
A theoretical study on the tuberculostatic drug isoniazid (ISO) and malic acid (AML), as well as the heterodimer (ISO-AML) was performed with a basis on density functional theory (DFT). The functional ωB97X-D was used to perform the DFT calculations, in association with the basis set 6-311++G(d,p). The integral equation formalism of the polarizable continuum model (IEFPCM) was used to study the solvation effects in methanol. Structural, electronic, spectroscopic and thermodynamic properties of ISO, AML, and the heterodimer ISO-AML were investigated, contributing to the study of these systems, and for their characterization.

Introduction
The low water solubility of crystalline drugs leads to low bioavailability and reduced pharmaceutical efficacy. The preparation of solid dispersions of the drugs is an alternative for improving their aqueous solubility, bioavailability, and therapeutic efficacy[1,2]. This type of intermolecular interaction between drug and coformer to obtain solid dispersions occurs mainly through hydrogen bonds, which are fundamental for obtaining coamorphous[3]. Computational investigations are essential to study the intermolecular interactions and to better understand the properties of solid dispersions[4].

Methodology:
The Gaussian 16 software was used for all the calculations in this work. We employed the DFT functional ωB97X-D in association with the basis set 6-311++G(d,p), considering the solvation effects in methanol with the integral equation formalism of the polarizable continuum model (IEFPCM), widely used in various DFT works[5,6]. The graphical interface software ChemCraft was used to manipulate the structures obtained from the CCDC (The Cambridge Crystallographic Data Center) database, explore the output files, and create the images from the results of the calculations. The software MultiWFN was used to get the electrostatic potential maps (EPMs). A scale factor of 0.957[7] was considered to correct calculated spectroscopic data, to a better fit of experimental and theoretical spectra. Different starting geometries were considered, based on optimized geometries of ISO and AML, to find the most stable interaction occurring in the heterodimer ISO-AML. Calculated variations of Gibbs free energy (ΔG^{298}), enthalpy (ΔH), and total electronic energy corrected with zeropoint vibrational energy (ΔE_{ZPVE}) indicated the most stable interaction found, considering also the basis set superposition error (BSSE).

Results
The electrostatic potential maps of the molecules in a vacuum and in methanol are presented in Figure 1. The regions in red color are electron-rich, while the regions in blue are electron-poor. These insights are important in the study of intermolecular interactions. The

thermodynamic data calculated in the study of the interactions occurring in the heterodimer are shown in Table 1. It confirms that the interaction shown in Figure 2 is the most favorable interaction in the heterodimer ISO-AML. It is possible to verify that a hydrogen bond occurs between the H(13) atom of AML and the N(2) atom of ISO in the heterodimer ISO-AML.

Table 1. Thermodynamic properties for the interaction in the heterodimr of ISO-AML, in kcal/mol.

Properties	ISO-AML (vacuum)	ISO-AML (methanol)
ΔH	-20.86	-14.73
ΔG^{298}	-11.91	-5.71
ΔE_{ZPVE}	-21.66	-15.54
BSSE	0.75	0.78
ΔE_{ZPVE} + BSSE	-20.91	-14.76

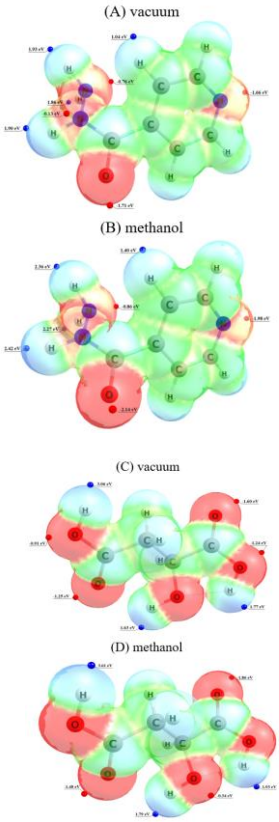


Figure 1. Electrostatic potential maps of ISO (a) and (b) and AML (c) and (d).

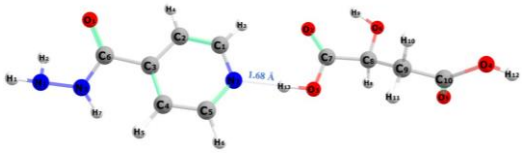
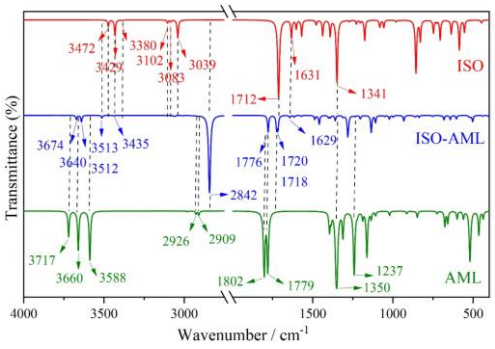
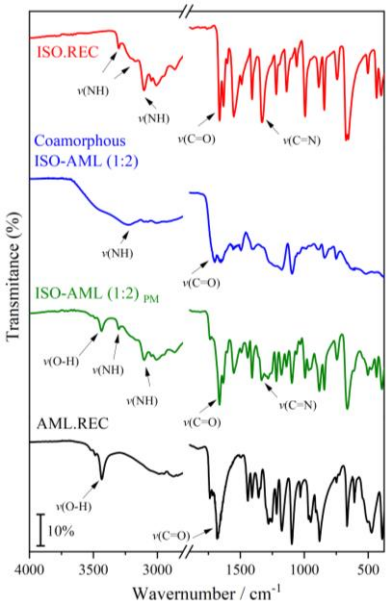


Figure 2. Optimized geometry of the heterodimer ISO-AML in a vacuum, as obtained from the DFT calculations.



(a)



(b)

Figure 3. Theoretical FT-IR spectra of ISO, AML and the heterodimer ISO-AML in a vacuum corrected with the scale factor 0.957 (a) and experimental FT-IR spectra (b).

Discussion

The EPMs of ISO (Figure 1) indicate a high electronic density around its most electronegative atoms (oxygen (O) and nitrogen (N) atoms), which are the most likely to interact with the hydroxyl and carboxyl groups of AML. We considered these insights to study the

interactions between the molecules in the heterodimer ISO-AML. In order to take into account the effects of the solvent on the interaction, computational calculations were also carried out in methanol using the IEFPCM method. This investigation revealed the importance of solvation in the thermodynamics of the interaction. The study confirmed that the interaction is more favorable in a vacuum, with a more negative ΔG^{298} value (Table 1). It validated the importance of hydrogen bonds in the formation of the material with the evaporation of the solvent. The distance between the N and H atoms is one of the parameters that determine the formation of hydrogen bonds, and a distance of 1.68 Å was found for the N···H hydrogen bonds. This evidence confirms the interaction in the heterodimer through hydrogen bond. Figure 3 shows the FT-IR spectra calculated for ISO, AML, and the heterodimer ISO-AML. The theoretical spectrum for the heterodimer shows changes in some significant vibrational bands compared to the theoretical spectra of ISO and AML calculated in a vacuum. A significant band shift is observed for the *ν*(O-H) hydroxyl group vibrational band, which undergoes a change from (3717 and 3660 cm^{-1}) in AML to (3674 and 3640 cm^{-1}) in the heterodimer. The vibrational band corresponding to the hydroxyl group of AML at 3588 cm^{-1} is not found in the spectrum for the heterodimer. This is due to hydrogen bonding interaction in the heterodimer, resulting in a vibrating band at 2842 cm^{-1}, which is not observed in ISO or AML spectra, these theoretical results are in agreement with the experimental results confirming the interaction between the compounds as observed in Figure 3 (b).

Conclusions

The theoretical study provided evidence to identify the most favorable interaction in the heterodimer ISO-AML. It confirms the occurrence of a hydrogen bond between the drug and the coformer in the solid dispersion of ISO with the AML coformer. Furthermore, we found that the method used is considerably accurate in providing structural, electronic, and spectroscopic data that agreed with experimental results. This information contributes to the characterization and further study of new solid dispersions.

Acknowledgements

Digital Research Alliance of Canada

References

1. SONG, D. *et al*. International Journal of Food Engineering 2023, 19 (1-2), 49-60.
2. HEALY, A. M. *et al*. Advanced drug delivery reviews 2017, 117, 25-46.
3. TANAKA, R. *et al*. Journal of Pharmaceutical Sciences 2021, 110 (9), 3289-3297.
4. CRISOSTOMO, S. *et al*. Letters in Mathematical Physics 2023, 113 (2), 42.
5. QUEIROZ, L. H. *et al*. *Molecular Pharmaceutics* 2024, 21 (3), 1272-1284.
6. SÁ, M. R. *et al*. *International Journal of Pharmaceutics* 2022, 615, 121500.
7. JOHNSON R. JOHNSON, R. NIST Standard Reference Database, v. 101, 2013.

Investigação computacional das barreiras na reação de redução de CO_2 em nanoclusters de cobre.

André Corrêa Souza, Caroline Zulle Vitorino, Breno Rodrigues Lamaguere Galvão.
acorrea.souza@hotmail.com

Palavras-Chave: Eletrocatálise, Cobre, DFT, Nanocluster

Abstract

The present work studies the barriers in the conversion of carbon dioxide (CO_2) into methane (CH_4) using a model copper catalyst containing 55 atoms, with a focus on the hydrogenation step of CO to CHO/COH. The study was conducted using DFT with the PBE+D3 and wB97X-D functionals some structures have been obtained at the PBE+D3 level, which are currently being optimized at the wB97X level for further analysis.

Introdução

Dentro da ciência atualmente, umas das questões mais relevantes é acerca do nosso meio ambiente e como nossos impactos negativos podem causar malefícios e até impedir nossa sobrevivência no futuro. Nesse sentido um assunto recorrente é o agravamento do aquecimento global causado pelas emissões do gás dióxido de carbono (CO_2), que por causa de sua natureza química é um dos componentes mais importantes nessa dinâmica.

Para a mitigação do aquecimento global é necessário a diminuição do CO_2 na atmosfera, que pode ser feito com a redução direta da liberação desse gás e/ou a utilização de métodos para converter esse gás em produtos de valor agregado que podem ser utilizados de forma sustentável em outras cadeias produtivas.

A conversão do CO_2 é difícil por causa de sua natureza química, e por isso é vantajoso a utilização de catalisadores. Porém, para o desenvolvimento de catalisadores eficientes é necessário o entendimento do mecanismo de reação do CO_2 até a formação dos produtos de valor agregado.

Atualmente, catalisadores de cobre são os mais eficientes para a conversão de CO_2 em metano (CH_4) [1][2][3]. Essa redução do CO_2 possui alguns mecanismos propostos na literatura, mas é consenso que a hidrogenação do CO é a etapa lenta de reação e o produto CHO é o mais provável de ser formado [1].

Até o momento atual, a maior parte dos estudos que visavam estudar as barreiras existentes na reação de CO_2 utilizaram o funcional PBE+D3, que pode não ter uma precisão quantitativa ideal e consequentemente a literatura ainda apresenta poucos resultados acerca da barreira dessa reação. O trabalho atual tem como objetivo desenvolver uma metodologia que corrobore com os resultados atuais e possibilite a utilização de funcionais com maior grau de precisão quantitativa para realizar o estudo completo da barreira em questão.

Metodologia

Os cálculos foram realizados utilizando DFT com os funcionais PBE+D3 [4] e wB97X-D. [5] Todos os cálculos foram realizados no programa ORCA com posterior análise das estruturas nos programas JMol e Avogadro. Todas as estruturas foram otimizadas primeiramente em PBE+D3 e seus resultados foram utilizados como ponto de partida para o desenvolvimento das estruturas em wB97X-D.

A estrutura de cobre utilizada como catalisador foi a estrutura icosaédrica de 55 átomos. Sítios de adsorção do tipo top, bridge e hollow foram avaliados com a adsorção das moléculas de CHO e COH para determinar a estrutura com menor energia. As estruturas escolhidas foram utilizadas como base para a adição de moléculas de água para a simulação explícita do solvente e realizou-se a otimização geométrica dessas estruturas. A procura de estruturas de TS foi feita utilizando o método NEB com posterior otimização das estruturas encontradas.

Resultados e Discussão

As estruturas otimizadas contendo o adsorbato e a estrutura de água foram modificadas com a transferência de um átomo de hidrogênio do CHO/COH para uma molécula de água com posterior otimização. Essas duas estruturas otimizadas foram utilizadas para a realização do NEB para verificar se existe e qual seria o TS.
Uma das superfícies já obtida foi a hidrogenação do CO com um hidrogênio advindo diretamente do cluster, como pode ser visto na Figura 1.

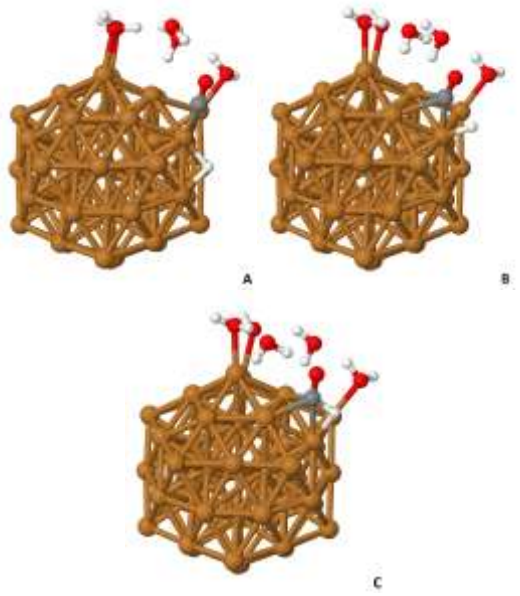


Figura 1 – Estruturas de hidrogenação do CO com hidrogênio fornecido diretamente pelo cluster em wB97X-D. (A) estrutura inicial, (B) estrutura de TS, (C) estrutura final.

O gráfico com as energias relativas dessas estruturas pode ser visto na Figura 2. É possível observar que as estruturas encontradas como mínimo e como TS são similares entre os dois níveis de cálculo. Além disso, é possível comprovar a existência da barreira nos dois níveis sendo que em wB97X-D o tamanho da barreira e a e energia de reação é muito superior quando comparado ao PBE+D3. Isso sugere que essa reação com o hidrogênio adsorvendo no cluster não é favorável de ocorrer.

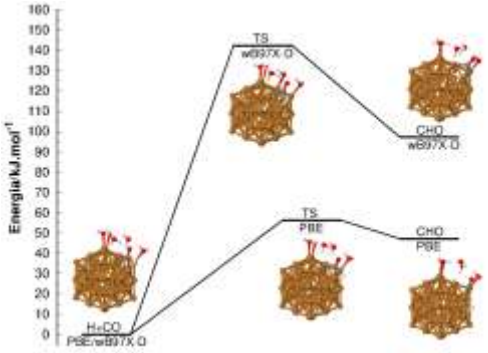


Figura 2 – Gráfico das energias para a hidrogenação do CO a partir de um hidrogênio adsorvido no cluster. Diagrama contendo energia em PBE+D3 e wB97X-D com ambos utilizando a estrutura contendo o CO adsorvido como referência.

Essas estruturas e outras obtidas em PBE+D3 estão sendo otimizadas no nível wB97X-D para futura comparação entre si e com a literatura atual.

Agradecimentos.

CEFET-MG, CNPq, CAPES, FAPEMIG (projeto APQ-00597-22).

Referências

1. LI, Yawei; CHAN, Siew Hwa; SUN, Qiang. Heterogeneous catalytic conversion of CO_2: a comprehensive, theoretical review. **Nanoscale**, v. 7, n. 19, p. 8663-8683, 2015.
2. SHI, C. et al. Barriers of electrochemical CO_2 reduction on transition metals. **Organic process research & development**, v. 20, n. 8, p. 1424–1430, 2016.
3. Verga, Lucas G., et al. "The role of site coordination on the CO 2 electroreduction pathway on stepped and defective copper surfaces." **Catalysis Science & Technology** 11.8 (2021): 2770-2781
4. Perdew, J. P.; Burke, K.; Ernzerhof, M. Generalized gradient approximation made simple. Phys. Rev. Lett., **American Physical Society**, v. 77, n. 18, p. 3865–3868, Oct. 1996.
ISSN 0031-9007, 1079-7114.

5. Chai, Jeng-Da; Head-Gordon, Martin. Long-range corrected hybrid density functionals with damped atom–atom dispersion corrections. **Physical Chemistry Chemical Physics**, v. 10, n. 44, p. 6615-6620, 2008.

Investigação computacional das barreiras na reação de redução de CO_2 em nanoclusters de cobre.

André Corrêa Souza, Caroline Zulle Vitorino, Breno Rodrigues Lamaguere Galvão.
Av. Amazonas, 5855, Bairro Gameleira. Belo Horizonte- MG
acorrea.souza@hotmail.com
Palavras-Chave: Eletrocatálise, Cobre, DFT, Nanocluster

Abstract
The present work studies barriers in the conversion of carbon dioxide (CO_2) into methane (CH_4) using a model copper catalyst containing 55 atoms, with a focus on the hydrogenation step of CO to CHO/COH. The study was conducted using DFT with the PBE+D3 and wB97X-D functionals some structures have been obtained at the PBE+D3 level, which are currently being optimized at the wB97X level for further analysis.

Introdução
Dentro da ciência atualmente, umas das questões mais relevantes é acerca do nosso meio ambiente e como nossos impactos negativos podem causar malefícios e até impedir nossa sobrevivência no futuro. Nesse sentido um assunto recorrente é o agravamento do aquecimento global causado pelas emissões do gás dióxido de carbono (CO_2), que por causa de sua natureza química é um dos componentes mais importantes nessa dinâmica.

Para a mitigação do aquecimento global é necessário a diminuição do CO_2 na atmosfera, que pode ser feito com a redução direta da liberação desse gás e/ou a utilização de métodos para converter esse gás em produtos de valor agregado que podem ser utilizados de forma sustentável em outras cadeias produtivas.

A conversão do CO_2 é difícil por causa de sua natureza química, e por isso é vantajoso a utilização de catalisadores. Porém, para o desenvolvimento de catalisadores eficientes é necessário o entendimento do mecanismo de reação do CO_2 até a formação dos produtos de valor agregado.

Atualmente, eletrocatalisadores de cobre são os mais eficientes para a conversão de CO_2 em metano (CH_4). [1][2][3] Essa redução do CO_2 possui alguns mecanismos propostos na literatura, mas é consenso que a hidrogenação do CO é a etapa que demanda maior potencial aplicado de reação e o produto CHO é o mais provável de ser formado [1].

Até o momento atual, a maior parte dos estudos que visavam estudar as barreiras existentes na reação de CO_2 utilizaram o funcional PBE+D3, que pode não ter uma precisão quantitativa ideal e consequentemente a literatura ainda apresenta poucos resultados acerca da barreira dessa reação. O trabalho atual tem como objetivo desenvolver uma metodologia que corrobore com os resultados atuais e possibilite a utilização de funcionais com maior grau de precisão quantitativa para realizar o estudo completo das barreiras envolvidas na eletroredução do CO_2

Metodologia
Os cálculos foram realizados utilizando DFT com os funcionais PBE+D3 [4] e wB97X-D. [5] A base escolhida para os primeiros testes foi def2-SVP considerando todos os elétrons, e pretende-se aumentar a precisão com a realização de cálculos com uma base maior. Todos os cálculos foram realizados no programa ORCA com posterior análise das estruturas nos programas JMol e Avogadro. Todas as estruturas foram otimizadas primeiramente em PBE+D3 e seus resultados foram utilizados como ponto de partida para o desenvolvimento das estruturas em wB97X-D.

A estrutura de cobre utilizada como catalisador foi a estrutura icosaédrica de 55 átomos. Sítios de adsorção do tipo top, bridge e hollow foram avaliados com a adsorção das moléculas de CHO e COH para determinar a estrutura com menor energia. As estruturas escolhidas foram utilizadas como base para a adição de moléculas de água para a simulação explícita do solvente e realizou-se a otimização geométrica dessas estruturas. A procura de estruturas de TS foi feita utilizando o método NEB com posterior otimização das estruturas encontradas.

Resultados e Discussão

As estruturas otimizadas contendo o adsorbato e a estrutura de água foram modificadas com a transferência de um átomo de hidrogênio do CHO/COH para uma molécula de água com posterior otimização. Essas duas estruturas otimizadas foram utilizadas na realização do NEB para verificar se existe e qual seria o TS.

Uma das superfícies já obtida foi a hidrogenação do CO com um hidrogênio advindo diretamente do cluster, como pode ser visto na Figura 1.

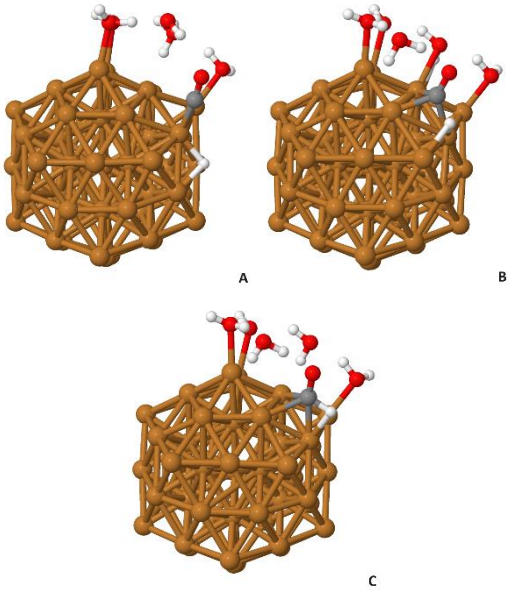


Figura 1 – Estruturas de hidrogenação do CO com hidrogênio fornecido diretamente pelo cluster em wB97X-D. (A) estrutura inicial, (B) estrutura de TS, (C) estrutura final.

O gráfico com as energias relativas dessas estruturas pode ser visto na Figura 2. É possível observar que as estruturas encontradas como mínimo e como TS são similares entre os dois níveis de cálculo. Além disso, é possível comprovar a existência da barreira nos dois níveis sendo que em wB97X-D o tamanho da barreira e a e energia de reação é muito superior quando comparado ao PBE+D3. Isso sugere que essa reação com o hidrogênio adsorvendo no cluster não é favorável de ocorrer.

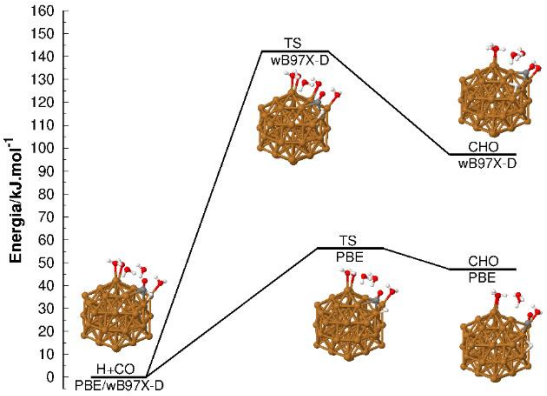


Figura 2 – Gráfico das energias para a hidrogenação do CO a partir de um hidrogênio adsorvido no cluster. Diagrama contendo energia em PBE+D3 e wB97X-D com ambos utilizando a estrutura contendo o CO adsorvido como referência.

Essas estruturas e outras obtidas em PBE+D3 estão sendo otimizadas no nível wB97X-D para futura comparação entre si e com a literatura atual.

Agradecimentos.

CEFET-MG, CNPq, CAPES, FAPEMIG (projeto APQ-00597-22).

Referências

1. LI, Yawei; CHAN, Siew Hwa; SUN, Qiang. Heterogeneous catalytic conversion of CO_2: a comprehensive, theoretical review. **Nanoscale**, v. 7, n. 19, p. 8663-8683, 2015.

2. SHI, C. et al. Barriers of electrochemical CO_2 reduction on transition metals. **Organic process research & development**, v. 20, n. 8, p. 1424–1430,2016.

3. Verga, Lucas G., et al. "The role of site coordination on the CO 2 electroreduction pathway on stepped and defective copper surfaces." **Catalysis Science & Technology** 11.8 (2021): 2770-2781

4. Perdew, J. P.; Burke, K.; Ernzerhof, M. Generalized gradient approximation made simple. Phys. Rev. Lett., **American Physical Society**, v. 77, n. 18, p. 3865–3868, Oct. 1996.
ISSN 0031-9007, 1079-7114.

5. Chai, Jeng-Da; Head-Gordon, Martin. Long-range corrected hybrid density functionals with damped atom–atom dispersion corrections. **Physical Chemistry Chemical Physics**, v. 10, n. 44, p. 6615-6620, 2008.

Promising TMDC-like optical and excitonic properties of the TiBr2 2H monolayer

André Luis de O. Batista[1], Maurício J. Piotrowski[2], and Alexandre C. Dias[3]
[1] Brasília - Distrito Federal, Brasil
[2] Pelotas - Rio Grande do Sul, Brasil
[3] Brasília - Distrito Federal, Brasil
alob696gmail.com
Keywords: $TiBr_2$ 2H monolayer; Crystalline structure; Phonon dispersion; Spin-orbit coupling (SOC); Electronic band structure; Hybrid functional (HSE06); Excitonic properties.

Abstract
The presented simulation protocol provides a solid foundation for exploring two-dimensional materials. Taking the TiBr2 2H monolayer as an example, this material displays promising TMDC-like optical and excitonic properties, making it an excellent candidate for optoelectronic and valleytronic applications. The direct band gap semiconductor (1.19 eV) is both structurally and thermodynamically stable, with spin–orbit coupling effects revealing a broken mirror symmetry in the K and K' valleys of the band structure, as confirmed by opposite values of the Berry curvature. A direct and bright exciton ground state was found, with an exciton binding energy of 0.56 eV. The study also revealed an optical helicity selection rule, suggesting selectivity in the valley excitation by specific circular light polarizations.

Introduction

Since the discovery of graphene in 2004, a vast and dynamic field in materials science has emerged, focusing on the study of two-dimensional (2D) materials. Transition-metal dichalcogenides (TMDCs) have attracted considerable attention over the past decade, particularly 2H monolayers of molybdenum (Mo) and tungsten (W), due to their intriguing valley physics. More recently, there has been increasing interest in exploring new classes of 2D materials, such as transition-metal dihalides (TMDHs), which show significant potential for further research. TMDCs are known for their valley physics and excitonic effects, which make them suitable for various nanoelectronic applications, including photovoltaic devices, spintronics, qubit generation, and more. The combination of spin–orbit coupling effects with the symmetry of the 2H structure allows access to valley degrees of freedom through specific optical helicity, enabling the manipulation and control of charge carriers in both valleys.

Our research aims to identify new materials with optical and excitonic properties similar to those of TMDCs, focusing on 2H monolayer systems within the TMDH family. These materials hold promise for the future design of spintronic and valleytronic devices. Theoretical studies have demonstrated that certain TMDHs, such as the PbI_2 monolayer, possess stable and desirable properties, including excitonic and spin–orbit coupling effects, potentially making them viable alternatives or even superior to TMDCs. However, research on group IV elements (Ti, Zr, Hf) in the formula MX_2 (where M is a transition metal and X is Cl, Br, I) has been limited, primarily focusing on Janus TiXY 2H monolayers and their electronic properties, valley physics, and Berry curvature. This study presents a proof of concept for the structural, stability, electronic, optical, and excitonic properties of the $TiBr_2$ 2H monolayer, a system that exhibits valley

physics similar to that of Mo and W TMDC 2H monolayers, suggesting it may have analogous applications.

To investigate the properties of the $TiBr_2$ 2H monolayer, we developed a calculation protocol. The atomic configuration of the proposed material features a honeycomb pattern similar to graphene and MoS_2 2H monolayers, with Ti atoms sandwiched between two Br layers. Structural optimization and total energy calculations were carried out using density functional theory (DFT) as implemented in the Vienna Ab initio Simulation Package (VASP). The electronic and structural properties were described using the semilocal exchange–correlation functional within the generalized gradient approximation (GGA), as proposed by Perdew, Burke, and Ernzerhof (PBE). However, it is well-known that the DFT–PBE framework tends to underestimate certain electronic properties like the bandgap due to self-interaction errors and poor treatment of weak interactions, so we employed the screened Coulomb hybrid exchange–correlation functional HSE06 to improve accuracy. Spin–orbit coupling (SOC) effects were also incorporated into the DFT calculations using the scalar-relativistic approximation to thoroughly investigate the valley physics and associated spin–valley configurations. For greater precision, SOC was applied to the valence states in both the DFT–PBE and DFT–HSE06 calculations using a second-variational approach. The number of bands included in these calculations was doubled relative to the number of electrons. The Kohn–Sham (KS) equations were solved using the all-electron projector augmented wave (PAW) method, where the KS states were expanded into plane waves. The equilibrium structure was determined through stress-tensor optimization and atomic force minimization, using a cutoff energy of 767.55 eV for the equilibrium configuration and 431.75 eV for other properties. Convergence was achieved when the atomic forces on each atom were less than 0.01 eV $Å^{-1}$, with a total energy convergence threshold of 10^{-6} eV. For Brillouin zone (BZ) integration, a k-mesh of 16 × 16 × 1 was used for most electronic properties, except for the density of states (DoS), which required a finer 32 × 32 × 1 k-mesh. To prevent unwanted interactions between the $TiBr_2$ 2H monolayer and its periodic images in the z-direction, a vacuum thickness of 16 Å was introduced, as the monolayer was constructed with periodicity in the xy-plane.

Phonon dispersion was calculated using the VASP (DFT–PBE) and Phonopy packages, employing the finite displacement method with a 4 × 4 × 1 supercell and a 4 × 4 × 1 k-mesh. Stability was further validated through ab initio molecular dynamics (AIMD) simulations, utilizing the Nosé thermostat over approximately 5 ps, with a time step of 1 fs at 300 K. To compute the excitonic and optical properties and the Berry curvature, we used the WanTiBEXOS package developed by our research group, which solves the Bethe–Salpeter equation (BSE) using a tight-binding Hamiltonian. This approach allowed us to rapidly compute these properties with a high degree of accuracy.

For this purpose, a maximally localized Wannier function tight-binding Hamiltonian (HSE06 + SOC) was constructed using the Wannier90 package, considering the d orbital projections for Ti and p orbital projections for Br. The BSE was solved using a 2D Coulomb truncated potential (V2DT) with 2 conduction and 2 valence bands. A k-mesh of 40 × 40 × 1 was employed to obtain the dielectric functions, with a smearing of 0.02 eV. Optical activity and dichroism in the first Brillouin zone, at the independent-particle approximation (IPA) level, were calculated according to the methodology proposed by Lu et al., with a modification in the circular dichroism where linear polarization was replaced by circular polarization in the mathematical expression. A k-mesh of 133 × 133 × 1 was adopted for these calculations, consistent with the BSE calculation protocol. This comprehensive

approach enabled a thorough investigation of the $TiBr_2$ 2H monolayer's potential for use in next-generation spintronic and valleytronic devices.

Text containing Introduction, Methodology, Results, Discussion, Conclusions, Acknowledgments and References

The crystalline structure of the $TiBr_2$ 2H monolayer was determined with a lattice parameter of 3.47 Å, a Ti–Br bond length of 2.47 Å, and a vertical Br–Br distance of 3.17 Å. To verify the stability of this structure, a two-step approach was implemented. First, phonon dispersion calculations were performed, showing no imaginary frequencies, which confirmed the dynamical stability of the monolayer. Additionally, vibrational frequencies were found to be below 10 THz. Second, an ab initio molecular dynamics (AIMD) simulation at 300 K was conducted, demonstrating that the structure remains stable under thermal fluctuations, as evidenced by the preservation of the structural motif throughout the simulation.

The electronic properties analysis revealed that the semiconductor nature of the $TiBr_2$ 2H monolayer is primarily due to contributions from Ti d-orbitals and Br p-orbitals near the Fermi level. The band structure calculations using DFT–PBE indicated an indirect band gap of 0.80 eV, with the valence band maximum (VBM) located at the K or K′ valleys and the conduction band minimum (CBM) between the valleys and the Γ point. Upon including spin-orbit coupling (SOC), the band gap slightly decreased to 0.76 eV, and the direct band gap in the K or K′ valleys was found to be 0.94 eV. The SOC also led to a spin degeneracy breaking in the valence bands around the K and K′ valleys, making these valleys energetically equivalent but with opposite spin configurations, a phenomenon often observed in Mo-based TMDCs. When the HSE06 hybrid functional was applied, the band gap was further corrected to 1.19 eV, which also became direct at the K and K′ valleys, with a slight increase in the spin degeneracy breaking.

The optical and excitonic properties of the $TiBr_2$ 2H monolayer were also investigated. The optical activity within the Brillouin zone (BZ) was found to be polarization-dependent. For circularly polarized light, the K valley is excited only by right-handed (σ+) polarization, while the K′ valley is excited by left-handed (σ−) polarization. The optical circular dichroism indicated a distinct optical response depending on the light helicity. In contrast, linear polarization activated both valleys, with different patterns depending on the polarization direction, resulting in linear optical dichroism. The optical activity in the K and K′ valleys under circular polarization was nearly twice as intense as under linear polarization.

Finally, the excitonic properties were examined, revealing a direct exciton ground state at the Γ point with an energy of 0.65 eV and a binding energy of 0.56 eV, attributed to the quantum confinement in the z-direction. The exciton band structure showed similarities to that of MoS_2, with additional local minima at the K and K′ valleys. The absorption spectra, calculated using the Bethe–Salpeter equation (BSE), confirmed that the exciton ground state is optically active, with distinct absorption peaks corresponding to excitons A and B at 0.65 eV and 0.74 eV, respectively, influenced by SOC. These excitonic characteristics are similar to those found in Mo and W-based TMDC monolayers. The analysis highlighted the importance of quasi-particle effects in determining the accurate absorption intensities, which were slightly dependent on the incident light polarization but consistent across circular and linear polarizations in the independent particle approximation (IPA).

Acknowledgements

The authors are thankful for financial support from the National Council for Scientific and Technological Development (CNPq, grant numbers 307345/2021-1 and 408144/2022-0), Federal District Research Support Foundation (FAPDF, grant 00193-00001817/2023-43), the Coordination for Improvement of Higher Level Education (CAPES), the Rio Grande do Sul Research Foundation (FAPERGS), and the German Federal Ministry of Education and Research (BMBF) for financial support of the project Innovation-Platform MaterialDigital (https://www.materialdigital.de) through project funding FKZ number: 13XP5094A. Part of this work was performed on the HoreKa supercomputer funded by the Ministry of Science, Research and the Arts BadenWürttemberg and by the Federal Ministry of Education and Research. In addition, the authors thanks the "Centro Nacional de Processamento de Alto Desempenho em São Paulo" (CENAPAD-SP, UNICAMP/FINEP – MCTI project) for resources into the 897 and 570 projects, Lobo Carneiro HPC (NACAD) at the Federal University of Rio de Janeiro (UFRJ) for resources into 133 project CIMATEC SENAI at Salvador – BA, Brazil, for the partnership and support through the Atos Computer, and "Laboratório Central de Processamento de Alto Desempenho" (LCPAD) financed by FINEP through CT-INFRA/ UFPR projects.

References

1. K. S. Novoselov, A. K. Geim, S. V. Morozov, D. Jiang, Y. Zhang, S. V. Dubonos, I. V. Grigorieva and A. A. Firsov, Science, 2004, 306, 666–669.
2. Q. H. Wang, K. Kalantar-Zadeh, A. Kis, J. N. Coleman and M. S. Strano, Nat. Nanotechnol., 2012, 7, 699–712.
3. J. Kang, S. Tongay, J. Zhou, J. Li and J. Wu, Appl. Phys. Lett., 2013, 102, 4774090.
4. F. Wu, F. Qu and A. H. MacDonald, Phys. Rev. B: Condens. Matter Mater. Phys., 2015, 91, 075310.
5. J. H. Correa, A. C. Dias, L. Villegas-Lelovsky, J. Fu, L. Chico and F. Qu, Phys. Rev. B, 2020, 101, 195422.
6. A. C. Dias, H. Bragança, J. P. A. de Mendonça and J. L. F. D. Silva, ACS Appl. Energy Mater., 2021, 4, 3265– 3278.
7 N. Thomas, S. Mathew, K. M. Nair, K. O'Dowd, P. Forouzandeh, A. Goswami, G. McGranaghan and S. C. Pillai, Mater. Today Sustainability, 2021, 13, 100073.
8. M. McGuire, Crystals, 2017, 7, 121.
9. V. V. Kulish and W. Huang, J. Mater. Chem. C, 2017, 5, 8734–8741.
10. Y. Wang, W. Wei, H. Wang, N. Mao, F. Li, B. Huang and Y. Dai, J. Phys. Chem. Lett., 2019, 10, 7426–7432.
11. C. M. O. Bastos, R. Besse, J. L. F. Da Silva and G. M. Sipahi, Phys. Rev. Mater., 2019, 3, 044002.
12. N. Zibouche, A. Kuc, J. Musfeldt and T. Heine, Ann. Phys., 2014, 526, 395–401.
13. J.-Y. Tsai, J. Pan, H. Lin, A. Bansil and Q. Yan, Nat. Commun., 2022, 13, 41467.
14. H. S. Borges, C. A. N. Júnior, D. S. Brandão, F. Liu, V. V. R. Pereira, S. J. Xie, F. Qu and A. M. Alcalde, Phys. Rev. B, 2023, 107, 035404.
15. T. Cao, G. Wang, W. Han, H. Ye, C. Zhu, J. Shi, Q. Niu, P. Tan, E. Wang, B. Liu and J. Feng, Nat. Commun., 2012, 3, 1882.
16. T. Kurumaji, S. Seki, S. Ishiwata, H. Murakawa, Y. Tokunaga, Y. Kaneko and Y. Tokura, Phys. Rev. Lett., 2011, 106, 167206.
17. Y. Tokunaga, D. Okuyama, T. Kurumaji, T. Arima, H. Nakao, Y. Murakami, Y. Taguchi and Y. Tokura, Phys. Rev. B: Condens. Matter Mater. Phys., 2011, 84, 060406.

Estudo de seletividade de design de novo em receptores de serotonina 5-HT2A, 5-HT6 e 5-HT7

Anelisa G. de Sousa[1], Guilherme D. R. Matos[2].
[1]Universidade de Brasília, Instituto de Química, Laboratório de Modelagem de Sistemas Complexos, Brasil.
[2]Stony Brook University, Department of Applied Mathematics and Statistics, EUA. *anelisa.gs@gmail.com*
Keywords: Design de novo, receptores de serotonina, seletividade.

Abstract

Serotonin receptors transmit signals in the nervous system and non-neuronal tissues. Given their role in cognition, anxiety, and depression, new ligands should target specific receptors. Using DOCK6, molecules were designed for 5-HT_{2A}, 5-HT_6, and 5-HT_7 receptors. Promising selective candidates for 5-HT_{2A} were found, guiding future DOCK6 improvements.

Introduction

Receptores de serotonina são componentes importantes da transmissão de sinais biológicos no sistema nervoso e em tecidos não-neuronais. Dada a associação desses receptores à depressão, cognição e até mesmo ao uso de drogas recreativas, o design de novos ligantes deve tentar buscar seletividade com o receptor de serotonina de interesse. Este trabalho propõe o uso de design *de novo* para a geração de ligantes seletivos (potencialmente específicos) para três receptores de serotonina, 5-HT_{2A} (PDB: 7WC6), 5-HT_6 (PDB: 7XTB) e 5-HT_7 (PDB: 7XTC)[1,2]. Para verificar a seletividade dos ligantes gerados pelo método *de novo*, o experimento computacional de *cross-docking* calcula a interação ligante-receptor nos demais sítios de ligação. A diferença de energia de interação de um ligante nos três receptores pode indicar a seletividade entre as diversas combinações de ligantes e receptores.

Metodologia

A geração de novas moléculas foi realizada por meio do software DOCK6[3] com o uso do algoritmo de design *de novo*[4,5]. Essa metodologia explora o espaço químico e cria moléculas a partir de uma biblioteca de fragmentos, levando em consideração propriedades de interesse (e.g.: energia de interação, descritores quimioinformáticos etc.) ao longo do processo de construção da molécula. O design foi executado no interior do sítio de ligação dos três receptores onde as moléculas geradas foram selecionadas ou descartadas de acordo com as suas energias de interação com o sítio de ligação. Os ensembles moleculares gerados em cada receptor foram, então, submetidos a *cross-docking*, onde os ligantes de um sítio foram ancorados nos sítios dos outros receptores com o propósito de separar ligantes promíscuos de ligantes mais seletivos.

Resultados e Discussões

Com o uso do D3N foram gerados 1202 ligantes para a proteína 5-HT_{2A}, 488 para a proteína 5-HT_6 e 1212 ligantes para a proteína 5-HT_7. Por meio da análise da energia de interação (energia eletrostática e energia contínua) entre os resíduos da proteína e os ligantes gerados foi feita a comparação entre ligantes capazes de se ligar a uma proteína de forma específica.

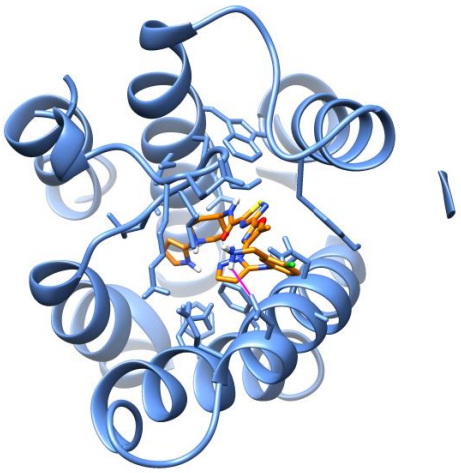


Figura 1. Ligante gerado no sítio do receptor (PDB: 7WC6).

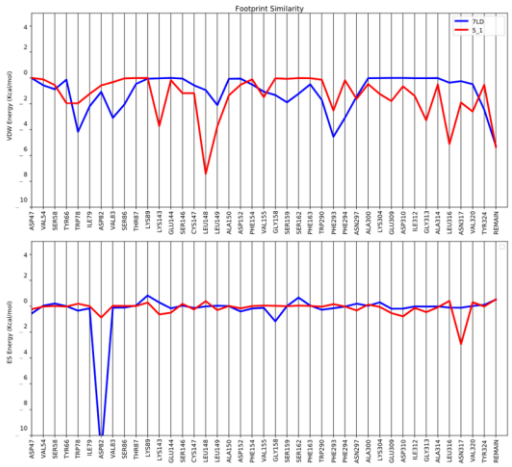


Figura 2. Gráfico com quarenta resíduos de maior interação com o receptor 5-HT_{2A}. Em azul a energia de interação do ligante natural dietilamida do ácido lisérgico, e em vermelho a energia de interação de uma das moléculas geradas.

Conclusões

O experimento conjunto de design de novo e *cross-docking* não revelou candidatos marcadamente seletivos para as proteínas 5-HT_6 e 5-HT_7, mas encontrou bons candidatos para o receptor 5-HT_{2A}. Ligantes escolhidos tem indicadores de seletividade quando as diferenças de energia de interação são grandes o suficiente para indicar uma interação preferencial. Estudos de energia livre por meio de cálculos alquímicos serão conduzidos para avaliar a estabilidade relativa das moléculas escolhidas no sítio ativo do receptor.

Agradecimentos

Agradeço ao LMSC, SEEDMOL, CAPES, CNPq, FAPDF.

Referências

1. Cao, D. et al. Science. 2022, v. 375, n. 6579, p. 403-411, 2022.
2. Huang, S. et al. Molecular cell. 2022, v. 82, n. 14, p. 2681-2695. e6, 2022.
3. Allen, W. J. et al. Journal of computational chemistry. 2015, v. 36, n. 15, p. 1132-1156.
4. Allen, W. J. et al. Journal of computational chemistry. 2017 v. 38, n. 30, p. 2641-2663.
5. Matos, G. D. R. et al. Journal of Chemical Information and Modeling. 2023, v. 63, n. 18, p. 5803-5822.

Graphical presentation of the atomic reactivity of the anti-SARS-CoV-2 agent EIDD-2801 (molnupiravir) molecule calculated with Fukui functions

Antonio L. Almeida[1], João B. L. Martins[2]
[1]*Universidade do Estado da Bahia (UNEB), Departamento de Ciências Exatas e da Terra, Rua Silveira Martins, 2555, Cabula, Salvador-BA, CEP:41.150-00. Brazil.*
[2]*Universidade de Brasília (UnB), Instituto de Química, CP 04478, Campus Universitário, Brasília, DF, 70919-970, Brazil.*
e-mail: alalmeida@uneb.br

Keywords: EIDD-2801, local reactivity, gas phase, solvent.

Abstract
EIDD-2801 has the potential for COVID-19 and treatment of seasonal and pandemic influenza. We present here, our results, on the local reactivity from the calculations of the Fukui Functions with the density functional theory, with the EIDD-2801 in the gas phase in solvents, water and dimethyl sulfoxide.

Introduction
EIDD-2801 is an orally bioavailable prodrug of the ribonucleoside analog EIDD-1931. EIDD-2801 has broad-spectrum antiviral activity against influenza viruses and various coronaviruses, such as SARS-CoV-2, MERS-CoV, SARS-CoV. EIDD-2801 has the potential for COVID-19 and treatment of seasonal and pandemic influenza. Much has been reported by the international press, news from laboratories that develop anti-Sars-CoV-2 research that EIDD-2801 has shown to be a very promising compound to eliminate the COVID-19 virus. EIDD-2801 can change the course of the disease in individual patients, stop the disease in the early stages, potentially reduce the time during which patients are infectious to others and change the course of the pandemic.

The recent years development in quantum chemistry methods, especially that of density functional theory (DFT) methods has made it possible for quantum chemistry calculations to reach accuracies comparable to those obtained in experiments for molecules of moderate sizes. The rapid development of computer technologies has greatly encouraged chemists to use quantum chemistry to understand and predict molecular properties and their reactions, properties of nanometer materials, and reactions and processes taking place in biological systems. Quantum chemistry is a very powerful tool to study the properties of molecules and their reactions.

For all calculations, we have obtained the stationary states, atomic charges, global molecular reactivity, highest occupied molecular orbital energy (HOMO), unoccupied molecular orbital of lowest energy (LUMO), ionization potential, electron affinity, electrophilicity index, chemical potential, electronegativity, hardness, softness and Fukui Functions for EIDD-2801 gas-phase and EIDD-2801 molecule in water and dimethyl sulfoxide (DMSO) solvents, have been investigated. In this work, based on quantum chemistry calculations, we verify the effect of solvents on all the molecular properties of the EIDD-2801 molecule studied here using the SMD (Solvent Model Density) method. For all calculations, obtaining the stationary states, geometric properties, we used *Density Functional Theory* (DFT) with CAM-B3LYP/aug-cc-pVTZ theory level in Gaussian09 Package Program. Finally, we use Time-dependent density theory, TD-DFT, for the analysis of excited states of the molecular states of the EIDD-2801 gas-phase and EIDD-2801 in water and DMSO solvents.

In the first row of Figure 1, we have the atomic charges of the EIDD-2801 molecule in its gas phase state, in the second row the molecule soaked in water and in the third row the molecule soaked in the DMSO solvent.

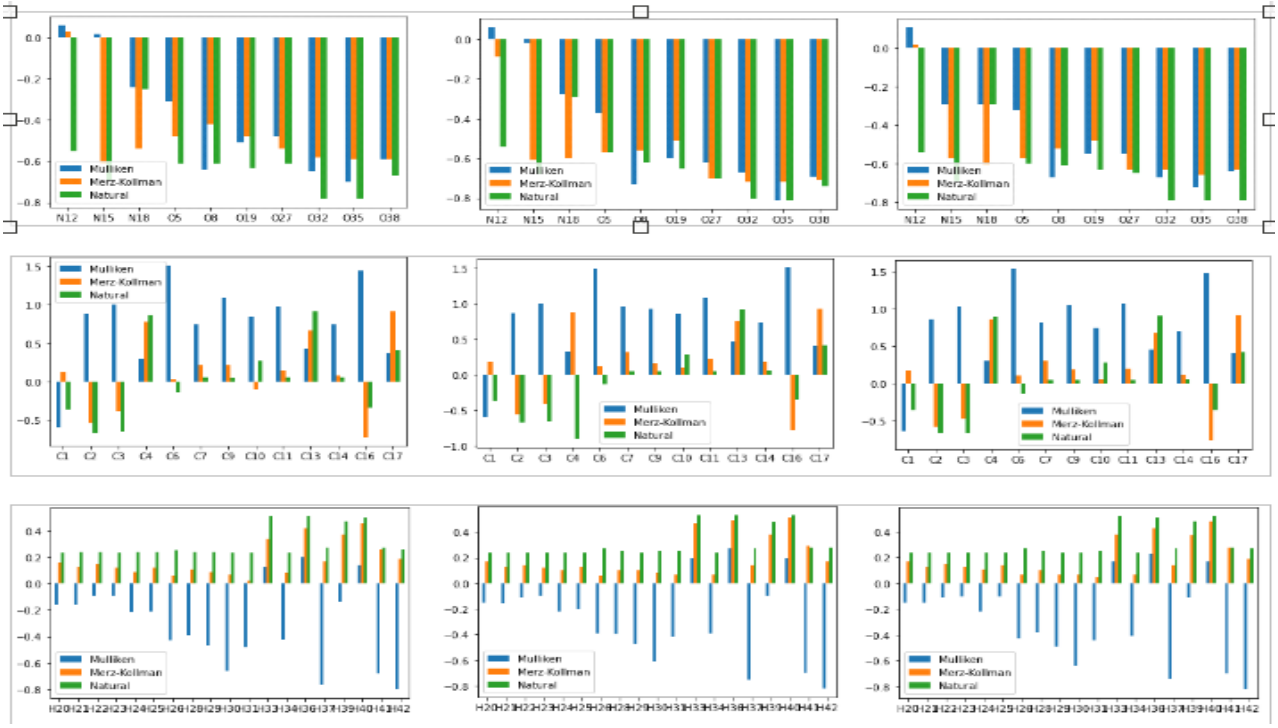


Figure 1- Mulliken, Merz-Kollman and Natural atomic charges

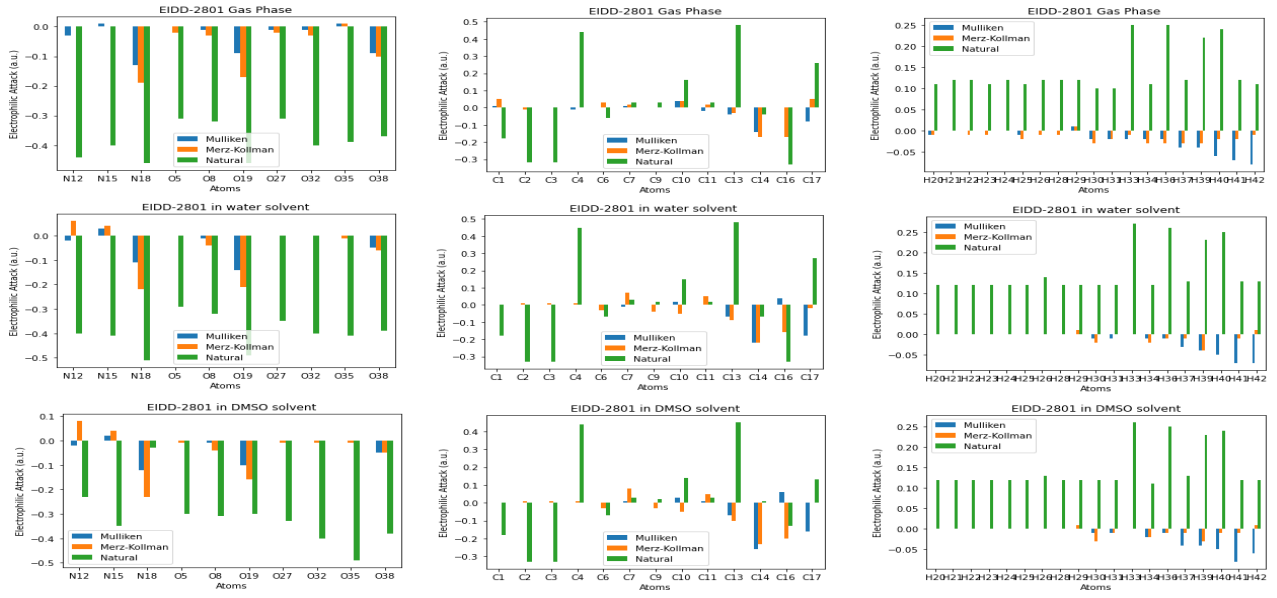


Figure 2 - Electrophilic Attack

The charge distribution methods and atomic reactivities present behaviors in their distributions that do not follow a trend, which can be used to understand the reactivity of the EIDD-2881 molecule. The results obtained require us to apply statistical methods and relationships that will need to be carried out in future work to provide better clarity on the molecular reactivity.

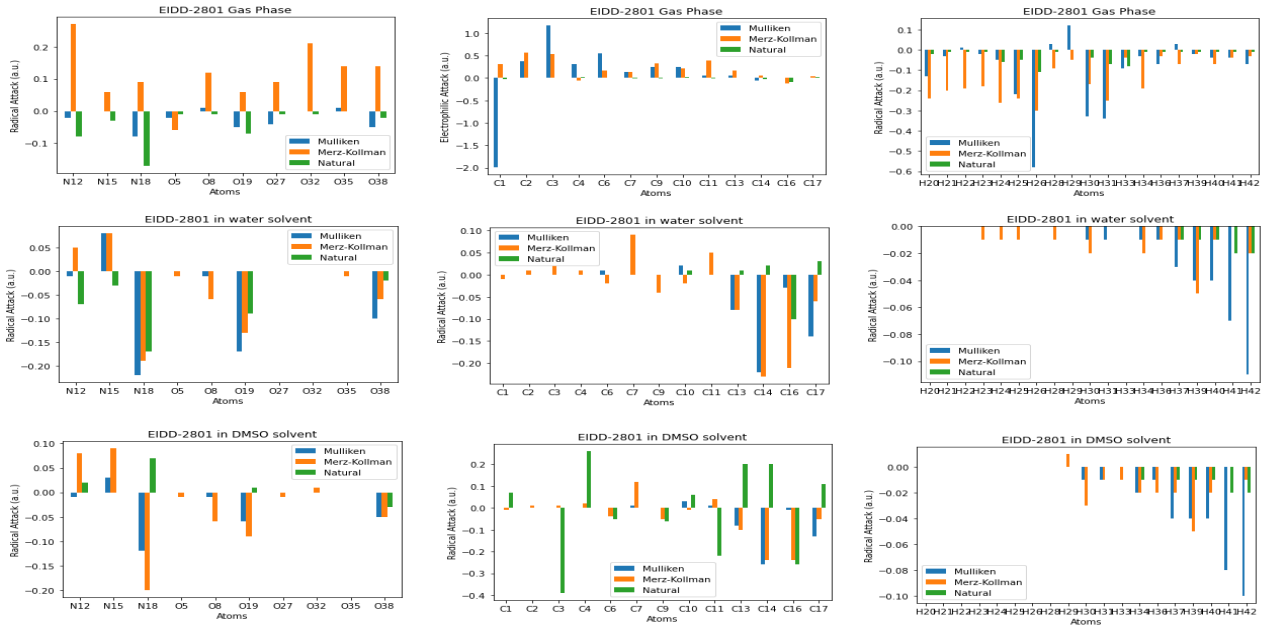


Figure 3- Radical attack

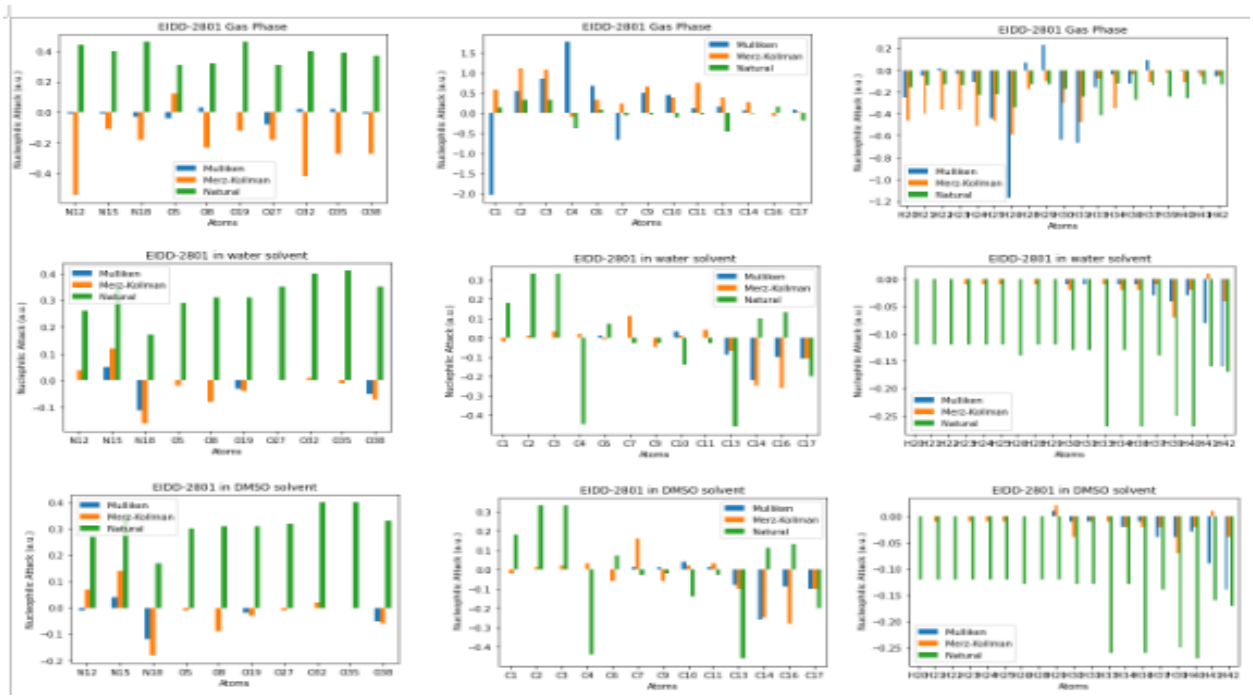


Figure 4 – Nucleophilic attack

Acknowledgements:
We thank UNEB and UnB for their hospitality and CAPES and CNPq for the financial incentive.References:

1. L. Padmaja, C. Ravikumar, D. Sajan, I. Hubert Joe, V.S. Jayakumar, G.R. Pettit, O.F. Nielsen, *J. Raman Spectrosc.*, 40 (2009) 419.
2. C. Ravikumar, I. Hubbert Joe, V.S. Jayakumar, *Chem. Phys. Lett.*, 460 (2008) 552.
3. R. G. Parr and R. G. Pearson, J. Am. Chem., 105 (1983) 7512.

Hydrogenation of Unsaturated Compounds Mediated by Intramolecular Frustrated Lewis Pairs

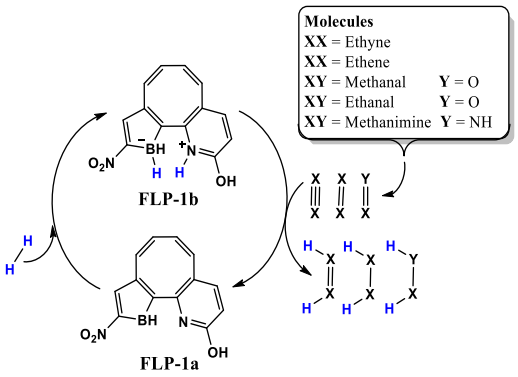
Antonio Rafael de Oliveira,[1] José Walkimar de Mesquita Carneiro,[2] and Roberto Luiz Andrade Haiduke[1]
[1]Departamento de Química e Física Molecular, Instituto de Química de São Carlos, Universidade de São Paulo, Av. Trabalhador São-Carlense, 400, 13560-970, São Carlos, SP, Brazil.
[2]Universidade Federal Fluminense, Niterói, RJ, Brazil.
rafaeldeoliveiraeu@gmail.com; haiduke@iqsc.usp.br; jose_walkimar@id.uff.br
Keywords: Hydrogenation; Frustrated Lewis pairs; unsaturated compounds; aminoborane; Intramolecular.

Abstract
This study explores the hydrogenation of unsaturated compounds using a substituted Frustrated Lewis Pair (FLP) system by means of Density Functional Theory. The results highlight the greater reactivity of simple imines and aldehydes compared to alkenes and alkynes, with lower reaction barriers, evidencing the potential of FLP in selective hydrogenation.

Introduction

The chemistry of Frustrated Lewis Pairs (FLPs), introduced by Stephen and collaborators,[1] originated from the observation of the reversible activation of the H_2 molecule in a metal-free system. Since then, the reactivity of FLPs has been extensively explored in the activation of small molecules and the hydrogenation of unsaturated organic compounds, including (imines, ketones, aldehydes, and CO_2).[2,3] FLPs are composed of a Lewis base (LB) and a Lewis acid (LA), both characterized by steric or structural hindrances that prevent the formation of a classical Lewis adduct.[4] These FLP systems can be classified as either intermolecular or intramolecular depending on the relative arrangement of their components (LB and LA).[5] The reactivity of FLPs is determined by a combination of factors such as the acidity and basicity of the Lewis centers, steric hindrance, and the functional groups attached to these centers.[6,7]

Hence, this study is focused on examining the activation of H_2 using the FLP-1a (Scheme 1) structure derived from cyclooctatetraene (COT)[8] by means of Density Functional Theory (DFT) calculations. The reactivity of this structure is evaluated along the catalytic hydrogenation of unsaturated compounds such as acetylene, ethylene, formaldehyde, acetaldehyde, and methanimine. A detailed discussion regarding the mechanism of this process provides a valuable theoretical framework that can guide the development of more efficient FLPs for hydrogenation applications.



Scheme 1. Hydrogenation reactions mediated by the FLP-1a vicinal aminoborane system considered in this study.

Methodology

The calculations were performed using the Gaussian 09 software (Revision D.01).[9] The M06-2X exchange-correlation functional[10] was employed along with def2-TZVP basis sets.[11] Structural optimizations aiming equilibrium geometries were conducted without the imposition of symmetry constraints. Thus, minimum

points (reactants, intermediates, and products) and transition states (TSs) are found and validated through vibrational frequency calculations. Additionally, Intrinsic Reaction Coordinate (IRC) calculations were performed to ensure that the TSs obtained indeed correspond to each reaction. The equilibrium structures were then used for energy analysis. All calculations are done in gas phase and thermodynamic properties are determined at 1 atm and 298.15 K.

Results

The analysis of thermodynamic results for the reactants, intermediates, and TSs (Enthalpies and Gibbs energies for barriers and elementary steps) reveals important information about the reactivity of the molecules studied with respect to the hydrogenation process. Hence, all global reactions have negative reaction enthalpy variations, ΔH_r, indicating that they are exothermic. As seen in Fig. 1, the reaction Gibbs energy variations, ΔG_r, are also negative, suggesting that the global reactions are spontaneous. In terms of Gibbs energies of activation, $\Delta G^{\ddagger}$, the ethene and ethyne molecules present the highest reaction barriers, while methanimine and aldehydes (formaldehyde and acetaldehyde) have the lowest barriers. This suggests that FLP-1a will lead to faster hydrogenation reactions of imines and aldehydes compared to alkenes and alkynes.

Discussion

The dissociation reaction of the H_2 molecule in the presence of FLP-1a, forming the intermediate FLP-1b, exhibits a $\Delta G^{\ddagger}$ value of 7.36 kcal/mol and a reaction energy ΔG_r of -4.27 kcal/mol. These values suggest that the H_2 dissociation reaction is thermodynamically favorable and fast at room temperature. The formation of FLP-1b is a crucial step, as this compound acts as an intermediate in the subsequent hydrogenation reactions. The negative reaction enthalpy indicates that the process is exothermic, contributing to the stability of FLP-1b, which can then react with the unsaturated compounds.

Specifically, as show in Fig. 1, the methanimine hydrogenation reaction stands out with the lowest reaction barriers, with a $\Delta G^{\ddagger}$ value of only 4.36 kcal/mol. Thus, the hydrogenation of methanimine is predicted to be faster compared to the same process in other unsaturated compounds analyzed. In addition, the reaction energy ΔG_r for methanimine is also significantly negative, -21.13 kcal/mol, indicating that this reaction is highly exergonic, which corroborates its spontaneity. Although the hydrogenation of formaldehyde has a slightly higher Gibbs activation energy than that of methanimine, $\Delta G^{\ddagger}$ = 8.01 kcal/mol, it should still provide a quite fast hydrogenation process at room temperature. The ΔG_r value of -5.57 kcal/mol is again exergonic. Similar considerations hold with respect to the other aldehyde considered, acetaldehyde.

In contrast, the hydrogenation reactions of ethyne and ethene show significantly higher barriers, with $\Delta G^{\ddagger}$ results from 28.98 kcal/mol above. Thus, these reactions should be much slower at room temperature, which implies a less effective hydrogenation process of these molecules compared to aldehydes and methanimine using the FLP-1a catalyst.

Therefore, based on Gibbs energy results, the hydrogenation reactions of imines and aldehydes catalyzed by the FLP system investigated here are found to be the most favorable ones. This suggests that these compounds would be preferentially hydrogenated under the conditions studied, reflecting their greater reactivity compared to alkenes and alkynes. Hence, FLPs might be used in selective hydrogenation routes.

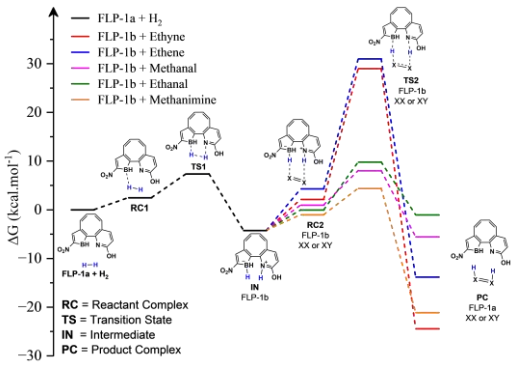


Figure 1. Reaction profiles for the hydrogenation reaction between FLP-1b species and unsaturated compounds (ethyne, ethene, formaldehyde, acetaldehyde and methanimine). Relative free energies computed at 298 K (ΔG).

These insights are highly relevant to the development of more efficient FLP systems to hydrogenation processes and can contribute to experimentalists by providing an alternative and less expensive approach to the development of new systems.

Conclusions

The results of this study show that the hydrogenation of methanimine and aldehydes (formaldehyde and acetaldehyde), mediated by the FLP-1a catalyst, provides quite small Gibbs energies of activation at room temperature, indicating a greater efficiency of these reactions compared to similar process using ethyne and ethene, for instance.

Thermodynamic and kinetic data show that methanimine is the most reactive of these unsaturated compounds as using the FLP-1a catalyst, with significantly lower $\Delta G^{\ddagger}$ values. Next, formaldehyde appears as the second most reactive unsaturated compound investigated here, followed closely by acetaldehyde.

Therefore, we can conclude that the theoretical investigation of FLPs in the hydrogenation of unsaturated compounds can provide a direction for the development of more efficient catalytic systems. Hence, the understanding of reaction barriers and relative reactivity of the different molecules contributes to advances in the design of new FLP-based catalysts.

Acknowledgements

The authors would like to thank the following institutions: IQSC-USP, UFF, CAPES (88887. 653938/2021-00), CNPq (306763/2021-4), and São Paulo Research Foundation (FAPESP – grant 2022/05138-0).

References

1. G.C. Welch, R.R.S. Juan, J.D. Masuda, D.W. Stephan. Reversible, Metal-Free Hydrogen Activation. *Science* **2006**, 314 (5802), 1124–1126.
2. D.W. Stephan. Frustrated Lewis Pairs: From Concept to Catalysis. *Acc. Chem. Res.* **2015**, 48 (2), 306–316.
3. J. Guo, M. Yan, D.W. Stephan. Frustrated Lewis pair chemistry of alkynes. *Org. Chem. Front.* **2024**, 11 (8), 2375–2396.
4. M. Heshmat, B. Ensing. Optimizing the Energetics of FLP-Type H_2 Activation by Modulating the Electronic and Structural Properties of the Lewis Acids: A DFT Study. *J. Phys. Chem. A* **2020**, 124 (32), 6399–6410.
5. G.A. Russell-Parks, T. Gennett, B.G. Trewyn. Balancing molecular level influences of intermolecular frustrated Lewis pairs (FLP) for successful design of FLP catalysts for hydrogen storage applications. *International Journal of Hydrogen Energy* **2023**, 48 (49), 18612–18633.
6. Md.N. Khan, Y. Van Ingen, T. Boruah, et al. Advances in CO_2 activation by frustrated Lewis pairs: from stoichiometric to catalytic reactions. *Chem. Sci.* **2023**, 14 (47), 13661–13695.
7. L. Liu, B. Lukose, P. Jaque, B. Ensing. Reaction mechanism of hydrogen activation by frustrated Lewis pairs. *Green Energy & Environment* **2019**, 4 (1), 20–28.
8. D. Zhuang, Y. Li, J. Zhu. Antiaromaticity-Promoted Activation of Dihydrogen with Borole Fused Cyclooctatetraene Frustrated Lewis Pairs: A Density Functional Theory Study. *Organometallics* **2020**, 39 (14), 2636–2641.
9. M. Frisch, G.W. Trucks, H.B. Schlegel, et al. Gaussian 09, revision D. 01; Gaussian, Inc., Wallingford CT, **2009**.
10. Y. Zhao, D.G. Truhlar. The M06 suite of density functionals for main group thermochemistry, thermochemical kinetics, noncovalent interactions, excited states, and transition elements: two new functionals and systematic testing of four M06-class functionals and 12 other functionals. *Theor Chem Account* **2008**, 120 (1–3), 215–241.
11. F. Jensen. Atomic orbital basis sets: Atomic orbital basis sets. *WIREs Comput Mol Sci* **2013**, 3 (3), 273–295.

Estudo de estrutura eletrônica e do perfil farmacofórico do Ponatinibe e derivados

Arthur A. Nascimento[1], Érica C. M. Nascimento[1], João B. L. Martins[1]
[1]Instituto de Química, UnB
alvesnascimentoarthur@gmail.com.
Keywords: Tyrosine Kinase Inhibitor (TKI), B3LYP, Leukemia Myeloid Cronic (LMC), BCR-ABL T315I

Abstract
In this work were studied and compared the differences between the electronic structure and structural properties coming from the hybrid basis set 6-311+g(d,p) and 6-311+g(2d,2p) applying the DFT theory with B3LYP functional for ponatinib and some derivatives molecules. They were compared based on Fukui indices, frontier orbitals, and the map using AI. This allows determining the need to expand to 2d,2p or if the gain in accuracy is not worthwhile.

Introdução

O Instituto Nacional do Câncer (INCA) estima que cada ano do triênio de 2023 a 2025 o Brasil apresentara 11540 casos de Leucemia. A leucemia mieloide crônica (LMC) é um tipo de leucemia caracterizada pela produção excessiva de glóbulos brancos, por ter uma evolução lenta e acontecer em células mieloides. (INCA; números de câncer, estimativas, 2023)

A LMC tem como fármaco de partida para seu tratamento o Imatinibe que é um inibidor de tirosina quinase (TKI). Porém atualmente o Ponatinibe é o único medicamente TKI efetivo para tratar pacientes com o mutagênico T315I da LMC. (FRANKFURT, Olga; Licht Jonathan D. Clin Cancer Res, 19(21), 2013)

Devido a sua toxicidade elevada, o Ponatinibe deixa de ser uma alternativa para tratar a LMC. Surgindo então a necessidade de novas propostas terapêuticas com o objetivo de diminuir os efeitos colaterais. Para encontrar novas moléculas derivadas do Ponatinibe é preciso entender sua estrutura eletrônica e o perfil de interações com o alvo enzimático.

Metodologia

Foi realizado o estudo de estrutura eletrônica e geométrica dos ligantes usando cálculos *ab intio* por meio da Teoria do Funcional de Densidade (DFT), usando o funcional híbrido B3LYP e as Funções de base 6-311+g(d,p) e 6-311+g(2d,2p), em meio solvatado com modelo de solvatação implícita SMD. Os cálculos foram realizados usando o software Gaussian 16. (FRISCH; Wallingford, 2016)

Os ligantes escolhidos para esse estudo foram o Ponatinibe, Vamotinibe e o N-[3,3-difluoro-2,3-dihydro-2-(4-methyl-1-piperazinyl)-1H-inden-5-yl]-3-(2-imidazo[1,2-b]pyridazin-3-ylethynyl)-4-methylbenzamide (31-Mi) (3a-p1). Essas moléculas foram escolhidas devido ao seu potencial de TKI.

Por meio das propriedades de estruturas eletrônicas calculadas foram obtidos os índices de reatividade e funções de Fukui (PARR; SZENTPÁLY; LIU, 1999) para propor qual tipo de reatividade prevalece na molécula. O mapa de potencial eletrostático foi renderizado para confrontar as regiões mais ativas dos ligantes com os resultados obtidos

Todos os dados obtidos do estudo de estrutura eletrônica e funções de Fuuki foram correlacionados utilizando a técnica de data mining Heatmap. Esse quantifica a semelhança das moléculas de acordo com os parâmetros alimentados sistemas.

Resultados

As principais diferenças entre as funções de base 6-311+g(d,p) e 6-311+g(2d,2p), foram algumas superestimações nos orbitais HOMO até HOMO-3 e LUMO até LUMO+3, a maior diferença foi no Ponatinibe. Resultando em uma diferença relevante no GAP entre as 2 funções de base,

onde o 6-311+g(2d,2p) teve um resultado mais próximo dos outros 2 fármacos.
Os LUMO+3 da função de base 6-311+g(d,p) tiveram um valor consideravelmente menores.

Conclusões

Tendo um tempo de cálculo consideravelmente maior e pouca diferença nos resultados entre as funções de base 6-311+g(d,p) e 6-311+g(2d,2p) a expansão se mostra desnecessária.

Acknowledgements

Este trabalho recebeu apoio institucional e financeiro da Universidade de Brasília, CNPq, CAPES e FAPDF.

References

1. INSTITUTO NACIONAL DE CÂNCER. Tipos de câncer: Leucemia. INCA. disponível em (https://www.gov.br/inca/pt-br/assuntos/cancer/tipos/leucemia) Acesso em: 05/2024
2. INSTITUTO NACIONAL DE CÂNCER. Números de câncer: Síntese de resultados e comentários. INCA. disponível em (https://www.gov.br/inca/pt-br/assuntos/cancer/numeros/estimativa/sintese-de-resultados-e-comentarios) Acesso em: 05/2024
3. FRISCH, M. J. et al. Gaussian 16, Revision C.01. Wallingford CT: 2016.
4. LU, Tian; CHEN, Feiwu. Journal of Computational Chemistry, 33, 580–592, 2012.
5. PARR, Robert G.; SZENTPÁLY, László V.; LIU, Shubin. E. Journal of the American Chemical Society, 121, 1922–1924, 1999.
6. DONGFENG, Zhang. et al.J. Med. Chem. 2021, 64, 7434−7452.
7. FRANKFURT, Olga; Licht Jonathan D. Clin Cancer Res, 19(21), 2013.
8. MATHEW, Thomas. et al. Bioorganic & Medicinal Chemistry Letters, 21, 3743–3748, 2011.
9. Tianjun, Zhou. et al. Chem Biol Drug Des, 75: 18–28, 2010.
10. Wei-Sheng, Huang. et al. J. Med. Chem, 53, 4701–4719 4701, 2010.
11. Wei-Sheng, Huang. et al. J. Med. Chem, 52, 4743–4756 4743, 2009
12. Thomas, O'Hare. et al. Cancer Cell, 16(5): 401–412, 2009

Electric Field Effects on Torsional Stiffness of Opened-Spiropyran Derivatives

Asdrubal Lozada-Blanco[1] Juliana Fedoce Lopes[1]
[1]Laboratório de Química Computacional - LaQC - Instituto de Física e Química, UNIFEI – Itajubá-MG - Brazil
aslozada@gmail.com
Keywords: Stress Tensor; QTAIM; AIMD; Spiropyran; Chromism

Abstract
A stress tensor stiffness analysis was applied to study electron density in opened spiropyran derivatives. Specifically, an evaluation was conducted on the effect of an electric field on the stiffness of critical bond critical points (BCPs) at pivot positions related to the torsion angles α, β, and γ of the merocyanine conformers TTT, TTC, TTC, and CTC. Our results show that for an interval of [-300,300]x10^{-4} a.u. of field strength, two sets of stiffness values are formed. Among these, CTC exhibits the lowest values, indicating higher electron density mobility in this case

Introduction

Chromism is the reversible change of color in substances arising from external factors or stimuli such as temperature, pressure, solvents, electric potential, pH and electron irradiation.[1,2] It has attracted attention due to its potential applications in the developing optical sensors and spectroscopic devices, photocatalysis, pharmacology, and others.[3]

Of interest among various chromism phenomena is the isomerization of spiropyrans (closed forms) to merocyanines (open forms).[4] While this isomerization is widely known as a photochromic process, recent years have seen increased research on how temperature variations, addition of metal ions, or application of electric potential differences affect the reversible switch between these two states.[5]

To obtain a local description of the electric field effects on the structural stability in the set of open rotational forms, merocyanines, we conducted an assessment based on the stress tensor[6] and the topology of the electronic charge density.[7]

Methodology

Four merocyanines (see the torsional model in Fig. 1), TTT, TTC, CTT, and CTC, were optimized at the M062X/Def2-TZVP level. The single point SCF calculations, with electric field strengths, Ex, Ey and Ez, in the range [-300x10^{-4} and 300x10^{-4}] a.u., were obtained at the B3LYP/SVP level.

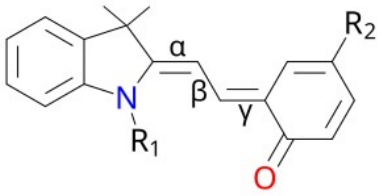


Fig. 1: Torsional model of Open-Spiropyran form. With dihedrals angles α, β and γ

A QTAIM analysis was performed for each geometric configuration to calculate critical points (NCP, BCP, RCP, and CCP), molecular graph, and ellipticity values in the electron charge density. Additionally, a stress tensor stiffness calculation was performed. The first calculation was done with Multiwfn[8], and the second with our own implementation for Multiwfn. The patch, written in Fortran language, can be found and downloaded from the repository

https://github.com/aslozada/Stress_tensor. Further discussion about this patch can be found at the Multiwfn Forum topic: "How to conduct a stress tensor analysis?"

Our implementation uses Bader's Stress Tensor model[7], and for the stiffness calculation we use the expression $S_\sigma = |\lambda_{1\sigma} / \lambda_{3\sigma}|$, where $\lambda_{i\sigma}$ are the eigenvalues of the stress tensor matrix.

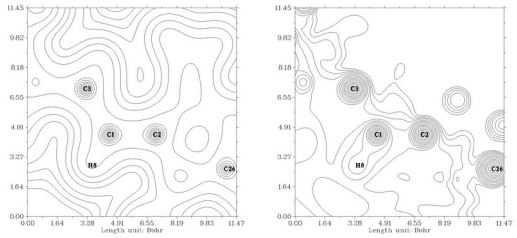
Results and Discussion

The stress tensor stiffness values computed for the optimized geometries of the merocyanine conformers (TTT, TTC, CTT, and CTC) at the BPCs corresponding to the torsion angles α, β, and γ are presented in Table 1. The values at α describe two sets of stiffness of the bond-path. In which the bond paths in TTT, CTT, and TTC are more rigid than the bond paths in CTC

Table 1: Stress tensor stiffness for merocyanine conformers at the corresponding pivots of the α, β, and γ rotation angles

	α	β	γ
TTT	4.21	2.36	2.4
TTC	4.24	2.35	2.39
CTT	4.25	2.36	2.41
CTC	4.11	2.36	2.41

Fig. 2 shows a contour map of electron density in the plane defined by the pivot corresponding to the torsion angle α. (a) and (b) depict the density values with and without applying an electric field, respectively. To define the upper limit of electric field application, a field strength of 2.0 a.u. was used before bond-path depletion. As can be observed, this electric field notably distorts the charge density.



(a) (b)

Fig. 2: Contour map of electron density in α pivot: a) without electric field, 0.0 a.u. and b) for a strong electric field, 2.0 a.u

An increase in the intensity of the applied electric field results in a reduction in stress tensor stiffness values. The maxima for this stiffness in each merocyanine conformer are found within the range [-50,50] a.u. Throughout the range of electric field applications, the two described groups remain unchanged. These results are shown in Fig. 3. For electric field strengths greater than 0.03 a.u., the electron density is strongly distorted, with some bond-paths formed and others depleted; therefore, the stiffness analysis can no longer be applied.

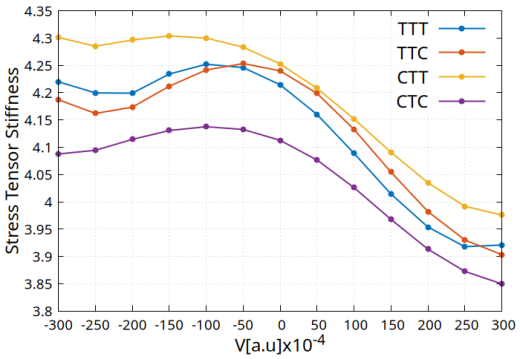


Fig. 3: Variation of the Stress tensor stiffness at the pivot α with the electric field

Conclusions

The stress tensor stiffness analysis is a useful tool for describing the responsiveness of electron density to external factors. Due to its vector nature, it also indicates the direction of electron density movement. In this study, framed within the context of the spiropyran-merocyanine isomerization process, the stress tensor stiffness values allow a detailed description of the ease of rotational distortion of electron density. Our results show that, in terms of the Stress tensor stiffness, the conformers of merocyanine can be grouped into two sets: one with TTT, CTT, and TTC, and another with CTC, which exhibit lower values.

Acknowledgements

We acknowledge financial support from the National Council for Scientific and Technological Development (CNPq -Brazil, grant 150836/2023-6), and Minas Gerais State Agency for Research and Development (Fapemig - Brazil). We also thank the Physics and Chemistry Institute of Federal University of Itajubá.

References

1. Morsumbuil, S.; Akçakokca Kumbasar. E. P.; IOP Conf. Ser.: Mater. Sci. Eng. 2018, 459, 012053

2.Bamfield, P; Hutchings, M; Chromic Phenomena: Technological Applications of Colour Chemistry; 2018, RSC

3. Abdollahi, A; Roghani-Mamaqani, H.; Razavi, B.; Prog. Poly. Sci. 2019, 98, 101149

4. Kortekaas, L; Browne. W. R.; Chem. Soc. Rev., 2019, 48, 3406

5. Wang, P-X; Bai, F-Q; Zhang, Z-X; Wang, Y-P; Wang, J; Zhang, H-X; Org. Elec., 2017, 45, 33

6. Jenkins, S; Kirk, S. R.; Next Generation Quantum Theory of Atoms in Molecules; 2023. Springer

7. Bader, R.F.W.; Atoms in Molecules: A Quantum Theory; 1990, Oxford University Press

8 Lu, T; Chen, F.; *J. Comput. Chem.*, 2012, 33, 580.

10º SIMPÓSIO DE ESTRUTURA ELETRÔNICA & DINÂMICA MOLECULAR
SEEDMOL 4 a 8 novembro | 2024
Pirenópolis, Goiás

Kanon: Software to compute chirality indices and assess molecular symmetry

Asdrubal Lozada-Blanco[1]
[1]Laboratório de Química Computacional - LaQC - Instituto de Física e Química, UNIFEI – Itajubá-MG - Brazil
aslozada@gmail.com
Keywords: Chirality; Hausdorff distance; Quaternions; Symmetry; Graphs; Nanostructures

Abstract
Kanon is an open-source software for computing chirality indices and assessing molecular symmetry. In the current version, kanon: i) computes chirality indices from nuclear arrangements, volumetric data, and real-valued functions, ii) computes graph automorphisms, iii) obtains the torsion degree of molecular surfaces, iv) builds surfaces by triangulation of volumetric data, and v) calculates standard molecular symmetry descriptors. Kanon is presented as an efficient tool for the study of nanostructured and supramolecular systems. Additionally, due to its modular structure, the addition of new functionalities or integration with other programs is facilitated.

Introduction

Symmetry, shape, and similarity are widely used concepts in areas such as chemistry, biochemistry, spectroscopy, material design[1], image analysis, and robotics, and they remain open problems in mathematics. Through these concepts, methodologies, techniques, and models for describing chirality in substances have been proposed for over a century[2]. Additionally, with the advent and growth of material development in increasingly larger scales and with more functionalities to evaluate, the need for more efficient methodologies to evaluate these properties or their derivatives becomes necessary.

Focusing on the analysis of these properties in supramolecular, nanostructured, and mesoscale models, an efficient computational implementation called *kanon* is presented for such calculations.

Kanon is an open-source software initiated at the Theoretical Chemistry Laboratory of the Federal University of São Carlos. In its current version, 1.3, it is available for collaboration to anyone interested.

Theoretical Background

Kanon implements two types of second-order chirality indices based on Euclidean distances and non-Euclidean distances: Hausdorff and Wasserstein.

In the Euclidean and Wasserstein models[3], the chirality indices, χ, are defined as follows:

$$\chi = \frac{d}{4T} Min_{(P,R,t)} D^2$$

where d represent the space dimensionality, P the allowed permutations, R the set of isometries, and D^2, are the sum of square or square difference between probability distributions. On the other hand, the Hausdorff-based chirality[4] index is defined as

$$\chi_H = \frac{d_{H_{min}}(Q, Q')}{d(Q)}$$

where $d_{H_{min}}$ is the minimized Hausdorff distance between a set and its mirror image, and *d(Q)* denotes the set's diameter. In both cases, the optimal superposition is treated as an eigenvalue problem, achieved through the optimal rotation described using quaternions as

$$\langle q|Bq\rangle$$

where q a unitary quaternion and B a 4x4 symmetric matrix.

The usage of kanon

Kanon is a stand-alone, serial, and parallelizable, Fortran code[5]. Its source code is compilable with Fortran compilers as GNU Fortran (GCC) or Intel Fortran Compiler, with the interface Openmp.

For installation, clone or download the source code from the github repository `github.com/aslozada/kanon`. There are two mechanism available: using teh makefile or the Fortran Package Manager (fpm). For the second case, use `fpm build`. These methods generate the executable binary `kanon`.

Kanon execution

To run kanon, a XYZ coordiantes file is needed. This file type can describe an arrangement of nuclei, a set of critical points of a real-valued function, or volumetric data. The simple execution mode is as follows:

```
./kanon <options> coor.xyz
```

By default, the output will be written to standard output. Below, some command-line options in the current version are described.

`--single`: Compute the chirality index from the coor.xyz file

`--pattern`: Input the pattern molecule XYZ file

`--image`: input a mirror image of molecule XYZ file

`--torsion`: compute the torsion angle for a molecular surfaces

`--monolayer`: compute the torsion angles in molecular monolayers models

`--bilayer`: compute the torsional angles in bilayers models

`--delaunay`: Build a set triangles on 2D surface

`--trajectory`: compute the chiral index for an ensemble of frames of XYZ files or trajectory

The point group and the generic symmetry descriptors are calculated by default.

Some results from kanon

Hausdorff Chirality Measure (HCM) for biphenyl model, input arrangement nuclei

Along the torsional angle, the HCM was calculated. The set of Cartesian coordinates or trajectory starts at 0º with point group D_{2h}, passes through an intermediate configuration D_2 at 45º, and reaches 90º with point group D_{2h}. The full trajectory ranges from 0º to 180º. The HCM describes minimum values for the structures with D_{2h} at 0º and 90º, and maximum values for the structures with D_2 at 45º and 135º. See Fig. 1.

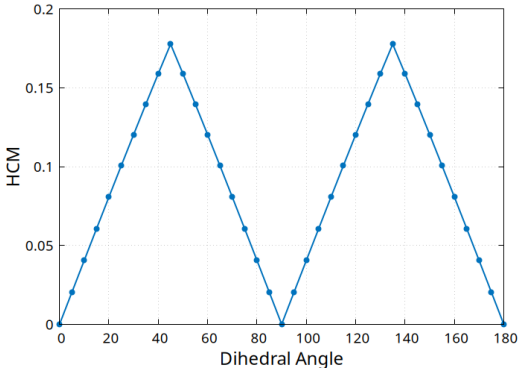


Fig. 1: HCM values along rotational dihedral angle in the biphenyl molecule model

Chirality measure from real valued-functions

This application can be performed using extrema values in R^3, such as Morse critical points or volumetric data.

Chirality index in nanostructure systems

The HCM was computed for Yoshida's C_{100} fullerenes. The values for C_1, D_5 and D_{2h} structure are 0.113, 0.088 and 0.00 respectively. See Fig. 2

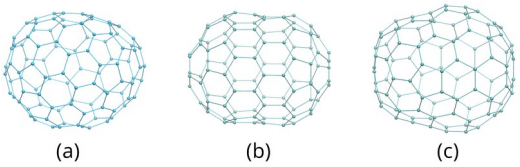


Fig. 2: Yoshida's C_{100} fullerene models: a) C_1, b) D_5 and c) D_{2h}

Folded monolayer orientations

The yellow arrows in Fig. 3 describe the local orientation of the surface of the magnetic monolayer nanostructure. Each normal vector is obtained by defining a set of triangular subsurfaces.

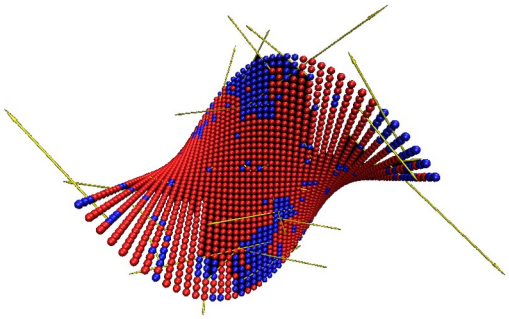
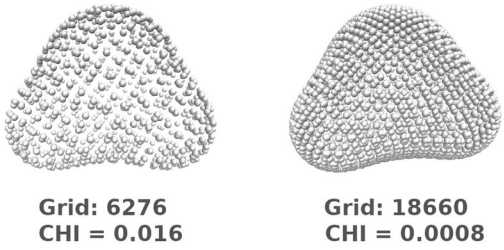


Fig. 3: Hyperbolic parabolid magentic nanostructure. The yellow arrow indicates the normal modes to surface

Volumetric data

The chirality is also calculated for a set of points in volumetric data. Figure 4 depicts the effect of grid quality on the x-values. The grid corresponds to isodensity values of 0.05 electron density of a water molecule. In this model, the variability is associated with the unequal description of spheroidal regions through triangulation.



Conclusion

Kanon is a useful tool for exploring properties associated with chirality, symmetry, and shape. Due to its efficiency in handling quaternion spaces and parallelization, it is a versatile tool for studying nanostructures and supramolecular systems. Kanon is presented to the community as an open-source tool intended for collaborative use or modification to meet research needs.

Acknowledgements

Kanon is a project started at the Theoretical Chemistry Laboratory (LQT) of the Federal University of São Carlos. The author thanks the laboratory for providing computational resources, physical infrastructure, and suggestions regarding the program's applicability.

References

1. Zhang, Y. et al.; Nano Lett., 2023, 23, 9280

2. Petitjean, M.; Entropy, 2003, 5, 271

3. Petitjean, M.; *J. Math. Phys. 2002*, 43, 4147

4. Buda, A.; T. Auf der Heyde; K. Mislow, Angew. Chem. Int. Ed., 1992, 31, 989

5. L. J. Kedward L. J. et. al.; Computing in Science & Engineering, 2022, 24, 63

DFT study of a heterodimer of the antihypertensive drug candesartan cilexetil with oxalic acid occurring in a solid dispersion

Moura, A. C.[1], Silva, A. P.[1], Ribeiro, P. R. S.[1], Lima A. D. S. G.[1], Lage, M. R.[1]
[1]Programa de Pós-Graduação em Ciência dos Materiais (PPGCM), Centro de Ciências de Imperatriz (CCIM), Universidade Federal do Maranhão (UFMA), Imperatriz, Maranhão, 65.900-410, Brazil.
Ayslla.moura@discente.ufma.br
Keywords: Candesartan Cilexetil; Oxalic Acid; Intermolecular Interaction; DFT; Solid Dispersion.

Abstract
In this work, a theoretical study of the antihypertensive drug candesartan (CAN) and acid oxalic (OXA), as well as of the heterodimer CAN-OXA, was carried out based on density functional theory (DFT). The electronic structure calculations were performed with the functional ωB97X-D combined with the basis set 6-311++G(d,p), considering solvation effects in methanol with the integral equation formalism of the polarizable continuum model (IEFPCM). Structural, electronic, spectroscopic, and thermodynamic properties of CAN, OXA, and the heterodimer CAN-OXA were studied, contributing to the characterization of these systems and a better understanding of their behavior in the body.

Introduction
Crystalline drugs are poorly soluble in water, resulting in their low bioavailability in the human body. Therefore, the search for strategies to improve the solubility of these drugs is essential. An outstanding strategy for this purpose is the preparation of solid dispersions using water-soluble coformers. Among these interactions, hydrogen bonding plays a significant role in the formation of new materials such as coamorphs. Therefore, theoretical studies using DFT are used to predict the interaction between the molecules. This type of theoretical study accelerates the development of new solid dispersions and provides deeper insights about their properties [1][2].

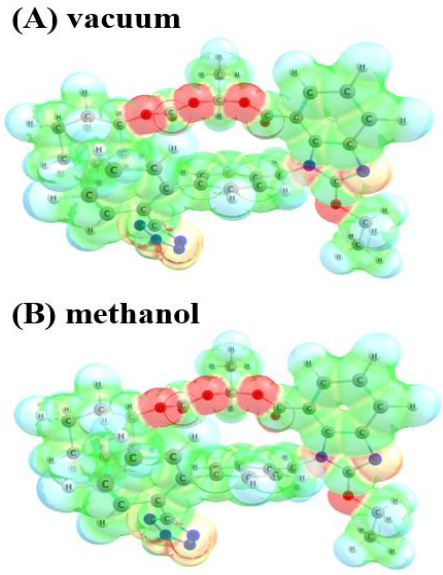
Methodology
The Gaussian 16 software was used for all the calculations in this work, employing the DFT functional ωB97X-D combined with the basis set 6-311++G(d,p), considering the solvation effects in methanol with the integral equation formalism of the polarizable continuum model (IEFPCM). The graphical interface software Avogadro was used to manipulate the structures obtained from the CCDC (The Cambridge Crystallographic Data Center) database to create the input files. The ChemCraft software was used to explore the output files and create the images. A correction factor of 0.957 [3] was applied to the spectroscopic data for a better fit of experimental and theoretical spectra. The different starting geometries tested to get the most stable interaction in the heterodimer CAN-OXA were built from the optimized geometries of CAN and OXA. Variations of Gibbs free energy (ΔG^{298}), enthalpy (ΔH), and total electronic energy corrected with zero-point vibrational energy (ΔE_{ZPVE}) were calculated in the search for the most stable interaction. Basis set superposition error (BSSE) was considered in the study of the interactions.

Results
Figure 1 presents the electrostatic potential maps of the molecules in vacuum and in methanol. The regions in red are electron-rich and can be considered the electron donor in the formation of hydrogen bonds, while the regions in blue are those prone to receive the electron density. Table 1 shows the thermodynamic parameters calculated in

the study of the interaction in the heterodimer, confirming that the interaction found is favorable. Figure 2 presents the optimized geometry of the most favorable interaction in the heterodimer CAN-OXA, from which it is possible to verify that the interaction is governed by hydrogen bonds occurring between the H(83) atom of OXA and the N(9) atom of CAN, as well as between the O(80) atom of OXA and H(79) atom of CAN.

Table 1. Thermodynamic properties for the interaction in the heterodimer CAN-OXA in kcal/mol.

Properties	CAN-OXA (vacuum)	CAN-OXA (methanol)
ΔH	-16.56	-9.79
ΔG^{298}	-4.21	1.53
ΔE_{ZPVE}	-16.66	-10.16
ΔE_{ZPVE} + BSSE	1.86	1.36



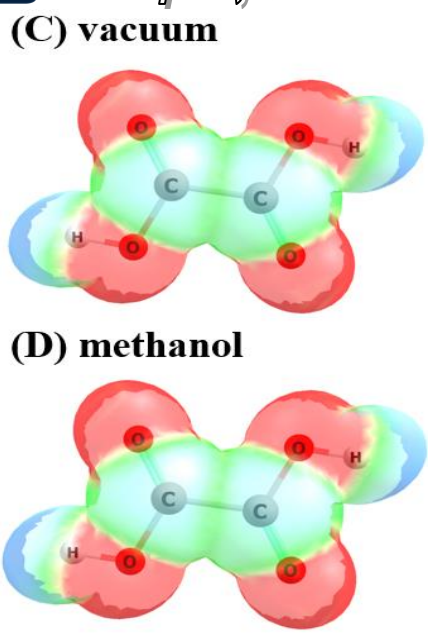


Figure 1. Electrostatic potential maps of CAN (a) and (b), and OXA (c) and (d).

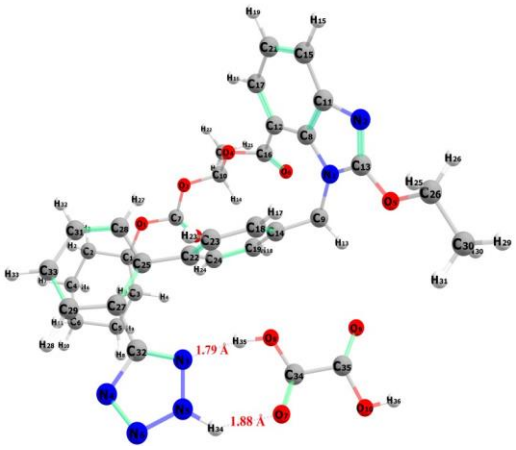


Figure 2. Optimized geometry of the heterodimer CAN-TRIS in a vacuum, as obtained from the DFT calculations.

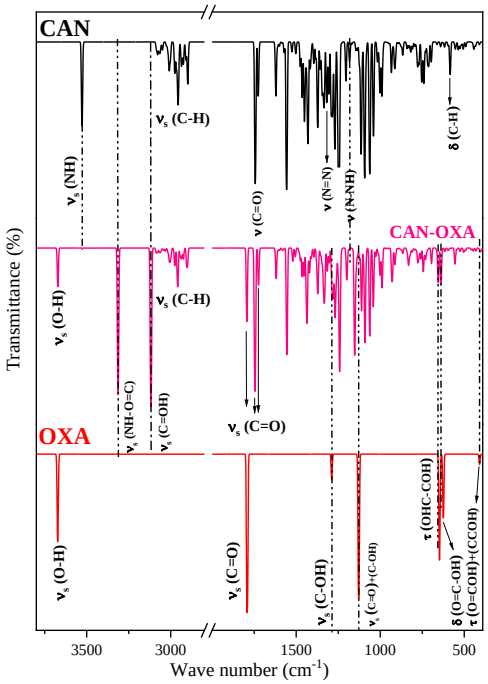


Figure 3. Theoretical FT-IR spectra of CAN, OXA and the heterodimer CAN-OXA in a vacuum corrected with the scale factor 0.957.

Discussion

The electrostatic potential maps (Figure 1) showed that the functional groups present in CAN (carbonyls, tetrazole group, ethers, and amines), corresponding to red regions, are those prone to interact with the carboxyl group in OXA. From this analysis, the study of the interaction between molecules was carried out. The computational calculations for the heterodimer CAN-TRIS were also developed in a vacuum and also in methanol, to account for the solvation effects on the interaction. It allowed us to observe that the solvation effects on the thermodynamics of the interaction are important since the interaction in a vacuum is favorable, with a negative value of ΔG^{298} (Table 1), while the ΔG^{298} in methanol is positive. This explains the formation of the material with the evaporation of solvent molecules. One of the determining evidence of the formation of hydrogen bonds is the distance between the O and H atoms. The distances in the interaction of the heterodimer CAN-OXA in a vacuum were 1.79 Å (N···H) and 1.88 Å (O···H), confirming the hydrogen bonds in the heterodimer studied. Figure 3 shows the FT-IR spectra of CAN, OXA and the heterodimer CAN-OXA, which provided additional evidence confirming the interaction between the drug and the coformer in the formation of the solid dispersion. This analysis was based mainly on the displacements of bands observed in the spectrum of the solid dispersion, caused by the interactions. But other changes were also observed in the spectrum of the solid dispersion in relation to those of CAN and OXA (indicated in the dashed line black) [5].

Conclusions

Through the theoretical study described, it was possible to find the most favorable interaction in the heterodimer CAN-OXA, confirming the occurrence of a hydrogen bond between the drug and the coformer. Also, it was confirmed that the method is accurate enough to provide structural, electronic, and spectroscopic data in good agreement with those obtained from the experiments, contributing to the characterization and a deeper study of the CAN, OXA, and the heterodimer CAN-OXA.

Acknowledgements

Digital Research Alliance of Canada

References

1. WANG, Bing et al. European Journal of Pharmaceutical Sciences, v. 96, p. 45-52, 2017.
2. WALDEN, Daniel M. et al. Molecules., v. 26, n. 1, p. 182, 2021.
3. Johnson R. Johnson, R. Computational Chemistry Comparison and Bench- mark Database, NIST Standard Reference Database 101 (National Institute of Standards and Technology, 2002). 2002. 2002;101: 2002.
4. Godfrey, Peter D.; Brown, R. D.; The Journal of Physical Chemistry A, v. 104, n. 2, p. 258-264, 2000.
5. Parthasarathi, R.; Subramanian, V. Characterization of hydrogen bonding. Hydrogen bonding—new insights, p. 1-50, 2006.

First Report on the Formation of a Secnidazole Coamorphous with Mandelic Acid: A Theoretical-experimental Study

João G. de Oliveira Neto[1], Ayslla C. Moura[1], Jailton R. Viana[1], Rossano Lang[2], Adenilson O. dos Santos[1], and Mateus R. Lage[1].
[1]Center for Social Sciences, Health, and Technology, Federal University of Maranhão - UFMA, 65900-410 Imperatriz, MA, Brazil.
[2]Institute of Science and Technology, Federal University of São Paulo - UNIFESP, 12231-280 São José dos Campos, SP, Brazil.
E-mail: *ayslla.moura@discente.ufma.br*
Keywords: Solid dispersions; Secnidazole; DFT calculations; Hirshfeld surfaces; ADME.

Abstract
The need to optimize pharmaceutical processes and drug a top priority for the pharmaceutical industry. This approach aims to enhance drugs' physicochemical and biopharmaceutical properties, including stability, solubility, bioavailability, and biological activity. In light of this, theoretical and experimental studies were conducted herein using the antimicrobial agent secnidazole (SNZ), an effective drug employed in the fight against neglected diseases. In this context, a solid dispersion of SNZ was prepared time using the isothermal evaporation method, with mandelic acid (MND) as a coformer. The research involved structural and thermal characterizations, as well as theoretical calculations of geometric, thermodynamic, and electronic properties based on density functional theory (DFT). Additionally, complementary computational assays explored Hirshfeld surfaces and estimated absorption, distribution, metabolism, and excretion (ADME) parameters of the starting materials. Biological experiments were developed to test this coamorphous against a variety of gram-positive and gram-negative bacteria. The X-ray diffraction (XRD) results revealed the formation of a new coamorphous in an equivalent molar proportion of SNZ and MND, indicating its physical stability for at least 60 days. DFT studies suggest an intermolecular drug-conformer interaction between the imidazole ring of SND and the carboxyl group of MND. This contact is also indicated through a detailed analysis of the favorable sites on the Hirshfeld surfaces corresponding to the individual chemical species. DSC data showed that the glass transition of the binary system occurs around 106 °C. Furthermore, the variation of Gibbs free energy, enthalpy, and electronic energy corrected with zero-point vibrational energy with the interaction indicate that the formation of the SNZ-MND coamorphous is spontaneous in vacuum. Additionally, antibacterial activity of this coamorphous was confirmed against Staphylococcus aureus, Streptococcus mutans, Klebsiella pneumoniae, and Pseudomonas aeruginosa species. Similarly, the ADME descriptors suggest a promising pharmacokinetic profile for developing future pharmaceutical agents based on the SNZ drug.

Introduction
The drug SNZ is classified as a powerful broad-spectrum antimicrobial and antiprotozoal medicament, exhibiting effective clinical treatment against several infections, including trichomoniasis, amoebiasis, among others [1]. However, due to its physical and pharmacokinetic limitations, the synthesis of binary solid dispersions has intensified over the years to overcome these adversities [2].
Although solid dispersions of SNZ, including salts and cocrystals, have been related in the literature, no coamorphous system has been previously reported [3]. To overcome the physical instability of SNZ,

we selected MND as the coformer to prepare a noncrystalline binary system. MND is widely used in the pharmaceutical industry due to its bioactive properties in treating skin diseases [4]. Our investigation aims to bridge this gap by designing a novel coamorphous formulation of SNZ and optimizing its physicochemical and biological properties.

Additionally, it is essential to understand how molecular units interact in an amorphous material, which is why computational calculations are widely used in these systems to adjust physicochemical properties and pharmacokinetic parameters [5]. DFT, for example, allows the elucidation of geometric, thermodynamic, and electronic parameters that provide a suitable description of molecular systems. In addition, theoretical methodologies based on Hirshfeld surfaces allow for the prediction of the contact sites between the chemical species forming the coamorphous.

In this context, here we report for the first time a SNZ coamorphous using the MND as a conformer (SNZ-MND). Its structural, thermal, and bactericidal properties were explored and discussed. Furthermore, computational calculations based on DFT, Hirshfeld surfaces, and ADME were employed to support the experimental results and provide parameters that help to contribute to the design of improved solid dispersions of SNZ.

Methodology

The coamorphous SNZ-MND was prepared by the isothermal evaporation method in 30 mL using an equimolar ratio (0.1 mol/L). The starting compounds SNZ and MND (both supplied by Sigma-Aldrich with purity >99%) were homogenized by magnetic rotation at 360 RPM for a period of 5 h. Subsequently, the solution was filtered and allowed to evaporate slowly under ambient conditions until the nucleation of the solid phase.

The SNZ-MND coamorphous and the starting materials SNZ and MND were characterized by XRD and DSC using a PANalytical diffractometer (model Empyrean) and a Shimadzu thermal analyzer (model DSC-60), respectively.

DFT calculations were performed on the SNZ-MND heterodimer and the individual molecules SNZ and MNZ. The structures were explored with Chemcraft 1.8 software and optimized from the ωB97X-D functional and the 6-311++G(d,p) basis set. In this methodology, the solvation effect in ethanol was considered using the integral equation formalism of the polarizable continuum model (IEFPCM), as implemented in the Gaussian16 software.

Interaction sites were identified from three-dimensional Hirshfeld surfaces using CrystalExplorer software, while pharmacokinetic descriptors were estimated using SwissADME software.

Microbiological experiments were conducted using four distinct bacterial strains, which were cultivated and supplemented in specific media, as described in the literature [6].

Results and discussion

A structural analysis via XRD showed that the SNZ-MND binary system has an amorphous nature, since it does not present Bragg reflections corresponding to the SNZ and MND phases, as shown in Fig. 1.

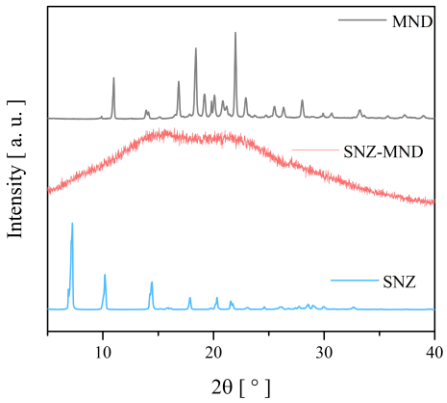


Fig. 1 – XRD pattern recorded at ambient conditions for the compounds SNZ, MND, and SNZ-MND.

In summary, the SNZ, and MND units in a 1:1 molar ratio interact through weak dispersive forces, tending to form a disordered atomic arrangement that results in a multiphase coamorphous solid dispersion. Furthermore, it was observed that the material remained amorphous for at least 60 days.

To understand how non-covalent interactions occur in the coamorphous

lattice of SNZ-MND, Hirshfeld surfaces were generated for the SNZ and MND species, as shown in Fig. 2. The reddish regions around the O, N, and H atoms indicate the sites suitable for the formation of intermolecular interactions.

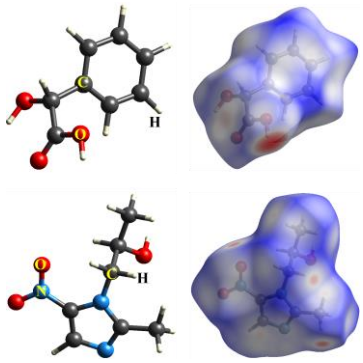


Fig. 2 – Hirshfeld surfaces of MND (up) and SNZ (down) molecules mapped according to normalized distance.

The optimized structure of the SNZ-MND heterodimer is shown in Fig. 3, where it is possible to verify that the contact occurs between the N atom that has free electrons present in the imidazole ring of SNZ and the O atom located in the carboxylic group of MND. In addition, the calculated thermochemical parameters indicate that this interaction is favorable and stabilizes the structural lattice (Table 1).

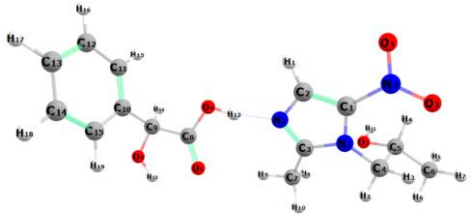


Fig. 3 – Optimized structure of SNZ-MND heterodimer calculated from the ωB97X-D/ 6-311++G(d,p) method.

Table 1. Thermodynamic properties for the interaction in the heterodimer CAN-OXA in kcal/mol.

Properties	SNZ-MND (vacuum)	SND-MND (methanol)
ΔH	-2.84	-0.51
ΔG^{298}	-13.04	-10.90
ΔE_{ZPVE}	-13.47	-11.33

Additionally, from the experimental DSC analysis, a glass transition was detected around 106 °C, which characterizes the amorphous lattice of SNZ-MND, corroborating the XRD data.

The antibacterial activity of the SNZ-MND coamorphous was confirmed through microbiological experiments against the bacteria Staphylococcus aureus, Streptococcus mutans, Klebsiella pneumoniae, and Pseudomonas aeruginosa, exhibiting minimum inhibitory concentrations of 50, 200, 100 and 50 µg/mL, respectively. The ADME results reinforce the antibacterial potential of SNZ-MND and present promising indices for improved SNZ-based drug development.

Conclusions

The first coamorphous system of SNZ was successfully obtained using the isothermal evaporation method, with MND as the conformer in equimolar proportions. Computational calculations revealed favorable interaction sites between chemical species, and DFT results confirmed spontaneous product formation. Additionally, the coamorphous system exhibited antibacterial activity against both gram-positive and gram-negative bacteria. ADME data suggest that this coamorphous formulation possesses pharmacokinetic properties suitable for drug development and enteral administration.

Acknowledgments

FAPEMA, CAPES, CNPq, Digital Research Alliance of Canada.

References

1. Pontes, A. G. O. et al.; J. Mol. Struct. 2024, 1311, 138374.
2. Muzny, C. A. Kissinger, P. J. J.; Sex. Transm. 2023, 50, 10.
3. Zheng, K. et al.; J. Mol. Struct. 2019, 1197, 727.
4. Jayaprakash, P. et al.; J. Mol. Struct. 2017, 1148, 314.
5. Sá, M. R. et al.; Int. J. Pharm. 2022, 615, 121500.
6. Oliveira Neto, J. G. et al.; J. Mol. Liq. 2024, 403, 124846.

10º SIMPÓSIO DE ESTRUTURA ELETRÔNICA & DINÂMICA MOLECULAR
SEEDMOL 4 a 8 novembro | 2024 Pirenópolis, Goiás

Reactivity of Phenolate-Based Zwitterions with CO_2 in the Aqueous Phase

Bruno Bercini de Araújo[1], Paulo Fernando Bruno Gonçalves[1]
[1]Instituto de Química – Universidade Federal do Rio Grande do Sul – UFRGS, Campus do Vale, Av. Bento Gonçalves, 9500, Agronomia, Porto Alegre – RS, 91509-900
bruno.bercini@gmail.com
Keywords: Chemical reactions; DFT; Green Chemistry; Zwitterions; CO_2 reactions.

Abstract

In this present work we studied the effect of electron donating and withdrawing groups in the reactivity of phenolate-based zwitterions with CO_2. Employing the ωB97XD functional and a mixture of triple and quadruple-ζ basis functionals we found that EDG have the general tendency to decrease the reaction energy barrier, ΔH and ΔG. A more complex effect was observed for EWG, as stronger character does not lead to an increase in reaction energy barrier.

Introduction

Reduction of atmospheric CO_2 is an ever-increasing major topic as the effects of climatic changes are more pronounced. To guarantee a viable earth to our future generations, methodologies of capture and reduction of carbon are necessary.

Within the wide range of methodologies developed, ionic liquids stands out due to their ecofriendly nature, low vapor pressure and efficacy.[1] However, their application encounter several challenges as high costs, high viscosity and density.[2,3]

In this context, ideal liquid sorbent is seen a work around those issues. In our work, Density Functional Theory (DFT) is employed to study the reactivity of phenolate-based zwitterions with CO_2 and substituents effects in their reactivity.

Methodology

All reactions were studied with DFT as implemented in the Gaussian 16 rev A.03 package.[4] The hybrid and range-separated functional ωB97XD was employed throughout all calculation. Range-separated functional are particularly recommended for assessing barrier heights[5] and the ωB97X functional family have demonstrated good performances in benchmarks sets.[6] Additionally, dispersion effects were incorporated using D2 empirical dispersion model defined in ωB97XD.[7]

For structure optimizations and vibrational analysis, the triple-ζ basis set DEF2-TZVPP was employed. Minimum energy structures were confirmed by the absence of imaginary frequencies, while transition states were identified by the presence of exactly one imaginary frequency. Energy calculations were performed with the DEF2-QZVPPD basis set. All thermodynamics quantities were evaluated at 298.15 K. Water was implicitly simulated with solvation model density (SMD).[8] Atomic charges were obtained with the CHELPG method.[9] Multiwfn was used to calculate Mayer bond orders.[10–13]

Results and Discussion

In our previously work, [3] we demonstrated that the phenolate based zwitterion is fully capable to react with CO_2 in aqueous medium. To modulate its reactivity, four substituents were chosen to either increase (electron donating groups, EDG) or decrease (electron withdrawing groups, EWG) the oxygen atomic charge. In Figure 1 illustrate the five molecules studied. Throughout the text, these compounds will be referred to by their respective substituents.

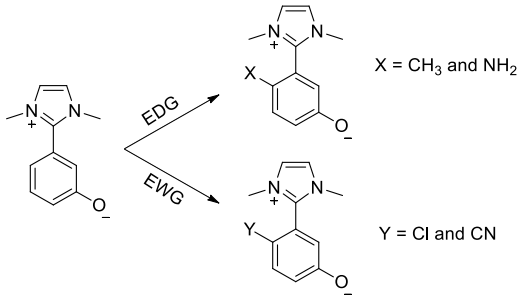


Figure 1. Phenolate based zwitterions studied.

The atomic charge on the oxygen atom behaves as expected as seen in Table 1. As NH_2 and CN substituent are the strongest donating and withdrawing groups, respectively, their effects are more pronounced.

Table 1. Oxygen atomic charge in all studied compounds.

Molecule	***Oxygen atomic charge***
Phenolate	-0.995
CH_3	-0.997
NH_2	-1.027
Cl	-0.974
CN	-0.918

Analysis of barrier heights, ΔH and ΔG, revealed that all reactions followed the same mechanism, regardless of the substituent. Generally, the phenolate ion facilitates the reaction between water (H_2O), which interacts with the oxygen atom of the phenolate, and carbon dioxide (CO_2), as depicted in Figure 2. This reaction results in the formation of a phenolate cation and carbonic acid.

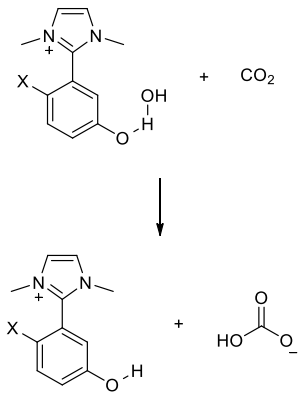


Figure 2. General reaction of the phenolate and water with CO_2.

It was observed that EDGs were effective in lowering the energy barriers, ΔH and ΔG, as seen in Table 2. These findings are consistent with observations reported in studies of ionic liquids based on phenolates.[1,14]

Table 2. Energy barriers, ΔH and ΔG in kcal·mol^{-1} for all reactions studied.

Molecule	***Barrier*** ***(kcal·mol^{-1})***	***ΔH*** ***(kcal·mol^{-1})***	***ΔG*** ***(kcal·mol^{-1})***
Phenolate	7.14	-7.43	-7.41
CH_3	6.87	-8.74	-9.80
NH_2	6.48	-10.04	-9.41
Cl	7.40	-6.32	-5.78
CN	6.99	-2.89	-3.31

For EWG, the results were not so clear as, according to the literature,[14] higher oxygen atomic charge (more positive) should lead to higher energy barriers. However, this fact was found not to be true for the cyan group, which is a stronger EWG than chlorine. The cyan group had an energy barrier 0.41 kcal·mol^{-1} than chlorine. A closer look on the EWG results, reveals that both, cyan and chlorine, has similar destabilizing effects on the transition state. However, the cyan group has a particular high destabilizing effect on the Phenolate+H_2O complex. This factor alone can explain the lower energy barrier associated with the cyan group.

In contrast, the ΔH and ΔG values followed our expectations as stronger EDG or EWG lead to lower and higher values, respectively.

To understand the influence of the substituents on the reaction, the Mayer bond order of the Phenolate-O-H-OH was analyzed in Table 3. We expected that a more negative charged the oxygen atom, stronger the O-H bond, leaving the OH^- more available to react with the CO_2.

Table 3. Mayer bond orders for the Phenolate-O-H-OH bond.

Molecule	***Mayer Bond Order Phenolate-O-H-OH***
Phenolate	0.19
CH_3	0.20
NH_2	0.21

Cl	0.19
CN	0.17

Despite of our expectations, the bond order had similar values, indicating that the substituent group does not significantly affect the phenolate and water interaction, instead, they primarily influence the stabilization of the phenolate itself.

Conclusion

Employing the ωB97XD/DEF2-QZVPPD//ωB97XD/DEF-TZVPP protocol we were able to study the reaction of five different phenolate based zwitterions with CO_2 in water. It was observed that EDG and EGW have different effects in energy barriers, ΔH and ΔG. For EDG, a stronger donor character of the substituent corresponds to a lower energy barrier. In contrast, the effect of EWGs is more complex; a stronger withdrawing character does not necessarily lead to higher energy barriers. The bond order analysis shows little to no effect of the substituent in the ability of the phenolate to interact with water.

Acknowledgements

This study was financed in part by the Coordenação de Aperfeiçoamento de Pessoal de Nível Superior - Brasil (CAPES) - Finance Code 001 and by the Conselho Nacional de Desenvolvimento Científico e Tecnológico (CNPq).

References

1. Sheridan, Q. R., Schneider, W. F. & Maginn, E. J. Role of Molecular Modeling in the Development of CO 2 –Reactive Ionic Liquids. *Chem. Rev.* **118**, 5242–5260 (2018).
2. Halliday, C. & Hatton, T. A. Sorbents for the Capture of CO2and Other Acid Gases: A Review. *Ind. Eng. Chem. Res.* **60**, 9313–9346 (2021).
3. Aydos, G. L. P. *et al.* Zwitterionic "Solutions" for Reversible CO2 Capture. *ChemSusChem* **16**, 1–13 (2023).
4. Frisch, M. J. *et al.* Gaussian 16, Revision A.03. (2016).
5. Bursch, M., Mewes, J. M., Hansen, A. & Grimme, S. Best-Practice DFT Protocols for Basic Molecular Computational Chemistry**. *Angew. Chemie - Int. Ed.* **61**, (2022).
6. Goerigk, L. *et al.* A look at the density functional theory zoo with the advanced GMTKN55 database for general main group thermochemistry, kinetics and noncovalent interactions. *Phys. Chem. Chem. Phys.* **19**, 32184–32215 (2017).
7. Chai, J. Da & Head-Gordon, M. Long-range corrected hybrid density functionals with damped atom-atom dispersion corrections. *Phys. Chem. Chem. Phys.* **10**, 6615–6620 (2008).
8. Marenich, A. V, Cramer, C. J. & Truhlar, D. G. Universal Solvation Model Based on Solute Electron Density and on a Continuum Model of the Solvent Defined by the Bulk Dielectric Constant and Atomic Surface Tensions. *J. Phys. Chem. B* **113**, 6378–6396 (2009).
9. Breneman, C. M. & Wiberg, K. B. Determining atom-centered monopoles from molecular electrostatic potentials. The need for high sampling density in formamide conformational analysis. *J. Comput. Chem.* **11**, 361–373 (1990).
10. Lu, T. & Chen, F. Multiwfn: A multifunctional wavefunction analyzer. *J. Comput. Chem.* **33**, 580–592 (2012).
11. Analyzer, A. M. W. & Lu, T. Multiwfn. **8**, (2024).
12. Mayer, I. Charge, bond order and valence in the AB initio SCF theory. *Chem. Phys. Lett.* **97**, 270–274 (1983).
13. Mayer, I. Improved definition of bond orders for correlated wave functions. *Chem. Phys. Lett.* **544**, 83–86 (2012).
14. Teague, C. M., Dai, S. & Jiang, D. E. Computational investigation of reactive to nonreactive capture of carbon dioxide by oxygen-containing Lewis bases. *ACS Natl. Meet. B. Abstr.* 11761–11767 (2011).

10º SIMPÓSIO DE ESTRUTURA ELETRÔNICA & DINÂMICA MOLECULAR
SEEDMOL 4 a 8 novembro | 2024 Pirenópolis, Goiás

Stability and induced magnetism by edge modification in HfS_2 nanoribbons

Bruno Guilherme Araujo Pimenta[1], Railson Vasconcelos[1], and Ricardo Gargano[1]
[1]Institute of Physics, University of Brasília, Campus Darcy Ribeiro, Brasília, DF, Brazil.
Email: *brunopimentafis@gmail.com* .
Keywords: nanoribbons ; armchair ; zigzag ; magnetism ; stability.

Abstract
The potential of HfS_2 nanoribbons in spintronics remains largely unexplored. This study investigates how the geometries of these nanoribbons, specifically armchair and zigzag structures, impact their properties. Understanding these effects could lead to advancements in spintronic applications.

Introduction

Since the successful isolation of the graphene monolayer [1] in contrast to thermodynamic intuition [2], two-dimensional materials have been extensively studied. This set of materials is known to possess remarkable electromagnetic properties [3], which allow for technological novelty. So far, devices such as sensors and transistors have been reinvented with low-dimensional materials, becoming more sensitive, compact, and efficient [4,5].

One subset of two-dimensional materials is the one composed of transition metal dichalcogenides (TMDs). The members of this subset commonly share desired properties, including reasonable bandgap values, chemical stability, and room-temperature mobility. One particular member of this subset is the HfS_2 monolayer. Current experimental prowess enables diverse methods for the synthesis of ultrathin HfS_2 films [6].

Ideally, spintronics-aimed materials ought to exhibit half metallic states and ferromagnetism simultaneously. In its pristine form, however, HfS_2 monolayers are non-magnetic semiconductors [7], constraining its applicability in spintronics. Several studies have shown the occurrence of intrinsic ferromagnetic states in TMDs through doping with transition metals and defect engineering [8]. In this context, another unexplored possibility is based on edge modification of the two basic ribbons that can be extracted from the HfS_2 monolayer, namely, armchair and zigzag. Motivated by these facts, we sought to evaluate the properties of pristine armchair and zigzag HfS_2 nanoribbons by means of ab initio calculations. In particular, we investigated the ribbons' structural stability and their band structure configuration. Additionally, effects resulting from edge modification and the ribbons' width were considered for all possible edge terminations. Most interestingly, we found that magnetic states arises for certain edge configurations.

Methodology

The geometric optimization and total energy calculations were conducted using spin-polarized density functional theory (DFT) within the SIESTA package [9]. The exchange-correlation functional was described using the Perdew–Burke–Ernzerhof (PBE) method [10] with the generalized gradient approximation (GGA) [11]. The calculations utilized Troullier-Martins pseudopotentials, a double-zeta polarized (DZP) basis set, a mesh cutoff of 380 Ry for the real-space grid, and a convergence criterion of 10^{-5} eV for the total energy. The nanoribbons were constructed with periodicity along the z-axis, and a vacuum spacing of more than 20Å in the x and y directions was used to prevent interactions between neighboring

ribbons. All structures were fully relaxed until the forces on each atom were less than 0.005 eV/Å. Regarding the total energy, the necessary integrals were evaluated using a 1 x 1 x 10 k-space grid constructed with the Monkhorst-Pack k-points mesh [12]. To validate the described methodology, we also simulated the monolayer itself and compared its optimized lattice parameters and energy gap with previously published results [13]. Our results closely match the latter.

Results

Figure 1 illustrates the studied HfS_2 ribbons of a particular width. For each ribbon, we evaluated its stability (Figure 2) as a function of the width, its band structure (Figure 3), and the resultant magnetic moments (Table 1).

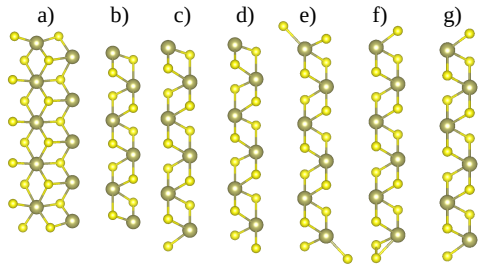


Figure 1: Studied optimized ribbons. a) Armchair, and b)-g) respective zigzag forms: HfHf, HfS_β, HfS_α, $S_\alpha S_\alpha$, $S_\alpha S_\beta$, $S_\alpha S_\alpha$.

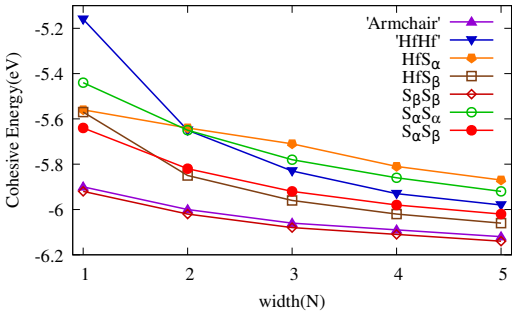


Figure 2: Cohesive energies for each ribbon as a function of width N.

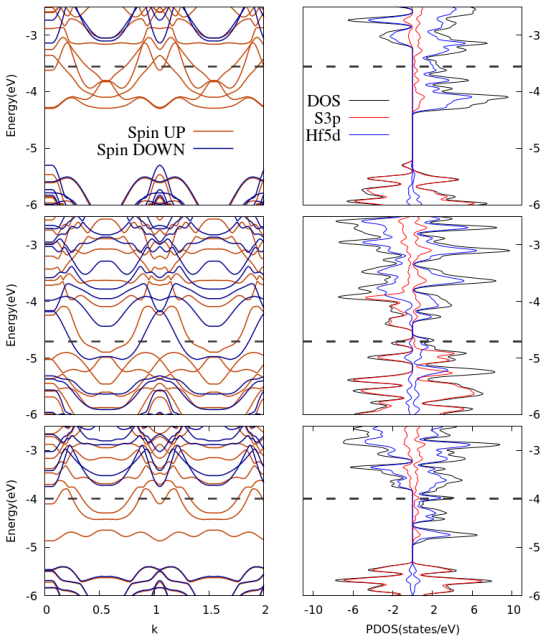


Figure 3: Band structure and density of states (DOS) of selected ribbons: HfHf, HfS_α, and HfS_β. The corresponding path in the Brillouin zone is Γ-B-D-Z.

Ribbons	$\mu(\mu_B)$
HfHf	4
HfS_α	2,7
HfS_β	2

Table 1: Total magnetic dipole moments for selected ribbons, expressed in Bohr magneton.

Discussion

From the obtained results, we observed that all the nanoribbons are very stable with low cohesive energies, as shown in Figure 2. Also, the significance of the geometry of the ribbons on the band structure is displayed in Figure 3. This reveals how edge modification can be used to tune the properties of HfS_2, allowing its ribbons to display semiconductor, metal, half-metal, and ferromagnetic states. Regarding induced magnetism, 3 of the 7 studied ribbons exhibited a non-zero total magnetic dipole moment: HfHf, HfS_α, and HfS_β. This corroborates the possibility of induced magnetism by modifying the nanoribbons' edges.

Conclusions

In this study, we have thoroughly examined the properties of pristine HfS_2 nanoribbons, considering all potential edge terminations. The optimization of the structures and the calculations of the cohesive energies suggest that every form of the nanoribbon is stable. Furthermore, 3 of the 7 structures exhibit magnetic states resulting from edge modification. At the same time, different band structure configurations have been observed, with the ribbons varying from semiconductor to metallic and half-metallic states. These results allow us to conclude that HfS_2 nanoribbons represent a promising candidate for spintronics applications, with properties that can be tuned by edge modification.

Acknowledgments

The authors acknowledge the financial support of CAPES, CNPq and FAP-DF.

References

1. S. Novoselov, A. K. Geim, S. V. Morozov, D.-e. Jiang,Y. Zhang, S. V. Dubonos, I. V. Grigorieva and A. A. Firsov, science, 2004, 306, 666–669.
2. N. D. Mermin, Physical review, 1968, 176, 250.
3. P. Miró, M. Audiffred and T. Heine, Chemical Society Reviews, 2014, 43, 6537–6554.
4. Choudhuri, P. Bhauriyal and B. Pathak, Chemistry of Materials, 2019, 31, 8260–8285.
5. P. Feng, L. Shen, M. Yang, A. Wang, M. Zeng, Q. Wu, S. Chintalapati and C.-R. Chang, Wiley Interdisciplinary Reviews: Computational Molecular Science, 2017, 7, e1313.
6. Wang, X. Zhang and Z. Wang, Journal of Nanoscience and Nanotechnology, 2018, 18, 7319–7334.
7. Ali, J.-M. Zhang, I. Muhammad, X.-M. Wei, I. Ahmad and M. U. Rehman, physica status solidi (b), 2020, 257, 1900768.
8. Xia, D. Gao and D. Xue, Nanoscale, 2021, 13, 12772–12787.
9. M. Soler, E. Artacho, J. D. Gale, A. García, J. Junquera, P. Ordejón and D. Sánchez-Portal, Journal of Physics: Condensed Matter, 2002, 14, 2745.
10. P. Perdew, K. Burke and M. Ernzerhof, Physical review letters, 1996, 77, 3865.
11. N. Troullier and J. Martins, Solid State Communications, 1990, 74, 613–616.
12. H. J. Monkhorst and J. D. Pack, Physical review B, 1976, 13, 5188.
13. Xingwang Zhang Denggui Wang and Zhanguo Wang. Recent advances in properties, synthesis and applications of two-dimensional hfs2.

10º SIMPÓSIO DE ESTRUTURA ELETRÔNICA & DINÂMICA MOLECULAR
SEEDMOL 4 a 8 novembro | 2024
Pirenópolis, Goiás

Computational evaluation of experimental models for exciton diffusion parameters

Bruno Guilherme Araujo Pimenta[1], Pedro Henrique de Oliveira Neto[1]
[1]Institute of Physics, University of Brasília, Campus Darcy Ribeiro, Brasília, DF, Brazil.
Email: *brunopimentafis@gmail.com* .
Keywords: diffusion length; quenching efficiency; experimental assumptions; exciton models.

Abstract
Diffusion length (L_D) measurements in organics are limited by assumptions about exciton behavior, which can result in inaccurate estimations of L_D. In this work, we conducted computational tests to evaluate the assumptions typically incorporated into experimental setups for estimating L_D.

Introduction

Understanding the energetic efficiency problem in organic photovoltaics (OPV) relies on investigating exciton's transport mechanisms. The transport properties of excitons in OPV systems are influenced by a myriad of factors, such as morphology, temperature, absorption coefficient α and excitation conditions. Experimentally, the typically determined parameter is the diffusion length L_D, which characterizes exciton dynamics. To measure L_D, experimentalists rely on spectroscopic techniques, such as *photoluminescence* (PL) quenching methods [1].

These measurements are constrained by assumptions about exciton behavior, which can lead to underestimating or overestimating L_D values. In the bilayer PL quenching method, two common assumptions are made: homogeneous excitation, characterized by an attenuation coefficient α=0, which implies a constant exciton generation rate G_0 along the OPV's depth (as opposed to an exponentially decaying generation rate when α>0), and negligible annihilation effects. Our results demonstrate that inaccurately assuming these conditions can significantly impact the estimation of L_D.

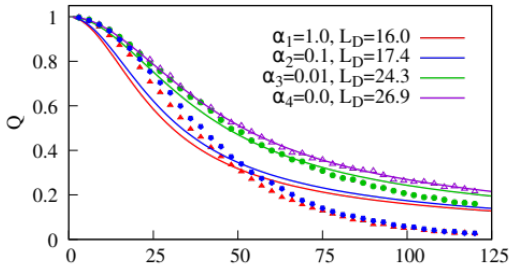
Methodology

To rigorously assess the error associated with these incorrect assumptions, we developed a custom kinetic Monte Carlo (KMC) algorithm that emulates exciton dynamics in organic materials [2]. KMC simulations were then performed on a 100 x 100 x L rectangular grid, where L emulates the bilayer position on the PL quenching method. The input probabilities for exciton hopping and fluorescence events utilized are the ones given by Förster Resonance Energy Transfer (FRET) [3, 4]. By counting the number of excitons that undergo the event of fluorescence (*Nf*) in the presence and absence of the quencher, we emulate the quantity of interest Q (known as quenching efficiency), which is defined as the ratio *Nf*/*N*, where *N* is the initial number of excitons in the grid.

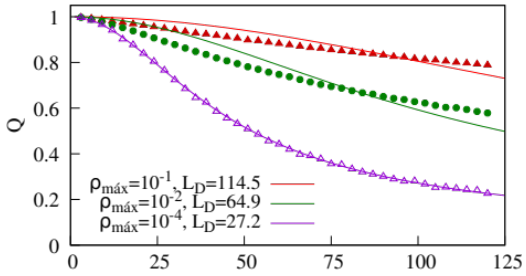
The typical assumptions made in this experimental setup were tested by evaluating how Q(L) changes when excitation and annihilation conditions — represented by the attenuation coefficient α and the initial exciton density $p_{máx}$, respectively — are modified. More specifically, by fitting the resulting plots according to $Q(L,\alpha=0)=(L_D/L)\tanh(L/L_D)$ [5], we can determine whether the diffusion length measured is overestimated or underestimated. In this framework, we use the expected value for comparison $L_D=R_F^3/r^2$, where R_F is the parameter known as Förster's radius and 'r' is the average distance between neighboring molecules, as determined by a combination of random-walk and FRET theories [6].

Results

The described methodology enabled the creation of the following plots corresponding to an arbitrary experimental enviroment, in arbitrary units of length:



In the first plot, the lines in the algorithm which emulates annihilation were turned off.



In the second plot, α was set to zero and annihilation lines in the algorithm were turn on. Also, $p_{máx}$ refers to the maximum concentration occurring in the respective grid.

In both cases, the input probabilities are the same and leads to a theoretical-statistical expected value for L_D=27 (R_F=3 and r=1), in the same arbitrary units of length.

Discussion

It is deduced from the first plot that the erroneous assumption of homogeneous generation of excitons leads to an *underestimation* of the diffusion length L_D, whereas the second plot indicates that the erroneous assumption of negligible annihilation leads to an *overestimation* of L_D. This can be seen by comparing the respective L_D values when α is increased from 0 (L_D=26.9), in the first case, and in the second case when the concentration is increased from 10^{-4} (L_D=27.2). Both of those values are in accordance with the expected value of 27.

Conclusions

In summary, we have conducted Kinetic Monte Carlo simulations to study excitons dynamics in a typical experimental setup for the bilayer PL quenching method. We aimed to evaluate computationally the common assumptions made in this setup, namely, homogeneous generation and negligible annihilation. It was found that the erroneous assumption of these conditions can significantly impact the measured value of the diffusion length L_D.

In a broader perspective, the algorithm developed in this study establishes a parametric way of evaluating exciton diffusion parameters. With this results, we hope to shed a light on experimental models commonly applied.

Acknowledgements

The authors acknowledge the financial support of CAPES, CNPq and FAP-DF.

References

1. TAMAI, Yasunari et al. The Journal of Physical Chemistry Letters, 6, 3417,3428 (2015)

2. BUENO, Fernando Teixeira et al. Modelling the quenching effect of chloroaluminum phthalocyanine and graphene oxide interactions: implications for photodynamic therapeutic applications. **Nanoscale Advances**, v. 5, n. 22, p. 6053-6060, 2023.

3. FÖRSTER, Th. Transfer mechanisms of electronic excitation energy. **Radiation Research Supplement**, p. 326-339, 1960.

4. DE SOUSA, Leonardo Evaristo et al. Triplet-to-singlet exciton transfer in hyperfluorescent OLED materials. **Journal of Materials Chemistry C**, v. 10, n. 12, p. 4914-4922, 2022.

5. DE Markov, C Tanase, PWM Blom, and J Wildeman. Simultaneous enhancement of charge transport and exciton diffusion in poly (p-phenylene vinylene) derivatives. Physical
Review B, 72(4):045217, 2005.

6. DE SOUSA, Leonardo Evaristo et al. Fast predictions of exciton diffusion length in organic materials. **Journal of Materials Chemistry C**, v. 7, n. 14, p. 4066-4071, 2019.

First-Principles Study of Graphenylene-Supported Single Atom Catalyst for Efficient Hydrogen Production

Caique Campos de Oliveira[1], Pedro Alves da Silva Autreto[1].
[1]Centro de Ciências Naturais e Humanas, Universidade Federal do ABC, Rua Santa Adélia 166, Bairro Bangu, 09210-170, Santo André – SP, Brasil.
pedro.autreto@ufabc.edu.br
Keywords: Green Hydrogen, Catalysis, Carbon nanostructure, DFT, CHE model.

Abstract

Green Hydrogen production by water electrolysis in the Hydrogen Evolution Reaction (HER) represents an alternative decarbonizing energetic sectors. Carbon-based nanostructures with high surface area and chemical stability are promising alternatives for scarce noble-metal catalysts. Specifically, Single Atom Catalyst (SACs) can effectively promote catalysis while reducing metal load and maximizing atomic efficiency. In this work, we apply first-principles calculations based on Density Functional Theory together with the Computational Hydrogen Electrode (CHE) model to investigate the catalytic activity of Graphenylene-based SAC using Sc, Ti, Mo, Zr, Pt, Ni and Co. Our results show that Sc and Ni are promising catalysts for HER with $\Delta G_H < 0.1$ eV. The catalytic activity is investigated in terms of charge transfer and the formation of bonding and anti-bonding states between the metal site and the H intermediate.

Introdução

A produção de hidrogênio verde pela eletrólise da água nas reações de evolução de hidrogênio (HER) é uma alternativa promissora para a produção e armazenamento de energia limpa. Contudo, tal tecnologia demanda o desenvolvimento de novos catalisadores eficientes e abundantes. Materiais bi-dimensionais baseados em carbono têm sido extensivamente estudados como catalisadores devido a abundância de matéria-prima, alta área superficial e boa condutividade eletrônica[1]. Além disso, a possibilidade de modificação das propriedades eletrônicas por meio da dopagem fornece uma estratégia para melhorar as atividades eletrocatalíticas dessas nanoestruturas em diferentes processos eletroquímicos. Em particular, a dopagem com metais de transição permite modificar a estrutura eletrônica do material modificando também suas propriedades catalíticas[2]. Neste trabalho, investigamos as propriedades catalíticas do Grafenileno (GPY) dopado com Sc, Ti, Mo, Zr, Pt, Co e Ni utilizando cálculos de primeiros princípios baseados na teoria do funcional da densidade (DFT). Átomos metálicos foram adsorvidos sobre o anel hexagonal da estrutura do GPY (cf. Figura 1), atuando como sítios para a adsorção de H. Os resultados obtidos para a atividade catalítica são estudados em termos da transferência de carga e em termos da formação de ligações químicas entre o sítio metálico e o intermediário de H.

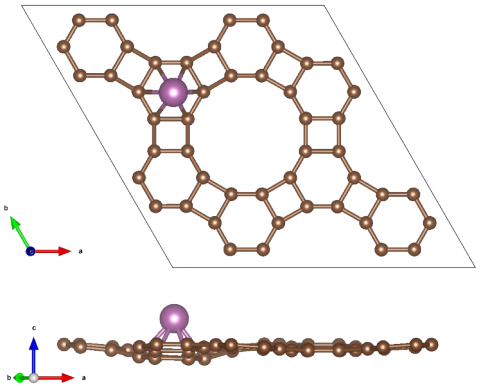


Figura 1: Supercélula 2x2 do GPY dopada com o átomo metálico no sítio hexagonal.

Metodologia

Cálculos de primeiros princípios baseados na teoria do funcional da densidade (DFT) foram conduzidos com o pacote computacional Quantum ESPRESSO[3] utilizando a parametrização de Perdew, Burke e Erzerhoff do gradiente generalizado (PBE-GGA)[4], com inclusão de efeitos de dispersão de longo alcance (van der Waals) por meio do termo de dispersão de energia implementado no funcional DFT-D3[5]. Orbitais de Kohn-Sham foram expandidos utilizando uma base de ondas planas com corte de 60 Ry e 480 Ry para a energia cinética e a densidade, respectivamente. A zona de Brillouin foi aproximada por um grid uniforme de (4x4x1) pontos k, conforme o esquema proposto por Monkhorst e Pack[6]. A atividade catalítica foi estudada por meio do modelo do eletrodo de hidrogênio computacional (CHE)[7], calculando a variação de energia livre para a adsorção do hidrogênio (ΔG_H):

$$\Delta G_H = E_{ads} + \Delta E_{ZPE} - T\Delta S$$

onde E_{ads} é a energia de adsorção do intermediário, calculada com base na molécula de hidrogênio em fase gasosa (E_{H2}):

$$E_{ads} = E_{surf+H} - \left(E_{surf} + \frac{1}{2}E_{H_2}\right)$$

E_{ZPE} é a variação de energia de ponto zero, relacionada com vibrações do intermediário adsorvido. S é a entropia, calculada em relação ao hidrogênio em fase gasosa. Tais contribuições são aproximadas por +0,24 eV, de acordo com trabalhos anteriores[8]. Em geral, bons catalisadores para a HER apresentam ΔG_H próximos de zero[2,6].

Resultados

O diagrama de energia livre para os metais selecionados é mostrado na Figura 2. Sc mostra a melhor atividade com ΔG_H = -0,04 eV, seguido por Ni (-0,07 eV). Ti, Mo, Zr e Co apresentam adsorção forte (ΔG_H << 0 eV) com valores de -0,32, -0,35, -0,23 e -0,45 eV, respectivamente. A Pt apresenta interação fraca com +0,21eV.

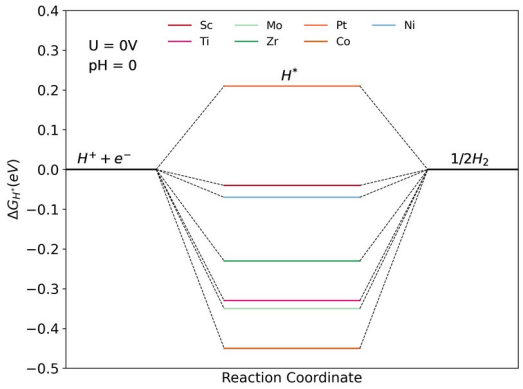


Figura 2: Diagrama de energia livre de adsorção do intermediário H para o GPY dopado com metais de transição.

Para compreender a origem da atividade catalítica, as cargas de Bader do intermedário de H após adsorção foram calculadas utilizando o software do grupo de Henkelman[9].

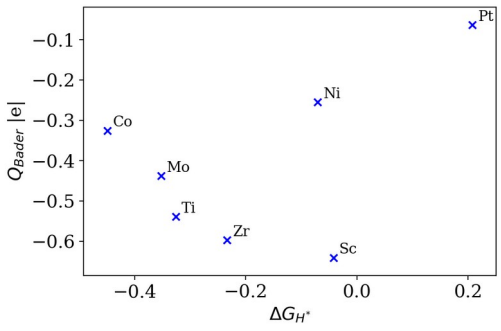


Figura 3: Gráfico de dispersão da carga de Bader transferida para o intermediário de H e o ΔG_H.

Os resultados são mostrados na Figura 2. Com excessão do Ni e Pt, observa-se que ΔG_H diminui a medida que a carga de Bader transferida para o H aumenta (o valor de Q_{Bader} fica mais negativo). No caso da Pt, a baixa transferência de carga pode explicar a fraca interação com o intermediário de H, resultando no ΔG_H positivo. Curiosamente, para o Ni observa-se um excelente ΔG_H apesar da baixa transferência de carga. Para entender tais resultados, a intensidade de ligação entre o intermediário de H e o metal foi calculada por meio da análise da população de Hamilton do orbital cristalino (COHP)[10], realizada com o software LOBSTER[11]. Nesta análise, estados ligantes (-COHP > 0) e anti-ligantes (-COPH < 0) são facilmente visualizados em função da energia.

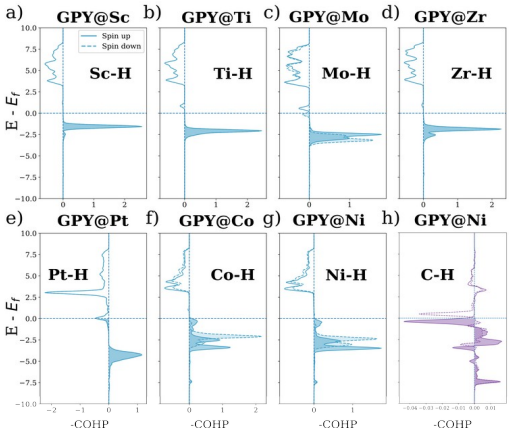


Figura 4: Análise da População de Hamilton do orbital cristalino (COHP) relativa ao a) Sc, b) Ti, c) Mo, d) Zr, e) Pt, f) Co, g) Ni e o intermediário de H. h) COHP relativa ao H e o C da matriz do GPY.

Os resultados para a COHP são mostrados na Figura 4. Sc, Ti, Mo e Zr, apresentam a formação de estados ligantes em -2 eV abaixo da energia de Fermi (E_{Fermi}), com a formação de estados anti-ligantes entre 3 e 8 eV acima de E_{fermi} (cf. Figura 4a-d). No caso da Pt observa-se um pico relacionado à estados anti-ligantes em 3 eV acima de E_{Fermi} e também um pico anti-ligante sobre E_{Fermi}. A maior contribuição dos estados anti-ligantes em conjunto com a baixa transferência de carga explicam a fraca interação com o intermediário de H, resultando no ΔG_H positivo. Co e Ni apresentam resultados similares, com a formação de mais estados ligantes entre -2 e -4 eV abaixo de E_{fermi}. Contudo, no caso do Ni observa-se também a formação de estados anti-ligantes relacionados à interação do intermediário de H com o C da matriz do GPY (Figura 4h). Tal interação (anti-ligante) pode estar relacionada com a modulação do ΔG_H para próximo de zero.

Agradecimentos

Os autores agradecem ao PRH.49 (PRH-ANP UFABC) pelo financiamento e à Central Computacional Multiusuário (CCM) da UFABC pelos recursos computacionais disponibilizados para a realização deste trabalho.

Referências

1. Chhetri M.; Ramachandra C. N.; Adv. Mater. 2019, 31 (13), 1803668.
2. Cui W.; Guo M.; Ji M.; Appl. Surf. Sci. 2022, 592, 153237.
3. Gianozzi P. et al.; J. Phys. Condens. Matter. 2017, 29(46), 465901.
4. Burke K.; Ernzerhof M.; Perdew J. P.; Phys. Rev. Lett. 1996, 18, 3865.
5. Antony J.; Ehrlich S.; Grimme S.; Helge K.; J. Chem. Phys. 2010, 132, 154104.
6. Monkhorst H. J.; Pack J. D.; Phys. Rev. B. 13 (12), 5188;
7. Bligaard T.; Jonsson H.; Kitchin J. R.; Lindqvist L.; Logadottir A.; Norskov J. K.; Rossmeisl J.; J. Phys. Chem. B. 2004, 108(46) 17886.
8. Bligaard T.; Chen J. G.; Kitchin J. R.; Logadottir A.; Norskov J. K.; Pandelov S.; Stimming U.; J. Electrochem. Soc. 2005, 152, J23.
9. Henkelman G.; Sanville E.; Tang W.; J. Phys. Condens. Matter. 2009, 21, 084204.
10. Bloechl P. E.; Dronskowski R.; J. Phys. Chem. 1993, 97 (33), 8617.
11. Deringer V. L.; Dronskowski R.; Maintz S.; Tchougreeff A. L. J. Comp. Chem. 2016 37 (11), 1030.

Transition metal doping effects on the electrical and magnetic properties of ITO studied by first principles calculations

C. A. Vilca Huayhua[1], B. D. Aparício Huacarpuma[1], F. F. Herrera Aragón[1], L. Villegas-Lelovsky[2,3], J. A. Huamani Coaquira[1]

[1]Institute of Physics, University of Brasília, Brasília, 70910900, DF, Brazil.
[2]Institute of Physics, Universidade Estadual Paulista Júlio de Mesquita Filho, São Paulo. Brazil.
[3]Institute of Physics, Federal University of São Carlos, São Paulo, Brazil

Email *cavilcahu@gmail.com*

Abstract

In this work, the effects of transition metals (Fe, Co, Ni) on the properties of ITO were studied using density functional theory (DFT). Our findings showed that magnetic ions produce changes in the lattice parameter and the appearance of new electronic states below the Fermi energy level, which cause a band gap closing. In addition, the results of spin-polarized electronic density of states (DOS) show asymmetry between the density of states of spin up and spin down, due to the *s-d* exchange interaction between the conduction band of ITO and the localized *d* band of the transition metals, suggesting the occurrence of ferromagnetism for the Fe, Co and Ni doped ITO compounds. Furthermore, the Fermi level was found superimposed to the conduction band, suggesting that these systems behave as electrically conductive materials. These electrical and magnetic properties make ITO interesting for spintronic applications.

Keywords: DFT calculation, Dilute magnetic conducting oxides; Spin polarized DOS.

Introduction

Indium Tin Oxide (ITO) is recognized as a *Transparent Conducting Oxide* (TCO), has low electrical resistivity (~10^{-4} ohm-cm) and high optical transmittance (>85%). making them interesting for optoelectronic applications. Currently, great interest has been aroused in the incorporation of magnetic impurities such as transition metals (Fe, Co, Ni, etc.) in transparent conductive oxides TCO, due to the possibility of generating magnetic order in the material. When ITO is doped with transition metals, it is possible to cause a magnetic order that, combined with optical and electrical properties, generates a *Dilute Magnetic Conducting Oxide* (DMC-O). One of the phenomena addressed is ferromagnetism at room temperature, which can have different origins such as the formation of clusters in the ITO structure [1], [2] oxygen-vacancy related bound magnetic polaron model and Zener-Ruderman-Kittel-Kasuya-Yoshida (RKKY) interactions [3], [4].

Methodology

Calculations were performed using density functional theory implemented in the *Quantum Espresso* simulation package [5], using the *Perdew−Burke-Ernzerhof* (PBE) functional. A cutoff energy of 600 eV and 4 × 4 × 4 k-point meshes were used for the total energy calculation. All structures were relaxed until the total energy converged and the total force was within 0.01 eV/Å on each atom. The cubic structure of In_2O_3 doped with Sn contains 48 oxygen, 29 indium and 3 tin atoms, the Sn atoms were introduced substitutionally into the In atoms, occupying the cationic sites 8b. Where the Sn dopant represents a doping ratio of ~9.4 %, which is within the doping range experimentally obtained for ITO compounds. Then, Fe, Co, Ni atoms were included to replace the In atoms, in the cationic position 8b.

Results and Discussion

Using DFT theoretical calculations, we obtained the lattice constant for ITO structures containing the different dopants. As observed in Fig. 1, the lattice parameter of the undoped ITO is 10.324 Å, and when we introduce the transition metal atoms substituting In atoms, the lattice constant is reduced in agreement with the Vergard's law. This decreasing trend is related to the smaller ionic radius of Fe^{3+} (r=0.785Å), Co^{2+} (r=0.740Å), Ni^{2+} (r=0.69Å), in comparison to the ionic radius of In^{3+} (r=0.81Å) which produce a decrease of the unit cell volume.

The formation energy for the different systems was obtained using the following formula:

$$E_F(defect) = E_F(Pristine) + \sum \pm n_i \mu_i \qquad (1)$$

Where $E_F(defect)$ is the total energy of the defect structure $E_F(Pristine)$ is the total energy of the defect-free structure, n_i is the number of corresponding species for the atoms and μ_i represents the chemical potentials of In, Fe, Co, Ni if either atom were added (+) or removed it would be (-). According to the results of the energy formation, it is suggested that the ITO structure doped with Co is energetically more favorable to be formed, presenting greater solubility compared to the systems doped with Fe and Ni.

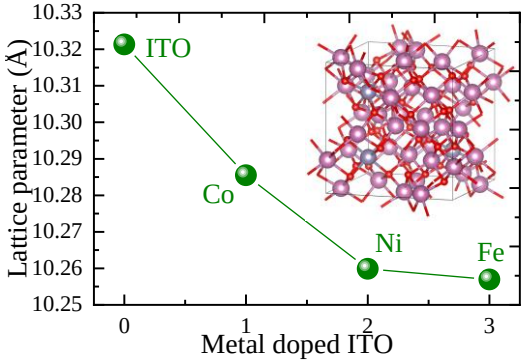


Fig. 1 Lattice constant as a function of three different transition metal dopants Fe, Co, Ni.

ITO does not show magnetic properties. When Fe, Co or Ni dopants are introduced on the structure, with 3.2% of doping substituting In atoms, we clearly see a change in the spin-polarized density of states (DOS) with the appearance of new electronic states below the Fermi level, within the band gap. It was determined a strong hybridization between the *d* orbitals and the conduction band, as shown in Fig. 2.

Table 1. Formation energy, magnetization and band gap energy obtained from DFT calculations.

Material	E_f (eV)	Mag. (emu/cell)	Gap (eV)
ITO	0	-	2.84
ITO:Fe	0.21	4.55	2.61
ITO:Co	0.15	0.48	2.67
ITO:Ni	0.24	1.99	2.52

The DOS for In, Sn and O are symmetric and the spin up and spin down for the Fe, Co, Ni dopants are asymmetric, which indicates the arising of a magnetic moment coming mainly from the d orbitals of dopant ions. It can lead to the spin polarization of carriers due to the *s-d* exchange interaction between the conduction band of ITO and the localized *d* electrons of the magnetic dopant [6]. Furthermore, a narrowing of the energy gap occurs, probably due to the formation of shallow levels at the top of the valence band and at the minimum of the conduction band [3].

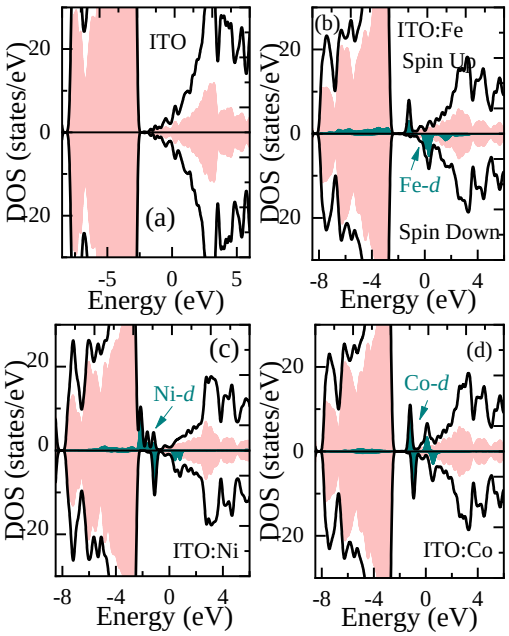


Fig. 2 Spin polarized DOS (a) ITO, (b) Fe doped ITO, (c) Ni doped ITO and (d) Co doped ITO.

Band structure calculations were performed using the exchange correlation function (PBE) commonly showing a typical underestimation of the bandgap in semiconductors and insulators calculated by DFT [7]. For our results, this underestimation does not affect our analyses. Figure 3(a) shows the band structure of ITO, with a bandgap energy of 2.3 eV and a Fermi level that is superimposed to the conduction band, which can allow electrons to move freely through the material, and the system behaves as a conducting material. When the magnetic ions (Fe, Co, or Ni) are introduced, it is notable to see changes in the band structure, as shown in figure (3)b-d. In addition, a slight decrease in the Fermi energy was observed suggesting that Fe^{3+}, Co^{2+} and Ni^{2+} ions could generate hole carries which partially compensate the n-type conductivity [8]. As the Fermi energy remains above the conduction band, still maintaining its n-type conductivity, thus forming a Dilute Magnetic Conducting Oxide (DMC-O).

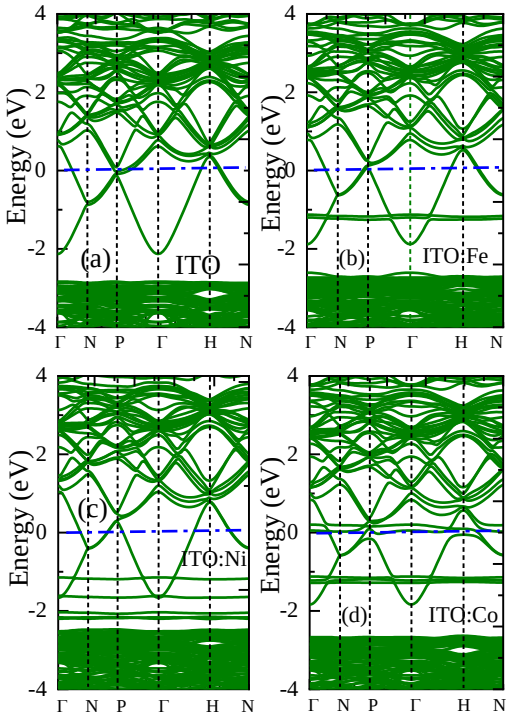


Fig. 3 Band structure (a) ITO, (b) Fe doped ITO, (c) Ni doped ITO and (d) Co doped ITO. Blue line represent the Fermi level.

Conclusions

Using first principles DFT calculations, structures of ITO doped with transition metals were successfully studied, showing changes in the ITO structure with a volume reduction, due to the smaller ionic radii of Fe, Co, Ni, in comparison to the In ionic size. Furthermore, the appearance of electronic states near to bottom of the conduction band causes a reduction in the band gap energy. From the spin-polarized DOS calculations, it was determined that the up and down spin densities are asymmetry, indicating that the magnetic moment comes from the Fe-*d*, Co-*d*, Ni-*d* ions, and the interaction between *s(p)* orbitals of ITO and the d orbitals of the magnetic ions can lead to the ferromagnetic order. Finally, ITO doped with transition metals remain as conductors, typical of highly degenerate transparent conducting oxides.

Acknowledgements

Brazilian agencies CNPq and Capes for financial support and INKARI from national university San Agustin de Arequipa for computational support.

References

[1] Ohno, T., et al. *Journal of Magnetism and Magnetic Materials* 310.2 (2007): e717-e719.
[2] Stankiewicz, Jolanta, Francisco Villuendas, and Juan Bartolomé. *Physical Review B* 75.23 (2007): 235308.
[3] Xing, P., Chen, Y., & Sun, S. *Journal of Semiconductors*, *34*(2), (2013), 023002.
[4] Peleckis, Germanas, Xiaolin Wang, and Shi Xue Dou. *Applied Physics Letters* 89.2 (2006).
[5] Giannozzi, Paolo, et al." *Journal of physics: Condensed matter* 21.39 (2009): 395502.
[6] Hakimi, A. M. H. R., et al. *Physical Review B* 82.14 (2010): 144429.
[7] Rosén, Johanna, and O. Warschkow. *Physical Review B* 80.11 (2009): 1152152.
[8] Aragón, F. F. H., et al. *Journal of Alloys and Compounds* 867 (2021): 158866.

Predicting the Os-187 NMR chemical shift in Os(II) complexes with new NMR-DKH basis set

Carolina Manhães Santos[1], Diego Fernando da Silva Paschoal[1]
[1]NQTCM: Núcleo de Química Teórica e Computacional de Macaé, Polo Ajuda, Instituto Multidisciplinar de Química, Centro Multidisciplinar UFRJ-Macaé, Universidade Federal do Rio de Janeiro, 27.971-525, Macaé, RJ, Brazil.
carolinamanhaessantos@gmail.com, diegopaschoal01@gmail.com.
Keywords: NMR; DFT; organometallic complexes; basis set; relativistic effects.

Abstract

In the present study a new NMR-DKH basis set was developed for Os atom and an empirical nonrelativistic protocol for predicting the δ^{187}Os NMR chemical shift in Os(II) complexes was proposed. For a set of 37 complexes, a mean relative error of only 4.30% was obtained at GIAO-OPBE/NMR-DKH/IEF-PCM(UFF) level.

Introduction

The nuclear magnetic resonance (NMR) spectroscopy of metal nuclei is a powerful tool for investigating the structure, reaction mechanisms, equilibrium and reactional kinetic of complexes, presenting great sensibility to structural modifications and being possible to carry in solution, which makes it a technique of particular interest to medicinal inorganic chemistry [1, 2, 3].

In parallel, osmoarene organometallic complexes show bioactive potential as anticancer agents, being able to attack DNA, cause endoplasmic reticulum stress and disturb electrochemical equilibrium inside cells through redox mechanisms [1]. Complexes of this type were also able to catalyze transfer hydrogenation reactions in quinones and enantioselective conversion of pyruvate in L-lactate or D-lactate [1, 4].

Osmium (Os) is a tricky nucleus to study through NMR due to the low sensitivity of its most suitable isotope, ^{187}Os, through the technique [1, 2]. The ^{187}Os isotope has a nuclear spin I = ½, gyromagnetic constant of 0.6192895 x 10^7 rad T^{-1} s^{-1} and natural concentration of 1.96%. The chemical shifts presented by the ^{187}Os nucleus are in a range slightly greater than 5,000 ppm.

Considering the experimental difficulties of ^{187}Os NMR, Computational Chemistry can make an important contribution. However, computational studies involving ^{187}Os NMR are scarce. Thus, we propose a computational study of Os-187 NMR chemical shift (δ^{187}Os) in osmoarene complexes.

Nonrelativistic and 4-components (4c) relativistic protocols were proposed for predicting the δ^{187}Os in Os(II) half-sandwich complexes. In addition, new relativistic NMR-DKH Gaussian basis set was constructed for Os atom.

Methodology

Initially, the NMR-DKH basis set for Os atom was developed following the same methodology developed by Paschoal et al. (2016) to develop the NMR-DKH for H-He, Li-Ne, Na-Ar, K-Ca, Ga-Kr, Rb-Sr, In-Xe, and Pt atoms [5].

A set of 37 Os(II) half-sandwich complexes with experimental δ^{187}Os available in the literature were selected [2]. The structure of the complexes was optimized considering three different protocols described by B3LYP/OSBS/def2-SVP/IEF-PCM(UFF), where OSBS (osmium basis set) = LANL2DZ, LANL2TZ(f), and def2-TZVP. Subsequently, NMR protocol at GIAO-PBE/NMR-DKH/IEF-PCM(UFF) level was applied for all optimized structures to define the best optimization protocol.

Furthermore, other DFT-Functionals (BP86, BLYP, OPBE, B3LYP, PBE0, TPSS, TPSSh, CAM-B3LYP, LC-OPBE, LC-wPBE, and LC-BLYP) were also applied to the best optimization protocol. The solvents considered in the calculations were the same used in the experimental data. The δ^{187}Os were determined through the linear correlation between experimental chemical shifts and calculated shielding constants, following a methodology that has previously been applied for Pt(0) and Pt(II) complexes giving good results [5, 6]. All these calculations were carried out in Gaussian 16 Rev. C.01 program.

In addition, 4-component relativistic calculations were performed for a set of four complexes selected from the previous group and for the internal reference complex, OsO_4, according the protocols 4c-DFT-Functional/dyall-vdz, where DFT-Functional = BLYP, BP86, PBE, KT2, B3LYP, and PBE0. These NMR calculations were carried out in the gas phase, considering the structures optimized with the best protocol in the first step. The 4c calculations were performed in ReSpect 5.1.0 program and the δ^{187}Os was calculated through the equation (1).

$$\delta^{187}Os = \sigma_{ref} - \sigma_{calc} \quad (1)$$

where σ_{calc} and σ_{ref} are the calculated shielding constants for the ^{187}Os nucleus in the studied complexes and in OsO_4 internal reference, respectively. The protocol that provided the best results were then applied for the complete set of 37 complexes and the chemical shift was determined using the same methodology.

Results and Discussion

Initially, the role of the osmium basis set (OSBS) in predicting the structure of Os(II) complexes were assessed. Protocols at B3LYP/OSBS/def2-SVP/IEF-PCM(UFF) level, with OSBS = LANL2DZ, LANL2TZ(f), and def2-TZVP, were tested. The calculated δ^{187}Os at GIAO-PBE/NMR-DKH/IEF-PCM(UFF) level was used as reference to define the best optimization protocol. From the calculated results, the mean relative error (MRE) for the set of 37 Os(II) complexes studied was of 4.5%, 4.3%, and 4.9% for the structures obtained with the OSBS LANL2DZ, LANL2TZ(f), and def2-TZVP, respectively. Thus, the B3LYP/LANL2TZ(f)/def2-SVP/IEF-PCM(UFF) level was the selected optimization protocol for the next steps.

The role of the DFT-Functional was also assessed in predicting the δ^{187}Os of Os(II) complexes. Computational protocols at DFT-Functional/NMR-DKH/IEF-PCM(UFF), considering a set of 11 DFT-Functionals were proposed.

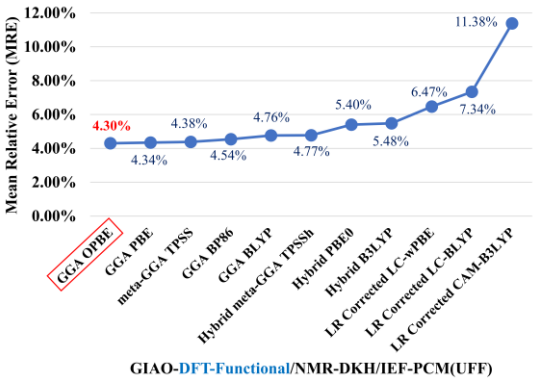


Figure 1. Calculated mean relative error (MRE) considering the δ^{187}Os of 37 Os(II) complexes at GIAO-DFT-Functional/NMR-DKH/IEF-PCM(UFF)//B3LYP/LANL2TZ(f)/def2-SVP/IEF-PCM(UFF) levels

The calculated results (Figure 1) show that the DFT-functional plays an important role in the description of δ^{187}Os, with MRD, considering the set of 37 Os(II) complexes studied, ranging from 4.30% (GGA OPBE) and 11.38% (LR corrected CAM-B3LYP). Overall, the GGA and meta-GGA functionals presented the best description of δ^{187}Os.

The best protocol was GIAO-OPBE/NMR-DKH/IEF-PCM(UFF), which presented an MRE of only 4.30%. The δ^{187}Os with this model was calculated according to equation presented in Figure 2, obtained from the linear correlation between σ_{calc} x δ_{expt} (Figure 2). From Figure 2, we also observe that the obtained angular coefficient of the linear correlation is close to -1 and the linear coefficient obtained is

of the same order of magnitude as the expected shielding constant of ^{187}Os nucleus in OsO_4. This is an indicator of a well-adjusted and physically consistent methodology since it makes the linear correlation equation similar to the equation that defines chemical shifts, which is $\delta = \sigma_{ref} - \sigma$.

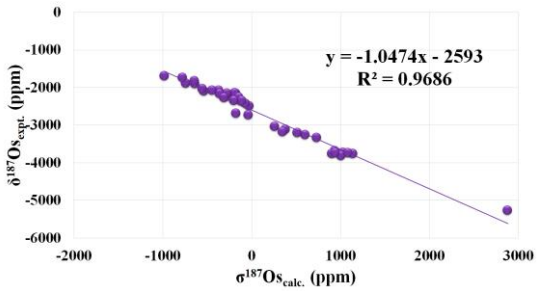


Figure 2. Linear correlation between $\sigma^{187}Os_{calc}$ and $\delta^{187}Os_{expt}$ with GIAO-OPBE/NMR-DKH/IEF-PCM(UFF)//B3LYP/LANL2TZ(f)/def2-SVP/IEF-PCM(UFF) protocol

Lastly, 4-components relativistic calculations were carried out for a set of four Os(II) complexes at GIAO-4c-DFT-Functional/dyall-vdz level, considering a set of six DFT-Functionals. The calculated results (Figure 3) show that protocol GIAO-4c-PBE/dyall-vdz presented the lowest MRE (2.15%), being selected for the study of the other complexes. When this protocol is applied to the set of 37 Os(II) complexes, an MRE of 5.08% was found.

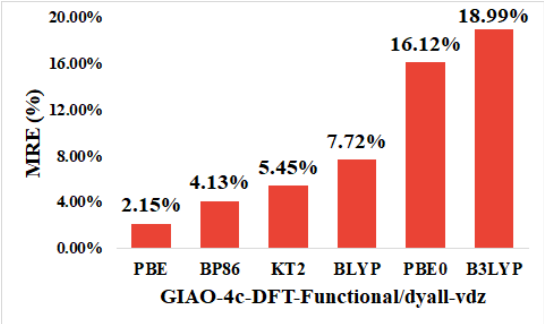


Figure 3. Mean relative error (MRE) calculated for a set of four Os(II) complexes at GIAO-4c-DFT-Functional/dyall-vdz level

These 4c results indicate that the empirical nonrelativistic model employing the NMR-DKH basis set can recover part of the relativistic effects not considered in the Hamiltonian, being an excellent alternative for the study of δ^{187}Os, with a lower computational cost.

Conclusion

In the present study, a computational protocol for predicting the δ^{187}Os in Os(II) complexes was proposed.

Considering a set of 37 Os(II) complexes, the best result was obtained with the protocol GIAO-OPBE/NMR-DKH/IEF-PCM(UFF), considering the structures obtained at B3LYP/LANL2TZ(f)/def2-SVP/IEF-PCM(UFF) level.

The mean relative error obtained was only of 4.30%, with a R^2 of 0.9686, in excellent agreement with the reference data obtained at GIAO-4c-PBE/dyall-vdz level (MRE of 5.08%).

In addition, a new NMR-DKH basis set for the Os atom was also proposed.

Acknowledgments

The authors would like to thank the Brazilian agency FAPERJ (E-26/201.336/2022 – BOLSA JCNE and E-26/210.070/2022 – DCTR), PIBIC-CNPq, and CAPES (Finance Code 001).

References

1. Needham, R. J. et al.; Dalton Trans. 2021, 50, 12970.
2. Bell, A. G. et al.; Organometallics 1996, 15, 3124.
3. Bühl, M.; Annu. Rep. NMR Spectrosc. 2008, 64, 77.
4. Bolitho, E. M. et al.; Organometallics 2021, 40, 3012.
5. Paschoal, D. et al.; J. Comput. Chem. 2016, 37, 2360.
6. e Silva, J. H. C. et al.; Magnetochemistry 2021, 7, 148.

REPOSICIONAMENTO DE FÁRMACOS E BUSCA POR NOVOS ANTIPLAQUETÁRIOS COM POTENCIAL MODO DE AÇÃO NO RECEPTOR P2Y12

*Caroline Reis Santiago Paschoal[1,2], Pryscila Santiago Rodrigues[1], Vinicius Schmitz Pereira Nunes[3], Paula Alvarez Abreu[2], Plínio Cunha Sathler[1].
[1]Universidade Federal do Rio de Janeiro, LABHEx, Faculdade de Farmácia, Ilha do Fundão, CEP 21941-902, Rio de Janeiro, RJ, Brasil.
[2]Universidade Federal do Rio de Janeiro, LAMCIFAR, Instituto de Biodiversidade e Sustentabilidade NUPEM, CEP 27965-045, Macaé, RJ, Brasil
[3]Universidade Federal do Rio de Janeiro, Programa de Pós-graduação em Produtos Bioativos e Biociências, CEP 27930-560, Macaé, RJ, Brasil
carolinesantiago@live.com.
Keywords: Agentes antiplaquetários; ADP; doenças cardiovasculares; P2Y12; triagem virtual.

Abstract
Current antiplatelet drugs have side effects, requiring more effective and less toxic medications. We aimed to identify antiplatelet candidates for the P2Y12 receptor using virtual screening, finding two promising molecules: mol 1 (IC_{50} 65.8 µM) and mol 2 (IC_{50} 92.5 µM). Studies emphasize important hydrophobic interactions.

Introdução

De acordo com a Organização Mundial de Saúde (OMS), as doenças não transmissíveis são as maiores causadoras de doenças no mundo, matando 41 milhões de pessoas todos os anos mundialmente, o equivalente a 71% das mortes. Só nas Américas esse número chega a 5,5% milhões de mortes. Dentre as quatro principais doenças não transmissíveis, destacam-se as doenças cardiovasculares (DCV), responsáveis pela maioria das mortes tanto nos países desenvolvidos como nos países em desenvolvimento nos últimos anos, totalizando cerca de 17,9 milhões de mortes anualmente, onde 85% ocorrem devido a acidentes vasculares cerebrais (AVCs) e ataques cardíacos. Em seguida vêm os casos de câncer, totalizando 9 milhões de mortes, seguidos pelas doenças respiratórias, com 3,9 milhões de mortes, e diabetes, com 1,6 milhão de mortes (OMS, 2023).
Diversas DCV ocorrem devido à obstrução vascular, ocasionada pela formação de um trombo no interior de um vaso sanguíneo (CANNON, 2013). Sendo classificadas em trombose arterial ou trombose venosa de acordo com a sua localização (MCBANE; WYSOKINSKI, 2012a). A agregação plaquetária é um dos principais eventos envolvidos no processo de formação dos trombos vasculares. Atualmente, os agentes antiplaquetários em uso clínico possuem severos efeitos indesejáveis, o que evidencia a importância da identificação de novos antitrombóticos mais eficazes e menos tóxicos. Assim, o trabalho tem como objetivo a busca de novos candidatos a fármacos com ação antiplaquetária no receptor P2Y12.

Metodologia

Inicialmente foi feita a modelagem comparativa no Modeller para obtenção da estrutura completa do receptor P2Y12 a partir do molde disponível no banco de dados de proteínas (PDB 4NTJ). Foi feita uma busca por antagonistas reversíveis conhecidos do receptor P2Y12 para estudar

o acoplamento molecular e prever a melhor pose bioativa. A validação do método foi realizada através de redocking com os programas Autodock Vina 1.2 e Autodock Vina 1.5.7. Em seguida, foi realizada a triagem virtual baseada no farmacóforo usando o servidor Pharmit tendo como base os grupos farmacofóricos e modo de ligação de antagonistas reversíveis já conhecidos. O servidor FAFDrugs foi utilizado para remoção das moléculas duplicadas e protonação em pH sanguíneo; análise de PAINS, DrugLike e subestruturas indesejáveis. Foi feito o docking molecular usando o Autodock Vina 1.2 e Autodock Tools 1.5.7 das estruturas selecionadas no sítio ativo e, posteriormente, aceitas mediante análise do farmacóforo e das energias de ligação. As substâncias foram analisadas quanto às suas propriedades físico-químicas no software Spartan'10 e as características farmacocinéticas e toxicológicas nos servidores admetSAR 2.0 e FAFDrugs 4.1. Em seguida, as substâncias mais promissoras foram adquiridas e testadas in vitro pelo teste de agregação plaquetária e foram avaliados os mecanismos biológicos que ocorrem com essas duas substâncias em condições termodinâmicas, através de estudos de dinâmica molecular com o software AMBER 18.

Resultados

Foi construído um modelo farmacofórico baseado na pose do ligante co-cristalizado AZD-1283 com 4 pontos, sendo 2 pontos aromáticos e 2 aceptores de ligação de hidrogênio e realizada a triagem virtual no banco de dados da empresa Sigma Aldrich, DrugBank e NuBBE, resultando em 18.604 moléculas filtradas. Após análise no servidor FAFDrugs, 8.900 substâncias foram selecionadas para o docking no receptor. Após inspeção visual e análise das interações, 48 moléculas mantiveram os pontos farmacofóricos propostos, sendo 15 disponíveis para aquisição. Desta forma, em caráter inicial, duas moléculas foram obtidas, o composto 5-Cloro-2-Metoxi-N-[2-(4-Sulfamoilfenil)etil]-benzamida e o fármaco doxasozina, provenientes da triagem virtual. Ambos foram testados quanto a sua agregação plaquetária induzida com ADP apresentando valores de concentração inibitória (IC_{50}) de 65,8 μM e 92,5 μM, respectivamente, com ticagrelor como controle positivo. Após estudos de dinâmica molecular, foi observado que essas duas substâncias fizeram contato com resíduos que apresentam boas contribuições hidrofóbicas, necessário para sua atividade. Porém, também foi observado que essas duas substâncias apresentaram contato com o resíduo R241, um resíduo envolvido na ativação do receptor, o que pode justificar seus baixos valores de agregação máxima.

Discussão

A administração de fármacos por via oral é muito utilizada devido à maior aderência do paciente e ao baixo custo. A solubilidade aquosa adequada, assim como a permeabilidade da membrana gastrointestinal são fundamentais para a absorção oral de fármacos (SOUZA; FREITAS; STORPIRTIS, 2007). Um dos filtros mais utilizados é o de Lipinski. A regra dos 5 (RO5), também conhecida como regra de Lipinski, consiste na aplicação de um conjunto de parâmetros visando a busca de novos fármacos com maior probabilidade de possuírem elevada absorção oral (DOAK et al., 2014). Foi feita uma análise da biodisponibilidade oral e absorção gastrointestinal in sílico comparada ao AZD-1283 e ticagrelor. Assim, todos os candidatos a fármacos apresentam alta absorção intestinal, assim como ticagrelor e AZD-1283. A biodisponibilidade oral quando comparada ao AZD-1283 e ticagrelor indicam que mol23, mol29, mol32, mol36, mol38 e mol44 apresentam baixa biodisponibilidade oral, assim como os compostos de referência.

Através dos dados obtidos por meio do teste de TP e TTPA não se observa efeito expressivo dos compostos doxasozina (mol10) e 5-Chloro-2-Methoxy-N-[2-(4-

Sulfamoylpheny)ethyl]-benzamide (mol48) sobre as vias extrínseca e intrínseca da coagulação sanguínea, respectivamente nas concentração avaliada (100 µM), uma vez que não houve ampliação em duas vezes, dos valores de T/Tc. Dessa forma é possível inferir que esses compostos terão uma ação direcionada para o processo de agregação plaquetária, referente a hemostasia primária. De forma promissora, mol48 e mol10 não apresentaram qualquer atividade hemolítica detectável em sua concentração de 100 µM, apresentando efetivo padrão de segurança na faixa de atividade referente ao IC50, enquanto o controle positivo Triton X-100 a 1% causou 100% de hemólise.

A análise de energia livre de ligação mostra que o melhor ΔG de ligação foi do ticagrelor, apresentando melhor afinidade. Mostrou, também, que a contribuição de vdw foi menor do que a eletrostática nos três complexos, sugerindo que as interações hidrofóbicas contribuem mais na afinidade dos ligantes pelo receptor do que as interações eletrostáticas.

Conclusões

Dos compostos triados, 2 foram adquiridos, sendo, 5-Cloro-2-Metoxi-N-[2-(4-Sulfamoilfenil)etil]-benzamida e doxasozina. Ambos foram testados quanto a sua agregação plaquetária induzida por ADP apresentando padrão inibitório com valores de IC_{50} de 65,8 µM e 92,5 µM, respectivamente. Nos testes de TP e TTPa não foram observados efeitos significativos dos compostos mol10 e mol48 sobre a coagulação, mostrando que eles terão uma ação direcionada para o processo de agregação plaquetária, e não possuem a tendência de promover um desequilíbrio na hemostasia. Ambos também apresentaram valores (abaixo de 10%) que prevejam boa hemocompatibilidade e nenhuma toxicidade. Estudos de dinâmica molecular identificaram que, apesar de apresentarem padrão inibitório no teste de agregação plaquetária, o contato com o resíduo R241, um resíduo envolvido na ativação do receptor, pode justificar seus baixos valores. Além disso, contatos com os resíduos F237 e L269, resíduos apolares, podem contribuir para a hidrofobicidade. O medicamento ticagrelor e a molécula AZD-1283, que apresentam boa resposta biológica, possuem valores de logP positivos, logo são mais lipofílicos. Assim, as análises das simulações de dinâmica molecular, propriedades físico-químicas e atividade biológica indicam que o logP é uma propriedade que pode ser usada para nortear a seleção das moléculas triadas visando uma avaliação do perfil biológico delas. Ainda, de acordo com as análises de dinâmica molecular, propor modificações nos substituintes das moléculas triadas, de forma que apresentem caráter mais hidrofóbico, também pode ser uma abordagem interessante.

Agradecimentos

FAPERJ, CNPq, CAPES.

Referências

Example:
1. Cannon, B. Nature. 2013, 493, S2–S3.
2. Doak, B. C.; Over, B.; Giordanetto, F.; Kihlberg, J. Chemistry & Biology. 2014, 21, 1115–1142.
3. MCbane, R. D.; WysokinskI, W. E. In: Mayo Clinic Cardiology: Oxford University Press, 2012, 484–498.
4. ORGANIZAÇÃO MUNDIAL DE SAÚDE, 2023.
5. Souza, j.; Freitas, z. m. f.; Storpirtis, S. Brazilian Journal of Pharmaceutical Sciences. 2007, 43.

Termogravimetria da Hidroxi-Chalcona (E)-3-(4-hidroxifenil)-1-p-tolilprop-2-en-1-ona (HXC): Análise de Estabilidade e Decomposição.

Cristiane Alves da Fonseca do Espírito Santo[1], Clodoaldo Valverde[2], Ademir João Camargo[3]
[1,2] Universidade Estadual de Goiás, Laboratório de Modelagem Molecular Aplicada e Simulações - LAMMAS, UEG, Anápolis-Go, Brasil.

[3]Universidade Estadual de Goiás, Laboratório de Química Teórica e Estrutural-LQTEA, Anápolis-Go, Brasil

cristiane.alves@ueg.br
Keywords: Análise Térmica; Hidroxi-Chalconas; degradação Térmica; estudo Termogravimétrico.

Abstract
Chalcones and their derivatives have attracted increasing attention from researchers in recent years due to their applications in materials science and diverse biological activities. Hydroxy-chalcone HXC is a chalcone derivative that has sparked interest in the research of new materials. In this context, this work analyzed the thermal stability and decomposition of HXC through thermogravimetric analysis (TGA). The thermogravimetric curve demonstrated that the HXC molecule presents two stages of mass loss in the temperature range between 112 and 560 °C (Δm =97%), proving to be a material with good thermal stability, favoring several technological applications for the compound where materials with good thermal stability are required.

Introdução

As chalconas e seus derivados têm atraído cada vez mais a atenção dos pesquisadores nos últimos anos devido às suas aplicações nas ciências dos materiais e às diversas atividades biológicas que apresentam, como propriedades antibacterianas, antifúngicas, citotóxicas e anti-inflamatórias. Além disso, as chalconas se destacam por sua fácil modelagem molecular e por serem precursoras dos flavonoides encontrados em vegetais, que são assimilados pelo organismo humano através da alimentação[1].

A hidroxi-chalcona HXC (Figura 1) é um desses derivados de chalcona que tem despertado interesse significativo na pesquisa de materiais devido às suas propriedades únicas. Sua estrutura química permite uma variedade de modificações, tornando-a uma candidata promissora para diversas aplicações tecnológicas e biomédicas. Entre as técnicas analíticas utilizadas para investigar as propriedades dessas moléculas, a termogravimetria (TG) se destaca por sua capacidade de fornecer informações detalhadas sobre a estabilidade térmica e os mecanismos de decomposição.

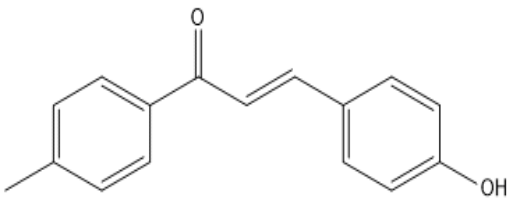


Figura 1- Estrutura molelular da Chalcona HXC.

A análise termogravimétrica (TGA) é uma técnica essencial na caracterização de materiais, permitindo avaliar como uma substância responde ao aumento de temperatura e quais são os produtos formados durante sua decomposição. Essa informação é crucial não apenas para entender a estabilidade de um material, mas

também para determinar suas possíveis aplicações em dispositivos eletrônicos, fotônicos e catalíticos. No caso das chalconas, a TGA pode ajudar a otimizar a síntese e o processamento desses materiais, ampliando seu uso em ciências dos materiais[2].

Neste contexto, este trabalho analisa a estabilidade térmica e decomposição da HXC através da TGA. Os resultados obtidos podem fornecer uma visão do comportamento térmico desta chalcona específica, evidenciando a importância das análises termogravimétricas na avaliação e desenvolvimento de novos materiais baseados em chalconas.

Metodologia

A síntese da chalcona HXC foi realizada através da reação clássica de condensação aldólica de *Claisen Schmidt* (figura 2), preparada pela reação de 4-hidroxibenzalaldeído (1) (3 mmol) em 1 mL de etanol com KOH (3 mmol). O precipitado obtido após 1 min, foi transferido para uma solução etanólica de 4-metilacetofenona (2) (2 mmol). A reação foi realizada à temperatura ambiente e seu progresso foi monitorado usando cromatografia em camada fina (TLC).

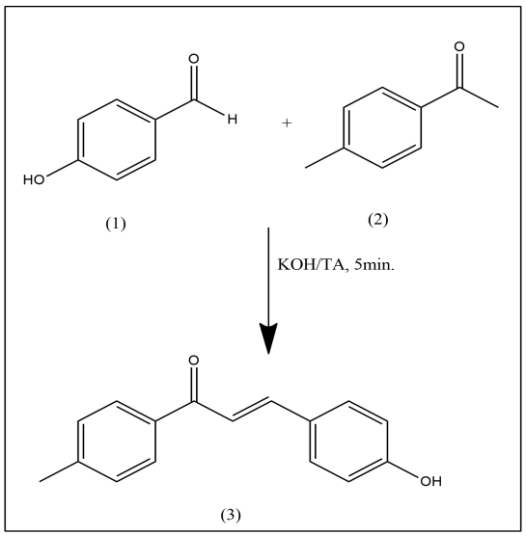


Figura 2- Síntese da Hidroxi-Chalcona (E)-3-(4-hidroxifenil)-1-p-tolilprop-2-en-1-ona (HXC)

O produto final foi coletado por filtração a vácuo e posteriormente purificado por cristalização em etanol. Um pó amarelo como produto (3) foi obtido. Os produtos químicos e solventes necessários foram obtido de fontes comerciais (Sigma-Aldrich). A TLC foi realizada utilizando placas de sílica gel e uma solução etílica sistema solvente acetato:hexano (1:9).

Para as análises termogravimétricas (TGA) e de termogravimetria derivada (DTG), foi utilized 1mg de amostra da Chalcona HXC cristalizada, pesada no próprio equipamento em cadinho de platina.

As análises TGA foram realizadas em analisador térmico (TGA-PYRIS 1, Perkin Elmer, EUA), sob atmosfera de gás Nitrogênio (N2), com vazão de 20 mL/min, razão de aquecimento de 10º C/min e faixa de temperatura de 25 a 600º C. As curvas de DTG foram obtidas a partir da derivada da curva de TGA, registrando-se a dTGA da massa em relação a temperatura (dm/dT) utilizando o software OriginPro2015®.

Resultados e discussão

O padrão de decomposição obtido para a chalcona HXC está demonstrado na figura Figura. 3.

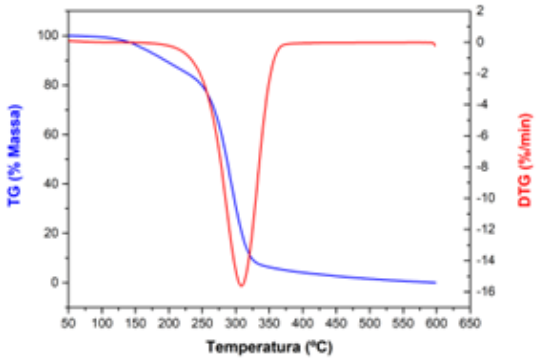


Figura 3- Termogramas das Curvas de TGA (Azul) e dTGA (Vermelho) para a Chalcona HXC.

A curva de TGA, mostra que o processo de decomposição térmica da HXC ocorre em dois estágios. O primeiro processo de perda de massa ocorre de 112 - 230ºC e essa perda inicial de massa (17%) possivelmente pode estar relacionada a umidade da amostra e/ou reagentes residuais[3]. A Segunda perda de massa ocorre de 245 -

560ºC, no qual há uma perda de massa acentuada na curva de TGA e observa-se que tal processo foi associado à decomposição da amostra (aproximadamente 80% de perda de massa). Além disso, a temperatura final de degradação (560°C) favorece diversas aplicações tecnológicas para o composto, quando materiais com boa estabilidade térmica são necessários.

Conclusão

Os experimentos de análise termogravimétrica são essenciais para caracterizar as propriedades térmicas das chalconas, fornecendo informações cruciais para seu desenvolvimento, síntese e aplicação em diversas áreas. A curva termogravimétrica (TG) demonstrou que a molécula de HXC apresenta dois estágios de perda de massa na faixa de temperatura compreendida entre 112 e 560 °C (Δm = 97%), se mostrando um material com boa estabilidade térmica.

Agradecimentos

Ao Centro de Análises, Inovação e Tecnologia em Ciência Naturais e Aplicadas da UEG – CA*i*Tec, localizado no Campus Central - Ciências Exatas e Tecnológicas da UEG, em Anápolis-GO, por ceder o laboratório para as análises termogravimétricas.

Referências

1.González-Sarrías, A.; Tomás-Barberán, F. A.; García-Villalba, R. Structural Diversity of Polyphenols and Distribution in Foods. Em: Dietary Polyphenols. [s.l.] Wiley, 2020. p. 1–29.

2. Olejnik, O.; Masek, A.; Kiersnowski, A. Thermal Analysis of Aliphatic Polyester Blends with Natural Antioxidants. *Polymers* 2020, *12*, 74. https://doi.org/10.3390/polym12010074

3. Karthikeyan, A., Suresh, J., Balaji, K., Anandhakumar, S., & Arun, A. (2022). Synthesis, characterization and antioxidant property of nano-scaled metal complexes of triazine based hydroxy chalcone. *Smart Science*, *11*(1), 192–203.

Revealing NDMA Formation: Mechanism, Kinetics and Regulatory Implications behind Theoretical Chemistry

Daniella C. Hilário de Paula[1], Pedro Henrique Ferreira Matias[1], Flávio O. Sanches-Neto[1,2] and Heibbe Cristhian B. de Oliveira[1].
[1]Laboratory of Electronic Structure and Molecular Dynamics, Federal University of Goias, Goiania, GO, Brazil.
[2] Federal Institute of Goias, IFG - Valparaiso de Goias Campus - GO, Brazil.
daniella_hilario@discente.ufg.br.

Keywords: nitrosamine, nitrosation, DFT, kinetic, thermodynamic.

Abstract

Recent discoveries of the presence of nitrosamines above acceptable limits in active pharmaceutical ingredients (APIs) and drug products (DPs) have motivated research into this subject and given rise to worldwide concern about these impurities. The kinetics and thermodynamics of N-nitrosodimethylamine (NDMA) formation were investigated using DFT. The comparative evaluation of the reactions studied showed that one is kinetically favored while the other is thermodynamically favorable.

Introduction

Nitrosamines are chemical substances characterized by containing a nitroso group linked to the nitrogen of an amine. These compounds can traditionally be formed from the reaction of a secondary or tertiary amine in the presence of nitrosating agents[1]. Although they have been reported since the 1950's, nitrosamines became a cause for concern for regulatory agencies such as the European Medicines Agency (EMA), the Food and Drug Administration (FDA) and the National Health Surveillance Agency (ANVISA) in 2018 when they were identified in active pharmaceutical ingredients (APIs) and drug products (DP)[2]. As this is a class of impurities with high mutagenic and carcinogenic potential, regulatory agencies, manufacturers of raw materials, pharmaceutical industries and researchers around the world are mobilizing to ensure the supply of safe medicines to the population, in other words, free of this type of impurity or, if present, with acceptable level[3].
It has become even more urgent to advance the frontier of knowledge regarding the chemistry of nitrosamine formation, their acceptable intake limits, the interaction of different impurities of this class in the body at cellular level, among other variables involved in this subject.
The purpose of this work is to investigate the kinetics and thermodynamics of the formation of N-nitrosodimethylamine (NDMA) from dimethylamine (DMA) and the nitrosating agents nitrosonium ion (NO^+) and dinitrogen tetraoxide (N_2O_4) using density functional theory (DFT).

Methodology

All the calculations were carried out using the Gaussian 16 software. The optimizations of the geometries and energies of the reactants, products, van de Waals complexes and transition states of the reactions studied were calculated with the M062X/def2tzvp level of theory. The contributions of ZPE (Zero Point Energy) were considered in the calculations of the energy barriers of these reactions. The thermodynamic and kinetic energy parameters were calculated as the difference between the energy of the products and reactants and the difference

between the energy of the transition state and that of the reactant structures, respectively.

Results and discussion

Figure 1 shows the potential energy surface for the nitrosation reaction of DMA and NO^+ (a - highlighted in blue on the left) and the reaction of DMA and N_2O_4 (b - highlighted in red on the right). Both reactions were found to be thermodynamically favorable. The energy barrier for 1.a is 3.4 kcal.mol^{-1} and for 1.b 15.4 kcal.mol^{-1}. A comparative analysis shows that reaction 1.a is kinetically favorable and reaction 1.b is thermodynamically favorable.

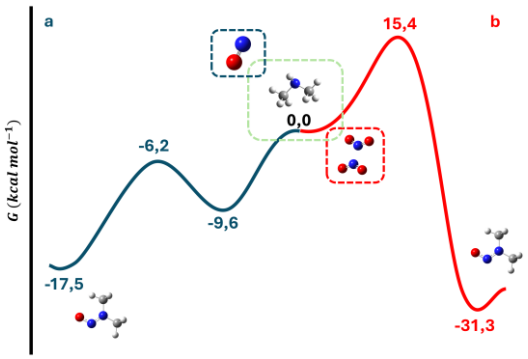


Figure 1: Representation of the energy barriers of the reactions studied.

Conclusion

Evaluating the energy barriers of nitrosation reactions represents a great opportunity to advance knowledge about the chemistry of nitrosamines and could enable the subsequent study of more complex reactions. The study suggests that the nitrosation reaction is favored by the reactants DMA and NO^+, but the thermodynamic results show that it will be necessary to carry out a more detailed evaluation of the case under study. The next steps in the research will be to evaluate molecular orbitals and the quantum theory of atoms and molecules to explain the difference in reactivity between the two proposed nitrosating agents. The kinetic constant of the reactions will also be calculated using DFT.

Acknowledgements

The authors would like to thank the Multiuser High Performance Computing Laboratory (LAMCAD) of the Federal University of Goias and the State University of Goias.

References

[1]LOPEZ-RODRÍGUEZ, Rocío *et al*. Pathways for N-Nitroso compound formation: secondary amines and beyond. Organic Process Research & Development, v. 24, n. 8, p. 1558-1585, 2020.
[2]Raphael Nudelman, *et al*. The Nitrosamine "Saga": Lessons Learned from Five Years of Scrutiny. Organic Process Research & Development 27 (10), 1719-1735, 2023.
[3]Schlingemann J, *et al*. The Landscape of Potential Small and Drug Substance Related Nitrosamines in Pharmaceuticals. J Pharm Sci. May;112(5):1287-1304, 2023.
[4]FRISCH, M. J.; TRUCKS, G. W.; SCHLEGEL, H. B. *et al.* Gaussian 16, Revision C.01 [Programa de Computador]. Wallingford CT: Gaussian, Inc., 2016.

Excitonic Effects in Quasi-2D Halide Perovskites with a Focus on Non-Toxic Metals.

Danilo Neves Silveira[1*], Alexandre Cavalheiro Dias[2], Luis Octavio de Araujo[1], Marco Antonio de Andrade Queiroz[1], Jônatas Favotto Dalmedico[3], Carlos Maciel de Oliveira Bastos[2], Celso Ricardo Caldeira Rêgo[4], Maurício Jeomar Piotrowski[3], Diego Guedes-Sobrinho[1*].
[1] Federal University of Paraná (UFPR), Department of Chemistry, Curitiba/PR, Brazil;
[2]Institute of Physics, International Physics Center, University of Brasília, Brazil;
[3]Federal University of Pelotas, Department of Physics, Pelotas/RS, Brazil;
[4]Karlsruhe Institute of Technology, Institute of Nanotechnology Hermann-von-Helmholtz-Platz, Karlsruhe, Germany.
**daniloneves@ufpr.br*
Keywords: Metal halide perovskites (MHPs), Density functional theory, DFT-1/2, MLWF-TB, BSE.

Abstract
Lead-free quasi-2D metal halide perovskites (quasi-2D MHPs) are promising materials for optoelectronic applications. This study develops a theoretical protocol to accurately analyze the structure, stability, and excitonic effects of zinc-based quasi-2D MHPs.

Introduction
Lead-free quasi-2D metal halide perovskites (quasi-2D MHPs) are promising for optoelectronic applications due to their low toxicity and high temperature stability. However, understanding their structural and optoelectronic properties, especially the role of excitons (electron-hole pairwise), is challenging because of their quantum-well behavior. This study proposes a theoretical protocol based on density functional theory (DFT) to characterize and analyze the stability of Cs_2ZnX (X = Cl_4, Br_2Cl_2, and I_2Cl_2) [1], using $Cs_2PbI_2Cl_2$ as a validation benchmark [2]. The electronic band gap is calculated using the relativistic quasi-particle approach (DFT-1/2) [3,4], which employs a weighted valence method protocol. Finally, the excitonic properties are characterized using the Bethe–Salpeter equation with the tight-binding method (MLWF-TB) [5,6].

Methodology and theoretical approach
We employed a multi-stage theoretical protocol thoroughly describe the excitonic properties of the materials, as illustrated in Figure 1.

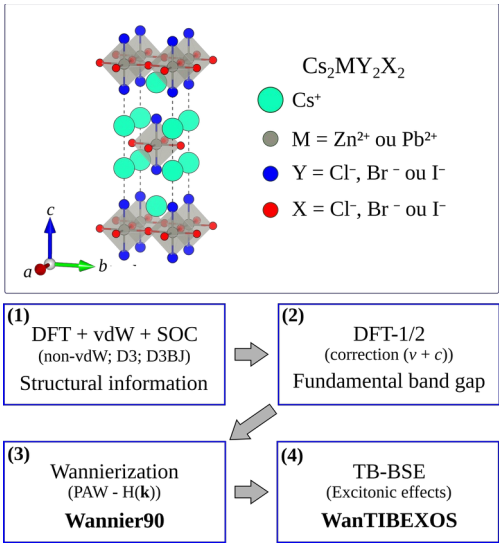


Figure 1: Unit cell representation of $Cs_2MY_2X_2$ (Y = apical; X = equatorial), and methodological steps.

The detailed methodological steps are as follows:

1. Structure optimization and thermodynamic study by using DFT+vdW

based on numerical solution from VASP code;

2. Analyzing the orbital contributions to VBM (valence band maximum) and CBM (conduction band minimum) in 2D–RP MHPs, using DFT-1/2 with spin-orbit coupling (SOC);

3. The optimized VBM-CBM corrections from DFT-1/2(SOC) to derive the TB Hamiltonian, $H(\mathbf{k})$, via the MLWF procedure with the Wannier90 package;

4. The obtained $H(\mathbf{k})$ was used in the WanTiBEXOS [5] code to solve the BSE, determining exciton binding energies and the optical absorption coefficient with excitonic effects.

Results and Discussion

Stability: A thermodynamic analysis of the enthalpy of formation was employed to discern two distinct stabilization mechanisms for the zinc and lead systems.

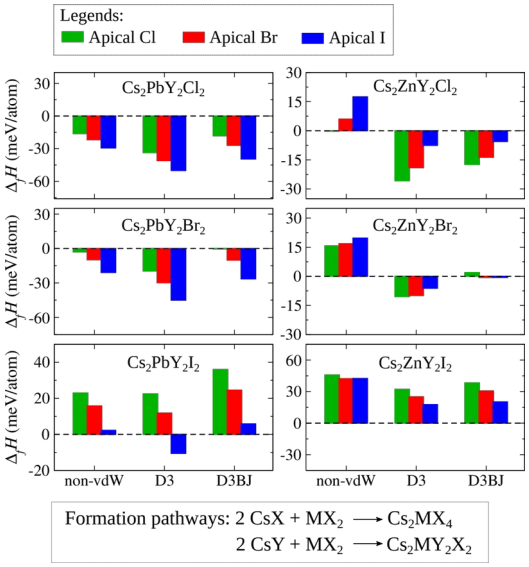


Figure 2: Enthalpy of formation for quasi–2D–RP MHPs. The colored bars represent the halides outside the plane in the apical direction. For Pb(Zn)-based MHPs, the apical sites are occupied by Cl, Br, and I.

The analysis was conducted by comparing the calculation protocols with the alternation of halides in equatorial and apical positions. The data pertinent to the analysis are depicted in Figure 2. It is evident that lead systems and the $Cs_2ZnY_2I_2$ type system (equatorial iodine) are stabilized when the smaller halides are positioned in the equatorial sites and the larger halides in the apical sites.

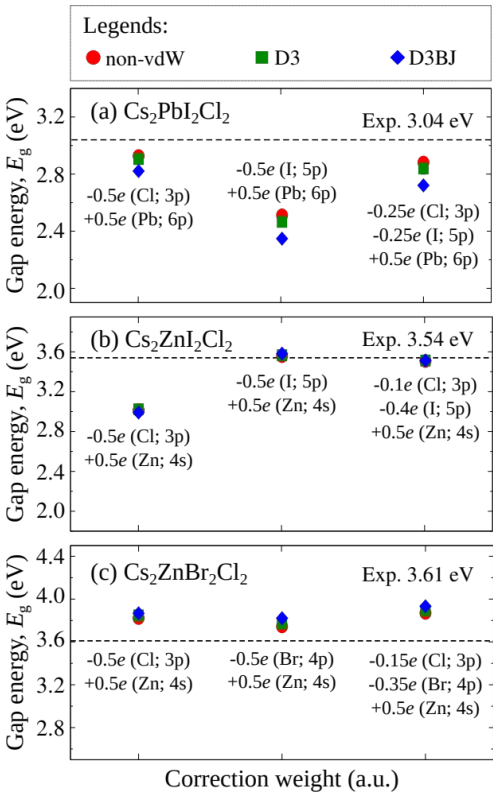


Figure 3: Calculated band gap energies using the DFT-1/2(SOC) protocol with non–vdW, D3, and D3BJ corrections. The variance in correction weights compared to experimental values is shown for: (a) $Cs_2PbI_2Cl_2$, (b) $Cs_2ZnI_2Cl_2$, and (c) $Cs_2ZnBr_2Cl_2$. Experimental band gaps can be visualized in references 1 (a) and 2 (b,c).

However, this tendency undergoes a sudden shift when bromine and chlorine halides occupy the equatorial positions in Zn systems, resulting in a decline in stability as the largest halide assumes an out-of-plane position. We proposed a mechanism for stabilization related to the radii of the central cations and their ability to arrange the spacer cation (Cs^+) within the cavities. In systems with low disposal capacity, cations tend to remain outside the octahedron lay-

ers, with the packing making the systems more stable. This phenomenon is observed in the $Cs_2ZnY_2X_2$ (Cl and Br) systems. In contrast, the $Cs_2PbY_2X_2$ and $Cs_2ZnY_2I_2$ systems, with larger radii and greater arrangement capacity, exhibit stabilization through packing and the formation of stronger bonds between the apical halides.

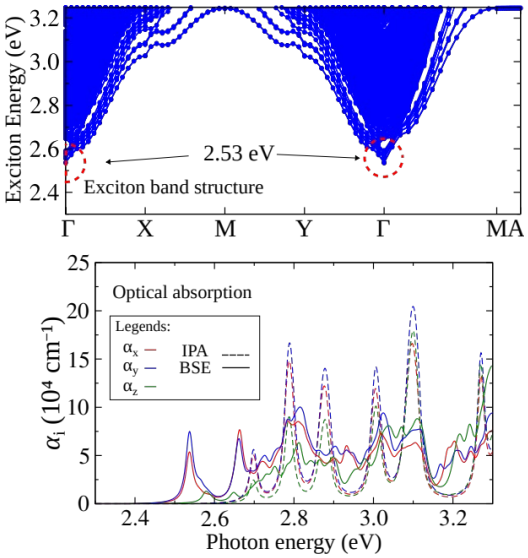


Figure 4: Excitonic properties of $Cs_2PbI_2Cl_2$, showing the exciton band structure with the lowest exciton transition highlighted, and optical absorption with (TB-BSE) and without (TB-IPA) excitonic effects.

The vdW protocol exhibited greater stability compared to non-vdW protocols, attributed to the inclusion of long-range interactions. Furthermore, structures relaxed with these protocols closely resembled the reference $Cs_2PbI_2Cl_2$ in relation to the lattice parameters. This was particularly evident in the case of D3BJ, with deviations being less than 1%.

Electronic structure: To calculate the band gap, which is often underestimated by local and semi-local exchange-correlation functional, the DFT-1/2 corrections were fully employed, adjusting VBM and CBM. In particular, for systems with halide alloys, a refined correction was applied considering the orbital contributions to the VBM, yielding the band gaps depicted in Figure 3.

Therefore, the calculated band gaps exhibit minimal deviations from experimental values, highlighting the effectiveness of the weighted approach that accounts for hybrid states in the VBM.

Excitonic effects: The TB Hamiltonian was parametrized by the DFT-1/2 electronic structure. To compute the exciton binding energy (E_b), the ground-state exciton energy was calculated by varying the exciton band structure. As an illustrative example for the reference system, Figure 4, E_b was calculated by subtracting DFT-1/2(SOC) band gap from the ground state exciton energy, resulting in a value of 160 meV. This value demonstrates a deviation of less than 1% from the experimental data. Furthermore, the optical absorption with polarized light was analyzed, which demonstrated a significant influence of excitonic interactions on optical properties.

Conclusions

This study investigated the structural, thermodynamic, electronic, and optical properties of quasi-2D inorganic MHPs based on Zn and Pb. The study focused on octahedral lattice rearrangement driven by Cs^+-halide interactions. Using DFT-1/2, we corrected electronic structures, achieving deviations of less than 10% from experimental values. The incorporation of TB+BSE exciton effects enabled the matching of $Cs_2PbI_2Cl_2$ exciton binding energies with a deviation of only 1%. These methods offer cost-effective accuracy, indicating potential applications of quasi-2D MHPs in optoelectronics.

Acknowledgments

PPGQ-UFPR, CAPES, LCPAD-UFPR, NACAD-UFRJ, CENAPAD-Unicamp and SENAI-CIMATEC.

References

1. Shankar, H. et al. ***J. Alloys Compd***. 2020, 844, 15614;
2. Li, J. et al. ***JACS***, 2018, 140, 11085.
3. Ferreira, L. et al. ***Phys. Rev. B.*** 2008, 78, 125116;
4. Guedes-Sobrinho, D. et al. ***Sci. Rep***. 2023, 13, 4446;
5. Dias, A. et al. ***Comput. Phys. Commun.*** 2023, 285, 11085;
6. Guedes-Sobrinho, D. ***J. Phys. Chem. C.*** 2024, 128, 7242.

10º SIMPÓSIO DE ESTRUTURA ELETRÔNICA E DINÂMICA MOLECULAR
SEED MOL
4 a 8 novembro | 2024
Pirenópolis, Goiás

Synthesis, structural characterization, and DFT study of a complex of Cu(II) with 2,2′-bipyridine and sulfate ligands

Abreu D. C.[1,2], Lage M.R. [2], Stoyanov, S.R.,[3] Santos A.O[2], Lima A. D. S. G. [2] and Viana J.R. [2]

[1] Instituto Federal de Educação, Ciência e Tecnologia do Maranhão – MA, Brasil.

[2] Universidade Federal do Maranhão – MA, Brasil

[3] Natural Resources Canada, CanmetENERGY Devon, AB, Canada

diego.abreu@ifma.edu.br

Keywords: DFT; PBE1PBE; Coordination Compounds; XDR; Vibrational Spectrocopy

Abstract

The complex [Cu(bpy)$(H_2O)_2(SO_4)_2$], where bpy is 2,2′-bipyridine, was synthesized by a new route, characterized by XRD and Raman and FT-IR spectroscopies, and DFT investigation. Results confirmed the synthesis and demonstrated the efficiency of PBE1PBE/6-311++G(d,p)/SDD for the computational study of thermodynamic and electronic properties.

Introduction

A literature review shows that copper complexes have been increasingly important in various fields of application, such as energy production [1]. From this perspective, the coordination compound [Cu(bpy)$(H_2O)_2(SO_4)_2$], first synthesized in 1974 by Tedenac [2], may represent alternative technological applications. This complex has an elucidated crystallographic structure, but there is a lack of comprehensive theoretical and experimental studies.

Methodology

In this work, the synthesis of the complex was carried out through a new route. By tutulometry, the 2,2'-bipyridine solution was slowly added to the Cu(II) sulfate solution, generating the complex as a precipitate. The product samples were experimentally analyzed using X-ray Diffraction (XRD), Fourier Transform Infrared Spectroscopy (FT-IR), and Raman. The theoretical study was conducted via density functional theory (DFT), with the DFT functional PBE1PBE associated with the 6-311++G(d,p) basis set for C, N, O, S, and H atoms, and the pseudopotential and valence electron basis functions of SDD basis set (Stuttgart-Dresden) [3]. The solvation effects were studied with the IEFPCM method [4]. The obtained data are presented below.

Results

Figure 1 shows the refinement of the experimental diffractogram using the Rietveld method [5]. Meanwhile, Table 1 presents the comparison of lattice parameters of the sample with the diffraction standard extracted from the *CIF* (crystallographic information file).

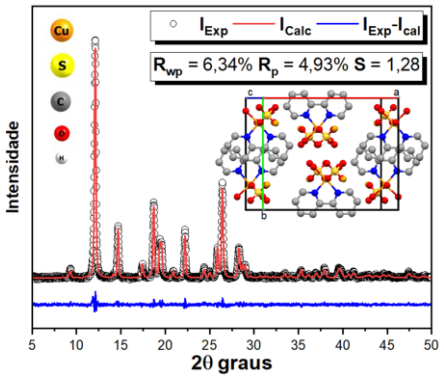


Figure 1. Rietveld refinement.

Table 1. Comparison of lattice parameters of the sample with data from the CIF.

Network Parameter	*Sample*	*Tedenac [2]*
***a* (Å³)**	15,06	15.136
***b* (Å³)**	12,38	12.464
***c* (Å³)**	6,96	6.999
α	90°	90°
β	105,9°	105.97°
γ	90°	90°
***Volume* (Å³)**	1249,08	1269,44

The optimized geometries obtained in this work from the DFT calculations, as well as the dipole moments and partial charges, are shown in Figure 2. Filled lowest energy (HOMO) and lowest energy (LUMO) frontier orbitals, as well as the electrostatic potential maps, can be seen in Figure 3.

In Figures 4 and 5, comparisons of the FT-IR and Raman spectra calculated in vacuum, methanol, and water are presented alongside

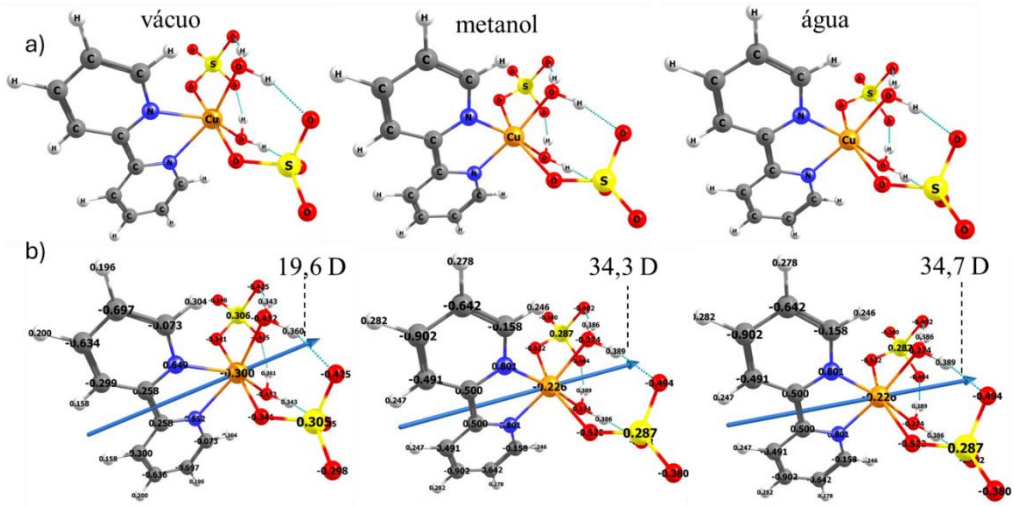


Figure 2. (a) Optimized geometry; (b) partial atomic charges and dipole moment calculated for the complex in vacuum, methanol and water.

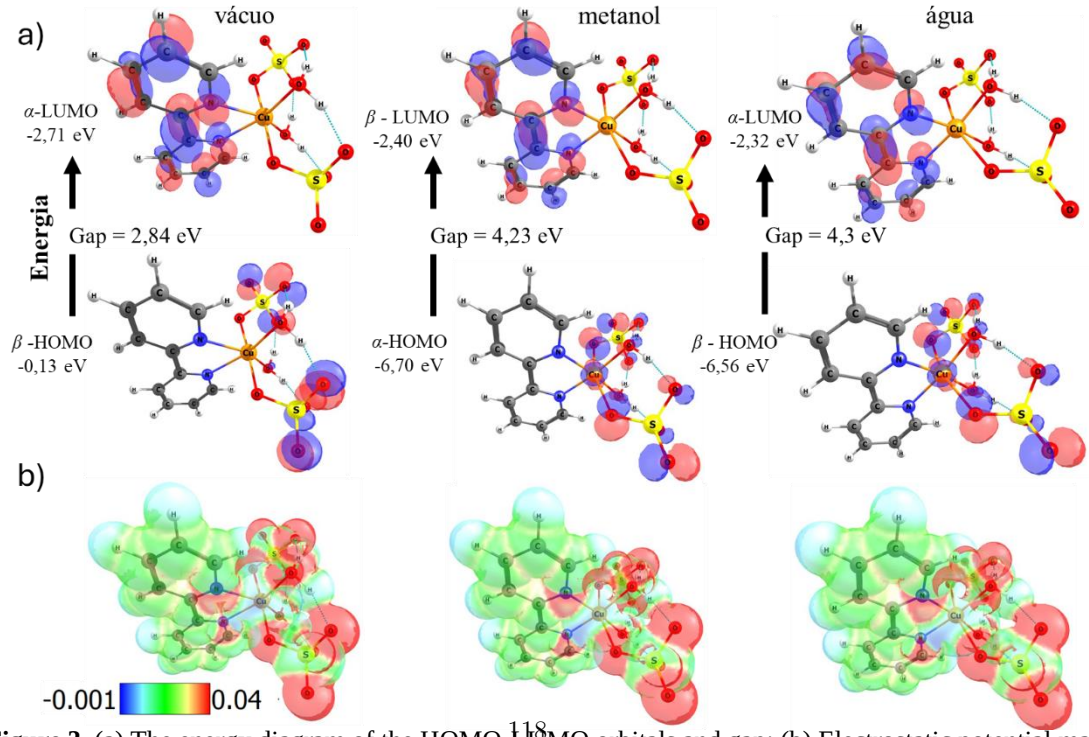


Figure 3. (a) The energy diagram of the HOMO-LUMO orbitals and gap; (b) Electrostatic potential map calculated for the complex in vacum, methanol and water.

the experimentally obtained spectra.

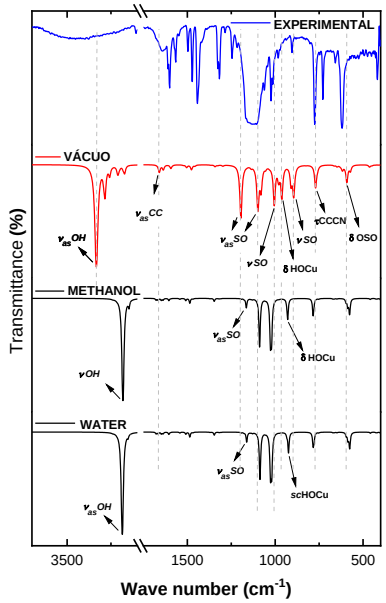


Figure 4. Comparison of FTIR spectra.

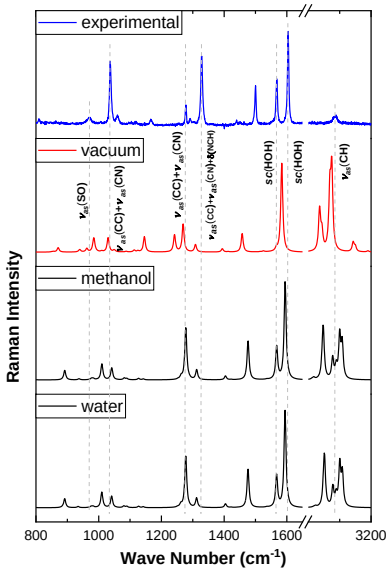


Figure 5. Comparison of Raman spectra

Discussion

The sample was obtained through a new, more straightforward route than the one proposed by Tedenac [2]. Refinement using the Rietveld method confirms that the complex in the obtained sample corresponds to the complex $[Cu(C_{10}H_8N_2)(H_2O)_2(SO_4)_2]$. The calculated FT-IR and Raman spectra correlate well with the experimental ones, corroborating our findings from XRD.

The DFT calculations provided additional information, which allowed us to study the electronic and thermodynamic properties of the titled complex.

It is worth noting that the ΔG^{298} of complexation is -871,3 kcal/mol in a vacuum, -187,96 kcal/mol in water, and -199,85 kcal/mol in methanol, confirming that the complexation is a spontaneous process. The dipole moment vector is oriented toward the sulfate groups, which makes sense since, in the electrostatic potential maps, it is possible to observe that this region has higher electron density. Furthermore, the small HOMO-LUMO gap suggests potential applications in electronics and energy production/storage [6].

Conclusion

The synthesis of the complex $[Cu(C_{10}H_8N_2)(H_2O)_2(SO_4)_2]$ was carried out through a new, more straightforward route. The obtention experimental characterization developed in this work confirmed the obtention of the complex. The results obtained from DFT calculations contributed to the characterization and provided additional information in the study of properties of the complex, also considering solvation effects on these properties.

Acknowledgements

LabMMol
Digital Research Alliance of Canada

References

[1] E. Chiyindiko, E. H. G. Langner, and J. Conradie, Molecules, vol. 27, no. 18, 2022, p. 6033.
[2] J.-C. Tedenac and E. Philippot, Journal of Inorganic and Nuclear Chemistry, vol. 37, no. 3, 1975, p. 846.
[3] P. Hohenberg and W. Kohn, Physical Review, vol. 136, no. 3B,1964, p. B864.
[4] G. Scalmani and M. J. Frisch, Journal of Chemical Physics, vol. 132, 2010, n°11.
[5] H. M. Rietveld, Acta Crystallogr, vol. 22, n° 1, 1967, pp. 151.
[6] Z. Ali, S. Abdalla, E. A. Hassan, Y. Umar, and M. M. Al-Mogren, Journal King Saud Univ Sci, vol. 34, n° 5, 2022, p. 102117.

10º SIMPÓSIO DE ESTRUTURA ELETRÔNICA E DINÂMICA MOLECULAR
SEEDMOL 4 a 8 novembro | 2024 Pirenópolis, Goiás

Structural and Optical Properties of Epoxy-functionalized Graphene Quantum Dots: A Theoretical Study

Edna S. M. Rodrigues[1], Nailton M. Rodrigues[2], João B. L. Martins[1].
[1]Instituto de Química, Universidade de Brasília, Brasília-DF
[2]Universidade Federal do Maranhão, São Luís-MA
edna_quimica@yahoo.com.br.
Keywords: coronene, conformations, optical absorption spectra.

Abstract
Density functional theory (DFT) and time dependent density functional theory (TDDFT) calculations have been performed to investigate the structural and optical properties of coronene ($C_{24}H_{12}$), as a model of GQD, and its derivatives functionalized with epoxy groups. It is observed that the epoxy groups distort the basal plane of the molecule and, as a consequence, the spectral profile varies with an increase in this oxygenated group.

Introduction

Since their discovery in 2004, graphene-based nanomaterials have attracted tremendous research interest. [1] Among graphene-based materials, the graphene quantum dots (GQDs) are of particular interest, because these materials are known for their optical properties, which are strongly influenced by a number of factors such as the their size (quantum confinement), shape, surface chemical composition (edge effect), or the functionalization with oxygenated groups including hydroxyl (-OH), epoxy (-O-), ether (-OCH_3), carbonyl (-(C=O)-), and carboxyl (-COOH) groups. [2]
Here the coronene molecule ($C_{24}H_{12}$) was selected as the model GQD, and the epoxide groups were covalently bonded to its basal plane.
In this work, we have used density functional theory (DFT) and time-dependent DFT (TDDFT) calculations to study the effect of the number of epoxy groups and conformational structure on the optical properties of a GQD. Based on the distribution of epoxy functional groups, our results provide a clear strategy for tuning the properties of GQDs.

Methodology

All calculations have been performed on the framework of Density Functional Theory[3] as implemented in the Gaussian16 (G16) program package[4]. The B3LYP hybrid functional was chosen for all calculations. Vibrational frequency calculations for the optimized geometries are carried out to obtain zero point vibrational energy (ZPVE). Excited state electronic structure and related optical properties of all molecular systems were calculated with time dependent density functional theory (TDDFT) methodology. TDDFT calculations were then performed for the first 30 states which were evaluated for the optical spectra, which were fitted with a Gaussian function with a half width at half maximum (HWHM) of 0.13 eV. The 6-311++G(d,p) basis set were chosen for the current study.

Results and Discussion

The relaxed structures $C_{24}H_{12}$ (D_{6h} symmetry) and epoxy-functionalized GQDs ($C_{24}H_{12}O$, $C_{24}H_{12}O_2$ and $C_{24}H_{12}O_3$, with point groups C_s, C_{2V} and C_s, respectively) are shown in the Figure 1. It is noted that the distortion of the basal plane of the $C_{24}H_{12}$ increases significantly as the number of epoxy groups increases. This can be explained by the conversion of sp^2 to sp^3 hybridization of carbon atoms (C-O-C).[5]

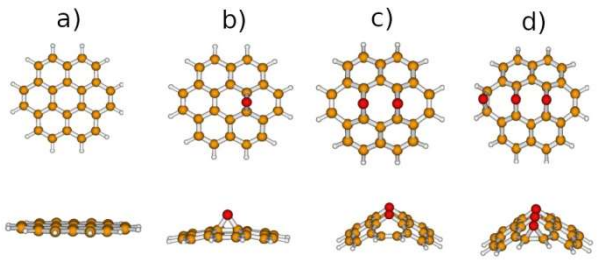


Figure 1: Top and side views of optimized geometries of the a) $C_{24}H_{12}$, b) $C_{24}H_{12}O$, c) $C_{24}H_{12}O_2$ and d) $C_{24}H_{12}O_3$ in gas phase. Color labels: yellow: C, red: O and white: H.

The energy levels of frontier orbitals are depicted in Figure 2. The results of HOMO−LUMO energy gap, showed that the presence of epoxy groups on the $C_{24}H_{12}$ molecule causes a slight increase in the the HOMO-LUMO gap ($C_{24}H_{12}O_2$ and $C_{24}H_{12}O_3$), except for the $C_{24}H_{12}O$. For Cui and Xue the different binding configurations of the epoxy groups influence the structural and orbital symmetries of the graphene lattice, resulting in variations in the bandgaps.[6]

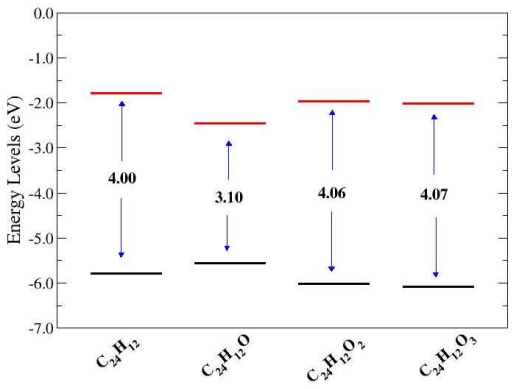


Figure 2: The highest occupied molecular orbitals (HOMOs) and lowest unoccupied molecular orbitals (LUMOs) of $C_{24}H_{12}$ and its epoxides molecules at the ground state.

To investigate the influence of the number (1-3) on the bands absorption of GQD model, we have performed TDDFT calculations of the optical spectra of $C_{24}H_{12}$, $C_{24}H_{12}O$, $C_{24}H_{12}O_2$ and $C_{24}H_{12}O_3$, which can be seen in the Figure 3.

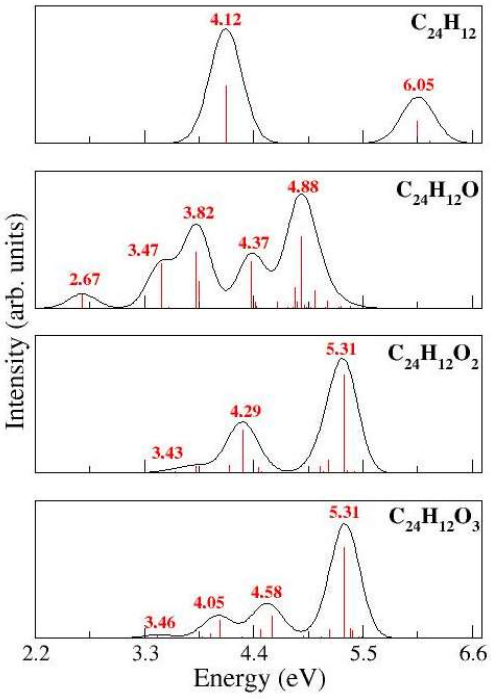


Figure 3: Optical absorption spectra of the $C_{24}H_{12}$, $C_{24}H_{12}O$, $C_{24}H_{12}O_2$ and $C_{24}H_{12}O_3$.

From Figure 3 it can be seen that the presence of epoxy groups affects the absorption spectral profile. This feature is due to the presence of epoxy groups that cause distortion of the carbon backbone, breaking structural and orbital symmetry.

The optical spectra of $C_{24}H_{12}$ show a spectral profile composed of two absorption bands (4.12 eV and 6.05 eV). The low energy peak at 4.12 eV is attributed to the transitions from its ground state (S_0) to the third (S_3) and fourth (S_4) excited states, and is related to the π–π* transitions (aromatic C–C bond). On the other hand, there are no transitions to states S_1 and S_2, since these are electronic transitions forbidden by the electric dipole. The absorption band at 6.05 eV is contributed by electronic excitations from S_0 to high energy degenerated excited states, such as $S_0 \rightarrow S_{25}$ and $S_0 \rightarrow S_{26}$, also attributed to the π–π* transition (aromatic C–C bond).

For the epoxy functionalized GQDs we can see the appearance of new bands which are not observed for $C_{24}H_{12}$. In the analysis of the spectra of the functionalized GQDs, a remarkable difference can be observed, in particular for $C_{24}H_{12}O$. This can be caused

by electronic excitations that are activated as a result of a change in the optical selection rules that take into account the newly appeared absorption peaks.

The electronic transition $S_0 \rightarrow S_1$ appear at 2.67 eV, 3.43 eV and 3.46 eV for $C_{24}H_{12}O$, $C_{24}H_{12}O_2$, and $C_{24}H_{12}O_2$, respectively. Therefore, it is observed that increasing the number of epoxy groups on GQD promotes blue-shift of the HOMO-LUMO absorption peak, which can be explained by the slight increase in the contribution of the oxygen orbitals to the orbitals involved in this electronic transition ($n \rightarrow \pi^* + \pi-\pi^*$, n refers to lone pair electrons of oxygen).

The highest intensity bands are located at 4.88 eV, for the $C_{24}H_{12}O$, and 5.31 eV for the $C_{24}H_{12}O_2$ and $C_{24}H_{12}O_3$. These bands are contributed by the electronic excitations from S_0 to several highenergy excited states and refer to $\pi-\pi^*$ transitions.

Conclusions

As revealed in this work, the structural and optical properties of GQD model ($C_{24}H_{12}$) is sensitive to the functionalization with epoxy groups. From a structural point of view, it has been shown that the progressive increase in the number of epoxides in the GQD causes greater distortion in the plane of the molecule. Moreover, introducing the epoxy group at the basal plane of the GQD model ($C_{24}H_{12}$) can activate the optically forbidden $S_0 \rightarrow S_1$ transition.

Acknowledgements

SEEDMOL, CAPES, CNPq, FAPDF.

References

1. K. S. Novoselov, A. K. Geim, S. V. Morozov, D. Jiang, Y. Zhang, S. V. Dubonos, I. V. Grigorieva, A. A. Firsov, Science 2004, 306, 666.
2. Li, Y.; Shu, H.; Niu, X.; Wang, J. J. Phys. Chem. C 2015, 119, 24950.
3. K. Burke J. Chem. Phys., 2012, 136, 150901.
4. M. Frisch, G. Trucks, H. Schlegel, G. Scuseria, M. Robb, J. Cheeseman, G. Scalmani, V. Barone, G. Petersson, H. Nakatsuji, X. Li, M. Caricato, A. Marenich, J. Bloino, B. Janesko, R. Gomperts, B. Mennucci, H. Hratchian, J. Ortiz, A. Izmaylov, J. Sonnenberg, D. Williams-Young, F. Ding, F. Lipparini, F. Egidi, J. Goings, B. Peng, A. Petrone, T. Henderson, D. Ranasinghe, V. Zakrzewski, J. Gao, N. Rega, G. Zheng, W. Liang, M. Hada, M. Ehara, K. Toyota, R. Fukuda, J. Hasegawa, M. Ishida, T. Nakajima, Y. Honda, O. Kitao, H. Nakai, T. Vreven, K. Throssell, Montgomery, Jr., J. Peralta, F. Ogliaro, M. Bearpark, J. Heyd, E. B.y K.N. Kudin, V. Staroverov, T. Keith, R. Kobayashi, J. Normand, K. Raghavachari, A. Rendell, J. Burant, S. Iyengar, J. Tomasi, M. Cossi, J. Millam, M. Klene, C. Adamo, R. Cammi, J. Ochterski, R. Martin, K. Morokuma, O. Farkas, J. Foresman and D. Fox, Gaussian 16 Revision C. 01, 2016, Gaussian Inc. Wallingford CT.
5. Odkhuu, D.; Shin, D.; R.S. Ruoff & Park, N. Scientific Reports, 2013, 3276.
6. Cui, P.; Xue, Y. Chem Eng J. 2022, 134052.

10º SIMPÓSIO DE ESTRUTURA ELETRÔNICA & DINÂMICA MOLECULAR
SEEDMOL 4 a 8 novembro | 2024 Pirenópolis, Goiás

Excitons in Nanoribbons Derived from Monolayer Biphenylene

E. J. A. Santos [1], Alexandre C. Dias [2], and L. A. Ribeiro Junior[3].

[1] Institute of Physics, University of Brasília, 70910-900, Brasília, Brazil.
[2] Institute of Physics, University of Brasília, 70910-900, Brasília, Brazil.
[3] Institute of Physics, University of Brasília, 70910-900, Brasília, Brazil.

emanueljose1215@hotmail.com, *alexandre.dias@unb.br*, *ribeirojr@unb.br*.

Biphenylene Monolayer (BPN), Boron Nitride, Nanoribbons, Electronic Properties, Optical Properties.

Abstract

In this study, we explore the structural and electronic properties of heterojunctions composed of biphenylene nanoribbons (BPN) and biphenylene-boron nitride (BPN-BN) through first-principles simulations. Biphenylene is a recently synthesized two-dimensional form of carbon, characterized by its square lattice of benzene rings. The introduction of boron nitride (BN) into BPN nanoribbons creates heterojunctions with unique properties due to the contrast between the metallic nature of BPN and the insulating properties of BN.

We employed density functional theory (DFT) calculations to investigate the stability of the BPN/BPN-BN heterojunctions, analyzing parameters such as binding energy, electronic structure, density of states, and excitonic properties. The results indicate that the interface between BPN and BPN-BN maintains good structural stability, enabling the formation of viable heterojunctions for electronic device applications.

The investigation of the electronic transport properties of the BPN-BN heterojunctions was conducted using first-principles calculations. The data indicated a significantly variable carrier mobility in the heterojunctions compared to pure BPN nanoribbons.

Another important aspect is the presence of excitons, which can significantly modify the optical properties of the nanoribbons. Excitons, quasi-particles formed by the binding of an electron with a hole through Coulombic forces, play a crucial role in determining the optical properties of the nanoribbons. Manipulating excitons in BPN and BPN-BN heterojunctions could lead to significant advancements in light-emitting technologies, photodetectors, and solar cells. This study highlights the capability of excitons to influence electronic interactions in heterojunctions, providing valuable insights for the development of efficient optoelectronic devices.

In conclusion, this study demonstrates that BPN-BN heterojunctions possess superior structural, electronic, and optical properties, making them promising for a wide range of technological applications. The detailed characterization of the heterojunctions opens new possibilities for nanoscale material engineering, offering valuable insights for future research and the development of advanced devices.

Introduction

Two-dimensional nanostructured materials, such as Biphenylene (BPN), are emerging as promising and cost-effective solutions for advanced optoelectronic applications [1]. Recently synthesized, BPN is composed of rings of 4, 6, and 8 carbon atoms, making it a fragile and lightweight material with a single-atom thickness [2]. Its properties include high stability, electrical conductivity, and transparency in both visible and ultraviolet spectra [3]. However, the lack of an energy bandgap limits its applications. Doping can open the bandgap [4]. Additionally, forming 2D networks with Boron and Nitrogen, such as h-BN, can enhance its properties and expand its applications [5].

In this work, inspired by theoretical and experimental results on h-BN/graphene heterojunctions [6], we utilized density functional theory (DFT) calculations to analyze the structural and electronic properties of BPN nanoribbons with BN domains of various sizes and periodicities. We found that these heterojunctions exhibit significant variations in band structures and charge distributions, suggesting advanced electronic applications and the possibility of excitonic insulation properties.

Methodology

In this study, we utilized density functional theory (DFT) calculations to analyze the structural and electronic properties of BPN nanoribbons with varied BN domains. The optimizations were performed using the Vienna Ab initio Simulation Package (VASP) [7], employing the generalized gradient approximation (GGA) and the Perdew-Burke-Ernzerhof (PBE) functional [8]. Due to the bandgap underestimation by PBE [9], we employed the Heyd-Scuseria-Ernzerhof (HSE06) hybrid functional [10] for a more accurate description.

Geometry optimization was conducted with a cutoff energy of 800 eV and a minimum atomic force of 0.01 eV/Å. A vacuum of 15 Å was applied to avoid spurious interactions between the nanoribbons and their periodic images. We used k-point meshes of 10×1×1 for structural optimization, 15×1×1 for electronic properties, and 30×1×1 for density of states (DoS).

The linear optical response was calculated in the independent particle approximation (IPA) and with excitonic effects using the Bethe-Salpeter equation (BSE) [11], with the WanTiBEXO code [12]. We described the single-particle levels with the maximally localized Wannier functions tight-binding Hamiltonian (MLWF-TB) [13] and solved the BSE with the 2D truncated Coulomb potential (V2DT). For the dielectric functions, a smoothing of 0.01 eV was used.

The BPN-BN-C structure contains 40 atoms per unit cell and specific lattice parameters. The BN-BPN bond lengths obtained are consistent with literature data [14]. Figure 1 illustrates the optimized structure of the BPN-BN-C nanoribbons.

Results

In this study, we investigated the structural, electronic, and optical properties of biphenylene (BPN) nanoribbon heterojunctions and their boron nitride analogs (BPN-BN) using density functional theory (DFT) calculations. The heterojunctions were proposed in nanoribbon forms with zigzag (ZZ) and armchair (AC) edges, and their structural and electronic transport characteristics were examined.

The proposed nanoribbons, including BPN-ZZ-BN-C-BN, BPN-AC-BN-C-BN, BPN-ZZ-C-BN-C, and BPN-AC-C-BN-C, exhibited significant structural stability. Most of the structures remained flat, except for BPN-AC-BN-C-BN, which showed a vertical tilt of 6.3º, indicating a topological modification. Passivation with hydrogen atoms at the non-periodic edges of the nanoribbons prevented charge imbalances, contributing to structural stability.

The partial density of states (PDOS) analysis revealed that, regardless of the edge type or chemical composition of the nanoribbon, the p orbitals of carbon atoms are predominant near the Fermi level. In armchair-type nanoribbons, a significant contribution from the p orbitals of nitrogen atoms in the valence states near the Fermi level was also observed. This indicates that the electrons in the carbon p orbitals play a crucial role in the electronic properties of the system.

The electronic band structures of the studied nanoribbon heterojunctions, both at the PBE and HSE06 levels, exhibited semiconductor behavior. Armchair-type nanoribbons displayed a fundamental bandgap ranging from 1.30 eV to 1.50 eV, while zigzag-type nanoribbons showed a fundamental bandgap ranging from 0.15 eV to 0.30 eV. The electronic properties of the heterojunctions are highly sensitive to the nanoribbon edges and atomic compositions, highlighting the differences in bonding that contribute to the structure's growth.

The distribution of the highest occupied crystal orbitals (HOCO) and lowest unoccupied crystal orbitals (LUCO), as well as the electron localization function (ELF), revealed a non-uniform distribution of orbitals along the armchair-type nanoribbon structures. In contrast, in zigzag-type nanoribbons, the HOCO and LUCO orbitals were more uniformly distributed among the carbon atoms.

The excitonic states of the nanoribbon heterojunctions, obtained by solving the Bethe-Salpeter equation (BSE), showed that the ground-state exciton for BPN-ZZ-BN-C-BN is direct, whereas for the other configurations, it is indirect. In zigzag-type nanoribbons, the ground-state exciton energy is below 0 eV, indicating that the Coulomb interaction between the electron and hole is greater than the electronic gap.

Conclusion

This study revealed that BPN-BN nanoribbon heterojunctions exhibit promising electronic and optical properties for applications in nanoscale optoelectronic devices. Zigzag-edged nanoribbons demonstrated semiconductor behavior with direct and indirect bandgaps, depending on the atomic composition. Armchair-type nanoribbons, although exhibiting indirect bandgaps, showed significant contributions from nitrogen orbitals in the valence states. The presence of direct and indirect excitonic states highlights the potential of these heterojunctions for future technological applications, including advanced semiconductor devices and sensors. The obtained results provide a detailed understanding of the electronic and structural properties of these nanoribbons, opening new perspectives for the development of two-dimensional materials with tunable properties for specific applications. Important references for this study include previous theoretical and experimental works on h-BN/graphene heterojunctions and analyses of two-dimensional materials, as referenced in the studies.

Acknowledgements

This work was financed by the Coordenação de Aperfeiçoamento de Pessoal de Nível Superior (CAPES), Conselho Nacional de Desenvolvimento Cientifico e Tecnológico (CNPq), and Fundação de Apoio à Pesquisa do Distrito Federal (FAP-DF). L.A.R.J. acknowledges the financial support from FAP-DF 00193.00001808⁄2022 − 71 grant and FAPDF-PRONEM grant 00193.00001247⁄2021 − 20, and CNPq grant 350176⁄2022 − 1. A.C.D acknowledges the financial support from FAP-DF 00193−00001817⁄2023−43 and 00193−00002073⁄2023−84 grants and CNPq 408144⁄2022−0 and 305174⁄2023 − 1 grants. L.A.R.J. and A.C.D acknowledges Núcleo de Computação de Alto Desempenho (N.A.C.A.D.) and for providing the computational facilities. This work used resources of the Centro Nacional de Processamento de Alto Desempenho em

São Paulo (CENAPAD-SP). L.A.R.J. and K.A.L.L. also acknowledge CAPES for partially financing this study - Finance Code 88887.691997/2022-00.

References

1. Dias, A. C.; Silveira, J. F. R. V.; Qu, F.; Wantibexos: A wannier based tight binding code for electronic band structure, excitonic and optoelectronic properties of solids. Computer Physics Communications, 2023, 285, 108636.

2. Fan, Q.; Yan, L.; Tripp, M. W.; Krejčí, O.; Dimosthenous, S.; Kachel, S. R.; Chen, M.; Foster, A. S.; Koert, U.; Liljeroth, P.; et al. Biphenylene network: A nonbenzenoid carbon allotrope. Science, 2021, 372, 852–856.

3. Kresse, G.; Hafner, J. J. P. R. B.; Ab initio molecular dynamics for open-shell transition metals. Physical Review B, 1993, 48, 13115.

4. Li, J.; Fan, X.; Wei, Y.; Chen, G.; Penta-bxny sheet: a density functional theory study of two-dimensional material. Scientific Reports, 2016, 6, 31840.

5. Mostofi, A. A.; Yates, J. R.; Lee, Y.-S.; Souza, I.; Vanderbilt, D.; Marzari, N.; wannier90: A tool for obtaining maximally-localised wannier functions. Computer Physics Communications, 2008, 178, 685–699.

6. Perdew, J. P.; Burke, K.; Ernzerhof, M.; Generalized gradient approximation made simple. Physical Review Letters, 1996, 77, 3865.

7. Ren, K.; Shu, H.; Huo, W.; Cui, Z.; Xu, Y.; Tuning electronic, magnetic and catalytic behaviors of biphenylene network by atomic doping. Nanotechnology, 2022, 33, 345701.

8. Salpeter, E. E.; Bethe, H. A.; A relativistic equation for bound-state problems. Physical Review, 1951, 84, 1232–1242.

9. Santos, R. M.; Giozza, W. F.; Sousa, R. T.; Silva Filho, D. A.; Santos, R. B.; Ribeiro Júnior, L. A.; A dft study on the electronic structure of in-plane heterojunctions of graphene and hexagonal boron nitride nanoribbons. Electronic Structure, 2021, 3, 024005.

10. Sun, Z.; Martinez, A.; Wang, F.; Optical modulators with 2d layered materials. Nature Photonics, 2016, 10, 227–238.

11. Veeravenkata, H. P.; Jain, A.; Density functional theory driven phononic thermal conductivity prediction of biphenylene: A comparison with graphene. Carbon, 2021, 183, 893–898.

12. Bafekry, A.; Faraji, M.; Fadlallah, M. M.; Jappor, H. R.; Karbasizadeh, S.; Ghergherehchi, M.; Gogova, D.; Biphenylene monolayer as a two-dimensional nonbenzenoid carbon allotrope: a first-principles study. Journal of Physics: Condensed Matter, 2021, 34, 015001.

13. Cohen, A. J.; Mori-Sánchez, P.; Yang, W.; Fractional charge perspective on the band gap in density-functional theory. Physical Review B, 2008, 77, 11.

14. Heyd, J.; Scuseria, G. E.; Efficient hybrid density functional calculations in solids: Assessment of the heyd–scuseria–ernzerhof screened coulomb hybrid functional. The Journal of Chemical Physics, 2004, 121, 1187–1192.

Study of the mechanical properties of WSe2 Nano-Origamis with Reactive Molecular Dynamics.

Érick Dos Santos Morais[1], Marcelo Lopes Pereira Júnior[2], Luiz Antônio Ribeiro Júnior[1].
[1]Institute of Physics, University of Brasília - UNB, Brasília - Brazil.
[2]Faculty of Technology, Department of Electrical Engineering, University of Brasília, UNB, Brasília-Brazil
221010407@aluno.unb.br.
Keywords: Transition metal dichalcogenides; Molecular dynamics. LAMMPS Software; WSe2.

Abstract

The research addresses the study of the mechanical properties of WSe2 Nano-Origamis through reactive molecular dynamics. Using computational simulations with the LAMMPS software [2] and the reax force field, we investigate the mechanical behavior of molecular kirigamis of WSe2. Kirigami is a process of creating patterns and shapes by cutting, stretching, or twisting materials. In molecular systems, kirigamis can be generated by manipulating the atomic structure of a material to create new molecular arrangements. Our study focuses on investigating the mechanical behavior of molecular kirigamis of WSe2 and their impact on the material's fracture patterns and elastic properties. To minimize modeling stresses, we equilibrate the system with the NPT ensemble for 50 ps and then apply uniaxial tension with the NVT ensemble at 300 K. We simulate the temporal evolution of atoms and molecules in the system using the Newton equations of motion and the Velocity-Verlet algorithm. Similar studies have been conducted on kirigamis of graphene and MoS2 [1], and this work builds on these previous findings to investigate WSe2. Our findings contribute to the fundamental understanding of WSe2, open up new avenues for material science research, and emphasizing the importance of utilizing advanced computational methods to investigate the properties of materials and their potential technological applications.

Introduction

In nanomaterials, structural modifications can lead to significant changes in their properties, and the "Kirigami" method, in particular, has shown potential for enhancing the elastic properties of nanomaterials. This method involves standardized cuts in the structure based on various parameters, as illustrated in Figure 1.

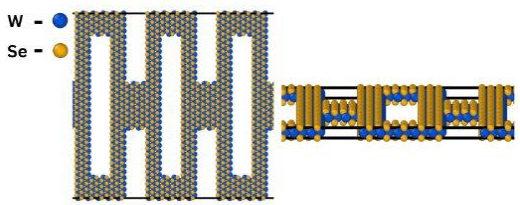


Figure 1: *Top and orthogonal views of the WSe2 Kirigami.*

In this study, molecular dynamics simulations were employed to investigate the influence of structural changes on the elastic properties of the material.

Methodology

Initially, the structure of a WSe2 nanosheet was obtained using an autonomously developed Python code. From this structure and using predefined parameters (depicted in Figure 2), the Kirigamis were constructed.

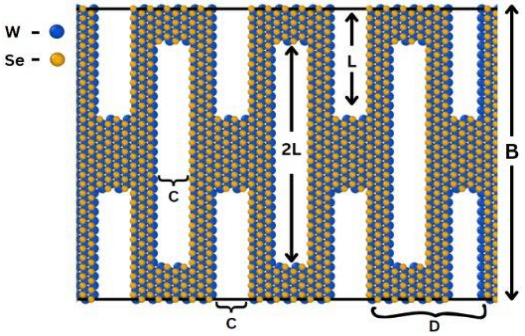


***Figure 2**. Parameters used in the Kirigami cutting*

With the Kirigami structures of WSe2, simulations are performed where uniaxial stress is applied in the periodic direction of the structure, using the LAMMPS software. The simulations are conducted using mainly the Stillinger-Weber[4] pottential.

The temperature used throughout the simulation was 300K (ambient temperature). Initially, the structure underwent an equilibration for 50 ps using the NPT ensemble. Then, the structure was thermalized for another 50 ps in an NVT ensemble. Finally, in an NVT ensemble, uniaxial strain was applied to the structure until it fractured.

Results

The simulations performed showed that the SW potential accurately describes the physical behavior of the systems.

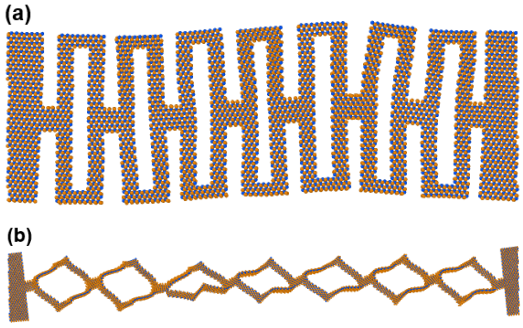


***Figure 3.** (a) Structure at the onset of strain application. (b) Structure under stress just moments before fracture.*

In the simulations conducted with the H phase and Zig-Zag chirality, a significant increase in the material's elasticity was observed as the value of the cutoff parameter W was increased, leading to a decrease in Young's modulus and a higher percentage of applied strain until the structure's fracture.

Figure 3 shows one of the stress-strain curves from the simulations. To fit this and other curves, a moving average was applied to the data, due to simulation noise, in order to facilitate the analysis. Figure 4 presents the changes in the stress curves for each applied parameter.

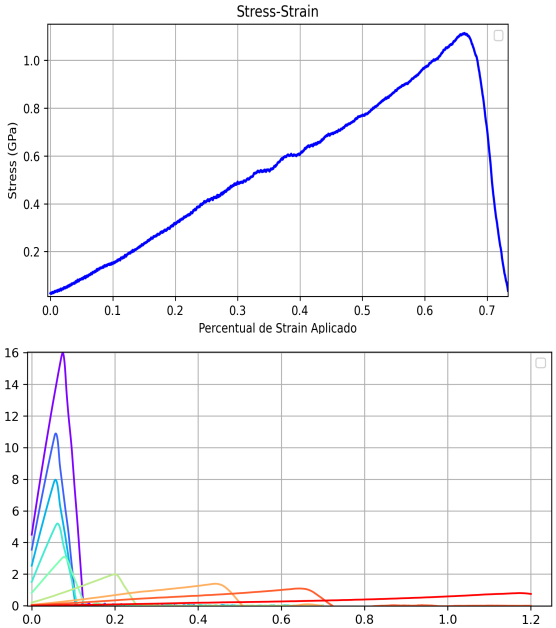


***Figure 4**. (a) Stress-strain curve of the kirigami for the cutoff parameters C=9.8177, W=90, D=39.27106. (b) Curves obtained by increasing the value of the parameter W while keeping the others constant.*

We can quantitatively observe the influence of the W parameter by examining Figure 5, which shows the Young's modulus as a function of the applied cutoff parameter value, and Figure 6, which represents the influence of W on the fracture strain percentage.

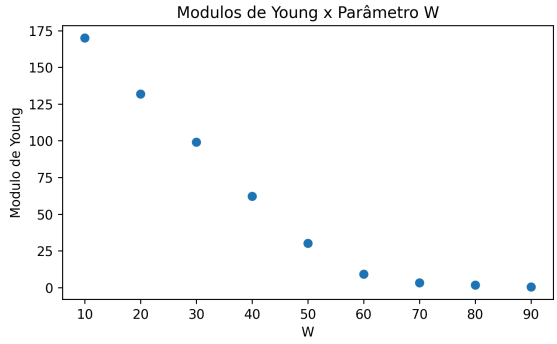


***Figure 5.** Young's modulus obtained for the kirigami structure as a function of the cutoff parameter W used in the structure's cutting process.*

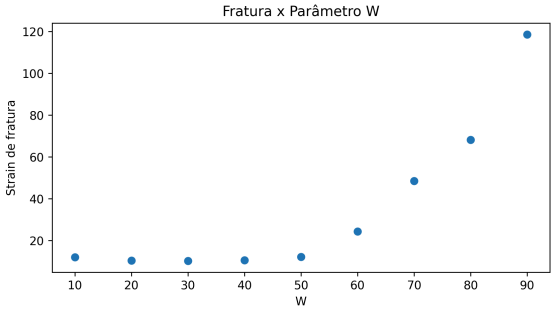


Figure 6. *Fracture strain percentage of the structure as a function of the cutoff parameter W.*

In future simulations, the goal is to continue analyzing the influence of other cutoff parameters, as well as whether these influences vary depending on the structure's phase or the applied chirality.

Acknowledgements

Thank you to the National Council for Scientific and Technological Development (CNPq), the Foundation for the Support of Research in the Federal District (FAP-DF), the Coordination for the Improvement of Higher Education Personnel (CAPES), and the University of Brasília (UnB) for their support.

References

1. HANAKATA, Paul Z. et al. Highly stretchable MoS 2 kirigami. Nanoscale, v. 8, n. 1, p. 458-463, 2016.

2. PLIMPTON, Steve. Fast parallel algorithms for short-range molecular dynamics. Journal of computational physics, v. 117, n. 1, p. 1-19, 1995.

3. VAN DUIN, Adri CT et al. ReaxFF: a reactive force field for hydrocarbons. The Journal of Physical Chemistry A, v. 105, n. 41, p. 9396-9409, 2001.

10º SIMPÓSIO DE ESTRUTURA ELETRÔNICA & DINÂMICA MOLECULAR
SEEDMOL 4 a 8 novembro | 2024 Pirenópolis, Goiás

Theoretical prediction of a novel class of electrides for applications in redox catalysis and quantum computing

Evangelos Miliordos[1], Andrei Evdokimov[1], Benjamin Jackson[2]
[1]Auburn University, Auburn, AL, USA
[2] Pacific Northwest National Laboratory, Richland, WA, USA.
emiliord@auburn.edu
Materials; Solvated electrons; Transition metals

Abstract
This high-level quantum chemical study reveals that metal complexes can accommodate bound diffuse electrons in their periphery making species, which mimic hydrogenic atoms. These complexes (called solvated electron precursors or SEPs) are present in concentrated metal ammonia solutions, where solvated electrons orbit around the positively charged metal ammonia skeleton. A typical example is $Li(NH_3)_4$, which has a $Li(NH_3)_4^+$ core and one peripheral electron populating a hydrogenic shell model but with the nuclear or jellium shell energy order: 1s, 1p, 1d, 2s, 2p, 1f, 2d. We demonstrate that transition metal ammonia complexes retain electrons in both their inner-d shell and the peripheral orbitals. In addition, two such complexes can bind together (like two hydrogen atoms producing molecular hydrogen) and form σ, σ*, π, π* orbitals identical to traditional diatomic molecules. The formation of dimers and polymers is confirmed experimentally in saturated lithium ammonia solutions, which create the so-called liquid or expanded metals. For the first time, we propose the bridging of two SEPs by replacing ammonia ligands with diamines or hydrocarbon chains. For small chains the two diffuse electrons couple into a closed-shell singlet, but for longer chains the two electrons prefer a triplet spin configuration. The spin coupling can be adjusted by the chain length and by decorating the chain with functional groups. We demonstrate that SEPs can capture, reduce, and convert CO_2 to industrial platform chemicals and that the spin of the diffuse electrons can be used as a qubit. Based on these results, we proposed the existence of novel 2d- and 3d-materials composed of linked-SEPs, which can serve both as redox catalysts and quantum computing materials.

Acknowledgements
The authors are indebted to Auburn University for financial support and especially the James E. Land endowment. This work was completed with resources provided by the Auburn University Easley Cluster. This material is based upon work supported by the U.S. National Science Foundation under Grant No. CHE-1940456.

References
1. Jackson, B. A.; Khan, S. N.; Miliordos, E.; Chem. Comm. 2023, 59, 10572.
2. Hartweg, S.; Barnes, J.; Yoder, B. L.; Garcia, G. A.; Nahon, L.; Miliordos, E.; Signorell, R.; Science 2023, 380, 1161.

10º SIMPÓSIO DE ESTRUTURA ELETRÔNICA & DINÂMICA MOLECULAR
SEEDMOL 4 a 8 novembro | 2024 Pirenópolis, Goiás

Analytical replicates to estimated affinity in molecular docking

Fabiani F. Triches[1,3], Tamires Martins[1,3], Francieli Triches[2], Cilene Lino-de-Oliveira[1,3]
[1]PhD program in Pharmacology, Center of Biological Sciences, Federal University of Santa Catarina, University Campus, Trindade, Florianópolis, SC – Brazil.
[2]Department of Mathematics, Center of Physic and Mathematics, Federal University of Santa Catarina, University Campus, Trindade, Florianópolis, SC – Brazil.
[3]Department of Physiological Sciences, Center of Biological Sciences, Federal University of Santa Catarina, University Campus, Trindade, Florianópolis, SC – Brazil.
fabianitriches@gmail.com, cilene.lino@ufsc.br
Keywords: Autodock Vina; consensus docking; DockThor; inhibition constant; Gold

Abstract
Estimated affinities with molecular docking may be more accurate with replicates. Indeed, variability of ligand positions in rankings of affinity drop substantially within three to ten analytical replicates, depending on the assay scenario (one or multiple macromolecules or programs or consensus).

Introduction
Molecular docking may identify the physical-chemical characteristics of macromolecule-ligand interactions in a virtual environment[1]. Affinities of docked complexes are useful to characterize compounds to be tested in pharmacological studies. Although more automatized and homogeneous than *in vitro* or *in vivo*, randomness and experimental choices also affect *in silico* assays. Consequently, the variance of affinity estimate *in silico* may be high. Indeed, affinities of docked complexes varied significantly with types of software, macromolecule, ligands, and protocols of dockings[3,4] In general, the impact of the sources of variability on analytical methods decrease with replicate strategies. However, the number of replicates or repetitions necessary to stabilize the values of affinities estimated with molecular dockings is uncertain. In this proof-of-concept study, antidepressants and *Drosophila melanogaster* dopamine transporter (dDAT) were docked in different scenario (different types of crystalized dDATs, programs, consensus docking calculations). Molecular dockings were repeated until affinity values reached stability. The hypothesis is that variability of the estimated affinity will drop with enlarged number of replicates.

Objective
The main goal of this study was to estimate the number of analytical replicates needed to stabilize the values of docked complexes affinities obtained with ensemble docking assays.

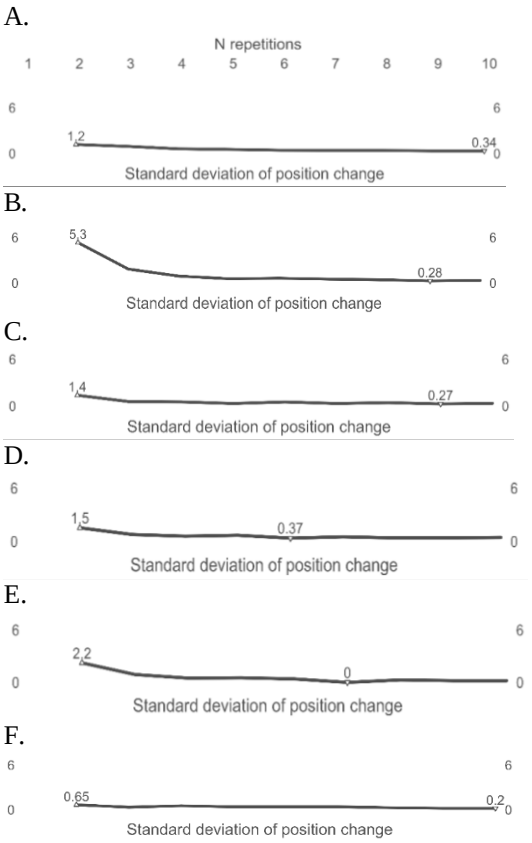
Methods
The docking parameters were selected according to previous work[4]. The following resources were employed in the docking studies: 11 dDAT (10 crystalized structures from PDB; 01 theoretical from AlphaFold); 26 prototypical antidepressants (from ZINC); 03 docking programs (Autodock Vina *v. 1.7*, DockThor, Gold *v. 2021.3.0*); 03 consensus-docking functions (ECR[3], ECR+MA[4], and LF+ECR+ MA). The delta G, score functions from Autodock of and DockThor, were used to calculate inhibition constant in *n* molar ($K_{i,}$)[4]. Ligands were organized in rankings of affinity values estimated of consensual scoring functions (ECR[3], ECR+MA[4], LF+ECR+ MA) or K_i[4]. In all rankings, the lower the position, the higher the affinity. The ordinal rankings, ECR[3] and ECR+MA[4], had number of positions equal to the number of ligands (n=26, 1 equal highest affinity and 26 equal the lowest affinity). The LF+ECR+MA[4] function ranked the ligands in a linear scale between 0 (highest affinity) and 1 (lowest affinity). Rankings based on *in silico* K_i[4] classified ligands according to

their estimated values, which are inversely proportional to ligands affinity. Six different experimental scenarios were investigated: 1. multiple ligands, one macromolecule, one program; 2. multiple ligands, one macromolecule, two programs; 3. multiple ligands, one macromolecule, three programs; 4. multiple ligands, multiple macromolecules, one program; 5. multiple ligands, multiple macromolecules, two programs; 6. multiple ligands, multiple macromolecules, three programs. For scenarios 1-3, dDAT PDB code 4XP9, randomly chosen from the list of 11 possible macromolecules, was docked with antidepressants in a single program at a time (Autodock Vina, DockThor, Gold). There was no need for consensus to obtain the rankings of antidepressants in the scenario 1 because every complex contributed with a unique score function *per* program (fitness or delta G). In scenarios 2 and 5, values of *in silico* K_i ranked the antidepressants. For scenarios 3, 4, and 6, multiple macromolecules or programs, consensus dockings (ECR, ECR+MA, LF+ECR+MA) ranked antidepressants. In scenario 3, the rankings ECR and ECR+MA were identical because only a macromolecule was docked with antidepressants in three programs. Each ranking was calculated with results of a single docking *per* ligand (k=1) or repetition of dockings *per* ligand (k=2 to 10 replicates). The number of ligands changing positions in the rankings and the standard deviations (SD) was computed for each repetition. For stability analysis, of all position changes in a repetition were calculated. The larger the SD the lower the stability and the smaller the SD the higher the stability of the ranking. Ratio between the largest and smallest SDs indicated the effectiveness of repetitions.

Results

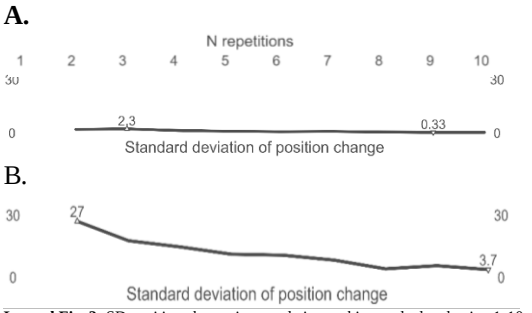
Values of initial SD were always larger than the last SD (Table 1). Scenario with the larger differences were the following: DockThor in scenario 01 and 04 (Fig 1); scenario 2 and 5 (Fig 2); ordinal and linear rankings in scenarios 3 and 6 (Fig. 3, Fig. 4). The differences in following scenario were small: Autodock Vina and Gold in scenarios 01 or 04 (Fig. 1). The differences in scenarios 2 and 5 (Fig 2); were intermediate.

Fig 1. Ordinal rankings scenario 1 and 4



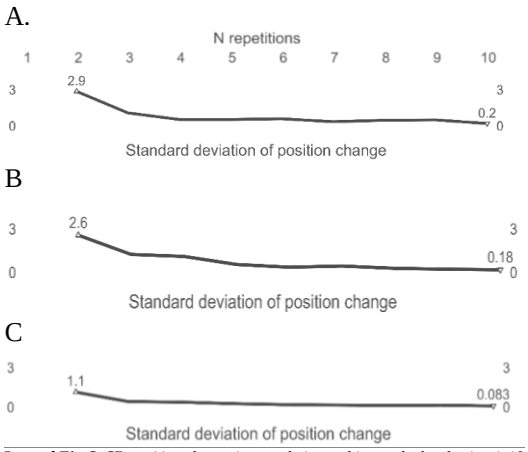
Legend Fig. 1: SD position change in cumulative rankings calculated using 1-10 replicas in the scenario 1 (A-C) or 4 (D-F), i.e. dDAT4XP (A-C) or 11 dDAT, 01 software (A, D. Autodock Vina; B, E. DockThor, C, F. Gold), and a ordinal ranking of scoring functions. Numbers over SD lines depict the highest or the lowest value of SD across ranking repetitions.

Fig 2. K_i rankings scenario 2 and 5



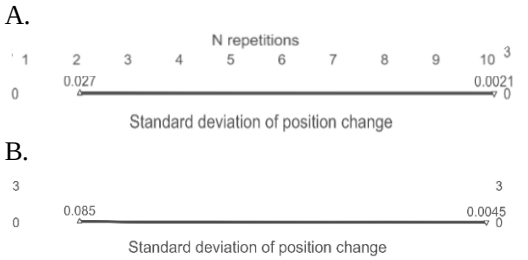
Legend Fig. 2: SD position change in cumulative rankings calculated using 1-10 replicas in the scenario 2 (A) or 5 (B), i.e. dDAT4XP (A) or 11 dDAT (B), 02 software (A, B, Autodock Vina, DockThor), and ranking of *in silico* K_i (A, B). Numbers over SD lines depict the highest or the lowest value of SD across ranking repetitions.

Fig 3. Ordinal consensus ranking scenario 3 and 6



Legend Fig. 3. SD position change in cumulative rankings calculated using 1-10 replicas in the scenario 3 (A) and 6 (B, C), i.e. dDAT4XP (A), 11 dDATs (A, B), 03 software (A, B, Autodock Vina, DockThor, Gold,), 02 consensus (A. Ordinal rankigns ECR or ECR+MA, B. Ordinal ranking ECR, C. Ordinal ranking ECR+MA). Numbers over SD lines depict the highest or the lowest value of SD across ranking repetitions.

Fig 4. Linear consensus rankings



Legend Fig. 4. SD position change in cumulative rankings calculated using 1-10 replicas in the scenario 3 (A) and 6 (B), i.e. dDAT4XP (A), 11 dDATs (B), 03 software (A, B, Autodock Vina, DockThor, Gold), 01 consensus (A, B, Linear ranking FL+ECR+MA.)

Discussion

Affinities estimate of docked antidepressants-dDAT varied across experimental conditions and number of replicates. In all these scenarios, SD values were larger in the repetition 2 than in the repetition 10. In general, effect of repetition was larger in scenario using DockThor and consensus docking with one or many macromolecules, in ordinal or linear rankings. Repetition has small effect in the scenario using Autodock Vina or Gold. Effect of repetition on rankings of K_i values was intermediate. Except for the ranking K_i in the scenario with many dDATs, other final values of SD were close to zero after ten repetitions. Together data indicate that analytical replicates stabilize rankings of affinities from a molecular docking or ensemble docking independent of the type of calculations used to obtain results. Further studies are necessary to understand if this concept applies to other types of docked complexes.

Table 1: Effect of repetitions *per* scenario

		SD position changes		
Scenario	Ranking	Initial	Final	Ratio
1 dDAT 1 software	Ordinal (Autodock)	1.2	0.3	3.4
	Ordinal (DockThor)	5.3	0.3	15.4
	Ordinal (Gold)	1.4	0.3	4
11 dDAT 1 software	Ordinal (Autodock)	1.5	0.4	3.4
	Ordinal (DockThor)	2.2	0.2	11.3
	Ordinal (Gold)	0.6	0.2	3.3
1 dDAT 2 software	K_i (nM)	2.0	0.3	5.9
11 dDAT 2 software	K_i (nM)	27.1	3.7	7.2
1 dDAT 3 software	Ordinal (ECR)	2.8	0.2	14.6
	Ordinal (ECR+MA)	2.8	0.2	14.6
11 dDAT 3 software	Ordinal (ECR)	2.6	0.2	14.4
	Ordinal (ECR+MA)	1.1	0.1	13.6
1 dDAT 3 software	Linear (LF+ECR+MA)	0.1	0.004	18.9
11 dDAT 3 software	Linear (LF+ECR+MA)	0.03	0.002	12.8

Conclusion

Analytical replicates in ensemble dockings increased the accuracy of the affinities estimate of docked complexes.

Acknowledgements

We thank Candinho L D B Junior for his assistance with Excel sheet calculations. Plots were prepared with R package ggplot2. Language was edited with Grammarly. We are thankful to financial support of Capes, CNPq, and Alexander von Humboldt Foundation.

References

1. BLANES-MIRA, C et al. *Molecules*, **2022**, 28, 1.
2. VERLI, H. *Bioinformática: da biologia à flexibilidade molecular*. cap 09, **2014**.
3. Palacio-Rodríguez, K. et al. *Sci rep*, **2019**, 9, 1.
4. Triches, F. F.; Triches, F.; De Oliveira, C. L. *MetX*, **2022**, 9.

Impacto dos ângulos de torção para modulação de cromóforos orgânicos visando aplicações fotovoltaicas.

Felipe Ferreira de Araujo Braz,[1] Daniel Francisco Scalabrini Machado.[1]
[1]Laboratório de Modelagem de Sistemas Complexos, Instituto de Química, Universidade de Brasília, Brasil.
200017659@aluno.unb.br
Keywords: DSSC, Density Functional Theory, TD-DFT, LHE, Electron Injection Driving Force.

Abstract
The use of organic dyes are a promising alternative for photovoltaics, termed as DSSC's. In this work, the impact of the dihedral angles of a D-p-A bithiophene-based chromophore on the electro-optical properties was investigated through TD-DFT calculations. The results suggested that imparting steric repulsions on the Acceptor would enhance the cell performance.

Introdução

Células fotovoltaicas vêm ganhando popularidade devido a sua fonte de energia verde. Porém, elas não são 100% sustentáveis. É comum a utilização de complexos de metais pesados, como o rutênio, os quais são difíceis de obter e descartar. Uma alternativa para este tipo de célula são as DSSC's (células solares sensibilizadas por corantes). Moléculas do tipo D-π-A (parte doadora de elétrons, parte com excesso de ligações π e parte aceptora de elétrons) são boas candidatas para este fim. O objetivo desse projeto é avaliar o impacto conformacional nas propriedades foto-eletrônicas para otimização dos parâmetros das DSSC's. Esta investigação se deu modificando o ângulo diedral entre os fragmentos D-π e A-π para determinar se existem outros ângulos ótimos que maximizem os parâmetros da célula.

Uma vez determinados os ângulos ótimos, propor-se-á modificar a estrutura molecular dos cromóforos originais para induzir a formação da conformação de interesse através de efeitos estéricos intramoleculares em posições cuidadosamente selecionadas. Neste trabalho o cromóforo selecionado é constituído por um grupo tri-fenilamina (D), 2,2'-bitiofeno (espaçador π) e ácido ciano-acrílico (A), como representado na Fig.1 [1]

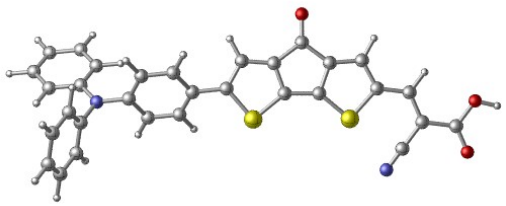


Fig. 1. Geometria molecular do pigmento orgânico investigado neste trabalho.

Metodologia

Nesse projeto, todos os cálculos foram conduzidos através do pacote computacional Gaussian 16. As geometrias moleculares foram otimizadas em nível DFT incluindo efeito de solvente com polaridades distintas de maneira implícita (SMD, solventes água e diclorometano) empregando o conjunto de funções de base 6-311G(d,p). Avaliou-se também a natureza da aproximação empregada no funcional de troca-correlação avaliando as propriedades geométricas e eletrônicas com os seguintes funcionais híbridos: B3LYP, CAM-B3LYP e WB97XD. A análise estrutural foi realizada através de um cálculo de varredura rígida dos ângulos diedrais entre os fragmentos D-π e A-π de maneira

independente no intervalo entre -90° e 90° com incrementos de 10°.
Em cada ângulo diedral foram realizados cálculos de estado excitado para obter as propriedades eletrônicas no primeiro estado excitado a fim de obter parâmetros fotofísicos como a força de oscilador e energia de excitação e gap HOMO-LUMO. Estas quantidades são usadas para computar os parâmetros de desempenho de célula como LHE (Light-Harvesting Efficiency), energia livre de injeção de elétrons, energia livre de regeneração, potencial de circuito aberto e fator de preenchimento (Fill Factor). [2]

Resultados e Discussão

Na Fig.2 observamos que o cromóforo é mais estável quando o grupo A encontra-se na forma planar e o grupo D nos ângulos equivalentes de ±25º.

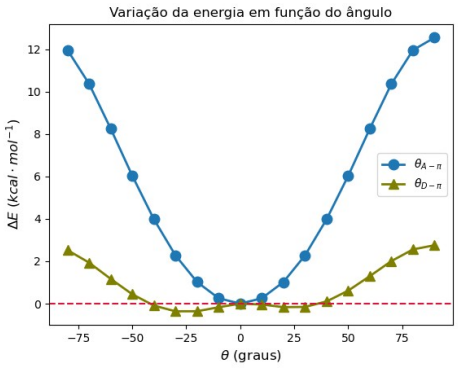


Fig.2. Barreiras energéticas de torção dos ângulos diedrais dos fragmentos doador e aceptor.

Um parâmetro importante utilizado para medir a tendência de injetar elétrons fotoexcitados é a Variação de Energia Livre de Gibbs de Injeção (ΔG_{inj}). Vemos na Fig. 3 que o impacto da torsão do grupo D é marginal neste parâmetro. Por outro lado, a torção do grupo aceptor melhora significativamente os valores de ΔG_{inj} quando o aceptor tende à perpendicularidade.

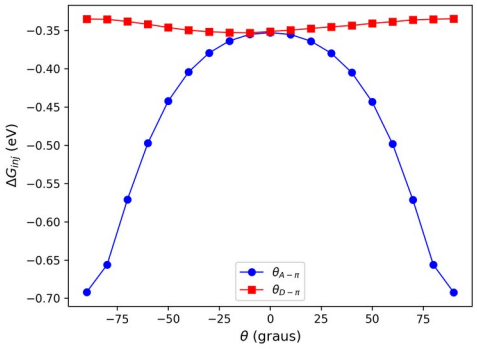


Fig. 3. Variação da energia livre de injeção de elétrons na banca de condução do TiO_2 a partir do pigmento em função do ângulo diedral dos fragmentos doador e aceptor.

Os resultados demonstrados acima indicam que uma alteração estrutural com o intuito de enviesar estericamente o diedro entre os fragmentos A-π da molécula em ±90º implicaria uma melhor eficiência dessa molécula como sensibilizador em DSSC's. Portanto, podemos sugerir uma modificação estrutural introduzindo um substituinte de tamanho e natureza química (retirador/doador) adequados no fragmento 2,2'-bitiofeno na posição 3.

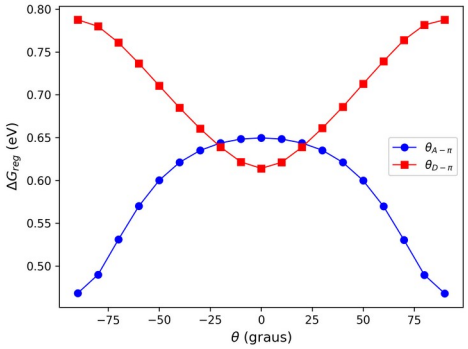


Fig.4. Variação da energia livre de regeneração de elétrons do pigmento a partir do eletrólito em função do ângulo diedral dos fragmentos doador e aceptor.

Conclusão

O design molecular para os ângulos diedrais D-π pode ocorrer com menor barreira nos dois sentidos. A torção do grupo A-π tem barreiras cerca de quatro vezes maior. A torção do grupo D-π tem um efeito significativo na transferência de carga

intramolecular. Além disso, a injeção de elétrons do corante para o TiO_2 é espontânea para todos os ângulos de torção devido ao valor negativo de ΔG_{in}. Isso leva à facilitação da transferência de carga pela redução da recombinação de carga e à melhoria da regeneração do corante, o que, por sua vez, leva a uma maior geração de fotocorrente pela conversão de mais luz em energia elétrica e, consequentemente, à melhoria da eficiência da célula solar. Pode-se concluir que a influência dos ângulos de torção ajustáveis afeta positivamente a eficiência das propriedades fotovoltaicas e, assim, melhora o desempenho do dispositivo. Sugere-se uma modificação química do composto original introduzindo substituintes que levem a um aumento do angulo diedral entre os fragmentos A-π.

Agradecimentos

Capes, CnPQ e FAP-DF

Referências

1. Bahrani, F.; Hameed, R.; Resan, S.; Al-anber, M. (2022). Acta Physica Polonica Series a. 141. 561-568.

2.Preat, J.; Jacquemin, D.; Michaux, C.; Perpète, E. (2010). Chemical Physics. 376. 56 - 68. 10.1016/j.chemphys.2010.08.001.

Pirenópolis, Goiás 10º SIMPÓSIO DE ESTRUTURA ELETRÔNICA & DINÂMICA MOLECULAR SEED MOL 4 a 8 novembro | 2024

Computational Study of Enantioselective Iminium Ion Catalysis in the Synthesis of Pyrroloindolines

Felipe Schoma Cardoso[1], Bruno M. Paz[1], Ataualpa A. C. Braga.[1]
[1]Instituto de Química USP, São Paulo, Brazil.
felipe_schoma@usp.br.
Keywords: Pyrroloinolines; Iminium Ion; Asymmetric Catalysis; Computational Chemistry; Non-covalent Interactions.

Abstract
Pyrroloindolines constitute an organic group that serves as the structural foundation for drugs such as Physostigmine. Other molecules within this group exhibit potential as novel drugs for cancer treatment. The asymmetrical synthesis of pyrroloindolines, catalyzed by an iminium ion, occurs through the activation of the catalyst with an aldehyde that reacts with tryptamine. The selectivity arises from the asymmetrical structure of the catalyst, which creates distinct non-covalent interactions between tryptamine and the catalyst, depending on the enantiomer formed. Mechanistic calculations at the B3LYP-D3BJ/def2-tzvp//B3LYP-D3BJ/def2-sv(p) level of theory, combined with an extensive conformational search using the software CREST, suggest an important role of the cocatalyst in the formation of the iminium ion. The activation barrier of this step decreases from 54.6 kcal/mol to 16.2 kcal/mol with the participation of the cocatalyst. Furthermore, the step involving the approach of tryptamine and the catalyst may not be responsible for the reaction selectivity, as the energy difference between the catalytic cycles of the two enantiomers is only 0.35 kcal/mol. Preliminary results point to a greater energy difference in the catalyst restoration step, indicating that this step may be responsible for the enantioselectivity of the catalysis.

Introduction

Stereochemistry is a determining factor in the biological activity of drugs. For example, we can cite the famous case of Thalidomide,[1] where one of the enantiomers had a sedative effect while the other caused teratogenic effects during pregnancy. Besides the academic interest, it is also of social interest to improve enantioselective synthetic routes for drugs, aiming to increase the selectivity of reactions, their yield, and economic viability. In this context, asymmetric catalysis presents itself as a powerful tool to achieve this goal. A notable example is the enantioselective catalysts developed by David MacMillan's group. In one of his works,[2] enantioselective catalysis of pyrroloindolines is presented, with excellent results in both selectivity and yield. However, even after all this time, the origin of this selectivity has not yet been unraveled.

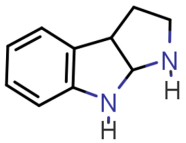


Figure 1. Pyrroloindoline structure.

Pyrroloindoline is a tricyclic structure with two chiral centers (Fig. 1), found in natural sources such as *Flustra foliacea* and *Physostigma venenosum*. It is already present in drugs like Physostigmine and shows great potential as a building block for new drugs in the treatment of cancer and tumors.[3] Due to this potential, this work aims to uncover the origins of selectivity in the asymmetric catalysis of pyrroloindolines with iminium ion catalysts (Fig. 2) using computational chemistry as a tool, with the objective of proposing changes in structures and experimental conditions to increase the selectivity and yield of the reaction.

This work focuses on the reaction of acrolein with tryptamine catalyzed by a second-generation MacMillan catalyst. Figure 2 shows a summarized catalytic

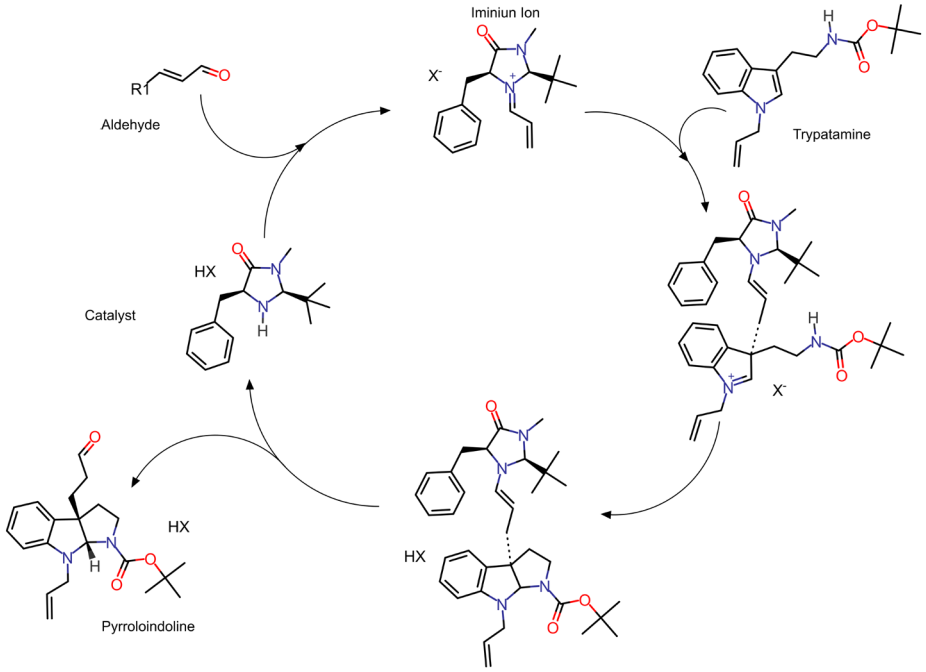


Figure 2. Catalytic cycle

cycle. It is believed that the steric hindrance of the catalyst promotes different non-covalent interactions depending on how the interaction with the tryptamine occurs. This difference may be the origin of the selectivity.

Methodology

The energy profile is obtained with suite of programs Gaussian 16, using the DFT performed using the functional B3LYP with D3BJ empirical dispersion. For geometry optimizations and frequency calculations, the def2-sv(p) basis set is used, and the electronic energy is corrected with the def2-tzvp basis set. The solvation effect is corrected using the SMD approach. Considering the importance of the different conformations the system can take, a conformational search is performed with CREST program, using GFN2-xTB as the primary method and GFN-FF as the secondary method. For solvation, the gbsa method is used.

Results

The formation of the iminium ion occurs in two stages: the attack of the catalyst on the protonated carbon of the acrolein and the subsequent formation of a water molecule (Fig. 3).

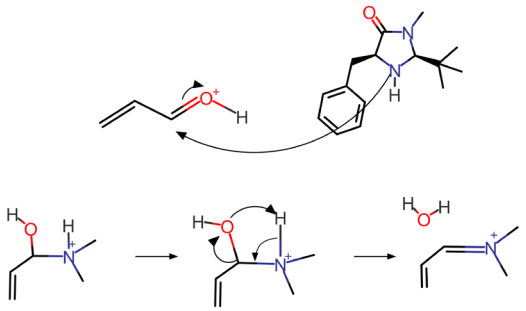


Figure 3. Iminium Ion formation.

The determining step is the formation of the water molecule, which has a prohibitive barrier of 54.6 kcal/mol under reaction conditions. The proposed alternative involves the use of TFA (trifluoroacetic acid) as a cocatalyst in the formation of the iminium ion (Fig. 4). In this proposal, the transfer of hydrogen to oxygen occurs in two stages, reducing the energy barrier to 16.2 kcal/mol.

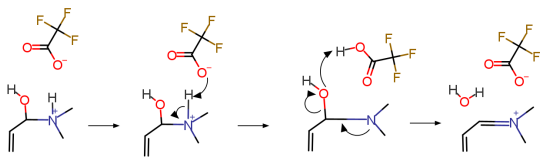


Figure 4. Iminium formation with cocatalyst

A conformational analysis using CREST was performed on the transition state resulting in the formation of the bond between the iminium ion and the tryptamine. Twenty-five conformers were studied for each enantiomer, with the energy difference between the barriers being only 0.35 kcal/mol, corresponding to barrier values of 15.7 kcal/mol and 16.1 kcal/mol, respectively.

To restore the catalyst, the reverse mechanism of iminium ion formation with the participation of the cocatalyst TFA was applied. Preliminary results indicate that, in this step, the energy barrier difference between the enantiomers is greater than in the previous step.

Discussion

The results produced so far indicate that the cocatalyst plays a more important role than previously thought. In addition to protonating the acrolein, the presence of the cocatalyst is crucial for the feasibility of the iminium ion formation and subsequently, in the restoration of the catalyst. Moreover, the steps involving the formation of the iminium ion and the bond formation between the catalyst and tryptamine show very similar barriers, making it still uncertain which state is the rate determining in the reaction. Preliminary data on the catalyst restoration suggest that this step may be the one determining the stereoselectivity of the catalysis. The next steps are to determine with certainty which step defines the enantioselectivity of the catalysis and to study this step through the lens of non-covalent interactions, using tools such as QTAIM and NCIPlot. With this information, it will be possible to suggest and test modifications that increase the enantiomeric excess of the catalysis.

Conclusion

This work demonstrates the importance of computational chemistry in elucidating reaction mechanisms, providing valuable information about the origins of experimental results. The project agrees with the experimental results and helps elucidate the origins of the enantioselectivity of the catalytic cycle. Additional results will help suggest modifications to improve yield and selectivity.

Acknowledgements

Felipe S. Cardoso thanks CNPq for Masters scholarship (Grant #131711/2023-7). A.A.C.B. acknowledges the financial support of FAPESP and CNPq (Grant #313720/2023-1).

Research developed with the assistance of HPC resources provided by the Superintendence of Information Technology at the University of São Paulo.

This research used the computing resources and assistance of the John David Rogers Computing Center (CCJDR) in the Institute of Physics “Gleb Wataghin”, University of Campinas. FAPESP (#2013/08293-7) and (#2019/17874-0).

References

1. MORO, Adriana; Invernizzi, Noela. História, Ciências, Saúde – Manguinhos, 2017, 24, 3, 603-622.

2. Joel F. Austin, Sung-Gon Kim, Christopher J. Sinz, Wen-Jing Xiao, and David W. C. MacMillan. Proceedings of the National Academy of Sciences. 2004, 101, 5482-5487.

3. Chika Takahashi, Katsuhiko Minoura, Takeshi Yamada, Atsushi Numata, Katsuhiko Kushida, Tetsuro Shingu, Sanji Hagishita, Hiroshi Nakai, Tomohiro Sato, Hiroshi Harada. Tetrahedron, 1995, Volume 51, Issue 12, 3483-3498.

Understanding triplet-to-singlet energy transfer pathways in organic systems

Fernando Teixeira Bueno[1], João Felipe Camargo Pinheiro[1], Tiago de Sousa Araújo Cassiano[1] and Pedro Henrique de Oliveira Neto[1,2].
[1]Institute of Physics, University of Brasília, Brasília-DF, 70910-900, DF, Brazil.
[2]International Center of Physics, Institute of Physics, University of Brasilia, Brazil
f.bueno1998@gmail.com
Keywords: exciton diffusion; conversion mechanisms; triplet to singlet transfers; nonradiative processes.

Abstract
The efficiency of organic optoelectronic devices rely on the energy carriers clear energy pathways for transfer and recombination. Multiresonance thermally activated delayed fluorescence molecules are known for their elevated quantum yield. Recent works have shown how powerful an adequate combination between MR-TADF hosts and dopants can be in terms of efficiency. The low energy gap between singlet and triplet excitation energies creates a realm of exciting possibilities to harvest triplet excitons as well as reducing the nonradiative losses of singlet excitons. This work provides a better understanding of how such host and dopant molecules influence the exciton diffusion.

Introduction

In the context of organic optoelectronic devices, their efficiency relies on the energy carriers clear energy pathways for transfer and recombination. The interplay between conversion and transfer processes is paramount to determine the efficiency of a device. Multiresonance thermally activated delayed fluorescence (MR-TADF) molecules have gained attention in the last couple years due to their noticeably large quantum yield and elevated reverse intersystem crossing rates[1]. Recent works have investigated the interactions and energy transfer mechanisms present in system comprised of TDBA based host molecules with v-DABNA used as a dopant[2,3]. Experimental observations point to extremely high rISC as expected as well as low nonradiative decay rates. By means of electronic structure calculations and computational simulations one can better understand the reasons for the experimentally observed phenomena. Traditionally, the rates that govern these systems can be obtained through spectra simulation, which derive from density functional theory (DFT) and its time-dependent extension (TD-DFT) in combination with the nuclear ensemble method. Nevertheless, MR-TADF molecules are known for low singlet-triplet energy gaps. Said gaps are not easily obtained via DFT calculations, even when using last generation functionals. This work aims to better understand the conditions under which MR-TADF can be adequately studied as well as identifying the characteristics in TDBA based host and the v-DABNA dopant that make those systems such prominent candidates for real use.

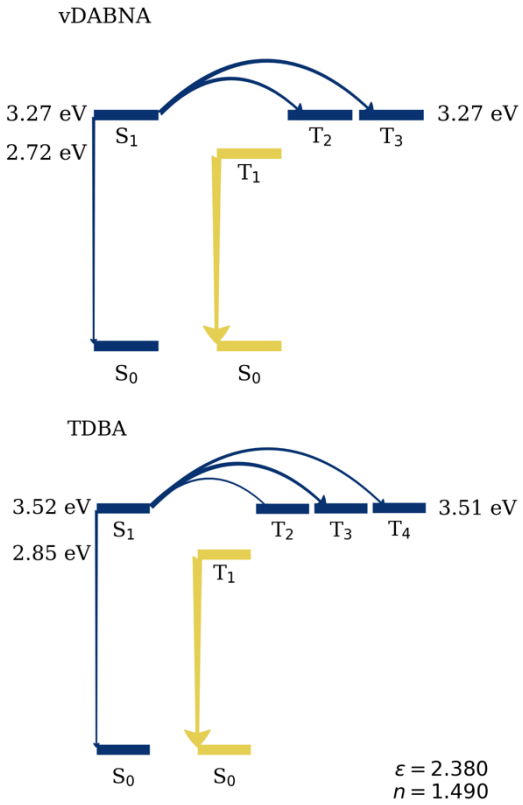
Methodology

By means of DFT and TD-DFT calculations using the polarization continuum model (PCM) with its perturbative state specific corrections in combination with the ROKS procedure and the nuclear ensemble method, absorption, fluorescence and phosphorescence spectra are simulated for a group of TDBA based host and the v-DABNA dopant molecule. Using said spectra, we are able to determine under which conditions nonradiative decay is

relevant as well as under which conditions rISC and triplet to singlet (TTS) transfers become efficient triplet harvesting mechanisms, which can lead to the high intensity QY.

Preliminary results

The figures below display the energy diagram for the vDABNA and TDBA energy diagrams.



As one can observe, the gap between the first singlet and triplet states (S_1 and T_1, respectively) is too elevated to make rISC a competitive approach. It is worth mentioning that the ensemble that generated such diagram is shifted in the absorption and fluorescence spectra when compared to experimentally obtained data. However, the phosphorescence spectra from both molecules is in good agreement with experimental data. This points to there being no cancelation of errors, further invalidating the diagram at hand.

Preliminary conclusions

Investigating complex systems and molecules with a wide variety of simultaneously occurring phenomena can be a difficult computational task using cost effective, although well tested and robust, DFT and TD-DFT methods. In the case of MR-TADF molecules specially, said task can only be achieved with appropriate corrections, given that the excitation energies are well off an acceptable margin of error. The miscalculation of these energies results in the neglect of highly relevant occurring phenomena, typically rISC and TTS. Thus, providing an ill conceived description of a desired physical system.

Acknowledgements

References

1. Park, Dongmin, et al. Nature Communications 14.1 (2023): 5589.
2. Hall, David, et al. Journal of Chemical Theory and Computation 18.8 (2022): 4903-4918.
3. Oda, Susumu, et al. Advanced Science 10.1 (2023): 2205070.

Aprendizado de máquina concilia curvatura no gráfico de Arrhenius com estrutura molecular de compostos orgânicos voláteis

Flávio O. Sanches-Neto[1], Valter H. Carvalho-Silva[2]
[1]Instituto Federal de Goiás, IFG-Câmpus Valparaíso de Goiás, GO 72876-601, Brazil.
[2]Modeling of Physical and Chemical Transformations Division, Theoretical and Structural Chemistry Group, Goiás State University, 75132-903, Anápolis, Brazil.
flavio.neto@ifg.edu.br
Palavras-chaves: QSAR, OH, SHAP, Aprendizado de Máquina

Resumo
Este estudo amplia pesquisas anteriores ao desenvolver modelos de aprendizado de máquina, com a aplicação da análise SHAP, para prever parâmetros cinéticos e interpretar os mecanismos de degradação de compostos orgânicos em ambientes aquáticos e atmosféricos. Os modelos, integrados em uma aplicação web de fácil utilização, demonstraram fortes correlações (R^2: 0,85–0,92) com dados experimentais, evidenciando a influência significativa de grupos doadores e retiradores de elétrons na reatividade dos radicais. Esses resultados contribuem para o aprimoramento de estratégias de tratamento mais eficazes e eficientes para a remoção de micropoluentes emergentes, promovendo avanços nas tecnologias de oxidação avançada em unidades de tratamento de água e ar.

Introdução

A ação climática tornou-se um foco central das conferências internacionais devido ao papel crucial das condições climáticas na existência humana e na qualidade ambiental. Uma preocupação significativa é o aumento dos poluentes orgânicos atmosféricos, particularmente compostos orgânicos voláteis (VOCs), resultantes da urbanização e industrialização. Os VOCs, liberados por meio de processos como pulverização e combustão, degradam a qualidade do ar e se espalham amplamente pela atmosfera. Esses poluentes reagem com radicais atmosféricos como a hidroxila (OH), levando à sua degradação. A constante de taxa dessas reações determina a rapidez com que os poluentes são removidos da atmosfera. Numerosos estudos investigaram a cinética de degradação de VOCs com radicais OH. Por exemplo, Gramatica et al. (2004b) e Öberg (2005) desenvolveram modelos QSAR para prever a reatividade do VOC com base na estrutura química, validados por dados experimentais com bom desempenho preditivo. Roy et al. (2011) destacaram a variabilidade nas previsões do modelo QSAR para diferentes compostos, enfatizando a necessidade de um modelo cuidadoso avaliação. Considerando a faixa de temperatura da troposfera de 200 K a mais de 600 K, é essencial estudar a constante de taxa das reações de degradação do OH nessa faixa para uma previsão precisa. Li et al. (2014) foram pioneiros em modelos QSAR que incorporam dependência de temperatura, mostrando bom desempenho preditivo. Gupta et al. (2016) desenvolveram ainda modelos QSAR para reatividade de OH e ozônio com dependência de temperatura, validados por dados experimentais, aprimorando a compreensão do comportamento dos poluentes atmosféricos. Com base nesses estudos fundamentais, o objetivo deste trabalho é prever a constante de taxa usando aprendizado de máquina combinado com impressões digitais moleculares, considerando a influência da temperatura.

Metodologia

Um conjunto de dados de 1543 poluentes atmosféricos com valores experimentais *de* k_{OH} foi compilado a partir da literatura. Esses valores, medidos sob várias condições, foram

convertidos em temperatura recíproca (1000 / T) e transformados em log para obter uma distribuição normal. Os compostos foram convertidos para o formato SMILES usando CIRpy e processados com RDKit para gerar impressões digitais MACCS e Morgan com diferentes comprimentos de bits. Três algoritmos de aprendizado de máquina - LightGBM, Random Forest (RF) e XGBoost - foram empregados para prever *os valores de kOH*. Os modelos foram implementados usando o pacote scikit-learn. O conjunto de dados foi dividido em um conjunto de treinamento (80%) e um conjunto de testes (20%) para validação interna e externa. As métricas de desempenho, incluindo RMSE, R^2 e outras, foram calculadas usando equações padrão. Um método de validação cruzada de 10 vezes foi usado para validação interna e a validação externa foi realizada usando um conjunto de dados de teste separado. O domínio de aplicabilidade (AD) foi avaliado usando o índice Tanimoto para medir a semelhança entre os compostos de consulta e o conjunto de dados de treinamento, garantindo previsões confiáveis. A interpretação mecanicista do modelo QSAR foi conduzida usando valores SHAP, que quantificam a contribuição de cada característica para as previsões do modelo, fornecendo informações sobre a importância das características individuais da impressão digital molecular.

Resultados e Discussões

Este trabalho expande uma pesquisa anterior, utilizando aprendizado de máquina para prever parâmetros cinéticos e interpretar a degradação de compostos orgânicos em ambientes aquáticos e atmosféricos. Desenvolvemos um modelo disponível na aplicação web gratuita (www.pysirc.com.br), que combina aprendizado de máquina com descritores moleculares (Morgan e MACCS). A figura compara o desempenho dos algoritmos Random Forest, XGBoost, e LightGBM, mostrando alta correlação entre valores experimentais e preditos de log(k_{OH}). Os modelos apresentaram valores de R^2 entre 0,85 e 0,92, com RMSE variando de 0,15 a 0,25, indicando alta precisão. O Q^2, medido por validação cruzada, variou entre 0,83 e 0,90, e o coeficiente de Pearson (r) ficou entre 0,91 e 0,95, confirmando a robustez dos modelos. A análise com o método SHAP confirmou que grupos eletronegativos e doadores de elétrons influenciam significativamente a reatividade dos radicais. Esses modelos aprimorados facilitam o uso e interpretação de dados cinéticos, potencializando o desenvolvimento de estratégias de tratamento para micropoluentes emergentes.

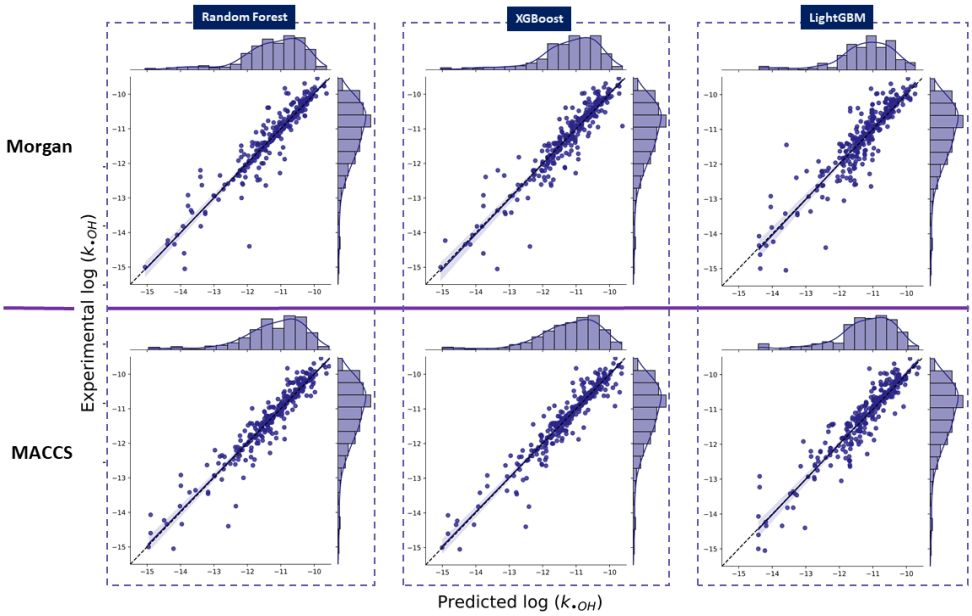


Figura 1: Comparação do desempenho dos modelos de aprendizado de máquina (Random Forest, XGBoost, e LightGBM) utilizando descritores moleculares Morgan e MACCS na predição do log(k_{OH}).

Conclusions

A expansão do estudo anterior através da aplicação de modelos de aprendizado de máquina mostrou-se eficaz na predição de parâmetros cinéticos e na interpretação dos mecanismos de degradação de compostos orgânicos em ambientes aquáticos e atmosféricos. Os modelos desenvolvidos, disponíveis na aplicação web (www.pysirc.com.br), demonstraram alta correlação entre valores experimentais e preditos de log(k_{OH}), com coeficientes de determinação (R^2) variando entre 0,85 e 0,92 e coeficientes de Pearson (r) entre 0,91 e 0,95. Além disso, a análise SHAP destacou a influência significativa de grupos eletronegativos e doadores de elétrons na reatividade dos radicais. Esses resultados indicam que os modelos propostos são ferramentas robustas e acessíveis para a análise cinética e interpretação mecanística de processos de oxidação radicalar. A plataforma desenvolvida tem o potencial de facilitar o desenvolvimento de estratégias mais eficazes para o tratamento de micropoluentes emergentes, contribuindo para a evolução das tecnologias avançadas de oxidação em unidades de tratamento de água e ar.

Acknowledgments

Gostaríamos de expressar nossa sincera gratidão ao Instituto Federal de Goiás (IFG), à Universidade Estadual de Goiás (UEG), à Coordenação de Aperfeiçoamento de Pessoal de Nível Superior (CAPES) e à Fundação de Amparo à Pesquisa do Estado de Goiás (FAPEG).

Referências

[1] MEI, Qiong et al, CEJ, 2019, 373, 668-676.
[2] GRAMATICA et al., PNAS, 2022, 119, 2113947119.
[3] OBERG et al., Chemosphere, 2021, 278, 130401.
[4] ROY et al., ES&T, 2021, 55, 12437-12448.
[5] LI et al., Atmos. Environ., 2022, 275, 119019.

10º SIMPÓSIO DE ESTRUTURA ELETRÔNICA & DINÂMICA MOLECULAR
SEED MOL
4 a 8 novembro | 2024
Pirenópolis, Goiás

Predicting the standard reduction potential of osmium(III) complexes with nitrogen-based ligands

Gabriel de S. Martins[1], Diego F. S. Paschoal[1]
[1]NQTCM: Núcleo de Química Teórica e Computacional de Macaé, Polo Ajuda, Instituto Multidisciplinar de Química, Centro Multidisciplinar UFRJ-Macaé, Universidade Federal do Rio de Janeiro, 27.971-525, Macaé, RJ, Brasil
gabrielmartins1102@gmail.com ; diegopaschoal01@gmail.com
Keywords: Osmium Complexes; Redox Potential, DFT, Basis set.

Abstract
In the present study the solvent effects, DFT functional, osmium and ligands basis sets in predicting the standard reduction potential of $[Os(NH_3)_6]^{+3/+2}$ redox system were assessed. The best protocol, mPW1LYP/def2-SVP/nqtcm-VDZP//IEF-PCM(Bondi) presented a relative deviation of only 0.4%.

Introduction

The anticancer activity of many transition metal complexes is related to redox processes, which alter several physicochemical properties of these complexes. Thus, understanding the redox potential can significantly contribute to understanding the mechanism of anticancer action of these complexes [1].

Considering the anticancer potential of osmium(III) complexes, the reduction potential is an essential property to be evaluated because the main mechanism involving these complexes depends on the reduction of the metal to osmium(II) [2,3].

The literature involving the computational prediction of the reduction potential of Os(III) complexes is very scarce. Furthermore, the deviations found in relation to the experimental values are relatively high [4,5].

Thus, the present study aims to propose a computational protocol for predicting the standard reduction potential (ε^0) of Os(III/II) complexes using the new nqtcm-VDZP basis sets.

Methodology

Initially, the redox system $[Os^{III/II}(NH_3)_6]^{+3/+2}$ (Figure 1), which has experimental data for ε^0 of -0,749 V obtained by cyclic voltammetry in water, with the standard hydrogen electrode (SHE) as reference, was selected. The ε^0 was calculated according to equation (1):

$$\varepsilon^0[V] = 27.21(G_{ox} - G_{red}) - \varepsilon^0_{abs}(SHE) \quad (1)$$

where $G_{ox/red}$ is the Gibbs free energy of the oxidized/reduced forms in hartree and SHE is the absolute potential of the standard hydrogen electrode, which had the value of 4.281 V considered.

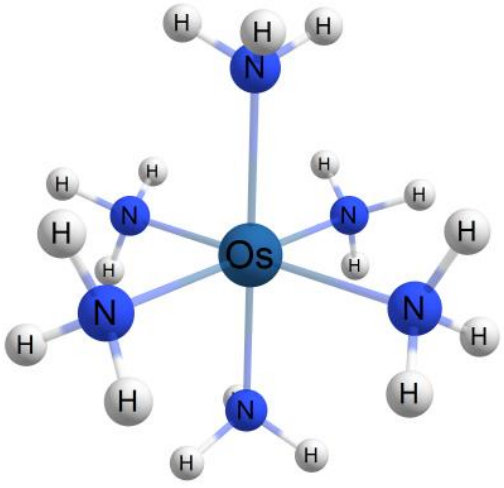


Figure 1: $[Os^{III/II}(NH_3)_6]^{+3/+2}$ redox system considered in the construction of computational protocol.

Thus, the Gibbs free energy $G^0_{i,aq}$ is the property calculated with the quantum mechanics calculations. The $G^0_{i,aq}$ was calculated according to equation (2):

$$G^0_{i,aq} = E_{el,aq} + G^0_{T,g} \quad (2)$$

Where the subscript "i" represents each reactive species, Os(III) and Os(II) complexes, $E_{el,aq}$ corresponds to the electronic energy plus nuclear repulsion in water, and $G^0_{T,g}$ is the thermal correction for Gibbs free energy calculated in the gas phase.

Initially, the role of the implicit solvent model was considered with the protocols B3LYP/def2-SVP//Solvent, Solvent = IEF-PCM(UFF), IEF-PCM(Bondi), and SMD. From these results, computational protocols considering a set of distinct 23 DFT functionals, 17 osmium basis sets (OSBS), and the def2-SVP and nqtcm-VDZP ligands basis sets (LBS) were proposed. The calculations were performed in GAUSSIAN 16 Rev. C.01 program.

Results and Discussion

First, the solvent effects were evaluated. The calculated results (Table 1) show that the inclusion of solvent effects and the implicit solvent model considered are of fundamental importance for predicting the ε^0. The relative deviation (RD) decreases from 1431% in the gas phase to 167% with the IEF-PCM(UFF) model, reaching 55% when the IEF-PCM(Bondi) model is considered.

Table 1. The role of the implicit solvent model in predicting the ε^0 of $[Os(NH_3)_6]^{+3/+2}$ with the B3LYP/def2-SVP//Solvent protocols.

Solvent models	ε^0 (V)	RD (%)
Gas phase	9.971	1431
IEF-PCM(UFF)	0.504	167.3
IEF-PCM(Bondi)	-0.340	54.61
SMD	-0.246	67.11
Experimental	-0.749	-

Furthermore, the role of the DFT functional, considering a set of 23 distinct functionals, were assessed at the DFT-Functional/def2-SVP/LBS//IEF-PCM(Bondi) levels, with the LBS = def2-SVP and nqtcm-VDZP. The nqtcm-VDZP is a new basis set developed in our group for ligands atoms.

The calculated results (Table 2) show a large variation of the relative deviations with the change of the DFT functional. However, a relationship with the functional class considered (GGA, meta-GGA, Hybrid, Hybrid meta-GGA, Long-range corrected) was not observed. Furthermore, the results also showed that the ligands basis sets play a fundamental role in the prediction of the reduction potential, with the values calculated with the LBS nqtcm-VDZP presenting a significantly better performance than that presented by the LBS def2-SVP. The best result was obtained with the mPW1LYP/def2-SVP/nqtcm-VDZP//IEF-PCM(Bondi) protocol, RD of only 0.4%.

Table 2. Calculated relative deviation (RD, %) from the experimental value for the ε^0 of $[Os(NH_3)_6]^{+3/+2}$ at DFT-Functional/def2-SVP/LBS//IEF-PCM(Bondi).

DFT-Functional	nqtcm-VDZP	def2-SVP
BLYP	12.4%	12.4%
BP86	3.4%	50.3%
OLYP	1.2%	110%
PBE	14.8%	22.6%
PW91	25.5%	44.1%
mPWLYP	14.2%	195.9%
mPWPW91	16.5%	178.4%
BPW91	11.5%	157.2%
M11L	57.0%	78.0%
MN15L	1.4%	349.2%
TPSS	8.9%	30.3%
B3LYP	8.6%	54.6%
B3P86	85.9%	229.0%
PBE0	5.1%	19.5%
mPW1LYP	0.4%	155.9%
mPW1PW91	6.5%	137.5%
B3PW91	10.6%	35.5%
TPSSh	3.1%	40.7%
M11	4.3%	37.5%
MN15	16.1%	490.9%
LC-BLYP	25.1%	105.4%
LC-wPBE	8.4%	77.8%
CAM-B3LYP	1.0%	39.0%

Finally, the role of the OSBS was also assessed at the BLYP/OSBS/LBS//IEF-PCM(Bondi) levels, considering a set of 17 OSBS. The GGA BLYP functional was considered to have presented the same RD with the LBS def2-SVP and nqtcm-VDZP. The calculated results (Table 3) show that the OSBS also plays a relevant role in

predicting the ε^0, with the use of an effective core potential (ECP) employing a triple- and quadruple-zeta polarized valence basis set resulting in a good description of the ε^0, RD smaller than ~3%.

Table 3. Calculated relative deviation (RD, %) from the experimental value for the ε^0 of $[Os(NH_3)_6]^{+3/+2}$ at BLYP/OSBS/LBS//IEF-PCM(Bondi).

OSBS/LBS	nqtcm-VDZP	def2-SVP
LANL2DZ	7.0%	17.0%
LANL2TZ	15.7%	21.0%
LANL2TZ(f)	19.3%	2.0%
def2-SVP	12.0%	12.4%
def2-TZVP	6.5%	30.0%
def2-TZVPP	3.2%	0.1%
def2-QZVP	1.2%	1.4%
cc-pVDZ-PP	3.9%	13.0%
cc-pVTZ-PP	3.4%	0.8%
cc-pVQZ-PP	10.7%	3.3%
aug-cc-pVDZ-PP	12.6%	11.0%
aug-cc-pVTZ-PP	8.4%	5.3%
aug-cc-pVQZ-PP	4.4%	11.1%
jorge-DZP	213.0%	15.0%
jorge-ADZP	228.0%	121.0%
jorge-TZP	474.0%	68.0%
jorge-ATZP	76.0%	89.0%

Conclusion

In the present study, we assessed the role of the solvent, DFT functional, osmium and ligands basis sets in predicting the ε^0 of the $[Os(NH_3)_6]^{+3/+2}$ complex.

The calculated results showed that all aspects considered in the computational protocol play an important role in the description of ε^0.

Besides, the new proposed nqtcm-VDZP ligands basis sets provided an excellent description of ε^0.

Furthermore, the calculated results showed that the construction of the computational protocol involves a compromise between DFT-Functional/OSBS/LBS//Solvent.

The protocols mPW1LYP/def2-SVP/nqtcm-VDZP//IEF-PCM(Bondi), RD of 0.4%, and BLYP/def2-TZVPP/def2-SVP//IEF-PCM(Bondi), RD of 0.1%, proved to be an excellent alternative for the study of the reduction potential in osmium complexes.

In the next step, these computational protocols will be validated in predicting the ε^0 of a set of osmium(III) complexes with nitrogen-based ligands.

Acknowledgments

The authors would like to thank the Brazilian agency FAPERJ (E-26/201.336/2022 – BOLSA JCNE and E-26/210.070/2022 – DCTR).

References

1. Zhang, P.; Sadler, P. J.; Eur. J. Inorg. Chem. 2017, 1541.
2. Baik, M.-H.; Friesner, R. A.; J. Phys. Chem. A 2002, 106, 7407.
3. Céron-Camacho, R. et al.; Molecules 2021, 26, 1563.
4. Srnec, M. et al.; J. Am. Chem. Soc. 2008, 130, 10947.
5. Rulísek, L.; J. Phys. Chem. C. 2013, 117, 16871.

Density functional optimizations for DFT calculations in Fermi-Hubbard Model

T. R. Pauletti[1], G. M. Tonin[1], I. M. Carvalho[1], T. Borges[2], and V. V. França[1]

[1]Chemistry Institute, São Paulo State University (UNESP), Av. Prof. Francisco Degni, 55, Araraquara, Brazil. Contact Phone: +55 016 3301-9500
[2]Mathematics, Federal Institute of Education, Rua Doutor Aldo Benedito Pierri, 250, Araraquara, Brazil. Contact Phone: +55 016 3303-2330

Contact email: gabriel.tonin@unesp.br

The advancement of experimental techniques for atom deposition in producing nanostructured materials has been crucial in quantum technology devices development, as quantum transistors [1]. To optimize such quantum technological applications, a theoretical investigation of their properties is essential, which invariably requires the quantum treatment of complex systems. Density Functional Theory (DFT) emerges as an efficient computation method for theoretical treatment of nanomaterial, solid, and cold atom properties. The efficiency of the electronic calculations via DFT depends however on the quality and precision of the density functionals used to describe the electronic correlations. For the one-dimensional Hubbard model, although we have robust analytical tools to obtain the ground-state energy of heterogeneous quantum systems via DFT in both non-magnetized [2] and magnetized systems [3], other quantities obtained from energy derivatives — such as magnetic susceptibility and chemical potential — are not well described by the current density functionals.

This study aims to enhance and optimize current density functionals for more precise DFT calculations of nanostructures described by the one-dimensional Hubbard model. Preliminary results for the ground state energy reveal an overall reduction in relative average error across the interaction strength range (from U=0t to U=40t, where t is the hopping term), with a 20% reduction in computational time. This initial improvement suggests the potential of our numerical code for functional optimizations to provide enhanced DFT calculations.

[1] Marchukov et al., Nat. Commun. 7, 13070 (2016).

[2] N. A. Lima et al., Phys. Rev. Lett. 90, 146402 (2003).

[3] V. V. França et al., NJP 14, 073021 (2012)

Stability and catalytic potential modulation of Au-alloys clusters supported on graphene

Gabriel Reynald Da Silva[1], Maurício J. Piotrowski[2], Alexandre C. Dias[3], Celso R. C. Rêgo[4], Diego Guedes-Sobrinho[1].

[1]Department of Chemistry, Federal University of Paraná, 81531-980 Curitiba/PR, Brazil.
[2]Department of Physics, Federal University of Pelotas, 96010-900 Pelotas/RS, Brazil.
[3]Physical Institute and International Center for Physics, University of Brasília, 70919-970 DF, Brazil.
[4]Institute of Nanotechnology Hermann-von-Helmholtz-Platz, Karlsruhe Institute of Technology, 76021 Karlsruhe, Germany.
gabriel.reynald@ufpr.br, *guedessobrinho@ufpr.br*.
Keywords: density functional theory (DFT); clusters alloys; graphene.

Abstract
Gold-based nanostructures catalysts face stabilization challenges on graphene due to weak affinity. This study employs density functional theory to explore how metal alloying impacts stability and catalytic potential. Group 10 alloys exhibit enhanced stability and comparable efficiency.

Introduction

Recent studies have highlighted Au-based nanostructures as a potential high efficiency catalysts for applications in energy production, such as in hydrogen evolution reactions (HER) and oxygen evolution reactions (OER) for H_2 production [1-3]. Nevertheless, stabilizing these nanostructures on cost-effective substrates like graphene (Gr) remains challenging due to the weak affinity between Au structures and Gr, stemming from the delocalized electron density of p_z carbon orbitals. Instead of chemically modifying the supports to enhance their attractiveness for adsorption, this study explores the impact of alloy formation on the stability and catalytic potential of Au-based nanocatalysts.

Methodology

With *ab initio* density functional theory (DFT) spin-polarized calculations approach with the exchange-corrlation functional developed by Perdew-Burke-Enzherhof (PBE), including empirical D3 van der Waals correction developed by Grimme, we examined the structural, electronic, and reactive properties of $M_{(n-x)}Au_x$ clusters (M = Ni, Pd, Pt, Cu, Ag) with atomicities n = 1–4, both in the gas-phase and when supported on Gr. The protocol was employed in Vienna *Ab initio* Simulation Package (VASP), which employs the Projector Augmented Wave (PAW) as basis set. The total energy convergence criteria was considered for lower than 1.0×10^{-6} eV, whereas 450 eV was employed for cutoff energy of the plane-waves, from which all the forces were minimized until 0.01 eV/Å. The Brillouin-zone integrations for the gas-phase clusters were performed only on the Γ point in a cubic box with 18 Å of size, conversely, for the clusters on Gr a **k**-mesh of 4×4×1 was employed for the 6×6×1 supercell.

Results

The stabilization of unary and binary clusters on Gr was investigated based on adsorptive stability, which is defined as the ability of the cluster to be anchored on the substrate, evaluated by adsorption energy (E_{ads}). Additionally, the thermodynamic formation stability of alloys was assessed using excess energy (E_{exc}), which determines the mixing/segregation tendency. Negative (positive) values of E_{ads} and E_{exc} signify fa-

vorable (unfavorable) adsorption and alloy formation, respectively. As seen in Figure 1(a), the most stable morphology for the adsorption of binary clusters on Gr occurs when the M atoms are directly bound on the surface. Panel (b) presents the E_{ads} for unary and binary clusters. Group 10 (Ni, Pd, Pt) alloys exhibit superior adsorptive stability compared to pure Au nanostructures (represented by the golden line), underscoring their potential as effective anchors between Au and Gr.

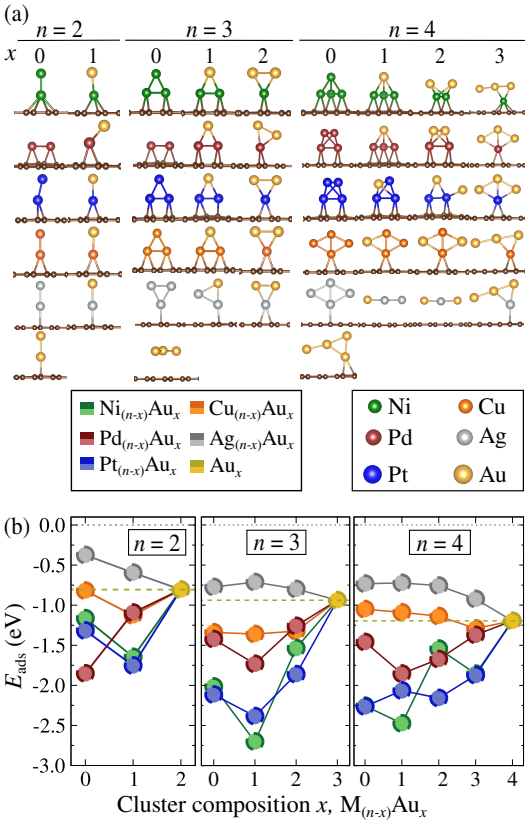


Figure 1: (a) The most stable configurations of unary and binary clusters adsorbed on graphene, and (b) their adsorption energy (E_{ads}) as a funciton of Au composition x.

Regarding thermodynamic formation stability, Figures 2(a) shows the E_{exc} for alloys in gas-phase and panel (b) for adsorbed systems. The influence of Gr on the thermodynamic stability tendencies of alloys is evident compared to those in the gas-phase. All the clusters exhibiting favorable formation in the gas-phase become more stable when adsorbed, whereas those ones with a tendency to segregate present favorable mixing.

The mechanisms underlying adsorptive and thermodynamic stability were investigated through ionic-covalent interactions between metal-metal and metal-Gr. This analysis employed charge population and covalent interaction analysis via the DDEC6 and COHP, respectively. The superior adsorption of alloys compared to their unary counterparts is attributed to the strengthened covalent C-M interaction when only Au occupies the exposed site of the cluster, a phenomenon not observed for Group 11 alloys. The favorable mixing tendencies arise from the stronger covalent interaction between M-Au compared to M-M and Au-Au interactions in alloys bonds.

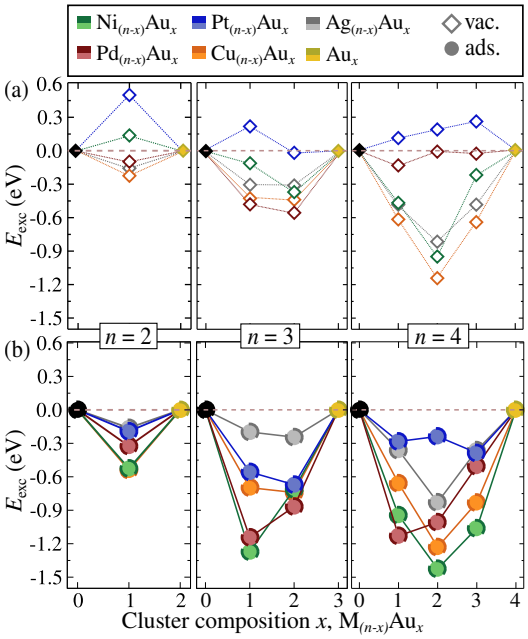


Figure 2: The excess energy (E_{exc}) of the most stable configurations of binary clusters in (a) gas-phase and (b) adsorbed on graphene as funciton of Au composition x.

Additionally, polarization of $M^{\delta+}$-$Au^{\delta-}$ bonds promotes electrostatic contribution for stability. The effect of adsorption promotes a favorable formation of all alloys by weakening the M-M bonds directly bonded to Gr. Moreover, Gr increases the electrostatic interaction between the metals, facilitating a greater charge transfer from M species to Au, forming a partially cationic $Au^{\delta-}$-$M^{\delta+}$/Gr bridge-like structure.

The d-band center (ε_d) model was employed to assess the catalytic potential of alloys in comparison to unary clusters. Based on

previous studies for the HER and OER, the optimal ε_d range was established to be -1 to -2 eV for catalysts [4,5]. Figure 3 illustrates the *d*-band centers for unary and binary adsorbed systems. It demonstrates that incorporation of Au into M_n results in modulation of the alloy's ε_d to closely align with

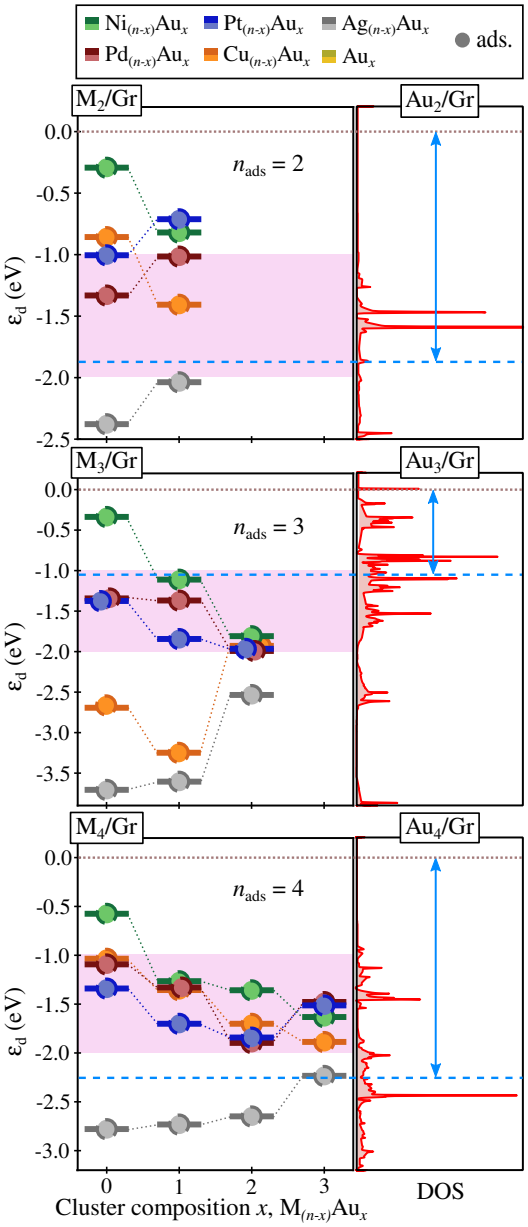


Figure 3: The *d*-band center (ε_d) of unary and binary adsorbed clusters as funciton of Au composition *x*. The density of states (DOS) and ε_d for pure adsorbed Au_n clusters are shown on the right side for each atomicity. The pink bar indicates the optimal ε_d range estimeted for HER and OER catalysts.

that of pure Au_n, either increasing or decreasing it relative to the Fermi level. The Group 10 alloys are notably influenced by Au, showing an optimal *d*-band center range suitable for HER and OER applications.

Conclusions

In conclusion, our *ab initio* calculations demonstrate a synergistic effect between Au and Group 10 (Ni, Pd, Pt) metals in better adsorptive stabilization of Au nanostructures on Gr by forming a $Au^{\delta-}$-$M^{\delta+}$/Gr bridge-like structure for anchoring. Moreover, the substrate influences direct in thermodynamic stability of alloys, where no segregating process is observed on Gr. The modulation by Au in Group 10 alloys, coupled with the exposure of Au in the adsorbed alloys morphology, positions these catalysts to be as efficient as pure Au catalysts. Our findings reveal the significant influence of the 2D surface on the physicochemical properties of alloys, particularly in terms of their stabilization and catalytic performance—an aspect often overlooked in previous studies. Furthermore, we have shown that alloying the nanocatalyst, rather than modifying the substrate's chemical composition, serves as a effective strategy for enhancing stabilization. This approach is especially advantageous given the inherent complexities associated with studying catalytic behavior in nanocatalysts supported on functionalized surfaces. Additionally, NiAu alloys emerge as catalytic candidates with stability and potential efficiency, along with offer reduced costs and non-toxicity.

Acknowledgements

We would like to thank CAPES for funding and LCPAD-UFPR, NACAD-UFRJ, CENAPAD-Unicamp, and SENAI-CIMATEC for providing computational resources.

References

1. Guedes-Sobrinho, D. *et al.* Phys. Chem. Chem. Phys. 2022, 24, 6515-6524.
2. Piotrowski, M. J. *et al.* J. Comput. Chem. 2022, 43, 230.
3. Guedes-Sobrinho, D. *et al.* J. Phys. Chem. C. 2017, 121, 27721-27732
4. Hu, Qi *et al.* Nat. Commun. 2022, 13, 3958.
5. Lyu, Xiao *et al.* Adv. Mater. 2020, 32, 2003493.

Augmenting Binding Mode Prediction Capabilities Using Graph Attention Neural Networks and Contact Maps.

LIMA, G. E.[1]; PANTALEÃO, S. Q.[1]; SCOTT, A. L.[1]
[1]Department of Mathematics, Computing, and Cognition (CMCC), Federal University of ABC, São Paulo, SP, Brazil.
glauco.endrigo@ufabc.edu.br
Keywords: Docking, Re-ranking, Deep Learning

Abstract

Understanding the intricate relationship between proteins and ligands is crucial for identifying potential drug candidates. The discovery of new candidates and comprehension of key chemical elements governing ligand-protein interactions in relevant biological targets have far-reaching implications.
Protein-ligand docking explores potential binding positions of a ligand on a specific molecular target and aims to predict the affinity of this interaction. However, the use of a rigid receptor, which fails to represent receptor flexibility, coupled with limitations in scoring functions and force fields, can have adverse effects on docking accuracy. Certain intermolecular interaction terms, such as solvation effects and entropy changes, are challenging to capture. In that sense, a significant limitation in molecular docking arises from the lack of confidence in scoring functions' ability to provide accurate binding energies. Because of that and many more reasons, the top-ranked solutions are not always the best. In this study, we propose employing a Graph Attention Network (GAT) to learn ligand-protein contact information and re-rank docking poses from conventional methods. Comparisons will be made with other approaches utilizing deep learning for binding affinity prediction. By leveraging (GAT), this research aims to re-ranck docking predictions by testing with strategies for descriptors of ligand-protein contact information, also including experiments with the recent mechanisms of attention in GAT, enabling a more comprehensive evaluation of the proposed method's effectiveness in addressing the limitations of conventional docking techniques.

Introduction

One challenge for docking protein/ ligand is to find an ideal function score. Several works show that the best pose is not always between the best ranked. The use of models of Deep Learning to rank against the results can be very useful when we perform docking protein-ligand [1].

Methodology

We selected a set with 284 complexes protein-ligand from the core data set of PDBbind and carried out docking calculations, using AutoDock Vina [2].

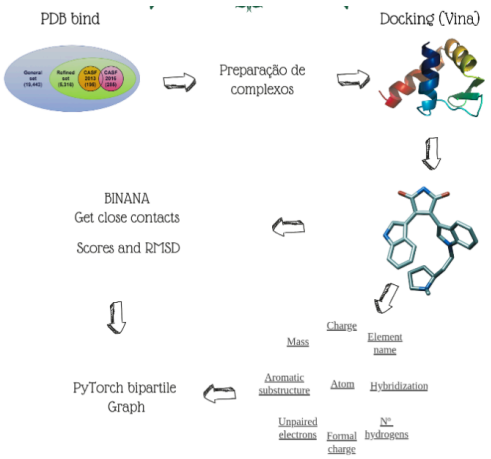


Figure 4: Flowchart illustrating the process of data collection, processing, and dataset construction for training. The final outcome is a graph-based dataset featuring atomic descriptors and labeled with positive or negative classifications.

Then, we took the first ten poses for each one and performed contact analysis with BINANA software.

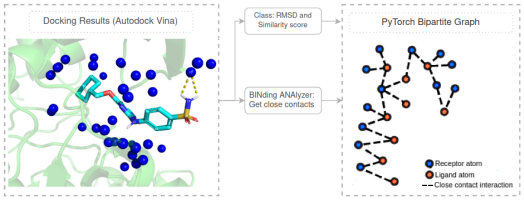


Fig 1: BINANA software and Python script to detect close-contact atoms, where close contact refers to atoms within 4 Å of each other.

For each pose, a bipartite graph is created in which atoms are the nodes and they have some atomic descriptors. A training database was built, with a subset of complexes, where each pose is mapped to a graph with descriptors and labeled as the positive or negative class according to a combination of RMSD and native contacts [3]. A Graph Attention Neural Network model was used to learn ligand-protein contact information.

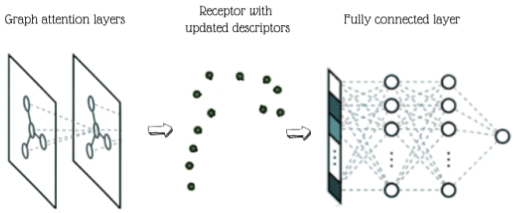
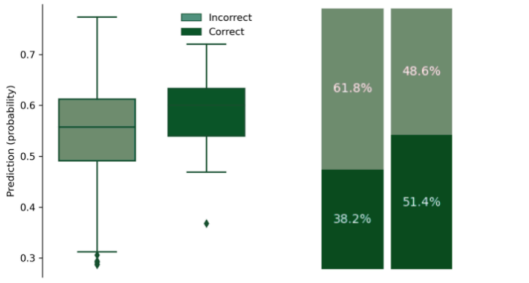


Fig 2: Graph Attention Neural Network with a fully connected layer.

Results and Discussion

The first results were promising. At this moment, we are trying to find the best set of descriptors to improve the performance of the model. In a second moment, when the descriptors are completely defined, the database for training and validation will be increased. We observed that the addition of pose rank, generated by Vina, added as a descriptor improved the results .After a detailed analysis of the results, it was observed that the model had learned only the ranking information. Consequently, we decided not to include this information as a descriptor, and this approach proved to be important.

When employing the core dataset for experimental purposes, the findings indicate the efficacy of the approach.



Distribution of probabilistic predictions made for classes known to be positive and negative, highlighting the model's strong performance in identifying positive classes.

By applying a filter with a prediction threshold greater than 0.5 to the first pose of each complex generated by AutoDock Vina, it is observed that a significant portion of negative cases would be excluded.

Fig 3: Results of the model.

Conclusions

The study, up until now, has worked with the core dataset and has demonstrated the benefit of employing a GAT model to enhance docking pose prediction accuracy and importance to consider the number of native contacts.

Acknowledgements

CAPES, Fapesp.

References

1. Guedes IA, Pereira FSS, Dardenne LE. Front,Pharmacol 9:10.3389/fphar.2018.010 89, 2018.

2. Liu, Z. et al. Bioinformatics 31:405-12, 2015.

3. Morrone, J.A. et al. J. Chem. Inf. Model. 60(9), 4170–4179, 2020.

Explorando o Mecanismo e a Cinética da Degradação Oxidativa da Epicloridrina pelo Radical OH: Uma Investigação em Química Quântica Computacional

Gustavo Gomes de Sousa[1*], José Roberto dos Santos Politi[1].
[1]Instituto de Química, Universidade de Brasília, Campus Universitário Darcy Ribeiro, 70910-000 Brasília, DF, Brasil.
*gustavo.gds.873@gmail.com

Keywords: Epicloridrina; Poluente recalcitrante; Processos Oxidativos Avançados; Radical hidroxila; cinética de reação

Abstract

In recent decades, the concentration of emerging pollutants in aquatic environments has risen due to improper industrial waste disposal. Epichlorohydrin, with extensive industrial uses and significant environmental and health risks, is a notable pollutant. This study examines its degradation using advanced oxidation processes (AOPs), effective in removing organic pollutants. Quantum chemical simulations with Gaussian 16 explored interactions between epichlorohydrin and hydroxyl radicals (OH), clarifying the reaction mechanisms and kinetics. Results identified multiple reactive sites on epichlorohydrin and many degradation mechanisms, producing various products. Lower activation barriers in mechanisms like Mec-B and Mec-C indicated higher kinetic rate constants and thermodynamic preference. Mec-A had higher activation barriers and lower reaction rates. Toxicity assessments showed degradation products were generally less toxic than epichlorohydrin. The study concludes that choosing the most suitable degradation mechanism should balance kinetic efficiency and environmental impacts, providing a foundation for better methods to remove epichlorohydrin from aquatic environments.

Introdução

Nas últimas décadas, o aumento na concentração de poluentes emergentes em ambientes aquáticos tem trazido preocupação devido ao elevado risco tóxico para a saúde aquática e humana [1]. Um exemplo significativo é a epicloridrina, recentemente regulamentada para monitoramento pelo Ministério da Saúde do Brasil, devido aos seus graves impactos ambientais e à saúde humana [2].

A epicloridrina (EPCH) foi incluída na lista negra de poluentes da Comissão das Comunidades Europeias em 1982 devido aos seus riscos potenciais [3]. Este composto pode causar efeitos adversos no sistema nervoso central, trato respiratório, fígado e rins, além de ser altamente irritante para os olhos e vias respiratórias [4]. A recalcitrância da epicloridrina torna os tratamentos convencionais ineficazes e economicamente inviáveis, exigindo abordagens alternativas para sua remoção.

Os Processos Oxidativos Avançados (POAs) [5,6] têm mostrado eficácia na degradação da epicloridrina em ambientes aquáticos. Pesquisas recentes buscam entender os mecanismos de degradação deste poluente e avaliar a toxicidade dos produtos resultantes. Estudos computacionais e teóricos são cruciais para elucidar a cinética de reação dos poluentes orgânicos e radicais hidroxila. Este estudo visa analisar detalhadamente a interação entre radicais OH e epicloridrina, contribuindo para a implementação de métodos mais eficazes de remoção, minimizando os impactos ambientais e riscos à saúde.

Metodologia

Todos os cálculos de química quântica foram realizados usando o pacote Gaussian 16. As propriedades eletrônicas e estruturais dos reagentes, do estado de transição e dos produtos foram determinadas no nível de cálculo MP2/aug-CC-PVTZ, a metodologia SMD foi empregada para simular o ambiente de solvatação aquosa. Os principais sítios reativos na epicloridrina foram identificados usando índices de Fukui, determinado através do pacote Multiwfn.

Os parâmetros cinéticos da reação foram determinados usando a teoria do estado de

transição deformado (*d*-TST), implementada no código Transitivity versão 1.0.3.

O estudo de toxicidade da epicloridrina e dos produtos provenientes da degradação foi conduzido usando o ECOSAR V2.0, um software que prevê a toxicidade de contaminantes orgânicos para organismos aquáticos e algas verdes.

Resultados e Discussão

Foram observados, através dos indicies de Fukui, dois principais sítios reativos na EPCH. Os quais promoveram a observação de três mecanismos reacionais distintos. Pode-se observar o caminho reacional de cada mecanismo presentes na Figura 1.

No Mec-A, observa-se a remoção de um átomo de cloro promovida pelo ataque do radical OH. Nos mecanismos Mec-B e Mec-C, o radical OH inicialmente ataca e abre a estrutura do epóxido, resultando na formação de um intermediário. Em seguida, no Mec-B, o epóxido é reconstruído pela eliminação do cloro, enquanto no Mec-C o intermediário se rompe, formando dois produtos menores.

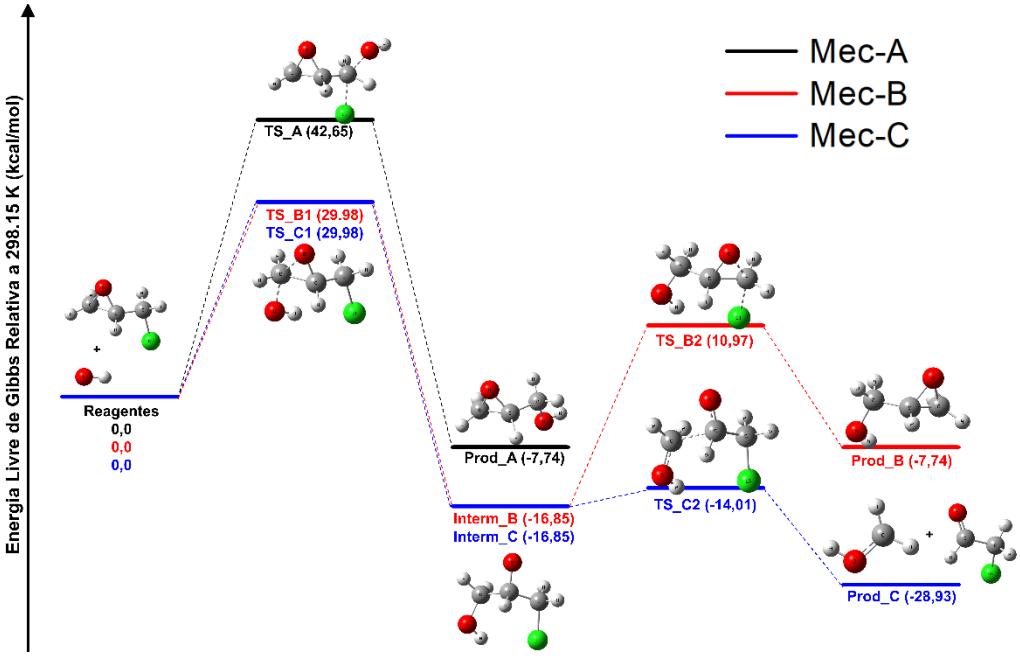


Figura 1 - Perfil de energia relativa correspondente aos Mec-A, Mec-B e Mec-C da degradação da Epicloridrina promovida pelo Radical Hidroxil.

Pode-se observar que, nos mecanismos Mec-B e Mec-C, as barreiras de ativação inicial são menores em comparação ao Mec-A, sugerindo uma preferência termodinâmica por esses mecanismos. As constantes cinéticas gerais para cada mecanismo de reação foram determinadas na faixa de temperatura de 273K a 373K, utilizando a metodologia desenvolvida por Murdoch [7,8], que considera cada barreira de ativação dos diferentes mecanismos.

As constantes cinéticas obtidas a 298K para os mecanismos Mec-A, Mec-B e Mec-C foram de $2{,}73\ x\ 10^{-36}\ cm^3 moleculas^{-1} s^{-1}$, $3{,}68\ x\ 10^{-27}\ cm^3 moleculas^{-1} s^{-1}$ e $3{,}68\ x\ 10^{-36}\ cm^3 moleculas^{-1} s^{-1}$, respectivamente.

Observa-se que, devido às barreiras de ativação mais baixas, as reações que ocorrem pelos mecanismos Mec-B e Mec-C tendem a apresentar constantes cinéticas mais altas. Isso indica que a menor barreira de ativação inicial nesses mecanismos resulta em uma taxa de reação mais elevada.

As toxicidades estimadas pelo ECOSAR para os compostos em relação a peixes, dáfnias e algas verdes estão apresentadas na Tabela 1, considerando os produtos formados em cada mecanismo de ação. Com base nos parâmetros

de toxicidade, observa-se que a degradação da EPCH, por meio de todos os mecanismos avaliados, tende a gerar produtos menos tóxicos do que a própria EPCH.

Tabela 1 - Toxicidade do EPCH e seus principais produtos gerados pelo ataque do radical OH (mg/L)

Organismos	Compounds				
	EPCH	Produto Mec-A	Produto Mec-B	Produto 1 Mec-C	Product 2 Mec-C
LC_{50} (Peixes, 96 h)	23,6	362	362	39,1	$1{,}88 * 10^3$
LC_{50} (Daphnia, 48 h)	21,2	$2{,}48 * 10^3$	$2{,}48 * 10^3$	42,9	881
EC_{50} (Algas verdes, 96 h)	21,8	$5{,}77 * 10^3$	$5{,}77 * 10^3$	20,4	297
ChV (Peixes, crônico)	1,86	0,059	0,059	14,4	147
ChV (Daphnia, crônico)	2,15	252	252	0,334	50,4
ChV (Algas verdes, crônico)	5,45	$1{,}36 * 10^3$	$1{,}36 * 10^3$	5,92	50,7

Conclusão

Este estudo utilizou metodologias computacionais para investigar a termodinâmica e a cinética da degradação de EPCH catalisada pelo radical OH. A análise dos índices de Fukui identificou como principais sítios de ataques a remoção do átomo de cloro e o ataque no carbono da estrutura do epóxido possibilitando a abertura do anel. Cada mecanismo reacional apresentou produtos distintos.

A análise energética dos perfis de reação indicou uma preferência por certos mecanismos devido a barreiras de ativação mais baixas, o que influenciou diretamente as constantes cinéticas. Os dados eletrônicos enfatizaram a importância da primeira etapa nos mecanismos de múltiplas etapas. Em particular, os mecanismos com barreiras de ativação mais baixas apresentaram constantes cinéticas mais altas, destacando a eficiência cinética de tais mecanismos.

A avaliação da toxicidade dos produtos revelou que a degradação do EPCH geralmente resulta em produtos menos tóxicos, exceto no caso do mecanismo Mec-C, onde foi observado o aparecimento de um produto ligeiramente mais tóxico que a EPCH. Esses resultados enfatizam a importância de considerar não apenas a cinética e a termodinâmica, mas também as implicações ambientais na escolha do mecanismo de reação, avaliando a formação de diversos produtos possíveis para os diferentes mecanismos de degradação.

Agradecimentos

O Conselho Nacional de Desenvolvimento Científico e Tecnológico do Brasil (CNPq, Brasil) financiou este trabalho.

Este trabalho foi financiado pela Fundação de Apoio à Pesquisa do Distrito Federal (FAPDF). Agradecimentos especiais ao Auxílio Financeiro para Estudantes e Pesquisadores - Edital DPG 0001/2022 da Universidade de Brasília.

References

1. M. Berkani, A. Smaali, Y. Kadmi, F. Almomani, Y. Vasseghian, N. Lakhdari, and M. Alyane, J Hazard Mater **421**, 126719 (2022).
2. Ministério da Saúde, (2017).
3. A. J. Van Den Wijngaard, D. B. Janssen, and B. Witholt, Microbiology (N Y) **135**, 2199 (1989).
4. D. C. Abbott, J R Soc Health **105**, (1985).
5. F. O. Sanches-Neto, B. Ramos, A. M. Lastre-Acosta, A. C. S. C. Teixeira, and V. H. Carvalho-Silva, Chemosphere **278**, 130401 (2021).
6. S. R. Kadam, N. L. Jadhav, A. B. Pandit, and M. K. Pejaver, Chemical Engineering and Processing - Process Intensification **166**, 108486 (2021).
7. J. R. Murdoch, J Chem Educ **58**, 32 (1981).
8. N. D. Coutinho, H. G. Machado, V. H. Carvalho-Silva, and W. A. da Silva, Physical Chemistry Chemical Physics **23**, 6738 (2021).

Avaliando o Desempenho de Supercapacitores à Base de Eletrodos Gêmeos e Não Gêmeos de Grafeno e Grafino

Henrique de Araujo Chagas[1], Thaciana Malaspina[2], Eudes Eterno Fileti[2] and Guilherme Colherinhas[1].
[1]Instituto de Física, Universidade Federal de Goiás, 74690-900, Goiânia, GO, Brasil.
[2]Instituto de Ciência e Tecnologia, Universidade Federal de São Paulo, 12247-014, São José dos Campos, São Paulo, Brasil.
hdachagas@gmail.com.
Keywords: Supercapacitor; graphene; graphyne; molecular dynamics; electrochemical energy.

Abstract
Graphene and graphyne electrodes are important for energy storage due to their unique properties. This study uses molecular dynamics simulations to explore supercapacitors with these electrodes and [Emim][BF4] and 1M NaCl@H_2O electrolytes. It examines electrode-electrolyte interactions, electric double layer characteristics, and capacitive performance, highlighting key differences and similarities between graphene and graphyne.

Introdução

Dispositivos de armazenamento de energia eletroquímica, como baterias e supercapacitores (SC), têm sido foco de intensas pesquisas devido ao seu papel crucial em diversas aplicações tecnológicas[1-5]. Dentro desse campo, os supercapacitores destacam-se por sua capacidade de armazenamento de energia e ciclos de vida prolongados. A pesquisa em supercapacitores pode ser dividida em duas abordagens principais, a manipulação da composição química do eletrólito para aumentar a condutividade e minimizar perdas[6-11] e o avanço no desenvolvimento de materiais utilizados como eletrodos, buscando materiais com alta área de superfície de contato, estabilidade robusta e boa condutividade elétrica[12-14].

O grafeno tem sido amplamente estudado devido às suas propriedades mecânicas, químicas e eletrônicas[12-14]. No entanto, limitações como a ausência de uma banda proibida e interações fortes entre folhas adjacentes de grafeno podem reduzir sua eficiência[1-5].

O grafino surgiu como uma alternativa e pode superar algumas limitações do grafeno[15-17]. Suas propriedades únicas, como maior distância intercamadas, estrutura porosa, maior área de superfície de contato, banda proibida intrínseca e capacidade eletroquímica, tornam-no um candidato promissor para aplicações de armazenamento de energia[12-14].

Metodologia

Neste trabalho, foram realizadas simulações de Dinâmica Molecular (DM) clássica para investigar supercapacitores com diferentes combinações de grafeno e grafino como eletrodos. Foram consideradas quatro combinações de eletrodos positivos e negativos: duas chamadas gêmeas (Modelo-1 e Modelo-2) compostas por grafeno/grafeno e grafino/grafino, respectivamente; e duas chamadas não gêmeas (Modelo-3 e Modelo-4) compostas por grafeno/grafino e grafino/grafeno, respectivamente. Foram utilizados dois modelos diferentes como eletrólito, o Líquido Iônico (LI) tetrafluoroborato de 1-etil-3-metilimidazólio [Emim][BF4] e uma solução aquosa de cloreto de sódio com concentração molar de 1 mol/L. A combinação de quatro pares de eletrodos e

dois eletrólitos resultou em um total de oito modelos de SC's.
Todos os modelos foram gerados a partir do software PACKMOL[18], com a inserção do eletrólito entre os eletrodos, separados por uma distância de 12 nm. A Figura 1 apresenta as caixas de simulação dos Modelos 1 e 2 para a solução aquosa de NaCl.

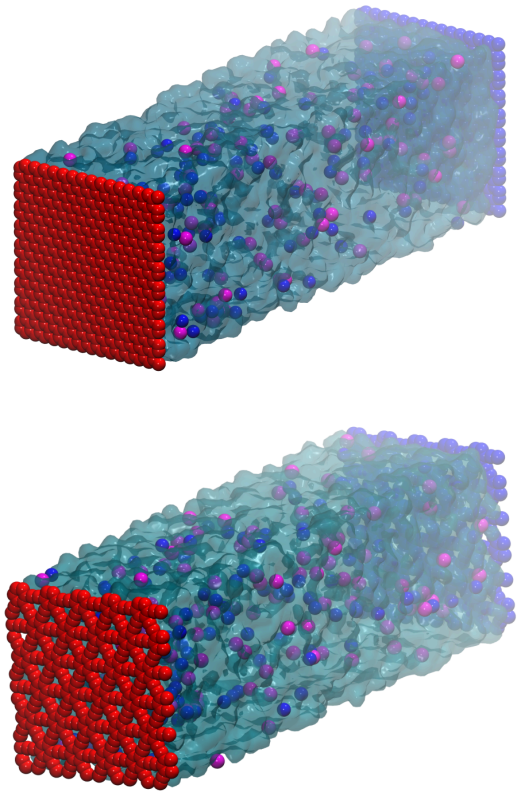


Figura 1: caixas de simulação dos Modelos 1 e 2 para a solução aquosa de NaCl.

Foram realizadas simulações de 30 ns utilizando o ensemble NVT a uma temperatura de 500 K. Além disso, foi empregado o método de carga fixa, com densidades de carga elétrica (σ) distribuídas sobre os eletrodos partindo de 0,0 a ±4,8 μC/cm².

Resultados e Discussão

Análise Energética da Dupla Camada Elétrica. Nota-se que a energia de interação eletrodo-eletrólito é cerca de cinco vezes maior para o LI quando comparado com a solução aquosa, além disso, as interações dos eletrodos de grafeno são maiores que as dos eletrodos de grafino. Isso pode estar associado à quantidade de átomos de carbono que compõem o eletrodo de grafeno (540 átomos) e grafino (360 átomos). É possível notar também que a interação de Lennard-Jones é de 5 a 10 vezes maior que a interação de Coulomb.

Propriedades Eletrostáticas. A densidade de carga aplicada aos eletrodos influenciam na formação da Dupla Camada Elétrica (EDL), produzindo um potencial eletrostático oscilante nessa região do dispositivo. A Figura 2 apresenta o perfil do potencial eletrostático para σ = 0,0 e ±4,8 μC/cm² para o Modelo-1 com o LI como eletrólito.

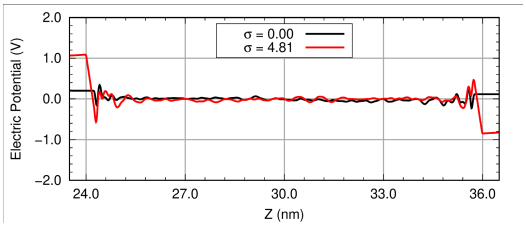


Figura 2: Potencial eletrostático para σ = 0,0 e ±4,8 μC/cm² para o Modelo-1 com o LI como eletrólito.

A energia armazenada em um supercapacitor (SC) é diretamente proporcional à capacitância e ao quadrado da diferença de potencial (DDP). Assim, foi analisada a densidade gravimétrica de energia armazenada nos dispositivos. Comparando o Modelo-1 com o Modelo-2 a uma DDP fixa de 1,8 V, observa-se que, para o dispositivo de grafino, a energia armazenada é cerca de 27% maior. Essa diferença pode ser ainda mais significativa em DDPs mais elevadas, indicando que o uso de eletrodos de grafino pode melhorar a capacidade de armazenamento de energia do dispositivo.

Conclusões

Simulações de DM foram empregadas para avaliar supercapacitores baseados em eletrodos de grafeno e grafino com dois eletrólitos: um LI [Emim][BF4 e uma solução aquosa de NaCl, totalizando oito modelos. A partir das análises das

interações energéticas da EDL e dos eletrodos, nota-se que as interações de van der Waals dominar a interação eletrodo-eletrólito. A capacitância dos dispositivos varia de 2,5 a 2,8 µF/cm², com desempenhos equivalentes entre os eletrodos de grafeno e grafino. O grafino demonstrou ser uma alternativa atraente por ser 33% mais leve e apresentar densidade gravimétrica de energia armazenada 27% maior a 1,8 V, justificando seu uso para aumentar a capacidade de armazenamento de energia de supercapacitores.

Agradecimentos

Este trabalho foi apoiado por bolsas de pesquisa do Conselho Nacional de Desenvolvimento Científico e Tecnológico – CNPq, da Coordenação de Aperfeiçoamento de Pessoal de Nível Superior – CAPES e da Fundação de Amparo à Pesquisa do Estado de São Paulo – FAPESP.

Referências

[1] E. Strandberg, S. Esteban-Martín, J. Salgado, A.S. Ulrich. Biophys J 96 (2009) 3223–3232.
[2] Y. Zhang, Q. Wan, N. Yang. Small 15 (2019) 1903780.
[3] A.G. Olabi, M.A. Abdelkareem, T. Wilberforce, E.T. Sayed. Renewable and Sustainable Energy Reviews 135 (2021) 110026.
[4] H. de Araujo Chagas, E.E. Fileti, G. Colherinhas J Mol Liq 360 (2022) 119494.
[5] H. de Araujo Chagas, E.E. Fileti, G. Colherinhas J Mol Liq 379 (2023) 121703.
[6] M. Sajjad, M.I. Khan, F. Cheng, W. Lu. J Energy Storage 40 (2021) 102729.
[7] C. Zhao, W. Zheng. Front Energy Res 3 (2015).
[8] H. Zhang, X. Liu, H. Li, I. Hasa, S. Passerini. Angewandte Chemie International Edition 60 (2021) 598–616.
[9] P. Lannelongue, R. Bouchal, E. Mourad, C. Bodin, M. Olarte, S. le Vot, F. Favier, O. Fontaine. J Electrochem Soc 165 (2018) A657–A663.
[10] M. McEldrew, Z.A.H. Goodwin, A.A. Kornyshev, M.Z. Bazant. J Phys Chem Lett 9 (2018) 5840–5846.
[11] L. Suo, O. Borodin, T. Gao, M. Olguin, J. Ho, X. Fan, C. Luo, C. Wang, K. Xu. Science (1979) 350 (2015) 938–943.
[12] Y. Li, J. Wu, C. Li, Q. Wang, L. Shen. ACS Omega 6 (2021) 10997–11004.
[13] N. Hou, X.H. Fang. Inorg Chem 61 (2022) 10756–10767.
[14] J. Zhou, Z. Xie, R. Liu, X. Gao, J. Li, Y. Xiong, L. Tong, J. Zhang, Z. Liu. ACS Appl Mater Interfaces 11 (2019) 2632–2637.
[15] R.H. Baughman, H. Eckhardt, M. Kertesz. J Chem Phys 87 (1987) 6687–6699.
[16] J. Kang, Z. Wei, J. Li. ACS Appl Mater Interfaces 11 (2019) 2692–2706.
[17] V.G. Desyatkin, W.B. Martin, A.E. Aliev, N.E. Chapman, A.F. Fonseca, D.S. Galvão, E.R. Miller, K.H. Stone, Z. Wang, D. Zakhidov, F.T. Limpoco, S.R. Almahdali, S.M. Parker, R.H. Baughman, V.O. Rodionov. J Am Chem Soc 144 (2022) 17999–18008.
[18] L. Martínez, R. Andrade, E.G. Birgin, J.M. Martínez. J Comput Chem 30 (2009) 2157–2164.

10º SIMPÓSIO DE ESTRUTURA ELETRÔNICA & DINÂMICA MOLECULAR
SEEDMOL 4 a 8 novembro | 2024 Pirenópolis, Goiás

Study of Mechanical Properties of DHQ-Graphene with Machine Learning Interatomic Potential (MLIP)

Hugo Xavier Rodrigues[1,2], Hudson Rodrigues Armando[1,2], Marcelo Lopes Pereira Júnior[3] and Luiz Antonio Ribeiro Júnior[1,2]

[1]Institute of Physics, University of Brasília, 70910-900, Brasília, Brazil.
[2]Computational Materials Laboratory, LCCMat, Institute of Physics, University of Brasília, 70910-900, Brasília, Brazil.
[3]University of Brasília, Faculty of Technology, Department of Electrical Enginnering, Brasília, Brazil.

rx.oguh@gmail.com, hrodrigues1729@hotmail.com, marcelo.lopes@unb.br, ribeirojr@unb.br

Keywords: Molecular Dynamics, Mechanical Properties, Machine Learning Potentials.

Abstract

In this study, we investigate the mechanical properties of DHQ-graphene, a theoretical corrosion-resistant carbon allotrope, using a combination of density functional theory (DFT) and classical molecular dynamics (MD) methods. We trained a machine learning interatomic potential (MTP) through ab initio molecular dynamics (AIMD) calculations to accurately model these properties. Our findings reveal that the mechanical characteristics of DHQ-graphene, including Young's modulus and Poisson's ratio, differ slightly from those reported in previous studies by Wang et al., likely due to the more stringent self-consistency convergence criteria applied in our DFT calculations. The stress-strain analysis indicates that DHQ-graphene lies on the threshold between ductility and brittleness, a property that could impact its practical applications. Additionally, our comparative study shows that the AIREBO and AIREBO-M parametric potentials approximate the ab initio and MTP results more closely than the ReaxFF and Tersoff potentials. These findings underscore the utility of MTP in accurately describing the mechanical behavior of novel 2D materials, providing a valuable tool for future research in this field.

Introduction

It has been 20 years since the synthesis of the first 2D carbon material called graphene, which initiated the search for new 2D carbon allotropes due to their electronic, optical, thermal, mechanical, and chemical properties [1]. Graphene, for instance, is a stable organic semimetal material that is optically transparent, with high thermal conductivity, a Young's modulus of approximately E = 1.0 ± 0.1 TPa, and a tensile strength of 130 GPa before breaking [2].

To study the mechanical properties of these materials, various methods, both theoretical and experimental, are employed depending on the scale of the structure. For 2D nanomaterials like graphene, small dimensions can reduce accuracy and negatively affect the reliability of experimental measurements of mechanical properties [3]. Therefore, accurate theoretical methods are necessary to investigate these properties.

DFT methods are known for their high accuracy, reproducibility, and flexibility, but they require significant computational

resources and cannot study systems with more than 1000 atoms, often neglecting temperature effects in ab initio calculations of mechanical properties [3. 4]. On the other hand, classical methods use interatomic potentials to describe interactions and can be categorized into two groups: parametric and non-parametric potentials [5]. The first group, which includes empirical potentials, can study the mechanical properties of materials at elevated temperatures with millions of atoms but often lacks accuracy and can overestimate tensile strength values, predicting nonphysical stress-strain curves [3,5]. Non-parametric potentials, however, can achieve greater accuracy and be improved through quantum mechanics calculations.

One type of non-parametric potential is the machine learning interatomic potentials introduced by Behler and Parrinello, which are trained using DFT-based datasets [6]. In 2016, Shapeev proposed a new approach for these non-parametric interatomic potentials, called Moment Tensor Potentials (MTP), which use machine learning methods to improve accuracy. [5]

As demonstrated by Mortazavi et al., these potentials can be used to study mechanical properties with classical molecular dynamics, achieving accuracy comparable to DFT calculations [3].

In this work, to study the mechanical properties of a theoretical corrosion-resistant carbon allotrope called DHQ-graphene, which cannot be described using empirical potentials but is similar to graphene, we trained an MTP using the MLIP package and DFT calculations with VASP. We then compared some of our results with those achieved by Wang et al [7].

Methodology

For this study, ab initio molecular dynamics (AIMD) using the Vienna Ab initio Simulation Package (VASP) were used to create a dataset for training the MLIP potentials.

In this work, the generalized gradient approximation (GGA), the Perdew-Burke-Ernzerhof (PBE) exchange-correlation functional [8], and the projector augmented-wave (PAW) method [9] were employed to analyze the mechanical properties of DHQ-Graphene, including elastic constants evaluation and classical stress-strain study. A cutoff energy of 500 eV was used, with a self-consistency convergence criterion of 10^{-7}eV, adopting a 3x4x1 Monkhorst-Pack K-point mesh in AIMDs and a 6x7x1 Monkhorst-Pack K-point mesh for the elastic constant calculations.

The training dataset was prepared through AIMD calculations performed on an 80-atom structure where DHQ-Graphene was stressed and stress-free, with the first being conducted at a fixed temperature and the second with varying temperatures.

With the dataset prepared, we utilized the LAMMPS package to examine the mechanical properties using the trained MTP, with a time step of 0.1 fs, comparing the results with those achieved by Wang et al., the achieved with parametric potentials and with the elastic constants calculations carried out in VASP with seven different applied strains (-0.015, -0.010, -0.005, 0.000, 0.005, 0.010, 0.015).

Results

In this study, we investigated the mechanical properties of DHQ-graphene using DFT calculations and classical dynamics, employing a machine learning interatomic potential trained through AIMD calculations.

The study of DHQ's mechanical properties reveals a small difference between the Young's moduli and Poisson's ratio obtained by Wang et al. and the data calculated using the elastic constants evaluated with VASP, which are as follows:

C11 = 230.2 GPa·nm, C12 = 60.88GPa·nm, C22 = 299.63 GPa·nm, and C44 = 82.43 GPa·nm. In Wang et al.'s work, they found a Young's modulus of 269 GPa·nm with a Poisson's ratio of 0.28 along the a-axis. In contrast, with VASP calculations, we found values of 217.89 GPa·nm and 0.203.

These values, obtained through VASP calculations, were found using a better self-consistency convergence criterion than that used in Wang et al.'s article, and are closer to those achieved through classical dynamics using the MTP with LAMMPS.

Furthermore, the stress-strain curve analysis and elastic constants results show that this material is on the threshold between a ductile and brittle material.

The comparative study of the mechanical properties of DHQ with MTP and the parametric potentials revealed that the AIREBO and AIREBO-M parametric potentials were those that reached values closer to ab initio calculations, and hence also close to those obtained with MTP, differing from the ReaxFF and Tersoff potentials.

Conclusions

This study highlights the effectiveness of using machine learning interatomic potentials (MTP) trained through AIMD calculations to investigate the mechanical properties of DHQ-graphene, a theoretical corrosion-resistant carbon allotrope. The comparison of our results with those obtained by Wang et al. demonstrates the importance of employing accurate self-consistency convergence criteria in DFT calculations, as evidenced by the closer alignment of our Young's modulus and Poisson's ratio values to those derived from ab initio methods.

Moreover, our findings indicate that DHQ-graphene exhibits mechanical properties that place it on the threshold between ductile and brittle materials, a characteristic that could have significant implications for its potential applications. The comparative analysis of different parametric potentials revealed that the AIREBO and AIREBO-M potentials closely replicate the mechanical properties predicted by both DFT and MTP calculations, whereas the ReaxFF and Tersoff potentials show greater deviations.

These results underscore the potential of MTP in providing a more accurate description of the mechanical behavior of novel 2D materials, particularly when empirical potentials fall short. Future studies could further explore the application of MTP to other carbon allotropes and investigate the temperature-dependent mechanical properties to fully realize the potential of DHQ-graphene in practical applications.

References

[1] K. S. Novoselov, A. K. Geim, S. V. Morozov, D. Jiang, Y. Zhang, S. V. Dubonos, I. V. Grigorieva, and A. A. Firsov. Electric field effect in atomically thin carbon films. Science, 306(5696):666–669, 2004.

[2] D.G. Papageorgiou, I.A. Kinloch, R.J. Young, Mechanical properties of graphene and graphene-based nanocomposite. Progress in Materials Science, 90:75–127, 2017.

[3] B. Mortazavi, X. Zhuang, T. Rabczuk, A. V. Shapeev. Atomistic modeling of the mechanical properties: the rise of machine learning interatomic potentials. Mater. Horiz., 10:1956–1968, 2023.

[4] Pan, J. Scaling up system size in materials simulation. Nature Computational Science, 1(2):95–95, Feb 2021.

[5] A. V. Shapeev. Moment tensor potentials: A class of systematically improvable interatomic potentials. Multiscale Modeling & Simulation, 14(3):1153–1173, 2016.

[6] Behler, J. & Parrinello, M. Generalized neural-network representation of high-

dimensional potential-energy surfaces. Phys. Rev. Lett., 98:146401, Apr 2007.

[7] Wang X, Chen L, Yuan Z, Rong J, Feng J, Muzammil I, Yu X, Zhang Y and Zhan Z. Dhq-graphene: a novel two-dimensional defective graphene for corrosion-resistant coating. J. Mater. Chem. A, 7:8967–8974, 2019.

[8] Salpeter, E. E.; Bethe, H. A.; A relativistic equation for bound-state problems. Physical Review, 1951, 84, 1232–1242.

[9] Kresse, G.; Daniel, J. From ultrasoft pseudopotentials to the projector augmented-wave method. Phys. Rev. B 1999, 59, 1758.

Unveiling new aspects of nonlocal correlations in 1D quantum phase transitions

Isaac Martins Carvalho[1].

[1]*Institute of Chemistry, São Paulo State University, 14800-090, Araraquara, São Paulo, Brazil.*

Accurately predicting the electronic structure of nanostructures remains a formidable challenge. In this context, Density Functional Theory (DFT) and Density Matrix Renormalization Group (DMRG) have emerged as powerful computational tools for addressing electronic correlation effects. We provide a brief overview of the fingerprints of entanglement in disordered systems, address issues in Density Functional Theory (DFT) for Hubbard models, and examine the impact of electric fields on one-dimensional fermionic systems. We will discuss in particular the $Ba_{2-x}Sr_xCuO_{3+\delta}$ cuprate chain within the framework of the extended Hubbard model resolved by using DMRG, highlighting how nonlocal correlations are related to charge fluctuations during the superconducting phase transition.

Quantum phase transitions in one-dimensional nanostructures: a comparison between DFT and DMRG methodologies

T. Paulleti[1], M. Sanino[1], L. Gimenes[1], I. M. Carvalho[1] and V. V. França[1]

[1]*Institute of Chemistry, São Paulo State University, 14800-090, Araraquara, São Paulo, Brazil.*

In the realm of quantum chemistry, the accurate prediction of electronic structure and properties of nanostructures remains a formidable challenge. Density functional theory (DFT) and density matrix renormalization group (DMRG) have emerged as two powerful computational methods for addressing electronic correlation effects in diverse molecular systems. We compare ground-state energies (e_0), density profiles (n), and average entanglement entropies ($\bar{S}$) in metals, insulators, and at the transition from metal to insulator, in homogeneous, superlattices, and harmonically confined chains described by the fermionic one-dimensional Hubbard model. While for the homogeneous systems, there is a clear hierarchy between the deviations, $D\%(\bar{S}) < D\%(e_0) < \bar{D}\%(n)$, and all the deviations decrease with the chain size; for superlattices and harmonic confinement, the relation among the deviations is less trivial and strongly dependent on the superlattice structure and the confinement strength considered. For the superlattices, in general, increasing the number of impurities in the unit cell represents lower precision in the DFT calculations. For the confined chains, DFT performs better for metallic phases, while the highest deviations appear for the Mott and band-insulator phases. This work provides a comprehensive comparative analysis of these methodologies, shedding light on their respective strengths, limitations, and applications.

Métodos Periódicos no Estudo de Adsorção de H_2S e SO_2 em IRMOF

Isaac Oliveira Miranda Magalhães[1], José Artigas dos Santos Laranjeira[3], Daniel Francisco Scalabrini Machado[1], Nailton Martins Rodrigues[2], Julio Ricardo Sambrano[3], João Batista Lopes Martins[1]
[1]Laboratório de Química Computacional, Instituto de Química, Universidade de Brasília. Brasil, 70910-900.
[2]Centro de Ciências Exatas e da Terra, Departamento de Química, Universidade Federal do Maranhão. Brasil, 65080-805.
[3]Departamento de Matemática, Faculdade de Ciências, Universidade Estadual Paulista. Brasil, 17033-360.
isaac.magalhaes@aluno.unb.br
Keywords: Adsorption; MOF; IRMOF; H_2S; SO_2.

Abstract
SO_2 and H_2S are common contaminants in natural gas and biomethane. Effective removal of these contaminants is crucial both in industry and the environment. In this scenario, MOFs are promising materials to promote the removal of these molecules. We used periodic DFT method to study the adsorption of H_2S and SO_2 on IRMOF1. The studies carried out demonstrate that IRMOF-1 is favorable to the adsorption of the suggested gases and that after adsorption the Chalcogen-Chalcogen interaction between sulfur is maintained.

Introdução

O gás natural é uma alternativa energética emergente com menor custo e impacto ambiental em comparação com a gasolina. Composto principalmente por metano (CH_4), ele precisa ser armazenado em cilindros de alta pressão para uso em veículos automotores, o que traz riscos significativos de explosão [1]. Pesquisas recentes indicam que materiais porosos, como as estruturas metal-orgânicas (MOFs), podem otimizar o armazenamento ao permitir maiores quantidades de gás a menores pressões, mitigando assim esses riscos [2].
As MOFs têm ganhado destaque devido às suas propriedades excepcionais, incluindo alta porosidade e estabilidade térmica e química [3-12].
Essas características as tornam promissoras para a captura de gases tóxicos como o sulfeto de hidrogênio (H_2S) e o dióxido de enxofre (SO_2), contaminantes comuns no gás natural e no biometano [13]. A remoção eficaz desses contaminantes é crucial para diversas aplicações industriais e ambientais, apresentando um desafio tecnológico relevante [14, 15].
Este estudo investiga a capacidade de adsorção dos gases H_2S e SO_2 na IRMOF-01.

Metodologia

Utilizamos inicialmente métodos de otimização em cálculos periódicos, por meio do CRYSTAL em níveis DFT com os funcionais B3LYP e HSE06 e seus correspondentes com correções de Grimme's em conjunto com a base TZVP-rev2 disponível nos conjuntos de base do CRYSTAL 17 [17, 18]. Foram realizadas análises NCI para a identificação do tipo de interação.

Resultados e Discussão

Foi observada uma redução no BandGap ao comparar a estrutura original (*bulk*) com a estrutura adsorvida. No caso do SO_2, o BandGap reduziu de 5,04 para 3,54 eV, o caso do H_2 para 4,77 eV enquanto para adsorção do $H_2S\cdots SO_2$ o valor obtido foi de

4,07 eV. Os resultados das otimizações com adsorção mostram a coordenação dos gases H_2S e SO_2 ao centro metálico, conforme ilustrado nas figuras 1 e 2 de análise NCI. Para adsorção $H_2S...SO_2$ os valores de energia de adsorção são apresentados na Tabela 1, ainda sem as correções BSSE.

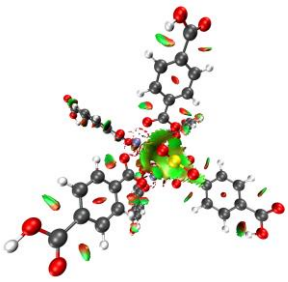


Figura 1. Análise NCI para gás SO_2.

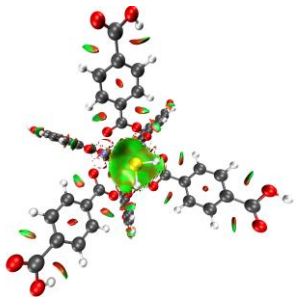


Figura 2. Análise NCI para gás H_2S.

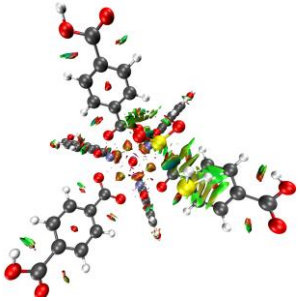


Figura 3. Análise NCI para gás $H_2S\cdots SO_2$.

Funcional	Gás	Energia (kcal·mol^{-1})
B3LYP	H_2S	-1,2169
	SO_2	-0,7877
	$H_2S\cdots SO_2$	-3,5954
B3LYP D3	H_2S	-13,3664
	SO_2	-14,7223
	$H_2S\cdots SO_2$	-19,4632
HSE06	H_2S	-6,11351
	SO_2	-8,41392
	$H_2S\cdots SO_2$	-8,7890
HSE06 D3	H_2S	-8,5609
	SO_2	-10,5898
	$H_2S\cdots SO_2$	-14,2111

Tabela 1. Valores para energias de adsorção.

Conclusões

Os estudos realizados demonstram que IRMOF-1 é favorável a adsorção dos gases sugeridos e que após a adsorção a interação Calcogênio-Calcogênio entre os enxofres se mantem. Para as três formas de adsorção vemos que a dominância é a interação de Van der Walls e uma leve repulsão devido a aproximação ao centro metálico e que dado a densidade eletrônica acaba gerando a estabilidade dos gases.

Agradecimentos

CAPES, CNPq, FAPDF.

Referências

1. Lozano-Castelló, D.; Alcañiz-Monge, J.; de la Casa-Lillo, M. A.; Cazorla-Amorós, D.; Linares-Solano, A. Fuel 2002, 81, 1777-1803.
2. Rodrigues, N. M.; Lisboa Dutra, J. D.; Martins, J. B. L.; Freire, R. O. Int. J. Quantum Chem. 2020, 121.
3. Koura, Z. E.; Rossi, G.; Calizzi, M. et al. Phys. Chem. Chem. Phys. 2018, 20, 221-231; Nguyen, H. T. T.; Doan, D. N. A.; Truong, T. J. Mol. Catal. A 2017, 426, 141-149.
4. Li, Z.; Xiao, G.; Yang, Q.; Xiao, Y.; Zhong, C. Chem. Eng. Sci. 2014, 120, 59-66.
5. Xia, L.; Liu, Q. et al. Comp. Mater. Sci. 2017, 126, 176-181; Müller, J. M.; Mesquita, G. C.; Franco, S. M. et al. Micropor. Mesopor. Mater. 2015, 204, 50-57.
6. Munoz, R.; Meier, L.; Diaz, I.; Jeison, D. Rev. Environ. Sci. Bio-Tech. 2015, 14, 727-7259.
7. Isaev, A. N. Russ. J. Phys. Chem. A 2016, 90, 601-699.
8. Politi, J. R. S.; Martins, J. B. L.; Cabral, B. J. C. J. Mol. Liq. 2022, 366, 120252.
9. Hunter, T.; Cooper, J. A. Ann. Rev. Biochem. 1985, 54, 897-930.
10. Melge, A. R.; Kumar, L. G.; K, P.; Nair, S. V.; K, Manzoor; Mohan, C. G. J. Biomol. Struct. Dyn. 2019, 37, 4747-4766.

11. Hubbard, S. R.; Mohammadi, M.; Schlessinger, J. J. Biol. Chem. 1998, 273, 11987-11990.
12. Zhang, L.; Lin, D.; Sun, X.; Ute Curth, U.; Drosten, C.; Sauerhering, L.; Becker, S.; Rox, K.; Hilgenfeld, R. Science 2020, 368, 409-412.
13. Martínez-Ahumada, E.; López-Olvera, A.; Jancik, V.; Sánchez-Bautista, J. E. et al. Organometallics 2020, 39 (7), 883-915.
14. Georgiadis, A. G.; Charisiou, N. D.; Yentekakis, I. V.; Goula, M. A. Chem. Proc. 2020, 2, 27.
15. Georgiadis, A. G.; Charisiou, N.; Yentekakis, I. V.; Goula, M. A. Materials (Basel) 2020, 13 (16), 3640.
16. Dubbeldam, D.; Calero, S.; Ellis, D. E.; Snurr, R. Q. et al. Molecular Simulation 2015, 42, 81-101.
17. Dovesi, R.; Erba, A.; Orlando, R.; Zicovich-Wilson, C. M. et al. WIREs Comput. Mol. Sci. 2018, 8, e1360.
18. Dovesi, R.; Saunders, V. R.; Roetti, C.; Orlando, R.; Zicovich-Wilson, C. M. et al. CRYSTAL17 User's Manual, University of Torino, Torino, 2017.

Studying the structural dynamics of the SARS-CoV-2 Spike protein in different pHs: identifying the optimal pH

Isabelle Alves Pereira[1], Ana Lígia Scott[1].
[1]Department of Mathematics, Computing, and Cognition (CMCC, Federal University of ABC, Santo André, São Paulo, Brasil.
isabelle.p@ufabc.edu.br
Keywords: *Spike protein; SARS-CoV-2; optimal pH; Brazil; ENM.*

Abstract
The Spike protein of SARS-CoV-2 plays a critical role in the virus's ability to invade human cells, facilitating its entry and infection. Several Spike mutations were found in the virus variants, which are related to higher transmissibility, pathogenicity, and resistance to neutralization antibodies. Understanding the structural dynamics and functional motion of this protein is essential as the virus continues to evolve and adapt. Keeping monitoring and analyzing the virus not only increases the control, but may also improve therapeutic strategies. In this study we aim to have more knowledge about the Spike's favorable pH and the influence of single mutations to comprehend the metastates and the structural dynamics of this macromolecule. Through the GISAID database we identified the frequent SARS-CoV-2 lineages in Brazil between May 2023 and May 2024. The genomic data was extracted from patients infected with these lineages, focusing on cases reported in Brazil, highlighting a set of mutations in all proteins of the virus (https://gisaid.org/). A wild-type (WT) and apo Cryo-EM SARS-CoV-2 Spike structure was used to prepare the protein in different pHs (7.5; 8;8.5;9) to determine the optimal pH for subsequent studies. To narrow the scope of this research we focused exclusively on sequences from Brazil and from a start we are evaluating the favorable pH state of the Spike protein to proceed with the analysis of the mutations. The analysis of structural dynamics and function motions on different pHs it is carrying on now.

Introduction
The Spike glycoprotein of SARS-CoV-2 plays a critical role in the virus's ability to invade human cells, facilitating its entry and infection. Several Spike mutations were found in the virus variants, which are related to higher transmissibility, pathogenicity, and resistance to neutralization antibodies. Having an understanding of the structural dynamics and functional motion of this protein is essential as the virus continues to evolve and adapt its mechanisms. Keep a track and analyze the virus not only increases the control, but may also improve therapeutic strategies.

The objective of this is to study the structural dynamics of the SARS-CoV-2 Spike glycoprotein, to have more knowledge about its favorable pH and the influence of single mutations to comprehend the metastates of this macromolecule.

Through the GISAID database we identified the frequent SARS-CoV-2 lineages in Brazil between May 2023 and May 2024. The genomic data was extracted from patients infected with these lineages,

focusing on cases reported in Brazil, highlighting a set of mutations in all proteins of the virus (https://gisaid.org/) [1]. For the analysis, the data was filtered to show only the mutations in the Spike protein and a frequency count of each mutation was conducted, having eliminated those that appeared only once and selecting the top 5% most frequent mutations for further studies, resulting in a total of 40 mutations. A wild-type (WT) and apo Cryo-EM SARS-CoV-2 Spike structure with 2.90Å resolution (PDB: 6XR8) was rebuilt using CHARMM-Gui to complete the missing residues [2] and the Solution Builder was used to prepare the protein in different pHs (7.5; 8; 8.5; 9) to determine the optimal pH for subsequent studies [3]. From the GISAID database we only extracted complete sequences and analyzed the Spike mutations, giving a total of 1.567 mutations.

To narrow the scope of this research we focused exclusively on sequences from Brazil and from a start we are evaluating the favorable pH state of the Spike protein to proceed with the analysis of the mutations. The analysis of structural dynamics and function motions on different pHs it is carrying on now, so a structural dynamics with Elastic Network Models using Prody can be performed.

Acknowledgements

UFABC, CAPES and FAPESP.

References

[1] S. Elbe, G. Buckland-Merrett, Data, disease and diplomacy: GISAID's innovative contribution to global health, Glob Chall 1 (2017) 33–46.

[2] S. Jo, T. Kim, V.G. Iyer, W. Im, CHARMM-GUI: a web-based graphical user interface for CHARMM, J. Comput. Chem. 29 (2008) 1859–1865.

[3] XIE, Y. et al. The pH effects on SARS-CoV and SARS-CoV-2 spike proteins in the process of binding to hACE2. 2021.

DFT study of a coordination complex of Cu(II) with nitrate, 1,10-phenanthroline and maleate ligands

Jailton R. Viana[1], Jad L. F. Simplicio[1], Diego C. Abreu[1], Marinaldo V. Souza Junior[1], João G. Oliveira Neto[1], Adenilson O. dos Santos[1], and Mateus R. Lage[1].
[1]Universidade Federal do Maranhão - UFMA, Programa de Pós-Graduação em Ciência dos Materiais - PPGCM, Centro de Ciências de Imperatriz - CCIm, Imperatriz-MA, Brasil.
E-mail: *jailton.viana@ufma.br*
Keywords: Coordination complex; DFT; Copper; 1,10-phenanthroline.

Abstract
Coordination complexes have been intensively studied because of their interesting properties and promising applications. Their design implies the applications of coordination complexes in energetic, optical, or biological fields, and it confirms the importance of studying their properties. This work reports the computational study of Cu(II) coordination complex with nitrate, 1,10-phenanthroline, and maleate ligands, via density functional theory (DFT). The geometric properties, thermodynamics, solvation effect, and frontier molecular orbitals were investigated in order to study the physicochemical characteristics of the complex. The optimized geometry confirms the square pyramidal structure around the metal ion, obtaining theoretical bond length and bond angle values close to the experimentally obtained. The variation of Gibbs free energy, enthalpy, and electronic energy corrected with zero point vibrational energy with the complexation indicates that the formation of the complex is spontaneous and exothermic. The HOMO-LUMO energy gap, as well as the chemical reactivity descriptors, show good stability of the complex.

Introduction

Computational studies of coordination complexes have been increasingly reported since understanding metal-ligand bonds at the atomic level provides a range of information. Geometric, electronic and thermodynamic properties of the complexes can also give rise to different applications and effects in functional materials [1].
To this end, electronic structure calculations using density functional theory (DFT) provide a wealth of knowledge capable of dictating the synthesis of compounds for different applications at a relatively low computational cost [2,3].
Copper is a trace element necessary for the physiological system, as it carries out biological oxidation-reduction reactions, is present in proteins, and has low toxicity [4].
The 1,10-phenanthroline is a bidentate chelating ligand with a flat heteroaromatic system and two juxtaposed nitrogen atoms that facilitate its coordination to transition metals [5]. Maleate is formed from maleic acid and also consists of a suitable ligand for forming coordination complexes.
This work aimed to calculate the optimized geometry of the Cu(II) coordination complex with nitrate, 1,10-phenanthroline and maleate ligands ($[CuMale_2NO_3Phen]^-$) in order to investigate its geometric, electronic, and thermodynamic properties, as well as the solvation effect on these properties.

Methodology

The structural information of the complex was obtained from the crystal structure deposited in the CCDC under the number 169759 [6]. The DFT calculations were carried out using the Gaussian 16 software, with the DFT functional PBE1PBE and the 6-311++G(d,p) basis set for C, O, N, and H atoms, and the SDD pseudopotential for the

Cu atom. The IEFPCM solvation method was used to account for solvation effects in the calculations in methanol and water solvents, additionally to the calculations performed in vacuum. The input and output files are analyzed with the Cremcraft software.

Results and discussion

The optimized geometries of the complex calculated in vacuum and in methanol and water solvents showed that its geometry is square pyramidal, with the Cu(II) bonded to the nitrogen atoms of the 1,10-phenanthroline, the oxygen atoms of the maleate and the oxygen of the nitrate ion. Figure 1 shows the optimized geometries of the superimposed.

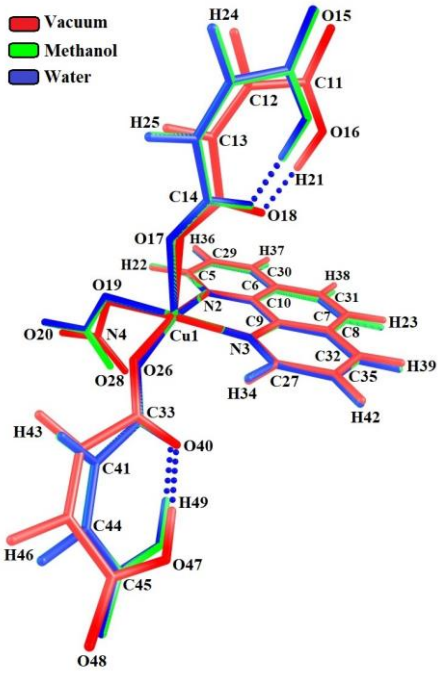


Fig. 1 – Optimized geometries of the $[CuMale_2NO_3Phen]^-$ complex calculated under vacuum and solvent conditions superimposed.

The calculated bond lengths and bond angles for the coordination complex were analyzed and compared with experimental data obtained from the literature [6], showing a good theoretical-experimental correlation, as shown in Table 1. However, little difference is expected since in the calculation we considered all the atoms of the complex free to move while the complex is stacked in the crystal lattice in the sample analyzed.

Tab. 1 – Theoretical bond length and bond angles of the $[CuMale_2NO_3Phen]^-$ complex

Atoms	Length (Å)			
	Exp.	ϖ_{vac}	ϖ_{met}	ϖ_{wat}
Cu1-N2	2.01	2.07	2.04	2.04
Cu1-N3	2.00	2.06	2.03	2.03
Cu1-O17	2.26	2.19	2.19	2.19
Cu1-O19	1.97	1.99	2.01	2.01
Cu1-O26	1.97	1.97	1.97	1.99
Angles (°)				
N2-Cu1-N3	82.09	79.83	81.32	81.37
N2-Cu1-O17	106.43	94.14	103.49	103.66
N2-Cu1-O19	92.79	89.51	92.21	92.28
N2-Cu1-O26	166.07	168.11	163.32	163.35
N3-Cu1-O17	95.45	93.17	96.96	97.06
N3-Cu1-O19	174.48	166.66	172.69	172.84
N3-Cu1-O26	94.59	98.12	95.70	95.68
O17-Cu1-O19	83.95	95.60	87.83	87.63
O17-Cu1-O26	87.30	97.67	93.15	92.96
O19-Cu1-O26	90.85	90.65	89.53	89.46

ϖ_{vac} = Calculated in vacuum, ϖ_{vac} = Calculated in methanol, ϖ_{vac} = Calculated in water

Thermodynamic data were calculated according to Equation 1, and their values are shown in Table 2. The results show negative values in all the calculated conditions, indicating that the complex formation reaction is spontaneous and exothermic. The solvent effect makes all the values obtained less negative because of the stabilization of charges.

$$\Delta X = X_{Comp.} - (X_{Phen} + X_{Cu} + 2.X_{Male} + X_{Nit}) \quad (1)$$

where X = G^{298}, H our E_{ZPVE}

Tab. 2 – Thermodynamic data of the $CuNO_3PhenMale_2$ complex

	Vacuum (kcal/mol)	Methanol (kcal/mol)	Water (kcal/mol)
ΔG^{298}	-616.67	-170.34	-161.86
ΔH	-659.71	-212.93	-204.18
ΔE_{ZPVE}	-659.81	-213.51	-204.80

Frontier molecular orbitals HOMO (highest occupied molecular orbital) and LUMO (lowest unoccupied molecular orbital) were calculated in therms of alpha (α) and betta (β) orbitals and their spatial distributions are shown in Figure 2. Changes in orbitals are also related to solvation effects.

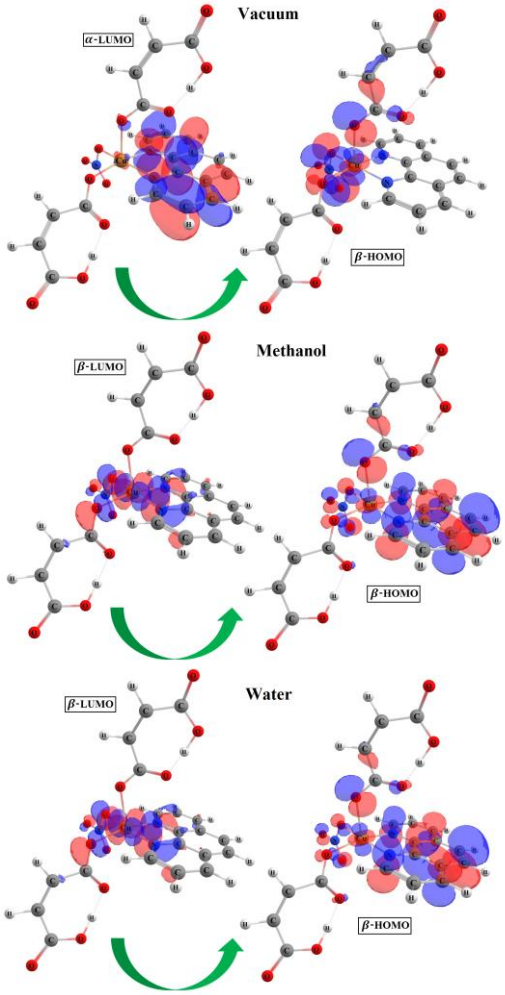


Fig. 2 – Frontier molecular orbitals of the CuNO3PhenMale2 complex calculated under vacuum and solvent conditions

The global chemical reactivity descriptors (GCRD), such as HOMO-LUMO energy gap (HLG), chemical potential (μ), hardness (η), softness (S) and electrophilicity (ω) were calculated and their values are shown in Table 3. The results indicate that the complex shows good stability, with solvent effects contributing to greater stability when compared to vacuum.

Tab. 3 – Molecular orbital energy values and global chemical reactivity indices.

GCRD (*eV*)	Mathematical expressions	$CuNO_3PhenMale_2$		
		Vacuum	Methanol	Water
E_{HOMO}	-	-4.53	-7.31	-7.35
E_{LUMO}	-	-0.53	-2.58	-2.64
HLG	$E_{LUMO}–E_{HOMO}$	4.00	4.73	4.71
μ	$(½).(E_{LUMO}+E_{HOMO})$	-2.53	-4.94	-4.99
η	$(½).(E_{LUMO}–E_{HOMO})$	2.00	2.36	2.35
S	$1/\eta$	0.25	0.21	0.22
ω	$\mu^2/2.\eta$	1.60	5.17	5.30

Conclusions

The DFT calculations provided accurate data to the study of the properties of the complex under investigation. The formation energy values indicated that the complex is formed from an exothermic and spontaneous reaction. The chemical reactivity indices indicate good stability of the complex and are useful for the study of its possible applications.

Acknowledgements

FAPEMA, CAPES, CNPq, Digital Research Alliance of Canada.

References

1. Hossain, E. Md.; Hasan, M. Md.; *et. al.*; *Spectrochim. Acta A.* 2015, **138**, 499.
2. Schleder, G. R.; Padilha, A. C. M.; *et. al.*; *J. Phys Mater.* 2019, **2**, 32001.
3. Nkunfli, N. K.; Ghogomu, J. N.; *et. al.*; *Comp. Chem.* 2015, **3**, 29.
4. Pereira, W. O.; Oliveira-Neto, J. G.; *et. al.*; *J. Mater. Sci.* 2024, **59**, 9502.
5. Bencini, A.; Lippolis, V.; *Coord. Chem. Rev.* 2010, **254**, 2096.
6. Zheng, Y. Q.; Sun, J.; Lin, J. L.; *J. Mol. Struct.* 2003, **650**, 49.

Efficient Exciton Transport in Organic Photovoltaics: A Monte Carlo Algorithm Study of Cascade Architecture

João Felipe Camargo Pinheiro[1], Larissa dos Santos Born[2], and Pedro Henrique de Oliveira Neto[3].
[1]Universidade de Brasília, Instituto de Física, Brazil.
[2]Universidade de Brasília, Instituto de Física, Brazil.
[3]Universidade de Brasília, Instituto de Física, Brazil.
[1]joaoffelipe886@gmail.com; lary_born@hotmail.com; pedrohenrique@unb.br.
Keywords: Excitons; Organic photovoltaic devices; Cascade Architecture; Monte Carlo Algorithm.

Abstract

Organic solar cells offer a sustainable alternative to traditional silicon-based photovoltaic technology. The efficiency of these cells is heavily influenced by their morphological structure, particularly in terms of exciton diffusion within the donor layer, which contains organic molecules arranged in various configurations. This research investigates the impact of cascade-oriented architectures within the donor layer on exciton transport efficiency towards the donor-acceptor interface[1]. The study involves segmenting the donor layer into sublayers composed of different organic materials, strategically arranged to optimize energy transfer towards the interface[2]. Electronic structure calculations using Density Functional Theory were performed on four organic molecules previously studied in experimental settings, and exciton diffusion was modeled using a Kinetic Monte Carlo algorithm. Our findings indicate that the material organization and the thickness of the sublayers play crucial roles in enhancing the solar cell's overall efficiency. This work provides significant insights into the design of organic photovoltaics, contributing to their potential for widespread adoption.

Introduction

In recent years, various sustainable energy production options have emerged. Among these, organic photovoltaic devices (OPVs) are a promising alternative, offering advantages such as being lighter and more versatile than their silicon-based counterparts, though they are currently less efficient [3]. However, OPV efficiency can be improved, and one approach is to implement a device with a cascade architecture. This architecture subdivides the device into layers of different materials, aiming to combine material properties to optimize specific processes within the device [1].

Among the many processes occurring in an OPV, exciton diffusion plays a crucial role. Excitons are quasiparticles characterized by a bound electron-hole pair state, making them charge-neutral energy carriers. Exciton diffusion is described via Förster Resonance Energy Transfer (FRET), which defines the rate of exciton transfer and decay. These rates can be used in a Monte Carlo algorithm that simulates the OPV device [4], allowing for the study of characteristics affecting its efficiency.

To compute the rates of processes described by Förster theory, it is necessary to calculate emission and absorption spectra for the materials. These spectra can be obtained for organic materials using the Nuclear Ensemble Method, via DFT and TD-DFT calculations [5].

In this work, we calculate the emission and absorption spectra for the molecules tetracene, rubrene, Dnt, and Dpt using the Nuclear Ensemble Method. Additionally, we study the effect of interface position in an OPV with cascade architecture using the aforementioned molecules.

Methodology

DFT calculations were performed using Q-Chem software at the wB97X-D level of theory, with the 6-31G(d,p) basis set. The functional parameter was tuned non-empirically to approximate results according to Koopmans' theorem.

Molecular absorption and emission spectra were calculated using the Nuclear Ensemble Method as implemented in the NEMO software. These spectra were used to calculate the exciton transfer and emission rates for singlet excitons.

Process rates were used in a Monte Carlo algorithm to simulate a cubic donor layer of an OPV device with periodic boundary conditions and a 200 nm length. The device simulated contains two organic materials separated by an interface, whose position can be varied as a parameter of the device. Simulations were performed one exciton at a time, for a total of one hundred thousand rounds.

To determine device efficiency, we initialized every exciton at the beginning of the donor layer and determined how many were able to traverse the entire donor layer. This is related to the efficiency of the device because, in real OPVs, excitons must reach an acceptor molecule. Therefore, we simulated devices that contain an acceptor material layer at the end of the donor layer.

Results

In **Figure 1**, we present the spectra for one of the molecules studied in different index of refraction media. These spectra, along with others calculated, were used to obtain the rates for the processes. The rates are given as a function of a parameter called the Förster radius. These radii, along with other molecular properties, are presented in **Table 1**. The rates were then used in a Monte Carlo algorithm. The results for the top efficiency of the device for each possible combination of two materials are presented in **Figure 2**.

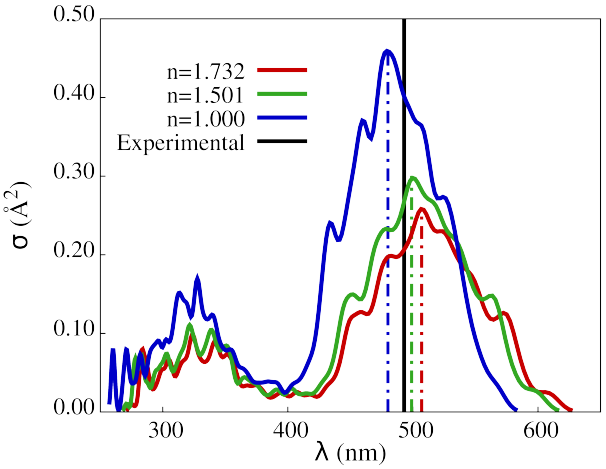


Figure 1: Absorption spectra for DPT molecule in different media and the comparison with experimental result should be made with the black and green vertical lines.

Table 1: Förster radii for the pair of molecules studied, radiative lifetimes and transition dipole moments.

		Aceitadora					
	R_F (nm)	Dnt	Dpt	Rbn	Ttn	$\tau_{teo.}$(ns)	$\mu(ea_0)$
Doadora	Dnt	5.12	5.11	5.51	2.96	8.980	1.8
	Dpt	5.11	5.10	5.50	3.10	9.103	1.8
	Rbn	4.55	4.59	5.16	2.18	8.914	2.0
	Ttn	5.32	5.27	5.34	4.18	14.41	1.2

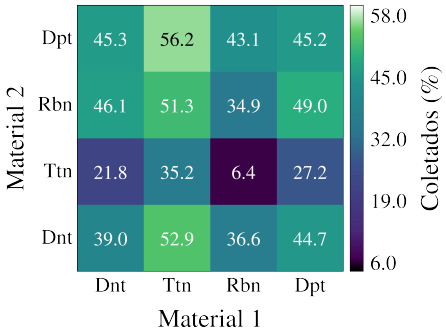


Figure 2: Exciton collection efficiency of the devices simulated.

Discussion

In **Figure 1**, we analyze how the refractive index plays a role in determining spectrum peak position. This result, along with the peak positions for the spectra of the other molecules, demonstrates the validity of the Nuclear Ensemble Method.

With the Förster radii table, we can predict that the Rbn/Ttn combination—in this order—is not a good candidate for an OPV device. This table also indicates that the Rbn/Ttn and Dnt/Ttn combinations are good candidates for an efficient device. These analyses are possible because the Förster transfer rate is proportional to the sixth power of the Förster radius, and the Förster radii for Ttn as the acceptor molecule are the lowest in the table. Given that excitons must traverse the entire donor layer and are all created at the beginning of the first material, Ttn as the second material would act as a barrier for excitons, making it the worst candidate for the second material. However, if Ttn is the first material, once excitons diffuse to the second material, the tetracene layer acts as a barrier, making backward exciton diffusion unlikely, thereby making it the best candidate for the first material in the device. These predictions are corroborated by the simulation results presented in **Figure 2**. We see that the least efficient device was the Rbn/Ttn pair, and the most efficient device was the Ttn/Dpt pair.

Conclusions

In this work, we studied the optoelectronic properties of certain organic materials and evaluated exciton transport in a cascade architecture OPV. We used DFT and TD-DFT calculations to describe the electronic structure of Dnt, Dpt, Rbn, and Ttn. In studying exciton transport, we employed a Kinetic Monte Carlo algorithm and obtained rates via FRET.

We observed the importance of the refractive index in the calculation of emission and absorption spectra, achieving excellent agreement with experiment, thus validating the Nuclear Ensemble Method for spectra calculation. Using Kinetic Monte Carlo simulations, we found that there is an interface position that can enhance the device's overall performance. For the molecules analyzed here, the best two-material combination is Ttn/Dpt, with 42% Ttn in the first sublayer and 58% Dpt in the second sublayer of the device's donor layer.

Acknowledgments

The authors acknowledge financial support from the Conselho Nacional de Desenvolvimento Científico e Tecnológico (CNPq).

References

4. de Sousa, Leonardo Evaristo, et al. *Chemistry of Materials* 31.17 (2019): 6818-6823.

5. de Sousa, Leonardo Evaristo, and Piotr de Silva. *Journal of Chemical Theory and Computation* 17.9 (2021): 5816-5824.

3. Kippelen, B., & Brédas, J. L. (2009). Organic photovoltaics. *Energy & Environmental Science*, *2*(3), 251-261.

2. Menke, S. Matthew; Tyler K. Mullenbach; and Russell J. Holmes.; *ACS nano* 9.4 (2015): 4543-4552.

1. Schlenker, Cody W., et al.; *Chemistry of Materials* 23.18 (2011): 4132-4140.

10º SIMPÓSIO DE ESTRUTURA ELETRÔNICA & DINÂMICA MOLECULAR
SEEDMOL 4 a 8 novembro | 2024 Pirenópolis, Goiás

Mechanistic insights into CO_2 electroreduction using a molecular Cu-porphyrin catalyst: A DFT approach

João V. F. da Costa and Ataualpa A. C. Braga

[1]Departamento de Química Fundamental, Universidade de São Paulo, São Paulo, Brazil
E-mail: ataualpa@iq.usp.br

Abstract

The rise in CO_2 emissions has intensified the search for solutions to mitigate the greenhouse effect. Electrocatalytic CO_2 reduction (CO_2RR) is a promising approach, converting CO_2 into valuable products like ethene and propene. This study aims to elucidate the CO_2RR mechanism using a copper-porphyrin catalyst.

Introduction

Molecular electrocatalysis based on 3d transition metal compounds plays a crucial role in various applications, including CO_2 reduction reaction (CO_2RR)[1-3], water splitting[4,5], oxygen reduction[6], and hydrogen evolution reactions[7]. In this context, Quantum Chemistry (QC) approaches can be employed to study reaction mechanisms, optimize ligand structures, and enhance selectivity toward products of industrial interest.

The first step in these theoretical studies is to identify a reliable Quantum Chemistry (QC) method, such as density functional theory (DFT), to accurately describe key thermodynamic properties commonly used in this type of application. One such property is the redox potential[8]. For first-row (3d) transition metal electrocatalysts, it is particularly challenging to establish a well-defined protocol for calculating redox potentials, as these systems can be large and often exhibit complex electronic structures.

Moreover, another challenge in studying the mechanism of CO_2 reduction employing these systems is the stabilization of critical intermediates such as M-CO_2 and M-CO (where M represents the metal center in the metalloporphyrin) through noncovalent electrostatic interactions[9], thus promoting the CO_2RR toward target products.

Here, the mechanistical aspects of CO_2RR employing a Cu-porphyrin catalyst (Figure 1) will be studied. This catalyst was synthesized in 2016 by Weng and coworkers[10]. A brief benchmark to calculate the redox potential for one electron reduction of this catalyst was conducted. Some protocols to calculate redox potential of transition metals complexes are available in the literature[11,12], and these two protocols were tested for the chosen catalytic system.

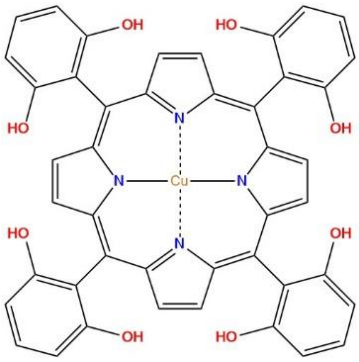


Figure 1. Chosen catalyst to further studies in the mechanism of CO_2RR[10].

Methodology

The DFT calculations are being done in Gaussian 16 C.01 software. To visualize the molecules, the softwares GaussView[13] and Chemcraft[14] are being used. For geometry optimization and frequency calculations, several functionals were tested, including PBE-D3(BJ)[15], TPSS-D3(BJ)[16], PBE0-D3(BJ)[17], B3LYP-D3(BJ)[18], and TPSSh-D3[19]. For all tested functionals, the dispersion effects (D3) proposed by Grimme and coworkers were included with the Becke-Johnson damping[20], except for the

TPSSh functional. All geometry and frequency calculations was done employing the Ahlrichs basis set def2-SVP and the single-point calculations was done with the Ahlrichs basis set def2-TZVP[21,22]. Geometries were optimized in water solution using the implicit SMD continuum solvation model[23].

In the first step of this study, two methodologies were employed to calculate the redox potential for a one electron reduction of Cu-porphyrin catalyst[11,12]. The equations involved for these calculations are shown below:

$$G^\circ = G_{\text{corr}}(\text{BS1}) + E_{el}(\text{BS2}) + \Delta G(\text{conc}) \quad (1)$$

$$E^\circ_{O/R} = \frac{G^\circ(O,aq) + n_p G^\circ(H^+,aq) + n_e G^\circ(e^-,g) - G^\circ(R,aq)}{n_e F} - E^\circ_{SHE} \quad (2)$$

$$E^\circ_{O/R} = \frac{G^\circ(O,aq) + G^\circ(FeCp^0,aq) - G^\circ(R,aq) - G^\circ(FeCp^+,aq)}{n_e F} + 0.64\,V \quad (3)$$

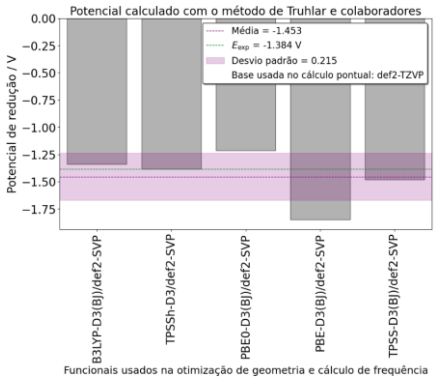
where, $G_{\text{corr}}(\text{BS1})$ is the thermochemical correction obtained from the geometry optimization end frequency calculation, $E_{el}(\text{BS2})$ is the corrected electronic energy from the single-point calculation for the optimized geometry using a more accurate basis set, and $\Delta G(\text{conc})$ is the correction related to solvation free energy, defined as the free energy to transfer a solute from the gas phase to the liquid phase. For this last term, the value adopted is +1.89 kcal.mol^{-1}, if the specie is at a partial pressure of 1 bar and being transferred to a solution of 1M at 298 K. In equation 1, BS1 mean **basis set 1** (def2-SVP basis set) and BS2 mean **basis set 2** (def2-TZVP basis set). The equation 2 was adapted from Truhlar and coworkers[11]. $G^\circ(H^+,aq)$ is assumed the value of -270,3 kcal.mol^{-1}, and it is the Gibbs free energy of a proton in water, that is obtained by the sum of the gas-phase Gibbs free energy of a proton (-6.3 kcal/mol) and its experimental solvation free energy in water (-264.0 kcal/mol), the Gibbs free energy of electron in gas-phase ($G^\circ(e^-,g)$) is equal to zero.

Moreover, the Gibbs free energy of the oxidized and reduced species was obtained according to equation 1, and all the redox potential reported here are relative to standard hydrogen electrode (SHE), and the experimental value of the absolute redox potential of the SHE (4.281 V) was used. In equation 3, that was adapted from Konezny *et al.*[12], the theoretical redox couple of ferrocene/ferrocenyl was considered in the redox potential calculation for a determined redox process in the catalytic cycle and their Gibbs free energies ($G^\circ(FeCp^0,aq)$, $G^\circ(FeCp^+,aq)$) were obtained in the same way as described in equation 1. Furthermore, a factor of 0.64V was summed to the calculated redox potential to convert this value in the SHE scale. This theoretical redox couple is widely used as reference in computational electrochemistry[10, 24-26].

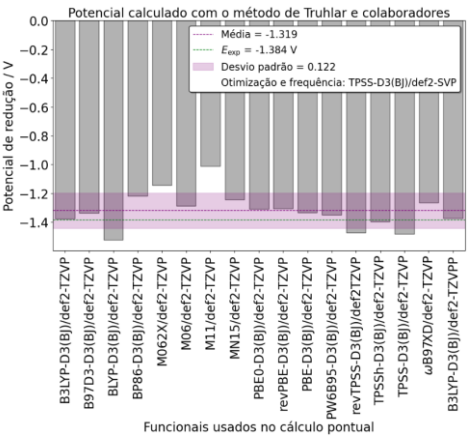
Results

Prior to start the mechanism elucidation for the CO_2RR in Cu-porphyrin system, it is important to consolidate a methodology to calculate the redox potential for each step in the catalytic cycle. To do this, a brief benchmark was conducted to explore some functionals that could work well in this study. The results obtained are summarized in Figure 2.

a



b



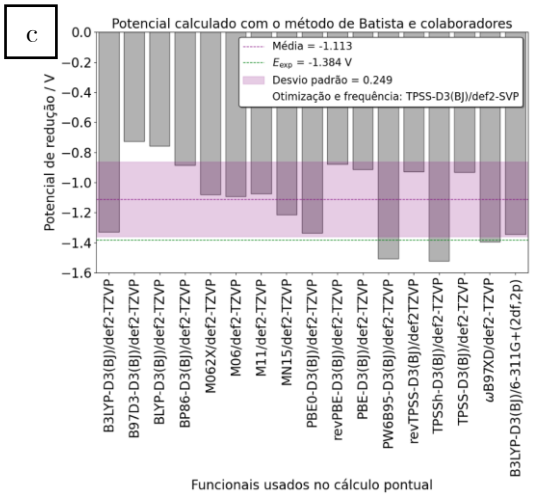


Figure 2. Potential redox calculations for a one electron reduction of Cu-porphyrin system using two types of methodologies available in the literature[11,12]. In (a), different functionals was tested in geometry optimization and frequency calculations. In (b) and (c), the geometry optimization and frequency calculations was done using TPSS-D3(BJ) functional, but in (b), it was employed the methodology proposed by Marenich *et al*[11]. In (c), it was done the methodology proposed by Konezny *et al.* [12].

In Figure 2a, five different functionals were tested in the first step of this mechanism, that consists of a one electron reduction for the Cu-porphyrin system. The two functionals that presented a good agreement with experimental results was the hybrid TPSSh and hybrid B3LYP functionals. These calculations was performed based on Truhlar and coworkers protocol[11]. The same protocol was adopted in the calculation of Figure 2b, but here, the geometry optimization and frequency calculation were done with meta-GGA TPSS-D3(BJ) functional with the dipersion correction proposed by Grimme and coworkers, and then, the single-point calculations was made with several functionals to evaluate their performance. The decision to use a meta-GGA functional for optimization was made to reduce the computational cost. In Figure 3c, it was adopted the methodology presented by Konezny *et al.* to calculate the redox potential for one electron reduction in the Cu-porphryin system[12], the geometry optimizations and frequency calculations was also done with the functional TPSS-D3(BJ) and several other functionals was tested in the single-point calculations. The latter methodology was not so effective for this system, as evidenced by the high deviation of the theoretical redox potentials obtained compared to the experimental redox potential reported by Weng *et al.*[10].

After this study, it was decided to proceed with the mechanistic investigation using the B3LYP-D3(BJ) functional for geometry optimization and frequency calculations. The construction of the energetic profile is underway, and some transition states and intermediates have already been found.

Conclusions

The methodology developed by Truhlar and coworkers[11] was suitable for predicting the redox potential in Cu-porphyrin system and it will be employed during the construction of energy profile for the CO_2RR. The TPSS-D3(BJ) functional provided good results in terms of redox potential prediction, but in some intermediates of the catalytic cycle, it was observed a considerable spin contamination. Therefore, the B3LYP functional was chosen for the next steps of this study.

In certain steps of the catalytic cycle, Proton-Coupled Electron Transfer (PCET) may occur to facilitate redox processes for specific intermediates. The energy profile, along with the identified transition states, will be presented.

Acknowledgments: FAPESP, CAPES and CNPq.

References

[1] Benson, E. E. *et al.*, Chem. Soc. Rev., **38**, 89-99 (2009).
[2] Francke, R. *et al.*, Chem. Rev., **118**, 4631-4701 (2018).
[3] Kinzel, N. W. et al., Angew. Chem., **60**, 11628-11686 (2021).
[4] Artero, V. et al., Angew. Chem., **50**, 7238-7266 (2011).
[5] Du, P. et al., Energy Environ. Sci., **5**, 6012-6021 (2012).
[6] Pegis, M. L. et al., Chem. Rev., **118**, 2340– 2391 (2018).
[7] Luo, G.-G. et al., Inorg. Chem. Front., **6**, 343-354 (2019).
[8] Marenich, A. V. et al., Phys. Chem. Chem. Phys., **16**, 15068– 15106 (2014).
[9] Azcarate, I. *et al.* J. Am. Chem. *Soc.*, **138**, 16639−16644 (2016).

[10] Weng, Z. et al., J. Am. Chem. Soc., **138**, 8076−8079 (2016).
[11] Marenich A. V. et al., Angew. Chem. Int. Ed., **51**, 12810 –12814 (2012).
[12] Konezny, S. et al., J. ,J. Phys. Chem. C, **116**, 10, 6349–6356 (2012).
[13] R. Dennington, T. Keith, J. Millam. GaussView. Semichem Inc., Shawnee Mission KS. 1999.
[14]Chemcraft - graphical software for visualization of quantum chemistry computations. https://www.chemcraftprog.com
[15] Perdew, J. P. et al., Physical review letters, **77**(18): 3865 (1996).
[16] Tao, J, Phys. Rev. Lett., **91**:146401 (2003).
[17] Adamo, C. The Journal of chemical physics, **110**(13): 6158-6170 (1999).
[18] Becke, A. D. The Journal of chemical physics, **96**(3):2155–2160 (1992).
[19] Staroverov, V. N. *et al.*, J. Chem. Phys., **119** 12129−12137 (2003).
[20] Grimme S. et al., The Journal of chemical physics, **132**(15), 2010.
[21] Weigend, F., Phys. Chem. Chem. Phys., **7**, 3297 (2005).
[22] Weigend, F., Phys. Chem. Chem. Phys., **8**, 1057 (2006).
[23] Marenich, A. V. et al., J. Phys. Chem. B , **113**, 6378−6396 (2009).
[24] Loipersberger et al., Inorganic chemistry, **59**(12) : 8146-8160 (2020).
[25] Loipersberger et al., Inorganic chemistry, **61**(18) : 6919-6933 (2022).
[26] Hong et al., ACS Catalysis, 13(5) : 3109-3119 (2023).

10º SIMPÓSIO DE ESTRUTURA ELETRÔNICA & DINÂMICA MOLECULAR
SEEDMOL 4 a 8 novembro | 2024
Pirenópolis, Goiás

Unveiling the tautomerism of sulfapyridine: Solvent effects on stability and ultraviolet/visible UV absorption spectra

José L. F. Santos,[1] Gabriel L. C. de Souza,[2] and Roberto L. A. Haiduke.[1]
[1] São Carlos Institute of Chemistry (IQSC), University of São Paulo (USP), 13560-970, São Carlos, SP, Brazil.
[2] Natural Science Center – Campus Lagoa do Sino (CCN), Federal University of São Carlos (UFSCar), 13565-905, Buri, SP, Brazil
jlfelix@usp.br

Keywords: sulfapyridine; tautomerism; microsolvation; density functional theory.

Abstract
Here, a theoretical investigation based on Density Functional Theory is carried out about the effects of microsolvation on the tautomerization mechanism and absorption ultraviolet/visible (UV/Vis) spectrum of sulfapyridine (SPY). First, the interconversion barriers of SPY (a sulfonamide) to its tautomer (sulfonimide) are probed. Hence, explicit solvation decreases this barrier height and induces a more spontaneous tautomer formation in aqueous solution. The similarity between the UV/Vis spectrum of this tautomer and the experimental one is another evidence that this tautomeric equilibrium cannot be ignored.

Introduction
Tautomerism is a fundamental chemical phenomenon among interconvertible compounds, known as tautomers, which coexist in dynamic equilibrium [1]. The solvent polarity can have a significant impact on the stability and distribution of tautomers in solution. This can influence the efficacy of processes such as the photodegradation of environmental contaminants and the bioavailability of drugs [2]. In addition, protic solvents, such as water and alcohols, can facilitate proton transfers, affecting the interconversion rates between tautomers and, consequently, their chemical properties [1,2].

Different tautomers can exhibit distinct absorption spectra due to variations in the electronic distribution and structures of the molecules [1,2]. These differences can be used to identify and quantify tautomers in solutions and mixtures, offering valuable insights into the composition and behavior of the compounds studied [1,2].

Thus, in the present work, a theoretical investigation is performed regarding the effect of microsolvation on the interconversion mechanism and stability of sulfapyridine (SPY) regarding its tautomeric form (TAUT) in aqueous solution, which are illustrated in Fig. 1. In addition, the ultraviolet/visible (UV/Vis) absorption spectra in gas phase, as well as in solutions with water and ethanol, are also reported.

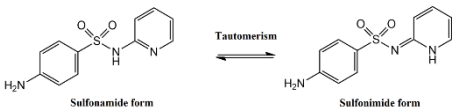


Fig. 1 – SPY tautomerization mechanism.

Methodology
Geometry optimizations and vibrational frequency calculations were performed at the PBE-D3(0)/cc-pVTZ level of theory in gas phase, as well as in solutions with water and ethanol, using the polarizable continuum model (PCM) [3]. Up to two explicit water molecules were also included in some of these calculations, which are carried out within Gaussian09 [4] package.

Next, to improve the stability description of SPY and TAUT in aqueous solutions, ONION (QM/XTB2) calculations were performed to include the explicit solvent. The quantum mechanical (QM) region, defined as the 28 atoms composing the SPY and TAUT structures, which were treated by using PBE-D3(BJ)/DEF2-TZVP with DEF2/J [5] auxiliary basis sets, while solvent effects were included with the Semiempirical Extended Tight-Binding Program Package (XTB2) [6] and the ALPB

[7] implicit solvent model. Geometry optimization and vibrational frequency calculations are done with this protocol. The initial structures for the clusters containing 43 water molecules were extracted from molecular dynamics (MD) calculations using the Autosolvate software [8].

Time dependent density functional theory (TD-DFT) with and without the Tamm-Dancoff approximation (TDA) were carried out with the CAM-B3LYP/DEF2-TZVP [9] level, along with DEF2/J auxiliary basis sets, to obtain the UV/Vis spectra of SPY and TAUT. These calculations were carried out in gas-phase and in solutions with water and ethanol, with the conductor-like polarizable continuum model (C-PCM) [10]. The number of states requested was 30 for singlet and 30 for triplet excitations. Onion, TD-DFT and TDA-DFT calculations were performed within the ORCA 5.04 package [11].

A temperature of 298.15 K was considered to thermodynamic properties.

Results and Discussion

First, the interconversion barriers for the SPY tautomerism mechanism in aqueous solution are presented in Fig. 2.

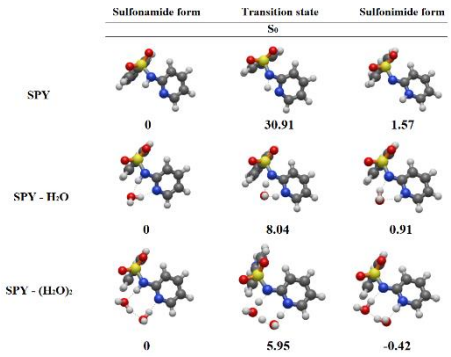


Fig. 2 - Equilibrium structures and relative Gibbs energies for the sulfapyridine tautomeric forms and the TS for the interconversion process (in kcal mol^{-1}).

Thus, the Gibbs activation energy decreases from 30.91 kcal.mol^{-1} with only implicit solvation (PCM) to 8.04 and 5.95 kcal.mol^{-1}, respectively, with the inclusion of one and two explicit water molecules. Furthermore, the formation of the tautomeric form is now spontaneous with two water molecules (-0.42 kcal.mol^{-1}). This indicates that the interconversion of SPY (sulfonamide) to its tautomeric form (sulfonimide) should occur much faster at room temperature as long as interactions with explicit solvent molecules are properly considered. In Fig. 3, the relative Gibbs energies obtained from ONIOM (QM/XTB2) calculations are illustrated. Now, the tautomeric formation becomes even more spontaneous along the increase of explicit solvent molecules, -8.60 kcal.mol^{-1}. Thus, it is possible to predict that the tautomeric form of SPY predominates in aqueous solutions at room temperature.

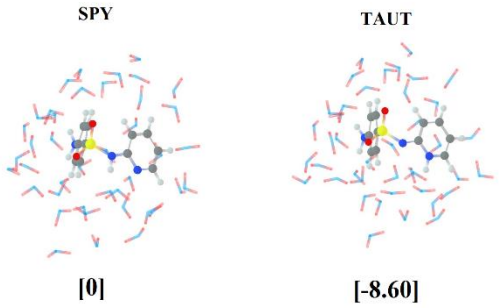


Figure 3 - Equilibrium structures and relative Gibbs energies for the sulfapyridine tautomeric forms obtained from ONIOM (QM/XTB2) with ALPB implicit solvation (in kcal mol $^{-1}$).

In the sequence, Fig 4. shows the UV/Vis absorption spectra for SPY and TAUT in gas-phase, as well as in solutions with water and ethanol. For comparison purposes, the TDA approach was also used in this work. Overall, TDA results in a blueshift in all spectra as compared to traditional TD-DFT data. In addition, the generalized oscillator strengths (GOSs) exhibit an increase of up to 60%. Solvent effects also led to band shifts and in an increase in GOSs, although the effect of the two different solvents on the spectra was practically identical. Although we did not find a complete spectrum of SPY in water, Velraj *et al.* (2014) obtained an experimental spectrum of SPY in ethanol, where the absorption bands observed are centered at 282, 258 and 211 nm [12]. Interestingly, the UV/Vis spectrum obtained for TAUT with the TDA approximation provides the closest accordance with the experiment, with absorption bands centered at 281, 240 and 219 nm in the region covered by the experimental apparatus. This seems to be a major evidence that the tautomer structure is the predominant form for this compound in ethanol.

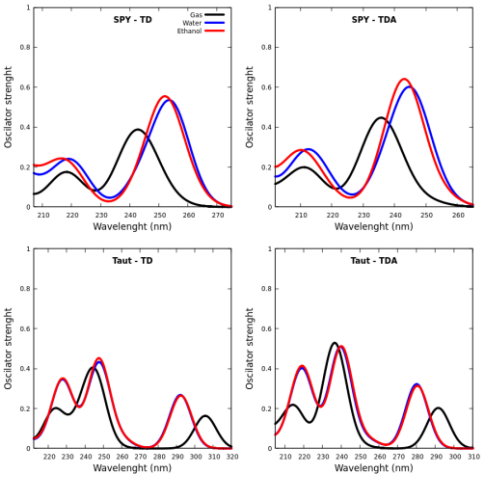


Fig. 4 - UV/Vis absorption spectra for SPY and TAUT obtained in gas-phase, water and ethanol.

Conclusions

In summary, we investigate the effects of microsolvation on the tautomerization mechanism and the UV/Vis absorption spectra of SPY (sulfonamide). The results obtained indicate that the interconversion is fast and the tautomeric form (sulfonimide) should be predominant in aqueous solution at room temperature. The absorption band around 290 nm, characteristic of the tautomeric form, was found in an experimental spectrum of SPY. This is evidence that the tautomeric equilibrium of SPY should be considered in studies concerning the biological activity or photodegradation mechanisms of SPY in protic solvents.

Acknowledgements

The authors thank the institutions that provided infrastructure and funding for this project: IQSC-USP, CNPq (141684/2022-4, 305401/2022-0, 403961/2021-1 and 306763/2021-4) and FAPESP (2022/14780-7, 2022/05138-0 and 2023/11043-4).

References

1. Antonov L, editor. Tautomerism: methods and theories. John Wiley & Sons; 2013.
2. Powling J, Bernstein HJ. The effect of solvents on tautomeric equilibria. Journal of the American Chemical Society. 1951 Sep;73(9):4353-6.
3. Mennucci B. Polarizable continuum model. Wiley Interdisciplinary Reviews: Computational Molecular Science. 2012;386-404.
4. M.J. Frisch et al., Gaussian 09, Revision D.01, Gaussian, Inc., Wallingford CT, 2013.
5. Weigend F, Ahlrichs R. Balanced basis sets of split valence, triple zeta valence and quadruple zeta valence quality for H to Rn: Design and assessment of accuracy. Physical Chemistry Chemical Physics. 2005; 3297-305.
6. Bannwarth C, Ehlert S, Grimme S. GFN2-xTB—An accurate and broadly parametrized self-consistent tight-binding quantum chemical method with multipole electrostatics and density-dependent dispersion contributions. Journal of chemical theory and computation. 2019:1652-71.
7. Ehlert S, Stahn M, Spicher S, Grimme S. Robust and efficient implicit solvation model for fast semiempirical methods. Journal of Chemical Theory and Computation. 2021;4250-61.
8. Hruska E, Gale A, Huang X, Liu F. AutoSolvate: A toolkit for automating quantum chemistry design and discovery of solvated molecules. The Journal of Chemical Physics. 2022.
9. Yanai T., Tew D. P. , Handy NC. A new hybrid exchange–correlation functional using the Coulomb-attenuating method (CAM-B3LYP). Chemical physics letters. 2004,51-7.
10. Cossi M, Rega N, Scalmani G, Barone V. Energies, structures, and electronic properties of molecules in solution with the C-PCM solvation model. Journal of computational chemistry. 2003, 669-81.
11 Neese F. The ORCA program system. Wiley Interdisciplinary Reviews: Computational Molecular Science. 2012.
12. Velraj G, Soundharam S. Structure, vibrational, electronic, NBO and NMR analyses of 4-amino-N-[2-pyridinyl] benzene sulfonamide (sulfapyridine) by experimental and theoretical approach. Journal of Molecular Structure. 2014, 475-86.

10º SIMPÓSIO DE ESTRUTURA ELETRÔNICA & DINÂMICA MOLECULAR
SEEDMOL 4 a 8 novembro | 2024
Pirenópolis, Goiás

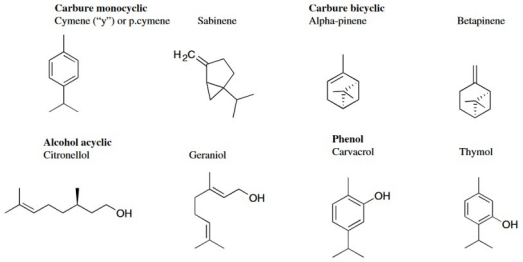
MODELAGEM MOLECULAR DE COMPOSTOS DE ÓLEOS ESSENCIAIS COM AÇÃO ANTIVIRAL: No Contexto do Ensino Médio.

Emmanuel R. F. Vasconcellos[1], Sávyo Aymar S. Maia[2], Eduardo N. N. da Silva[3], Júlia L. M. Marra[4] e Josenaide P. do Nascimento[5].
[1-4]Centro Educacional GISNO, Quadra SGAN 907, Bloco A, Brasil/Brasília/DF.
[5]Instituto de Química da UnB, Brasil/Brasília/DF.
josenaide.nascimento@unb.br
Keywords: Antivirals; Computational and Theoretical Chemistry; Essential Oils; Basic Education.

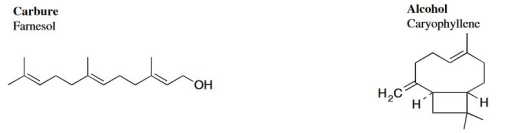
Abstract
We aim is to invest efforts in carrying out projects that make it possible to show the methods and resources of Theoretical and Computational Chemistry to public high school students. This way, it involves them in research aimed at their learning and interest in this area.

Introdução
Os óleos essenciais são extraídos e obtidos por destilação a vapor de plantas ou prensagem a frio do pericarpo de frutos cítricos. São compostos principalmente de mono e sesquiterpenos e de fenilpropanoides, metabólitos que conferem suas características organolépticas[1].
Possuem grande aplicação na industria de perfumaria, cosméticos, alimentos e em composições farmacêuticas e orais e comercializados na sua forma bruta ou beneficiada, fornecendo substâncias purificadas como o limoneno, citral, citronelal, eugenol, mentol e safrol[1-3].
Esses óleos são bastante usados em tratamentos médicos e têm se mostrado promissores contra diversos agentes patogênicos, além de exibir propriedades antimicrobianas, como antifúngica, antibacteriana, antiviral e antiparasitária[3-4]. Podendo até interagir com alvos proteicos para desencadear uma resposta biológica[5-6].
Nesse contexto, foram selecionados uma série de compostos originários de óleos essenciais com o objetivo de investigar a Relação Estrutura e Atividade Biológica (*SAR*), por meio da análise das propriedades moleculares calculadas e relacionadas com a atividade estrutura molecular, a fim de compreender como os descritores moleculares podem contribuir para previsão das estruturas relevantes que podem explicar a ação entre os compostos e a atividade antiviral de forma acessível aos estudantes da rede pública de ensino do Distrito Federal.

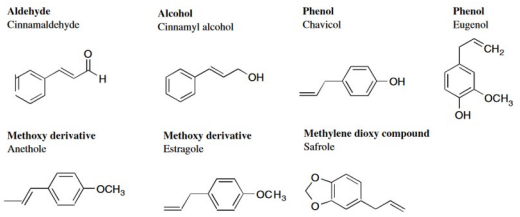
Metodologia
Foram selecionados da literatura dezenove (19) compostos majoritários identificados em óleos essenciais, os quais possuem alguma aplicação farmacológica[3] (Figura 1).
Figura 1. Estrutura química de isolados presentes no óleo essencial
Terpenos e Monoterpenos



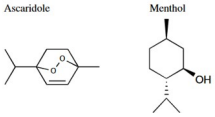
Sesquiterpenos



Compostos aromáticos



Terpenóides ou Isoprenóides



A construção, otimização da geometria e minimização da energia das estruturas (Figura 1) foram realizadas no programa HyperChem Professional. Todas as estruturas foram calculadas na forma neutra, no vácuo sem qualquer restrição geométrica. Nos cálculos de Mecânica Molecular foram utilizado o campo de força Merck Molecular Force Field 94 (MMFF94)[7], em seguida as geometrias de todos os compostos foi otimizada aplicando-se o método semi-empíricos, o Hamiltoniano Austin Model 1 (AM1).

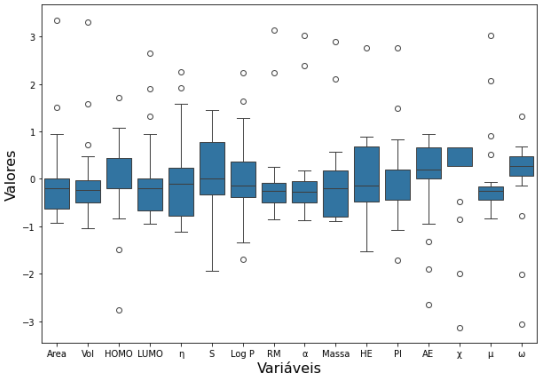
Os cálculos teóricos dos descritores moleculares para a determinação dos parâmetros físico-químicos foram obtidos através do programa HyperChem, e os descritores eletrônicos foram calculados através do programa Gaussian03W.

Estes dados gerados foram inicialmente tratados com método Análise de Componentes Principais (Principal Component Analyses – PCA) para reduzir o número de variáveis, pois o mesmo gera uma combinação linear entre as 27 variáveis iniciais. Em seguida aplicou-se a técnica exploratória de análise de Cluster, este pré-tratamento de dados é apropriado para resolver os problemas contraídos na análise, como por exemplo, a redução de informações redundantes através da colinearidade.

Resultados

Estudo da relação estrutura e atividade, com base nas análises estatísticas dos valores de média, desvio padrão e coeficiente de variação percentual de cada descritor molecular calculado, permitiu observar que de modo geral os compostos estudados apresentam um perfil similar (Figura 2), apesar dos óleos essenciais possuírem composição química extremamente complexa devido à presença de constituintes altamente funcionalizados (Figura 1), com diferentes esqueletos de carbono e uma grande variedade de derivados oxigenados.

Figura 2. Resultado da análise de Cluster para os descritores moleculares



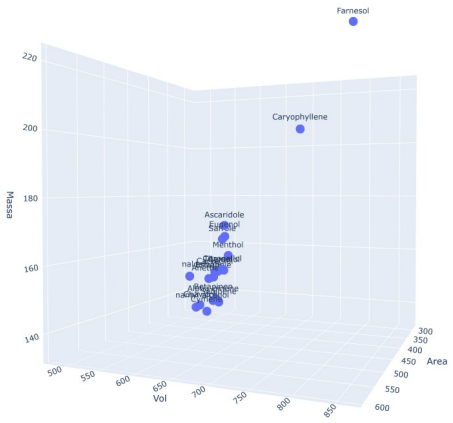
Os terpenoides, de modo geral, classificam-se de acordo com o esqueleto de carbono. Os menores terpenos contêm uma única unidade de isopreno (C5) e são chamados de hemi-terpenos ou meio-terpenos. À medida que as unidades de isopreno vão sendo metabolizadas pelo organismo da planta, a partir dos diversos estímulos genéticos e epigenéticos, são originados os monoterpenos (C10), sesquiterpenos (C15), diterpenos (C20), triterpenos (C30), tetraterpenos (C40), dentre outras classificações de acordo com a quantidade de carbonos na molécula e/ou unidades de isopreno presentes.

Ao analisar amplitude dos descritores originais (Figura 3), pode-se observar a separação dos descritores área, volume e massa, que culminou com a distinção dos compostos Caryophyllene e Farnesol, de acordo com a classe Sesquiterpenos, separando corretamente as estruturas menos semelhantes, enquanto que os demais compostos apresentaram maior similaridade estrutural (esqueleto de carbono).

Estes resultados corroboram com a literatura já que estes compostos avaliados apresentam moderada atividade antiviral (32,1%) para ensaio de redução de placa e HSV-1. Sendo que o Eugenol apresenta

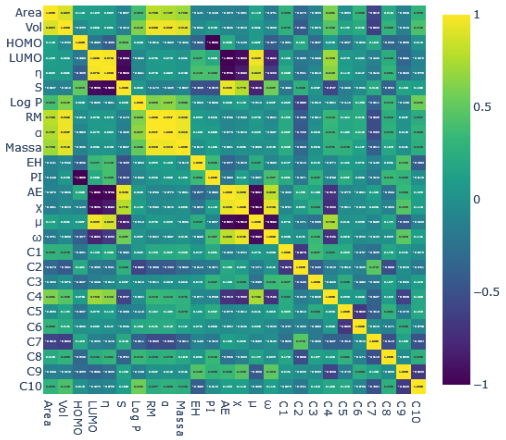
uma atividade elevada (75-85%) para ensaios da gripe tipo A (H1N1).

Figura 3. Correlação entre as propriedades estruturais por agrupamento de Cluster



Resultados de correlação de Pearson para todas as variáveis (Figura 5), mostraram que os coeficientes de correlação mais próximos dos valores extremos (-1 ou 1) indicam alta correlação entre si.

Figura 5. Correlação de Pearson entre os descritores calculados



Para avaliar a adequação glogal da análise fatorial calculou-se o teste de esfericidade de Bartlettt com Qui² = 2720,37 e p-valor = 0,0, os resultados indicam que estes descritores são significativos, pois ao comparar a matriz de correlações com a matriz identidade de mesma dimensão obteve-se matrizes diferentes, ou seja, a análise é aplicável.

Discussão

Pouquíssimos mecanismos são propostos na literatura para explicar a atividade antiviral dos óleos essenciais, dos quais entende-se que a inibição da infecção é devida ao dano direto causado à integridade da membrana celular pelos componentes lipofílicos do óleo essencial, o que afeta diretamente a manutenção do pH celular e o equilíbrio de íons inorgânicos. A ação antiviral está mais consistentes com os constituintes monoterpênicos, apesar de que ainda precisam de maiores evidências, estes compostos podem auxiliar de diferentes formas, sugerindo um promissor agente antiviral, nota-se a necessidade de maiores estudos para elucidação de possíveis mecanismos.

Conclusão

A demonstração das técnicas, desenho estrutural e cálculo dos descritores forneceu aprendizados de suma importância aos estudantes do Ensino Médio. É certo que houveram algumas predições desfavoráveis, porém, as moléculas ainda podem ser otimizadas em técnicas de modelagem molecular e assim evoluírem para modelos de QSAR.

A partir do exposto consideramos oportuno investir esforços na realização de projetos que possibilitem mostrar os métodos e recursos da Química Teórica e Computacional a estudantes do Ensino Médio da Rede Pública.

Acknowledgements

IQ/UnB CNPq

References

1. Bizzo, H. R.; Hovell, A. M. C.; Rezende, C. M. Quím. Nova 2009, 32, 588.
2. Campelo, L. M. L.; Sá, C. G.; Feitosa, C. M.; Sousa, G. F.; Freitas, R. M. Rev. Bras. de Plan. Med. 2013, 15, 708.
3. Bakkali, F. S.; Averbeck, D.; Averbeck, M. Food and Chem. Tox. 2008, 46 446.
4. Winska, K., W. Maczka, J. Łyczko, M. Grabarczyk, A. Czubaszek and A. Szumny. 2019, 24, 2130.
5. Da Silva, J. K. R.; Figueiredo, P. L. B.; Byler, K. G. and Setzer, W. N. 2020, 21, 3426.
6. Sousa et al., Ind. Crops and Prod. 2015, 65, 71.
7. Halgren T. A. J. Comp. Chem. 1996, 17, 490.

10º SIMPÓSIO DE ESTRUTURA ELETRÔNICA & DINÂMICA MOLECULAR
SEED MOL
4 a 8 novembro | 2024
Pirenópolis, Goiás

Dodecanophene as anode for Potassium-Ion Battery (KIB)

Juan Rafael Gomez Quispe[1], Pedro Autreto Alves Da Silva[1].
[1]Centre of Natural and Human Sciences, Federal University of ABC, Santo Andre, Sao Paulo, Brazil.
*pedro.autreto@ufabc.edu.br
Keywords: Potassium Ion Battery, Density Functional Theory, Graphene Allotrope

Abstract
This study explores dodecanophene as a potential anode material for potassium-ion batteries (KIBs). Its unique properties, including intrinsic metallic behavior, strong potassium adsorption, and low diffusion barriers, suggest it could enhance KIB performance, making it a promising candidate for this application.

Introduction
Dodecanophene is a two-dimensional carbon allotrope characterized by a unique structure comprising 3-, 6-, and 12-membered carbon rings, which imparts distinctive properties such as intrinsic metallic behavior and high structural stability under stress[1]. Additionally, it exhibits significant optical activity across the infrared, visible, and ultraviolet spectra, making it suitable for electronic and optoelectronic applications. The material demonstrates mechanical anisotropy, with Young's modulus that varies according to the direction of the applied stress, indicating variable resistance. Moreover, it maintains structural stability at high temperatures, underscoring its potential as a robust material for industrial applications.

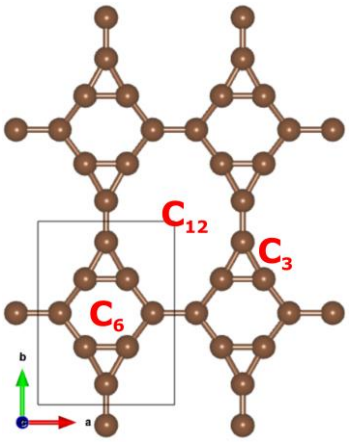


Fig. 1. Top view of Dodecanophene structure, C6, C12 and C3 represent the hexagonal, dodecagonal and triangular carbon rings.

This study assesses the feasibility of using dodecanophene as an anode material in potassium-ion batteries (KIBs). Due to its unique physical and electronic properties, dodecanophene has the potential to enhance energy storage capacity, charge-discharge efficiency, and the durability of KIBs, positioning it as a promising candidate for this emerging technology.

Methodology
Density Functional Theory (DFT) calculations were performed using the SIESTA[2] software on a 2 x 1 supercell of a dodecanophene sheet. Periodic boundary conditions with a 20 Å vacuum space were applied. Kohn-Sham orbitals were expanded using a double-zeta basis set, augmented with polarization orbitals. Optimized pseudopotentials and atomic bases from the SIMUNE database were employed, along with the Perdew-Burke-Ernzerhof (PBE) exchange-correlation functional. Brillouin Zone (BZ) sampling utilized a 7 x 6 x 1 irreducible Monkhorst-Pack (MP) k-point grid. The total energy convergence threshold was set to 1 x 10^{-4} eV, and geometry optimizations were conducted using the conjugate gradient (CG) algorithm, ensuring forces on ions were minimized to less than 0.01 eV/Å.

Adsorption Energy Calculations

$$E_{ads} = E_{dodecanophene+K} - (E_{dodecanophene} + E_{K_{bcc}})$$

Adsorption Energy Calculations(N)

$$E_{ads}(N) = E_{N-K+dodecanophene} - (NE_{K_{bcc}} + E_{dodecanophene})$$

Theoretical Specific Capacity(mAh/g)

$$C = N_{max} \times \frac{F}{M}$$

Open Voltage Circuit

$$OCV = \left(\frac{E_{dodecanophene} + NE_{K_{bcc}} - E_{N-K+dodecanophene}}{Ne} \right)$$

Charge density difference

$$\Delta\rho = \rho_{dodecanophene+K} - \rho_{dodecanophene} - \rho_{K_{bcc}}$$

Results

Figure 2 presents the electronic band structure and density of states for the dodecanophene sheet, revealing a non-zero band gap indicative of its intrinsic metallic nature. Figure 3 illustrates the charge density difference for potassium adsorption on the C6 and C12 carbon rings, allowing a qualitative analysis of the strong interaction between potassium atoms and adsorption sites, with adsorption energies of -0.60 eV and -0.96 eV, respectively. The effect of potassium atom concentration on adsorption energy is shown in Figure 4, where an optimal value of N=2 K atoms is identified with a maximum adsorption energy of -1.0 eV.

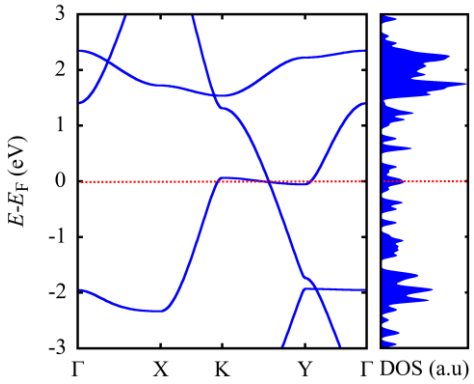


Fig. 2. Electronic band structure and density of states (DOS) of Dodecanophene.

The energy barriers for potassium diffusion paths on the dodecanophene sheet are depicted in Figure 5(a, c, d), showing values of approximately 0.39 eV and 0.40 eV for paths 1 and 2. Additionally, Figure 5(b) presents the open-circuit voltage, which measures the stability of the charge-discharge rate. The average voltage of 0.42 V suggests good cyclability for potassium-ion batteries.

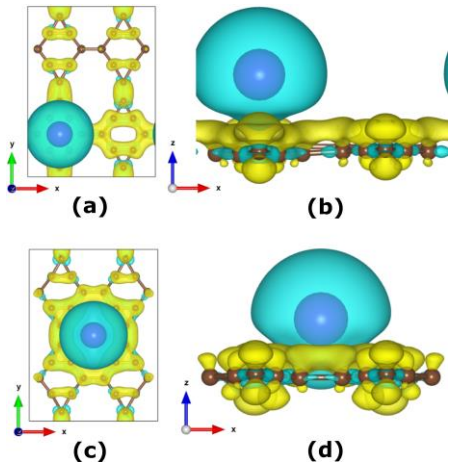


Fig. 3. Charge density difference plots of K absorbed structures on C6 (a and b) and C12 (c and d) carbon rings. The isosurface value is taken to be 0.001 e/Ang³.

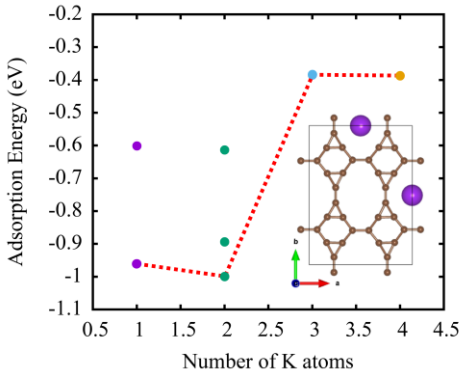


Fig. 4. Adsorption Energy values in function of number of K atoms. The inset figure corresponds to the optimal of 2 atoms K adsorbed Dodecanophene.

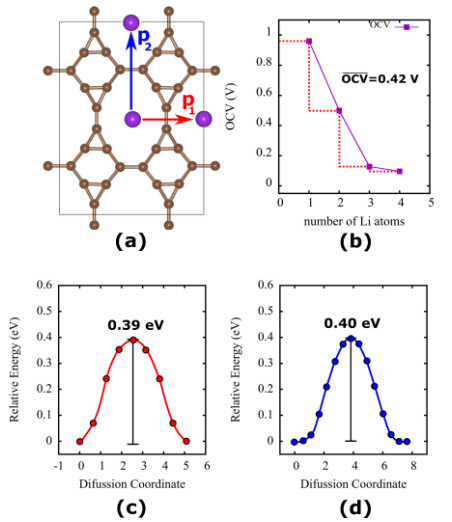


Fig. 5. (a) Diffusion paths of K atoms on Dodecanophene, (b) open voltage circuit (OCV) values. Diffusion energy barrier for p_1 and p_2 paths.

Discussion

The findings of this study demonstrate the potential application of dodecanophene as an anode material for KIBs. The adsorption energy values indicate strong adsorption of potassium atoms onto the dodecanophene sheet, which is beneficial for storage within the carbon structure. Moreover, dodecanophene's intrinsic metallic nature is advantageous for battery applications, as the anode requires good electrical conductivity. The concentration effects on adsorption energy suggest a maximum adsorption of 4 potassium atoms, corresponding to a theoretical specific capacity of 557.852 mAh/g, which compares favorably with graphene's capacity in lithium-ion batteries. Furthermore, the open-circuit voltage calculation indicates good cyclability, and the low diffusion energy barriers imply that potassium atoms can efficiently diffuse through the structure.

Conclusions

In conclusion, this study supports the potential of dodecanophene as an anode material for potassium-ion batteries, with its intrinsic properties, favorable adsorption energy, and low diffusion barriers indicating its suitability for this application.

Acknowledgements

Thanks the UFABC Multiuser Computational Center (CCM-UFABC) for the computational resources provided.

References

1. Lima, K. A. L.; Monteiro, F. F.; Santos, E. J. A.; Alves, R. A. F.; Giozza, W. F.; Ribeiro, L. A.; Mater. Today Commun. 2024, 40, 109455.

2. Garcia, A.; Papior, N.; Akhtar, A.; Artacho, E.; Blum, V.; Bosoni, E.; Brandimarte, P.; Brandbyge, M.; Cerdá, J.; Corsetti, F.; Cuadrado, R.; Dikan, V.; Ferrer, J.; Gale, J.; García-Fernández, P.; García-Suárez, V.; García, S.; Huhs, G.; Illera, S.; Junquera, J.; J. Chem. Phys. 2020, 152, 204108.

3. Ernzerhof, M.; Scuseria, G. E.; J. Chem. Phys. 1999, 110, 5029-5036.

10º SIMPÓSIO DE ESTRUTURA ELETRÔNICA & DINÂMICA MOLECULAR
SEEDMOL 4 a 8 novembro | 2024
Pirenópolis, Goiás

Polarização de novos conjuntos relativísticos de funções de base Gaussianas sem prolapso variacional de qualidade duplo- e triplo-ζ: elementos dos blocos *d*

Julielson dos Santos Sousa,[1] Eriosvaldo Florentino Gusmão,[1] Anne Kéllen de Nazaré dos Reis Dias,[1] Roberto Luiz Andrade Haiduke.[1]

[1] *Departamento de Química e Física Molecular*, Instituto de Química de São Carlos, USP, São Carlos, SP- Brasil.
julielson@usp.br

Palavras Chave: Prolapso variacional; Funções de polarização; Conjuntos duplo-ζ; Conjuntos triplo-ζ.

Abstract

A series of relativistic prolapse-free Gaussian basis sets of double- and triple-ζ quality has been augmented by correlation/polarization functions for *d*-block elements. Here, we report the (aug-)RPF-2Z and (aug-)RPF-3Z sets for Sc−Hg.

Introdução

A proposta da equação de Dirac em 1928 [1] representou um marco na física teórica ao unificar a mecânica quântica com a teoria da relatividade especial. Essa equação descreve o comportamento dos elétrons relativísticos, levando em conta tanto suas propriedades ondulatórias quanto os efeitos da relatividade. A implementação prática dessas ideias impulsionou estudos na estrutura eletrônica dos átomos e moléculas, revelando a importância dos efeitos relativísticos em sistemas químicos [2]. Esses efeitos são particularmente relevantes para elementos pesados, onde a velocidade dos elétrons próximos ao núcleo é significativa em comparação com a velocidade da luz.

A consideração dos efeitos relativísticos permitiu uma compreensão mais precisa das propriedades químicas e físicas desses elementos, influenciando áreas como a química quântica e a espectroscopia. O objetivo deste trabalho é avançar no desenvolvimento de novos conjuntos de funções de base Gaussianas sem prolapso variacional de qualidade duplo- e triplo-ζ, RPF-2Z e RPF-3Z, e de suas versões com funções difusas extras (aug) para elementos do bloco *d*, Sc−Hg.

Metodologia

O presente trabalho abordou a escolha de funções de correlação/polarização (C/P) a serem incluídas nos conjuntos relativísticos sem prolapso variacional de funções de base Gaussianas primitivas de tamanhos pequeno e médio, que foram previamente desenvolvidos no grupo [3, 4], almejando gerar conjuntos de qualidade duplo- e triplo-ζ para cálculos moleculares.

Para orientar tal processo de seleção, foi utilizada a energia de correlação eletrônica de cálculos multi-referenciais de interação de configurações com excitações simples e duplas (MR-CISD) dos elétrons de valência realizados dentro do formalismo de 4 componentes, via Hamiltoniano Dirac-Coulomb. Quando disponível, a correção de Davidson foi utilizada. Os conjuntos de base foram sempre usados na forma descontraída, em paralelo com as condições de balanço cinético. Uma aproximação foi usada para tratar as integrais de repulsão intereletrônica em termos de funções *small*, (SS|SS), visando reduzir a demanda por recursos computacionais [5].

A Teoria de Pares Acoplados com excitações simples e duplas iterativas, juntamente com uma correção perturbativa para substituições triplas (DC-CCSD-T), considerando um espaço ativo para os elétrons de valência e spinors virtuais com energia até 20 ua, foi escolhida para cálculos investigativos de distâncias de equilíbrio (r_e) e frequências vibracionais harmônicas (ω_e), determinadas por um ajuste polinomial de quarta ordem. Os momentos dipolares (μ) foram obtidos nas geometrias de equilíbrio experimental [6,7]. Todos esses cálculos foram feitos para moléculas diatômicas do tipo MH e MF (M = Cu, Ag e Au) e os resultados são comparados com aqueles de conjuntos de base do tipo dyall.v2z e dyall.v3z [8,9,10,11,12]Além disso, o programa computacional empregado em todos esses cálculos foi o DIRAC 23 [13,14].

Resultados e discussões

Os elementos do bloco *d* são mais complicados que aqueles dos blocos *s* e *p*. Isso ocorre porque a definição do espaço de valência agora precisa incluir elétrons *d*. Inicialmente, o estudo consistiu em selecionar a quantidade apropriada de funções a serem incorporadas aos conjuntos relativísticos de funções primitivas Gaussianas de tamanhos pequeno e médio, sem prolapso variacional, e, em seguida, escolher os expoentes dessas funções. Em outras palavras, foram selecionadas funções C/P para os elementos do bloco *d* do quarto ao sexto período.

Caso as simetrias das funções a serem adicionadas já estejam presentes nas primitivas destes átomos (*s*, *p*, *d* ou *f*), são consideradas funções mais difusas dessas simetrias para compor o conjunto C/P, pois o efeito delas para a energia de correlação pode ser relevante. Por outro lado, caso essa simetria não esteja presente no conjunto de primitivas, as funções C/P necessárias são obtidas a partir de funções de momento angular duas unidades menor (para minimizar o número de funções *small* geradas pelo balanço cinético).

Inicialmente, foi verificada a necessidade de incluir duas funções difusas do tipo *p* no conjunto C/P. Além disso, uma função mais difusa do tipo *d* foi também adicionada ao conjunto C/P desses elementos. Isto foi feito para ambos os conjuntos, RPF-2Z e RPF-3Z.

Em seguida, no caso do conjunto RPF-2Z, uma função *f* foi incluída, resultando em [2*p*,1*d*,1*f*] funções C/P para os elementos do bloco *d*. Por sua vez, para o conjunto RPF-3Z, foram adicionadas ainda 2 funções *f* e uma função *g*, provendo [2*p*,1*d*,2*f*,1*g*] funções C/P para tais átomos.

Depois, uma função difusa extra foi incluída para cada simetria presente nos conjuntos RPF-2Z e RPF-3Z, para obter os conjuntos aug-RPF-2Z e aug-RPF-3Z, que são indicados para tratar sistemas aniônicos ou com ligações fracas.

Todos esses conjuntos foram avaliados através de cálculos moleculares, que mostraram um desempenho satisfatório, quando comparados aos conjuntos de Dyall.

Conclusão

Neste estudo, foram adicionadas funções de correlação/polarização baseadas nos resultados de cálculos MR-CISD, com o objetivo de fornecer conjuntos de qualidade duplo-ζ e triplo-ζ sem prolapso variacional (RPF-2Z e RPF-3Z) e suas versões complementadas com funções difusas extras (aug). Os resultados confirmam a eficácia das metodologias empregadas na análise das moléculas diatômicas MH e MH (M = Cu, Ag e Au), mostrando precisão nos cálculos de distâncias de equilíbrio, frequências vibracionais e momentos dipolares.

Referências

[1] P.A.M. Dirac, Proc. R. Soc. Lond. Ser. A, 1928, 117, 610–624.
[2] Pyykko, P. Annu. Rev. Phys. Chem. 2012, 63 45-64
[3] E.F. Gusmão, R.L.A. Haiduke, J. Comput. Chem., 2022, 43,1901.
[4] Gusmão, E. F.; Haiduke, R. L. A. *J. Comput. Chem.* 2023, 44, 2478–2485.

[5] Visscher, L. Theor. Chem. Acc. 1997, 98, 68−70.
[6] Huber, K. P.; Herzberg, G. H. "Constants of Diatomic Molecules" in *NIST Chemistry WebBook*, NIST Standard Reference Database No. 69, Eds. P. J. Linstrom and W. G. Mallard, National Institute of Standards and Technology: Gaithersburg, MD. https://doi.org/10.18434/T4D303 (accessed Jul 17, 2024).
[7] Haynes, W. CRC Handbook of Chemistry and Physics, 94th Edition; 100 Key Points; CRC Press, 2016.
[8] Dyall, K. G. *Theor. Chem. Acc.* 1998, 99, 366–371.
[9] Dyall, K. G. *Theor. Chem. Acc.* 2002, 108, 335–340.
[10] Dyall, K. G. *Theor. Chem. Acc.* 2006, 115, 441–447.
[11] Dyall, K. G. *Theor. Chem. Acc.* 2016, 135, 128.
[12] Dyall, K.G. unpublished
[13] DIRAC, a relativistic ab initio electronic structure program, Release DIRAC22 (2022), written by L. Visscher *et al.*
[14] Saue, T.; Bast, R.; Gomes, A. S. P.; Jensen, H. J. A.; Visscher, L.; Aucar, I. A.; Di Remigio, R.; Dyall, K. G.; Eliav, E.; Fasshauer, E.; et al. *J. Chem. Phys.* 2020, **152**.

Agradecimentos

Os autores agradecem à Fundação de Amparo à Pesquisa do Estado de São Paulo (FAPESP - número de concessão 2022/05138-0) e ao Conselho Nacional de Desenvolvimento Científico e Tecnológico (CNPq - números de concessão 306763/2021-4 e 2018/168778-1) pelo apoio financeiro. Este estudo foi financiado em parte pela Coordenação de Aperfeiçoamento de Pessoal de Nível Superior – Brasil (CAPES) – Código de Financiamento 001 (88887.658222/2021-00 e 88887.653823/2021-00).

Low-lying Excited States of Polyenes: The Contribution of σ-π Electron Correlation to the Description of Ionic States

Julio C. V. Chagas[1,2], Reed Nieman[2], Hans Lischka[2], and Francisco Bolivar Correto Machado[1]
[1]Department of Chemistry, Aeronautics Institute of Technology, São José dos Campos, São Paulo, Brazil, 12228-900.
[2]Department of Chemistry and Biochemistry, Texas Tech University, Lubbock, Texas, United States of America, 79409.
fmachado@ita.br
Keywords: multireference; electronic structure; excited states; electron correlation.

Abstract
In this work, we use high-level multireference methods to investigate the electronic spectra of linear all-*trans* polyenes, with a particular focus on characterizing the ionic $1^1B_u^+$ state. By applying a balanced treatment, we demonstrate the effect of enhancing the σ-π dynamic electron correlation on transition densities and excitation energies.

Introduction

The study of linear all-*trans* polyenes has a long tradition due to their spectral properties, which arise from the structure of their low-lying excited-state manifold. The three lowest excited states (2^1Ag^-, 1^1Bu^+, and 1^1Bu^-) have attracted considerable attention, both experimentally and theoretically.[1] This work focuses on their description from an electronic perspective.
The wave functions of ionic states are primarily composed of singly excited determinants, whereas those of covalent states are more complex, with significant contributions from doubly excited determinants.[2] Consequently, uniformly describing both covalent and ionic states using a single computational method is notoriously challenging. The multiconfigurational self-consistent field (MCSCF) method, which effectively captures the static electron correlation in covalent states, encounters significant accuracy issues when applied to ionic states. Specifically, excitation energies for ionic states are typically overestimated by about 1−2 eV when using an active space that includes only valence π-electrons and π-orbitals.[3] Several strategies have been proposed to mitigate this issue, such as expanding the active space to include additional unoccupied π-orbitals, incorporating σ-orbitals into the active space, and modifying the one-electron basis set.[4]
In this work, we provide an accurate and balanced treatment of both ionic and covalent excited states in all-*trans* unsubstituted polyenes containing $6 \leq N \leq 12$ π-electrons. We also perform a detailed analysis to examine the impact of progressively increasing σ-orbital correlation on both excitation energies and transition densities, contributing to a deeper understanding of the wave functions of ionic states and the general electronic structure of polyenes at the multireference level.

Methodology

We performed geometry optimizations of unsubstituted all-*trans* polyenes containing $6 \leq N \leq 12$ π-electrons using the long-range corrected hybrid ωB97X-D functional with the cc-pVTZ basis set, employing the Gaussian 16 software package.[5]
Based on the optimized geometries, we conducted a comprehensive analysis of the singlet excited states $2^1A_g^-$, $1^1B_u^+$, and $1^1B_u^-$, utilizing both non-dynamic and dynamic correlation treatments. Vertical excitation

energies for transitions between the ground state and the aforementioned states of interest were computed using a range of computational methods, including complete active space self-consistent field (CASSCF), multireference configuration interaction expansion truncated to single and double excitations (MR-CISD), and multireference averaged quadratic coupled-cluster (MR-AQCC) approaches.[6]

Both non-dynamic and dynamic correlation treatments were conducted using the cc-pVDZ basis set, encompassing all valence π-electrons and valence π-orbitals of each molecule. For the dynamic correlation treatment, 50% of the σ space (evenly distributed between reference occupied and virtual orbitals) was frozen. All the multireference calculations were performed using the Columbus program system.[7] Wave function analyses were conducted using the TheoDORE 3.1.1 program package.[8]

Results and Discussion

First, it should be noted that the ionic $^1B_u^+$ state results from a HOMO-LUMO transition. A treatment primarily involving non-dynamic electron correlation at the CASSCF level presents significant issues regarding excitation energies from the ground state to the ionic $^1B_u^+$ state (Figure 1). The CASSCF method considerably overestimates the excitation energies. At this level of methodology, the ionic $^1B_u^+$ state lies not only above the $2^1A_g^-$ state, but also above the covalent $^1B_u^-$ state, causing the ionic state to become the second excited state of B_u symmetry.

The relative ordering of the excited states throughout the series of all-*trans* linear polyenes remains a topic of ongoing debate. However, for polyenes with $6 \leq N \leq 12$ π-electrons, it is generally accepted that the lowest singlet excited state is the $2^1A_g^-$, followed by the $1^1B_u^+$ state.

The inclusion of dynamic electron correlation through MR-CISD, along with appropriate size-extensivity corrections significantly stabilizes the ionic $1^1B_u^+$ state.

The transition densities (Figure 2), given as the product of the hole and electron NTOs, have crucial implications for the energetics of an excited state. First, it is important to note that the transition densities of covalent states ($2^1A_g^-$, and $2^1B_u^-$) are centered around the bonds, whereas they are localized on the atoms for the ionic state.

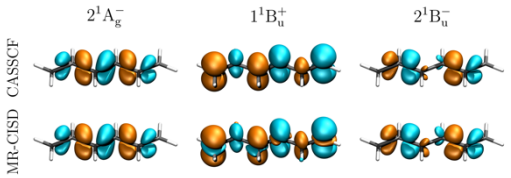


Figure 2. Transition densities (isovalue: 0.002 au) between the ground state and excited states in hexatriene computed at the CASSCF and MR-CISD levels.

Similarly to the observations for excitation energies, no appreciable difference is found between the transition densities calculated using CASSCF and MR-CISD+P wave functions for covalent states. Strikingly, this is not the case for the $1^1B_u^+$ state, where new contributions in the σ-system appear. To understand this phenomenon, it is noteworthy that the energy of singlet excited

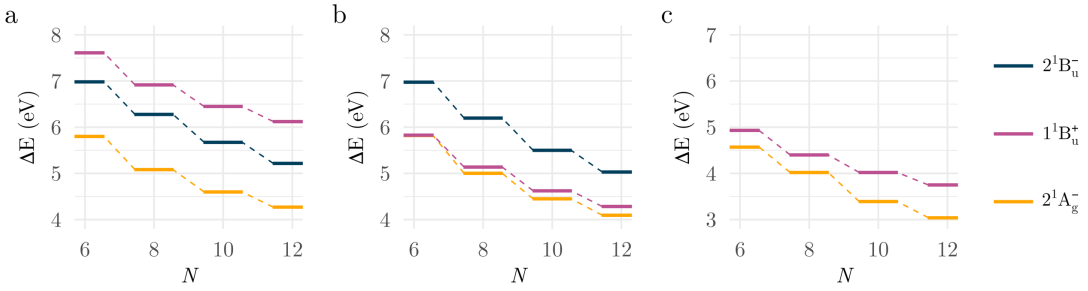


Figure 1. Vertical singlet excitation energies of polyenes with N π-electrons computed using a) CASSCF, b) MR-CISD+P, and c) Experimental estimates for the gas phase.

states is proportional to the transition density self-repulsion. The repulsive term can be compensated by σσ* excitations, yielding opposing terms in the transition density.[9] As a result, to overcome the energetic penalty associated with a transition density with high self-repulsion, a few σ-contributions are mixed into the wave function to partially cancel out the repulsion, resulting in a lower energy.

The effect of enhancing the σ-π dynamic electron correlation on transition densities and excitation energies was also analyzed (Figure 3). When considering size-extensivity errors, freezing 50% of the σ space has no significant impact on the excitation energies or transition densities of hexatriene. However, as a higher percentage of σ-orbitals are frozen, the excitation energies are increasingly affected, and the contributions from the σ-system vanish. Furthermore, the size-extensivity correction plays an important role in the $1^1A_g^-$ to $1^1B_u^+$ excitation energies. This correction loses its effect as a higher percentage of the σ space is frozen, to the point where the dynamic treatment considers only the π space, and no appreciable distinction is observed between MR-CISD and MR-CISD+P or MR-AQCC.

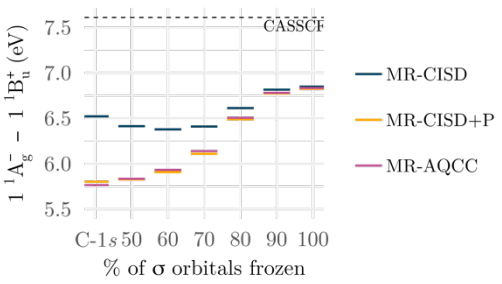


Figure 3. Influence of freezing σ-orbitals in hexatriene on the excitation energies between $1^1A_g^-$ and $1^1B_u^+$, computed at the MR-CISD and MR-AQCC levels of theory. The dashed line represents the CASSCF reference energy.

Conclusions

In this work, we investigated the general electronic structure of polyenes at the multireference level. Our study includes vertical transition energies and density matrix analyses from the ground state to the excited states. To overcome the energetic penalty associated with transition densities exhibiting significant self-repulsion, which would arise from a pure HOMO-LUMO transition, a few σ-contributions are mixed into the wave function to partially cancel out the repulsion, thereby yielding a lower energy state. Crucially, an accurate description of ionic states requires an extensive treatment of σ-π electron correlation, which gives rise to effects that cannot be captured by considering the π space alone.

Acknowledgements

This work was supported by Conselho Nacional de Desenvolvimento Científico e Tecnológico (Grant Nos. 164766/2021-9, 307168/2022-0), Fundação de Amparo à Pesquisa do Estado de São Paulo (Grant No. 2022/16385-8), Coordenação de Aperfeiçoamento de Pessoal de Nível Superior (Grant No. 88887.877979/2023-00), and U.S. National Science Foundation (Grant No. 2107923).

References

1. Schmidt, M.; Tavan, P. J. Chem. Phys. 2012, 136, 124309.
2. Khokhlov, D.; Belov, A. J. Phys. Chem. A 2020, 124, 5790–5803.
3. do Monte, S. A.; Spada, R. F. K.; Alves, R. L. R.; Belcher, L.; Shepard, R.; Lischka, H.; Plasser, F. J. Phys. Chem. A 2023, 127, 9842–9852.
4. Boggio-Pasqua, M.; Bearpark, M. J.; Klene, M.; Robb, M. A. J. Chem. Phys. 2004, 120, 7849–7860.
5. Frisch, M. J.; Trucks, G. W.; Schlegel, H. B. et al. Gaussian 16 Revision C.01, 2016.
6. Lischka, H.; Nachtigallová, D.; Aquino, A. J. A.; Szalay, P. G.; Plasser, F.; Machado, F. B. C.; Barbatti, M. Chem. Rev. 2018, 118, 7293–7361.
7. Lischka, H.; Shepard, R.; Shavitt, I. et al. COLUMBUS, an Ab Initio Electronic Structure Program, 2017.
8. Plasser, F. J. Chem. Phys. 2020, 152, 084108.
9. Kimber, P.; Plasser, F. Phys. Chem. Chem. Phys. 2020, 22, 6058–6080.

Explorando Como as Dimensões do Sistema e as Condições Periódicas de Contorno Influenciam a Simulação de Dinâmica Molecular das Nanostruturas de Auto-Montagem do Peptídeo A_6H.

Karinna Mendanha[1] e Guilherme Colherinhas[1]
[1]Instituto de Física, Universidade Federal de Goiás, Goiânia, GO, Brasil.
karinnamendanha@discente.ufg.br

Dinâmica Molecular; Peptídeo; Ligação de Hidrogênio; Tempo de Vida da Ligação de Hidrogênio; Condições Periódicas de Contorno.

Abstract

This work studies the effects of PBC on the properties and HB dynamics using molecular dynamics simulations of alanine and histidine peptide membranes. Small surface areas can lead to non-convergent values, affecting mobility and HB lifetimes, which increase by ~19% without PBCs.

Introdução

Uma maneira teórica de estudar estruturas de peptídeos com alta confiabilidade é através de simulações de Dinâmica Molecular (MD). No entanto, o processo de modelagem molecular pode envolver várias aproximações, e durante as simulações computacionais de MD, é possível, em alguns casos, identificar efeitos indesejados que não representam com precisão o sistema macroscópico real. Uma maneira de mitigar tais efeitos é controlando as dimensões da caixa simulada através da imposição de condições de contorno periódicas (PBC).

O artigo de Klauda et al. destaca que a constante de difusão lateral de lipídios varia significativamente com o tamanho do sistema simulado, mostrando um efeito de tamanho finito dramático que afeta a correlação de difusão entre os lipídios. Portanto, a escolha do tamanho da membrana simulada é crucial para evitar artefatos e garantir que as propriedades dinâmicas e estruturais observadas sejam representativas de sistemas reais, justificando a necessidade de simulações em maior escala e refinamentos nos métodos.

Metodologia

Um peptídeo foi construído utilizando o programa Pymol com base em uma sequência de aminoácidos: seis alaninas (A) e uma molécula de histidina (H) com estrutura de β-folha, com terminação zwitteriônica $-NH_3^{1+}$ e $-COO^{1-}$ mapeada pelo campo de força CHARMM36. Assim, utilizando as ferramentas do Gromacs, foi construído um dímero usando dois monômeros A_6H, um invertido em relação ao outro, como mostrado na Figura 1. Este dímero foi então replicado 10:10 vezes nos eixos x e y, formando a estrutura de nanomembrana de β-folha A_6H (referida aqui como A_6H-11). O sistema então foi solvatado.

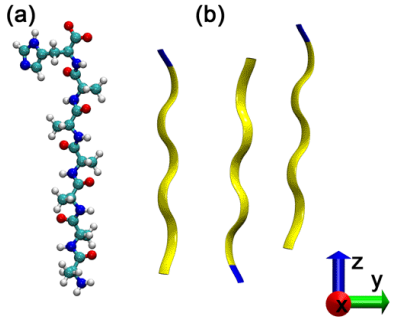


Figura 1: (a) Monômero representado por átomos e imagens em fita. (b) Dímero de dois peptídeos A6H formados por alanina (A) e histidina (H).

O modelo de nanomembrana A6H-11, solvatado, foi simulado sequencialmente alternando entre os conjuntos termodinâmicos NPT e NVT a cada 2 ns. Novos modelos foram criados com base na configuração equilibrada da A_6H-11, variando o número de réplicas ao longo dos eixos x e y. Os modelos A_6H-12, A_6H-13, A_6H-22, A_6H-23 e A_6H-33 apresentam diferentes dimensões, permitindo comparar a estrutura A_6H-11 com a região central do A_6H-33 para avaliar o impacto das PBCs. A Figura 2 ilustra essas configurações iniciais.

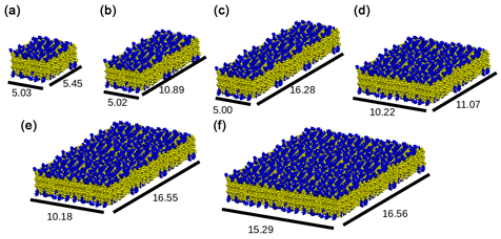


Figura 2: Estruturas iniciais das nanomembranas de peptídeos (dimensão da caixa em x e y em nm). (a) A_6H-11; (b) A_6H-12; (c) A_6H-13; (d) A_6H-22; (e) A_6H-23; e (f) A_6H-33. Amarelo representa alanina e azul representa histidina.

Todos os novos modelos são submetidos a uma nova sequência de simulações MD-NPT e MD-NVT e após confirmar que todos os sistemas estão em equilíbrio termodinâmico, uma nova fase de produção MD-NPT é realizada, onde os sistemas são simulados por 100 ns.

Resultados e Discussão

Energia de Coulomb e de van der Waals

As energias de interação entre os resíduos não apresentam grande variação, porém nossos resultados também mostram que a interação E_C(Ala-água) varia entre -2,3% e 3,8% ao comparar o Modelo A_6H-11 com os Modelos A_6H-12 e A_6H-33, indicando que o tamanho da membrana influencia essa interação. A interação coulombiana entre histidina e água é crucial para as características hidrofílicas/hidrofóbicas da superfície da membrana, aumentando com a área da membrana. A E_C para histidina-água pode subir até 2,5% ou descer até 5% dependendo do modelo comparado.

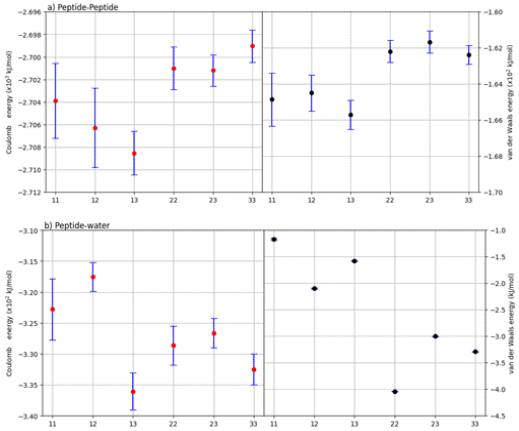


Figura 3: Média da energia coulombiana em vermelho e média da energia de van der Waals em preto.

Isso indica uma conclusão clara de que, energeticamente, a membrana não exibe uma modificação global nos valores de E_C ou E_{VDW}. No entanto, os resultados sugerem que a energia de interação entre o resíduo e a água pode ter interpretações distintas quando uma superfície de membrana maior é considerada no processo de simulação. Ressaltamos que esses resultados para energias vdW e Coulômbicas não invalidam os resultados anteriores obtidos para modelos menores de membrana, mas destacam que, energeticamente, a estimativa obtida com modelos menores pode ser satisfatória, dependendo do caso avaliado. Para uma melhor análise desse impacto, a seguir faremos uma comparação direta dos valores de energia de interação exclusivamente entre o A_6H-11 e o centro da membrana A_6H-33, que representa exatamente o mesmo grupo de peptídeos que o A_6H-11, mas livre das PBCs.

Comparamos a interação Coulômbica (EC) e a interação de van der Waals (EVDW) entre o modelo A_6H-11 (com área superficial menor) e um segmento correspondente no centro do modelo A_6H-33 (sem PBCs). O objetivo foi avaliar os efeitos das condições de contorno periódicas (PBCs) no A_6H-11 comparando com uma região central do A_6H-33, que representa a mesma estrutura sem PBCs. A região central do A_6H-33 é mais estável

comparada ao modelo A_6H-11, com interações mais intensas na simulação de membrana maior. Isso sugere que uma estrutura simulada com dimensões maiores pode representar melhor as características reais da membrana, enquanto modelos menores com PBCs podem não capturar detalhes específicos. Esses resultados destacam que, apesar das simulações menores fornecerem informações úteis, simulações em maiores dimensões oferecem uma visão mais precisa das propriedades da membrana.

Dinâmica das ligações de hidrogênio

Os resultados para o número de HBs mostram um valor médio consistente para o número de HBs/N, independentemente do tamanho do sistema estudado, indicando que, ao avaliar sistemas completos sob PBCs semelhantes, não há variação significativa no número médio de HBs. O valor da energia livre de Gibbs para a quebra das HBs converge para valores que mantêm uma diferença entre os resultados abaixo de 1 kJ/mol. No entanto, a vida útil das HBs entre peptídeos varia quando obtida para os sistemas de membrana menores e maiores.
A análise detalhada das HBs revela variações sutis nas interações Ala-água e Ala-His com o aumento da área da membrana. Além disso, a comparação entre o modelo A_6H-11 e a região central do modelo A_6H-33, que possuem o mesmo número de peptídeos simulados, mas com e sem restrições impostas pelas PBCs, respectivamente, destaca o impacto das PBCs na interpretação das propriedades médias e energéticas das HBs. Existem diferenças significativas nas características das HBs e na estabilidade estrutural, demonstrando uma diferença significativa na duração dessas interações, o que pode afetar a interpretação e avaliação da estabilidade e robustez do material, impactando diretamente sua aplicação. Assim, essas análises energéticas e dinâmicas das HBs enfatizam a importância de considerar o tamanho da membrana na interpretação dos resultados.

Gráfico de Ramachandran e MSD

A análise dos gráficos de Ramachandran e do Coeficiente de Difusão Lateral de Einstein forneceu informações valiosas sobre a mobilidade e o comportamento estrutural dos peptídeos nos sistemas estudados. Observou-se que o modelo menor exibe menos flexibilidade do que o previsto para o modelo central quando simulado livre de PBCs. Assim, nosso estudo compara um sistema de peptídeos de tamanho convencional com um sistema maior, investigando o impacto das PBCs, que são menos pronunciadas na parte central da estrutura da membrana na simulação com o maior caixa.

Conclusão

Os resultados mostram que as interações eletrostáticas não variam significativamente com o tamanho da membrana, mas as interações de van der Waals, especialmente entre alanina e água, são influenciadas pelo tamanho da membrana. A análise das ligações de hidrogênio revela diferenças significativas entre modelos com e sem PBCs, afetando a estabilidade e robustez do material. Esses achados destacam a importância de considerar o tamanho da membrana na simulação para obter uma representação mais precisa das propriedades e dinâmicas dos sistemas auto-organizáveis.

Acknowledgements

Agradecemos ao CNPq, CAPES e LaMCAD/UFG.

References

1. Andrade, D.; Oliveira, L. B. A.; Colherinhas, G. J. Mol. Liq. 2020, 302, 112610.

2. Klauda, J. B.; Brooks, B. R.; Pastor, R. W. J. Chem. Phys

3. Luzar, A.; Chandler, D. Nature 1996, 379, 55–57

Molecular Analysis of the Selective Inhibition of the Stress-inducible human Heat Shock Protein 70 (Hsp70) Performed by the Allosteric Inhibitor VER-155008

Maria Carolina Barbosa da Silva[1], Carlos Gefferson Silva Falabelo[2], Elvis Santos Leonardo[3], Fábio Rogério dos Santos[2], Claudir Oliveira[2], Kauê Santana da Costa[4,*], Paulo Sergio Taube Junior[4]

[1]Laboratório de Simulação Computacional e Educação Científica, Programa de Pós-Graduação de Biociências - Universidade Federal do Oeste do Pará

[2] Laboratório de Simulação Computacional e Educação Científica, Instituto de Ciências da Educação, Universidade Federal do Oeste do Pará

[3]Laboratório de Simulação Computacional e Educação Científica, Programa de Pós-graduação em Genética, Conservação e Biologia Evolutiva - Instituto Nacional de Pesquisa da Amazônia.

[4]Laboratório de Simulação Computacional e Educação Científica Instituto de Biodiversidade e Florestas - Universidade Federal Do Oeste do Pará

* Corresponding author*: kaue.costa@ufopa.edu.br*

Keywords: Hsp70, cancer cells, allosteric inhibitor, binding affinity, computational methods

Abstract

The stress-inducible human heat shock protein 70 (Hsp70) plays a crucial role in supporting the survival and proliferation of cancer cells, which are marked by rapid growth and genomic instability. Cancer cells often increase Hsp70 expression to manage this stress, utilizing these chaperones to ensure the correct folding of key oncogenic proteins. Hsp70 is recognized as a cutting-edge target for developing new anticancer drugs. However, targeting Hsp70 has proven highly challenging. The compound VER-155008 functions as an allosteric inhibitor of the ATP binding site on Hsp70. Moreover, the molecular details of how these inhibitors bind and the subsequent allosteric conformational changes in Hsp70 remain unexplored. This study aims to use computational methods to investigate the selectivity and binding affinity of these compounds, as well as the allosteric conformational changes occurring in Hsp70. We have elucidated the binding affinity and conformational changes induced by VER-155008 in Hsp70 through advanced computational methods, including molecular docking and molecular dynamics simulations. Our findings suggest that the inhibitor stabilizes Hsp70 in a half-open conformation, forming two hydrogen bond interactions with the residues Arg340 and Asp364, thus effectively disrupting the ATPase activity of the protein and impairing its chaperone's function.

Introduction

The stress-inducible human heat shock protein 70 (Hsp70, also known as Hsp72 or HspA1A) is a promising target for cancer therapy due to its critical roles in cellular protection and protein folding. Hsp70, a highly conserved molecular chaperone, assists in protein folding, prevents aggregation, and supports cell survival under stress conditions such as heat and oxidative stress. In cancer, Hsp70 helps cancer cells survive and proliferate amid rapid growth and genomic instability by maintaining the proper folding of oncogenic proteins. This reliance on Hsp70 in cancer cells has led to the development of new chemotherapy strategies targeting

Hsp70's activity or its protein-protein interaction network. Hsp70 has two functional domains: the nucleotide-binding domain (NBD) and the substrate-binding domain (SBD).

The NBD, which performs ATPase activity, is divided into two lobes, while the SBD is split into α and β subdomains. Despite various druggable sites being identified, targeting Hsp70 has proven challenging due to its constant ATP/ADP exchange at the NBD, which hinders the binding of potential inhibitors. Additionally, Hsp70's structural similarity to other family members, like Hsc70, complicates drug development. Few compounds have shown inhibitory activity against stress-inducible Hsp70, and the detailed molecular interactions and conformational changes induced by these inhibitors remain largely unexplored. VER-155008, a small molecule inhibitor, has been shown to bind to the nucleotide-binding site of Hsp70 and stabilize it in a half-open conformation, acting as an ATP-competitive inhibitor.

Computational Methods

The Hsp70-VER-155008 protein complex was obtained by X-ray crystallography (PDB ID: 4IO8, resolution: 2.58 Å). From this structure, the Hsp70 protein was separated from the ligand and modeled using the Swiss-Model web server, aiming to correct potential structural errors. The protein's protonation state was optimized at pH 7.0 using the PDB2PQR server. Molecular dynamics (MD) simulations of 50 ns were performed using the Amber22 software package for the Hsp70 protein in its apo form and in complex with the VER-155008 ligand. The initial structures for the simulations were prepared from the models obtained after modeling and protonation. The systems were solvated in a TIP3P water model and neutralized by adding a chloride ion.

The MD simulations included the following steps: energy minimization, gradual heating to 300 K, equilibration, and finally, production of the 50 ns of molecular dynamics. Analysis of the trajectories included the calculation of root mean square deviation (RMSD) to assess structural stability and root mean square fluctuation (RMSF) to identify flexible regions of the protein structure.

Results

Based on the analysis of residue interactions from the 50 ns molecular dynamics simulation, seven hydrogen bonds were identified using the Visual Molecular Dynamics (VMD)**.** We noted a hydrogen bond between Asp364 and Asn362 with a significant occupancy of 45.40%. This indicates a relatively stable interaction between these residues throughout the simulation. This interaction may be important for the stability of the protein structure or for protein-ligand interactions. We noted that a structural water molecule forms a hydrogen bond interaction with Gly337 (79.52%) showing a highest occupancy over the molecular dynamics simulation, which suggests that it plays a crucial role to the stability of the structure. A hydrogen bond between the side chain of Arg340 and Asp364 showed an occupancy of 53.28%. This interaction suggests a significant contribution to the structural stability of the protein, indicating that these residues may be involved in an important interaction for protein conformation. The observed hydrogen bonds provide insights into the structural stability of the protein and the potential contributions of specific residues and water molecules to this stability. High-occupancy interactions, such as those between the structural water and the residue Gly337, and Arg340 with Asp364, are particularly important and suggest that these residues play critical roles in maintaining the protein's structure.

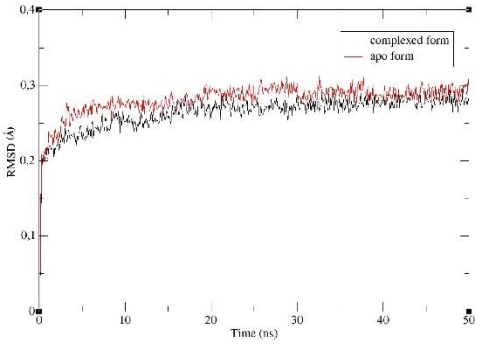


Figure 1: Comparison of structural stability of Hsp70 protein in its apo and ligand-bound forms. 50 ns MD simulation.

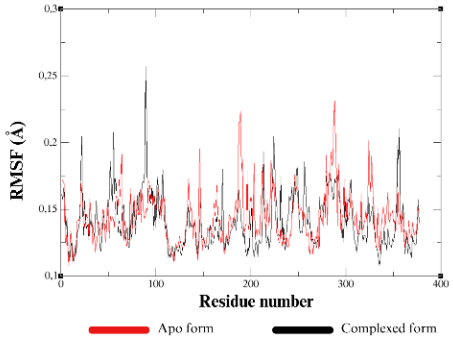


Figure 2: Molecular dynamics simulations identified specific regions of the Hsp70 that undergo changes in flexibility upon binding of the VER-155008.

Conclusion

This study highlights the potential of VER-155008 as a selective allosteric inhibitor of the human Heat Shock Protein 70 (Hsp70), a critical player in cancer cell survival and proliferation. We have elucidated the binding affinity and conformational changes induced by VER-155008 in Hsp70 through advanced computational methods, including molecular docking and molecular dynamics simulations. The findings suggest that the inhibitor stabilizes Hsp70 in a half-open conformation, effectively disrupting its ATPase activity and potentially impairing the chaperone's function in oncogenic protein folding.

The insights gained from this research offer new insights for the development of novel anticancer therapies targeting this essential protein. Future studies should focus on in vitro and in vivo evaluations of VER-155008's efficacy and its potential synergistic effects with existing chemotherapeutic agents. Overall, this work contributes to the growing body of knowledge aimed at exploiting Hsp70 as a therapeutic target in cancer treatment.

Acknowledgements

The authors are grateful to the *Pró-reitoria de Pesquisa, Pós-graduação e Inovação Tecnologica* (Proppit/Ufopa) and to the *Centro Tecnológico de Computação Científica Aplicada* for the access to the computational facilities of the Tapajós Supercomputer.

References

1. Howe, M. K.; Bodoor, K.; Carlson, D. A.; Hughes, P. F.; Alwarawrah, Y.; Loiselle, D. R.; Jaeger, A. M.; Darr, D. B.; Jordan, J. L.; Hunter, L. M.; Molzberger, E. T.; Gobillot, T. A.; Thiele, D. J.; Brodsky, J. L.; Spector, N. L.; Haystead, T. A. J. Identification of an Allosteric Small-Molecule Inhibitor Selective for the Inducible Form of Heat Shock Protein 70. Chem. Biol. 2014, 21 (12),1648–1659. https://doi.org/10.1016/j.chembiol.2014.10.016.
2. Howe, M. K., Speer, B. L., Hughes, P. F., Loiselle, D. R., Vasudevan, S., & Haystead, T. A. J. (2016). An inducible heat shock protein 70 small molecule inhibitor demonstrates anti-dengue virus activity, validating Hsp70 as a host antiviral target. *Antiviral Research*, 81, 81-82.
3. Zhang, P.; Leu, J. I. J.; Murphy, M. E.; George, D. L.; Marmorstein, R. Crystal Structure of the Stress-Inducible Human Heat Shock Protein 70 Substrate-Binding Domain in Complex with Peptide Substrate. PLoS One 2014, 9 (7), 1–11. https://doi.org/10.1371/journal.pone.0103518.
4. Murphy, M. E. The HSP70 Family and Cancer. Carcinogenesis 2013, 34 (6), 1181–1188. https://doi.org/10.1093/carcin/bgt111.

Hierarchical Clustering Algorithms Applied to the Evaluation of Afatinib Derivatives Modeled for the Inhibition of the BCR-ABL Enzyme

Kelvyn M.L. Rocha[1], Érica C.M. Nascimento[2], and João B.L. Martins[1,2].
[1]Departamento de Farmácia, Universidade de Brasília, Câmpus Universitário Darcy Ribeiro, Asa Norte, 70910-900, Brasília-DF, Brasil.
[2]Instituto de Química, Universidade de Brasília, Câmpus Universitário Darcy Ribeiro, Asa Norte, 70910-900, Brasília-DF, Brasil.
232100389@aluno.unb.br
Keywords: Hierarchical Clustering, Machine Learning, Afatinib, Chronic Myeloid Leukemia

Abstract
A Hierarchical Algorithm was applied to the evaluation of several afatinib derivatives aiming to identify groups and consistencies between these molecules and commercially available BCR-ABL inhibitors. Similarities were found regarding ponatinib, which was clustered together with one of the derivatives and approached several others, while imatinib remained a relatively isolated molecule.

Introduction
Chronic Myeloid Leukemia is a non-solid malign disease characterized by the uncontrolled proliferation of white blood cells of the myeloid lineage [1]. The pathological mechanism of this disease is heavily dependent on the mutant tyrosine-kinase enzyme BCR-ABL, which originates from the translocation of the 9th and 22nd pairs of chromosomes [2].
Given the oncogenesis capabilities of the BCR-ABL enzyme, its inhibition through the tyrosine-kinase inhibitors class of drugs is the main treatment strategy. This proved effective, with imatinib being the first successful molecule in this endeavor. However, the use of imatinib promotes the development of severe therapeutic resistance [3]. In this context, ponatinib emerged as the main effective alternative, but it is associated with serious cardiovascular adverse effects [4,5]. Thus, there is need for the design of new molecules capable of inhibiting the BCR-ABL enzyme and this may be achieved by the repurposing of other inhibitors, such as afatinib, through molecular modeling and rational design modifications [6].
These derivatives may be evaluated and compared to the commercially available molecules through many tools, including machine learning techniques such as hierarchical clustering algorithms, which allow for the detailed comparison of ligands using large sets of data (e.g.: electronic properties and molecular descriptors) [7].

Methodology
New afatinib derivatives were modeled using various strategies, such as bioisosterism, simplification, and regioisomerism. Then the Absorption, Distribution, Metabolism, Excretion (ADME) and electronic properties of these structures were obtained through the SwissADME [8] online tool and DFT calculations at B3LYP/6-311+G(d,p) level, respectively. Additionally, this data was used to determine the Pearson correlation index [9] of the designed ligands. The ADME and electronic properties as well as the correlation results were then compiled into two input matrices (A_{13x23} and A_{13x13}, respectivelly) that were subjected to the following hierarchical clustering algorithm:

Let $\boldsymbol{C_0} = \{\boldsymbol{1}, \cdots, \boldsymbol{n}\}$ be the set containing all objects and their indices and $C = \{C_0\}$ the set of all clusters and splinter groups found until the current iteration. Then, until $|C| = n$, the current cluster with largest diameter can be found through:

$$C_* = argmax_{C \in C}\ max_{i_1, i_2 \in C}\ \delta(i_1, i_2)$$

This new C_* cluster is used to obtain a new splinter group by finding the object $i^*$with most dissimilarity to the rest of the cluster, through the following equation:

$$i^* = argmax_{i \in C_*} \frac{1}{|C_*| - 1} \sum_{j \in \frac{C_*}{i}} \delta(i,j)$$

Then i^* can be removed from its original cluster and put into the new splinter group $C_{new} = \{i^*\}$. This operation must be repeated until C_* is empty, with objects migrating to C_{new}. This migration must be performed considering dissimilarity to both the splinter group and C_*, according to:

$$i^* = argmax_{i \in C} D(i)$$

With the definition of $D(i)$ being:

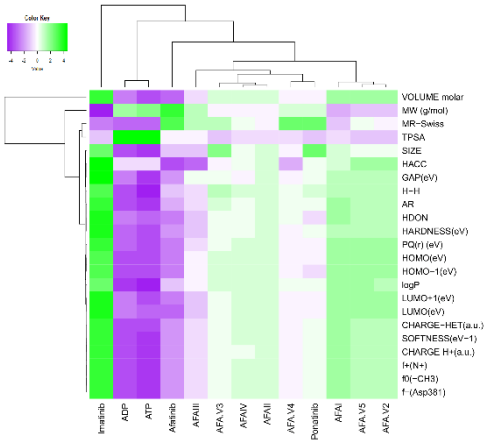
$$D(i) = \frac{1}{|C_*| - 1} \sum_{j \in \frac{C_*}{i}} \delta(i,j) - \frac{1}{|C_{new}|} \sum_{j \in C_{new}} \delta(i,j)$$

The iterations stop when $D(i^*) < 0$, with the migration of i^* and addition of C_{new} to C after each step. All these operations were done using the R programming language and necessary libraries (*ggplot2* and *stats*). ATP and ADP were also included in these calculations, serving as reporter molecules to validate the clustering algorithm. The results were outputted as clustering heatmaps with relevant dendrograms for visualization.

Results

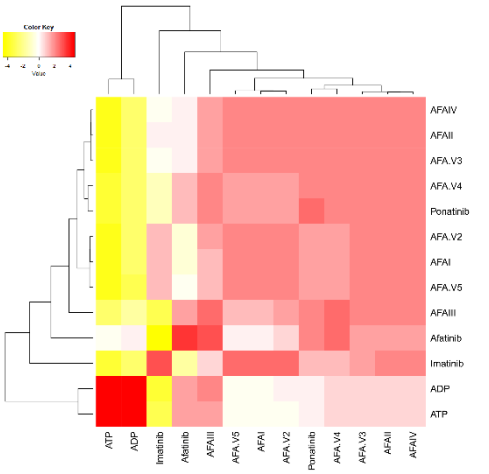
Figures 1 and 2 show the clustering heatmaps of the studied properties and the correlation between the ligands. The first important observation is that, in both cases, the ADP and ATP molecules are organized in the same cluster, indicating successful validation of the clustering algorithm used. Afatinib was shown to be closely related to ATP and ADP, while imatinib was shown to be a relatively isolated molecule. Of the designed molecules, AFA.V4 was clustered with ponatinib due to their similar physicochemical properties, which can be observed through their color palettes. Another cluster, closely related to that of ponatinib, was formed with AFA(I), AFA.V5, and AFA.V2

Figure 1. Clustering heatmap of the studied molecules and their properties.



The correlation hierarchical heatmap mimics the disposition of Figure 1. ADP and ATP were clustered together, while ponatinib again approached AFA.V4, consistent with what was observed in Figure 1. A high correlation was observed homogeneously in most pairings of the modeled molecules, which is to be expected since these structures were obtained through small modifications

Figure 2. Clustering heatmaps showing the studied molecules and their correlation levels.



Conclusions

The hierarchical clustering algorithm used in this study was able to discern a pattern between several different molecules, using two arbitrary sets of data. The clusters observed may point to adequate replacements for imatinib and ponatinib. Refinement of these results may be achieved through the use of other algorithms, such as PCA, aiming to eliminate noisy or unnecessary descriptors while providing maximum variance. These first findings suggest that the algorithm should be able to evaluate larger sets of molecules and data competently, implementing proper machine learning models to the study of the current and future BCR-ABL inhibitors.

Acknowledgements

The authors wish to thank the University of Brasília, FAPDF, CNPq, and CAPES

References

1. Sawyers, C.L. Chronic Myeloid Leukemia. *N. Engl. J. Med.* **1999**, *340*, 1330–1340.
2. Kang, Z.J.; Liu, Y.F.; Xu, L.Z.; Long, Z.J.; Huang, D.; Yang, Y.; Liu, B.; Feng, J.X.; Pan, Y.J.; Yan, J.S.; et al. The Philadelphia Chromosome in Leukemogenesis. *Chin. J. Cancer* **2016**, *35*, 48, doi:10.1186/S40880-016-0108-0.
3. Claudiani, S et al. The Argument for Using Imatinib in CML. *Hematol. Am. Soc. Hematol. Educ. Progr.* **2018**, *2018*, 161–167, doi:10.1182/ASHEDUCATION-2018.1.161.
4. O'Hare, T.; Shakespeare, W.C.; Zhu, X.; Eide, C.A.; Rivera, V.M.; Wang, F.; Adrian, L.T.; Zhou, T.; Huang, W.S.; Xu, Q.; et al. AP24534, a Pan-BCR-ABL Inhibitor for Chronic Myeloid Leukemia, Potently Inhibits the T315I Mutant and Overcomes Mutation-Based Resistance. *Cancer Cell* **2009**, *16*, 401–412, doi:10.1016/j.ccr.2009.09.028.
5. Massaro, F.; Molica, M.; Breccia, M. Ponatinib: A Review of Efficacy and Safety. *Curr. Cancer Drug Targets* **2018**, *18*, 847–856, doi:10.2174/1568009617666171002142659.
6. Rocha, K.M.L.; Nascimento, É.C.M.; Martins, J.B.L. Investigation on the Interaction Behavior of Afatinib, Dasatinib, and Imatinib Docked to the BCR-ABL Protein. *J. Mol. Model.* **2021**, *27*, doi:10.1007/S00894-021-04925-8.
7. Kaufman, L.; Rousseeuw, P. Divisive Analysis (Program DIANA). In *Finding Groups in Data: An Introduction to Cluster Analysis*; Wiley, 1990; pp. 253–279 ISBN 978-0-470-31748-8.
8. Daina, A.; Michielin, O.; Zoete, V. SwissADME: A Free Web Tool to Evaluate Pharmacokinetics, Drug-Likeness and Medicinal Chemistry Friendliness of Small Molecules. *Sci. Reports 2017 71* **2017**, *7*, 1–13, doi:10.1038/srep42717.
9. Schober, P.; Schwarte, L.A. Correlation Coefficients: Appropriate Use and Interpretation. *Anesth. Analg.* **2018**, *126*, 1763–1768, doi:10.1213/ANE.0000000000002864.

Enhancing Exciton Transport in Organic Optoelectronics through Energetic Disorder Analysis

Larissa S. Born[1], Leonardo E. Sousa[2], and Pedro Henrique O. Neto[1,3]
[1]Institute of Physics, University of Brasília, 70919- 970 Brasília, Brazil.
[2]Department of Energy Conversion and Storage, Technical University of Denmark, Anker Engelunds Vej 301, 2800 Kongens Lyngby, Denmark.
[3]International Center of Physics, University of Brasília, 70919- 970 Brasília, Brazil.
bornfis22@gmail.com
Keywords: dynamic disorder, static disorder, exciton diffusion, organic optoelectronic devices.

Abstract

Exciton transport in organic materials can be affected by different types of energetic disorder. By combining electronic structure calculations and kinetic Monte Carlo simulations, we investigate the effects of static and dynamic disorders on exciton diffusion in AlQ_3 thin films. Our findings highlight that higher static disorder regimes raise energy barriers, hindering transport, while the presence of dynamic disorder mitigates these barriers, enhancing energy transport. This study underscores the importance of considering both disorder types for optimizing organic optoelectronic devices.

Introduction

Singlet exciton diffusion is essential for the performance of organic optoelectronic devices, such as OLEDs and solar cells [1]. Effective energy transfer influences OLED color saturation and the efficiency of photogeneration in solar cells and photodetectors. The Förster mechanism largely governs energy transport in these devices, with exciton hopping rates affected by energy level alignment at individual sites. Energetic disorders, due to molecular arrangements and vibrations, can either hinder or enhance energy transfer [2]. Assessing these effects is crucial for evaluating energy transfer properties.

Traditional methods for estimating photophysical properties, such as the Franck-Condon approximation, are unsuitable for organic molecules that undergo significant geometric changes upon excitation [3]. The nuclear ensemble method (NEM) provides an alternative by accounting for vibronic effects. NEM calculates transition moments for various displaced geometries, reflecting the impact of exciton coupling on intramolecular motion.

Static energetic disorder, caused by intermolecular interactions, and dynamic disorder, linked to molecular vibrations, both significantly influence energy transport [4]. Experimental studies on AlQ3 thin films show that increasing temperature reduces photoluminescence lifetime and energy while enhancing energy transport, suggesting that dynamic disorder can improve energy transfer even in the presence of static disorder.

This work investigates the effects of static and dynamic disorder in AlQ3 thin films. Using the NEM, we estimate absorption and emission ensembles to assess relevant quantities across different nuclear conformations. Exciton dynamics are simulated using a Kinetic Monte Carlo (KMC) algorithm. Our results indicate that dynamic disorder enhances exciton kinetic properties, while higher levels of static disorder hinder them. These findings highlight the importance of considering different types of disorder in the study of exciton diffusion properties.

Methodology

We conducted electronic structure calculations of the S0 and S1 states for the AlQ3 molecule using DFT and TD-DFT with the ωB97X-D functional and a 6-31G(d,p) basis set in Gaussian 16. The range separation parameter was non-empirically tuned to $\omega = 0.1564$ bohr^{-1}. The PCM model was used for geometry

optimization and normal mode analyses, with a dielectric constant of ε = 3.11 and a refractive index of 1.77.

Photophysical properties were estimated using the protocol described in reference [3], estimating absorption and fluorescence spectra at 75 K and 300 K with ensembles of 500 geometries. This protocol can be interpreted as averaging over a molecule's excited state lifetime, where it adopts several geometries before transitioning to another state. For this interpretation to hold, the transition rate between geometries must be infinite; otherwise, the process isn't ergodic, and ensemble and time averages cannot be equated. Thus, the ensemble approach yields rate estimates in the adiabatic approximation.

A non-adiabatic rate k_{nad} corresponds to the frequency with which a molecule in a particular geometry switch to a different one. If k_{nad}=0, the molecule's photophysical properties are fixed. When k_{nad} approaches infinity, geometric changes become instantaneous, returning to the adiabatic limit.

KMC simulations were performed using the Xcharge software [5]. These simulations allow excitons to jump between neighboring sites via the FRET mechanism, fluoresce via a fluorescence decay rate, or undergo a non-adiabatic rate transition. We estimated the FRET rates following the procedure outlined in reference [6]. In the KMC algorithm, dynamic disorder was considered through the non-adiabatic rate, and static disorder was modeled by sampling energy values E_{st} from a Gaussian distribution centered at zero with a standard deviation σ_{st}. This distribution encompasses all the energies in the corresponding ensemble.

Results and Discussion

Figure 1(a) shows the absorption and emission spectra of the AlQ3 molecule at 300K obtained from the NEM. In Figure 1(b), the Förster radius distribution for the geometry pairs of the absorption and emission ensembles is presented. The dashed line indicates the Förster radius calculated from Figure 1(a). The distribution reveals that there are Förster radii larger than those calculated in Figure 1(a).

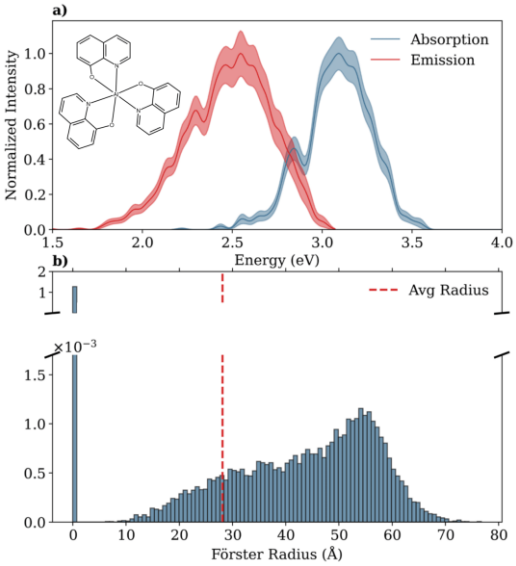


Figure 1 – Photophysical proprieties of AlQ3 systems simulated by NEM.

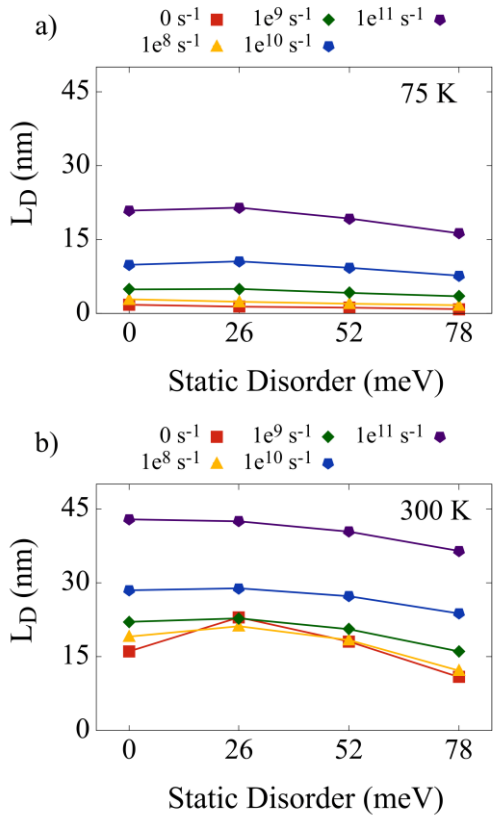


Figure 2 – Diffusion length of AlQ3 as a function of static disorder for different dynamic disorder regimes for ensemble in 75K (figure a) and 300K (figure b).

Figure 2 illustrates the variation of the diffusion length as a function of static disorder for different regimes of dynamic disorder at temperatures of 75 K (Figure 2a) and 300 K (Figure 2b). The results indicate that the diffusion length can increase with static disorder, regardless of the dynamic disorder regime. However, for higher levels of static disorder, the diffusion length decreases. In all regimes of static disorder, an increase in dynamic disorder favors the diffusion length.

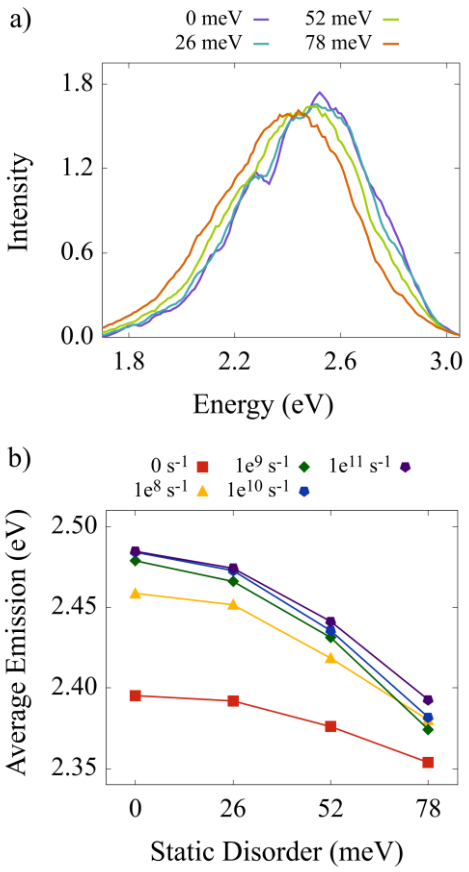


Figure 3 – Figure a presents emission spectra for different static disorders and figure b presents average energy emission as a function of static disorder for different dynamic disorder regimes.

Figure 3(a) presents the emission spectrum obtained from the KMC simulations for different regimes of dynamic disorder for the 300K ensembles. It is possible to observe a redshift of the absorption peak as the static disorder increases. Figure 3(b) shows the average exciton emission from the simulations as a function of static disorder for different regimes of dynamic disorder. Our results demonstrate that dynamic disorder increases the average exciton emission energy, while an increase in static disorder decreases it. This suggests that increased static disorder raises the energy barriers between sites, hindering energy transport. In contrast, dynamic disorder mitigates these energy barriers through vibrational effects, thereby favoring energy transport.

Conclusion

In this study, we investigated the impact of static and dynamic disorder on exciton diffusion in AlQ_3 thin films using electronic structure calculations and kinetic Monte Carlo simulations. We found that static disorder generally impedes energy transport by raising energy barriers, while dynamic disorder enhances it by mitigating these barriers through vibrational effects. Our results highlight the importance of considering both types of disorder to accurately assess exciton diffusion properties, which is crucial for optimizing the performance of organic optoelectronic devices like OLEDs and solar cells.

Acknowledgements

This work was supported by the financial support from Brazilian Research Councils CNPq, CAPES, and FAPDF.

References

1. Ma, D. Aggregation-Induced Emission, 2021, 171.
2. de Silva P. and Van Voorhis, T. The journal of physical chemistry letters, 2018, 9, 1329.
3. De Sousa, L.; De Silva, P. The Journal of Physical Chemistry A, 2023, 127, 8200.
4. Rebentrost, P., Mohseni, M., & Aspuru-Guzik, A. (2009). The Journal of Physical Chemistry B, 2009, 113, 9942.
5. https://github.com/LeonardoESousa/xcharge
6. de Sousa, L., Bueno, F., and Silva, G., da Silva Filho, D. and Neto, P. H. (2019). Journal of Materials Chemistry C, 2019, 7, 4066.

Structural and Photocatalytic Characterization of g-C_3N_4 Conformers.

Letícia C. S. Faria[1], Francisco, B. C. Machado[1], A. J. A. Aquino[2], Hans Lischka[3], Leonardo T. Ueno[1], Luiz F. A. Ferrão[1].
[1] Departamento de Química, Instituto Tecnológico de Aeronáutica, Brasil.
[2]Departament of Mechanical Engineering, Texas Tech University, Lubbock, TX, EUA.
[3]Departament of Chemistry and Biochemistry, Texas Tech University, Lubbock, TX, EUA.
leticiacarolaine@ita.br
Keywords: Photocatalysis, g-C3N4, Solar water Splitting, Charge Analysis, thermodynamics Bandgap criteria.

Abstract
Photocatalysis offers a promising approach for converting solar energy into storable fuels, such as hydrogen generated through solar water splitting, which is essential for CO_2 reduction. In this study, we investigated several nitrogen-containing molecules based on or related to the graphitic carbon nitride (g-C_3N_4), a catalyst known for its visible light activity, low cost, and layered structure. We also evaluated 10 different conformations of g-C_3N_4 to assess their suitability for H_2O and CO_2 reduction based on thermodynamic bandgap criteria. To characterize these systems, we used the ionization energy calculations (M06/DEF2-SV(P)), excitation energy (TDDFT//M06/DEF2-SV(P)), natural population analysis (NPA) charges, and charge transfer analysis in the S_1 state. The results indicated that heptazine has the lowest excitation energy (2.98 eV), falling within the visible spectrum, while urea has the highest excitation energy (6.78 eV), meeting the thermodynamic criteria for CO_2 reduction. Additionally, five systems show minimal variation in their properties, suggesting that they function as building blocks of g-C_3N_4.

Introduction
Photocatalysis presents a promising mechanism for converting solar energy into storable fuels, with solar water splitting being particularly notable for producing hydrogen, a critical step for CO_2 reduction. In recent years, novel organic photocatalysts have gained significant attention due to their use of π-conjugated aromatic compounds, which enable the development of diverse photocatalytic materials [1, 2]. Graphitic carbon nitride (g-C_3N_4), a polymeric semiconductor, has emerged as a highly sought-after material in photocatalysis due to its visible light activity, easy accessibility, low cost, chemical stability, and distinctive layered structure. These materials can adopt different stoichiometries and incorporate various dopants. In this study, we investigated 10 different conformations of g-C_3N_4 and analyze their physicochemical properties to determine if these structures meet the key criteria for H_2O and CO_2 reduction in photocatalysis. The fundamental pillars of photocatalysis are light absorption, charge separation, adsorption, oxidation-reduction, and the final product after desorption [1]. Below, we will explore each of these in detail

- Light Absorption: Structures that absorb light within the visible spectrum are particularly desirable, as these photocatalysts are more effective at harnessing solar energy.
- Charge Separation: This involves the separation of photoinduced charge carriers, specifically electrons from the conduction band minimum (CBM) and valence band maximum (VBM) [1, 2].
- Absorption of the target structure: The photocatalyst must exhibit weak interactions with reduction targets, such as H_2O and CO_2, in the excited state S_1, where the chemical reaction occurs according to Kasha's rule [1].
- Oxidation-reduction reactions: These are surface redox reactions in which

photoinduced electrons and holes drive different half-reactions independently.

• Desorption of the Product: For the reaction to proceed effectively, the edge of the conduction band minimum (CBM) must be more negative than the reduction potential of CO_2/ H_2O while the edge of the valence band maximum (VBM) must be more positive than the oxidation potential of water [1]. In this study, we will focus on two of these critical aspects: the thermodynamic criteria of these conformers and their charge transfer (CT) analyses.

Methodology

The g-C_3N_4 has basic melamine and melem structures that lead to various structural arrangements. Below is a list of the conformers investigated in this work: a) melamine ($C_3H_6N_6$) this structure serves as a precursor for the synthesis of g-C_3N_4; b) melam ($C_6H_6N_{11}$), a dimer of melamine; c) tri-melamine ($C_9H_9N_{15}$); d) triazine ($C_{12}H_{12}N_{20}$) defined by a quadruple arrangement of melamine and its derivative poly-triazine imide (PTI) ; e) poly-triazine imide (PTI) ($C_{18}H_{18}N_{30}$); f) melem ($C_6H_6N_{10}$); g) polymeric form of g-C_3N_4, a cutout of the polymeric structure of g-C_3N_4 structure ($C_{18}H_8N_{27}$); h) g-C_3N_4 heptazine ($C_6H_3N_7$); i) oxygen-doped urea (CN_2O); j) cyanamide (CH_2N_2) [3, 4]:

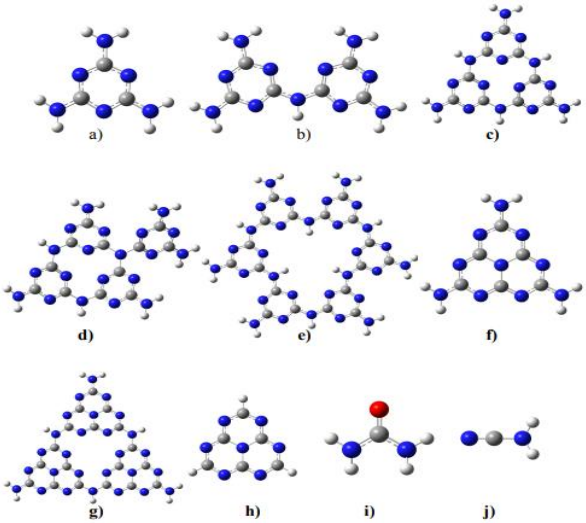


Figure 1: Representation of the different g-C_3N_4 conformers studied in this work.

For all structures, we calculated the ionization energy (difference between the neutral and cationic structure) using M06/DEF2-SV(P), and the first singlet excited state using TDDFT//M06/DEF2-SV(P). The electronic structure calculations were carried out using Gaussian G09 [7]. Charge analyses were performed using the TheoDORE [5, 6], which divides the molecule in fragments, allowing for the determination of charge transfer in S_1 for each fragment. Additionally, NPA calculations were employed to further evaluate the charge distribution.

Results and Discussion

We first calculated the ionization potential (blue bars – Fig. 2) and the energy of the first singlet excited state (orange bars – Fig 2) for each structures using the aforementioned methodology. These calculations provide the electronic structures energies for the studied conformers analogous to the band structures of g-C_3N_4. These energies can be examined in terms of the absolute energy scale, as well as the redox potentials for CO_2/CO, H_2O /OH $^{\cdot}$+H^+, H^+/H_2 and H_2O /O_2 . Such analyses offer insights into the thermodynamic driving force required for the reduction of water and CO_2. In Fig. 2 we present the results on both energy vs. vacuum and potential vs. SHE (Standard Hydrogen Electrode) scales, correlating the theoretical values with the experimental (SHE) values reported in the literature [2]. See below:

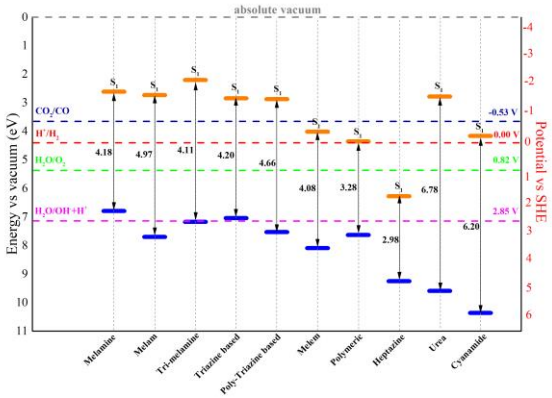


Figure 2: Graph of the thermodynamic criteria for each basic conformer of the g-C_3N_4 structure. The orange bars represent the energy S_1, and the blue bars represent the ionization energy.

Fig. 2 shows that heptazine exhibits the lowest excitation energy (2.98 eV), while

urea shows the highest excitation energy (6.78 eV), meeting the thermodynamic reduction criteria for all the reductions reported here. Interestingly, the excitation energies of the first five compounds (a-e) show minimal variation, suggesting that these compounds serve as fundamental building blocks of g-C_3N_4. This implies that enlarging the structure as seen from the melamine to poly-triazine variations, results in slight changes in the analyzed physicochemical properties. Fig. 3 presents the HOMO and LUMO intrinsic bonding orbitals for each fragment. These orbitals were calculated using the PBE functional and the def2-SV(P) basis set in the IboView program [8].

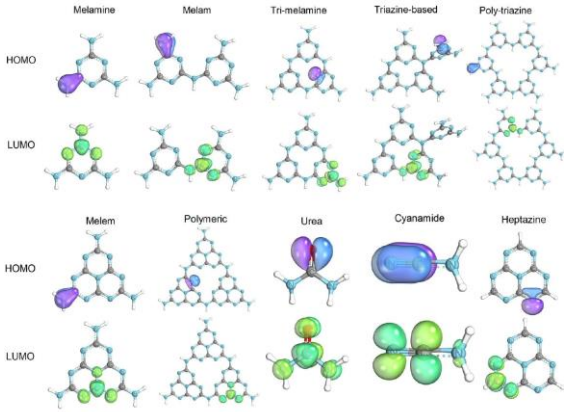


Figure 3: HOMO and LUMO orbitals for each of the fragments studied here using IboView//PBE//DEF2-SV(P).

Next, we analyze the charge transfers in S_1 using two different e (Fig. 4). The first diagram, shown in blue, displays the S_1 values calculated with TDDFT/M06/DEF2-SVP, as previously described. The second diagram, presented in red, lists the charge transfer values for each structure obtained from the TheoDORE program. The third diagram provides the NPA results for each atom in S_1, calculated using the M06/DEF2-SV(P) methodology. This analysis offers a charge distribution within the molecule, with atoms depicted in different colors: intense green indicates positive charges, intense red colors signify negative charges, and neutral colors represent neutral atoms There is no Table to refer here.

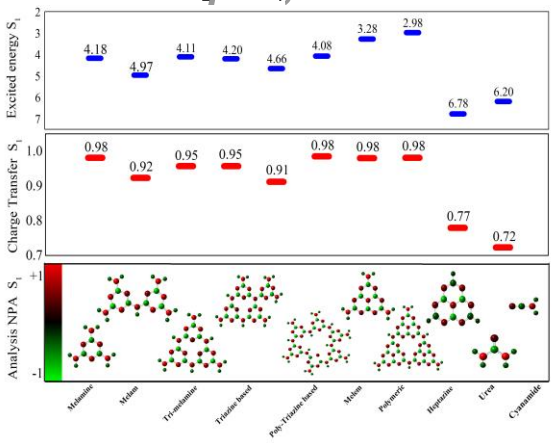


Figure 4: Charge transfers in S_1 for each structure related to energy S_1.

Conclusion:

The results indicate that heptazine exhibits the lowest excitation energy, while urea has the highest excitation energy, meeting the thermodynamic criteria for reduction. The first five conformations displayed minimal variation in the analyzed properties, suggesting that they function as building blocks with similar characteristics. Overall, these findings suggest that g-C_3N_4, regardless of the specific conformation, maintains strong photocatalytic properties according to the thermodynamic criteria, making it a promising candidate for applications in water splitting and CO_2 reduction.

Acknowledgements

CAPES, CNPQ, FAPESP.

References

1 LAGHAEI, Milad et al. Journal of Materials Chemistry A, 2023, 11, 23.
2 LU, Chengwei et al. Journal of Colloid and Interface Science, 2024, 668.
Varma, R. S.; Singh, A. P.; J. Indian Chem. Soc. 1990, 67, 518.
3 YI, Yuhui et al. RSC advances, 2022, 12.
4 MA, Dandan et al. Coordination Chemistry Reviews, 2024, 500.
5 PLASSER, Felix. The Journal of chemical physics, 2020, 152, 8.
6 PLASSER, Felix, et al. Journal of chemical theory and computation, 2012, 8, n. 8.
7 FRISCH, A. Wallingford, 2009. USA, 25, 470.
8 KNIZIA, Gerald. 2013, 9, 11.

Desenvolvimento de NEQs para inibição da agregação β-amilóide

Letícia de Almeida Nascimento[1], Érica Cristina Moreno do Nascimento, João Batista Lopes Martins
[1]Laboratório de Química Computacional, Instituto de Química, Universidade de Brasília, CP 4478, Brasília-DF, Brasil.
leticiaalm2000@gmail.com.
Keywords: Alzheimer; β-amilóide; docking molecular; canabinóides; *in silico*

Abstract

This study used electronic structure combined with in silico simulations for the rational design of new chemical entities with the aim of proposing new candidate molecules for inhibiting the aggregation of β-amyloid protofilaments related to the development of neurodegenerative diseases.

Introdução

A doença de Alzheimer é a causa mais comum de demência. Configura-se como uma doença neurodegenerativa progressiva marcada por sintomas como problemas de memória, linguagem e pensamento.[1]

A DA se apresenta com marcadores patológicos, o acúmulo de placas da proteína β-amilóide, supressão dos níveis colinérgicos de acetilcolina, hiperfosforilação da proteína Tau e a formação de emaranhados neurofibrilares no meio sináptico.[2]

Ao longo dos tempos, novas forma terapêuticas foram estudadas visando encontrar ligantes que atuem em diversos alvos farmacológicos associados a DA.[3] O uso de moléculas que apresentam ação neuroprotetora[4] também se faz presente, como é o caso da utilização dos fitoterápicos como os canabinóides, moléculas as quais estão presentes na planta *Cannabis Sativa*.[5]

A modulação do sistema endocanibinóide emergiu como uma estratégia potencialmente atraente para o tratamento da DA, visto que últimas descobertas em modelos de roedores com DA mostraram efeitos promissores do uso dos canabinóides na redução da deposição de placas amilóides e na estimulação da neurogênese do hipocampo.[6]

Logo, o Δ^9-tetrahidrocanabinol (THC) é, dentre todos os fitocanabinóides presentes no vegetal, responsável pelos principais efeitos farmacológicos causados pelo consumo de planta, tanto pela ação psicotrópica do uso recreativo, quanto pelos benefícios medicinais.[5]

Sendo assim, este trabalho visa colaborar com a busca de novas alternativas terapêuticas multialvos para o tratamento da Doença de Alzheimer. Desta forma, foram desenhadas novas entidades químicas por meio de metodologias computacionais *in sílico* de heterodímeros com a proteína alvo β-amilóide (Aβ 1- 42, com código 2BEG).

Metodologia

A partir das estruturas precursoras Δ^9-tetrahidrocanabinol (THC) e 9-amino-1,2,3,4-tetrahidroacridina (THA) foram modeladas novas entidades químicas (NEQ) heterodiméricas por meio da técnica de isosterismo usando os softwares ChemDraw Ultra[7] e Gaussview.[8] Foram gerados os heterodímeros THC0, THC1, THC2, THC3 e THC4.

As conformações obtidas em uma primeira otimização aplicando o campo molecular MM2, foram posteriormente submetidas a uma nova otimização de geometria, cálculo de frequências e modos vibracionais por meio do método DFT com o funcional B3LYP e função de base 6-311+G(d,p) aplicando o modelo de solvatação implícita

SMD através do pacote computacional Gaussian09.[9].

A caracterização dos parâmetros de absorção, distribuição, metabolismo, excreção e toxicidade (ADMET), foram conduzidos para todas as moléculas, por meio do software ADMETlab 3.0.[10] A fim de analisar as propriedades eletrônicas e conformacionais das moléculas postuladas, foi realizado estudo das interações não-covalentes por meio de estudos de NCI e ELF usando o programa Multiwfn.[11]

Colaborando com o intuito de determinar as interações intermoleculares presentes entre os resíduos componentes dos protofilamentos de Aβ (1-42) e os ligantes estudados, um estudo de docking molecular foi conduzido com o algoritmo AutoDock 4.2.6[12], por meio do pacote AutoDock Tools[12] e os seus resultados foram analisados através do software de visualização Discovery Studio Visualizer.[13] O estudo de docking foi no modo rígido/rígido, no qual as estruturas das enzimas e dos ligantes foram definidas de forma rígida, e do tipo rígido/flexível no qual algumas ligações das estruturas das NEQ, especificamente na região de conexão entre os monômeros foram deixadas sem restrições de movimento.

Resultados e Discussão

Os parâmetros obtidos da absorção, distribuição, metabolismo, excreção e toxicidade dos ligantes, mostraram que, em sua totalidade nenhuma molécula apresentou qualquer índice de tumorigenicidade ou mutagenicidade, sugerindo de maneira teórica, satisfatória biossegurança. Por sua vez, ressalta-se que apenas o composto THC4 apresentou alta absorção gastrointestinal e resultado positivo para permeabilidade à BHE (Barreira Hematoencefálica), aproximando-se assim ao THC e THA, em relação a sua possível ação no Sistema Nervoso Central (SNC).

Os NEQs desenhados, mostraram tamanho molecular na faixa de 18,00 a 22,60 Å. E volumes molares, no intervalo de 553,40 a 743,92 $Å^3 \cdot mol^{-1}$. Novamente, apenas a molécula THC4 exibiu menor resultado para essas propriedades, o que em estudos de docking molecular apresentou-se mais adequado para o acoplamento deste ligante aos protofilamentos de Aβ (1-42).

Os orbitais moleculares de fronteira, HOMO, dos ligantes propostos, encontram-se dispostos na porção referente ao monômero do Δ^9-THC, ao redor do grupo fenol e nos dois átomos de oxigênio. Por outro lado, os orbitais LUMO foram observados sobre o monômero do THA, sobre a região dos anéis condensados e dos átomos de nitrogênio da molécula, como pode ser visto na Figura 1. Assim, presumisse papel distinto, para cada monômero, durante a ação farmacológica dos heterodímeros frente a Aβ (1-42), conforme mostrado na Figura 1.

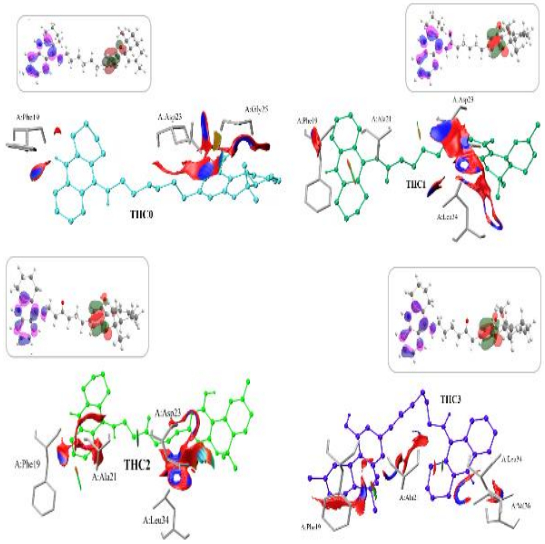


Figura 1. Estudo das interações não-covalente, NCI e ELF, e orbitais moleculares de fronteira Homo (cores vermelho e verde) e Lumo (cores rosa e azul).

Nos estudos de docking molecular, os heterodímeros mostraram que suas conformações de maior energia de interação, scores maiores do que o estabelecido pelo monômero do Δ^9-THC. A maioria das moléculas desenhadas apresentaram interações de ligação de hidrogênio com o resíduo Phe19 do protofilamento da cadeia A da proteína Aβ (1-42) e NEQ THC4 exibiu o melhor potencial inibitório (score -8,80 kcal/mol) seguido do THC3, THC2, THC0 e THC1 (Figura 2).

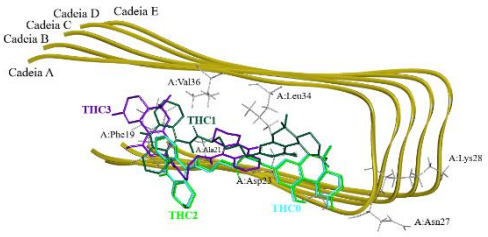


Figura 2. Resultados do estudo de docking molecular frente aos protofilamentos Aβ (1-42).

Por fim, os resultados dos estudos de NCI e ELF corroboraram com os resultados e observações feitas para o estudo de docking molecular, visto que também indicaram uma possível colaboração da presença do grupo funcional carbonila para afinidade dos ligantes ao biorreceptor Aβ (1-42), sugerindo uma maior capacidade a moléculas em doar ou aceitar átomos de hidrogênios.

Conclusão

Concluímos que técnicas e metodologias de química teórica combinadas a simulações *in silico* são capazes de auxiliar no desenho racional de novas entidades químicas com ação inibidora ao protofilamento Aβ.

Assim como, a molécula THC4 se destacou em maior parte de todos os estudos realizados. Apresentou maior potencial inibitório, com score -8,80 kcal/mol, alta absorção gastrointestinal e permeabilidade a barreira hematoencefálica.

Os resultados obtidos indicam que o desenvolvimento de abordagens terapêuticas frente a anti-agregação amilóide, corroborando com a busca de alternativas multi-alvo para o tratamento de doenças neurodegenerativas são uma alternativa promissora.

Agradecimentos
Unb, FAP-DF, CNPq e LQC.

Referências

1. Alzheimer's & Dementia, 19, 4, 1598–1695, 1 abr. 2023.
2. Twarowski, B.; H, M. Intern. Jour. of Mol. Scie., 24, 7, 1 abr. 2023.
3. Tian, S. et al. Mini rev. in med. Chem., 21, 15, 2039–2064, 15 fev. 2021.
4. Kanchi, P. K.; D, A. K. Jour. of Mol. Grap. and Model., 105, 107889, 1 jun. 2021
5. Grotenhermen, F. Clin. Pharm. 2003 42:4, 42, 4, 327–360, 30 set. 2012.
6. Abate, G.; U, D.; T, S. Biology, 10, 6, 1 jun. 2021.
7. Cousins, K. R. Jour. of the Amer. Chem. Soc., 127, 11, 4115–4116, 1 mar. 2005.
8. Nielsen, A.B. H, A.J. (2009) Gauss View 5.0, Inc., Pittsburgh.
9. Frisch, M. J. et al. Gaussian 09, Revision D.01. GaussianWallingford, 2009.
10. Fu, L. et al. Nucleic acids research, 4 abr. 2024.
11. Lu, T.; C, F. Jour. of Comp. Chem., 33, 5, 580–592, 15 fev. 2012.
12. Morris, G. M. et al. Jour. of Comp. Chem., 30, 16, 2785–2791, 27 dez. 2009.
13. Systèmes, D. Discovery Studio. BIOVIA San DiegoDassault Systèmes, 2015.

Desenvolvimento de novas moléculas com potencial atividade neuroprotetora: rede neural recorrente

Letícia de Almeida Nascimento[1], Rafael Campos[1], Érica Cristina Moreno do Nascimento[1,2], João Batista Lopes Martins[1,2]
[1]Faculdade de Saúde, Farmácia, UnB, Brasil.
[2]Laboratório de Química Computacional, Instituto de Química, Universidade de Brasília, CP 4478, Brasília-DF, Brasil.
leticiaalm2000@gmail.com.
Keywords: Alzheimer; Acetilcolinesterase; AChEI's; Redes neurais; PCA.

Abstract
Neurodegenerative diseases represent a major challenge in the search for new drugs. With the increase in life expectancy worldwide, the search for new drugs with potential neuroprotective activity has grown in industry and academia. Computational chemistry methods through *in silico* simulation, such as modeling biological systems as enzymes and proteins, are an important tool in initial studies in the search for new drugs. Advances in data science methodologies, techniques such as machine learning algorithms and neural networks, together with computational chemistry methods, could optimize the initial phase of the search for new drugs, increasing the assertiveness of candidate molecules and reducing subsequent costs in experimental studies.

Introdução
As doenças neurodegenerativas abrangem uma gama de doenças clinicamente diversas, as quais crescem de forma exponencial com o aumento da expectativa de vida.[1] A exemplo as doenças de Alzheimer (DA), Parkinson (DP) e esclerose lateral amiotrófica (ELA), que são caracterizadas pela presença de agregados proteicos patogênicos, nas fendas sinápticas correspondentes, e relacionados com a degeneração progressiva de neurônios no cérebro e a perda de funções cognitivas.[2]
Apesar da DA ser responsável por 60% a 80% de todos os casos de demência, seu tratamento concentra-se apenas em minimizar os sintomas apresentados pelos portadores da doença.[3] Nesse contexto, a hipótese colinérgica é atualmente a principal escolha para o tratamento da DA por meio dos inibidores da proteína Acetilcolinesterase (AChEIs). [4,5]
O principal objetivo da terapia colinérgica, consiste em inibir seletivamente a proteína hAChE, mantendo assim, os níveis adequados do neurotransmissor acetilcolina nas fendas sinápticas.[6] Logo, a hAChE faz parte dos alvos enzimáticos mais investigados acerca da inovação em abordagens terapêuticas para a DA.
Redes neurais podem ser programadas de forma recursiva com a finalidade de codificar informações sobre determinado conjunto de moléculas e gerarem novas entidades químicas, a partir do conjunto inicial, com potencial terapêutico[7-11]. A verificação da correlação do perfil farmacofórico das moléculas geradas e sua atividade inibitória frente ao alvo terapêutico por meio de ferramentas de ciência de dados, como a análise multivariada dos descritores através da análise dos componentes principais (PCA), e estudos da energia de interação via docking molecular é uma estratégia para verificação da viabilidade da aplicação destas técnicas.
Este trabalho tem por objetivo empregar técnicas de simulações de sistema bioquímicos, cálculos de química teórica e computacional, bem como, métodos de inteligência artificial e ciência de dados, para o desenho racional de estruturas moleculares com possível potencial terapêutico para o tratamento de doenças neurodegenerativas.

Metodologia
As moléculas avaliadas foram obtidas por meio de uma rede neural recorrente (RNN) desenvolvida utilizando a arquitetura de

células de memória de curto-longo prazo (do inglês, *Long short-term memory*-LSTM)[12,13], acoplada a um modelo do tipo autocodificador variacional (do inglês, *variational autoencoders*-VAE)[14].

A rede utilizou como dados de entrada para treinamento os denominados SMILES (do inglês, *simplified molecular-input line-entry system*), obtidos de três bases de dados distintas.

Foram exploradas 310253 (> 310 K unidades) moléculas, obtidas nos bancos de dados públicos ZINC[15]e GDB[16] e um terceiro banco de dados privado, obtido por nosso grupo, sem critério inicial de seleção do banco de dados de input. Estruturas conformacionais das moléculas dos ligantes, foram otimizadas em campo de força mecânica molecular MM2[17], seguido de uma otimização usando método semi-empírico PM3[18] para um primeiro ajuste de geometria e dados de estrutura eletrônica (EE).

O estudo das interações receptor-ligante foi conduzido por meio da técnica de docking molecular através do software GOLD (do inglês, *Genetic Optimization for Ligand Docking*)[19] usando os algoritmos GoldScore e ChemScore. As coordenadas das estruturas cristalográficas da proteína hAChE foram obtidas por meio do banco de dados Protein Data Bank (PDB)[20] sob código 6O4X.

Por serem novas moléculas desenvolvidas in sílico, faz-se necessário a caracterização dos parâmetros de absorção, distribuição, metabolismo, excreção e toxicidade (ADMET), a partir do software SwissADME.[21]

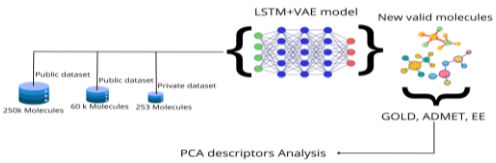


Figura 1: Esquema demonstrando o fluxo de trabalho (workflow) desenvolvido.

Resultados e Discussão

A análise dos componentes principais (PCA) exibiu para as 29 propriedades ADMET avaliadas, variância acumulada igual a 90,54% para as seis primeiras componentes principais, conforme mostrado na Figura 2.

De mesmo modo, as propriedades que obtiveram os maiores pesos (*loadings*) foram as relacionadas às propriedades de: solubilidade (ESOL logS Solubility (0,261) na PC1, log Kp para PC2 e Ali Solubility (0,54) para PC3); bioviabilidade (Bioavailability Score (0,56) na PC4) e síntese química (Synthetic Accessibility (0,43), na PC5).

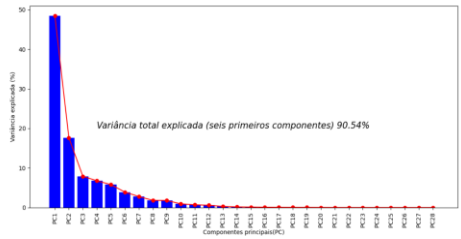


Figura 2: Variância acumulada para as seis primeiras componentes principais.

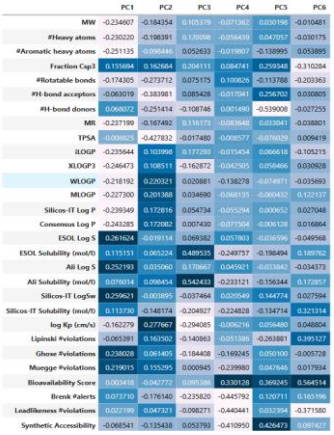


Figura 3: Valores dos loadings para as seis primeiras componentes principais.

Os resultados de docking obtidos nas simulações com a hAChE e as interações intermoleculares formadas foram analisadas por meio dos parâmetros de correlação GoldScore Fitness e ChemScore Fitness, o qual permite predizer quais ligantes formam complexos mais estáveis com os resíduos do sítio ativo da hAChE. E ainda, o parâmetro ChemScore ΔG com a finalidade de prever as afinidades de ligação dos complexos formados e estimar a energia livre de Gibbs.

A molécula de código MRLe48 foi a candidata com maior valor de GoldScore Fitness (63,487%) ChemScore ΔG -36,58 kcal/mol), enquanto a THA apresentou valores de 56,281% e -35,84 kcal/mol, respectivamente. A análise conformacional do complexo formado com melhor rank, exibe a formação de interações do tipo ligação de hidrogênio com os átomos de

hidrogênio pertencentes aos átomos de nitrogênio da molécula e o resíduo Asp74, bem como a interação do tipo π-alquil com o resíduo Trp286, que são interações importantes para a inibição da hAChE por AChEIs clássicas como o donepezil e a galantamina[4].

Ressalta-se que o composto MRLe6 (com Golscore Fitness de 59,023 % e ChemScore ΔG de -38,46 kcal/mol), apesar de não ser uma das moléculas com maior potencial para os parâmetros analisados, apresentou um dos perfis conformacionais mais semelhantes ao exibido pelo fármaco tacrina[20]. Formou as interações chaves do tipo ligação de hidrogênio com os resíduos His447 e interações do tipo π-alquil e π-sigma com os resíduos Tyr337 e Trp86, em uma distância de, 2,96 e 2,55 Å respectivamente.

Conclusão

A associação dos métodos de química teórica e computacional, as simulações *in silico* às inovações de métodos de inteligência artificial são estratégias promissoras para auxiliar na busca de novas abordagens terapêuticas para as doenças neurodegenerativas.

Nossa estratégia de associar dados de estrutura eletrônica, às metodologias recursivas de Machine Learning e Inteligência Artificial foi exitosa ao gerar moléculas, dentre todo o conjunto gerado pela rede neural, com possível potencial inibitório frente a hAChE, a exemplo da MRLe6 que mimetiza o perfil de interação apresentado pelo inibidor tacrina.

Agradecimentos

UnB, FAPDF, CNPq e LQC.

Referências

1. Sengupta, U.; K., R. Prog. in Neuro., 214, 102270, 2022.
2. Raghunathan, R.; T., K.; W., L. C. Inter. Jour. of Mol. Sci., 23,16,9299, 2022.
3. Rostagno, A. Inter. Jour. of Mol. Scie., 24, 1, 107, 2022.
4. Nascimento, É. C. M. et al. Journ. of Chem. Infor. and Model., 57, 4, 958–976 2017.
5.Nascimento, L. A.; N., É. C. M.; M., J. B. L. Journ. of Mol. Model., 28, 9, 1–13, 2022.
6. Zhou, S.; H., G. Chem. Biol. & Drug Design, 98, 6, 997–1006, 2021.
7. Ertl, P., L., R., M, E., & P. V. *ArXiv:1712.07449*, 2017.
8. Bjerrum, E. J., & T., R. *ArXiv Preprint ArXiv:1705.04612*, 2017.
9. Ma, C., & Z., X. *Proc.s of the 30th ACM Intern. Conf. on Infor. & Know. Manag.*, 1181–1190, 2021.
10. Walters, W. P., & B., R. *Accou. of Chem. Resea.*, *54*(2), 263–270, 2020.
11. Ullanat, V. *14th Intern. Conf. on Innov.s in Infor. Tech. (IIT)*, 102–107, 2020.
12.Kingma, D. P., & W., M. (2013). *ArXiv:1312.6114*.
13.Hochreiter, S., & S., J. (1997). *Neur. Comp.*, *9*(8), 1735–1780.
14. Gers, F. A., S., J., & C., F. (2000). *Neur. Comp.*, *12*(10), 2451–2471.
15 Irwin, J. J., & Shoichet, B. K. ZINC. *Jour. of Chem. Infor. and Model.*, *45*(1), 177–182, 2005.
16 Fink, T., & Reymond, J.-L. *Journ. of Chem. Inform. and Model.*, *47*(2), 342–353, 2007.
17. KAO, J; L., D; A., MM2/M0MM Force. Param. for Azoal.. 12, 7286–7291, 1988.
16. Cramer, C. J. Ess. of Comp. Chem., 2004.
18. Jones, G. et al. Jour. of Mol. Biol., 267, 727–748, 1997.
19. BERMAN, H. M. et al. Nucleic Acids Research, 28, 1, 235–242, 2020.
20. DAINA, A.; M., O.; Z., V. Scien. Rep. 2017 7:1, 7, 1,1–13, 2017.
21. GERLITS, O. et al. Chem.-Biol. Inter., 309, 108698, 2019.

Investigação Quanto-Mecânica para Síntese Racional de Polímeros Molecularmente Impressos Visando a Detecção de Contaminantes Emergentes

Linara Tarusa Damascena Correa[1] and Daniel Francisco Scalabrini Machado[1].
[1]Laboratório de Modelagem de Sistemas Complexos, Institute of Chemistry of University of Brasília, Brazil.
linara.tarusa@gmail.com
Keywords: DFT, MIP, and Emerging Contaminants.

Abstract

The project entails a theoretical investigation of Molecularly Imprinted Polymers (MIPs) for the detection of emerging contaminants: carbamazepine, diclofenac, and trimethoprim. The objective is to determine the interaction energies between the template molecule (drug) and the functional monomer to facilitate the formation of non-covalent complexes utilizing Density Functional Theory (DFT) calculations.

Introduction

Molecularly Imprinted Polymers (MIPs) are highly cross-linked materials with cavities that exhibit high affinity and selectivity for specific compounds. Therefore, they are widely used in industry, particularly for the separation of substances in environmental contexts due to their molecular recognition capabilities.[1]

Currently, the presence of substances used in pharmaceuticals has been found in large quantities in effluents. These drugs have been classified as recalcitrant Emerging Contaminants (ECs) because current technologies are not effectively applied to remove them from the environment. Examples include Diclofenac (DCF), an anti-inflammatory, and Carbamazepine (CBZ), an anticonvulsant, frequently found in sewage treatment plants in municipalities in worldwide;[2,3] Trimethoprim (TMP), prescribed to treat respiratory diseases.[4]

Without a rational approach to developing MIPs, the selection of functional monomers (FMs) often relies on a laborious task of trial and error. In this context, computational chemistry is an extremely relevant tool to ensure the production of polymers with high affinity based on the strongest interaction (more negative ΔE).[1] Additionally, they allow the study of key parameters that determine the properties of MIPs, such as the molecular nature of the functional monomer (FM) that interacts non-covalently with the target molecule, the T-FM concentration ratio, the cross-linking agent, and the polymerization conditions, such as temperature and solvent.

The present work aims to study the interactions of the template molecules with the functional monomers acrylamide (ACR), methacrylic acid (MAA), itaconic acid (IA) and vinylpyridine (VP). In addition, the influence of the crosslinking agents ethylene glycol dimethacrylate (EGDMA), pentaerythritol tetraacrylate (PETA) and trimethylolpropane triacrylate (TMPTA) was investigated, as shown in Figure 1.

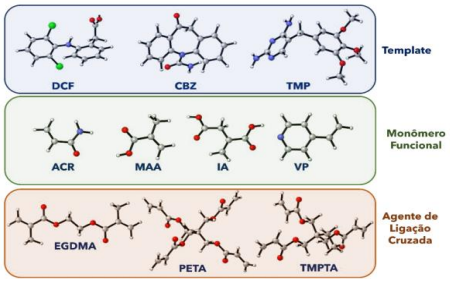


Figure 1. Molecular structure of the chemical species studied in this work.

Methodology

In the first step, the structures were optimized at semi-empirical level using the PM6 method with the GaussView program. To create the initial structure of the potential T+FM complexes, a classical simulation was performed using the PcModel 10.0 program employing the MMFF94 force field in order to correct the arbitrary initial positioning of the species drawed by the user, guided by the Electronic Potential Maps (MPEs).

At the quantum level, Density Functional Theory (DFT) was employed to obtain the electronic energies and structural properties using the M062X exchange-correlation functional because it's good description of London dispersion interactions.[5] The 6-31G(d,p) basis function set were used to represent the atomic orbitals that will form the molecular orbitals, so the M062X/6-31G(d,p) theoretical chemistry model was adopted due to its success in the study of other MIPs reported in the literature.[6] Finally, the interaction energy calculation to evaluate the best T:FM ratio was performed using the following expression:

$$\Delta E = E_{T+nMF} - (E_T + N_{FM}) \qquad (1)$$

where n = 1, 2, 3 is the number of FMs included in the calculation. The ΔE_1 interaction energy between the van der Waals complexes with the cross-linking agent (ALC) were calculated using Equation 2:

$$\Delta E_i = E_{T+nMF-AGL} - (E_T \text{ or } M + E_{ALC}) \qquad (2)$$

Since the molecular imprinting process usually occurs in a solvent, the polarizable continuum model (PCM) was employed, specifically the IEFPCM model. The interaction energy in solution ΔE_{solv} was evaluated using four different solvents (acetonitrile, dichloromethane, dimethyl sulfoxide, and tetrahydrofuran) was calculated using Equation 3:

$$\Delta E_2 = \Delta E - \Delta E_{solv} \qquad (3)$$

All the described calculations were corrected for Basis Set Superposition Error (BSSE) using the CounterPoise method. Finally, the GoodVibes program were used to extract the thermodynamic properties.

Results and Discussion

1. Estabilty of complex

Analysis of the interaction energy between T-FM complexes revealed that solvent polarity affects T-FM complexation, potentially leading to competition between chemical bonds.[7,8] Therefore, based on this, it can be concluded that apolar solvents, especially THF, favored pre-polymerization more, as evidenced by more negative energies, as shown for example in figure 2.

Regarding the effect of increasing T-FM ratios, it is observed that there is a growing stabilization of the complexes with the increase in the number of M molecules. This effect is due to the increase in the number of attractive interactions with the presence of more neighboring molecules.

Analyzing the monomers, VP presented the worst interaction and IA the best. Vinylpyridine has only one binding site located on the aromatic ring, making it difficult to establish multiple bonds in the same way as itaconic acid, as shown for example in figure 2.

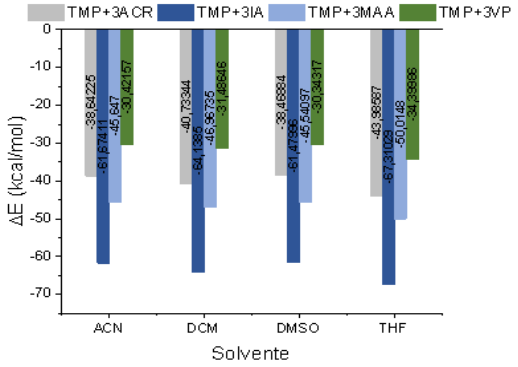


Figure 2. Energy's analyze of TMP interacting with n-template in different solvents.

In the study of cross-linking agents, it was observed that the combination of MIPs and cross-linking agent should favor the formation of more active binding sites.[9] Thus, the cross-linking agent PETA was the one that best established binding energy, as it has four acrylate functional groups, allowing the molecule to make more hydrogen bonds, as shown for example in figure 3.

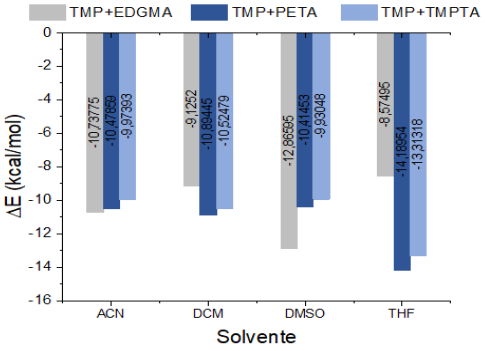


Figure 3. Energy's analyze of TMP interacting with cross-linking agent in different solvents.

2. Complexation Thermodynamics

In all cases, it is observed that at lower temperatures and with a smaller amount of monomers bound to the template, complexation formation is more spontaneous since the Gibbs free energy is more negative for these situations. The ΔG *versus* T plots showed that the quasi-harmonic corrections had marginal effects, since the curves are nearly superimposed.

Conclusions

The study concluded that the solvent-template interaction increases with polarity. Itaconic acid was the best monomer due to its multiple binding sites, while vinylpyridine was the worst. Complexes with three monomers are more spontaneous but less favorable with increasing temperature. Analyzing the crosslinker, PETA were the best crosslinking agents. So it was concluded that DFT was effective in describing the energies, aiding in the optimization of MIP synthesis.

Acknowledgements

I would like to thank my advisor and co-author, Professor Dr. Daniel Francisco Scalabrini Machado. From the very first moment you began guiding me, you have always been attentive and patient. I would also like to express my gratitude for the support from the Laboratory of Modeling and Complex Systems, especially to Master Sandro Francisco de Brito and Professor Dr. Guilherme Duarte Ramos Matos. Finally, I acknowledge the research funding agencies, FAP-DF, CAPES and CnpQ.

References

1. Sousa, M. D.; Barbosa, C. M.; *Quim. Nova* **2009**, *32*, 1609.
2. Daniel Harris, BA, Lynn McNicoll, MD, Gary Epstein-Lubow, MD, and Kali S. Thomas, P.; Usselman, C. W. N. S. S. J. R. B.; *Physiol. Behav.* **2017**, *176*, 139.
3. Ginebreda, A.; Muñoz, I.; de Alda, M. L.; Brix, R.; López-Doval, J.; Barceló, D.; *Environ. Int.* **2010**, *36*, 153.
4. Borozniak, R.; Reut, J.; Tretjakov, A.; Lomaka, A.; Öpik, A.; Syritski, V.; *J. Mol. Recognit.* **2017**, *30*, 1.
5. Zhao, Y.; Truhlar, D. G.; *Theor. Chem. Acc.* **2008**, *120*, 215.
6. Khan, M. S.; Pal, S.; *J. Mol. Recognit.* **2018**, *31*, 1.
7. Song, X.; Wang, J.; Zhu, J.; *Mater. Res.* **2009**, *12*, 299.
8. Mohajeri, S. A.; Karimi, G.; Khansari, M. R.; *Anal. Chim. Acta* **2010**, *683*, 143.
9. Ceylan, G.; Emik, S.; Yalcinyuva, T.; Sunbuloğlu, E.; Bozdag, E.; Unalan, F.; *Polymers.* **2023**, *15*, 1.

Benchmarking entre energias calculadas por MM e por SAPT em Sistemas Opioides

Luana Lemos Reis[1], Dr. Guilherme Duarte Ramos Matos[1,2] e Dr. Daniel Francisco Scalabrini Machado[1].
[1]Laboratório de Modelagem de Sistemas Complexos, Instituto de Química, Universidade de Brasília – LMSC / IQ / UnB.
[2]Department of Applied Mathematics and Statistics, Stony Brook University.
Email of the corresponding author [in italics].
Keywords: Molecular Docking; Symmetry-Adapted Perturbation Theory; Benchmark; Opioids.

Abstract
Balancing cost and accuracy in computational chemistry is essential. Comparing molecular docking and SAPT on opioid receptors reveals docking's limitations in predicting electrostatic interactions, especially for charged residues. Significant discrepancies highlight the need to improve docking scoring functions, enhancing accuracy.

Introduction

Na química computacional, é crucial equilibrar o custo computacional e a precisão das análises. O docking molecular é uma técnica eficiente para triagens em larga escala, permitindo gerar múltiplas poses de ligação que podem ser posteriormente avaliadas por técnicas mais precisas. No entanto, as previsões feitas pelo *docking*, baseadas em interações eletrostáticas e de dispersão usando campos de força, muitas vezes carecem de precisão comparadas a métodos de mecânica quântica [1]. A Teoria de Perturbação Adaptada por Simetria (SAPT) oferece uma análise mais detalhada e precisa das forças intermoleculares, embora a um custo computacional mais elevado [2].
Comparar as interações intermoleculares calculadas via Mecânica Molecular e Mecânica Quântica em receptores opioides, permite avaliarmos as magnitudes de diferença entre as técnicas [3]. Esse benchmark tem potencial de auxiliar no aprimoramento de funções de *scoring function*, utilizadas no *docking*.

Methodology

Os sistemas opioides MOR (PDB: 8F7R), KOR (PDB: 8F7W) e DOR (PDB: 8F7S) foram preparados utilizando o programa GROMACS com os campos de força AmberFF14SB e GAFF2. As energias de interação foram determinadas pelo programa DOCK6, sendo particionadas em interações por resíduo, também conhecidas como *Footprint* Energético, usando parâmetros não ligantes dos campos AmberFF14SB e GAFF2. A partir desses *footprints*, selecionaram-se pares resíduo-ligante para realização de cálculos nos níveis SAPT0 e FI/SAPT, empregando o conjunto de função de base jun-cc-pvdz.

Results

A análise das energias de interação eletrostática obtidas pelo *docking* demonstrou uma precisão considerável para resíduos neutros. No entanto, resíduos eletricamente carregados, como no sistema MOR, com glutamato 126 e aspartato 149, apresentaram diferenças de até 5,71 k cal·mol^{-1}.
A comparação das energias de interação revelou que, para o resíduo aniônico aspartato 149, a diferença entre os valores obtidos pelo *docking* e pelo SAPT foi a mais acentuada, alcançando aproximadamente 98,08 k cal·mol^{-1}.

Discussion

Observou-se que as energias de interação eletrostática calculadas pelos métodos quânticos foram superiores às obtidas por Mecânica Molecular.

Os resultados indicam que o *docking* possui limitações na precisão das interações eletrostáticas, especialmente para resíduos carregados.

A discrepância observada para o aspartato 149 sugere que o método de *docking* pode subestimar a importância das interações eletrostáticas, principalmente de resíduos com cadeias laterais carregadas.

Comparar os dados de *docking* com os obtidos por métodos quânticos, como o SAPT, fornece uma visão mais detalhada das forças intermoleculares, o que é crucial para melhorar as funções de *scoring function*.

Conclusions

Os resultados deste estudo indicam que resíduos eletricamente carregados, especialmente aniônicos, apresentam maiores discrepâncias nas energias de interação calculadas por *docking* em comparação com métodos quânticos, como SAPT.

Essas diferenças destacam a possibilidade de aprimorar as funções de *scoring function* usadas no *docking*, especialmente para interações eletrostáticas.

Ajustes no modelo de *docking*, como escalonar a magnitude das interações eletrostáticas, possivelmente levarão a uma geração de poses mais adequadas.

Acknowledgements

CAPES, CNPq, FAPDF

References

[1] Allen WJ, et al., "DOCK 6: Impact Of New Features and Current Docking Performance," J. Comput. Chem., vol. 36, no. 15, pp. 1132-1156, Jun 5, 2015.

[2] D. G. A. Smith, L. A. et al., "Psi4 1.4: Open-Source Software for High-Throughput Quantum Chemistry," J. Chem. Phys., vol. 152, no. 18, 184102 (2020).

[3] Wang Y, et al., "Structures of the Entire Human Opioid Receptor Family," J. Cell., vol. 186, no. 2, pp. 413-427.e17, 2023.

Estudo Computacional dos Mecanismos TICT e ESIPT de um novo Pigmento Baseado no Núcleo BTD

Luana Lemos Reis[1] e Daniel Francisco Scalabrini Machado[1]
[1]Laboratório de Modelagem de Sistemas Complexos, Instituto de Química, Universidade de Brasília – LMSC / IQ / UnB – Brasília, DF, 70910-900
luana.reis@aluno.unb.br
Keywords: Fluorescence; Quenching; BTD; TICT; ESIPT.

Abstract
This work explores the photophysical properties of the BTD-4AS pigment, focusing on TICT and ESIPT mechanisms. Computational analysis revealed that cLR corrections are crucial, and ESIPT is enhanced in polar environments. These findings guide future studies on fluorescence quenching mechanisms.

Introdução

Investigar os mecanismos de quenching é essencial para otimizar suas propriedades de fluorescência. Compreender e controlar esses processos permite projetos moleculares personalizados com intensidade, sensibilidade e cores de emissão ajustáveis, avançando assim tanto o conhecimento fundamental quanto as aplicações práticas em diversos campos [1, 2, 3]. Recentemente, a doutoranda Ms. Raíssa Kelly Correa de Paiva, orientada pelo Prof. Dr. Brenno Amaro da Silveira Neto (Laboratório de Química Medicinal – LaQuiMeT), sintetizaram uma base de Schiffer com características fluorescentes como ilustra a figura 1.

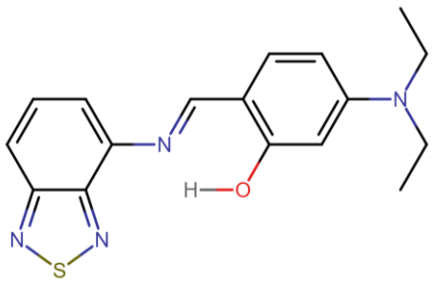


Figura 1. Molécula sintetizada pela equipe do LaQuiMeT, denominada de BTD-4AS.

O corante sintetizado, denominado pelos autores de BTD-4AS teve suas propriedades fotofísicas caracterizadas.
O espectro de emissão de fluorescência foi determinado em soluções de várias polaridades em que foi observado que o aumento da polaridade do meio acarreta na extinção da emissividade do pigmento. A extinção da fluorescência pela água também é observada no caso de muitas outras sondas fluorescentes. Apesar da ampla aplicação de tais sondas, as causas da extinção de fluorescência pela água são insuficientemente claras até hoje. Na literatura são propostos vários mecanismos de extinção da fluorescência de corantes orgânicos em solventes polares, como: Extinção Estática; Extinção Dinâmica; Transferência de Elétron Fotoinduzida (PET); Transferência de Carga Intramolecular (ICT); Transferência Protônica em Estado Excitado (ESIPT). Esses mecanismos podem agir isoladamente ou em conjunto, dependendo das propriedades específicas do corante e do solvente. Além disso, a concentração do agente extintor e a temperatura também podem influenciar a extensão da extinção da fluorescência. Para compreender os mecanismos de quenching de fluorescência do cromóforo BTD-4AS e explorar modificações estruturais que possam melhorar suas propriedades fotofísicas, investigamos a torção intramolecular e a transferência de carga por meio de abordagens da química teórica e computacional.

Metodologia

Os cálculos teóricos deste trabalho baseiam-se em princípios de mecânica

quântica, utilizando o software Gaussian16 [4, 5]. As geometrias do estado fundamental e do estado excitado foram otimizadas utilizando a Teoria do Funcional de Densidade (DFT) e dependente do tempo (TD-DFT), respectivamente [6, 7, 8]. Os cálculos empregaram o funcional cam-B3LYP e o conjunto de base def2TZVP [9, 10]. Simulações de solvente foram realizadas usando o Modelo de Continuidade Polarizável (PCM) [11, 12].
Foram utilizados os programas Multiwfn e VMD para cálculos de pontos críticos e visualizações de gradientes de densidade [13, 14].

Resultados e Discussão

Os resultados das otimizações da BTD-4AS torcida com correção linear cLR (*Corrected Linear Response*) estão compreendidos na Figura 2.

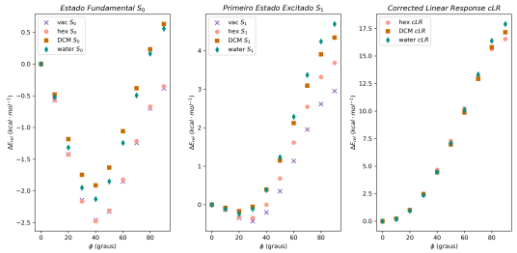


Figura 2. ΔE_{rel} (kcal·mol^{-1}) por ϕ (graus) em vácuo, em hexano, em diclorometano e em água no estado fundamental, no primeiro estado excitado e com correção da resposta linear, da esquerda para a direita, respectivamente.

A correção do LR é relevante quando utilizando PCM, pois para cálculos para obtenção de energias de excitação em solução, referente a excitações que envolvem expressivo rearranjo de densidade, o LR se mostra insuficiente por não considerar a relaxação de densidade dependente da polarização do solvente.
Com as estruturas otimizadas fixamos o comprimento da ligação –OH entre 0,8 e 2,2 Å, construindo curvas de energia potencial e obtendo correções termodinâmicas. A figura 3 ilustra a análise de ESIPT.

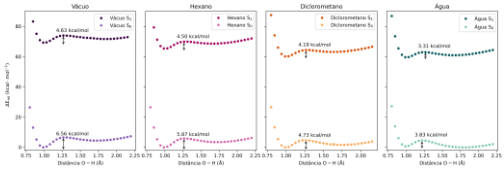


Figura 3. ΔE_{rel} (kcal·mol^{-1}) por Distância O–H (Å) do estado fundamental e primeiro estado excitado em vácuo, em hexano, em diclorometano e em água, da esquerda para a direita, com os respectivos valores de barreira energética.

Podemos observar que a barreira energética diminui com o aumento da polaridade do solvente. Assim como o estado ceto se estabiliza com o aumento da polaridade. Esses resultados indicam que o ESIPT é facilitado em meios polares.

Conclusão

Foi constatado que a correção linear cLR é essencial em sistemas como o da BTD-4AS, onde há um rearranjo significativo da densidade eletrônica. Além disso, a conclusão de que o mecanismo de ESIPT é facilitado em meios polares sugere que a forma ceto, estabilizada pelo aumento da polaridade, merece ser explorada em estudos futuros.
A extinção da fluorescência da BTD-4AS parece ser influenciada por múltiplos fatores, o que abre caminho para investigações adicionais em outros mecanismos de *quenching*.

Agradecimentos

CAPES, CNPq, FAPDF.

Referências

1. Duangkamol, C.; et al.; Dyes Pigments 2023, 216, 111365. https://doi.org/10.1016/j.dyepig.2023.111365
2. Meng, X.; et al.; Spectrochim. Acta A Mol. Biomol. Spectrosc. 2022, 265, 120383. https://doi.org/10.1016/j.saa.2021.120383
3. Wang, C.; et al.; Angew. Chem. Int. Ed. 2020, 59, 10160.

https://doi.org/10.1002/anie.201916357
4. Dennington, R.; Keith, T. A.; Millam, J. M.; GaussView Version 6, 2019.
5. Frisch, M. J.; et al.; Gaussian˜16 Revision C.01, 2016.
6. Adamo, C.; Jacquemin, D.; Chem. Soc. Rev. 2013, 42, 845. https://doi.org/10.1039/C2CS35394F
7. Kohn, W.; Sham, L. J.; Phys. Rev. 1965, 140, A1133. https://doi.org/10.1103/PhysRev.140.A1133
8. Laurent, A. D.; et al.; Phys. Chem. Chem. Phys. 2014, 16, 14334. https://doi.org/10.1039/C3CP55336A
9. Yanai, T.; et al.; Chem. Phys. Lett. 2004, 393, 51. https://doi.org/10.1016/j.cplett.2004.06.011
10. Weigend, F.; Ahlrichs, R.; Phys. Chem. Chem. Phys. 2005, 7, 3297. https://doi.org/10.1039/b508541a
11. Marenich, A. V.; et al.; J. Phys. Chem. B 2009, 113, 6378. https://doi.org/10.1021/jp810292n
12. Scalmani, G.; et al.; J. Chem. Phys. 2006, 124, 094107. https://doi.org/10.1063/1.2173258
13. Humphrey, W.; et al.; J. Mol. Graph. 1996, 14, 33. https://doi.org/10.1016/0263-7855(96)00018-5
14. Lu, T.; Chen, F.; J. Comput. Chem. 2012, 33, 580. https://doi.org/10.1002/jcc.22885
15. Bannwarth, C.; et al.; J. Chem. Theory Comput. 2019, 15, 1652. https://doi.org/10.1021/acs.jctc.8b01176
16. Grimme, S.; J. Chem. Theory Comput. 2019, 15, 2847. https://doi.org/10.1021/acs.jctc.9b00143
17. Grimme, S.; et al.; J. Phys. Chem. A 2021, 125, 4039. https://doi.org/10.1021/acs.jpca.1c00971

10º SIMPÓSIO DE ESTRUTURA ELETRÔNICA E DINÂMICA MOLECULAR
SEEDMOL 4 a 8 novembro | 2024 Pirenópolis, Goiás

Experimental and DFT study of a solid dispersion of the drug clofazimine with *p*-aminobenzoic acid coformer

Lucas Aires de Sousa[1], and Mateus Ribeiro Lage [2].
[1]Faculty of Pharmaceutical Sciences - Araraquara Campus Araraquara Highway, Jaú, Km 01 - s/n - Campos Ville - Araraquara/SP - CEP 14800-903, Brazil.
[2]Balsas Science Center - CCBL, MA-140, KM 04, Balsas/MA, CEP: 65800-000, Brazil.
lukarelio.aires@gmail.com
Keywords: Clofazimine; Density Functional Theory; Solubility.

Abstract

Clofazimine (CFZ) is an antibacterial drug used to treat Hansen's disease. This drug has poor solubility in aqueous media, which may compromise its efficiency in oral administration. Previous studies showed that the solubility of this compound is increased with the obtention of its salts. In this work, we carried out experimental investigations of a salt of CFZ with PABA coformer and its precursors, combined with a theoretical study of the molecules CFZ and PABA, of the ions $CFZH^+$ and $PABA^-$, as well as of the heterodimer $CFZH^+$-$PABA^-$. We developed this work employing two experimental techniques (FT-IR spectroscopy and diffuse reflectance UV-Vis spectroscopy) and DFT theoretical calculations. In the experimental FT-IR analysis, the shift in bands corresponding to vibrational modes of groups involved in the interaction of the ions, such as the N-H stretching (3324 cm^{-1} and 1482 cm^{-1}) and COO^- symmetrical stretching, indicate the salt formation, which is confirmed with the theoretical calculations. Furthermore, the UV-Vis spectrum of the salt exhibits new bands not observed in the starting compounds, also contributing to the characterization of the material. The variation of Gibbs free energy of interaction was the parameter used to confirm that the interaction in the heterodimer is favorable. Additionally, TD-DFT results help to explain electronic transitions, which is also in good agreement with the experimental data obtained. The experimental and theoretical results obtained help for a better understanding of the salt formation from favorable intermolecular interactions between $CFZH^+$ and $PABA^-$, also contributing to a deeper characterization of the material.

Introduction

Clofazimine (CFZ) is a compound known for its low solubility in aqueous media, a characteristic that can be modulated through the use of coformers, resulting in a significant increase in the dissolution rate and bioavailability of the drug. CFZ is used in medicinal cocktails, composed of first-generation drugs such as rifampicin and dapsone, for the treatment of leprosy[1].

The preparation of solid dispersions has been a promising alternative to increase the dissolution rate and solubility of drugs in the body, resulting in a significant increase in their bioavailability[2]. The most common solid dispersions include salts, co-crystals and co-amorphs, with solid salt dispersions obtained from the interaction between the formed ions of the drug and the coformer at room temperature[2].

CFZ has been used to prepare solid co-crystal and salt dispersions using pharmacologically acceptable coformers such as methanesulfonic acid, maleic acid, isonicotinic acid, nicotinic acid, malonic acid and *p*-aminobenzoic acid (PABA).

Although these materials have been prepared and characterized experimentally, theoretical studies of these systems are scarce in the literature. Computational chemistry studies involving electronic structure calculations based on quantum chemistry principles can significantly

contribute to further investigation of the electronic and structural properties of chemical compounds and the formation of solid dispersions[3].

All calculations were performed using the ωB97X-D DFT[4,5] functional, a long-range corrected hybrid functional, and the 6-311++G(d,p)[6] basis set, as implemented in the *Gaussian 16* software. The ωB97X-D DFT functional was selected for its accuracy for thermodynamic properties of organic compounds and for describing long-range atom-atom interactions. Furthermore, the polarizable continuity model in the Integral Equation Formalism version (IEFPCM)[7] was used to simulate the solvation effects, using ethanol as the solvent.

We also calculated the electronic chemical potential (μ), defined as μ=-(ELUMO+EHOMO)/2, the hardness (η), defined as η = (ELUMO - EHOMO)/2, the softness (s), defined as s = 1/η, and the global electrophilicity, defined as ω = μ²/2η. The optimized geometries of different interactions were then obtained, and we determined the most favorable one based on the calculated thermodynamic parameters. The vibrational frequencies were calculated after each geometry optimization calculation, to confirm that each obtained geometry was a minimum on the potential energy surface, when all calculated vibrational frequencies are positive.

The calculated thermodynamic parameters indicated that the ionic interaction between CFZ and PABA is thermodynamically favorable, with negative variations in $\Delta EZPVE$, ΔH and ΔG^{298}, suggesting that the formation of the $CFZH^+$-$PABA^-$ solid salt dispersion is spontaneous. The simulated spectra of the optimized geometries showed good agreement with the available experimental data, corroborating the accuracy of the theoretical calculations performed.

The results obtained in this theoretical study confirm the affinity between CFZ and PABA to form solid salt dispersions, corroborating the experimental data indicating the formation of solid dispersions with high stability and increased solubility. The use of the DFT functional ωB97X-D and the basis set 6-311++G(d,p) proved to be suitable for describing the intermolecular interactions and predicting accurate thermodynamic properties.

The theoretical contribution of this work is significant, providing a deeper understanding of the electronic and structural interactions between CFZ and PABA, which may be useful for the development of new pharmaceutical formulations with improved therapeutic performance.

This theoretical study on clofazimine and p-aminobenzoic acid confirmed the feasibility of forming solid dispersions of $CFZH^+$ $PABA^-$ salt, with favorable thermodynamic parameters and simulated spectra that correspond well to the experimental data. The methodologies employed proved to be effective in predicting electronic and structural properties, contributing to the advancement of the understanding of intermolecular interactions in pharmaceutical systems. These findings highlight the importance of theoretical studies in complementing experimental data, enabling the development of drugs with better solubility and bioavailability characteristics, potentially expanding their therapeutic application.

Table 1. Values of reactivity indexes calculated for CFZ, $CFZH^+$, PABA, and $PABA^-$.

Reactivity index	**CFZ**	**$CFZH^+$**	**PABA**	**$PABA^-$**
E_{HOMO}*	-7.26	-8.13	-8.08	-3.71
E_{LUMO}*	-1.04	-2.05	0.41	3.11
Gap HOMO-LUMO*	6.23	6.07	8.49	6.82
Chemical potential (*μ*)*	-4.16	-5.10	-3.84	-0.30
Hardness (*η*)*	3.11	3.04	4.25	3.41
Softness (*s*)**	0.32	0.33	0.24	0.29
Electrophilicity (*ω*)*	2.77	4.28	1.73	0.01

*Given in eV;

**Given in eV^{-1}.

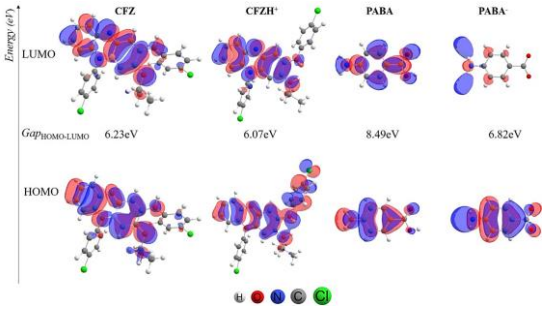


Figure 1. HOMO and LUMO molecular orbitals in ethanol.
Source: Author

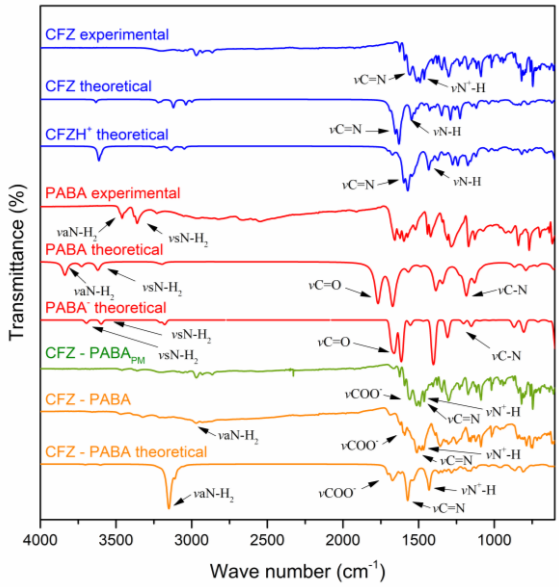


Figure 2. Experimental FT-IR and simulated spectra for CFZ, $CFZH^+$, PABA, $PABA^-$, and of the heterodimer $CFZH^+$-$PABA^-$, in ethanol.
Source: Author

Acknowledgements
The authors are grateful to the Coordenação de Aperfeiçoamento de Pessoal de Nível Superior (CAPES) and to the Fundação de Amparo à Pesquisa e Desenvolvimento Científico e Tecnológico do Maranhão (FAPEMA) for the financial support.

References

1. KAR, H. K.; GUPTA, R. Dermatol. Clin. 2015, 33, 1, 55-65.
2. SOUSA, M. L. et al. J. Mol. Struct. 2020, 128226.
5. BOLLA, G.; NANGIA, A. Cryst. Growth Des. 2012, 12, 12, 6250-6259.
3. BECKE, A. D. J. Chem. Phys. 2014, 140, 18, 18A301.
4. CHAI, J.-D.; HEAD-GORDON, M. Phys. Chem. Chem. Phys. 2008, 10, 44, 6615-6620.
5. SHAM, L. J. KOHN, W. Phys. Rev. 1996, 145, 2, 561.
6. DITCHFIELD, R. H. W. J.; HEHRE, Warren J.; POPLE, John A. J. Chem. Phys. 1971, 54, 724-728.
7. TOMASI, J.; MENNUCCI, B.; CAMMI, R. Chem. Rev. 2005, 105, 8, 2999-3094.

10º SIMPÓSIO DE ESTRUTURA ELETRÔNICA E DINÂMICA MOLECULAR
SEEDMOL 4 a 8 novembro | 2024 Pirenópolis, Goiás

Experimental and DFT study of a solid dispersion of the drug clofazimine with *p*-aminobenzoic acid coformer

Lucas Aires de Sousa[1], and Mateus Ribeiro Lage [2].
[1]Faculty of Pharmaceutical Sciences - Araraquara Campus Araraquara Highway, Jaú, Km 01 - s/n - Campos Ville - Araraquara/SP - CEP 14800-903, Brazil.
[2]Balsas Science Center - CCBL, MA-140, KM 04, Balsas/MA, CEP: 65800-000, Brazil.
lukarelio.aires@gmail.com
Keywords: Clofazimine; Density Functional Theory; Solubility.

Abstract

Clofazimine (CFZ) is an antibacterial drug used to treat Hansen's disease. This drug has poor solubility in aqueous media, which may compromise its efficiency in oral administration. Previous studies showed that the solubility of this compound is increased with the obtention of its salts. In this work, we carried out experimental investigations of a salt of CFZ with PABA coformer and its precursors, combined with a theoretical study of the molecules CFZ and PABA, of the ions $CFZH^+$ and $PABA^-$, as well as of the heterodimer $CFZH^+$-$PABA^-$. We developed this work employing two experimental techniques (FT-IR spectroscopy and diffuse reflectance UV-Vis spectroscopy) and DFT theoretical calculations. In the experimental FT-IR analysis, the shift in bands corresponding to vibrational modes of groups involved in the interaction of the ions, such as the N-H stretching (3324 cm^{-1} and 1482 cm^{-1}) and COO^- symmetrical stretching, indicate the salt formation, which is confirmed with the theoretical calculations. Furthermore, the UV-Vis spectrum of the salt exhibits new bands not observed in the starting compounds, also contributing to the characterization of the material. The variation of Gibbs free energy of interaction was the parameter used to confirm that the interaction in the heterodimer is favorable. Additionally, TD-DFT results help to explain electronic transitions, which is also in good agreement with the experimental data obtained. The experimental and theoretical results obtained help for a better understanding of the salt formation from favorable intermolecular interactions between $CFZH^+$ and $PABA^-$, also contributing to a deeper characterization of the material.

Introduction

Clofazimine (CFZ) is a compound known for its low solubility in aqueous media, a characteristic that can be modulated through the use of coformers, resulting in a significant increase in the dissolution rate and bioavailability of the drug. CFZ is used in medicinal cocktails, composed of first-generation drugs such as rifampicin and dapsone, for the treatment of leprosy[1].

The preparation of solid dispersions has been a promising alternative to increase the dissolution rate and solubility of drugs in the body, resulting in a significant increase in their bioavailability[2]. The most common solid dispersions include salts, co-crystals and co-amorphs, with solid salt dispersions obtained from the interaction between the formed ions of the drug and the coformer at room temperature[2].

CFZ has been used to prepare solid co-crystal and salt dispersions using pharmacologically acceptable coformers such as methanesulfonic acid, maleic acid, isonicotinic acid, nicotinic acid, malonic acid and *p*-aminobenzoic acid (PABA).

Although these materials have been prepared and characterized experimentally, theoretical studies of these systems are scarce in the literature. Computational chemistry studies involving electronic structure calculations based on quantum chemistry principles can significantly

contribute to further investigation of the electronic and structural properties of chemical compounds and the formation of solid dispersions[3].

All calculations were performed using the ωB97X-D DFT[4,5] functional, a long-range corrected hybrid functional, and the 6-311++G(d,p)[6] basis set, as implemented in the *Gaussian 16* software. The ωB97X-D DFT functional was selected for its accuracy for thermodynamic properties of organic compounds and for describing long-range atom-atom interactions. Furthermore, the polarizable continuity model in the Integral Equation Formalism version (IEFPCM)[7] was used to simulate the solvation effects, using ethanol as the solvent.

We also calculated the electronic chemical potential (μ), defined as μ=-(ELUMO+EHOMO)/2, the hardness (η), defined as η = (ELUMO - EHOMO)/2, the softness (s), defined as s = 1/η, and the global electrophilicity, defined as ω = μ²/2η. The optimized geometries of different interactions were then obtained, and we determined the most favorable one based on the calculated thermodynamic parameters. The vibrational frequencies were calculated after each geometry optimization calculation, to confirm that each obtained geometry was a minimum on the potential energy surface, when all calculated vibrational frequencies are positive.

The calculated thermodynamic parameters indicated that the ionic interaction between CFZ and PABA is thermodynamically favorable, with negative variations in $\Delta EZPVE$, ΔH and ΔG^{298}, suggesting that the formation of the $CFZH^+$-$PABA^-$ solid salt dispersion is spontaneous. The simulated spectra of the optimized geometries showed good agreement with the available experimental data, corroborating the accuracy of the theoretical calculations performed.

The results obtained in this theoretical study confirm the affinity between CFZ and PABA to form solid salt dispersions, corroborating the experimental data indicating the formation of solid dispersions with high stability and increased solubility. The use of the DFT functional ωB97X-D and the basis set 6-311++G(d,p) proved to be suitable for describing the intermolecular interactions and predicting accurate thermodynamic properties.

The theoretical contribution of this work is significant, providing a deeper understanding of the electronic and structural interactions between CFZ and PABA, which may be useful for the development of new pharmaceutical formulations with improved therapeutic performance.

This theoretical study on clofazimine and p-aminobenzoic acid confirmed the feasibility of forming solid dispersions of $CFZH^+$ $PABA^-$ salt, with favorable thermodynamic parameters and simulated spectra that correspond well to the experimental data. The methodologies employed proved to be effective in predicting electronic and structural properties, contributing to the advancement of the understanding of intermolecular interactions in pharmaceutical systems. These findings highlight the importance of theoretical studies in complementing experimental data, enabling the development of drugs with better solubility and bioavailability characteristics, potentially expanding their therapeutic application.

Table 1. Values of reactivity indexes calculated for CFZ, $CFZH^+$, PABA, and $PABA^-$.

Reactivity index	**CFZ**	**$CFZH^+$**	**PABA**	**$PABA^-$**
E_{HOMO}*	-7.26	-8.13	-8.08	-3.71
E_{LUMO}*	-1.04	-2.05	0.41	3.11
Gap HOMO-LUMO*	6.23	6.07	8.49	6.82
Chemical potential (μ)*	-4.16	-5.10	-3.84	-0.30
Hardness (η)*	3.11	3.04	4.25	3.41
Softness (s)**	0.32	0.33	0.24	0.29
Electrophilicity (ω)*	2.77	4.28	1.73	0.01

*Given in eV;

**Given in eV^{-1}.

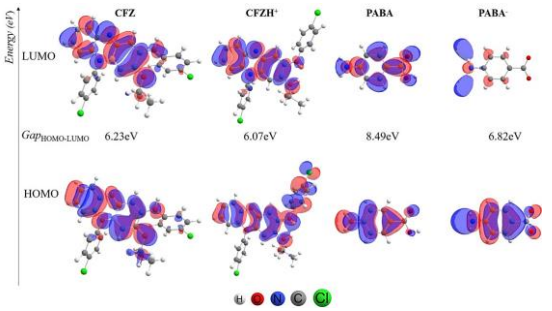


Figure 1. HOMO and LUMO molecular orbitals in ethanol.
Source: Author

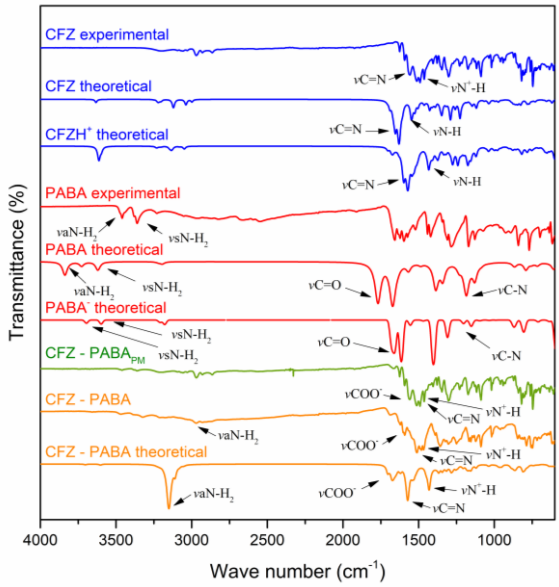


Figure 2. Experimental FT-IR and simulated spectra for CFZ, $CFZH^+$, PABA, $PABA^-$, and of the heterodimer $CFZH^+$-$PABA^-$, in ethanol.
Source: Author

Acknowledgements
The authors are grateful to the Coordenação de Aperfeiçoamento de Pessoal de Nível Superior (CAPES) and to the Fundação de Amparo à Pesquisa e Desenvolvimento Científico e Tecnológico do Maranhão (FAPEMA) for the financial support.

References

1. KAR, H. K.; GUPTA, R. Dermatol. Clin. 2015, 33, 1, 55-65.
2. SOUSA, M. L. et al. J. Mol. Struct. 2020, 128226.
5. BOLLA, G.; NANGIA, A. Cryst. Growth Des. 2012, 12, 12, 6250-6259.
3. BECKE, A. D. J. Chem. Phys. 2014, 140, 18, 18A301.
4. CHAI, J.-D.; HEAD-GORDON, M. Phys. Chem. Chem. Phys. 2008, 10, 44, 6615-6620.
5. SHAM, L. J. KOHN, W. Phys. Rev. 1996, 145, 2, 561.
6. DITCHFIELD, R. H. W. J.; HEHRE, Warren J.; POPLE, John A. J. Chem. Phys. 1971, 54, 724-728.
7. TOMASI, J.; MENNUCCI, B.; CAMMI, R. Chem. Rev. 2005, 105, 8, 2999-3094.

Optimizing Molecular Descriptors for Reliable Adsorption Energy Prediction on Transition Metal Nanoclusters

Lucas B. Pena†, Felipe V. Calderan‡, Marcos G. Quiles‡, Breno R. L. Galvão†, Juarez L. F. Da Silva¶

†Federal Center for Technological Education of Minas Gerais, 30421-169, Belo Horizonte, MG, Brazil

‡Institute of Science and Technology, Federal University of São Paulo, 01109-010, SP, Brazil

¶São Carlos Institute of Chemistry, University of São Paulo, PO Box 780, 13560-970, São Carlos, SP, Brazil

e-mail: lucas.bernardesp205@gmail.com

The field of nanocatalysis has shown great potential for sustainable energy solutions, such as the conversion of pollutant molecules into valuable chemicals and fuels. Namely, atomically precise metal nanoclusters are promising catalysts for CO2 reduction, H2 production, water splitting, and other electrochemical processes.[1] Computational research on these systems often rely on computationally expensive density functional theory (DFT) calculations for analyzing a great diversity of nanocluster structures, catalytic intermediates and adsorption sites.

Due to this problem, a rapid advancement of machine learning for predicting molecular properties has been observed.[2] One critical aspect of this progression is feature engineering, which involves the extraction and selection of molecular descriptors that substantially influence model performance. However, there remains a notable gap in understanding the importance of molecular descriptors in modeling adsorption energies on nanoclusters. This gap is due to constraints in database variability or a lack of comprehensive understanding of widely-used molecular descriptors such as the Coulomb Matrix (CM), Many Body Tensor Representation (MBTR), Atomic Centered Symmetry Functions (ACSF), and Smooth Overlap of Atomic Orbitals (SOAP), which have been recently developed in the DScribe project as a python package.[3]

In this study, we address the challenge of predicting adsorption energies on nanocluster systems across a wide variety of molecules associated with catalytic processes. By utilizing a meticulously curated database of DFT-calculated adsorption energies, containing over 400,000 samples across diverse molecule-nanocluster combinations, we focus on exploring the significance of the molecular descriptors mentioned earlier. Our systematic analysis and engineering of features from molecular geometries aim to provide interpretability of how these descriptors influence the accuracy and reliability of adsorption energy predictions. This work not only bridges the existing gap in the field but also sets the stage for the development of more efficient machine learning models in nanocatalysis, potentially accelerating the discovery of sustainable energy solutions.

Acknowledgements:

CNPq, CINE, FAPESP-SHELL project 2017/1 231 1631-2, FAPEMIG project APQ-00597-22.

References:

[1] Yuan, X.; Zhu, M. Recent Advances in Atomically Precise Metal Nanoclusters for Electrocatalytic Applications. Inorganic Chemistry Frontiers, 2023, 10, 3995–4007. https://doi.org/10.1039/d3qi00656e.

[2] Yao, Z.; Lum, Y.; Johnston, A.; Mejia-Mendoza, L. M.; Zhou, X.; Wen, Y.; Aspuru-Guzik, A.; Sargent, E. H.; Seh, Z. W. Machine Learning for a Sustainable Energy Future. Nat Rev Mater 2022, 8 (3), 202–215. https://doi.org/10.1038/s41578-022-00490-5.

[3] Himanen, L.; Jäger, M. O. J.; Morooka, E. V.; Federici Canova, F.; Ranawat, Y. S.; Gao, D. Z.; Rinke, P.; Foster, A. S. DScribe: Library of Descriptors for Machine Learning in Materials Science. Computer Physics Communications 2020, 247, 106949. https://doi.org/10.1016/j.cpc.2019.106949.

Biodegradable electrolyte alternative for energy storage in supercapacitors

Lucas de Sousa Silva[1] and Guilherme Colherinhas de Oliveira[2]
[1]Instituto de Física, Universidade Federal de Goiás, 74690-900, Goiânia, GO, Brazil.
[2]Instituto de Física, Universidade Federal de Goiás, 74690-900, Goiânia, GO, Brazil.
lucas_sousa@discente.ufg.br
Keywords: Energy storage; supercapacitors; amino acid ionic liquids; graphene; molecular dynamics.

Abstract
This study explores energy storage in supercapacitors (SCs) using amino acid-derived ionic liquids (AAILs) and graphene electrodes through Molecular Dynamics (MD) simulations. By examining 1-ethyl-3-methylimidazolium (Emim) and alanine (Ala) with various hydration levels and charge densities, we find significant energy storage capacity and biodegradability potential.

Introduction
Energy storage in supercapacitors (SCs) occurs through the Electric Double Layer (EDL) [1-3]. When a potential difference is applied across the terminals of the SC, ions from the electrolyte are attracted near the electrode surfaces, forming the EDL. These devices have the advantage of not involving any electrochemical processes, only electrostatic ones [4], which gives them a longer lifespan with extended charge cycles.

Constructing a good SC requires careful evaluation of the materials comprising the electrodes and electrolyte. One material that has attracted attention from the scientific community is graphene, due to its interesting properties such as high electrical conductivity, high thermal conductivity, mechanical strength, and flexibility [5]. In the context of energy generation and storage, graphene also stands out, particularly in the 2-3 V range [6].

Furthermore, there are various possibilities for choosing the electrolyte, which can be organic, solid, or even an ionic liquid (IL) [7, 8]. Among the numerous types of ILs available, amino acid-based ILs (AAILs) are noteworthy, composed of amino acids (AAs). Indeed, this new class is prominently featured due to its biodegradable properties [9, 10], making them environmentally viable. Additionally, their versatility is highlighted as they consist of functional groups that can be chemically modified [9].

Thus, this study aimed to evaluate the structural electrical properties of a SC composed of graphene electrodes and an electrolyte composed of 1-ethyl-3-methylimidazolium (Emim) and alanine (Ala), denoted as [Emim][Ala], using Molecular Dynamics (MD) concepts.

Methodology
We modeled the device considering the simulation box dimensions as x = 3.708 nm, y = 3.8529 nm, and z = 12 nm. We used the AA-IL density information from Ref. [11] with charge scaling to adjust the density values in more detail, using +1 for [Emim] and -1 for [Ala]. With these density values, we calculated the maximum number of molecules that would completely fill the simulation box based on the molecular weight of each molecule. The software Packmol [12] was used for the modeling. It's worth noting that two vacuum columns were added after each supercapacitor (each with a length of 24 nm along the z-axis), as we employed periodic boundary conditions and aimed to avoid any electrode interactions. To reinforce this, the simulations were conducted with fixed electrodes. Figure 1 shows the

representation of the simulated model without any water added.

After the modeling process, we established the parameters for the MD simulations. The initial simulations aimed to achieve thermodynamic equilibrium of the system, while the final simulation aimed to obtain the electrical properties. To achieve equilibrium, we performed 20 simulation cycles. The simulations were conducted using an NVT ensemble at a constant temperature of 500 K (employing the *v-rescale* temperature coupling method every 0.1 s) and a pressure of 1.013 bar. The number of steps varied significantly across simulations, ranging from 10^4 to 5 x 10^7, allowing us to explore the system's evolution over different time periods. Electrostatic interactions were handled using *Cut-Off* and PME methods with cut-off radii set to 1.2 nm. For this methodological framework, we utilized the software GROMACS [13]. It is important to emphasize that we analyzed cases where the electrodes were subjected to charge densities of 0.00, 2.40, and 4.81 µC/cm² using the fixed charge model.

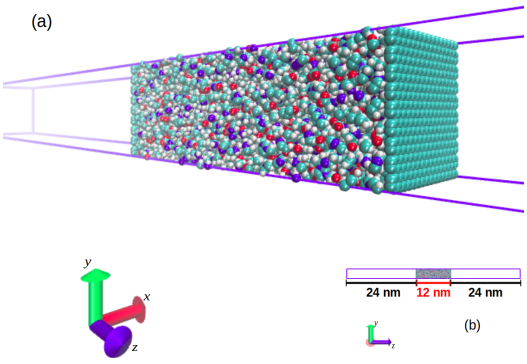


Figure 1: Standard simulated SC model. Here we present the configuration featuring [Emim][Ala] without added water as the electrolyte: (a) Perspective view of the model rotated at 45º; (b) Orthogonal view showing the complete simulation box.

Results

The electric potential values on the electrodes were obtained directly from the MD simulations. the results of the potential along the z axis of the capacitor can be observed in Figure 2.

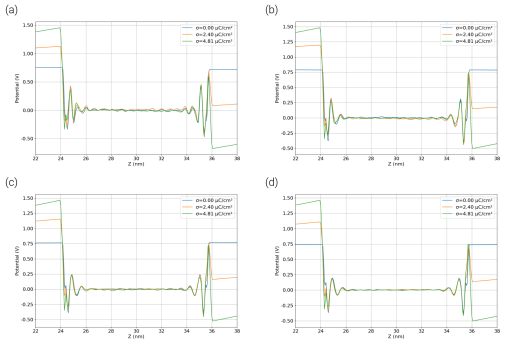


Figure 2: Potential values along the z axis of the SC for: (a) [Emim][Ala]; (b) [Emim][Ala] + 10% water; (c) [Emim][Ala] + 20% water; (d) [Emim][Ala] + 30% water.

With the potential values on the positive and negative electrodes for each charge density, we performed a linear fit to determine the capacitance of the device. Through this analysis, we found that for the device with the electrolyte in its pure form, i.e., without any water addition, the capacitance was 2.30 µF/cm². However, for hydrations at 10% and 20%, the capacitance values were found to be 2.42 µF/cm². In contrast, with hydration at 30%, the capacitance increased to 2.45 µF/cm². This increase in capacitance with increasing electrolyte hydration suggests a potential enhancement in the device's energy storage capability, as stored energy is directly proportional to capacitance.

Discussion

As a rule, computational analyses of materials aim to anticipate characteristics and properties that enable their applicability in industry or everyday life. Indeed, we can conclude that this study demonstrates these aspects. Through Molecular Dynamics simulations, we observed that using AAILs as electrolytes in supercapacitors could be a promising alternative for energy storage, and it is an environmentally friendly choice due to their biodegradable properties. Furthermore, our model aimed to enhance these biodegradable properties by studying the energy storage behavior as the electrolyte hydration progressed. In addition to contributing to environmental aspects, the addition of water is also very

interesting from an economic standpoint, as it makes these devices cheaper and lighter.

Acknowledgements

The authors acknowledge the financial support of the Brazilian agencies CNPq and CAPES, Brazil.

References

1. Chagas, H. A.; Fileti, E. E.; Colherinhas, G. J. Mol. Liq. 2022, 360, 119494.
2. da Silva, D. A. C.; Paulista Neto, A. J.; Pascon, A. M.; Fileti, E. E.; Fonseca, L. R. C.; Zanin, H. G. J. Phys. Chem. C 2021, 125 (10), 5518-5524.
3. Shim, Y.; Kim, H. J.; Jung, Y. Faraday Discuss. 2012, 154, 249-263.
4. Xia, L.; Yu, L.; Hu, D.; Chen, G. Z. Mater. Chem. Front. 2017, 1 (4), 584-618.
5. Cardoso, W. B.; Avelar, A. T.; de Almeida, N. G; Colherinhas, G. J. Phys. Chem. A 2019, 123 (9), 1790-1795.
6. Huang, Y.; Liang, J.; Chen, Y. Small 2012, 8, 1805-1834.
7. Lian, C.; Liu, H.; Wu, J. J. Phys. Chem. C 2018, 122 (32), 18304-18310.
8. Oliveira, L. B. A.; Fonseca, T. L.; Colherinhas, G. J. Mol. Liq. 2024, 393, 123662.
9. Ohno, H.; Fukumoto, K. Acc. Chem. Res. 2007, 40 (11), 1122-1129.
10. Hou, X. D.; Liu, Q. P.; Smith, T. J.; Li, N.; Zong, M. H. PLOS ONE 2013, 8 (3), e59145.
11. Fileti, E. E.; Chaban, V. V. Chem. Phys. Lett. 2014, 616–617, 205-211.
12. Martínez, L.; Andrade, R.; Birgin, E. G.; Martínez, J. M. J. Comput. Chem. 2009, 30 (13), 2157-2164.
13. Abraham, M. J.; Murtola, T.; Schulz, R.; Páll, S.; Smith, J. C.; Hess, B.; Lindahl, E. SoftwareX 2015, 1–2, 19-25.

Interaction of Methanol with Chemical Environment: Zeolite Adsorption and Supercritical Intermolecular Interactions through VPT2 and AIMD Vibrational Spectra under Varying Thermodynamic Conditions

Lucas Gonçalves Randolli[1], Thiago Mineo Mizumoto[1], Dr. Leonardo José Duarte[1,2], Dr. Lenin José Díaz Soto[1], Prof. Dr. Ataualpa A. C. Braga[1].
[1]Institute of Chemistry, University of São Paulo, São Paulo - SP, Brazil.
[2]Center of Chemistry, University of Coimbra, Coimbra, Portugal.
lrandolli@iq.usp.br
Keywords: Zeolites; DFT; AIMD; Anharmonicity; Supercritical Fluids.

Abstract

Vibrational modes of protonated methanol interacting with its surroundings are knowingly anharmonic. We used DFT to compute harmonic and anharmonic spectra of MeOH adsorbed to a model of HZSM-5 (MFI). Spectra of liquid and supercritical methanol obtained from MD simulations were also evaluated.

Introduction

The dehydration of Methanol to Dimethyl Ether (DME) process has the potential of gaining great importance on a methanol-based, low-carbon economy. Recent, still unpublished experimental work showed that increasing the methanol pressure can substantially boost catalytic performance of the acid H-ZSM-5 (MFI) zeolite for this process. However, the reasons for such an effect are still unknown, partially because detailed spectroscopic data are difficult to be obtained on operando conditions. In order to investigate this effect from first principles calculations, we have been working on a suitable model that appropriately describes both the interaction between the catalyst and its substrates and the effects of the supercritical regime on the energetics of the process.

In a first step, we determined the MeOH adsorption free energy to the MFI T12 site in the supercritical regime by including harmonic thermodynamic corrections, but large discrepancies with published values for the adsorption enthalpy [3] suggested a further refinement of the model was necessary. We also tested several methods for optimizing a cluster model for the structure of MFI's straight channel (Fig. 1).

Anharmonic coupling is knowingly present in the interaction of protonated methanol with the chemical environment [2]. They are especially relevant when it comes to adsorption on zeolites, can become even more pronounced when subjected to high pressures and must be included in calculations when computing vibrational corrections for thermodynamics. On a second step, we strived to use Vibrational Perturbation Theory (VPT2) to compute the anharmonic spectrum of MeOH adsorbed to MFI. Interactions with both a 2T cluster model of MFI's T12 site and 2 neighboring MeOH molecules are being evaluated and compared with harmonic data.

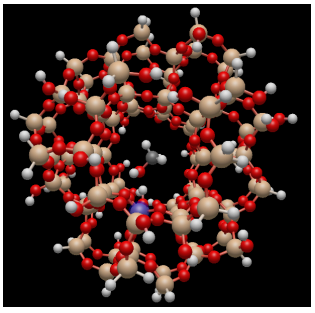


Figure 1: Methanol physisorbed to the spheric cluster model developed in this work. Geometry obtained on r²SCAN-3c level of theory

Raman spectra of pure methanol has been shown to change in the supercritical region

due to stronger intermolecular interactions [1]. Thus, in a third stage, we began to run Molecular Dynamics simulations of liquid and supercritical methanol in order to characterize those interactions and look for anharmonicity of vibrational modes. AIMD spectra will be presented and compared to gas phase results by the time of the Symposium.

We thus expect to better understand the behavior of Methanol and H-ZSM-5 on different temperatures and pressures, providing insights for further refinement of our static DFT model for the process.

Methodology

In order to investigate the effect of the methodology for reproducing the experimental MFI structure, we constructed a spheric cluster to model the straight channel of the zeolite. Using a homemade Python script, the resulting cluster containing 322 atoms (Fig. 1) was extracted from the unit cell available on the International Zeolite Association (IZA) database. One semiempirical approach, three composite methods and eight density functionals were tested. Resulting geometries were compared to the original crystallographic one by calculating the Root Mean Square Deviations (RMSD) value.

Methanol adsorption energies were firstly calculated with the ωB97X-D3BJ/def2-TZVP level of theory, from the r²SCAN-3c geometries, with vibrational corrections thermodynamics computed in the harmonic quasi-RRHO approximation.

Regarding the contribution of anharmonic modes in the vibrational correction for the MeOH adsorption free energy, VPT2 calculations are being performed using the QM/MM scheme (B3LYP//UFF), with def2-SVP basis set for oxygens, carbons and hydrogens, and SDD effective core potential basis set for aluminum and silicon, on a 2T cluster model (Figure 3a).

Molecular Dynamics simulations are being performed on a 32 Methanol molecules simulation box on Periodic Boundary Conditions. Equilibration runs were firstly performed with the LAMMPS force-field, and subsequent runs are being performed using the BLYP Density Functional Approximation with a 70 Ry cutoff. The simulations are being performed on the liquid (300 K, 1 bar) and supercritical (600 K, 200 bar) regimes. Classical MD trajectories were obtained on an equivalent model using the LAMMPS force field. Spectra obtained from AIMD simulations will be compared with classical MD results.

Geometries were optimized using ORCA 5.0.4, and VPT2 calculations are being performed using Gaussian16. AIMD calculations are being performed on CP2K 2024.1, and classical MD trajectories were obtained with LAMMPS.

Results

In the first part of the work, the performance of different methods for determining the structure of MFI was evaluated. Table 1 shows the RMSD values and total calculation time for each method.

Geometry Optimization			
Method	RMSD (Å)	Number of cores	Total Calculation Time
GFN2-xTB	0.1850	4	00d03h54min
PBEh-3c	0.1316	8	16d15h36min
B97-3c	0.1551	8	09d21h14min
r²SCAN-3c	0.0941	8	04d08h10min
BP86-D3BJ/def2-SVP	0.1757	8	2d8h42min
B97-D3/def2-SVP	0.1656	8	3d6h12min
PBE-D3BJ/def2-SVP	0.1729	8	2d7h46min
revPBE-D3BJ/def2-SVP	0.1900	8	2d11h16min
r²SCAN-D3BJ/def2-SVP	0.1496	8	3d12h20min
TPSS-D3BJ/def2-SVP	0.1622	8	2d09h48min
TPSSh-D3BJ/def2-SVP	0.1415	8	10d03h38min
PBE0-D3BJ/def2-SVP	0.1190	8	8d06h17min

Table 1: Performance of electronic structure methods for geometry optimizations of the bare silica cluster.

Table 2 shows the methanol adsorption free energy calculated in this study using the ωB97X-D3BJ/def2-TZVP level of theory with harmonic vibrational corrections. The enthalpy is compared to the values previously reported by Piccini, Alessio and Sauer [3].

Adsorption Energies				
Method	Author	Temperature	ΔG (kJ/mol)	ΔH (kJ/mol)
ωB97X-D3BJ/def2-TZVP	This work	500K	-114	-248
MP2/PBE+D	Piccini, Alessio and Sauer	300K	-28	-84

Table 2: Adsorption energies for MeOH in MFI.

The geometry of methanol adsorbed to a 2T cluster model of MFI used to perform QM/MM (B3LYP//UFF) harmonic and

anharmonic VPT2 frequency calculations is shown on Figure 2.

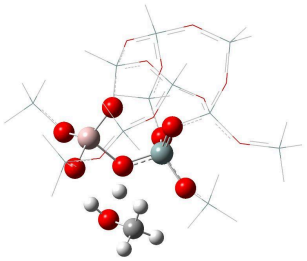


Figure 2: 2T Cluster model used in the VPT2 calculations. QM atoms are shown in a ball and stick fashion, MM are shown with sticks only.

Infrared spectra obtained for the model above with the QM/MM B3LYP/UFF level of theory are presented in Figure 3.

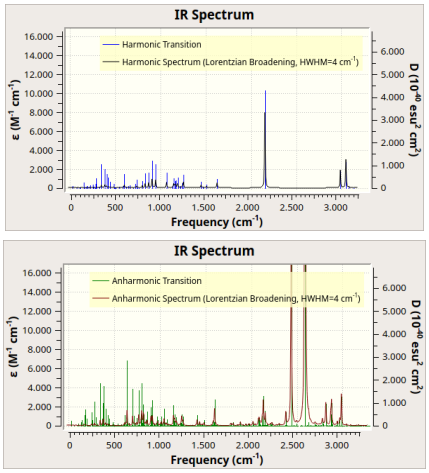


Figure 3: Harmonic (above) and anharmonic (below) spectra of adsorbed MeOH obtained from QM/MM B3LYP/UFF calculations.

Reliable double-hybrid VPT2 results and AIMD spectra have not been obtained yet, and should be presented by the time of the symposium.

Discussion

The smallest RMSD value was obtained with the r²SCAN-3c composite method. The computational cost of this approach is similar to that of a meta-GGA, making it a promising method for optimizing the geometry of zeolite.

Large disparities between our harmonic calculations for the free energy of adsorption and published values imply that anharmonic corrections should be included, which prompted us to perform VPT2 calculations. Preliminary results show high intensity combination bands associated with the motion of the zeolitic proton that suggest an impact on energetics, but it should still be further evaluated with double-hybrid B2PLYP calculations.

Since AIMD spectra in the supercritical regime are yet to be obtained, the need to include explicit MeOH molecules to model the supercritical regime in our calculations cannot be debated yet.

Conclusions

The r²SCAN-3c composite method has proven to be suitable for geometry optimizations of H-ZSM-5 clusters. Harmonic calculations in vacuum showed to be insufficient to properly compute the energetics of methanol dehydration by H-ZSM-5. By the time of the symposium, we expect data from anharmonic VPT2 calculations and AIMD simulations will help us answer whether anharmonic effects or interactions in the supercritical regime must be included in our model in order to better describe the phenomenon of interest.

Acknowledgements

We thank FAPESP, CAPES and FUSP for funding, as well as prof. Mauro Carlos Costa Ribeiro and Dr. Abner Massari Sampaio from IQ-USP for the support and fruitful conversations about Molecular Dynamics simulation.

References

1. Kimura, Y.; Fukura, T.; Asada, Y.; Ueno, M.; Yasaka, Y.; J. Mol. Liq. 2017, 245, 11–16.
2. Lin, C.-K.; Huang, Q.-R.; Li, Y.-C.; Nguyen, H.-Q.; Kuo, J.-L.; Fujii, A.; J. Phys. Chem. A 2021, 125, 1910–1918.
3. Piccini, G.; Alessio, M.; Sauer, J.; Phys. Chem. Chem. Phys. 2018, 20, 19964–19970.

Electronic band structure and magnetic properties of doped silicene

LuccaMoraes Gomes[1], Andreia Luisa da Rosa[1], Flavio Bento de Oliveira[1]
[1]Instituto de Física, Universidade Federal de Goiás, Av.Esperança 74690-900, Goiânia, Goiás, Brasil.
luccanok@discente.ufg.br, andreialuisa@ufg.br, flaviobentooliveira@gmail.com.
Keywords: Silicene; Diffusion; Chromium; DFT; Spintronic.

Abstract

Magnetic nanomaterials have been deeply investigated due to it's fantastic properties and potential application in spintronics. Ferromagnetic materials is the fundamental materials applied on several devices used to read write and process data. New studies shows that antiferromagnetic materials could be used to enhance the already existent spintronic devices to increase the decoherence time and increase the reliability of the information storage. The present work aims to explore the magnetic and structural properties of the Cr adsorbed and doped silicene in several concentrations, directions and conformations of silicene, such as monolayer silicene, dumbbell silicene and bilayer silicene on several different stack modes. Cr adsorbed silicene is a strong candidate for spintronic applications mainly on AFM state.

Introduction

The growing interest in low-dimensional materials has led to the emergence of important ramifications in scientific knowledge such as the emergence of nanoscience and nanotechnology. Nanometer scale materials exhibit behaviors distinct from those of structural macroscopic. Due to associated quantum effects, these materials can possess new properties such as high electronic mobility and thermal conductivity, in addition to greater mechanical resistance. On the other hand, silicon is a material whose technological application is well established, and obtaining this material in nanostructured form expands its possibility of integration into current technology. Doping with open shell elements can be used to adjust the silicene band gap and at the same time introduce new functions, for example turning the material into a ferromagnet or into a antiferromagnet. This properties could led to spintronic applications.

However, several aspects of silicene doped with transition metals still remain unanswered, such as solubility limits of dopant, site preference for adsorption and doping and formation of magnetic domains. The objective of this work is to investigate the diffusion doping of Chromium atoms on silicene. Bilayer silicene was also investigated. We found that some metals introduce new magnetic properties into silicene, in addition to form metal alloys with it. Doped silicene seems to be promising for the application of these materials in electronic and magnetic devices.

Methodology

The method used to such investigation is the plane-wave-based Density Functional Theory (DFT). The generalized gradient approximation (GGA) with Perdew–Burke–Ernzerhof (PBE) function was used as exchange and correlation functional. The electrons wave functions were built using the PAW method.

Results

The present work has had some interesting results. NEB (Nudged elastic band) method was performed to obtain the

diffusion barrier for a parallel path (hollow to hollow) and for a transverse path for the diffusion of Cr atom in silicene. Both chosen paths presents a high barrier which means that the Cr atom will not move easily to an adjacent hollow after being adsorbed in silicene (stable adsorption), and the Cr atom will not cross the monolayer it will probably diffuse into silicene. It was possible to observe that the adsorption of Cr atoms pair in silicene has a preferential adsorption direction, (Arm-chair). The adsorption of Cr atoms pair in low concentrations in arm-chair direction is considerably more stable in AFM state. Dumbbell silicene adsorbed with Cr atoms were also investigated and the system has had a significant structural difference in AFM and FM states, despite of the AFM state is more stable compared to FM state [1].

The bilayer silicene was investigated in six different stack modes and also adsorbed with Cr atoms. The six different Cr adsorbed bilayer silicene presented a very interesting property which is the bucking dependence for the total magnetic moment. The larger is the buckling the smaller is the magnetic moment. Charge density difference were performed on Cr adsorbed monolayer silicene and bilayer silicene. One was able to notice that for low concentrations of Cr adsorbed in monolayer silicene the charge density was very localized, as well as for considerably high concentrations of Cr adsorbed bilayer silicene. This is a very interesting result since this material has potential applications in spintronics. This localized states could be explored for data storage. Another spintronic application is that controlled strain could be used to toggle between AFM and FM states and consequently used to generate binary data by using principles of spintronic [2].

Conclusions

Cr adsorbed silicene is a promising materials to spintronics applications. Most systems are more stable in AFM state. Strain-controlled could be used to generate information, due to AFM-FM state transition. NEB calculations shows high energy barriers for the site transition of Cr atom, therefore the system present a good stability when adsorbed with Cr atoms. Cr adsorbed bilayer silicene has shown a relation between the magnetic and the structural properties.

Acknowledgements

I thank my family for always supporting me in my work. I thank Professor Andreia Luisa da Rosa for guiding me in the development of my research and career. Special thanks to Flávio Bento for helping with the development of the project. To my friends. And to cenapad, Lamcad, LNCC, and CAPES for offering structure for the research.

References

1. R. Zheng, Y. Chen, J. Ni, Highly tunable magnetism in silicene doped with Cr and Fe atoms under isotropic and uniaxial tensile strain, Applied Physics Letters 107 (26) (2015) 263104.

2. Li Shuang, Ao Zhimin, Zhu Jiaji, and Ren Jichang. Strain controlled ferromagnetic- antiferromagnetic transformation in mn-doped silicene for information transformation devices. J. Phys. Chem. Lett., 8:1484–1488, 2017.

3. LI, S. et al. Strain Controlled Ferromagnetic-Antiferromagnetic Transformation in Mn-Doped Silicene for Information Transformation Devices. The Journal of Physical Chemistry Letters, v. 8, n. 7, p. 1484–1488, 20 mar. 2017.

4. LEONI, T. et al. Demonstration of the Existence of Dumbbell Silicene: A Stable Two-Dimensional Allotrope of Silicon. The Journal of Physical Chemistry C, v. 125, n. 32, p. 17906–17917, 6 ago. 2021.

5.

Interações de Solvatação do Ácido Indolacético em Água: Análise da Função de Distribuição Radial e CPMD

Núbia Maria Nunes Rodrigues[1], Lilian Tatiane Ferreira de Melo Camargo[2], Ademir João Camargo[1], Luciano Ribeiro[1,*]

[1] Grupo de Química Teórica e Estrutural de Anápolis, Câmpus Central, Universidade Estadual de Goiás (UEG), Anápolis – GO – Brasil

[2] Instituto Federal de Educação, Ciência e Tecnologia de Goiás, 75131-457, Anápolis, GO, Brazil

lribeiro@ueg.br

Keywords: Car-Parrinello Molecular Dynamics; Solvation; Radial Distribution Function; Hydration Shell

Abstract

This study used Car-Parrinello molecular dynamics to investigate the solvation of indoleacetic acid (IAA) in a system with 90 water molecules. The study focused on the interactions between the hydrogen atoms of IAA and the oxygen atoms of the water molecules. The radial distribution function analysis showed that the water molecules form a distinct hydration layer around the H_{19} and H_{22} sites, indicating significant solvation interactions. The O_{13} site also showed relevant solvation, highlighting the importance of these interactions for the stability of IAA in aqueous solution. These results, obtained using the Car-Parrinello method, provide a solid foundation for future research on the molecular dynamics of IAA in different environments.

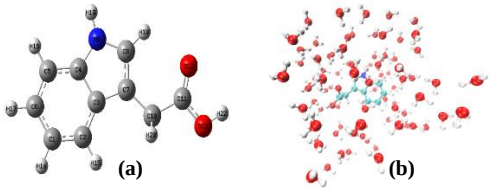
Introduction

As auxinas, os primeiros hormônios vegetais conhecidos, são fundamentais na regulação do crescimento das plantas [1]. O ácido indolacético (IAA) é a principal auxina, regulando processos como divisão, expansão e diferenciação celular, além do desenvolvimento de frutos [2].

Produzido principalmente no ápice e folhas jovens, o IAA estimula a abertura estomática e o movimento de água nas raízes [1]. Diversos microrganismos, como bactérias e fungos, podem produzir IAA, tornando-os potenciais produtores comerciais [3]. Investigamos, por meio de cálculos ab initio, a solvatação do IAA em meio aquoso para entender suas interações moleculares [1].

Methodology

A dinâmica molecular foi realizada no programa CPMD (versão 4.1) para a dinâmica molecular de Car-Parrinello, usando o funcional PBE Cálculos estáticos foram feitos no Gaussian 16. A análise topológica das interações interatômicas foi realizada com a teoria de Bader usando o *multiwfn* 3.7. As trajetórias CPMD foram analisadas para obter a FDRP, TMR e ligações de hidrogênio. O VMD 1.9.3 foi usado para visualização. A simulação do IAA isolado (Fig 1a) durou 60 ps, e com 90 moléculas de água, 40 os (Fig 1b). O ensemble NVT foi mantido a 300 K com termostatos Nosé-Hoover e integração Velocity-Verlet.

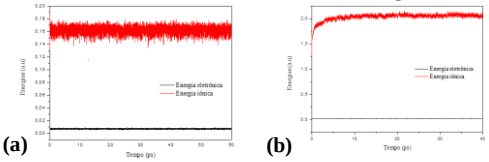


(a) **(b)**

Figura 1. a) Estrutura molecular do IAA (vácuo) com os rótulos numéricos. b) Solvatação do IAA durante a simulação.

Results and Discussion

A Figura 2a e 2b mostram a separação adiabática entres os subsistemas para a molécula do IAA no vácuo e na água.



(a) **(b)**

Figura 1. a) Estrutura molecular do IAA (vácuo) com os rótulos numéricos. b) Solvatação do IAA durante a simulação.

A Figura 2 mostra a RDF dos átomos de oxigênio das moléculas de água nos sítios H19 e H22 do IAA, com picos bem definidos entre 1,35–2,55 Å (Figura 2a) e 0,85–2,45 Å (Figura 2b), com picos em 1,95 Å e 1,45 Å, respectivamente. A integral da RDF indica 0,95 e 0,93 molécula de água na primeira esfera de hidratação. A RDF g(Hw_O_13) revela um pico claro entre 1,35 Å e 2,45 Å, com um pico em 1,95 Å e uma média de 1,42 átomos de hidrogênio (Figura c).

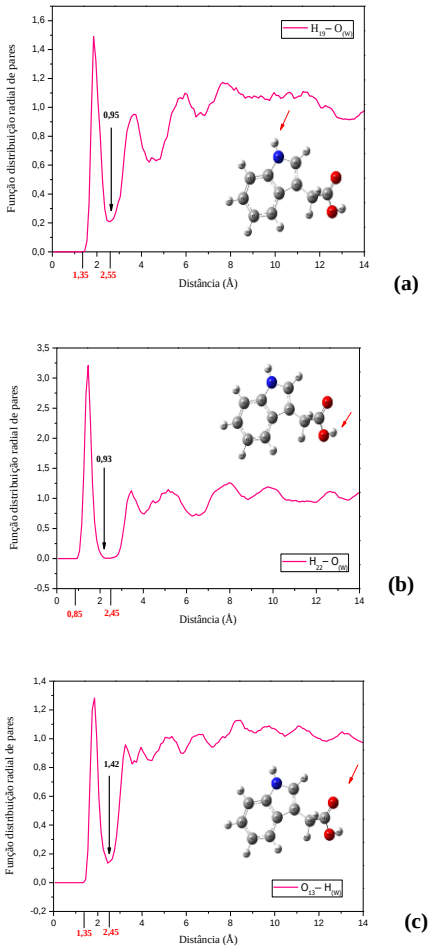


Figura 2. a) FDRP para os átomos a) H19, b) H22 e c) O13 do IAA com os átomos de água durante a simulação.

Conclusion

Concluímos que a solvatação do IAA em água revela interações específicas e bem definidas entre os átomos de hidrogênio do IAA (H19 e H22) e os átomos de oxigênio das moléculas de água. A análise da RDF mostra que as moléculas de água formam uma camada de hidratação distinta em torno dos sítios H19 e H22, com picos claros indicando fortes interações de solvatação. A presença de 0,95 e 0,93 molécula de água na primeira esfera de hidratação ao redor dos sítios H19 e H22, respectivamente, destaca a importância dessas interações na estabilidade da solvatação. Adicionalmente, a análise do sítio O13 mostra uma solvatação igualmente significativa, evidenciada pelo pico na RDF e pela média de 1,42 átomos de hidrogênio das moléculas de água interagindo nessa região. Esses dados contribuem para uma compreensão mais aprofundada das propriedades de solvatação do IAA, fornecendo informações cruciais para futuras investigações sobre a dinâmica molecular do IAA em diferentes ambientes.

Acknowledgements

Agradecemos à Universidade Estadual de Goiás pelo apoio logístico e à bolsa de doutorado concedida à discente Núbia Maria Nunes Rodrigues.

References

1. Gadallah MAA (2000) Journal of Arid Environments 44:451–467.
2. Enders TA, Strader LC. American Journal of Botany 102:180–196.
3. Bunsangiam S, Thongpae N, Limtong S, Srisuk N (2021) Scientific Reports 11:13094.

Thermodynamic Stability and Electronic Properties of Polymorphic Perovskite Alloys

Luis O. de Araujo[1], Celso R. C. Rêgo[2], Wolfgang Wenzel[2], Maurício J. Piotrowski[3], Alexandre C. Dias[4], and Diego Guedes-Sobrinho[1].
[1]Department of Chemistry, Federal University of Paraná, Curitiba, 81531-980, Paraná, Brazil. [2]Institute of Nanotechnology Hermann-von-Helmholtz-Platz, Karlsruhe Institute of Technology, Karlsruhe, Baden-Württemberg, Germany.
[3]Department of Physics, Federal University of Pelotas, Pelotas, 96010-900, Rio Grande do Sul, Brazil. [4]Institute of Physics and International Center of Physics, University of Brasília, Brasília, 70919-970, DF, Brazil.
araujo.phys.chem@gmail.com
Keywords: Metal halide perovskites (MHPs); Hybrid Perovskite Alloys; Generalized Quasichemical Approximation (GQCA), Density Functional Theory, DFT-1/2.

Abstract
Employing an automated cluster expansion within the generalized quasichemical approximation (GQCA), we explored the impact of polymorphic features on the electronic properties, configurational disorder, and thermodynamic stability of $FA_{1-x}Cs_xPbI_3$ perovskite alloy, revealing how the effective radius of cations into the cuboctahedral voids, their dipole moments, and temperature influence the structural motifs in their respective inorganic frameworks. Through a complete first-principles protocol including relativistic effects such as spin-orbit coupling (SOC), the low-cost DFT-1/2 quasiparticle correction, and a generalized ensemble encompassing multiple polymorphs, we found a critical temperature of about 427.7 K for the alloy, which is stable against phase segregation for $x<0.15$ above 100 K. Our findings advocate for the rational design of thermodynamically stable compositions to applications in solar cells by calculating power conversion efficiencies via the spectroscopic limited maximum efficiency (SLME) model, from which we obtained high efficiencies of about 31–32% for $FA_{1-x}Cs_xPbI_3$, with $0.0<x<0.20$ as potential photovoltaic candidates at room temperature.

Introduction
Metal halide perovskites (MHPs) are promising materials for photovoltaic (PV) devices, presenting impressive power conversion efficiencies (PCE) exceeding 26%, e.g., for $FAPbI_3$.[1] However, the intrinsic chemical instability of hybrid MHPs is challenging to manufacture long-term stable solar cells, which has motivated alloying strategies between Cs cations and organic ones to form $A_{1-x}Cs_xPbI_3$ (e.g., A = MA, FA). However, the correlation between the polymorphic nature of MHPs *in operando* and their electronic properties (connected with PCE values) through empirical approaches is not trivial, potentially hampered in the alloying context.[2,3]
Cubic MHPs as polymorphous networks have a local structure that differs from the global *Pm-3m* space group, whose low symmetry structural motifs (B-metal off-center displacements within octahedra, octahedral rotations, positional rearrangements of the A cations within the cuboctahedral voids, and second-order Jahn-Teller distortions) are not experimentally characterized by X-ray diffraction (XRD) technique due to the long coherence length.[2] Thus, investigations about

the impact of those motifs on the thermodynamic stability and electronic properties of MHP alloys from an atomistic perspective are scarce, while a reliable mapping of the composition dependence through experiments to investigate phase transitions or the gap energies requires high financial costs involving reagents and material characterization. Thus, there is a wide field to develop *ab initio* protocols to capture this polymorphism through proper construction of the alloys' thermodynamic ensembles, with automation procedures being highly desirable to speed up data acquisition. Here, we investigated the impact of polymorphism on the thermodynamic properties of $FA_{1-x}Cs_xPbI_3$ alloy, developing an automated workflow within the SimStack framework to make their cluster expansions based on the generalized quasichemical approximation (GQCA).[1] From this, we characterized the alloy's polymorphic features and their influence on the gap energies and PCE as a function of composition and temperature, being able to make predictions about this material for application in solar cells.

Methodology

The thermodynamic properties of $FA_{1-x}Cs_xPbI_3$ alloy were calculated through the GQCA, wherein their polymorphs were expanded into an ensemble of 22 cluster classes that are statistically and energetically independent.[1] Since we focus on analyzing a cubic crystal structure with multiple polymorphic elements, the following set of configurations was explored to compose our thermodynamic ensemble: $a^-a^-a^+$ (stablest isostructural limit), $a^-a^-a^-$ (metastable isostructural limit), ROT (random octahedral tilts), which were identified by their octahedrons rotations pattern via Glazer's notation.[1,2] For each polymorph, clusters were automatically constructed by using the symmetry operations of the *Pm-3m* space group, as implemented in the Simstack via the SOD-2022 Workflow active node (Wano, Fig. 1). DFT calculations were made through DFT-VASP Wano by using the PBE approximation for exchange-correlation functional, in which spin-orbit coupling (SOC) was included. All needed data were transformed in a database by DB-Generator, which was passed to a Colab notebook in a subsequent step for GQCA calculations. DFT-1/2 quasiparticle correction was employed to compute the alloy's gap energies by making the electron half-ionization from 5p orbitals of I atoms. Following this, we employed the spectroscopic limited maximum efficiency (SLME) model to compute the material's PCE at 300 K, making thermodynamic averages over the respective polymorphic ensemble.[3]

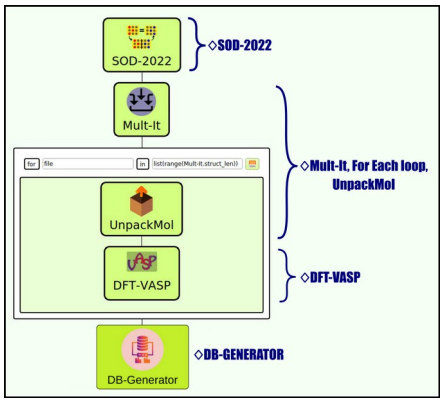


Figure 1. WaNos used to construct the Simstack-based Workflow to automatize the polymorphic alloy's calculations within the GQCA approach.

Results and Discussion

The calculated phase diagram for $FA_{1-x}Cs_xPbI_3$ alloy is shown in Fig. 2. From this, segregation preferentially occurs when $x > 0.20$, since FA is about 40% larger than Cs and its incorporation into perovskite becomes increasingly unfavorable as the matrix becomes richer in Cs for the $a^-a^-a^+$ polymorph, which presents higher statistical contributions (40-70%) to the alloy at 300 K. This finding is in good accordance with experimental reports, which suggest the limit for Cs content in the cubic phase of $FA_{1-x}Cs_xPbI_3$ to be about 15–20% at room temperature, and the bulk $FA_{0.9}Cs_{0.1}PbI_3$ compound being stable at the same temperature.[1]

The gap energies computed with the GQCA+DFT-1/2+SOC protocol are presented in Fig. 3. When we put together all the effects

of individual polymorphs, an excellent agreement was obtained between the calculated E_g values and their experimental counterparts, evidencing the importance of polymorphic degrees conferring to the cation alloy its experimentally measured properties.

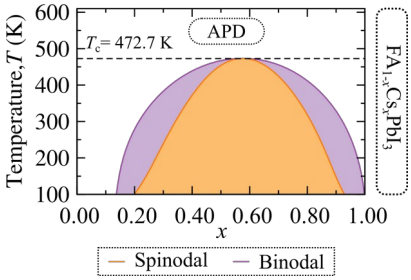


Figure 2. Phase diagram calculated for $FA_{1-x}Cs_xPbI_3$ system showing the binodal (purple) and spinodal (orange) lines.

In addition, our results here also evidence the importance of statistical protocols in the alloy treatise from an *ab initio* perspective, since only the analysis of gap energies cannot allow distinguishing between the different polymorphic contributions to the alloy.

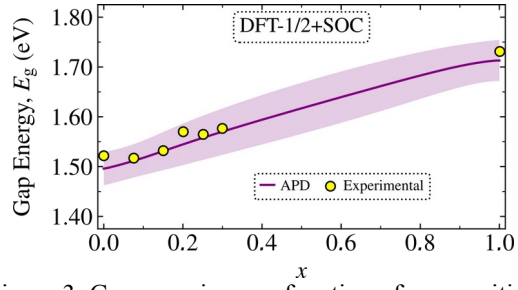


Figure 3. Gap energies as a function of composition for $FA_{1-x}Cs_xPbI_3$ at T = 300 K. Available experimental reports are shown as symbols filled in yellow.[1]

As a general trend, PCE values computed for $FA_{1-x}Cs_xPbI_3$ via SLME model follow the behavior of E_g shown in Fig. 3, where compositions with lower E_g values presented higher PCE. The latter is dominated by the polymorph with the highest probability at 300 K, being $a^-a^-a^+$ for $0.0 < x < 0.50$ and ROT for $0.50 < x < 1.00$, with PCE for $FA_{0.9}Cs_{0.1}PbI_3$ system at room temperature being near to 31%.

Conclusions

We performed a systematic first-principles investigation about the polymorphic features of $FA_{1-x}Cs_xPbI_3$ pseudo-cubic alloy, analyzing the impact of mixing organic and inorganic cations on its thermodynamic and electronic properties. Our calculated phase diagram correlated well with the experimental findings about the system analyzed here, allowing us to verify how different polymorphic contributions can affect its thermodynamic stability. The obtained gap energies were in excellent agreement with the available experimental reports, reflecting the statistical nature of the MHP alloys from the FA-cation configurational disorder and the disorder from the polymorphic nature intrinsic to the MHPs. Joining together the statistical features of GQCA with the SLME model, we computed the corresponding alloy's PCEs *in operando* conditions of temperature, in direct connection with their main application in solar cell devices, making a breakthrough in the rational design of thermodynamically stable MHP cation alloys for optimized PV applications via automated workflow technologies.

Acknowledgments

The authors thank the Atos, CIMATEC SENAI (BA), LCPAD, CAPES (finance Code 001), CNPq (grant number 307345/2021-1 and 408144/2022-0), BMBF, FAPDF (grant 00193-00001817/2023-43), CENAPAD-SP (UNICAMP/FINEP-MCTI project), Lobo Carneiro HPC (NACAD, UFRJ) and KIT.

References

1. de Araujo, L. O.; Rêgo, C. R. C.; Wenzel, W. *et al*. npj Comput. Mater. 2024, 10, 146.
2. de Araujo, L. O. Rêgo, C. R. C.; Wenzel, W. *et al*. J. Phys. Chem. C 2022, 126, 4, 2130.
3. de Araujo, L. O. Rêgo, C. R. C.; Wenzel, W. *et al*. J. Comput. Chem. 2023, 44 (14), 1395.

PCHY a rationally designed peptide with inhibition potential for SARS-CoV-2 RBD

Luiz Felipe M.A. Benicio,[1] Érica C.M. Nascimento,[2] Aisel Valle Garay,[3] Sonia M. Freitas,[3] João Batista Lopes Martins[1,2]
[1] Universidade de Brasília, Faculdade de Ciências da Saúde, Departamento de Farmácia, Brasília-DF, Brasil;
[2] Universidade de Brasília, Laboratório de Química Computacional, IQD, 70910900, Brasília-DF, Brasil.
[3] Universidade de Brasília, Instituto de Biologia, Laboratório de Biofísica Molecular, Brasília-DF, Brasil.
lipembenicio@gmail.com
Keywords: BTCI, SARS-CoV-2, ONIOM, Docking.

Abstract

Type

SARS-CoV-2 Omnicron variant stands out as a negative legacy left by the COVID pandemic due to its high mutation rate, particularly in the Spike protein, a key bioreceptor involved in viral infection. To investigate the inhibitory potential of BTCI-derived peptides, we selected two Spike protein structures for study: the original coronavirus Spike protein (S_C), which lacks mutations, and the Omicron variant Spike protein (S_O), which contains residue mutations. In this work we provide insights into the possible molecular interactions and inhibition tendencies of BTCI-derived peptides against S_C and S_O Spike proteins, contributing to the development of effective therapeutic strategies against those targets.

Introdução

A pandemia do COVID-19 impactou negativamente os sistemas de saúde e a vida de acometidos pelo SARS-CoV-2 em todo o mundo diminuindo a qualidade de vida com sequelas de longo prazo.[1] O surgimento da variante Omicron (B.1.1.529) é uma consequência da pandemia que continua a levantar preocupações devido às suas mutações na proteína Spike(S) e possibilidade de doença grave com quadro de óbito em indivíduos comprometidos.[1,2] O monitoramento das mutações nos resíduos do domínio de ligação ao receptor (RBD) e sua correlação com mecanismo de escape antigênico e outbreak continua a ser realizado.[3]

Dadas as tendências de mutação no RBD, selecionamos a proteína Spike do coronavírus inicial (S_C) e da variante Omicron (S_O) para avaliar os efeitos inibitórios de um grupo de peptídeos derivados do *black-eyed pea trypsin/chymotripsin inhibhitor* (BTCI). Esses peptídeos, desenvolvidos a partir de inibidores de proteases Bowman-Birk pelo Grupo de Biofísica Estrutural da Universidade de Brasília (UnB), são denominados PTRY9L, PTRY9D, PTRY8, PTRY6 e PCHY.[4]

Neste estudo, realizamos análises de docking para avaliar o potencial de inibição e as interações dos peptídeos derivados do BTCI contra as proteínas Spike S_C e S_O. Além disso, conduzimos estudos ONIOM no sistema PCHY-S_C e PCHY-S_O com objetivo examinar as variações de carga dos átomos dos sistemas e averiguar as interações observadas no docking.

Metodologia

Estruturas cristalográficas da proteína Spike do SARS-CoV-2 foram obtidas através do Protein Data Bank (PDB)[5], códigos 7A93 e 7T9J (Uniprot: P0DTC2) para as proteínas S_C e S_O.[6,7] A região de binding (RBD), resíduos Pro330 a Ser530, foi

selecionada e analisada em cada estrutura. Em seguida, realizamos os estudos de protonação com PropKa em pH 7.0 dos RBDs.[8]

Os peptídeos ligantes PCHY, PTRY9D, PTRY9L, PTRY8 e PTRY6 foram otimizados utilizando método/funcional B3LYP/6-311+G(d,p) com intuito de obter o ponto mínimo de energia por meio do pacote Gaussian 16.[9]

Realizamos o estudo de docking com o algoritmo de docking AutoDock 4.2.[10] Utilizamos o carbono β do resíduo Leu452 como ponto central para da caixa. As mutações presentes nas estruturas foram levadas em consideração para o dimensionamento das caixas. Os parâmetros de acoplamento utilizados com o algoritmo genético Lamarckiano (LGA), com número de soluções ajustados para 100, avaliações em $40x10^6$ e tamanho populacional para 150. Os resultados foram visualizados com o Discovery Studios e Virtual Molecular Dynamics (VMD).[11,12]

As soluções Receptor-Ligante utilizadas no ONIOM para os sistemas PCHY-S_C e PCHY-S_O foram obtidas a partir do estudo de Docking. Realizamos a divisão do sistema de ONIOM em duas camadas, a camada Alta (PM6) constituída pelo inibidor e os aminoácidos 448-454, 469-471 e 470-506; e a camada Baixa (AMBER) composta pelos demais aminoácidos. Utilizamos o Gaussian 16.[9]

Resultados

Para a análise, levaremos em consideração que o RBD é uma região promiscua e que peptídeos não apresentam a mesma energia de interação que ligantes pequenos. Assim, as interações geradas pelo estudo de docking (Tabela 1) demonstram que os peptídeos derivados do BTCI apresentam uma energia de interação (scores), abaixo de -9.0 kcal/mol. Demonstrando que os peptídeos apresentam potencial de interação intermediário com os alvos, entre -4.0 kcal/mol e -7.0 kcal/mol. O peptídeo PCHY apresentou as soluções com melhor score para S_C e S_O, respectivamente -6.37 kcal/mol e -6.70 kcal/mol. Assim como o peptídeo Ptry6 apresentou a solução com menor score para ambos os alvos, respectivamente -1.01 kcal/mol e -0.25 kcal/mol.

Tabela 1. Scores obtidos a partir do Docking com o AutoDock 4.2: a) RBD do S_C, b) RBD do S_O.

Peptídeo	*Spike Inicial (7A93)*	*Spike Ômicron (7T9J)*
PTRY9D	-4.61	-4.69
PTRY9L	-4.52	-3.57
PTRY8	-3.63	-3.40
PTRY6	-1.01	-0.25
PCHY	-6.37	-6.70

Através da imagem 1, demonstramos as interações realizadas pelo PCHY. Observamos que o PCHY realiza 8 ligações de hidrogênio, 2 interações π-Alkil e uma interação desfavorável com o S_C. Já com o S_O o PCHY realizou 5 ligações de hidrogênio, 2 interações π-Alkil e 1 interação π-Sulfur. Observamos que o Pchy apresentou mais interações com o S_C quando comparado com o S_O.

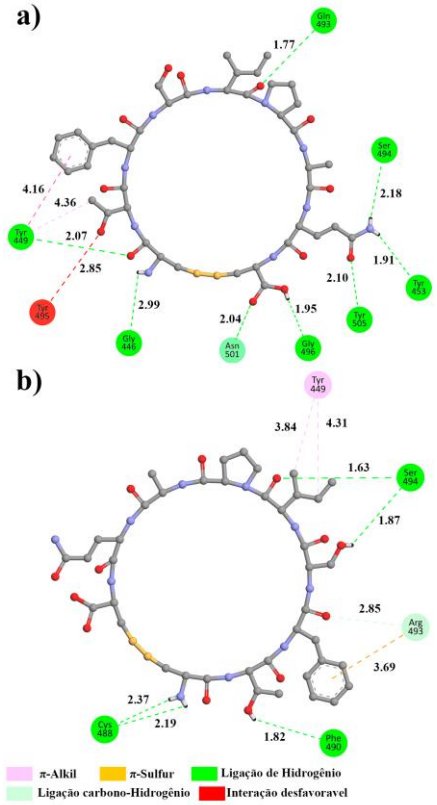


Imagem 1. Interações observadas com o Pchy com os alvos: a) RBD do SC, b) RBD do SO.

As mutações nos resíduos G496S, N501Y e Y505H afetaram negativamente a interação com resíduo, demonstrando que as

interações não estão mais presentes. A mutação Q493R alterou a natureza da interação de 1 pote de hidrogênio para uma ponte de hidrogênio e uma interação π-sulfur. As soluções geradas para o Pchy foram utilizadas para os estudos de ONIOM.

Os estudos de ONIOM demonstraram ambos os sistemas apresentaram variação das cargas atômicas nos resíduos do receptor. As cargas com maiores variações apresentadas para os alvos S_C e S_O foram o CG da Tyr453 com -1.456 Mulliken e o CA da Arg493 com 0.882 Mulliken respectivamente. Ambos os resíduos, Tyr453 e Arg493, realizam interações com o peptídeo PCHY, demonstrando que as interações foram reproduzidas.

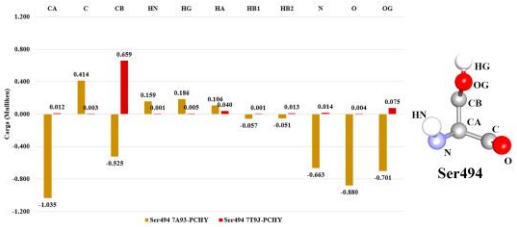


Imagem 2. Comparação da variação de carga em Mulliken dos átomos dos resíduos da Ser494 dos sistemas PCHY-S_C e PCHY-S_O.

Observamos que a diferença nas interações da Ser494 (Figura1) foi reproduzida nas cargas do ONIOM (Figura 2). As variações de cargas nos átomos HG, OG, CB, C para o S_O e nos átomos O, C, CA para o S_C demonstra que as interações ocorrem com diferentes conjuntos de átomos.

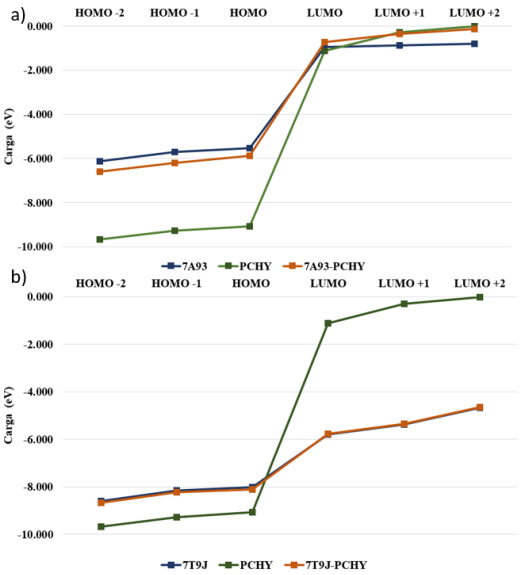


Imagem 3. Comparação dos orbitais HOMO-2 ao HOMO+2 dos sistemas.

Observamos na imagem 3 que o GAP (LUMO-HOMO) dos alvos apresentou aumento quando em complexo com o peptídeo PCHY de -4.594 eV para –5.157 eV no S_C e aumento de -2.228 eV para -2.343 eV no S_O. O aumento observado no GAP dos complexos indica tendência de diminuição da reatividade da Spike quando na presença do PCHY, assim como que a diminuição da reatividade é maior no S_C que no S_O.

Conclusão

Os estudos de docking demonstram que os peptídeos apresentam interações com resíduos de interesse da proteína Spike. O estudo também demonstra que os resíduos 493 quando sofre mutação ainda se encontra realizando interação com o peptídeo PCHY. Os resultados do estudo de ONIOM sugerem que as interações diminuem a energia do complexo gerando maior estabilidade. Reforçando o potencial dos peptídeos para estudos de maior complexidade.

Agradecimentos

FAP-DF, CNPq, CAPES e UnB.

Referências

1. Afrashtehfar, K.I.; *Int. J. Environ. Res. Public Health* **2023**, *20*, 3099.
2. Mengist, H.M.; *Front. Chem.* **2021**, *9*.
3. Harvey, W.T.; *Nat. Rev. Microbiol.* **2021**, *19*, 409–424.
4. Fernandes, J.P.C.; *Arch. Biochem. Biophys.* **2019**, *665*, 79–86.
5. Berman, H.M. *Nucleic Acids Res.* **2000**, *28*, 235–242.
6. Mannar, D.; *Science (80-.).* **2022**, *375*, 760–764.
7. Benton, D.J.; *Nature* **2020**, *588*, 327–330.
8. Søndergaard, C.R.; *J. Chem. Theory Comput.* **2011**, *7*, 2284–2295.
9. Frisch, M. J.; Gaussian 16, Revision C.01 2016.
10. Forli, W.; AutoDock Version 4. *Citeseer* **2012**, 1–66.
11. BIOVIA, Dassault Systèmes, Discovery Studio Visualizer 2021.
12. Humphrey, W.; VMD: Visual Molecular Dynamics. *J. Mol. Graph.* **1996**, *14*, 33–38.

Analysis of promising ligands for treatment of type-2 diabetes targeting GPR119

Luiz Felipe M.A. Benicio (PG),[1] Érica C.M. Nascimento (PQ),[2] João Batista Lopes Martins[1,2]

[1] Universidade de Brasília, Faculdade de Ciências da Saúde, Departamento de Farmácia, Brasília-DF, Brasil;

[2] Universidade de Brasília, Laboratório de Química Computacional, IQD, 70910900, Brasília-DF, Brasil.

lipembenicio@gmail.com

Keywords: GPR119; Docking; ADMET; Screening.

Abstract

Type 2 diabetes is a worldwide growing epidemic related to insulin response diminishing. A promisor receptor to the manage this condition is G protein coupled receptor 119 (GPR119) showing activity lowering glucagon levels and releasing insulin through GLP-1 pathway. However, little is known about how prosperous ligands ADMET profile and interaction pattern with GPR119. In this work we performed a ADMET study and molecular docking methodology considering different conformations of GPR119 against GPR119 agonist molecules. GPR119 pockets analysis was performed with PDB crystallographic structures. Heatmap correlating ADMET study and docking study showed clusters between crystallized molecules and selected molecules, indicating similar interactions mechanism.

Introdução

Acometendo cerca de 90% dos casos de diabetes registrados, a diabetes do tipo 2 (DM2) ou diabetes mellitus é uma doença metabólica crónica que quadruplicou seus casos nas últimas três décadas[1]. A causa da DM2 está relacionada a diminuição da resposta a insulina, com o principal fator a diminuição de secreção de insulina por células β-pancreáticas ao decorrer do tempo [1]. Uma forma de combate a DM2 é o estimulo de vias que causam a liberação de insulina por meio de incretinas [2]. O receptor acoplado a proteína G 119 (GPR119) quando ativado, estimula o peptídeo-1 similar ao glucagon (GLP-1) que estimulam o receptor de GLP-1 liberando insulina e diminuindo o glucagon[2].

Assim o GPR119 se tornou um promissor alvo para o desenvolvimento de fármacos para DM2 com baixos efeitos adversos [3]. Caracterizado na classe das Rodopsina, o GPR119 está classificado como um receptor órfão devido a diversas possibilidades de ligantes endógenos, como a lisofosfatidilcolina (LSC), e sintéticos que realizam asua ativação [4]. Entre os ligantes sintéticos, destacam-se AR231453 (8WL) e o MBX-2982 (8VP) que são reconhecidos como agonistas orais de alta eficácia, apresentando efeitos no controle de glicemia em ensaios clínicos de fase 2[3]. Derivados de nortropanol (M16, M26 e M27), pirazolopirimidinas (M1 a M6 e M13 a M15) e ciclohexanos spirocíclicos (M17 a M25) demonstraram atividade na GPR119 com potencial hipoglicemiante[5–8].

Desta forma, realizamos estudos para analisar descritores farmacocinéticos e toxicológicos (ADMET) de moléculas com atividade relatada para a GPR119 assim como o estudo de docking destas moléculas com estruturas cristalográficas da GPR119 com o intuito de analisar o padrão de interação com resíduos chave e correlacionar os dados obtidos e consequentemente os ligantes por meio de heatmap.

Metodologia

As estruturas cristalográficas do receptor GPR119 foram obtidas do **Protein Data**

Bank (PDB)[9], depositadas com códigos 7WCM, 7WCN, 7XZ5 e 7XZ6 (Uniprot: P63092)[3,4]. Analisamos as estruturas cristalográficas e selecionamos apenas as estruturas correspondentes aos receptores de interesse. Realizamos o estudo de protonação dos resíduos do receptor com o software APBS, propka3.5.1, por meio do campo de forma AMBER com pH 8.0[10]. Após, realizamos estudo de possíveis sítios de interação da GPR119 e suas propriedades através do GeoMine[11].

Um conjunto de 1548 ligantes reconhecidos por possuir atividade no GPR119 foram selecionados através do banco de dados GPCRdb[12]. Em seguida, análises das propriedades ADMET foram conduzidas com o ADMETlab 3.0[13]. Ligantes que apresentavam toxicidade aguda, genotoxicidade, carcinotoxicidade ou mutagenicidade no estudo de ADMET foram excluídos. Ao final da seleção, ajustamos a conformação de distância de ligação e ângulos de 21 ligantes utilizando o campo de força MM2 com o Chem3Dpro.

O re-docking dos ligantes cristalizados com as suas respectivas estruturas cristalográficas foi utilizado como validação para o estudo de docking. Realizamos o re-docking com o algoritmo do AutodockVina[14] utilizando script automatizado para docking e extração de dados, Fastdock_LQC. As diferenças presentes nos cristais e seus ligantes demandaram a formação de caixas adaptadas para cada estrutura cristalográfica com diferentes dimensões e centros. Utilizamos o ponto central de cada ligante presente em sua respectiva estrutura cristalográfica como o centro das suas caixas. . O re-docking gerou os RMSDS (Å) e energia de binding (kcal/mol): 0.4854 e -15.50; 0.4682 e -14.10; 0.4031 e -17.60; 0.2069 e -14.10, respectivamente para os cristais 7WCM, 7WCN, 7XZ5 e 7XZ6. Realizamos os estudos de docking com os mesmos protocolos utilizados no re-docking. Visualizamos os resultados por meio do software Discovery Studio Visualizer[15] e Virtual Molecular Dynamics (VMD)[16].

Com o intuito de avaliar as similaridades dos ligantes selecionados e também a correlação destas propriedades com os resultados do estudo de docking, para correlacionar propriedades e interação com o alvo biológico. Realizamos um estudo de correlação dos dados obtidos performado por meio da técnica de data mining Heatmap (mapa de cores) usando o software HeatLQC.

Resultados

A GPRC119 apresentou 9 possíveis sítios de interação. Analisamos que o sítio com maior potencial de interação (drugscore) consiste com o sítio com ligantes na estrutura cristalizada (Figura 1) [3]. A profundidade (Å) do principal sítio para os diferentes cristais foram calculadas como 40.5; 40.28; 21.67 e 26.31. Conjuntamente, para a sua profundidade observamos os volumes ($Å^3$) tidos como 1685.95, 1928.90, 1411.33 e 1018.94 respectivamente. Observamos que as propriedades espaciais e drugscore das estruturas não seguem a mesma tendência.

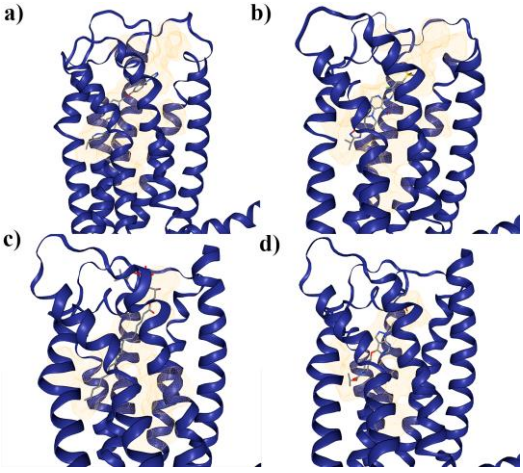


Figura 1. Estruturas cristalográficas 7WCM(a), 7WCN(b), 7XZ5(c) e 7XZ6(d) e seus respectivos ligantes, com o principal sítio de interação em superfície amarela.

Os resíduos do sítio estudado possuem características apolares (63%), polares (30%), carga negativa (4,5%) e carga positiva (3%). Os resíduos M82, V93, I136, F157, F174, W238, F241, R262 e W265 são considerados os resíduos polares com maior potencial de interação com fármacos e estes permaneceram aptos para a realização de interações nas estruturas analisadas [4].

O estudo do perfil ADMET dos ligantes demonstrou que os ligantes possuem tamanho compatível com o sítio estudado (volume médio de 433.51 $Å^2$), baixa capacidade de absorção intestinal (-4.807 médio de Caco2), baixa capacidade de absorção em barreiras lipídicas (PAMPA médio de 0.336) e alta seletividade para o alvo (promiscuidade média de 0.067).

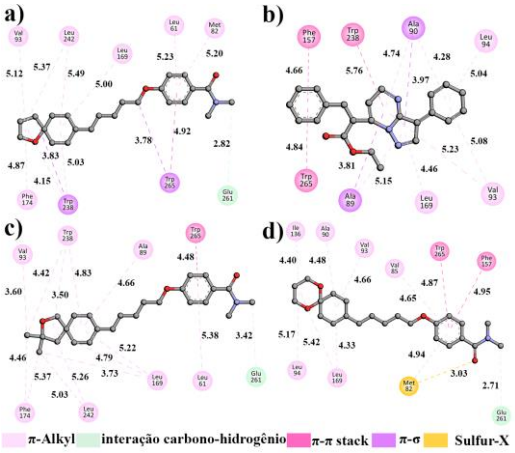


Figura 2. Representação 2D dos resultados de docking dos complexos: (a) 7WCM-M27, (b) 7WCN-M14, (c) 7XZ5-M19 e (d) 7XZ6-M18.

As melhores soluções do docking consistem com os ligantes presentes nas estruturas cristalizadas. Dentre os ligantes não cristalizados testados, o ligante com melhor score (energia de interação em kcal/mol) para cada cristal foi M27 (-12.30); M14 (-13.00); M19 (-13.50) e M18 (-11.20) respectivamente (Figura 2). A maioria das interações observadas pelos ligantes são de natureza hidrofóbica. Os ligantes demonstraram interações do tipo π-π ou π-σ com o resíduo Trp265, considerado essencial para a conformação ativa do receptor [3].

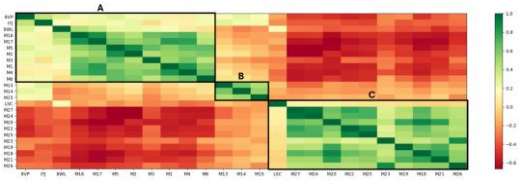


Figura 3. Heatmap com dados de ADMET e docking dos 21 ligantes.

O Heatmap demonstra a clusterização de 3 grupos. O grupo A é formado pelos ligantes 8WL, 8VP, I7J, nortropanol M16, pirazolopirimidinas M1 a M6 e spirocíclico M17. O grupo B contém as pirazolopirimidinas M13, M14 e M15. O grupo C é composto pelos ligantes LSC, nortropanol M26 e M27, e os spirocíclicos M18 a M25.

Conclusão

Os estudos das estruturas cristalográficas demonstram que a natureza do sítio de interação é hidrofóbica e que o receptor se adapta ao ligante, indicando mais de uma possibilidade de conformação ativa da GPR119 [3,4]. Os estudos de ADMET demonstram que os ligantes possuem propriedades condizentes com fármacos orais sem absorção para ação sistêmica e baixa chance de efeitos adversos. As soluções do docking demonstram que os ligantes interagem com resíduos V93, I136, F157, F174, W238 e W265 críticos para a ativação da GPR119[3]. O heatmap demonstrou a clusterização de dois grandes grupos, A e C. Os ligantes pertencentes ao grupo A apresentaram características similares à fármacos enquanto os ligantes do grupo C se assemelham à lipídeos.

Agradecimentos

FAP-DF, CNPq, CAPES e UnB.

Referências

1. Zheng, Y; *Nat. Rev. Endocrinol.* **2018**, *14*, 88–98.
2. Ahrén, B. *Nat. Rev. Drug Discov.* **2009**.
3. Qian, Y.; et al. *Nat. Commun.* **2022**, *13*, 7033.
4. Xu, P.; et al. *Nat. Struct. Mol. Biol.* **2022**, *29*, 863–870.
5. Alper, P.; et al. *Bioorg. Med. Chem. Lett.* **2014**, *24*, 2383–2387.
6. Azimioara, M.; et al. *Bioorg. Med. Chem. Lett.* **2014**, *24*, 5478–5483.
7. Xia, Y.; et al. *Bioorg. Med. Chem. Lett.* **2011**, *21*, 3290–3296.
8. Harada, K.; et al. *Bioorg. Med. Chem. Lett.* **2018**, *28*, 1228–1233.
9. Berman, H.M. **2000**, *28*, 235–242.
10. Jurrus, E.; et al. *Protein Sci.* **2018**, *27*, 112–128,
11. Diedrich, K.; Graef, J.; *Bioinformatics* **2021**, *37*, 424–425.
12. Pándy-Szekeres, G.; et al ; *Nucleic Acids Res.* **2023**, *51*, D395–D402.
13. Xiong, G.; et al. *Nucleic Acids Res.* **2021**, *49*, W5–W14,
14. Trott, O.; Olson, A.J. *J. Comput. Chem.* **2010**, *31*, 455–461.
15. Biovia, D. *Discovery Studio Visualizer (V21.1.2.20298). (2021)*;
16. Humphrey, W.; *J. Mol. Graph.* **1996**, *14*, 27–28.

Efeitos da Distribuição de Energia e Captura na Difusão de Éxcitons: Simulações de Monte Carlo em Materiais Orgânicos

Maria Vitória G. R. Dias[1], Fernando Teixeira Bueno[1], e Pedro Henrique O. Neto[1,2]
[1]Instituto de Física, Universidade de Brasília, 70919-970, Brasília-DF, Brasil.
[2]Centro Internacional de Física, Universidade de Brasília, 70919-970, Brasília-DF, Brasil.
maria.vit.2004@gmail.com
Keywords: desordem energética; difusão de éxcitons; dispositivos optoeletrônicos orgânicos; simulação de Monte Carlo.

Abstract
The efficiency of optoelectronic devices, such as LEDs and organic photovoltaics, depends on understanding energy transfer mechanisms involving excitons, quasiparticles formed by an electron-hole pair. Exciton diffusion typically occurs via Förster resonance energy transfer, influenced by factors like exciton emission lifetime, Förster radius, intermolecular distance, and energy differences between sites. Recent data suggest a shift from normal to subdiffusive regimes, potentially due to energy trapping effects within the crystal lattice. This study uses kinetic Monte Carlo simulations to explore exciton diffusion under various energy distributions. Findings show that energy trapping can independently induce a subdiffusive regime, significantly affecting the diffusion length.

Introdução

Desde a sua descoberta, os dispositivos optoeletrônicos orgânicos têm se destacado em comparação com os materiais inorgânicos devido à flexibilidade, leveza, sustentabilidade e baixo custo de produção. A eficiência desses dispositivos depende fortemente da dinâmica dos éxcitons, quasipartículas quânticas formadas pelo estado ligado entre um elétron e um buraco, essenciais para o transporte de energia em materiais orgânicos[1]. Para éxcitons do tipo singleto, o processo de difusão é modelado pelo mecanismo de transferência de energia por ressonância Förster (FRET), caracterizado pela transferência não radiativa de excitação de uma molécula para outra. As taxas desse mecanismo dependem do tempo de vida de emissão do éxciton, bem como de parâmetros como a distância intermolecular e a variação de energia entre sítios[2].

Estudos experimentais recentes indicam uma transição do regime de difusão de éxcitons, de normal para subdifusivo, atribuída à captura de éxcitons provocada por variações de energia em redes cristalinas[3]. A difusão é medida pela evolução temporal do deslocamento quadrático médio dos éxcitons[4], parâmetro altamente influenciado por flutuações energéticas em nanoescala, uma característica intrínseca de cada material. Em materiais onde esse fenômeno é acentuado, outros processos, como interações entre éxcitons e fusão ou fissão excitônica, tornam-se menos relevantes para a difusão.

Neste trabalho, realizamos simulações da difusão de éxcitons em redes cristalinas com variações de energia de sítio, buscando determinar o impacto dessas variações em aspectos como o comprimento de difusão, a possível concentração espacial de recombinação radiativa e a mudança no regime difusivo. As simulações utilizaram um modelo de Monte Carlo Cinético (KMC), onde foi controlada a morfologia e as variações energéticas do cristal estudado. O tetraceno, amplamente investigado como

semicondutor orgânico, foi escolhido como modelo para este estudo.

Metodologia

A taxa de transferência Förster, em função da variação de energia ao longo de uma rede cristalina, é expressa por:

$$k_F = \frac{1}{\tau}\left(\frac{RF}{r+\alpha\mu}\right) e^{\frac{-(\Delta E+|\Delta E|)}{2k_B T}}$$

onde τ representa o tempo de vida do éxciton, r é a distância intermolecular, αμ é um fator de correção para pequenas distâncias, com μ sendo o momento de dipolo de transição, RF é o raio de Förster, ΔE a diferença de energia entre os sítios, k_B a constante de Boltzmann, e T a temperatura.

A simulação dinâmica de transporte e recombinação radiativa dos éxcitons foi baseada nas taxas de FRET e de emissão, dada por 1/τ. No modelo de KMC, essa dinâmica foi implementada em uma rede cúbica de moléculas de tetraceno, com uma distância intermolecular de 1 nm, utilizando condições de contorno periódicas.

Inicialmente, foi gerada uma variação de energia ao longo dos sítios da rede, seguida pela criação aleatória de um éxciton. A cada passo temporal na simulação, foram calculadas as taxas de transferência FRET para os seis primeiros vizinhos, além da taxa de emissão. A probabilidade de ocorrência de cada evento foi determinada pela razão entre a taxa correspondente e a soma total das taxas, com o evento selecionado sendo definido por sorteio aleatório.

Foram implementados dois tipos de variação de energia nos sítios. Na primeira, a distribuição de energia é proporcional a ns^2, onde ns é o número do sítio em relação ao centro da rede. Na segunda, a distribuição segue a mesma regra para ns maiores que um limite inferior, enquanto para ns menores que esse limite, a energia é mantida constante. As funções de distribuição de energia utilizam uma constante multiplicativa "a", que define a amplitude, variada entre $10^{-5}k_BT$ e $10^{-4}k_BT$ eV. O limite inferior utilizado na segunda forma de variação de energia foi variado entre $5\times10^{-3}k_BT$ e $3k_BT$ eV. Além disso, o número de sítios na rede foi ajustado entre 200 e 2000.

Resultados e Discussão

Foi implementado o modelo de KMC com a distribuição de energia proporcional a ns^2 e um total de 200 sítios. Resultados iniciais foram obtidos ao variar a amplitude da energia. Observou-se um possível acúmulo espacial de emissões e uma mudança no regime difusivo.

A Figura 1 apresenta histogramas das posições de emissão dos éxcitons para três valores crescentes do fator 'a', mostrados nas imagens a-c. Nesses gráficos, nota-se que, à medida que o fator 'a' aumenta, a distribuição se torna mais estreita e com um pico mais pronunciado. Isso sugere que há um efeito de captura de éxcitons em torno do ponto de menor energia, resultando em uma maior concentração de emissões nessa região.

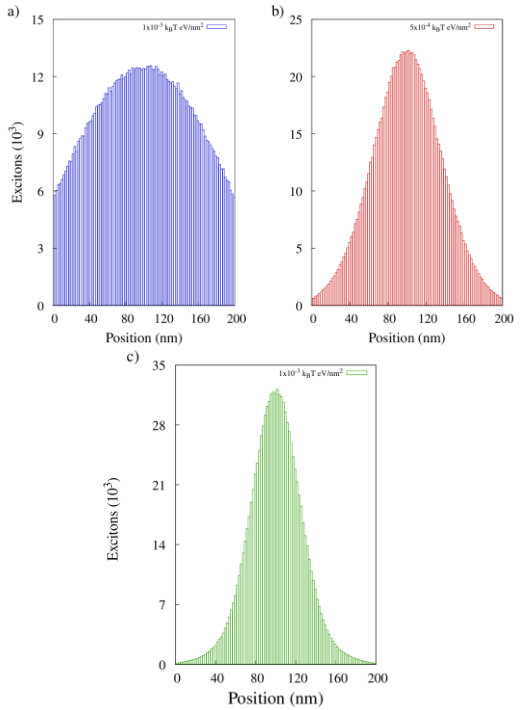


Figura 1: histogramas das posições de emissão dos éxcitons ao longo de uma rede de 200 nm, considerando diferentes variações de energia nos sítios: a)1×10^{-5} eV, b) 5×10^{-4} eV e c)1×10^{-3} eV.

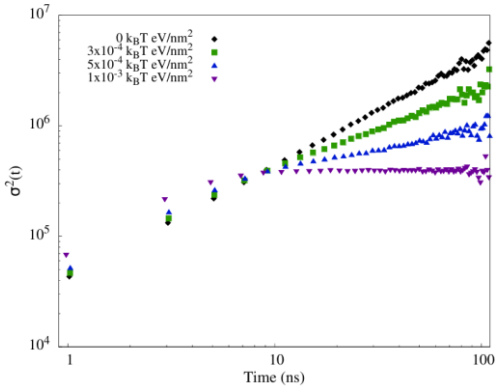


Figura 2: deslocamento quadrático médio dos éxcitons em função do tempo para diferentes amplitudes de variação de energia nos sítios.

Na Figura 2, é exibido um gráfico do deslocamento quadrático médio em função do tempo. Os dados refletem diferentes amplitudes do fator 'a' e incluem uma condição sem alteração de energia (curva em preto). Observa-se um único regime difusivo quando não há modificação na energia dos sítios. No entanto, quando a variação de energia é aplicada, verifica-se que, nos momentos iniciais (t < 10 ns), há um regime que posteriormente muda para uma subdifusivo. Essa transição se torna mais evidente à medida que o fator 'a' aumenta.

Esses resultados indicam que alterações na amplitude têm um impacto significativo na dinâmica e difusão dos éxcitons em uma rede. Além disso, outras abordagens para a distribuição de energia, como a segunda forma apresentada, onde parte da distribuição é proporcional a ns^2 e outra é mantida constante, podem provocar diferentes efeitos nessa dinâmica.

Conclusão

Neste estudo, foi investigado como diferentes distribuições de energia nos sítios de uma rede cristalina influenciam a dinâmica de difusão de éxcitons em materiais orgânicos. Utilizando simulações de Monte Carlo Cinético, foram analisados os efeitos de variações na amplitude de energia e diferentes formas de distribuição na rede, observando-se mudanças significativas no regime difusivo e no acúmulo espacial de emissões. Os resultados destacam a importância do controle da distribuição de energia para otimizar a eficiência de dispositivos optoeletrônicos.

Agradecimentos

Este trabalho contou com o apoio financeiro dos Conselhos de Pesquisa Brasileiros CNPq, CAPES e FAPDF.

Referências

3. Akselrod GM, Deotare PB, Thompson NJ, Lee J, Tisdale WA, Baldo MA, Menon VM, Bulović V. Nature communications. 2014 Apr 16;5(1):3646.

2. de Sousa LE, da Silva Filho DA, de Silva P, Ribeiro L, de Oliveira Neto PH. Advanced Theory and Simulations. 2020 Aug;3(8):2000042.

1. Kippelen B, Brédas JL. Energy & Environmental Science. 2009;2(3):251-61.

4. Oliveira FA, Ferreira RM, Lapas LC, Vainstein MH. Frontiers in Physics. 2019 Feb 19;7:18.

BCS and FFLO superconducting states in ultracold atomic gases

M. Sanino*, I. M. Carvalho, and V. V. França
Institute of Chemistry, São Paulo State University, Araraquara, Brazil

Spin-imbalanced fermionic systems offer a significant opportunity for exploring novel states. Among them is the phase separation between different superfluid phases. The types and sequences of these emerging phases may depend on spin-imbalance, trap shape, and on-site interaction strength. Here, we investigate the properties of such systems within an attractive fermionic Hubbard model and their relation to the phase diagram of the homogeneous system. Our preliminary results show the emergence of a structure, which includes both the BCS (conventional Cooper pairs superfluidity) and FFLO (Fulde-Ferrell-Larkin-Ovchinnikov exotic superfluid) states. More interestingly, by calculating the second derivative of the on-site energy term with respect to the polarization, we observe a negative magnetic susceptibility-like behavior in the FFLO phase, which may be related to magnetic shielding. Additionally, we show that the system's magnetic susceptibility decays to its minimal value around the universal critical polarization $P_c = 1/3$.

Topological phases in one-dimensional superfluid Hubbard chains probed by entanglement measures

M. Sanino[*,1], I. M. Carvalho[1], F. Iemini[2,3] , and V. V. França[1]
[1]Institute of Chemistry, São Paulo State University, Araraquara, Brazil.
[2]Institute of Physics, Federal Fluminense University, Niterói, Brazil.
[3]Institute for Physics, Johannes Gutenberg University Mainz, D-55099 Mainz, Germany.
marina.sanino@unesp.br
Keywords: three up to five, separated; by semicolons; include commas, within terms only; required, [Times New Roman, 10].

Abstract
Quantum simulations involving ultracold atoms confined by optical potentials provide an ideal platform for investigating quantum phase transitions driven by atomic interaction strength, particle density, and geometry — challenging to be probed and explored in solid-state systems. In this work, we investigate the one-dimensional attractive Hubbard model under optical confinement using Density Matrix Renormalization Group calculations. We consider not only the BCS regime, characterized by weakly coupled Cooper pairs, but also the strongly dimer regime, BEC, as well as the BCS-BEC crossover driven by the strength of the atomic interactions. We analyze both single-site and half-chain bipartite entanglement for several densities, interaction and confinement strengths. Our findings reveal that entanglement exhibits a non-monotonic behavior as a function of the interaction strength or the filling factor, fingerprinting a quantum phase transition induced by harmonical confinement. Double occupancy probabilities and superconducting order parameter profiles confirm the presence of a quantum phase transition driven by the charge density: from a trivial superfluid to a non-trivial topological structure, composed by an insulator bulk surrounded by superfluid edges. We numerically depict a phase diagram, in Fig. 1, routing the parameters for optimizing this topological superfluidity structure which could be explored in future quantum devices.

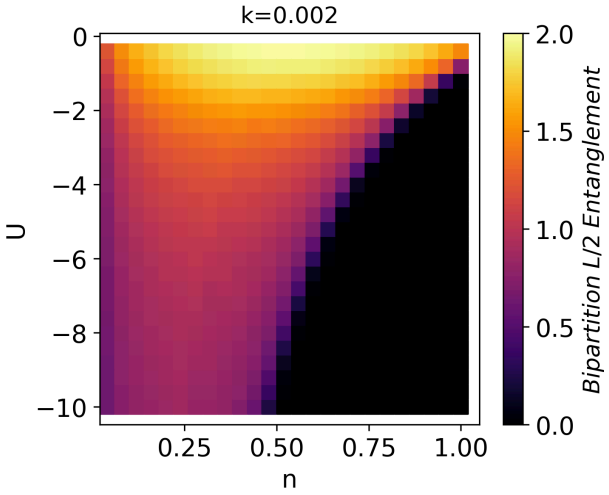


Figure 1. Phase diagram using half-chain bipartite entanglement for confined chains.

Efeitos da hidrogenação e do estiramento nas propriedades eletrônicas do TPH-grafeno

Matheus Rodrigues de Amorim Medina[1], Pedro Alves da Silva Autreto[1].
[1]Centro de Ciências Naturais e Humanas, Universidade Federal do ABC (UFABC), Rua Santa Adélia 166, Bairro Bangu, 09210-170, Santo André-SP, Brazil.
theus.m@hotmail.com
Keywords: DFT; Molecular Dynamics; Graphene; Hydrogen; Strain

Abstract
Since its discovery and synthesis, graphene has been regarded as a highly promising material due to its exceptional mechanical, thermal, electronic, and optical properties. However, its utility in certain electronic applications is constrained by the absence of a band gap in its pure form. To address this limitation, various strategies have been proposed, including the development of novel graphene-based materials, chemical functionalization, and elastic deformation. Among these, chemical functionalization, through processes such as hydrogenation and/or fluorination, as well as elastic deformation, has been extensively investigated. These methods have demonstrated significant outcomes, notably the induction of an adjustable band gap, thereby enhancing the material's applicability.
This study employs first-principles calculations using density functional theory (DFT) and reactive molecular dynamics (MD) simulations to explore the structural and electronic effects of hydrogenation and deformation in Tetra-Penta-Hepta (TPH)-graphene, a metallic variant of graphene. The DFT results indicate a modification in the electronic structure. MD simulations reveal a distinctive pattern of hydrogenation, which aligns with the DFT predictions. Additionally, the simulations demonstrate that the optimal hydrogenation sites are influenced by the applied strain.

Introdução

Desde sua descoberta, o grafeno é considerado um material promissor, devido a suas incríveis propriedades mecânicas, térmicas e eletrônicas. Essas propriedades levaram ao estudo do grafeno para as mais diversas aplicações tecnológicas.

Apesar das diversas possibilidades de aplicações do grafeno, novos materiais bidimensionais baseados em carbono foram propostos e sintetizados desde sua descoberta, com diferentes propriedades que aumentam a gama de possíveis aplicações destes materiais.

Assim, neste trabalho exploramos como as propriedades do TPH-grafeno [1], um material sintetizado de caráter metálico, são afetadas por métodos de funcionalização química por meio da hidrogenação e da deformação elástica de sua estrutura.

Metodologia

Neste trabalho foram realizadas simulações computacionais baseadas em métodos quânticos (DFT) e clássicos (MD) para se obter a variação das propriedades do TPH-grafeno.

Os cálculos clássicos foram realizados pelo código computacional *Large-scale Atomic/Molecular Massively Parallel Simulator* (LAMMPS)[2].

Nestas simulações uma super-célula do TPH-grafeno foi exposta a uma atmosfera de hidrogênio sob diferentes regimes de deformação para se determinar o processo de hidrogenação e o efeito da deformação neste.

Os cálculos quânticos foram realizados pelo código computacional SIESTA[3]. Nestes, foram obtidas as propriedades eletrônicas do sistema hidrogenado sob diferentes regimes de deformação da estrutura.

Resultados e Discussões

As simulações de dinâmica molecular mostraram um padrão de hidrogenação dos sítios do TPH-grafeno que variaram com a deformação da estrutura. Estes resultados concordam com as energias de ligação obtidas pelos cálculos de DFT.

Os resultados dos cálculos de DFT mostraram que a hidrogenação provoca uma alteração da estrutura eletrônica do TPH-grafeno pela abertura de um "band-gap", levando a estrutura de um caráter metálico para um semicondutor.

Agradecimentos

Este trabalho foi apoiado pelo Programa de Recursos Humanos da Agência Nacional do Petróleo, Gás Natural e Biocombustíveis – PRH-ANP, suportado com recursos provenientes do investimento de empresas petrolíferas qualificadas na Cláusula de P, D&I da Resolução ANP no 50/2015. Também agradeço a Central Computacional Multiusuário (CCM) da UFABC pela disponibilidade de clusters.

Referências

1. LI, Jin et al. The Journal of Physical Chemistry Letters 2021, 12, 2, 732-738.

2. Thompson, A. P. et al. Computer Physics Communications 2022, 271, 108171.

3. ARTACHO, Emilio et al. physica status solidi (b) 1999, 215, 1, 809-817.

Evidências teóricas e experimentais para a formação do radical ânion carbonato ($CO_3^{-\bullet}$) na atmosfera

Murielly Fernanda Ribeiro Bihain[1], Grasiele Soares Cavallini[1], Douglas Henrique Pereira[1,2].
[1]Programa de Pós-Graduação em Química, Universidade Federal do Tocantins, Campus Gurupi -Badejos, Caixa Postal 66, CEP: 77 402-970, Gurupi, Tocantins, Brasil
[2]Departamento de Química, Instituto Tecnológico de Aeronáutica (ITA), São José dos Campos, CEP: 12228-900 SP, Brasil.

murielly.fernanda@mail.uft.edu.br

Palavras-chave: Radical ânion carbonato; Química atmosférica; Simulação computacional.

Abstract
Troposphere is the lowest layer where the oxidation reactions responsible for the atmospheric self-purification of contaminants occur, which are initiated mostly by hydroxyl radicals ($HO^{\bullet}$). In this context, the objective of the present work was to carry out theoretical and experimental studies on the formation of the carbonate anion radical ($CO_3^{-\bullet}$) in the atmosphere and evaluate the spontaneity of chemical reactions that occur at molecular. Experimental tests to evaluate the formation of $CO_3^{-\bullet}$ in the atmosphere were conducted using rainwater samples containing 5, 10, and 15 mg L^{-1} of sodium carbonate, and the addition of methylene blue dye was used to indicate the formation of the $CO_3^{-\bullet}$ by monitoring its degradation. Exposure of the samples to solar radiation led to a greater degradation of the dye in rainwater samples with higher concentrations of bicarbonate. The determination of the alkalinity of the samples revealed that the predominant chemical species in the medium was the bicarbonate anion and that the increase in its concentration promotes the formation of $CO_3^{-\bullet}$. As a result of the simulation of the reactions with the radicals $HO^{\bullet}$, $HOO^{\bullet}$, and $CO_3^{-\bullet}$ at the level of theory MP2/6–311++G (2df,p), it was obtained that the formation of the radical $CO_3^{-\bullet}$ is possible. The simulations were carried out in aqueous phase with implicit solvent, in the gas and showed the same trends. Furthermore, the reactions involving $CO_3^{-\bullet}$ with atmospheric molecules are spontaneous ($\Delta rG^{298}<0$) for electron-rich groups as H_2S compounds, indicating that the radical $CO_3^{-\bullet}$ can react with some atmospheric molecules, and thus contribute to the atmospheric oxidation mechanisms.

Introdução
A troposfera concentra grande parte dos poluentes gasosos e por isso possui uma alta capacidade oxidativa que ocorre através de reações iniciadas por radicais atmosféricos, o que contribui para o restabelecimento da qualidade do ar [1,2].
Além do radical hidroxila ($HO^{\bullet}$), que se torna o principal agente oxidante diurno outros radicais também podem existir e agir como oxidantes na troposfera, como por exemplo o radical ânion carbonato ($CO_3^{-\bullet}$), que pode ser formado solar através da reação do $HO^{\bullet}$ com carbonato (CO_3^{2-}) ou ânions de bicarbonato (HCO_3^-) por meio da fotólise, como mostra a Reação abaixo [3].

$$HCO_3^-/CO_3^{2-} + HO^{\bullet} \rightarrow H_2O\ /HO^- + CO_3^{-\bullet}$$

Através da Química Teórica é possível com analisar reações à nível molecular e compreender os mecanismos de autodepuração. Neste contexto, o objetivo do trabalho foi estudar teoricamente as reações químicas que ocorrem na atmosfera, em especial com o radical $CO_3^{-\bullet}$ e avaliar a possibilidade deste na atmosfera por meio de ensaios experimentais utilizando amostras de água de chuva, as

quais apresentam em sua composição íons carbonato e bicarbonato.

Materiais e métodos

1. Parte experimental

Foi feita a coleta de água da chuva na região central de Gurupi-TO, Brasil e realizado o estudo de degradação de azul de metileno (16 $\mu molL^{-1}$) em um experimento com diferentes concentrações de (CO_3^{2-}), onde foi preparado soluções de azul de metileno com água da chuva tendo a adição de carbonato de sódio nas concentrações de 0, 5, 10, 15 $mg.L^{-1}$, além da solução controle utilizando água destilada. O ensaio foi realizado na ausência e na presença de radiação solar, em ambos os ensaios o tempo de duração do ensaio foram de 2 horas.

A formação dos radicais foi detectada por espectrofotometria UV-Vis (PG Instruments, modelo T60) em 664 nm, devido a degradação do corante.

2. Parte teórica

As moléculas referentes as reações da atmosfera foram construídas pelo programa GaussView e otimizadas até o mínimo de energia utilizando o método *ab initio* de perturbação irrestrita de segunda ordem (UMP2) e função de base 6-311++G (2df,p) As simulações foram realizadas sem a inclusão do solvente e com a inclusão de um solvente implícito. Para as simulações de solventes o efeito da água foi considerado na otimização e em todos os cálculos utilizando o modelo de solvente contínuo SMD.

Os cálculos da Energia reacional de Gibbs a 298,15 Kelvin foram realizadas de acordo a Equação 1.

$$\Delta_r G = \sum G_P - \sum G_R \quad (1)$$

Em que $\sum G_P$ é a soma individual da energia de Gibbs das moléculas do produto e $\sum G_R$ é a soma individual da energia de Gibbs das moléculas dos reagentes.

Todos os cálculos foram realizados com o programa Gaussian.

Resultados e discussão

- Experimento 3

Com o intuito de detectar a contribuição dos íons carbonato/bicarbonato para formação de radicais, foram adicionadas diferentes concentrações de carbonato de sódio na água da chuva. Considerando que a água da chuva apresentou alcalinidade de 4,6 $mg.\ L^{-1}$, com a adição do carbonato de sódio, as demais amostras apresentaram alcalinidade de 9,6; 14,6 e 19,6 $mg.\ L^{-1}$

A partir dos resultados obtidos foi possível observar que sem radiação ocorre uma degradação inicial nos primeiros 30 minutos, mas depois a degradação se estabiliza. No ensaio com radiação, as eficiências de degradação foram crescentes com o aumento do tempo de exposição solar.

A partir de 1 hora e meia de exposição solar a condição de 14,6 $mg.L^{-1}$ de alcalinidade demonstrou uma maior eficiência de degradação do corante, no entanto, na concentração de 19,6 $mg.L^{-1}$ a eficiência de degradação diminui. Esse comportamento pode ser explicado a partir da concentração de bicarbonato que decai na amostra de água da chuva com adição de 15 $mg.L^{-1}$ de carbonato de sódio (alcalinidade de 19,6 $mg.L^{-1}$). Dessa forma, pode-se concluir que a presença do ânion bicarbonato, proveniente da solubilização do ânion carbonato na água, é o principal responsável pela formação do $CO_3^{-\bullet}$ na água da chuva.

Como o carbonato é proveniente de partículas do solo presentes na atmosfera, a alcalinidade de 15 $mg.L^{-1}$ poderia ser alcançada de forma natural, principalmente em chuvas após longos períodos sem chuva, como por exemplo, as primeiras chuvas do Estado do Tocantins após 6 meses de estiagem. No entanto, a maior alcalinidade registrada nas coletas foi de 11,5 $mg.\ L^{-1}$. Os ânions bicarbonato podem se originar não apenas do material particulado, mas também da solubilização do CO_2 atmosférico na água da chuva [4].

- Parte teórica

Além da oxidação pelo radical hidroxila, uma outra hipótese seria a formação do radical $CO_3^{-\bullet}$, uma vez que o mesmo pode ser formado na atmosfera dada a predominância do bicarbonato na água da

chuva que contribui para a formação do radical ânion carbonato (ΔrG^{298} = -9,59 kcal mol^{-1}). A Tabela 1 mostra algumas das reações com os radicais $HO^{\bullet}$, $HOO^{\bullet}$ substituídos pelo $CO_3^{-\bullet}$.

Tabela 1. Energia reacional de Gibbs a 298 K (ΔrG^{298}) para algumas das principais reações atmosféricas com o $CO_3^{-\bullet}$. O resultado foi obtido no nível MP2/6–311++G (2df,p) e os valores estão em kcal mol^{-1}.

Reações	Δ_rG^{298} Solvente implícito	Δ_rG^{298} Sem solvente
1b. CH_4 + $\mathbf{CO_3^{-\bullet}}$ → $H_3C^{\bullet}$ + HCO_3^-	-1,42	6,01
7b. NH_3 + $\mathbf{CO_3^{-\bullet}}$ → $H_2N^{\bullet}$ + HCO_3^-	4,53	11,36
8b. H_2S + $\mathbf{CO_3^{-\bullet}}$ → $HS^{\bullet}$ + HCO_3^-	-14,01	-6,94
11b. $\mathbf{CO_3^{-\bullet}}$ + HNO_3 → HCO_3^- + $^{\bullet}NO_3$	15,02	16,95

Através dos resultados apresentados na Tabela 1 é possível observar que com o solvente, as reações 1b e 8b são espontâneas ($\Delta_rG^{298} < 0$), embora os valores de Δ_rG para as reações 1b sejam muito próximos de zero. Para os resultados sem solvente, apenas a reação com H_2S foi espontânea (Δ_rG^{298} =-6,94 kcal mol^{-1}). Os resultados mostraram que o radical ânion carbonato pode reagir espontaneamente com sulfeto de hidrogênio (H_2S), o que pode ser justificado porque o radical $CO_3^{-\bullet}$ é um oxidante seletivo, e sua seletividade é para grupos ricos em elétrons como compostos contendo nitrogênio, enxofre e moléculas aromáticas [5, 6]

Conclusão

Os resultados do presente trabalho sobre reações atmosféricas demonstraram que é possível formar o radical $CO_3^{-\bullet}$. Os cálculos teóricos da mudança de energia de Gibbs da reação a 298,15 K mostraram que $CO_3^{-\bullet}$ pode ser formado pela reação de carbonato e bicarbonato com o radical hidroxila e que o radical ânion carbonato reage preferencialmente com moléculas ricas em elétrons como H_2S.

Na parte experimental, observou-se que a água de chuva natural pode apresentar alcalinidade suficiente para realizar a degradação de espécies atmosféricas. A predominância do bicarbonato aumenta a capacidade de formar radicais ânion carbonato. Assim, conclui-se que os dados teóricos e experimentais confirmam que o $CO_3^{-\bullet}$ pode ser formado na água da chuva e pode atuar como um agente oxidante troposférico, especialmente para oxidação de moléculas ricas em elétrons.

Agradecimentos

Os autores agradecem o apoio da CAPES (Código 001), a Fundação de Amparo à Pesquisa do Estado de São Paulo # 2023/17727-2, o Centro de Engenharia e Ciências Computacionais (apoio financeiro da FAPESP, #2013/08293–7 e #2017/11485–6) e do Centro Nacional de Processamento de Alto Desempenho em São Paulo (CENAPAD), pelos recursos computacionais.

Referencias

[1] Bihain, M.F.R., Oh, L.B.C., Teixeira, K.C., Cavallini, G.S., Pereira, D.H., 2023. Atmospheric Pollution Research 14, 101783.

[2] Yunping, L., Chunsheng, Z., 2009. Advances in Earth Science 24, 488.

[3] Wojnárovits, L., Tóth, T., Takács, E., 2020. Science of The Total Environment 717, 137219.

[4] Lan, X., Dai, Y., Jing, W., Meng, X., Liu, F., Wang, S., He, A., Li, N., 2022. Journal of Molecular Graphics and Modelling 114, 108182

[5] Liu, Y., Wang, T., Ge, Q., You, W., Li, K., Wang, W., Xie, L., Wang, L., Fang, X., Ruan, X., Yang, L., Wang, R., Zhang, L., 2024. JGR Atmospheres 129, e2023JD040017.

[6] Zhou, Y., Chen, C., Guo, K., Wu, Z., Wang, L., Hua, Z., Fang, J., 2020. Water Research 185, 116231.

Avaliação de Alcaloides da Biodiversidade Brasileira como Inibidores Potenciais do Inflamassoma NLRP3: Triagem Virtual, Análise de Toxicidade e Dinâmica Molecular.

Nalberth Batista Farias[1], Renato Araújo da Costa[2], João Augusto Pereira da Rocha[3] Nalanda da Silva Maués[4], Ana Lilian Luz Rodrigues[5].
[1] Laboratório de Biologia Molecular, Evolução e Microbiologia. Abaetetuba-PA. Brasil.
[2] Laboratório de Biologia Molecular, Evolução e Microbiologia. Abaetetuba-PA. Brasil.
[3] Laboratório de Biologia Molecular, Evolução e Microbiologia. Abaetetuba-PA. Brasil.
[4] Laboratório de Biologia Molecular, Evolução e Microbiologia. Abaetetuba-PA. Brasil.
[5] Laboratório de Biologia Molecular, Evolução e Microbiologia. Abaetetuba-PA. Brasil.
narthbatista@gmail.com
Triagem Virtual; Dinâmica Molecular; NLRP3; Inflamassoma.

Abstract
NLRP3 (Nod-like receptor protein 3) belongs to the NOD-like receptor family, which is activated by pathogens and damage-associated signals to form a multimeric protein complex, known as the NLRP3 inflammasome. Activation of the NLRP3 inflammasome leads to the release of proinflammatory cytokines IL-1β and IL-18, thereby inducing pyroptosis, a programmed cell death mechanism. Dysregulation of the NLRP3 inflammasome pathway is closely related to the development of many human diseases, such as neuroinflammation, metabolic inflammation, and immunological inflammation. Emerging studies have suggested the NLRP3 inflammasome as a potential drug target for inflammatory diseases. Several specific molecules have been recently identified to target the NLRP3 inflammasome pathway directly or indirectly and alleviate the related disease pathology. This review summarizes the recently evolving scenario of the development of small molecule inhibitors that target the NLRP3 inflammasome pathway.

Introduction

O inflamassoma NLRP3 é um complexo multiproteico que desempenha um papel crucial na resposta do sistema imunológico inato a vários insultos patogênicos e sinais de perigo (Kim, 2022). Após a ativação, o inflamassoma NLRP3 desencadeia a maturação das citocinas pró-inflamatórias interleucina-1β (IL-1β) e interleucina-18 (IL-18) através do recrutamento e ativação da caspase-1 (Yao *et al.*, 2024). Embora esta resposta inflamatória seja essencial para a defesa do hospedeiro contra patógenos, a ativação desregulada do inflamassoma NLRP3 tem sido implicada na patogênese de numerosos distúrbios inflamatórios e metabólicos, incluindo doença de Alzheimer, doença de Parkinson, aterosclerose, gota, diabetes tipo 2 e câncer (Blevins *et al.*, 2022; Y*AO et al.*, 2024). Estudos baseado em simulações de triagem virtual e dinâmica molecular foram aplicadas com sucesso à descoberta de inibidores do inflamassoma NLRP3, fornecendo informações valiosas sobre as interações moleculares e a dinâmica que governa a ligação ao alvo (PATIL et al., 2022; SANTOS NASCIMENTO; AQUINO; SILVA-JÚNIOR, 2022). Sendo assim, neste estudo, empregamos um fluxo de trabalho de triagem virtual combinado com simulações dinamica molecular (DM) de todos os átomos para avaliar o potencial de um conjunto diversificado de alcalóides da biodiversidade brasileira como inibidores do inflamassoma NLRP3. As descobertas deste estudo contribuem para os esforços contínuos no desenvolvimento de novas estratégias terapêuticas para atingir o inflamassoma NLRP3 e distúrbios inflamatórios associados.

Metodologia

Triagem Virtual Baseada em MMGBSA.

A estrutura cristalina da proteína NLRP3 (PDB ID 7ALV) (Dekker *et al*., 2021) foi utilizada como alvo, com MCC950 como inibidor de referência. Um total de 288 alcaloides do banco de dados NuBBEDB foram filtrados usando a Regra de Lipinski (Lipinski *et al*., 2001) para obtenção de moléculas semelhantes a fármacos. A triagem virtual foi conduzida no ChemFlow (Barreto Gomes *et al*., 2023), com encaixe molecular realizado no PLANTS (Korb; Stützle; Exner, 2009). Os ligantes foram parametrizados com GAFF2 e cargas RESP, seguidos de simulações de dinâmica molecular (1ns) para cálculo da energia livre de ligação via MMGBSA (Sun *et al*., 2018).

Análise de Toxicidade.

Os 10 alcaloides com melhores energias de ligação foram submetidos a uma análise de toxicidade abrangente, incluindo hepatotoxicidade, citotoxicidade, carcinogenicidade e mutagenicidade, utilizando o servidor PROTOX (Banerjee *et al*., 2018).

Simulação de Dinâmica Molecular.

Para analisar a dinâmica e as interações dos compostos selecionados, do inibidor MCC950 e da proteína Apo, foram realizadas simulações de dinâmica molecular usando o Amber22. Os estados de protonação foram definidos no servidor H++, e os sistemas foram solvatados em caixa de TIP3P com 12 Å, neutralizados com íons, e minimizados em quatro etapas. Após um aquecimento de 200 ps e equilíbrio de 500 ps, foi conduzida uma produção de 200 ns. O RMSD, RMSF e ligações de hidrogênio foram analisados para avaliar a estabilidade.

Resultados e Discussão

No estudo atual, os alcaloides do banco de dados NuBBE foi usado para triagem virtual contra a proteina NLRP3. Os 10 principais compostos foram selecionadas para análise de toxicidade usando o servidor PROTOX-2.

Os compostos NuBBE_1362 e NuBBE_1361 mostraram-se inativos para hepatotoxicidade, carcinogenicidade, mutagenicidade e citotoxicidade, tornando-os candidatos favoráveis para inibidores da NLRP3. Sendo assim, foram selecionados para e etapa de simulação de dinâmica molecular.

Os compostos NuBBE_1361 e NuBBE_1362 foram submetidos a simulação de dinâmica molecular e compardos com o inibidor conhecido da proteína NLRP3, MCC950 (TAPIA-Abellán *et al*., 2019). Essa comparação é importante para avaliar a eficácia dos compostos em potencial como inibidores da proteína alvo. Os gráficos de RMSD e RMSF foram são mostrados na figura 1. traçados para os complexos formados pelos compostos NuBBE_1361, NuBBE_1362 e MCC950, além da proteína Apo (Figura 1). O complexo NLRP3-NuBBE_1362 e complexo NLRP3-MCC950, tornaram-se estáveis após 25 ns. O complexo NLRP3-NuBBE_1361 tornou-se estável após, aproximadamente, 80ns e a proteína Apo estabilizou após 50ns. Os valores médios de RMSD para a proteína Apo e os complexos NLRP3-MCC950, NLRP3-NuBBE_1361 e NLRP3-NuBBE_1362 foram de 4,52, 411, 4,37 e 4,35 Å, respectivamente. Os valores baixos de RMSD para o NuBBE_1362 e MCC950 indicaram fortemente o aprimoramento da estabilidade conformacional que a proteína obteve na presença dos compostos, inibindo o seu sítio ativo. Isso sugere que as interações foram energeticamente favoráveis e contribuíram para a estabilidade dos complexos. Outro componente essencial na determinação da estabilidade de um complexo proteínaligante é RMSF (Figura 1), a flutuação dos resíduos ao longo da simulação. Os resíduos exercem um papel crucial na formação estável para a forte ligação de um complexo proteína-ligante

(Costa *et al.*, 2023). De acordo com a Figura 1, as flutuações mais notáveis foram observadas principalmente na região de alça da proteína que possui uma maior flexibilidade. O complexo NLRP3-NuBBE_1362 apresentou um menor número de flutuações dos resíduos, comprados com o complexo NLRP3-MCC950 e com a proteína Apo. Isso sugere que o NuBBER_1362 se liga ao sítio ativo da proteína NLRP3 sem causar mudanças significativas em sua conformação. Esses achados sugerem que a interação essencial entre o NuBBE_1362 e o sítio de ligação da NLRP3 contribui para preservar a estabilidade da proteína, indicando que este composto é um potencial inibidor da NLRP3.

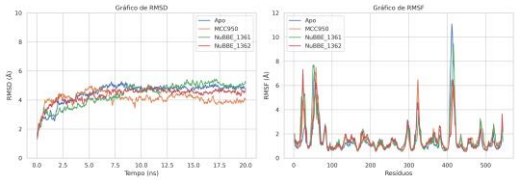


Figura 1: Gráficos RMSD e RMSF para complexos NLRP3 durante trajetórias de 200 ns.

Além disso, as ligações de hidrogênio formadas por NuBBE_1361, NuBBE_1362 e MCC950 durante a simulação foram plotadas para analisar a extensão da interação com o inflamassoma NLRP3. O NuBBE_1362 formou 2 ligações de hidrogênio com a Tyr310 e Arg445. Enquanto o MCC950 formou 2 ligações de hidrogênio, com os resíduos Ala95 e Glu496 durante a simulação. Após a simulação, ambos os compostos, interagiram com resíduos-chave, Ala95 e Arg448 relacionados à ativação do NLRP3. Esses resultados estão de acordo com o estudo realizado por Dekker et al. (Dekker *et al.*, 2021; Santos Nascimento; Aquino; Silva-Júnior, 2022), em que indicaram a presença destes resíduos como aminoácidos chave para a ativação desta proteína.

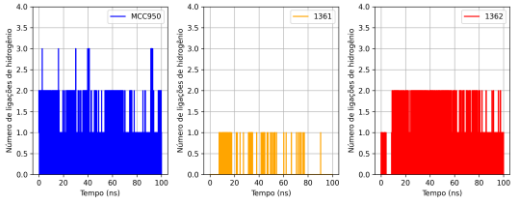


Figura 2: Número de ligações de hidrogênio durante o tempo de simulação.

Conclusões

Os resultados obtidos destacam o potencial dos alcaloides NuBBE_1362 e NuBBE_1361 como inibidores promissores do inflamassoma NLRP3, superando o inibidor sintético MCC950 em termos de afinidade de ligação e estabilidade conformacional. A análise de toxicidade revelou que ambos os compostos são seguros, não apresentando riscos significativos de hepatotoxicidade, carcinogenicidade, mutagenicidade ou citotoxicidade. As simulações de dinâmica molecular reforçam a eficácia dos compostos em manter a estabilidade estrutural da NLRP3, sugerindo que eles poderiam servir como uma base para o desenvolvimento de novos agentes terapêuticos. Estudos futuros poderão incluir a validação experimental desses compostos em modelos celulares e a síntese de análogos estruturais para otimizar suas propriedades farmacológicas.

Agradecimentos

Ao CNPq pela bolsa concedida.

Referências

1. KIM, S.-K. The Mechanism of the NLRP3 Inflammasome Activation and Pathogenic Implication in the Pathogenesis of Gout. **Journal of Rheumatic Diseases**, v. 29, n. 3, p. 140–153, 1 jul. 2022.

2. HONG, Y. et al. MCC950 alleviates seizure severity and angiogenesis by inhibiting NLRP3/ IL-1β signaling

pathway-mediated pyroptosis in mouse model of epilepsy. **International Immunopharmacology**, v. 126, p. 111236, 5 jan. 2024.

3. DEKKER, C. et al. Crystal Structure of NLRP3 NACHT Domain With an Inhibitor Defines Mechanism of Inflammasome Inhibition. **Journal of Molecular Biology**, v. 433, n. 24, p. 167309, 3 dez. 2021.

4. PY, B. F. et al. Caspase-11 Controls Interleukin-1β Release through Degradation of TRPC1. **Cell Reports**, v. 6, n. 6, p. 1122–1128, 27 mar. 2014.

5. BARRETO GOMES, D. E. et al. ChemFlow─From 2D Chemical Libraries to Protein–Ligand Binding Free Energies. **Journal of Chemical Information and Modeling**, v. 63, n. 2, p. 407–411, 23 jan. 2023.

6. KORB, O.; STÜTZLE, T.; EXNER, T. E. Empirical Scoring Functions for Advanced Protein−Ligand Docking with PLANTS. **Journal of Chemical Information and Modeling**, v. 49, n. 1, p. 84–96, 26 jan. 2009.

7. FANUCCHI, S. et al. Immune genes are primed for robust transcription by proximal long noncoding RNAs located in nuclear compartments. **Nature Genetics**, v. 51, n. 1, p. 138–150, jan. 2019.

8. KERUR, N. et al. cGAS drives noncanonical-inflammasome activation in age-related macular degeneration. **Nature Medicine**, v. 24, n. 1, p. 50–61, jan. 2018.

9. FONSECA, B. M. et al. Increased expression of NLRP3 inflammasome components in granulosa cells and follicular fluid interleukin(IL)-1beta and IL-18 levels in fresh IVF/ICSI cycles in women with endometriosis. **Journal of Assisted Reproduction and Genetics**, v. 40, n. 1, p. 191–199, 1 jan. 2023.

10. TAPIA-ABELLÁN, A. et al. MCC950 closes the active conformation of NLRP3 to an inactive state. **Nature Chemical Biology**, v. 15, n. 6, p. 560–564, jun. 2019.

Seleção e Avaliação Toxicológica de Produtos Naturais como potenciais Inibidores da Proteína VEGFR-2

Nalanda da Silva Maués[1], Renato Araújo da Costa[2], Nalberth Batista Farias[3], Flavia da Silva Soares[4].
[1] Laboratório de Biologia Molecular, Evolução e Microbiologia. Abaetetuba-PA. Brasil.
[2] Laboratório de Biologia Molecular, Evolução e Microbiologia. Abaetetuba-PA. Brasil.
[3] Laboratório de Biologia Molecular, Evolução e Microbiologia. Abaetetuba-PA. Brasil.
[4] Laboratório de Biologia Molecular, Evolução e Microbiologia. Abaetetuba-PA. Brasil.

mauesnalanda@gmail.com
Palavras-chave: VEGFR-2, Produtos Naturais, Triagem Virtual.

Abstract

In this study, the inhibition of the VEGFR-2 protein by natural products from Brazilian biodiversity was evaluated using virtual screening with the NuBBE database. Out of 1,448 analyzed compounds, the top 10 with the best binding free energy (MM-GBSA) were selected for toxicity and drug-likeness analysis. Compounds NuBBE_980 and NuBBE_981 showed superior affinity to sorafenib and were non-toxic in the conducted tests, standing out for significantly interacting with key residues of VEGFR-2. These compounds also demonstrated in vitro cytotoxic potential, suggesting they may be promising for anticancer therapies and angiogenesis inhibition.

Introdução

O Receptor de Fator de Crescimento Endotelial Vascular Tipo 2 (VEGFR-2) é um receptor tirosina quinase (RTK) que é responsável por regular a angiogênese (formação de novos vasos sanguíneos a partir de vasos pré-existentes) (El-Meguid et al., 2022). Trata-se de um processo fisiológico natural indispensável que auxilia no crescimento de células e reparo de tecidos (Modi; Kulkarni, 2019). No entanto, quando superexpresso, pode contribuir com o processo cancerígeno de muitas células, estando envolvido na ocorrência de vários tipos de câncer, em especial, o câncer de mama (El-Meguid et al., 2022).

Medicamentos comumente utilizados em tratamentos cancerígenos com inibidores de VEGFR-2 como o sorafenib, apesar de inibirem a atuação do receptor, acabam por gerar resistência ao medicamento, devido à ocorrência de efeitos colaterais adversos, o que, por consequência, resulta em uma eficácia limitada do fármaco (Li et al., 2014). Em vista disso, novos inibidores de VEGFR-2 menos tóxicos e mais acessíveis vêm sendo desenvolvidos para a formulação de fármacos no tratamento do câncer de mama.

No presente estudo, utilizamos um fluxo de trabalho de alto desempenho para selecionar moléculas de produtos naturais da biodiversidade brasileira presente no banco de dados NuBBE (Núcleo de Bioensaios Biossíntese e Ecofisiologia de Produtos Naturais), objetivando o desenvolvimento de potenciais inibidores da proteína VEGFR-2.

Metodologia

Foi realizada a triagem virtual com compostos do Banco de Dados de Núcleos de Bioensaios, Ecofisiologia e Biossíntese de Produtos Naturais (NuBBEDB) (Russo et al., 2023), que possui 2223 compostos naturais. Após filtragem com base na "Regra dos 5" de Lipinski (Lipinski et al., 2001), selecionamos 1448 compostos. Utilizamos a estrutura cristalina da proteína do Protein Data Bank (PDB: 4ASD) em complexo com sorafenib (BAY) (El-Meguid et al., 2022). A proteína VEGFR-2 foi preparada para análise, e a triagem virtual foi realizada com o fluxo ChemFlow (Barreto Gomes et al., 2023). O DockFlow fez o encaixe molecular utilizando o programa PLANTS (Korb, Stützle e Exner, 2009), o LigFlow a parametrização e atribuição de cargas aos compostos, e o ScoreFlow reclassificou as poses utilizando os métodos MM/PBSA ou MM/GBSA, conforme implementado no MMPBSA.py do AmberTools22. Em seguida, foram selecionadas as 10 moléculas com melhores energias de ligação para análise de toxicidade com base nos parâmetros de hepatotoxicidade, neurotoxicidade, carcinogenicidade, mutagenicidade e citotoxicidade, usando ProTox II (Banerjee et al., 2018). Apenas moléculas inativas nos

testes foram consideradas para etapas subsequentes. Por fim, foram analisadas interações com resíduos-chave da proteína para selecionar o melhor composto para simulações de dinâmica molecular.

Resultados e Discussão

A triagem virtual é uma ferramenta crucial para identificar compostos promissores em grandes bibliotecas de produtos naturais. Neste estudo, 1.448 produtos naturais do banco de dados NuBBE foram avaliados quanto à interação com o sítio ativo da proteína VEGFR-2. Para minimizar falsos positivos, a energia livre de ligação dos compostos foi calculada usando o método MM-GBSA e os compostos foram reclassificados com base nesses valores. Dez compostos foram selecionados para avaliação adicional, incluindo análise de toxicidade e semelhança a fármacos. A Tabela 1 apresenta esses compostos juntamente com seus valores de energia livre de ligação e resultados das análises.

Tabela 1. Valores de energia livre MMGBSA, teste de toxidade e semelhança a fármacos.

Comp	MMGBSA (kcal/mol)	Hepa	Carci	Muta	cito	Semelhança a fármacos
1800	-56,14	Inactive	Inactive	Inactive	Inactive	-9,4
980	-55,33	Inactive	Inactive	Inactive	Inactive	3,3
412	-50,59	Inactive	Inactive	Inactive	Inactive	-7,5
981	-50,5	Inactive	Inactive	Inactive	Inactive	3
2218	-50,09	Inactive	Inactive	Inactive	Inactive	-1,5
1807	-49	Inactive	Inactive	Inactive	Inactive	-13
1862	-48,73	Inactive	Inactive	Inactive	Inactive	-5,4
306	-48,69	Inactive	Inactive	Inactive	Inactive	-10
2221	-48,63	Inactive	Inactive	Inactive	Inactive	-1,7
BAX	-47,95	Active	Inactive	Inactive	Active	

De acordo com a Tabela 1, os dez produtos naturais selecionados apresentaram valores de energia livre de ligação MM-GBSA mais favoráveis do que o inibidor de referência, sorafenib (BAX). Esses valores mais baixos indicam uma afinidade de ligação mais forte ao sítio de ligação da proteína VEGFR-2 (Sahakyan, 2021). Além disso, todos os compostos mostraram-se inativos em relação aos parâmetros de hepatotoxicidade, carcinogenicidade, mutagenicidade e citotoxicidade, conforme avaliação pelo PROTOX-II. A análise de semelhança a fármacos realizada pelo software DataWarrior revelou que os compostos NuBBE_980 e NuBBE_981 apresentaram valores positivos de probabilidade de similaridade medicamentosa, destacando-se como bons candidatos a medicamentos.

Esses dois compostos foram então selecionados para uma análise das interações com os resíduos de aminoácidos do sítio ativo da proteína VEGFR-2 e comparados com as interações observadas para o inibidor sorafenib, conforme mostrado na Figura 1.

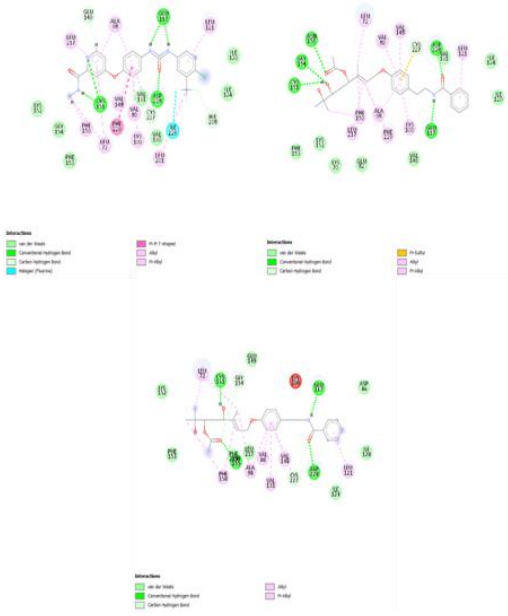


Figura 1. Interações realizadas pelos compostos BAX (A), NuBBE_980 (B) e NuBBE_981 (C) com os resíduos do sítio ativo da proteina VEGFR-2.

O composto mais eficaz para o encaixe com VEGFR-2 foi o NuBBE_980, que apresentou uma energia livre de ligação MM-GBSA de -55,33 kcal/mol. Este composto estabeleceu fortes interações com VEGFR-2, evidenciadas pela formação de cinco ligações de hidrogênio com os resíduos Glu117, Cys151, Gly154, Asn155 e Asp228, além de interações hidrofóbicas adicionais no sítio ativo da proteína. O NuBBE_981, com uma energia livre de ligação MM-GBSA de -50,50 kcal/mol, mostrou quatro interações de hidrogênio com os resíduos Glu117, Cys151, Asn155 e Asp228, além de interações hidrofóbicas com outros resíduos do sítio ativo (Figura 1). As interações de hidrogênio com os resíduos Glu117, Cys151 e Asp228, também observadas com o inibidor de referência sorafenib, corroboram nossos resultados.

Tanto o NuBBE_980 quanto o NuBBE_981 já foram relatados por possuírem potencial citotóxico in vitro em linhagens de células cancerígenas (Sribuhom et al., 2017). Agora, eles também demonstram uma forte afinidade com o sítio ativo da proteína VEGFR-2. Esta descoberta é de grande relevância, pois sugere que essas moléculas podem atuar diretamente no alvo terapêutico VEGFR-2, além de terem o potencial de serem desenvolvidas como candidatos promissores para novas terapias anticâncer. A combinação de interações robustas com VEGFR-2 e a citotoxicidade previamente

estabelecida reforça o potencial desses compostos em inibir a angiogênese, um processo crucial no desenvolvimento e progressão de tumores (Salimi et al., 2022). Assim, os resultados destacam a importância dos compostos NuBBE_980 e NuBBE_981 como potenciais inibidores da VEGFR-2, justificando uma investigação mais aprofundada para seu desenvolvimento como agentes terapêuticos contra o câncer.

Conclusões

Os compostos naturais NuBBE_980 e NuBBE_981 mostraram forte potencial como inibidores da VEGFR-2, com energia de ligação mais favorável que o sorafenib e inatividade em testes de toxicidade. Suas interações robustas com resíduos críticos do sítio ativo da VEGFR-2 e evidência de citotoxicidade in vitro destacam sua importância para novas terapias anticâncer. A combinação de alta afinidade e baixa toxicidade sugere que esses compostos podem superar limitações dos medicamentos atuais. Assim, NuBBE_980 e NuBBE_981 são candidatos promissores para desenvolvimento clínico como novos agentes terapêuticos contra o câncer.

Referências

1. EL-MEGUID, Eman A. et al. Novel benzothiazole-based dual VEGFR-2/EGFR inhibitors targeting breast and liver cancers: Synthesis, cytotoxic activity, QSAR and molecular docking studies. **Bioorganic & Medicinal Chemistry Letters**, v. 58, p. 128529, 2022.

2. MODI, Siddharth J.; KULKARNI, Vithal M. Vascular endothelial growth factor receptor (VEGFR-2)/KDR inhibitors: medicinal chemistry perspective. **Medicine in Drug Discovery**, v. 2, p. 100009, 2019.

3. LI, Jing et al. In silico discovery of potential VEGFR-2 inhibitors from natural derivatives for anti-angiogenesis therapy. **International journal of molecular sciences**, v. 15, n. 9, p. 15994-16011, 2014.

4. MANNOCHIO-RUSSO, Helena et al. Twenty-five years of natural products research in NuBBE. **Frontiers in Natural Products**, v. 2, p. 1252092, 2023.

5. LIPINSKI, Christopher A. et al. Experimental and computational approaches to estimate solubility and permeability in drug discovery and development settings. **Advanced drug delivery reviews**, v. 46, n. 1-3, p. 3-26, 2001.

6. BARRETO GOMES, Diego E. et al. ChemFlow─ From 2D Chemical Libraries to Protein–Ligand Binding Free Energies. **Journal of Chemical Information and Modeling**, v. 63, n. 2, p. 407-411, 2023.

7. KORB, Oliver; STUTZLE, Thomas; EXNER, Thomas E. Empirical scoring functions for advanced protein− ligand docking with PLANTS. **Journal of chemical information and modeling**, v. 49, n. 1, p. 84-96, 2009.

8. BANERJEE, Priyanka et al. ProTox-II: a webserver for the prediction of toxicity of chemicals. Nucleic acids research, v. 46, n. W1, p. W257-W263, 2018.

9. SAHAKYAN, Harutyun. Improving virtual screening results with MM/GBSA and MM/PBSA rescoring. **Journal of Computer-Aided Molecular Design**, v. 35, n. 6, p. 731-736, 2021.

10. SRIBUHOM, Thurdpong et al. Benzoyltyramine alkaloids atalantums A–G from the peels of Atalantia monophylla and their cytotoxicity against cholangiocarcinoma cell lines. **Journal of Natural Products**, v. 80, n. 2, p. 403-408, 2017.

11. SALIMI, Abbas et al. The use of machine learning modeling, virtual screening, molecular docking, and molecular dynamics simulations to identify potential VEGFR2 kinase inhibitors. **Scientific Reports**, v. 12, n. 1, p. 18825, 2022.

Desenho de novos heterodímeros do Ladostigil e da Huprina W como proposta à inibidores da AChE humana.

Nicolas Ricardo de Melo Alves[1], Érica Cristina Moreno Nascimento[1], João Batista Lopes Martins[1].
[1]Laboratório de Química Computacional, Instituto de Química, Universidade de Brasília, Campus Darcy Ribeiro, Asa Norte.
nicolasrmalves@gmail.com.
Keywords: Heterodimers, Alzheimer's Disease, Acetylcholinesterase, Docking, ADMET.

Abstract
The cholinergic hypothesis sets the inhibition of acetylcholinesterase enzyme (hAChE) as an alternative way to reduce the Alzheimer's disease symptoms. In this work, 30 new hybrids heterodimers as potential inhibitors of the hAChE were designed. The better ranked molecules presented 3 carbons atoms and an amide or alkene group on its linker (bridge) between the monomers of Ladostigil and the Huprine W ligands.

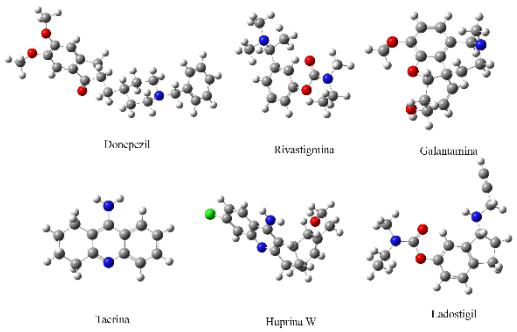
Introdução

A doença de Alzheimer (DA) é uma doença neurodegenerativa associada a cerca de 70% dos casos de demência, perda de memória e perdas cognitivas. Atualmente essa demência é uma das principais causas de morte e causadora de dependência entre a população idosa mundialmente[1].

A principal via de tratamento da DA leva em consideração a chamada hipótese colinérgica. Esta hipótese, por sua vez, sugere que a neurodegeneração estaria diretamente associada ao déficit colinérgico que é observado em pacientes com a DA. Esta hipótese propõe a inibição da ação da enzima acetilcolinesterase (AChE) sobre o neurotransmissor acetilcolina (ACh) no meio sináptico. O mecanismo de ação da AChE consiste na hidrólise da acetilcolina em acetato e colina que por sua vez em outro momento será restaurada nos neurônios pré-sinápticos em ACh para a manutenção das sinapses. A inibição da AChE ocorre diretamente no seu sítio ativo, chamado Gorge, constituído de uma entrada estreita e repleta de resíduos aromáticos com um alargamento na base do sítio, onde se encontra a tríade catalítica Ser203-Glu334-His447.[2]

Neste trabalho, novas entidades químicas (NQE) foram desenhadas como candidatos a inibidores da acetilcolinesterase humana (hAChE) e tiveram seu potencial estudado por meio de suas propriedades farmacocinéticas, e docking molecular.

Figura 1 – Inibidores clássicos da acetilcolinesterase humana.



Metodologia

Os ligantes aqui estudados foram modelados usando técnicas de heterodimerização e bioisosterismo[2]. Partindo das estruturas do ladostigil e da huprina W, novas entidades químicas foram desenhadas utilizando softwares de visualização de moléculas. As NQE desenhadas foram modeladas por meio de estudos de absorção, metabolismo, distribuição, eliminação e toxicidade (ADMET)[4], assim como seus potenciais enquanto inibidores da hAChE avaliados, por meio de técnicas de docking molecular. Os resultados obtidos no estudo ADMET foram utilizados para realizar um estudo de

correlação entre estas propriedades e ligantes clássicos através de um heatmap.

O docking molecular foi realizado usando os algoritmos AutoDock 4 e AutoDock Vina[5] contidos no pacote MGLTools. O cristal da proteína utilizado está complexado com o donepezil e depositado no PDB com o código 6O4W. A estrutura foi preparada a partir da remoção do ligante, moléculas de água, glicerol e íons nitrato. A grid box indicada para o programa cobria todos os resíduos presentes no sítio ativo da enzima. Os testes foram realizados com o algoritmo lamarckiano de 100 soluções, 36 milhões de avaliações e uma população de 300.

Resultados

A partir das técnicas de drug design utilizadas, 30 novas estruturas foram obtidas variando o número de carbonos e a função orgânica do grupo de ponte que conecta os dois monômeros. Os resultados dos estudos de ADMET (Figura 2) mostraram que estes novos heterodímeros apresentam, em sua maioria, área de superfície polar elevada (TPSA), alta capacidade de absorção gastrointestinal e relativa capacidade de permeabilidade na barreira hematoencefálica.

A presença de anéis aromáticos nitrogenados derivados da quinolina nos ligantes, somado à presença de funções orgânicas oxigenadas/nitrogenadas no grupo espaçador aumenta a TPSA, dificultando a capacidade dos ligantes de permear membranas como a barreira hematoencefálica. Apenas as moléculas que eram capazes que ultrapassar esta barreira, aquelas que se encontram dentro do círculo amarelo na Figura 2, foram consideradas para continuação do estudo.

Os resultados de docking molecular mostraram que todas as moléculas apresentaram boa capacidade inibitória dado o resultado das energias de ligação dos complexos formados com a hAChE. No geral, as moléculas que contêm 5 carbonos em seu grupo de ponte tiveram um resultado mais energético, ou seja, formaram um complexo menos estabilizado com a proteína. Em contrapartida, aquelas com 3 carbonos no grupo de ponte obtiveram melhores resultados de energia de interação e forma selecionadas para eventuais estudos de estrutura eletrônica e dinâmica molecular (Figura 3). Este resultado parece concordar com os observados no heatmap (Figura 4), onde observamos maior correlação destas com ligantes clássicos e de estrutura conhecida. Paralelamente, as moléculas que continham os grupos amida e alcano no seu grupo de ponte tiveram um desempenho notavelmente melhor, com energia de interação 1,44 kcal/mol menor que os demais. As NQEs com grupos éster e cetona na sua composição também mostraram uma boa inibição

Figura 2 - Gráfico BOILED-Egg das novas entidades químicas desenhadas.

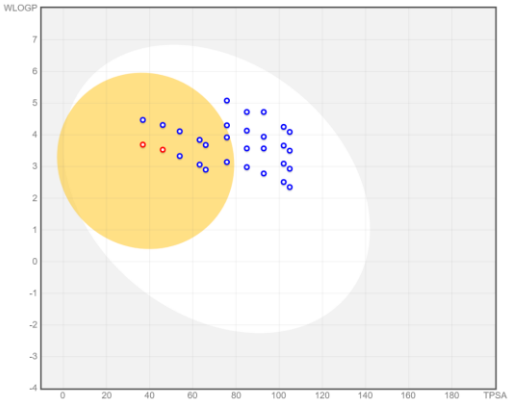


Figura 3 - Resultado de docking molecular das moléculas de melhor resultado ADMET.

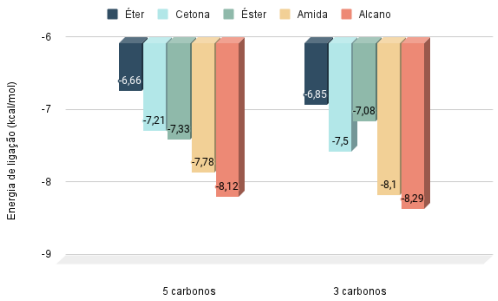
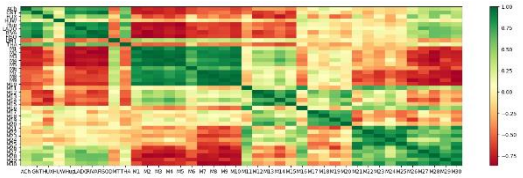


Figura 3 – Visualização heatmap da correlação dos dados ADMET das NQEs e ligantes clássicos.



Conclusão

O presente estudo permitiu o desenho de novas estruturas candidatas a inibidores da AChE. A partir do estudo ADMET de cada NEQ individualmente observou-se que o efeito da presença dos anéis aromáticos nitrogenados da quinolina parece diminuir a permeabilidade das moléculas na barreira hematoencefálica, alvo das NQEs. Entretanto, 10 dessas moléculas tiveram resultado positivo e promissor, sendo levadas em sequência para estudos mais detalhados. Em concordância com o estudo heatmap dos ligantes, as moléculas que continham apenas 3 carbonos no grupo espaçador resultaram em melhores resultados de docking, principalmente com as funções alcano e amida. Estas seguirão em estudos e terão suas estruturas otimizadas e serão estudadas através de seus orbitais moleculares de fronteira,

Agradecimentos

FAPDF, UnB, CNPq, LQC.

Rerefências

1. ALZHEIMER'S ASSOCIATION. 2023 Alzheimer's disease facts and figures. Alzheimer's and Dementia, v. 19, n. 4, p. 1598–1695, 1 abr. 2023.

2. DHAPOLA, R. *et al.* Oxidative stress in Alzheimer's disease: current knowledge of signaling pathways and therapeutics. Molecular Biology ReportsSpringer Science and Business Media B.V., 2 jan. 2024.

3. MEZEIOVA, Eva *et al.* Huprine Y–Tryptophan heterodimers with potential implication to Alzheimer's disease treatment. Bioorganic & Medicinal Chemistry Letters, v. 43, p. 128100, 2021.

4. DAINA, Antoine; MICHIELIN, Olivier; ZOETE, Vincent. SwissADME: a free web tool to evaluate pharmacokinetics, drug-likeness and medicinal chemistry friendliness of small molecules. Scientific reports, v. 7, n. 1, p. 42717, 2017.

5. MORRIS, Garrett M. et al. AutoDock4 and AutoDockTools4: Automated docking with selective receptor flexibility. Journal of computational chemistry, v. 30, n. 16, p. 2785-2791, 2009.

Viriális: A Web-based Software to Calculate the Second Virial Coefficient

Alberto Seleto de Souza[1], Patricia RP Barreto[2]
[1]Departamento de Engenharia de Materiais, Escola de Engenharia de Lorena da USP - Área II - Lorena – SP,
[2]Laboratório Associado de Plasma, Instituto Nacional de Pesquisas Espaciais, CP515, São José dos Campos – SP – Brasil.
Email of the corresponding author: *patricia.barreto@inpe.br*
Keywords: Monte Carlo Integration, Potential Energy Surface, Second Virial Coefficient, Interactive web based program, non linear regression.

Abstract
Viriális calculates the second virial coefficient of AB diatomic molecules as well as A_2-B_2 polyatomic molecules. It performs a nonlinear fitting, generating a potential energy surface according to the generalized fifth-degree Rydberg function and the Pirani potential. Thus, *Viriális* returns the second virial coefficient in terms of temperature.

Introduction
Viriális has been developed through the Python programming language to calculate the second virial coefficient in function of temperature, B(T). Centering on the molecular system of A_2-B_2 type as a rigid rotor, the intermolecular interaction energy $V(R, \theta_a \theta_b, \varphi)$ is defined as[1]:

$$V(R, \theta_a \theta_b, \varphi) = 4\pi \sum_{L_a, L_b, L} V^{L_a, L_b, L}(R) Y^{L0}_{L_a L_b}(\theta_a \theta_b, \varphi)$$

Where R is the distance between the centers of mass, θ_a and θ_b are the angles between the molecule axis and the center of mass coordinates, and φ is the dihedral angle between A_2 and B_2. $Y^{L0}_{L_a L_b}$ represents the bipolar spherical harmonics, and $V^{L_a, L_b, L}$ momentums, that are define as function of the leading configurations (LCs) and can be described with the Pirani potential[2] and the fifth degree Rydberg potential[3].
The goal of this work is to obtain the value of the second virial coefficient through a computational numeric method hosted in the web, so other research can avail from it.

Methodology
Using outputted ab initio points from simulation software such as *Molpro, Gaussian, and SAPT, etc*, it was possible to create a code that fits these points to the fitting function of choice, and calculates *B* varying with temperatures (*T*) using Monte Carlo integration through the *VEGAS* library. To evaluate the efficiency of the code, the virial equation of state for mixture[4,5] is used, and compared via RMSE. The final outputs are a downloadable information table, and plots of *B x T*, *V x R*, and $V^{L_a, L_b, L}$ *x R*. In this work, the molecules used were H_2F_2, F_2F_2, and H_2Cl_2 and H_2H_2.

Results
The software can be accessed through https://virialis.streamlit.app/[6]. Figure 1 represents the Home Page of *Viriális*.



Fig. 1: Virialis homepage

From there, the user can read the instructions on how to use it, and proceed to page "Fitting", where he can input his ab initio point's files and choose the desired PES.

Once the fitting is done, the energy information is displayed in a plot, and the generated information can be used as input for page "Polyatomic Molecules A_2B_2. There, a few options ought to be specified, such as the number of temperatures, and the PES of choice once again.

Figure 2 illustrates the main results for H_2-H_2, F_2-F_2, H_2-F_2 and H_2-Cl_2 systems, while Table 1 shows the RMS for the second virial coefficient calculated using Rydberg and Pirani Potential with reference data.

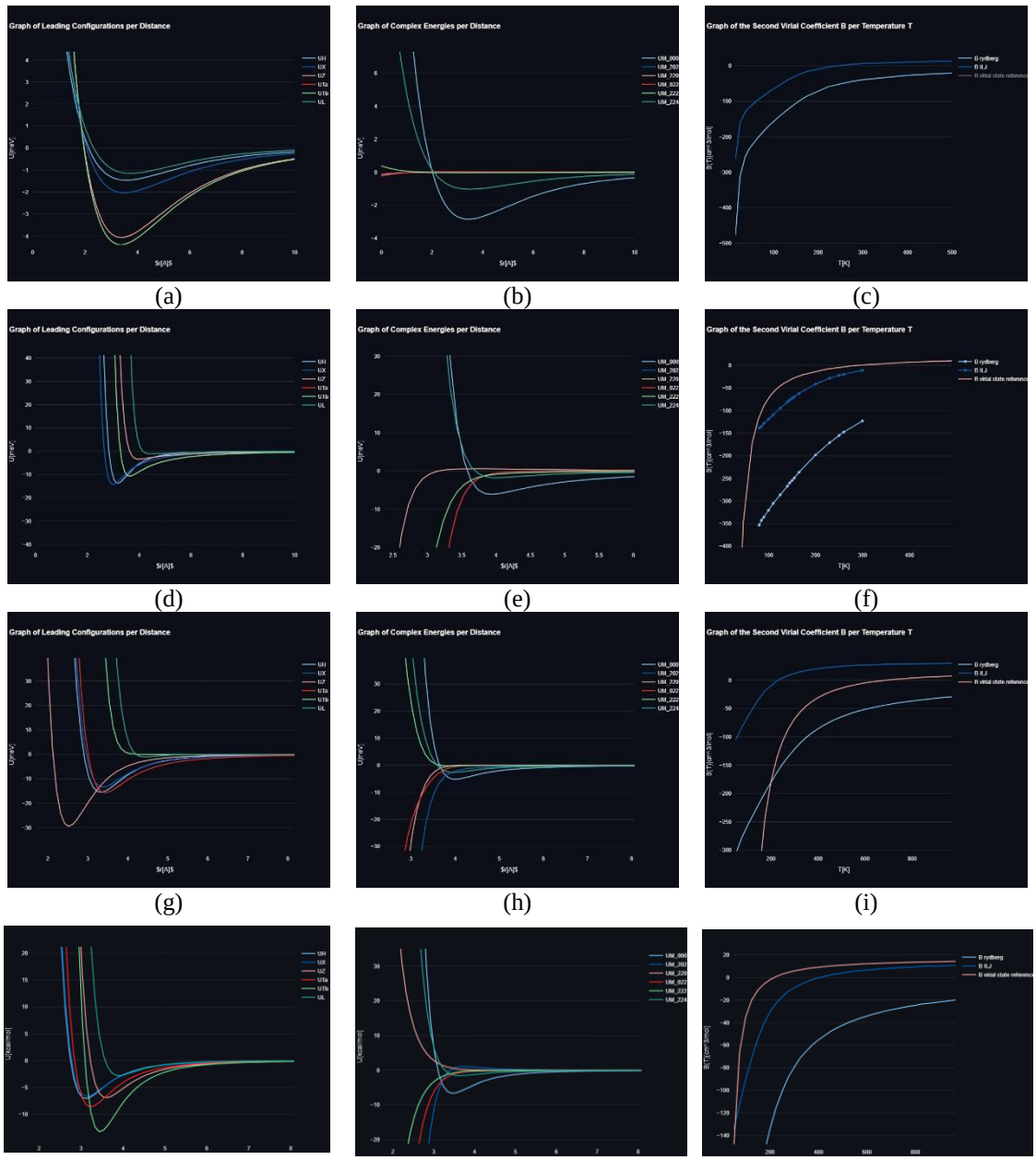


Fig. 2: Leading configuration (LC), momentums (ν_{ijk}) and second virial coefficient (B(T)): (a) LC for H_2-H_2 using Rydberg Potential, (b) ν_{ijk} for H_2-H_2 using Rydberg Potential, (c) B(T) for H_2-H_2, (d) LC for F_2-F_2 using Pirani Potential, (e) ν_{ijk} for F_2-F_2 using Pirani Potential, (f) B(T) for F_2-F_2, (g) LC for H_2-Cl_2 using Rydberg Potential, (h) ν_{ijk} for H_2-Cl_2 using Rydberg Potential, (i) B(T) for H_2-Cl_2 using Pirani Potential, (j) LC for H_2-F_2 using Pirani Potential, (k) ν_{ijk} for H_2-F_2, (l) B(T) for H_2-F_2,

Figs 2(a),(d), (g) and (j) shows the ab initio fitting using Rydberg and/or Pirani Potential. Looking at this figure, we cannot see a big difference between them. The mean RMS, for all leading configurations and systems, are 0.61 and 0.71 for Rydberg and Pirani Potential, respectively. The moments ν_{ijk}, are presented in Figs 2(b), (e) (h) and (k), they are very similar considering these two different potentials. The second virial coefficients are given in Figs. 2(c), (f), (i) and (l), and are compared the results for the two different potential and reference data. While the Rydberg Potential gives smaller mean RMS, it presents a bigger difference for the virial coefficient for all systems analyzed. The main reason for that is the construction of the potential. The Rydberg Potential is a fifth grade polynomial times an exponential; it is easier to do the fitting, while the Pirani Potential has a physical meaning, related with the hardness of the interacting system and reproduces the correct behavior of the long range for a wide variety of systems[7].

Table 1: RMS for the second virial coefficient between reference data and different potential fitting

	Rydberg	Pirani
H_2-H_2	137.025	47.318
F_2-F_2	169.145	28.513
H_2-Cl_2	41.536	10.524
H_2-F_2	93.096	19.694

Conclusions

Viriális' addresses the objectives of the research, providing reliable and consistent results. While the outcomes demonstrate the software's potential in calculating the B(T) of A_2-B_2 and A-B type systems, there is room for further optimization and enhancement.

Acknowledgements

I would like to thank the National Council for Scientific and Technological Development (CNPq) for their financial support, which made this research possible.

References

1. BARRETO, P. et al., J. Mol. Spectrosc. 337, 163, 2017
2. Pirani, F.; et al., Chem. Phys. Lett., 394, 37. 2004
3. Rydberg, R.. Eur. Phys. J. A, 73, 376, 1931.
4. DYMOND, J. H. et al. Virial coefficients of pure gases. 2002.
5. T.P. Van, U.K. Deiters, Chem. Phys. 485, 67, 2017
6. ADEL, A.; BREZEANU, G.; GREITZER, R. et al. Streamlit: The fastest way to create data apps. 2020. https://www.streamlit.io
7. Albernaz A. F., at al., J. Phys. Chem. A, 120, 5315, 2016.

ESTUDO DAS PROPRIEDADES GEOMÉTRICAS E ELETRÔNICAS DO CORTISOL USANDO DINÂMICA MOLECULAR *AB INITIO*

Paulo Henrique Silva Miranda; Ademir João Camargo;

Universidade Estadual de Goiás

RESUMO

O cortisol, um glicocorticoide endógeno com propriedades anti-inflamatórias de grande amplitude, desempenha papel vital na regulação de diversas funções fisiológicas, incluindo o metabolismo, a resposta ao estresse e a modulação imunológica. Este hormônio, ao se ligar ao receptor intracelular de glicocorticoides, exerce uma influência crucial na regulação celular e tecidual, bem como na resposta imunossupressora e anti-inflamatória. A aplicação de simulações de dinâmica molecular e métodos computacionais surge como uma abordagem essencial para investigar as mudanças conformacionais do cortisol em nível atômico, fornecendo subsídios importantes para o desenvolvimento de novos fármacos.

O presente estudo tem como objetivo principal investigar as propriedades geométricas e eletrônicas do cortisol nas fases sólida, líquida e gasosa, utilizando a teoria do funcional da densidade e dinâmica molecular *ab initio*. Entre os objetivos específicos, destaca-se a análise do arranjo supramolecular e das interações intermoleculares do cortisol no estado sólido, cálculos das propriedades geométricas e eletrônicas na fase gasosa, a realização de dinâmica molecular em fase gasosa e aquosa, e a caracterização das ligações de hidrogênio com moléculas de H_2O.

Durante o período inicial da pesquisa, foi realizado um levantamento bibliográfico abrangente sobre o cortisol, evidenciando a necessidade de estudos mais aprofundados para uma caracterização precisa e para a exploração de seu potencial terapêutico. Este esforço resultou na elaboração de uma revisão sistemática que sublinhou a importância dos métodos computacionais e das simulações de dinâmica molecular na análise dessas moléculas.

Os resultados parciais indicam a relevância da investigação das propriedades do cortisol para a pesquisa farmacêutica. As perspectivas futuras incluem a expansão contínua da pesquisa bibliográfica, cálculos avançados das propriedades geométricas e eletrônicas, aprofundamento na dinâmica molecular e na análise das ligações de hidrogênio, além da caracterização dos estados excitados e avaliação da estabilidade fotoquímica do cortisol. Espera-se que este trabalho contribua de maneira significativa para o avanço do conhecimento científico sobre os glicocorticoides, oferecendo insights valiosos para o desenvolvimento de novos tratamentos farmacológicos.

ABSTRACT

Cortisol, an endogenous glucocorticoid with broad-spectrum anti-inflammatory properties, plays a vital role in regulating various physiological functions, including metabolism, stress response, and immune modulation. By binding to the intracellular glucocorticoid receptor, cortisol exerts crucial influence on cellular and tissue regulation, as well as immunosuppressive and anti-inflammatory responses. The application of molecular dynamics simulations and computational methods is essential for investigating the conformational changes of cortisol at the atomic level, providing significant insights for the development of new pharmaceuticals.

This study aims to investigate the geometric and electronic properties of cortisol in solid, liquid, and gaseous phases using density functional theory and ab initio molecular dynamics. Specific objectives include analyzing the supramolecular arrangement and intermolecular interactions of cortisol in the solid state, calculating the geometric and electronic properties in the gaseous phase, performing molecular dynamics in both gaseous and aqueous phases, and characterizing hydrogen bonds with H_2O molecules.

During the initial phase of the research, an extensive literature review on cortisol was conducted, highlighting the need for more in-depth studies for precise characterization and exploration of its therapeutic potential. This effort resulted in a systematic review underscoring the importance of computational methods and molecular dynamics simulations in analyzing these molecules.

Preliminary results indicate the relevance of investigating cortisol's properties for pharmaceutical research. Future perspectives include continuous expansion of the literature review, advanced calculations of geometric and electronic properties, further molecular dynamics studies, and analysis of hydrogen bonding, as well as characterizing excited states and evaluating the photochemical stability of cortisol. It is anticipated that this work will significantly contribute to the advancement of scientific knowledge on glucocorticoids, providing valuable insights for the development of new pharmacological treatments.

Characterization of Ground and Excited States and Photophysical Properties of Hypericin and Modified Structures

Paulo Ricardo de Carvalho Magalhães[1], Julio Cesar Verli Chagas[1], and Francisco Bolivar Correto Machado[1]
[1]Departamento de Química, Instituto Tecnológico de Aeronáutica, Brasil
fmachado@ita.br
Keywords: photodynamic therapy; singlet fission; aromaticity.

Abstract
Hypericin exhibits properties for Photodynamic Therapy (PDT) against cancer, which is based on the interaction between a photosensitizer (PS), light with a specific wavelength, and molecular oxygen, promoting the selective destruction of the target tissue. The proposed mechanisms first involve the excitation of the PS to the triplet state. One possibility for the PS to have a populated triplet state is to exhibit thermodynamic properties of singlet fission ($E(S_1) \geq 2\ E(T_1)$ and $E(T_2) > 2\ E(T_1)$). Thus, this study used Density Functional Theory (DFT) methods, ωB97X-D and CAM-B3LYP with the def2-TZVP basis set, to investigate the structural and electronic properties of hypericin and modified structures. The analyzed structures are Phenanthro[1,10,9,8-opqra]perylene (HPA) (a), and through the implementation of substituents, other structures were studied until reaching the hypericin molecule. The stability of the ground state was analyzed by the energy difference (ΔE) between S_0 and T_1; aromaticity by the Harmonic Oscillator Model of Aromaticity (HOMA); and radical character by the Fractional Occupation Number Weighted Density (FOD). Some excited states were calculated using time-dependent (TDDFT). The main conclusions were that the disruption of π-electron delocalization by the inclusion of a ketone in Phenanthro[1,10,9,8-opqra]perylene-7,14-dione (b) makes the rings with the ketone antiaromatic and increases the aromaticity of the four side rings. The addition of hydroxyl groups forms hydrogen bonds in the molecule (c), increasing the aromaticity of the antiaromatic rings in (b). The addition of more hydroxyl or methyl groups breaks the planarity, with little alteration in aromaticity. TDDFT results indicate that no molecule meets the singlet fission criterion. However, it was observed that there is a proximity between S_1 and Tn, which may favor the population of the T_n state by Intersystem Crossing (ISC).

Introdução
O primeiro registro de caso de hipericismo foi identificado no início do século XIX, tendo a hipericina como responsável. Desde então, a hipericina é estudada para ser utilizada na Terapia Fotodinâmica (PDT) contra o câncer [1] que é baseada na interação dinâmica entre um fotossensibilizador (PS), luz com um comprimento de onda específico e oxigênio molecular, promovendo a destruição seletiva do tecido alvo. [2] Os mecanismos propostos preveem primeiramente a excitação do PS para o estado tripleto. Nesse sentido, é importante entender a estabilidade e a estrutura eletrônica do PS a fim de compreender o mecanismo que leva a estados tripletos populados. Uma das possibilidades é o PS apresentar as propriedades termodinâmicas favoráveis para realizar a fissão singleto (*singlet fisson*).[3]

Metodologia
O presente trabalho utilizou métodos de estrutura eletrônica da química computacional, para estudar as

propriedades estruturais e eletrônicas dos estados fundamentais e excitados da hipericina e de algumas estruturas moleculares da hipericina modificada utilizando métodos da Teoria do Funcional da Densidade (DFT) com os funcionais ωB97X-D, CAM-B3LYP e M06L, e com o conjunto de funções base def2-TZVP. As estruturas moleculares analisadas partiram do Phenanthro[1,10,9,8-opqra]perylene (HPA) (a) e, por meio da implementação de substituintes, outras estruturas foram estudadas até chegar na molécula da hipericina. A estabilidade do estado fundamental foi analisada pela diferença de energia entre o estado fundamental S_0 e primeiro estado excitado de multiplicidade tripleto T_1 (ΔE S_0-T_1). A aromaticidade foi avaliada pelo índice *Harmonic Oscillator Model of Aromaticity* (HOMA) [4], que é baseado na estrutura geométrica. Por definição,

$$HOMA = 1 - \frac{1}{n}\sum \alpha_i\left(R_{Opt} - R_i\right)^2$$

em que α é uma constante empírica escolhida para resultar em HOMA = 0 para o composto de referência não aromático. Quando R_i é igual a R_{Opt} (1,388 Å para C-C), o sistema é considerado aromático (benzeno) e HOMA=1. Quando HOMA < 0, o sistema é classificado antiaromático. O caráter radicalar foi estimado pelo método *Fractional Occupation Number Weighted Density* (FOD) [5], que propõe uma densidade fracionária que considera a contribuição de elétrons fortemente correlacionados. A inspeção da densidade dá-se pela Equação

$$\rho^{FOD}(r) = \sum_i^N \left(\delta_1 - \delta_2 f_i\right)\left|\psi_i(r)\right|^2$$

O quadrado dos orbitais ψ_i's é à densidade de probabilidade, os f_i's introduzem a parcela dos números de ocupação fracionários. Integrando a densidade fracionária (ρ^{FOD}) em todo o espaço, obtém-se o N_{FOD}, que fornece o valor quantitativo referente ao número total de elétrons desemparelhados. Alguns estados excitados foram calculados via métodos *time-dependent* (TDDFT) que permitiram analisar se as estruturas estudadas apresentam as propriedades termodinâmicas favoráveis para a fissão singleto ($E(S_1) \geq 2\ E(T_1)$ e $E(T_2) > 2\ E(T_1)$ [3].

Resultados

Pelo índice Homa (Fig.1) verifica-se que, do ponto de vista da estabilidade estrutural, a quebra na deslocalização dos elétrons π pela inclusão da cetona na molécula (b) faz com que os anéis em que ele se encontra ligada se tornem antiaromáticos, consequentemente há um aumento da aromaticidade dos quatro anéis das laterais. A adição de hidroxilas forma pontes de hidrogênio na molécula (c) aumentando a aromaticidade dos anéis previamente antiaromáticos em (b). O acréscimo de mais hidroxilas ou grupos metil levam a uma quebra de planaridade das moléculas devido a impedimentos estéricos, fazendo com que haja uma pequena alteração na aromaticidade. Os valores de HOMA nos diferentes métodos seguem a mesma tendência e em acordo com resultados anteriores calculados para alguns sistemas [6].

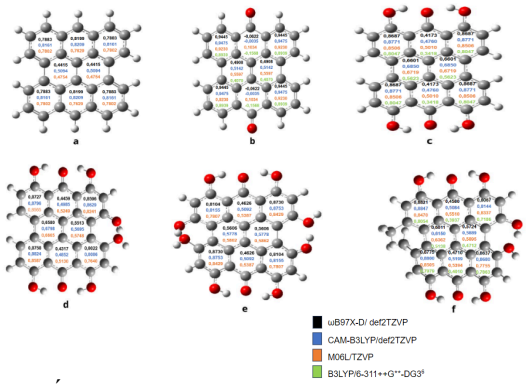


Fig.1 Índice HOMA

A estabilidade eletrônica pelo gap ΔE (S_0-T_1) (Fig.2) e pelo N_{FOD} (Fig.3), mostra que a molécula (a) apresenta um caráter *open-shell* maior (N_{FOD}=1,016) e um gap menor, conferindo, portanto, menor estabilidade entre as moléculas analisadas. A estrutura (b) é a de maior

estabilidade, pois apresenta um caráter *closed-shell* e gap maiores. Para as demais há uma diminuição sutil da estabilidade, valores de gap e N_{FOD} ligeiramente menores. Os valores de gap ΔE (S_0-T_1) entre os métodos ωB97X-D e CAM-B3LYP são um pouco maiores dos que os apresentados por M06L, porém continuam seguindo a mesma tendência.

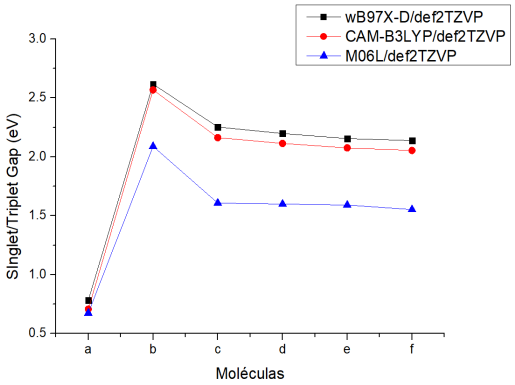


Fig.2 Gap ΔE (S_0-T_1) Vertical

Os resultados TDDFT (Fig.5) indicam que nenhuma molécula atende o critério de fissão singleto. Porém, foi observado que há uma proximidade entre S_1 e T_n, o que pode favorecer a população do estado T_1 por Conversão Intersistema (ISC). A molécula (a) apresenta um alto caráter *open-shell*, e desta forma, o resultado TDDFT descreve o estado tripleto como o mais estável.

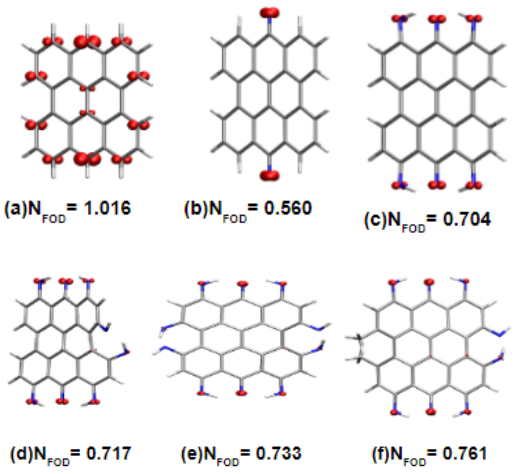


Fig.3 N_{FOD} calculados por ωB97X-D.

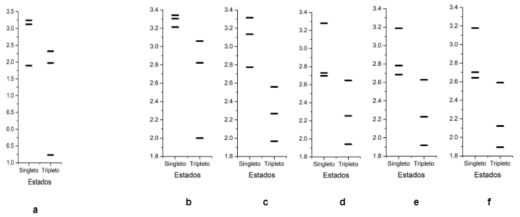


Fig.5 Diagrama de níveis de energia por TD-CAM-B3LYP

Conclusão

O presente trabalho analisando a estrutura da hipericina e estruturas moleculares similares constatou que nenhuma atende aos critérios de singleto fission, mas que que há uma proximidade entre S_1 e T_n, o que pode favorecer a população do estado T_1 por Conversão Intersistema (ISC). A hipericina, por sua vez, apresentou propriedades de estabilidade intermediárias entre a molécula (a) e a (b).

Acknowledgements

O presente trabalho foi realizado com apoio da Coordenação de Aperfeiçoamento de Pessoal de Nível Superior - Brasil (CAPES) - Código de Financiamento 001, CNPq (Processos Nos. 307168/2022-0 e 164766/2021-9) e FAPESP (Processo No. 2022/16385-8).

Referências

1. Andrade, G. *et al.*: Photodiagnosis and Photodynamic Therapy, 2021, 35, 102343.
2. Rocha, L. G. B.: *Ph.D., Thesis*, University of Coimbra, 2015.
3. M. B. Smith, J. Michl.: Chem. Rev., 2010, 110, 6891.
4. (a) Kruzewski, J., T.M. Krigowski.: Tethrahedron Lett.1972, 36, 3839.
(b) Dobrowolski J.C.: ACS Omega, 2019, 4, 18699.
5. Bauer C.A., et al.: Chemistry. 2017, 23(25), 6150.
6. Szymanski S., Majerz I.: *J.Nat. Prod.*, 2019, 82(8), 2106.

Improving Optical Property Predictions in Solvated Systems: Combining tuning of RSH functional and sequential QM/MM approach

Pedro Henrique Ferreira Matias[1], Mateus Rodrigues Barbosa[1], Daniel Francisco Scalabrini Machado[2], Heibbe Cristhian Benedito de Oliveira[1].
[1]Instituto de Química - Universidade Federal de Goiás.
[2]Instituto de Química - Universidade de Brasília.
phfmatias@discente.ufg,br.
Keywords: DFT; TD-DFT; JGAP; Solvated System.

Abstract

This study presents an advanced approach to improving optical property predictions in solvated systems by combining range-separated hybrid (RSH) functional tuning with a sequential quantum mechanics/molecular mechanics (QM/MM) methodology. Para-Nitroaniline (pNA) was selected as the model molecule due to its well-known photophysical properties and its frequent use as a reference system in similar studies. The research utilizes time-dependent density functional theory (TD-DFT) to calculate the photophysical properties of pNA, with water as the solvent. By implementing a sequential QM/MM solvation method using the DICE software, and optimizing the functional using the Golden Omega algorithm, this study effectively reduces computational costs while maintaining high accuracy. Notably, the study achieves a 9.92% relative error between the theoretical predictions and experimental data in the optimized solvated system, which is a marked improvement compared to previous methodologies. The findings underscore the potential of combining RSH functional tuning with explicit solvation methods to enhance the reliability and accuracy of theoretical models in solvated environments.

Introduction

Discrepancies between theoretical and experimental results can arise from the choice of molecular modeling. Add solvation effects can enhance theoretical accuracy. Another way is performing functional optimization. However, trying to mix this practice with solvation methodologies, some barriers arise. Optimizing RSH functionals in implicit solvation methodologies leads to artificially low values of range separation parameter ω (bohr^{-1})[1]. Looking for explicit solvation methodologies, HOMO and LUMO orbitals become spread over onto solvent molecules instead of solute[2]. The present work aims to overcome the problems of functional optimization in solvated systems combining the JGAP tuning scheme with explicit solvation methodology carried out by s-QM/MM.

Methodology

The para-Nitroaniline (pNA) molecule was the object of study due to its frequent use as a reference system for property responses as it is a π conjugated system with high π delocalization and push-pull mechanism.

Photophysical properties were calculated using TD-DFT in Gaussian 16 software[3]. The solvent employed was Water. OPLS parameters were obtained through the LigParGen server[4]. The s-QM/MM solvation method was performed using

DICE[5] software in conjunction with ASEC-FEG approximations with 1 solute and 500 solvent molecules. Functional optimization was performed by Golden Omega software in Python 3.x/C++ programming language. The golden ratio search algorithm was implemented to reduce computational cost. The procedure was performed in order to minimize the equation (1):

$$Jgap(\omega) = \sqrt{(Jip)^2 + (Jea)^2} \quad (1)$$

Results

The functional optimization process resulted in 0.27 ω (bohr^{-1}) for all systems.

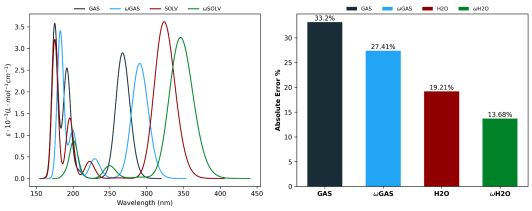


Fig 1. Theoretical UV-Vis spectrum (left), Relative error between theoretical and experimental (right). Dark blue is the isolated system, light blue is the optimized isolated system, red is the solvated system, and green is the optimized solvated system.

In Fig 1 (left), a red shift is observed in optimized systems and the inclusion of the charge points also presents a redshift. This behavior is due to the optimization process minimizing the GAP, leading to low-energy excitation. Also, due to the polarity of water, the charge points stabilize the solute LUMO, decreasing the GAP and consequently leading to redshift. The relative errors present a trend, when the approximation becomes more robust the relative error decreases, the lowest being the solvated optimized with 9.92% of error.

Conclusion

The combination of RSH functional optimization with explicit solvation using a QM/MM approach effectively enhances the accuracy of optical property predictions in solvated systems. This methodology not only reduces the relative error between theoretical and experimental results but also demonstrates a significant improvement in modeling solvated environments, and enables coupling functional optimization in solvated systems. The approach provides a robust framework for accurately predicting photophysical properties in complex solvated systems, making it a valuable tool for future computational studies in chemistry.

Acknowledgements

CNPq, CAPES, FAPEG, LAMCAD, PPGQ-UFG, IQ-UFG, LMSC-IQ-UNB, LEEDMOL-IQ-UFG.

References

1. Bhandari et. al., JCTC, 2018, 14. 6287–6294.
2. de Queiroz, T. JCP, 2015, 143.
3. Frisch, M. J. et al. Gaussian 16 Revision C.01. 2016; Gaussian Inc. Wallingford CT.
4. Dodda, L. S et. al., Nucleic Acids Research, 2017, 45. W331–W336.
5. Coutinho, K et. al., Journal of Chemical Information and Modeling, 2020, 60. 3472–3488

Efeitos conformacionais nas propriedades fotovoltaicas de cromóforos orgânicos sensibilizadores de células solares

Pierre C. S. Junior[1], Daniel F. Scalabrini Machado[1]
[1]Laboratório de Moléculas e Sistemas Complexos (LMSC) – Instituto de Química – Universidade de Brasília – Brasil.
pierrecarlosj@gmail.com, danielscalabrini@unb.br.
Keywords: DSSC's, DFT, conformers, chromophores, charge transfer.

Abstract

We have assed the chemical structure of a series of dipolar chromophores typically employed in DSSC's. The thermal effects on the photovoltaic and electronic parameters of the dyes by determining the conformational ensemble at room temperature. The conformational effects rendered significative impacts on the parameters for the case of flexible fragments.

Introdução

Desde a demonstração pioneira do potencial das Células Solares Sensibilizadas por Cromóforos Orgânicos (em inglês Dye-Sensitized Solar Cells - DSSC) como uma tecnologia fotovoltaica econômica, pesquisas em larga escala e esforços intensos para o desenvolvimento de novos materiais vêm impulsionando o campo.[1] Beneficiadas por inovações contínuas em materiais e na engenharia de dispositivos, as células sensibilizadoras à base de rutênio alcançaram eficiências validadas de até 11,1%.[2] No entanto, a escassez de rutênio e a toxicidade de metais pesados impulsionaram a busca por alternativas livres de metais nos últimos anos. Cromóforos orgânicos se destacam por sua alta flexibilidade no design e síntese molecular, abrindo um universo de possibilidades para exploração científica.
As DSSC's são consideradas dispositivos de conversão de energia solar ambientalmente amigáveis e de baixo custo de produção, consistindo tipicamente em uma estrutura do tipo D-π-A.[1] Este tipo de design dos cromóforos, visa, como peça-chave do funcionamento das DSSC's, utilizar o cromóforo com a função de absorver fótons e injetar os elétrons foto excitados na banda de condução do semicondutor no anodo (geralmente baseados em óxido de titânio).
Comumente, a viabilidade de um cromóforo orgânico visando aplicações fotovoltaicas é analisada através do espectro de absorção UV-vis. Esta análise é importante para caracterizar a eficiência do sensibilizador que deve apresentar altos coeficientes de extinção molar afim de coletar os fótons mais abundantes do espectro solar que se encontram majoritariamente na região do visível e IV-próximo.[3]
Neste trabalho, investigamos diferentes combinações de grupos doadores, aceptores e pi-espaçadores do tipo D-π-A mais comumente encontrados na literatura afim de estabelecer a melhor combinação que otimize os parâmetros eletrônicos associados a eficiências das DSSC's. Para este fim, buscou-se levar em consideração os efeitos térmicos nestes parâmetros através da contribuição estatística de cada conformação acessível na temperatura ambiente.

Metodologia

Inicialmente, foram geradas cento e cinquenta moléculas a partir de cinco doadores de elétrons; dez espaçadores π-conjugados e três doadores de elétrons. Os fragmentos de DSSC's estão ilustrados na Figura 1.

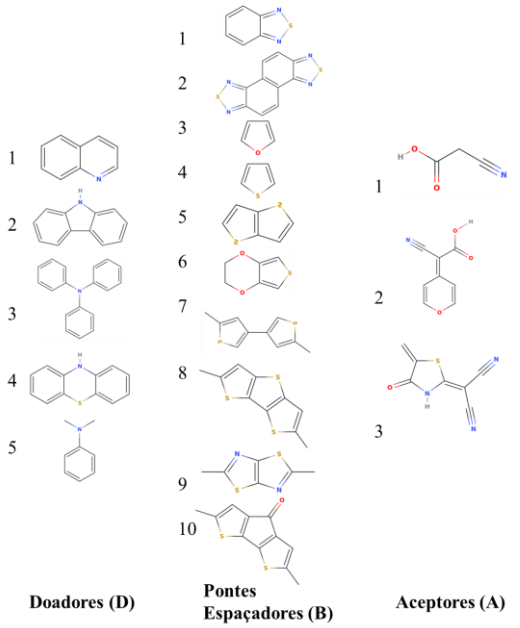


Figura 1 - Estrutura molecular das unidades constituintes dos cromóforos do tipo D-π-A investigados neste trabalho.

As conformações de cada DSSC's formada, foram então avaliadas com o programa CREST[4] para uma busca geométrica inicial. Por questões de capacidade computacional, foi usado o método composto GFN2-xTB//GFN-FF[5,6]. Neste método a amostragem e otimizações são feitas no nível GFN-FF, que são anexadas por um calculo de *single-point* no nível GFN2-xTB. Para melhor classificação dos confórmeros então gerados, o programa CENSO[7] foi empregado. Nele, a partir do arquivo final do CREST os confórmeros foram otimizados em nível DFT utilizando o funcional r²scan-3c[8] e a função de base def2-mTZVPP.

Após essa primeira otimização, os cromóforos (com todos os seus confórmeros) passaram por cálculos TD-DFT utilizando o programa Gaussian 16. A escolha do funcional (CAM-B3LYP) e função de base (6-31G(d,p)) selecionados a partir de testes de benchmarking para esse tipo de molécula.

Em seguida, foi utilizado o programa Multiwnf[9] para extração de parâmetros necessários para análise e verificação da viabilidade do pigmento em potencial.

Resultados

A nomenclatura dos cromóforos foi feita da seguinte forma: os doadores (D) foram numerados de 1 a 5; pontes espaçadoras (B) foram numerados de 1 a 10 e os aceptores foram numerados de 1 a 3. A molécula chamada de D1B1A1 é composta do doador (1), ponte (1) e aceptor (1).

Com o Multiwfn foram extraídos parâmetros que são fundamentais para compreender a natureza fotofísica das transições eletrônicas. Estes parâmetros permitem avaliar se a transição de carga é majoritariamente do tipo CT, algo fundamental em uma célula solar. Até a data para submissão do resumo, estão finalizadas 20% do total das moléculas. Abaixo estão alguns dados extraídos. Na Fig. 2 são apresentados os valores médios (sobre todas as conformações seguindo a estatística de Boltzmann na temperatura de 298K) para os parâmetros CT. Na Fig. 3 é apresentado a energia livre de injeção e elétrons médio (298K) na banda de condução do TiO_2.

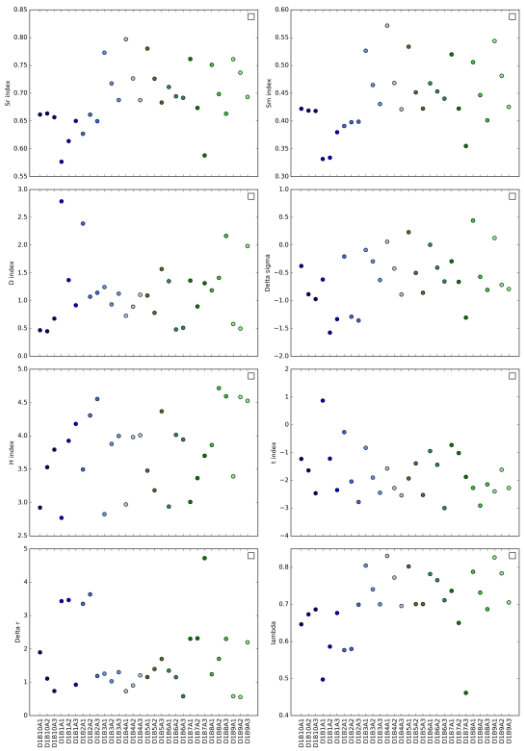


Figura 2 - Parâmetros extraídos do Multiwfn.

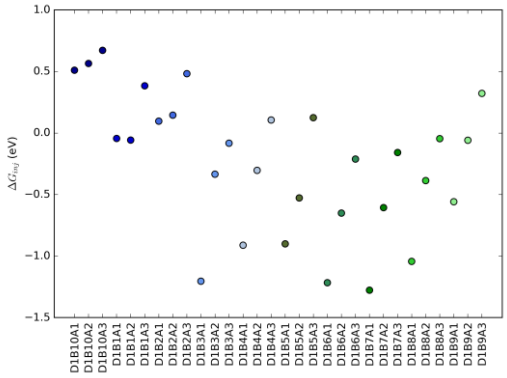


Figura 3 – Energia livre de injeção de elétrons médio (298K) sobre a banda de condução do TiO_2.

Discussão e Conclusões

Na Fig. 2 vemos que a distância entre os centróides da densidade de elétron-buraco associado à transição eletrônica para o primeiro estado excitado é maximizada no pigmento D1A1B1 e este tem boa separação espacial, caracterizado por valores de índice t positivo. As demais moléculas apesar de terem valores de DCT comparáveis não apresentam uma boa separação espacial (índice t negativo). Na Fig. 3 os cálculos DFT revelaram que a molécula D1A1B1 embora tenha forte caráter CT, não consegue espontaneamente injetar elétrons na banda de condução do TiO_2. Outros cromóforos com menor caráter CT tiveram melhor desempenho com relação a este parâmetro de eficiência de célula solar. Em suma, é preciso investigar o efeito do meio, pois este pode ser substancial modificando as conclusões derivadas de cálculos em fase gás.

Agradecimentos
SEEDMOL, CAPES, CNPq, FAPDF.

References
1. O'Regan, B.; Grätzel, M. ;*Nature* **1991**, *353*.
2. Chiba, Y.; Islam, A.; Watanabe, Y.; Komiya, R.; Koide, N.; Han, L. ;*Japanese Journal of Applied Physics, Part 2: Letters* **2006**, *45*.
3. Kitamura, T.; Ikeda, M.; Shigaki, K.; Inoue, T.; Anderson, N. A.; Ai, X.; Lian, T.; Yanagida, S. ;*Chemistry of Materials* **2004**, *16*.
4. Pracht, P.; Grimme, S.; Bannwarth, C.; Bohle, F.; Ehlert, S.; Feldmann, G.; Gorges, J.; Müller, M.; Neudecker, T.; Plett, C.; Spicher, S.; Steinbach, P.; Wesołowski, P. A.; Zeller, F. ;*Journal of Chemical Physics* **2024**, *160*.
5. Spicher, S.; Grimme, S. ;*Angewandte Chemie - International Edition* **2020**, *59*.
6. Bannwarth, C.; Ehlert, S.; Grimme, S. ;*J Chem Theory Comput* **2019**, *15*.
7. Grimme, S.; Bohle, F.; Hansen, A.; Pracht, P.; Spicher, S.; Stahn, M. Efficient Quantum Chemical Calculation of Structure Ensembles and Free Energies for Nonrigid Molecules. *Journal of Physical Chemistry A* **2021**, *125*.
8. Grimme, S.; Hansen, A.; Ehlert, S.; Mewes, J. M. ;*Journal of Chemical Physics* **2021**, *154*.
9. Lu, T.; Chen, F. ;*J Comput Chem* **2012**, *33*.

Estudo teórico da adsorção de 17β-estradiol e 17α-etinilestradiol no óxido de grafeno reduzido

Raabe Freitas dos Santos[1], Murielly Fernanda Ribeiro Bihain[1], Douglas Henrique Pereira[1,2]

[1]Programa de Pós-Graduação em Química, Universidade Federal do Tocantins, Campus Gurupi -Badejos, Caixa Postal 66, CEP: 77 402-970, Gurupi, Tocantins, Brasil
[2]Departamento de Química, Instituto Tecnológico de Aeronáutica (ITA), São José dos Campos, CEP: 12228-900 SP, Brasil.

Corresponding author. Email: freitas.raabe@mail.uft.edu.br.

Keywords: Hormones; DFT; Interactions.

Abstract

The 17β-estradiol (E2) and 17α-ethinyl estradiol (EE2) are the main causes of estrogenic activities in aquatic bodies and sewage, mainly affecting the male and female reproductive systems, causing various disorders such as menstrual irregularities, infertility, endometriosis, polycystic ovary syndrome, spontaneous abortions and other illnesses. One technique for removing hormones from water bodies is using adsorption and the use of reduced graphene oxide (rGO) is interesting because rGO has excellent adsorption properties. In this context, the work aims to theoretically evaluate the interaction, bonds and interaction energies that occur between the interaction of E2 and EE2 with the rGO matrix. The frontier molecular orbitals (HOMO and LUMO) and the molecular electrostatic potential (MEP) were analyzed and it was shown that the interactions between the adsorbate and the adsorbent can occur through hydrogen bonds (HBs), -H ··· π and π ··· π interactions. The binding energy (ΔE_{Bind}) values showed that the interaction can occur, the enthalpies show that the process is exothermic and the Gibbs energy showed that only the adsorption of E2 hormones with the rGO matrix is spontaneous. The structural properties demonstrate classical hydrogen bonds, which vary between 1.924 Å and 2.781 Å. The QTAIM topological parameters categorized the nature of the interactions, where almost all were electrostatic, and also allowed the evaluation of unconventional hydrogen bonding interactions. The distribution of peaks in NCI analysis indicated the presence of Van der Waals interactions predominantly between the adsorbate adsorbent. In this way, it can be confirmed that the study showed the efficient use of the rGO matrix for the treatment of effluents that contain the hormones E2 and EE2 and in particular for the removal of 17β-estradiol.

Introdução

Os hormônios 17β-estradiol (E2) e o 17α-etinilestradiol (EE2) podem afetar os sistemas reprodutivos masculino e feminino causando diversos distúrbios, além de frequentemente encontrados em corpos aquáticos e no esgoto [1-3]. A adsorção é uma técnica que se destaca para retirada de contaminantes de água residuária [4], assim o uso de óxido de grafeno reduzido (rGO) apresenta ser interessante, pois possui excelentes propriedades adsortivas [5]. Neste contexto, o trabalho tem como objetivo avaliar teoricamente a interação, ligações e energias de interação que

ocorrem entre os hormônios E2 e EE2 com a matriz r-GO.

2. Materiais e métodos

Os cálculos foram realizados usando a Teoria do Funcional de Densidade (DFT) com o nível de teoria M06-2X/6-31G(d,p) e solvente implícito (SMD). As estruturas foram construídas com o programa GaussView e os cálculos de otimização e frequência realizados com o programa Gaussian 09. Os cálculos da teoria quântica de átomos em moléculas foram realizados com o pacote AIMALL. Análises de interação não covalente (NCI) foram realizadas usando o programa Multiwfn. Os programas VMD e gnuplot foram usados para visualizar os dados gerados pelas análises NCI e RDG, respectivamente.

3. Resultados e discussão

Os orbitais HOMO e LUMO e o mapa de potencial eletrostático demonstraram que as interações entre o adsorvato e o adsorvente podem ocorrer por meio de ligações de hidrogênio e interações -H ··· π e π ··· π. Os valores de Energia de ligação evidenciaram que a interação ocorre. As entalpias mostraram que o processo é exotérmico e os valores de energia de Gibbs mostraram que apenas a adsorção do hormônio E2 com a matriz rGO é espontânea. Os valores dos comprimentos das ligações de hidrogênio clássicas variam entre 1,924 Å a 2,781 Å. Os resultados gerados pela QTAIM categorizaram a natureza das interações em que quase todas foram eletrostáticas e permitiu avaliar as ligações de hidrogênio não convencional. A distribuição de picos no RGD na análise NCI, indicou a presença de interações de Van der Waals predominantemente entre o adsorvente adsorvato.

4. Conclusões

A análise estrutural revelou que ocorreram interações entre os átomos de oxigênio da matriz e os átomos de hidrônio dos hormônios por meio de ligações de hidrogênio, interações -H ··· π e π ··· π. As energias revelaram que as interações podem ocorrer, que são exotérmicas e que a formação dos complexos rGO-E2 são espontâneas. As análises QTAIM e NCI mostraram que as interações são fracas do tipo van der Waals para todos os complexos. Por fim, considerando os bons resultados da interação dos Hormônios com a matriz de oxido de grafeno reduzido é possível inferir que matriz rGO apresenta ser um candidato promissor para uso em remediação ambiental, em especial para águas contaminadas com E2 e EE2, que pode incentivar estudos experimentais para aplicações futuras.

5. Agradecimentos

Os autores agradecem o apoio da CAPES (Código 001), a Fundação de Amparo à Pesquisa do Estado de São Paulo # 2023/17727-2, o Centro de Engenharia e Ciências Computacionais (apoio financeiro da FAPESP, #2013/08293–7 e #2017/11485–6) e do Centro Nacional de Processamento de Alto Desempenho em São Paulo (CENAPAD), pelos recursos computacionais.

6. Referências

1. Báez, M.L.; García, A.; Martínez, I.; González, C.; Gómez, M.; Rodríguez, B. Int. J. Electrochem. Sci. 2024, 19, 100538.

2. E. Nazari, E.; Suja, F. Rev. Environ. Health. 2016, 31, 465–491.

3. Chen, J.; Wang, X.; Ge, X.; Wang, D.; Wang, T.; Zhang, L.;Tanguay, R.L.; Simonich, M.; Huang, C.; Dong, Q, Environmental Pollution 2016, 218, 702–708.

4. Leal, P.V.B.; Pereira, D.H.; Papini, R.M.; Magriotis, Z.M. J. Environ. Chem. Eng. 2021, 9, 105503.

5. Ngoc, Tri, N.; Ho, D.Q.; Tran Gia Bao, N.; Tien Trung, N. Chem. Phys. 2024, 579, 112207.

10º SIMPÓSIO DE ESTRUTURA ELETRÔNICA & DINÂMICA MOLECULAR
SEEDMOL 4 a 8 novembro | 2024 Pirenópolis, Goiás

Study of the Electronic Structure and Characterization of the Pharmacophoric Profile of Cannabinoids via DFT and Artificial Intelligence

Rafael de Almeida Cordeiro[1], Érica C. M. Nascimento[1], João B. L. Martins[1]
[1] Laboratory of Computational Chemistry, Institute of Chemistry,
University of Brasília, Darcy Ribeiro Campus, Asa Norte
Email: rfaelalmeida4@gmail.com
Keywords: CB2, Minor canabinoides, Docking molecular, Data Mining

Abstract

Cannabis sativa contains delta-9-tetrahydrocannabinol (THC) and cannabidiol (CBD). THC is psychoactive compound, while CBD, is a non-psychoactive, may treat pain and inflammation via the endocannabinoid system, which includes two receptors known as Cannabinoid Receptor Type 1 and Type 2 (CB_1R and CB_2R). The CB_2 receptor is known for its involvement in immune modulation system. This study uses semi-empirical methods to optimize 18 molecules structures and models how minor cannabinoids activate CB2 receptors through ADMET, Molecular Docking, and Data Mining. Docking simulations, including the CB2-stable inhibitor 9GF, were conducted using AutodockTools4 and AutoDock4. Electronic structure analyses with PM6 and PM7 methods in Gaussian 16 provided insights into orbital energies and reactivity, highlighting Desmodianone E as a potent CB2R inhibitor. These findings suggest promising therapeutic potential for minor cannabinoids in *Cannabis sativa.*

Introduction

The extract from the Cannabis sativa plant has been used for various purposes due to the variety of bioactive molecules in its composition. The predominantly identified and most studied molecules are delta-9-tetrahydrocannabinol (THC) and cannabidiol (CBD)[1]. THC is recognized for its psychoactive effect and its side effects, which limit its use for medicinal purposes. On the other hand, CBD does not have psychotropic effects and shows potential therapeutic use in the treatment of chronic pain and inflammatory processes[2]. The action of these molecules occurs through the endocannabinoid system, which consists of cannabinoid receptors CB_1R and CB_2R, which are signaled by endogenous molecules such as anandamide (AEA) and 2-arachidonoylglycerol (2-AG)[3]. The CB_2R receptor has shown to be a promising therapeutic target due to its immunomodulatory role[4].

The present work aims to perform both structure optimization using semi-empirical methods and to computationally model the activating action of minor cannabinoids on the CB2R receptor via ADMET studies, Molecular Docking, and Data Mining.

Methodology

The structure of the selected CB_2 protein has the code 8GUR and is found in the **Protein Data Bank** (PDB, with a crystallography resolution of 2.84 Å)[5].The inhibitor 9GF (2-[(1R,2R,5R)-5-hydroxy-2-(3-hydroxypropyl)cyclohexyl]-5-(2-methyloctan-2-yl)phenol) forms a stable complex with CB_2, and this molecule was used as a reference for the study with the proposed molecules[6]. Using the bioreceptor in question, molecular docking simulations were performed with 18 molecules including the reference, using the AutodockTools4 computational package with the AutoDock4 algorithm, employing the rigid/rigid method[6]. To validate the method and the selected parameters, redocking was performed with the reference molecule 9GF, which resulted in a score of

-10.52 kcal/mol and an RMSD value of 0.4595 (Figure 1).

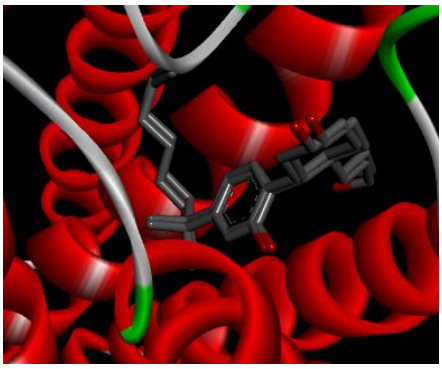


Figura 1-Validation of chosen method by redocking with 9GF molecule.

The study of electronic structure to obtain the lowest energy conformation of the ligands was performed through calculations considering redundant coordinates and frequencies, using the semi-empirical methods PM6 and PM7 in a solvated environment with the CPCM implicit solvation model[6]. For this stage, the Gaussian 16 computacional simulation package will be used[6]. From the electronic structure study, its results will be used for determining reactivity indices.

ADMETlab 3.0 studies were conducted to evaluate the pharmacological properties of the studied ligands[7]. The data obtained from ADMET and molecular docking studies wereanalyzed using the HeatMap technique to identify which studied molecules have the highest correlation with the reference molecule (9GF), indicating them as potential candidates for CB_2 receptor inhibitors.

Results

The values obtained from scores generated by molecular docking simulations demonstrated a good inhibition capacity of the receptor of interest. Comparing with the reference, the binding energy of the best candidate molecule, Desmodianone E, was approximately -10.1 kcal/mol. ADMET studies also presented pharmacological parameters that were largely favorable and safe for the selected cannabinoids compared to the reference molecule.

From the study of electronic structure, it was possible to understand how orbitals are involved in interactions with the receptor. Additionally, the electronic parameters have revealed a spectrum of energy levels and their reactivity.

Conclusão

The selected molecules exhibited parameters that were sufficiently satisfactory as CB_2 agonist ligands, representing a promising yet underexplored alternative through minor components found in the *Cannabis sativa* plant.

From the electronic structure, we were able to investigate both the role of orbital energy levels and the electronic density distribution of minor cannabinoids regions in their interaction with the CB2 receptor.

Acknowledgements

This work was developed with assistance and resources from FAP-DF, UnB and CNPq.

References

1. CROCQ, M.-A. History of cannabis and the endocannabinoid system. **Dialogues in Clinical Neuroscience**, v. 22, n. 3, p. 223–228, set. 2020.
2. AMIN, M. R.; ALI, D. W. Pharmacology of Medical Cannabis. Em: BUKIYA, A. N. (Ed.). **Recent Advances in Cannabinoid Physiology and Pathology**. Cham: Springer International Publishing, 2019. v. 1162p. 151–165.
3. PROSPÉRO-GARCÍA, O. et al. Endocannabinoids as Therapeutic Targets. **Archives of Medical Research**, Special Issue: Mental Health. v. 50, n. 8, p. 518–526, 1 nov. 2019.
4. GRABON, W. et al. CB2 receptor in the CNS: From immune and

neuronal modulation to behavior. **Neuroscience & Biobehavioral Reviews**, v. 150, p. 105226, 1 jul. 2023.

5. LI, X. et al. Structural basis of selective cannabinoid CB2 receptor activation. Nature Communications, v. 14, n. 1, p. 1447, 15
6. Morris, G. M. *et al.* AutoDock4 and AutoDockTools4: Automated docking with selective receptor flexibility. *J Comput Chem* **30**, 2785–2791 (2009).
7. FU, L. et al. ADMETlab 3.0: an updated comprehensive online ADMET prediction platform enhanced with broader coverage, improved performance, API functionality and decision support. Nucleic acids research, 4 abr. 2024.

Descritores clássicos e quânticos no desenho de potenciais inibidores da enzima hAChE: data analytics

Rafael do Couto Campos de Jesus[1], Nicolas Ricardo de Melo Alves[2], Érica Cristina Nascimento Moreno[1,2], João Batista Lopes Martins[1,2].
[1]Faculdade de Saúde, Farmácia, UnB, Brasil.
[2]Laboratório de Química Computacional, Instituto de Química, UnB, Brasil.
lopes@unb.br
Keywords: Electronic structure, Rational drug-design; PCA; heatmap; Alzheimer's disease.

Abstract
Searching for new chemical entities to be used in Alzheimer's Disease treatment can be very useful. In this work, we used methods such as heatmap and principal component analysis to highlight the role of a few selected ADMET and electronic structure properties.

Introdução
A Doença de Alzheimer (DA) é uma forma de demência que apresenta sintomas como perda de memória, falhas cognitivas, dificuldades de realizar atividades no dia a dia, entre outros. Estima-se que cerca de 10 milhões de novos casos surgem todo ano por todo o mundo[1].
A curva crescente de casos torna a DA uma doença de atenção da comunidade científica e com o aumento da expectativa de vida global, faz-se necessário novas formas de entender como prevenir a doença, descobrir suas causas e seus respectivos sintomas[2]. O fluxo de novas moléculas estudadas para candidatos a inibidores da acetilcolinesterase humana (hAChE), colocam a DA em primeiro lugar no ranking de doenças estudadas[3]. A hAChE é a enzima alvo para o tratamento dos sintomas moderados da DA[4].
Este estudo propõe associar técnicas de data mining, estrutura eletrônica, predição ADMET e drug design para correlacionar os inibidores clássicos da AChE com moléculas amplamente estudadas, como as da família dos canabinoides raros, e novas moléculas desenhadas a partir dos inibidores clássicos da hAChE[4].

Metodologia
A correlação entre os ligantes estudados foi feita por meio de propriedades farmacocinéticas e de estrutura eletrônica. As moléculas de canabinoides raros foram selecionados, considerando o crescente interesse por esta classe de moléculas devido ao potencial terapêutico destas entidades químicas como agentes neuroprotetores[5-8]. O outro grupo de moléculas foi selecionado a partir de novas entidades químicas desenhadas a partir de técnicas de heterodimerização e bioisosterismo, a usando como monômeros os inibidores clássicos: huprina W[10] e o ladostigil[11]. As propriedades de absorção, distribuição, metabolismo, eliminação e toxicidade (ADMET) foram preditas usando a plataforma web SwissADME[12] e o aplicativo Osiris[13]; enquanto os cálculos de estrutura eletrônica foram realizados com o método DFT/6-311+G(d,p)/SMD. A similaridade e correlação entre as moléculas estudadas foram avaliadas por meio de algoritmo de matriz de similaridade desenvolvido no nosso laboratório (LQC. UnB), aplicando mapas de calor (HeatMap). Para redução do espaço amostral e definição de significância na classificação e correlação entre as moléculas estudadas foi usada a técnica de análise dos componentes principais (PCA), a fim de identificar os descritores de maior peso através da análise dos loadings.

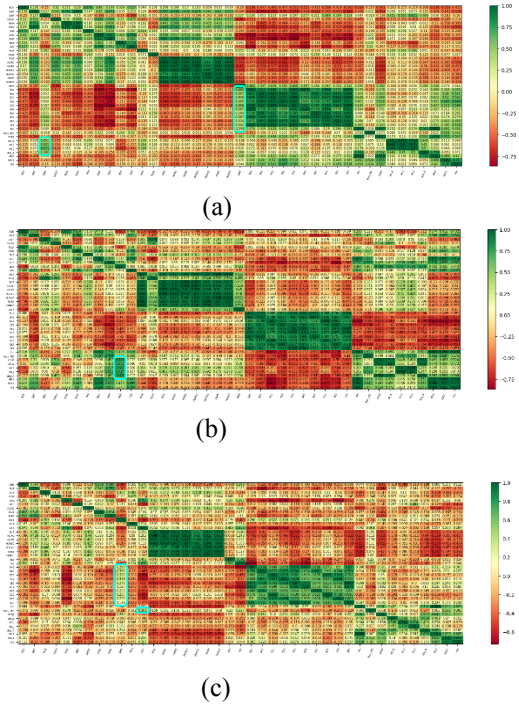
Resultados e Discussão
Os resultados obtidos por meio do HeatMap mostrados na Figura 1, com correlações

com valores entre -1 e 1 sendo que a maior correlação se dá com valores >0, destacam que as moléculas desenvolvidas com as estratégias de *drug design* apresentaram correlação positiva (0.128 à 0.322), de modo geral com o inibidor clássico dímero da tacrina (DMT), assim como o tetrahidrocanabinol (THC) apresentou correlação (0.361) com a dopamina (DOP). Apesar de apresentarem elementos semelhantes nas suas estruturas como grupos hidrofóbicos e aromáticos, isso não foi suficiente para que as moléculas de canabinóides apresentassem correlação significativa com os novos ligantes propostos. Estas correlações estão destacadas na Figura 1c.

Considerando apenas as propriedades de estrutura eletrônica, os ligantes da classe dos canabinóides apresentaram bons resultados de correlação com os ligantes clássicos, com destaque para as correlações da benserazida (bsz) com o canabidiol (cnbd) e a série das radulaninas (rdl-n), representados e destacados na figura 1b. Para este caso, os valores variaram de 0.692 à 0.793.

As radulaninas correlacionaram de forma positiva (0.386 à 0.621) com o donepezil (DNP), considerando exclusivamente as propriedades ADMET. Os ligantes propostos, apresentaram uma correlação notável também com o DMT (0.284 à 0.484), um dímero da tacrina (THA), o que está em linha com o esperado uma vez que o DMT é também de um dímero ligado por uma cadeia hidrofóbica (Figura 1a).

Quanto à correlação, ao associarmos os descritores advindos dos cálculos de estrutura eletrônica (EE), o espalhamento dos dados foi observado, havendo redução dos valores das correlações (Figura 1c). O valor máximo e mínimo para os descritores EE foram de +0.999 para HURXC com HURYC e de -0.867 para o 5C2 com hd11, já para os descritores ADMET, os valores foram de +0.992 para o rdl_I com rdl_A e de -0.863 da HUP com 5T2. Considerando todos os dados, os valores máximos e mínimos de correlação foram de +0.997 entre a HURY com HURYC e de - 0.779 entre 3S2 com HUP.



(a)

(b)

(c)

Figura 1: HeatMap com propriedades ADMET (a), com propriedades EE (b) e com propriedades ADMET e de EE juntas (c).

A análise dos componentes principais (PCA) com número de PCs igual a n-1, sendo **n** o número de descritores usados na matriz de covariância, mostrou que os dados acumulam uma separação igual a 58.97% para as três primeiras componentes (PC1, PC2 e PC3). Reduzindo o espaço dimensional para 17 descritores com os maiores pesos (loadings), a variância acumulada para as três primeiras PCs aumentou para 75.50%. Os descritores mais significativos foram as propriedades: Dipolo, HOMO-4, HOMO-3, HOMO-2, HOMO-1, HOMO, LUMO, GAP, H2 (ESP), tamanho, volume, peso molecular (MW), átomos pesados, átomos pesados aromáticos, ligações rotacionáveis, refratividade molar e permeabilidade na barreira heamtoencefálica (BBB).

Em convergência com o observado na mineração de dados (HeatMap), as propriedades de EE foram os descritores com maior peso para a análise das propriedades, uma vez que das remanescentes, estas representam quase

dois terços do total. Os loadings de maior peso para as duas primeiras PCs foram o GAP (diferença de energia entre o orbital HOMO e LUMO) e a capacidade de permeabilidade dos ligantes na barreira hematoencefálica, o que era esperado uma vez que estas podem ser usadas para entender a capacidade dos ligantes de adentrarem a matriz celular do cérebro e interagir com a AChE e a reatividade de cada ligante.

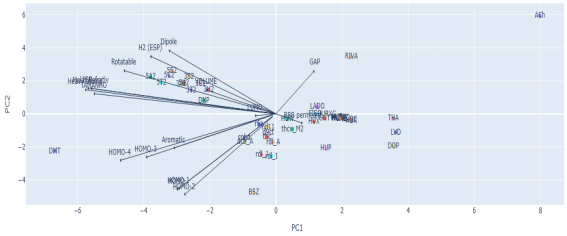
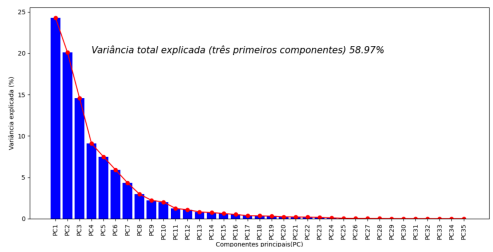
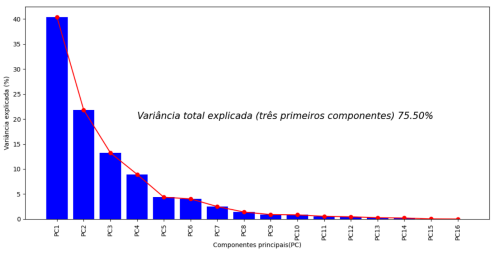


Figura 3: *Feature space* com os 17 descritores com os maiores loadings.



(a)



(b)

Figura 3: Variância acumulada para as 35 PCs (a), e para as 17 de com os maiores loadings(b).

Conclusão

Através de propriedades ADMET e propriedades de estrutura eletrônica, novos potenciais inibidores e uma série de moléculas selecionadas da família dos canabinoides tiveram seus resultados correlacionados com ligantes clássicos e amplamente estudados.

Os descritores de estrutura eletrônica foram mais sensíveis a separação entre os diferentes grupos no HeatMap, sendo estas as responsáveis por apresentar uma melhor descrição da sua correlação. Este resultado foi evidenciado pela análise dos componentes principais, que apresentou uma maior variância acumulada quando a maioria dos descritores utilizados eram advindos dos cálculos de estrutura eletrônica.

As principais correlações com ligantes clássicos foram observadas com o donepezil e a dopamina, com destaque para alguns fitoquímicos análogos aos canabinoides como às radulaninas.

Agradecimentos

UnB, FAPDF, CNPq e LQC.

Referências

1. WHO, World Health Organization https://www.who.int/news-room/fact-sheets/detail/dementia, 2023, March 15.

2. Wise, J. British Medical Journal Publishing Group, 2024.

3.DONG, Rui et al. Frontiers in human neuroscience, v. 13, p. 259, 2019.

4. DHAPOLA, R. *et al.* Molecular Biology ReportsSpringer Science and Business Media B.V., 1 dez. 2024

5. MEZEIOVA, Eva *et al.* Bioorganic & Medicinal Chemistry Letters, v. 43, p. 128100, 2021.

6. Meyer, E., de Mattos, B. A., Kirchhoff, F., & de Oliveira, R. M. W.*Revista Brasileira de Farmacognosia*, 1–13, 2021.

7. Zagzoog, A., Mohamed, K. A., Kim, H. J. J., Kim, E. D., Frank, C. S., Black, T., Jadhav, P. D., Holbrook, L. A., & Laprairie, R. B.*Scientific Reports*, *10*(1), 20405, 2020.

8. Zeine, R. R., & Teasdale, B. W.IGI Global, 2023.

9. Rodriguez, C. E. B., Ouyang, L., & Kandasamy, R. *Behavioural Pharmacology*, *33*(2 & 3), 130–157, 2022.

10.CAMPS, Pelayo et al.. Journal of medicinal chemistry, v. 43, n. 24, p. 4657-4666, 2000.

11. YOUDIM, Moussa BH et al. Journal of neuroscience research, v. 79, n. 1‐2, p. 172-179, 2005

Daina, A., Michielin, O., & Zoete, V. (2017). SwissADME. *Scientific Reports*, *7*(1), 42717.

12. SANDER, Thomas et al. Journal of chemical information and modeling, v. 49, n. 2, p. 232-246, 2009.

13. Frisch, M. J.; Trucks, G. W.; Schlegel, H. B.; Scuseria, G. E.; Robb, M. A.; Cheeseman, J. R.; Scalmani, G.; Barone, V.; Petersson, G. A.; Nakatsuji, H.; Li, X.; Caricato, M.; Marenich, A. V.; Bloino, J.; Janesko, B. G.; Gomperts, R.; Mennucci, B.; Hratch, D. J. (2016). *Gaussian 16, Revision C.01*.

Máquinas de vetores de suporte para classificação de moléculas de interesse terapêutico a partir de diagramas NCI

Rafael Campos[1], Érica Cristina Moreno[2], João Batista Lopes Martins[2]
[1]Faculdade de Saúde, Farmácia, UnB, Brasil.
[2] Laboratório de Química Computacional, Instituto de Química, UnB, Brasil.
lopes@unb.br.
Keywords: support vector machines; NCI; DFT; machine learning; computational vision.

Abstract
Molecular classification is a complex task, even for experienced chemists. Molecular structures could be quite similar in different scenarios, for example if they were isomers or if they share common functional groups which is common in pharmacophore drugs. Non-covalent-interaction(NCI) diagrams applied Density Functional Theory(DFT) to obtain non-covalent interactions presented in a molecule. NCI could be used as a very accurate fingerprint of a molecule, but these diagrams could be hard to interpret for non-specialists and even for them it could be very difficult to interpret in the case of similar molecules. In present work we develop a machine learning algorithm to classify molecules from non-covalent interactions (NCI) diagrams using Support-Vector-Machines. Our algorithm obtained scores greater than 90% showing the efficacy of the methodology for classification.

Introdução
Classificação molecular é uma importante área da química, sendo empregada para identificação de compostos através de diferentes técnicas como espectroscopia de infravermelho e ressonância magnética nuclear. Todavia, com o avanço tecnológico, o desenvolvimento de aprendizado de máquina para classificação de moléculas vem sendo amplamente estudado[1-5], o que mostra a relevância da utilização de ferramentas de data science na química.
Dentre as diversas técnicas utilizadas para classificação em aprendizado de máquina, as máquinas de vetores de suporte (do inglês *support vector machines*-SVM) destacam-se como um dos principais algoritmos de machine learning para classificação, tendo sido desenvolvido por Boser e Guyon em 1992[6].
Diagramas NCI (non-covalent-interaction) ou diagramas RDG, são diagramas gerados a partir do método RDG (reduced density gradient). O método RDG é utilizado para o estudo de interações não covalentes, sendo possível visualizar os tipos de interações não covalentes no gradiente de densidade reduzida em regiões de baixa densidade eletrônica.
Diagramas RDG fornecem descrições únicas de moléculas candidatas a fármacos, por computarem as interações não covalentes efetuadas pela molécula, que são consideravelmente relevantes na interação receptor-ligante em biossistemas. No presente estudo, foi desenvolvido um algoritmo SVM acoplado a PCA para classificar imagens de diagramas NCI gerados com o programa Multiwfn[7].

Metodologia
Dado um conjunto de dados $\{x_i, d_i\}^{i = 1, 2,..., N}$ onde x_i são os dados de entrada e d_i os rótulos, considerando que os dados sejam separáveis, o algoritmo SVM busca traçar um hiperplano ótimo que separa corretamente os dados de entrada.

CÓDIGO	Molécula
Arac1	Trans-Arachidin-1(Arachidin 1)
Arac2	Trans-Arachidin-2(Arachidin 2)
Cmg	Carmagerol
CnbdA	Cannabinolic acid
CnbdD	Cannabinodiol
Cnbrpl''	Cannabiripsol
D9CT	Delta-9-cis-tetrahydrocannabinol
DcbA	DecarboxyAmorfrutin A
DdaA	DemetyldocarboxyAmorfrutin A
DmdD	Desmodianone D
DmdE	Desmodianone E
Dnp	Donepezil
HD11	(10α − hydroxy − Δ9, 11 − hexahydrocannabinol)
Hhc	Hydroxy-helicannabigerol(Heli-Cannabigenol)
Ithc	Isotetrahydrocannabinol
Lvd	Levodopa
McdC	Machaeridiol C
McdD	Machaeridiol D
McrA	Machaeriol A
Omcnb	O-methyl-Cannabinol

Figura 1. Tabela com codificação dos nomes das moléculas estudadas.

Para tanto o algoritmo inicialmente converte as imagens em vetores multidimensionais com f_{mn} elementos do tipo float, em seguida a dimensionalidade dos dados é reduzida através da análise dos componentes principais (PCA) por fim, os dados são inseridos em uma SVM com kernel linear. Para avaliar a performance do modelo foi calculado a acurácia média(A) das previsões.

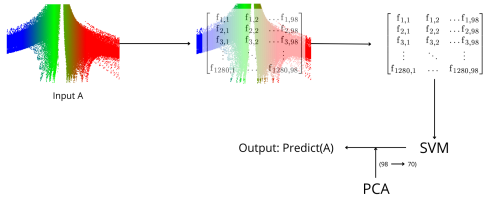
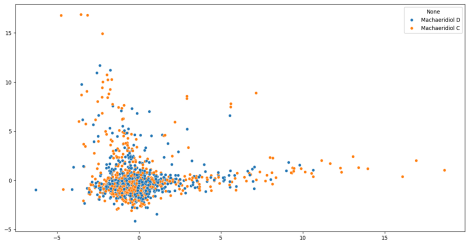


Figura 2. Esquema representativo do algoritmo desenvolvido.

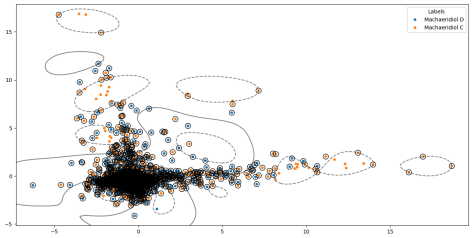
Resultados e Discussão

A separação efetuada pelo algoritmo SVM em plano bidimensional com os vetores de suporte representados pelas circunferências de cor preta e com o hiperplano ótimo representado como uma reta para kernel linear e como linhas radiais completas e tracejadas para kernel radial, foi analisada, buscando compreender a estrutura dos dados(tensores) gerados pelo modelo.

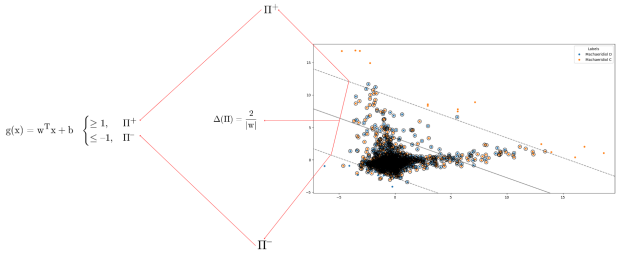
Apesar do modelo ter obtido melhores resultados utilizando um kernel linear, é possível notar que a estrutura dos dados gerados em duas dimensões pelo modelo é não linear, uma vez que os hiperplanos gerados em kernel radial, separaram os dados de forma mais satisfatória. Por tanto, este resultado indica que o modelo gera dados não lineares localmente (baixa dimensionalidade), aproximando-se da linearidade globalmente (elevada dimensionalidade).



(a)



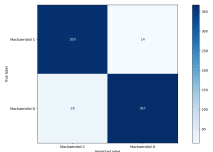
(b)

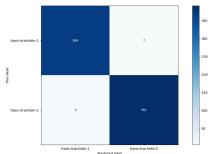


(c)

Figura 3. Diagramas bidimensionais das moléculas McdC (laranja) e McdD (azul) (a); com separação usando kernel radial (b); e linear (c).

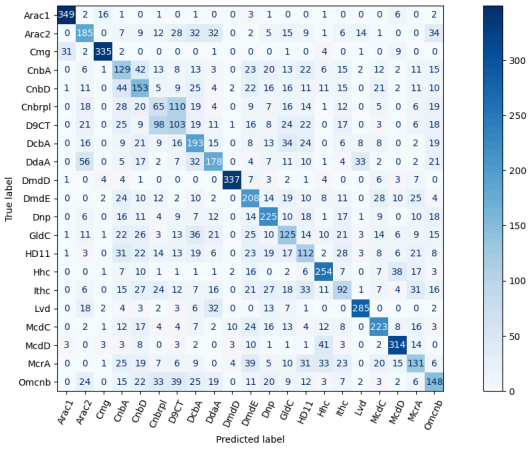
Foram geradas matrizes de confusão para avaliar a acurácia do modelo. O modelo apresentou elevada acurácia na predição de moléculas estruturalmente semelhantes como o McdD e o McdC e o Arac1 e Arac2. A matriz de confusão global (com todas as moléculas estudadas), obteve valor superior a 50%, demonstrando a robustez do modelo, uma vez que o erro associado ao aumento de classes na matriz de confusão, tende a diminuir a acurácia em modelos binários de classificação.





A=94.53 **A=98.57**

Figura 4. Matriz de confusão com dados de treino para classificação das moléculas McdC e McdD(a);e Arac1 e Arac2(b).



A =55.98

Figura 5. Matriz de confusão com dados de treino para classificação de todas as moléculas do estudo.

Conclusões

O modelo desenvolvido teve assertividade considerável na classificação de derivados canabinoides como flavonoides e terpenoides com alta acurácia (acima de 90%), demonstrando-se uma potencial ferramenta para classificação de moléculas semelhantes, tendo como dados de base exclusivamente dados das interações NCI. São necessários mais experimentos computacionais com outras moléculas a fim de aprimorar a validação do modelo.

Acknowledgements

Os autores agradecem a FAPDF e ao CNPQ pelo auxílio financeiro para realização deste trabalho e a todo time LQC.

References

1. Srivastava, G. N., Malwe, A. S., Sharma, A. K., Shastri, V., Hibare, K., & Sharma, V. K. *Genomics*, 2020,*112*(4), 2823–2832.
2. Liu, A. L., Venkatesh, R., McBride, M., Reichmanis, E., Meredith, J. C., & Grover, M. A. *ACS Applied Polymer Materials*, 2020, *2*(12), 5592–5601.
3. Das, S., & Chakrabarti, S.*Scientific Reports*, 2021, *11*(1), 1761.
4. Adeshina, Y. O., Deeds, E. J., & Karanicolas, J. *Proceedings of the National Academy of Sciences*, 2020, *117*(31), 18477–18488.
5. Li, J., Telychko, M., Yin, J., Zhu, Y., Li, G., Song, S., Yang, H., Li, J., Wu, J., & Lu, J. *Journal of the American Chemical Society*, 2021, *143*(27), 10177–10188.
6. Boser, B. E., Guyon, I. M., & Vapnik, V. N. *Proceedings of the Fifth Annual Workshop on Computational Learning Theory*, 1992, 144–152.
7. Lu, T., & Multiwfn, R. 2.6. 1; University of Science and Technology Beijing: Beijing, China, 2013;(b) T. Lu, F. Chen. *J. Comput. Chem*, *33*, 580.

Photophysical Properties investigation of Benzothiadiazole Derivatives: A Machine Learning and Computational Chemistry Approach

Rafael Ferreira Veríssimo[1], Pedro Henrique Ferreira Matias[1], Flávio Olímpio Sanches-Neto[1], Brenno Amaro Da Silveira Neto[2], Heibbe Cristhian Benedito de Oliveira[1, *].
[1]Instituto de Química, Universidade Federal de Goiás, Goiânia, Brasil.
[2]Instituto de Química, Universidade de Brasília, Brasília, Brasil.
heibbe@ufg.br
Keywords: Benzothiadiazole, Machine Learning, Photophysics.

Abstract

This work applies machine learning techniques to predict the photophysical properties of benzothiadiazole (BTD) derivatives. A supervised machine learning model was trained, using Random Forest, XGBoost and Neural Networks, to make predictions based on the structural and electronic characteristics of these derivatives. The model training and validation used a dataset of BTD derivatives obtained through web scraping of experimental data from the Elsevier database, which included properties of system solvation. The model's performance was evaluated using cross-validation with coefficient of determination (R^2), root mean square error (RMSE), and mean absolute error (MAE) as metrics. Model interpretability was achieved using the SHAP algorithm to correlate the most important features with the physicochemical properties of BTD derivatives.

Introduction

2,1,3-Benzothiadiazole (BTD) is a bicyclic molecule composed of a benzene ring fused to a 1,2,5-thiadiazole.

Due to the presence of nitrogen and sulfur, as well as the sharing of π-electrons through resonance, this class of compounds exhibits intrinsic properties such as a small separation between HOMO-LUMO orbitals, fluorescence, phosphorescence, and thermodynamic and photochemical stability[1].

The BTD system in chemistry is significant due to its luminescent properties, enabling its use as a biological marker, as demonstrated by Neto and collaborators (2020). Fluorescence allows the visualization of unique cellular structures, enhancing the understanding of biological processes[2].

Therefore, the use of machine learning to correlate photophysical and electronic properties with the structural properties of this system allows both the classification and prediction of these properties for new molecules[3].

In light of this information, the present work addresses the creation of a database for molecules of the 2,1,3-benzothiadiazole class, cataloging their photophysical properties.

Additionally, it proposes the creation of a machine learning model with the aim of understanding the relationship between the structural, electronic, and photophysical properties of the BTD system, as well as predicting photophysical properties for new molecules.

Methodology

Using an API key provided by ScienceDirect and web scraping techniques, data on the photophysical properties of BTD derivatives was automatically collected using Python 3.x.

Additionally, all molecules were converted to SMILES (simplified molecular-input line-entry system) using RDKit.

Also, physicochemical properties of BTD derivatives were included to address the absence of conformational information from RDKit, such as normalized transition energy (ETN) and dielectric constants for solvents.

SMILES were converted into a molecular fingerprint known as Morgan Fingerprint (MF), and a scan of the MF length was conducted using the following values: 512, 1024, 2048, 3072, 4096, and 8192.

Scikit-learn was employed to implement machine learning models, including XGBoost and Random Forest, while the Keras library was used to implement neural networks using TensorFlow.

The metrics were assessed using the coefficient of determination (R^2), mean absolute error (MAE), root mean squared error (RMSE), and explained variance (Q^2). Additionally, cross-validation was performed to evaluate potential issues of model overfitting and underfitting, employing K-Fold cross-validation.

To interpret the results of the machine learning model predictions, SHAP (Shapley Additive Explanations) was utilized[4].

SHAP assigns importance values to each feature, elucidating how each feature contributes to the model's predictive outcomes. This methodological approach enhances understanding by quantifying the impact of individual features on the model's predictions.

Results

A study was conducted to compare different bit values and radii within the scope of the molecular descriptor MF. The radius was varied from 1 to 6, and the bits ranged between 512, 1024, 2048, 3072, 4096, and 8192.

After training the model with the different bit values and radii and evaluating performance, it was observed that a bit value of 512 with a radius of 3 was the best combination. This pair introduced the least bias to the model and had a lower computational cost. Table 1 and figure 1 illustrate the obtained results.

Table 1: The nine best combination of Bit and length of Morgan Finger Prints.

Model	R2	Q2	RMSE	MAE
XGBRegressor_512_3	0.825	0.827	20.072	7.441
XGBRegressor_2048_4	0.824	0.825	20.137	7.239
XGBRegressor_4096_6	0.824	0.824	20.174	7.283
XGBRegressor_2048_6	0.821	0.821	20.309	7.621
XGBRegressor_2048_5	0.820	0.821	20.363	7.567
XGBRegressor_1024_6	0.819	0.820	20.412	7.458
XGBRegressor_8192_5	0.819	0.821	20.417	7.455
XGBRegressor_4096_5	0.819	0.820	20.426	7.596
XGBRegressor_2048_2	0.817	0.817	20.562	7.848

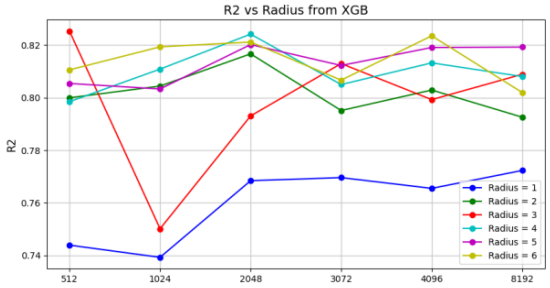


Figure 1: Correlation graph between fingerprint bit size, radius, and the R^2 coefficient from the model training using XGBoost.

Using SHAP for model interpretability, it was possible to identify the most important features and correlate them with the structural properties of BTD derivatives. This approach provided insights into how these structural features influence the photophysical properties of BTD derivatives.

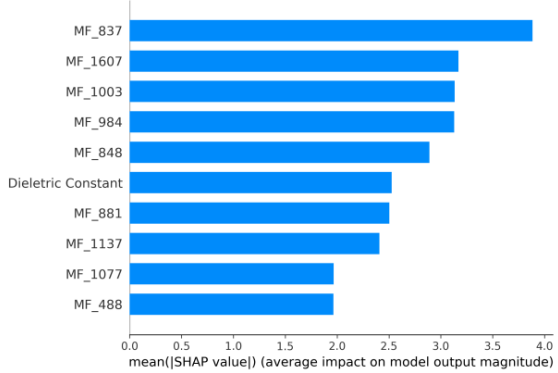


Figure 2: The most important descriptors for the model, generated using the SHAP algorithm.

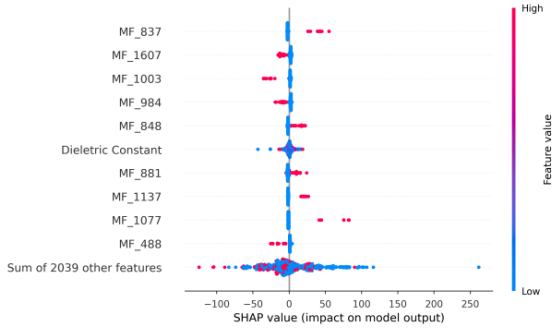


Figure 3: Feature importance graph of the model generated using the SHAP algorithm, where blue points represent the absence of the feature, while red points indicate its presence.

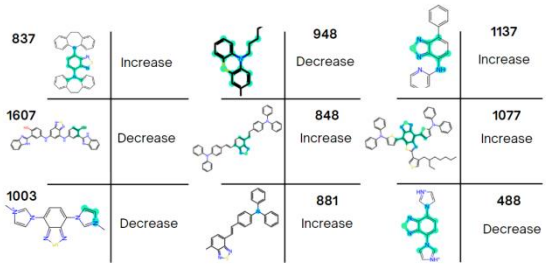


Figure 4: Representation of the most important substructures for the model, generated using the Morgan fingerprint algorithm and analyzed by SHAP.

Figure 2 highlights the importance of features for the model, revealing that fingerprint 837 had the greatest impact.

Complementing this result, Figure 3 illustrates the nature of this impact, whether positive or negative. It is observed that the presence of bit 837 leads to an increase in the maximum absorption property, while the presence of bit 1607 results in a decrease in this property.

Figure 4 displays the most important substructures for the model, generated using the Morgan fingerprint algorithm and analyzed by SHAP.

Additionally, Figure 4 shows that the presence of the BTD core, when substituted at certain positions by nitrogen atoms, increases the maximum absorption.

Conversely, the presence of a phenolic group reduces it. Similarly, insights into the subsequent details can be intuitively inferred by combining the information from Figures 3 and 4.

As this is still a work in progress, additional results will be obtained by expanding the database to include electronic structure calculations that account for solvent effects, dipole moments for accurate determination of structural conformations, and TD-DFT calculations.

Improving the model through cross-validation methods and hyperparameter optimization, as well as developing a web interface to facilitate its use.

Acknowledgements
Capes, IQ-UFG, LEEDMOL.

References

1. Neto, B. A. D.; Lapis, A. A. M.; da Silva Junior, E. N.; Dupont, J. 2,1,3-Benzothiadiazole ´ and Derivatives: Synthesis, Properties, Reactions, and Applications in Light Technology of Small Molecules. European Journal of Organic Chemistry 2013, 2013, 228–255.
2. Mota, A. A. R.; Carvalho, P. H. P. R.; Guido, B. C.; de Oliveira, H. C. B.; Soares, T. A.; Correa, J. R.; Neto, B. A. D. Bioimaging, cellular uptake and dynamics in living cells of a lipophilic fluorescent benzothiadiazole at low temperature. Chem. Sci. 2014, 5, 3995– 4003.
3. Wei, J.; Chu, X.; Sun, X.-Y.; Xu, K.; Deng, H.-X.; Chen, J.; Wei, Z.; Lei, M. Machine learning in materials science. InfoMat 2019, 1, 338–358.
4. Lundberg, S. M.; Lee, S.-I. In Advances in Neural Information Processing Systems 30; Guyon, I., Luxburg, U. V., Bengio, S., Wallach, H., Fergus, R., Vishwanathan, S., Garnett, R., Eds.; Curran Associates, Inc., 2017; pp 4765–4774.

10º SIMPÓSIO DE ESTRUTURA ELETRÔNICA & DINÂMICA MOLECULAR
SEEDMOL 4 a 8 novembro | 2024 Pirenópolis, Goiás

Title: Doping and magnetization effects in metal-insulator transitions driven by electric fields

[1]Daniel Arisa, [1]Isaac M. Carvalho, [1]Ramiro M. dos Santos,[1]Vivian V. França
[1]Institute of Chemistry, São Paulo State University, 14800-090 Araraquara, São Paulo, Brazil
ramiromarcelo2@gmail.com
Keywords: Mott insulators, Hubbard model; electrical field, quantum phase transitions

Abstract
Quantum phase transitions induced by electric fields have garnered attention in quantum chemistry and condensed matter physics, especially in dipole systems like Hubbard dimers. Using Density Matrix Renormalization Group (DMRG) calculations, we explore the metal-insulator transition at half-filling and find an intermediate metallic phase suppressed by doping or increased polarization.

Introduction

Mott insulators are materials that, despite having partially filled bands and theoretically behaving as good conductors, act as insulators due to strong electronic correlations between electrons.[1] This anomalous behavior cannot be explained by conventional band theory, as intense Coulomb interactions (denoted as term U) negate electron itinerancy, creating a Mott gap, which is an energy barrier separating the ground state from the first excited state, rendering electronic transport infeasible.[2] This insulating regime exhibits intriguing magnetic properties resulting from the spin coupling of localized electrons, often leading to the antiparallel alignment of neighboring electron magnetic moments.[3]

When an external potential, such as harmonic confinement or an electric field, is introduced, electronic correlations may shift, allowing a transition to a metallic regime where charge fluctuations are permitted.[5] This transition reflects the complex competition between the external potential, which promotes metallicity, and the local electronic correlations responsible for insulating behavior.

In contrast, band insulators, unlike Mott insulators that arise from strong electronic correlations, are described by conventional Bloch theory, with insulating properties derived from their electronic band structure. When the valence band is fully occupied, there exists a significant energy gap between it and the conduction band, freezing electron mobility as no states are available for itinerancy; electrons remain confined, filling sites with n_i=2. Only a sufficiently strong external potential can overcome this gap, transitioning the system to a metallic regime. With a fully filled valence band, band insulators are diamagnetic, have zero net magnetism, lack intrinsic magnetic moments, and exhibit low sensitivity to an external magnetic field.

In this work, we aim to investigate phase transitions in strongly correlated fermionic systems using the Hubbard model. By expanding the chain size from four to 32 sites, we enable a more precise characterization of phase transitions, including charge and spin gaps. The study focuses on how spin-charge separation manifests in strong interaction regimes and the relationship between the charge gap and potential. Additionally, it identifies the emergence of a non-monotonic metallic phase between insulating states, providing insights into the oscillatory behavior associated with phase transitions. The findings suggest future investigations considering the effects of magnetization and doping.

Methodology

In this work, we apply the Hubbard model to describe strongly correlated fermionic systems.6 In its one-dimensional form, the model approximates the interactions and movements of fermions within a chain of L sites, where each site can hold a maximum of two fermions with opposite spins, according to the Pauli exclusion principle. The model identifies four quantum states: empty, doubly occupied, spin-up, and spin-down. It can represent both homogeneous systems, which have no external potentials and result in uniform particle density, and heterogeneous systems, characterized by boundary conditions and non-zero potentials that induce local density variations.

Periodic boundary conditions (PBC) create cyclic continuity, while open boundary conditions (OBC) lead to Friedel oscillations near the boundaries due to limited degrees of freedom.[7,8] In its simplest form, the model addresses the on-site Coulomb interaction U and the hopping t between neighboring sites. The Hamiltonian includes site-specific Coulomb interaction U_i, hopping t_{ij}, and an external potential $v_{i\sigma}$, which simulates spatial heterogeneities typical of real materials.

Results

Despite the promising results obtained with a four-site chain, the size limitation causes significant errors due to edge effects, introducing Friedel oscillations that smooth transitions and compromise the precision of the results. To overcome these limitations, the chain size was increased to 32 sites, reducing edge effects and allowing for a more comprehensive analysis of the different magnetized states. This increase enables the acquisition of more realistic electronic properties and provides a more precise analysis of the phase transitions in the system, especially regarding charge mobility and magnetic correlations. This expanded approach reveals more defined phase transitions and better characterization of the energy gaps associated with the system, such as the charge gap and the spin gap.

In strong interaction regimes, the separation of spin and charge is observed, which is typical of strongly correlated systems, with the charge gap exhibiting a linear relationship with the potential in band insulating states. The analysis of the gaps, in comparison to metrics such as quantum entanglement, allows for a deeper understanding of the system's phases, showing the oscillatory behavior as an intrinsic characteristic and suggesting pathways to explore phase transitions and excitations in strongly correlated systems.

Conclusions

In terms of half-chain entanglement and double occupancy, our results indicate that a non-monotonic metallic phase emerges between the two insulating states, characterized by oscillatory behavior that reveals an exotic and complex electron itinerancy. To gain a deeper understanding of this phenomenon, further calculations incorporating the effects of magnetization and doping are essential. These analyses will help us propose a more effective mechanism to accurately describe the nature of electronic itinerancy along the chain, elucidating the intricate interplay between the interaction strength (U) and the applied potential (V). Such insights could significantly enhance our understanding of the underlying dynamics in strongly correlated systems.

Acknowledgements

D.A. is supported by Coordenação de Aperfeiçoamento de Pessoal de Nivel Superior - Brasil (CAPES) - Finance Code 001. R.M.S. acknowledges financial support from the São Paulo Research Foundation Fapesp (Grants No. 2024/10789-5) I.M.C. is supported by São Paulo Research Foundation Fapesp (Grant No. 20XX/XXXXX-X). V.V.F. is supported by São Paulo Research Foundation Fapesp (Grant No. 2021/06744-8) and the National Council of Technological and Scientific Development CNPq (Grants No. 403890/2021-7 and No. 140854/2021-5).

References

1. N. F. Mott. T.; Proceedings of the Physical Society. Proc. Phys. Soc. A 1949, 62, 416.
2. M. Imada.; A. Fujimori.; Y. Tokura.; Review of Modern Physics 1998 ,70, 1039
3. Y. J. Lee.; Y. Kim.; H. Gim.; K. Hong.; H. W. Jang.; Adv. Mater. 2023, 2305353 .
4. M. Kitatani, L. Si.; O. Janson, R. Arita, Z. Zhong.; K. Held.; npj Quantum Materials 2022, 5, 59.
5. M. Vekić.; S. R.; White Phys. Rev. B 1995, 53, 14552
6.Carlos A. Jiménez-Hoyos and Gustavo E. Scuseria Phys. Rev. B 2015, 92, 08510
7. Minmin Xue.; Zhili Hu.; Hu Qiu.; Chun Shen.; Wanlin Guo.; Zhuhua Zhang.; National Science Review, 2021,9,9
8.M. Greiner.; O. Mandel.; T. Esslinger.; T.W. Hänsch.; I. Bloch.; Nature 2002,39,415.

Investigation Nonlinear Optical Properties of N-Pyrimidinyl Stilbazolium Crystals Using DFT Method

Renato Medeiros[1], Leandro R. Franco[2], Francisco A. P. Osório[3], Clodoaldo Valverde[1,4], Marcos A. Castro[3] and Tertius L. Fonseca[3].
[1]Universidade Estadual de Goiás, Anápolis-Go, Brasil.
[2] Department of Engineering and Physics, Karlstad University, Karlstad, Sweden.
[3] Instituto de Física, Universidade Federal de Goiás, Goiânia-GO, Brasil.
[4] Universidade Paulista, Goiânia-GO, Brasil

renato.medeiros@ueg.br.
Keywords: Ionic Crystals; Hyperpolarizabilities, Susceptibilities; Electrostatic Embedding.

Abstract

Density functional theory (DFT) and time-dependent DFT (TD-DFT) were used to study the nonlinear optical (NLO) properties of phenolic N-pyrimidinyl stilbazolium cationic chromophore in non-centrosymmetric crystals. The OPR chromophore features a strong electron donor (4-hydroxyphenyl group) and acceptor (N-pyrimidinyl pyridinium group). Using CAM-B3LYP, the second-order nonlinear susceptibility tensor values range from 64.00 to 80.34 pm/V (static) and 162.09 to 175.52 pm/V (1907 nm). The third-order susceptibility is also notable. The TD-CAM-B3LYP model explains the first hyperpolarizability values in the crystalline phase, showing potential for various NLO applications.

Introduction

The development of efficient nonlinear optical (NLO) organic salt crystals is crucial for high-speed optical modulators, field detectors, frequency conversion, and terahertz wave generation. Highly polar organic NLO crystals like 4-N,N-dimethylamino-4'-N'-methyl-stilbazolium tosylate (DAST) have demonstrated second harmonic generation (SHG) efficiency 1000 times greater than urea[(1)]. DAST derivatives, such as DSTMS and DAPSH, show notable NLO properties, with interionic interactions in crystalline states significantly impacting their molecular hyperpolarizability *(β)*.

Recently, new organic salt crystals with large second-order optical nonlinearity were developed for various applications. The cationic chromophore OPR (4-(4-hydroxystyryl)-1-(pyrimidin-2-yl)pyridinium) includes an N-pyrimidinyl pyridinium electron acceptor with two electron-withdrawing groups (EWGs)[(2)]. Three benzenesulfonate anions - 4-vinylbenzenesulfonate (VBS), 4-methylbenzenesulfonate (T), and 4-chlorobenzenesulfonate (CBS) - serve as counterions. These OPR-based crystals exhibit isomorphic structures with P1 space group symmetry and contain one pair of molecules per unit cell. The introduction of EWGs and a phenolic electron donor promotes non-centrosymmetric crystal structures with parallel chromophore orientation. SHG measurements of OPR crystals are comparable to those of DAST and other benchmark NLO crystals.

The primary aim of this work is to determine the linear and nonlinear optical properties of highly efficient N-pyrimidinyl stilbazolium-salt crystals and compare them with those of the previously studied organic stilbazolium-salt crystal (DAPSH). We analyze the crystalline effects on the dipole moment, linear polarizability, and first and second hyperpolarizabilities of OPR-based crystals with different benzenesulfonate anions. These crystals exhibit very large

macroscopic second-order optical nonlinearity. Using a methodology combining electrostatic embedding and quantum mechanics (QM) calculations, we estimate the second-order and third-order nonlinear susceptibilities. Our results show that the NLO properties of OPR-based crystals are highly promising for various nonlinear optical applications.

Methodology and Computational Details

To account for electronic polarization effects from the crystalline structure, an iterative procedure was used to determine the in-crystal dipole moment (μ) of OPR-CBS, OPR-T, and OPR-VBS molecules within their respective crystalline environments. The procedure begins with partial atomic charges derived from fitting an electrostatic potential grid (CHELPG) based on CAM-B3LYP charge density of isolated molecules. These charges, derived from the QM region, undergo a self-consistent process accounting for environmental effects. CHELPG charges of surrounding molecules in closest unit cells are used in the QM calculations, and the cycle iterates until the dipole moment converges. This method, which describes the inhomogeneous polarizing field, has been applied to estimate the linear and nonlinear susceptibilities of nonionic organic crystals and the polarization of organic molecules in solution[3]. Linear parameters for the OPR-based crystals, such as the dipole moment, average linear polarizability, first-order susceptibility, and linear refractive index, were calculated.
Crystal field effects on OPR-anion molecules were modeled by including the electrostatic field of surrounding molecules in a cluster of 9×9×9 unit cells, each containing one pair of molecules. All QM calculations were performed with the Gaussian 16 program using experimental structures determined by X-ray.

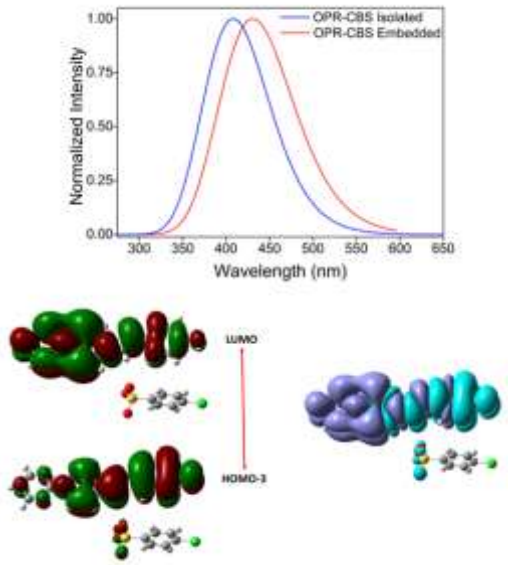
Results and Discussion

The basis set effects on the ground state dipole moment of OPR-CBS, OPR-T, or OPR-VBS compounds in solid phase were investigated. Results show minimal impact of diffuse functions when comparing CAM-B3LYP calculations with 6-311++G(d,p) and 6-311G(d,p) basis sets. Dipole moment convergence, crucial for non-centrosymmetric crystalline packing, was observed. Hyperpolarizability values were more sensitive to basis set effects. The in-crystal dipole moment converged to values smaller than isolated unit cell values, contrasting with DAPSH crystal results. Partial charges indicated charge separation in the ground state, influenced by electrostatic embedding. Linear polarizability increased slightly in the crystalline environment, with minor influence from dispersion effects. The largest component of the linear refractive index at 1907 nm was comparable across OPR-based crystals, akin to the DAPSH crystal's refractive index result.
The environment polarization effects significantly enhance the total first hyperpolarizability (β_{tot}) relative to linear polarizability for OPR-based crystals. Embedded static values of β_{tot} show increases between 16-30% compared to isolated unit cell values. β_{tot} values are affected by crystal polarization, with notable increases observed in the dynamic values, especially for OPR-CBS. The β_{yyy} component exhibits significant increases due to crystal polarization, while the β_{zzz} component decreases markedly. At 1907 nm, dispersion effects are moderate, with β_{tot} values augmented by factors of 35-33%. At 1097 nm, increases around 200% are observed, possibly due to a resonant effect. Our CAM-B3LYP estimates for the largest diagonal component of the second-order nonlinear susceptibility tensor ($\chi_{yyy}^{(2)}$) are significant, ranging from 64.00 to 80.34 pm/V in the static regime and from 162.09 to 175.52 pm/V at 1907 nm. These results are notable compared to DAPSH, a promising material for THz wave generation[4,5]. The point charge distribution affects the first hyperpolarizability of the cationic chromophore, with β_{tot} values overestimated by about 10% compared to embedded unit cell results. These findings demonstrate the impact of counterion nature and position on the optical properties of

ionic crystals. Point charge distribution affects the first hyperpolarizability of the cationic chromophore, overestimating β_{tot} values by about 10% compared to embedded unit cell results. These findings underscore the impact of counterion nature and position on the optical properties of ionic crystals.

The absorption spectra of both isolated and embedded unit cells of the OPR-CBS crystal show one dominant transition, indicating π-π* transitions. In OPR-CBS, OPR-T, and OPR-VBS crystals, the dominant transition involves excitation from HOMO-3 to LUMO, indicating intramolecular charge transfer from a 4-hydroxyphenyl donor group to an N-pyrimidinyl pyridinium acceptor group. This charge transfer is illustrated in the molecular orbitals and density difference patterns shown in Figure 1. The polarization effects of the environment cause slight red shifts in the π-π* transition when moving from isolated to crystalline phases. OPR-based crystals absorb light in the visible range, with OPR-CBS having a maximum absorbance around 430 nm, resulting in a perceived complementary color of yellow/orange.

Figure 1: Theoretical UV–Vis absorption spectra of unit cell of OPR-CBS crystal. The frontier orbitals involved in the dominant transition and change in electron density.



Acknowledgements

The authors gratefully acknowledge the financial support of CNPq, CAPES, and FAPEG (PRONEX) agencies (Brazil) as well as the computer resources of the LaMCAD/UFG laboratory. LRF acknowledge the Swedish National Infrastructure for Computing (SNIC) at National Supercomputer Centre at Linköping University (NSC) for providing the computational infrastructure.

References

1. Marder, S. R.; Perry, J. W.; Schaefer, W. P. Synthesis of Organic Salts with Large Second-Order Optical Nonlinearities. Science 1989, 245, 626-628. https://doi.org/10.1126/science.245.4918.6.

2. Kim, S.-J.; Kim, S.-I.; Jazbinsek, M.; *et al*. Design Strategy of Highly Efficient Nonlinear Optical Orange-Colored Crystals with Two Electron-Withdrawing Groups. Adv. Photonics Res. 2022, 3, 2100350. https://doi.org/10.1002/adpr.202100350.

3. Aguiar, A. S. N.; dos Santos, V. D.; Borges, I. D.; *et al*. Bromine Substitution Effect on Structure, Reactivity, and Linear and Third-Order Nonlinear Optical Properties of 2,3-Dimethoxybenzaldehyde. *J. Phys. Chem. A* **2022**, *126*, 7852–7863. https://doi.org/10.1021/acs.jpca.2c04658.

4. Figi, H.; Mutter, L.; Hunziker, C.; *et al*. Extremely Large Nonresonant Second-Order Nonlinear Optical Response in Crystals of the Stilbazolium Salt DAPSH. J. Opt. Soc. Am. B 2008, 25, 1786-1793. https://opg.optica.org/josab/abstract.cfm?URI=josab-25-11-1786.

5. Valverde, C.; Medeiros, R.; Franco, L. R.; Osório, F. A. P.; Castro, M. A.; Fonseca, T. L. Theoretical Investigation on the Linear and Nonlinear Optical Properties of DAPSH Crystal. Sci. Rep. 2023, 13, 8616. https://doi.org/10.1038/s41598-023-35442-8.

10º SIMPÓSIO DE ESTRUTURA ELETRÔNICA & DINÂMICA MOLECULAR
SEEDMOL 4 a 8 novembro | 2024 Pirenópolis, Goiás

Complete basis set extrapolations using the new relativistic prolapse-free Gaussian basis sets of the RPF-XZ family (X = 2, 3, and 4)

Roberto Luiz Andrade Haiduke[1]
[1]Departamento de Química e Física Molecular, Instituto de Química de São Carlos, Universidade de São Paulo, Av. Trabalhador São-Carlense, 400, 13560-970, São Carlos, SP, Brazil.
haiduke@iqsc.usp.br
Keywords: variational prolapse; complete basis set extrapolations; relativistic calculations; double ionization potentials.

Abstract
Complete basis set extrapolations are successfully used with the new relativistic prolapse-free Gaussian basis sets, RPF-XZ (X = 2, 3, and 4), in four-component Coupled Cluster Theory calculations with single, double and perturbative triple substitutions for double ionization energy determinations in simple atomic systems.

Introduction

Important relativistic effects in chemistry are frequently encountered in different properties [1]. However, the electronic structure treatments based on the four-component formalism, which is one of the most advanced methodologies to include such effects, require specifically tailored basis sets. However, these basis sets can suffer from variational prolapse, which is an incompleteness issue associated to a poor description of inner electrons that can lead to smaller energy results than the exact values [2,3]. Hence, basis sets with variational prolapse are not recommended for calculations of properties more dependent on inner electron distributions. A few years ago, relativistic prolapse-free Gaussian basis sets of quadruple-ζ quality (RPF-4Z) were developed [4-6]. Our research group is now working on generating double- and triple-ζ quality members of the RPF-XZ family, which is almost finished for *s* and *p*-block elements [7].

Thus, Complete Basis Set (CBS) extrapolation schemes can be used to achieve more accurate electronic energies by carrying out calculations with basis sets of different sizes within a family [8]. However, considering relativistic calculations, it is mandatory to address the variational prolapse problem before extrapolations are employed or else the electronic energies will inevitably lead to wrong absolute results, which can will tend to be significantly smaller than the exact values.

Here, the RPF-XZ family (X = 2, 3, and 4) will be used to achieve extrapolated CBS results including high level treatments for relativistic effects and electronic correlation in order to obtain double ionization energies for some closed shell atoms (He, Be, Mg, Ca, Sr, Ba, and Ra).

Methodology

The Dirac-Coulomb (DC) Hamiltonian was used in all calculations, which are performed with DIRAC23 [9,10]. The default Gaussian nuclear model and light speed value are used. Uncontracted basis sets are considered here. Moreover, repulsion integrals between *small* functions generated by kinetic balance conditions, (SS|SS), are replaced for an approximation [11]. The energy results are obtained in four-component Coupled Cluster Theory calculations with single, double and perturbative triple excitations, DC-CCSD(T), with an active space composed by valence plus sub-valence electrons and virtual spinors up to 100 atomic units (*au*).

Two common extrapolation equations [12,13] are evaluated here for obtaining CBS results for energies (E_{CBS}):

$$E(X)=E_{CBS}+AX^{-3} \quad \text{or} \quad (1)$$

$$E(X)=E_{CBS}+A(X+½)^{-4}\,, \quad (2)$$

where $E(X)$ represents the energy obtained with a basis set of a certain cardinal number (X = 2, 3, and 4 for the RPF-XZ family) and A is a parameter. Thus, these CBS estimates require two calculations.

Results and Discussion

The double ionization process investigated here is based on calculations for closed-shell systems, a neutral atom and its double cation (A and A^{2+}), that is:

$$A \rightarrow A^{2+} + 2e^{-} \quad (3)$$

Hence the total energies of A and A^{2+} are obtained by the extrapolations presented in eqs. (1) and (2). Thus, the double ionization results are compared to experimental data [14]. Table I illustrates the mean absolute deviations (MADs) and mean signed errors (MSEs) obtained with the RPF-XZ basis sets. As one can see, there is a clear improvement pattern as the cardinal number increases, with MADs decreasing from 0.23 to 0.08 eV, although the calculations always underestimate the double ionization data.

In the sequence, the CBS extrapolations are considered in Table II. Hence, the results are obtained from pairs of basis sets, that is, the pairs formed by the smallest and the largest sets, labelled respectively as (2Z,3Z) and (3Z,4Z). As one can notice, the (2Z,3Z) values from CBS extrapolations point to a clear improvement in the overall results individually obtained from the smallest basis sets, with MADs (around 0.09 and 0.10 eV) and MSEs (nearby -0.09 and -0.10 eV) similar to those from the RPF-4Z set. Further, the best MADs (0.05 eV) and MSEs (around -0.04 and -0.05 eV) are those from (3Z,4Z) CBS extrapolations.

Table I: Results obtained for double ionization energies in DC-CCSD(T) calculations and experimental data (in eV).

	RPF-2Z	RPF-3Z	RPF-4Z	Exp[a]
He	78.72	78.91	78.98	79.01
Be	27.50	27.51	27.52	27.53
Mg	22.34	22.43	22.57	22.68
Ca	17.82	17.88	17.93	17.98
Sr	16.52	16.59	16.63	16.73
Ba	15.05	15.08	15.09	15.22
Ra	15.03	15.26	15.29	15.43
MAD	0.23	0.13	0.08	
MSE	-0.23	-0.13	-0.08	

[a] From reference [14].

Table II: Results obtained for double ionization energies in DC-CCSD(T)/CBS calculations (in eV).

	(2Z,3Z)		(3Z,4Z)	
	eq. (1)	eq. (2)	eq. (1)	eq. (2)
He	79.00	78.98	79.04	79.02
Be	27.51	27.51	27.53	27.53
Mg	22.46	22.46	22.67	22.64
Ca	17.91	17.91	17.97	17.96
Sr	16.63	16.62	16.66	16.66
Ba	15.10	15.09	15.10	15.10
Ra	15.35	15.33	15.31	15.31
MAD	0.09	0.10	0.05	0.05
MSE	-0.09	-0.10	-0.04	-0.05

Conclusions

The results obtained here demonstrate that the RPF-XZ family (X = 2, 3, and 4) of relativistic Gaussian basis sets can be successfully used in CBS extrapolation schemes.

Acknowledgements

The author is grateful to São Paulo Research Foundation (FAPESP) for financial support (2022/05138-0). The funding from National Council for Scientific and Technological Development (CNPq) is also acknowledged (306763/2021-4).

References

[1] Pyykkö, P. *Annu. Rev. Phys. Chem.* 2012, 63, 45.
[2] Faegri Jr, K. *Theor. Chem. Acc.* 2001, 105, 252.
[3] Tatewaki, H.; Mochizuki, Y. *Theor. Chem. Acc.* 2003, 109, 40.
[4] Teodoro, T.Q.; da Silva, A.B.F.; Haiduke, R.L.A. *J. Chem. Theory Comput.* 2014, 10, 3800.
[5] Teodoro, T.Q.; da Silva, A.B.F.; Haiduke, R.L.A. *J. Chem. Theory Comput.* 2014, 10, 4761.
[6] Teodoro, T.Q.; Visscher, L.; da Silva, A.B.F.; Haiduke, R.L.A. *J. Chem. Theory Comput.* 2017, 13, 1094.
[7] Sousa, J.S.; Gusmão, E.F.; Dias, A.K.N.R., Haiduke, R.L.A. 2024, in preparation.
[8] Feller, D. *J. Chem. Phys.* 1992, 96, 6104.
[9] DIRAC, a relativistic ab initio electronic structure program, Release DIRAC23 (2023), written by Bast, R.; Gomes, A.S.P.; Saue, T.; Visscher, L.; Jensen, H. J. Aa. with contributions from several authors (https://doi.org/10.5281/zenodo.7670749, see also https://www.diracprogram.org).
[10] Saue, T.; Bast, R.; Gomes, A.S.P.; Jensen, H.J.A.; Visscher, L.; Aucar, I.A.; Di Remigio, R.; Dyall, K. G.; Eliav, E.; Fasshauer, E.; Fleig, T.; Halbert, L.; Hedegård, E.D.; Helmich-Paris, B.; Iliaš, M.; Jacob, C.R.; Knecht, S.; Laerdahl, J.K.; Vidal, M.L.; Nayak, M.K.; Olejniczak, M.; Olsen, J.M.H.; Pernpointner, M.; Senjean, B.; Shee, A.; Sunaga, A.; van Stralen, J.N.P. *J. Chem. Phys.* 2020, 152, 204104.
[11] Visscher, L. *Theo. Chem. Acc.* 1997, 98, 68.
[12] Helgaker, T.; Klopper, W.; Koch, H.; Noga, J. *J. Chem. Phys.* 1997, 106, 9639.
[13] Martin, J.M.L. *Chem. Phys. Lett.* 1996, 259, 669.
[14] Kramida, A., Ralchenko, Yu., Reader, J. and NIST ASD Team (2023). NIST Atomic Spectra Database (version 5.11), [Online]. Available: https://physics.nist.gov/asd [Fri Aug 02 2024]. National Institute of Standards and Technology, Gaithersburg, MD. DOI: https://doi.org/10.18434/T4W30F

10º SIMPÓSIO DE ESTRUTURA ELETRÔNICA & DINÂMICA MOLECULAR
SEED MOL
4 a 8 novembro | 2024
Pirenópolis, Goiás

Degradação do Picloram por Radicais •OH em Meio Aquoso: Um Estudo Teórico com Campos Elétricos Externos Orientados (OEEFs)

Rodrigo Alves Costa[1], Flávio O. Sanches-Neto[1,2], Luciano Ribeiro[1]
[1] Grupo de Química Teórica e Estrutural de Anápolis, Câmpus Central, Universidade Estadual de Goiás (UEG), Anápolis – GO – Brasil
[2] Instituto Federal de Educação, Ciência e Tecnologia de Goiás, 72876-601, Valparaíso de Goiás, GO, Brazil

rodrigoalvesc@outlook.com

Keywords: Reaction Kinetics; Computational Chemistry; SMD Solvation Model

Abstract

This study presents a theoretical investigation of picloram degradation by •OH radicals in aqueous media, employing quantum chemistry calculations and reaction rate theories in the presence of Oriented External Electric Fields (OEEFs). The results indicate that the application of OEEFs significantly increases the reaction rate constant, accelerating the degradation of picloram. The proposed approach proves effective in optimizing oxidation processes of pollutants in aqueous systems, suggesting a promising method for the environmental treatment of pesticides.

Introduction

Os agrotóxicos, como o Picloram (4-amino-3,5,6-tricloro-2-piridinocarboxílico), desempenham um papel crucial na agricultura, impactando a economia global e a saúde humana [1], ver Figura 1.

Derivado da piridina, o picloram (veja a Figura 1) é amplamente utilizado como herbicida no controle de diversas culturas e plantas daninhas, mas apresenta riscos significativos ao meio ambiente e à saúde [2]; [1, 3].

A reação dos radicais •OH com poluentes orgânicos é frequentemente complexa e envolve vários mecanismos: i) adição de •OH a um anel aromático ou outras ligações insaturadas, ii) abstração de átomo de hidrogênio e/ou iii) transferência de elétron único.

Assim, o foco deste trabalho é fornecer uma compreensão detalhada do mecanismo e da cinética da degradação do picloram mediada por radicais •OH, utilizando uma combinação de cálculos de química quântica, teoria da taxa de reação acompanhada de um campo elétrico externos orientados (OEEFs), da expressão em tradução livre do inglês (*oriented external electric fields*).

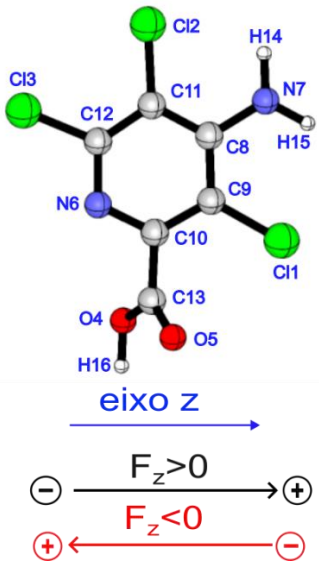


Figura 1 - A estrutura tridimensional do composto picloram e a convenção de polaridade adotada para o OEEF no software Gaussian 16.

Methodology

A estrutura eletrônica dos reagentes, produtos e estados de transição foi calculada no nível B2PLYP/6-31G(d) (veja a Figura 1) com o modelo de solvatação de densidade (SMD). O modelo SMD tem sido amplamente utilizado para simular o ambiente aquoso na elucidação dos mecanismos de degradação de pesticidas, sendo menos exigente computacionalmente

do que outros modelos de contorno (Luo et al., 2018).

Detalhes sobre outros níveis de cálculos serão apresentados posteriormente. Os pontos estacionários foram caracterizados por cálculos analíticos de frequências harmônicas. Os cálculos de química quântica foram realizados usando o pacote Gaussian 16 (Frisch et al., 2016).

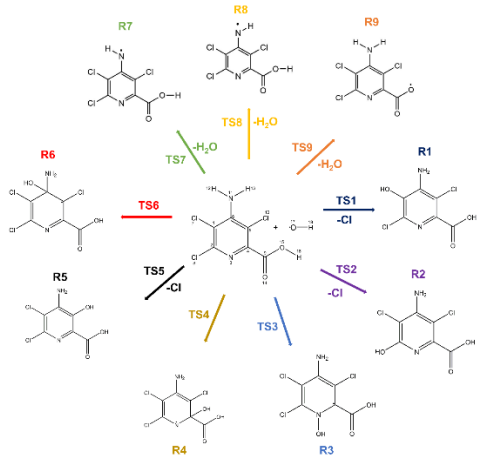


Figura 2 - Esquema de reações de abstração de átomo de hidrogênio e adição com picloram e radicais •OH.

Results and Discussion

A Tabela 1 mostra a constante cinética da reação de degradação estimada pela aplicação de um campo elétrico externos orientados (OEEFs), apenas ao canal reativo k_{R1} (para a nomenclatura apropriada, veja a Figura 1), pelo ataque de •OH calculadas no nível B3LYP/6-31+G(d) com o modelo de solvatação contínua SMD.

Tabela 2 – Apresenta a constante cinética da reação de degradação do picloram.

T. (K)	k_{R1}	
	[Ref. 1]	OEEFs (field=x-10)
250k	1.01E-14	6.91E-14eV
273.15k	1.45E-14	8.84E-14eV
298.15k	2.03E-14	1.11E-13eV
300k	2.07E-14	1.12E-13eV
310k	2.33E-14	1.22E-13eV

Conclusions

Este trabalho apresentou um estudo teórico da degradação do picloram por radicais •OH em meio aquoso, utilizando uma combinação de cálculos de química quântica e teorias de taxa de reação na presença de Campos Elétricos Externos Orientados (OEEFs). Os valores calculados foram comparados com resultados teóricos e experimentais [1]. Os resultados iniciais indicam que a adição de •OH ao picloram, na presença de OEEFs, ocorre de maneira mais eficiente, resultando em um aumento da constante cinética. Esse aumento na constante cinética implica em uma degradação mais rápida do picloram. A aplicação de campos elétricos mostrou-se eficaz em melhorar a eficiência da oxidação, sugerindo um potencial estratégia para acelerar processos de degradação de poluentes como o picloram em sistemas aquosos.

Acknowledgements

A UEG pela bolsa de Mestrado.

References

1. **Sanches-Neto FO, Ramos B, Lastre-Acosta AM, Teixeira ACSC, Carvalho-Silva VH**. Aqueous picloram degradation by hydroxyl radicals: Unveiling mechanism, kinetics, and ecotoxicity through experimental and theoretical approaches. *Chemosphere* 2021;278:130401.

2. **Abramović B, Šojić D, Despotović V, Vione D, Pazzi M, *et al.*** A comparative study of the activity of TiO2 Wackherr and Degussa P25 in the photocatalytic degradation of picloram. *Appl Catal B* 2011;105:191–198.

3. **Ghauch A**. Degradation of benomyl, picloram, and dicamba in a conical apparatus by zero-valent iron powder. *Chemosphere* 2001;43:1109–1117.

Employment of Carbon Nanostructures for the Detection and Capture of Pollutants in Gaseous environment

Rodrigo A. Lemos Silva [1,2], Daniel F. Scalabrini Machado[3], Heibbe C. B. de Oliveira[4], Demétrio A. da Silva Filho[5] and. Luciano Ribeiro[2]

[1] Grupo de Modelagem Computacional de Sistemas Físicos, Atômicos e Moleculares – GMCFAM, Instituto Federal de Educação, Ciência e Tecnologia de Goiás (IFG), Câmpus Jataí, CP 75804-714, Jataí, GO, Brasil
[2] Grupo de Química Teórica e Estrutural de Anápolis, Câmpus Central – Sede Anápolis de Ciências Exatas de Anápolis, Universidade Estadual de Goiás, Anápolis, Brasil
[3] Laboratório de Modelagem de Sistemas Complexos (LMSC), Instituto de Química, Universidade de Brasília, 70919-970, Brasília, Brasil
[4] Laboratório de Estrutura Eletrônica e Dinâmica Molecular (LEEDMOL), Instituto de Química, Universidade Federal de Goiás, Goiânia, Brasil
[5] Grupo de Semicondutores Orgânicos, Instituto de Física, Campus Darcy Ribeiro, Universidade de Brasília, CP 4478, Brasília 70919-970, DF, Brasil;

Keywords: Molecular modeling, Carbon nanostructures, Carbon sequestration, Synthetic fuels, Detection, and capture of agricultural pesticides.

Abstract

The increase in extreme weather events has raised alarms worldwide, with prolonged droughts, intermittent rains, and heatwaves threatening human and other species' existence. To address this, urgent efforts to mitigate climate change effects and preserve the environment are needed. Prioritizing new technological strategies to remove pollutants from the atmosphere and water is crucial. These technologies could reduce greenhouse gas concentrations and aid in developing synthetic fuels, meeting the energy demands of a carbon-dependent society. This research aims to conduct a theoretical study using molecular computational modeling to explore carbon nanostructures, especially fullerenes, for detecting, capturing, and reusing pollutants, thus promoting synthetic fuel production and other valuable raw materials.

Introduction

According to data from Climate Central [1], the year 2023 had average temperatures 1.3°C higher than the historical average values in 175 countries, including Brazil. Observations from the World Meteorological Organization (WMO) and the National Institute of Meteorology (Inmet) [2] indicate that 2023 was the hottest year on record since the beginning of the historical series in 1950. Data such as these increasingly highlight the urgency of promoting actions to combat climate change.

Given the current scenario, this work intends to conduct a theoretical study, employing Density Functional Theory (DFT), to verify the feasibility of using organic nanomaterials, in their pure and doped forms, for the detection and capture of potential greenhouse gases. Additionally, the use of oriented external electric fields will be employed to enhance the effectiveness of these nanomaterials.

Methodology

The geometric structural, electronic, and energetic properties of the molecules were determined using Density Functional Theory (DFT) with the ωB97XD functional, coupled with the 6-31G(d) 6-31G (d) [3, 4] e 6-311+G (d,p) [5, 6] basis sets.. All computational calculations were carried out using the Gaussian 16 quantum chemistry program suite [7].

The supramolecular approach was employed to calculate the adsorption energies as presented in Equation 1,

$$E_{ads} = E_{complex} - \left(E_{CBZ} + E_{C_{59}X}\right), \quad (1)$$

The effects of Basis Set Superposition Error (BSSE) was corrected using the counterpoise method [8]. The investigation of intermolecular interactions was performed using the Quantum Theory of Atoms in Molecules (QTAIM) [12–14] and the Reduced Density Gradient (RDG) index [15, 16].

Results and Discussion

As it is a work in progress, it will be presented in the following the partial results obtained along the last years. These results are for the detection and capture of CO, CO_2 and N_2 molecules by the C_{20} fullerene and the doped $C_{19}Si$ fullerene, presented in Figure 2. The results presented bellow were published in the paper "Harnessing Greenhouse Gases Absorption by Doped Fullerenes with Externally Oriented Electric Field" [17]

Adsorption Energies between C_{20} Fullerene and CO, CO_2, and N_2 Molecules

In pristine form, the most interacting system is formed by the C_{20}-CO_2 dimer. Interaction energies of C_{20}-CO and C_{20}-N_2 are similar, so there is no clear selectivity towards these two molecules. Our theoretical results indicate that the complexes studied in the present work are about twice as stable as the complexes investigated by Vessally et al. [18], which can be attributed to both the basis set and the functional chosen for the calculation.

For the doped fullerenes, the results indicate that the adsorption energies, when compared to the E_{ads}values of pristine fullerenes, increased for the adsorption of carbon monoxide and carbon dioxide. For C_{19}Si-N_2, a decrease in the energy module E_{ads} is observed when the calculation is performed with the level ωB97XD/6-31G(d).

For ease of interpretation, the energy values for the second theoretical level are shown in parentheses. The results show that E_{ads} increases, in contrast to the pristine fullerene. It is observed that there is an increase in the E_{ads} reaching values of −0.703 eV (−0.738 eV) for C_{19}Si-CO and -0.068 eV (-0.077 eV) for C_{19}Si-CO_2. The values of E_{ads} obtained with ωB97XD/6-311+G(d,p), resulted in a slight increase in the interaction between nitrogen gas and doped fullerene (E_{ads} values observed for the C_{19}Si-N_2 dimer were -0.017 eV (-0.045 eV)). For the C_{19}Si-CO, system, the CO reorients to interact in a perpendicular configuration. For C_{19}Si-CO2 and C_{19}Si-

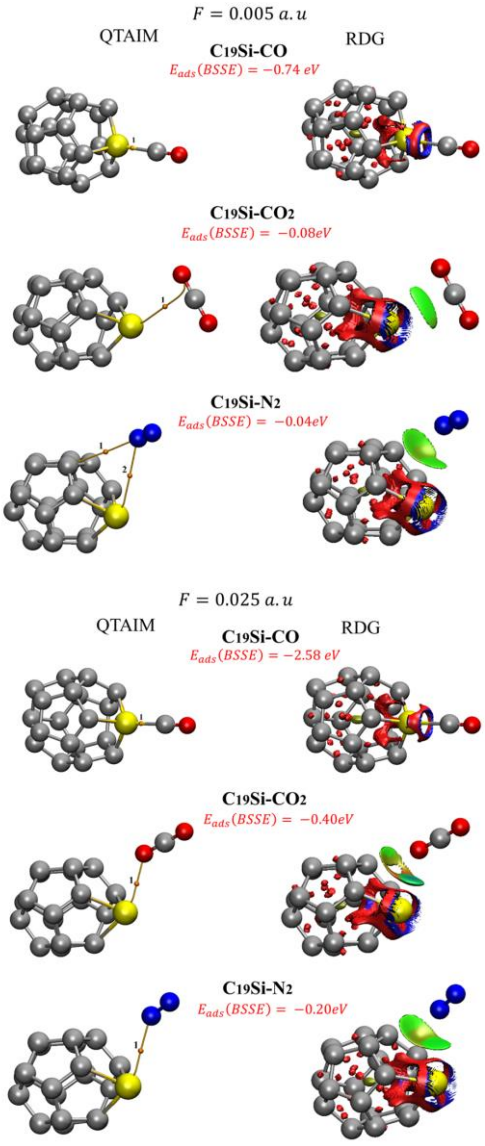


Figure 1 Critical bond points, BCP, RDG isosurfaces and adsorption energies (in eV), E_{ads}, for the dimers formed by C20 and C19Si fullerenes with the adsorbed gas molecules. The results were obtained with the theoretical level ωB97XD/6-311+G(d,p). On top are shown the results for $F = 0.005\ a.u.$, on the left button the results presented are for $F = 0.025\ a.u.$ are presented.

N2, the molecules remain interacting in a parallel orientation.

Electric Field Effect on the Adsorption Energies

The External Oriented Electrical Field (EOEF) effect on the adsorption energies for the doped fullerene with field, F, in the range of $0.005\ a.u.$ and $0.025\ a.u.$, are presented in Figures 1 and 2. It is seen that F and E_{ads} show direct proportionality, and for the C_{19}Si-CO system, this increase appears almost linear. On the other hand, for the C_{19}Si-CO_2 and C_{19}Si-N_2 systems, F affects E_{ads}, with a prominent parabolic behavior as corroborated by fitting correlation polynomial expressions on the F vs. E_{ads} portrayed in Figure 2.

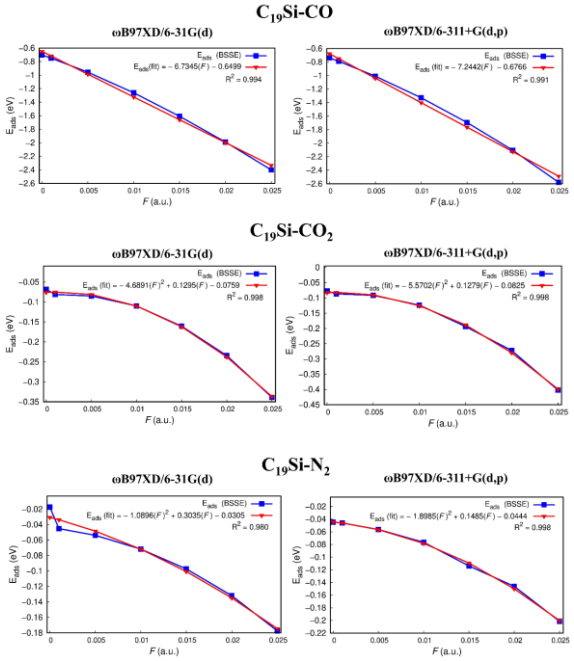


Figure 2 Theoretical, E_{ads}, and fitted, $E_{ads}(fit)$, adsorption energies as a function of the electric field, F. Figure obtained from ref. [17].

The bond character was evaluated under the QTAIM and RDG scheme. Special attention must be given to the C_{19}Si-CO which presented a dipolar interaction character, at the ωB97XD/6-31G(d) level and a polar-covalent character for the ωB97XD/6-311+G(d,p) level when $F < 0.0150\ a.u.$. Beyond $F = 0.015\ a.u.$, C_{19}Si starts to show a tendency to interact with CO through an interaction with partial polar-covalent character for both theoretical levels. This observation agrees with the E_{ads} values obtained for C_{19}Si-CO (Figures 1 and 2) and with the directionality observed for the interaction between CO and C_{19}Si shown in Figure 1.

Conclusions

It can be observed that doping with a Si atom enabled the adsorption of the mentioned chemical species to the C_{19}Si cage. Moreover, the application of an EOEF showed the potential to increase the fullerene-gas interaction. In this context, the C_{19}Si-CO interaction was the most favored. The QTAIM and RDG analyses also showed a change in the interaction character in the C_{19}Si-CO. These results show the potential of doping and EOEF for greenhouse gas detection and capture.

Acknowledgments

IFG, Câmpus Jataí. UEG. Fundação de Amparo à Pesquisa do Estado de Goiás – FAPEG. PROFIX-JD - Programa de Apoio à Fixação de Jovens Doutores no Brasil, CHAMADA PÚBLICA FAPEG/CNPQ Nº 09/2022. QTEA. e GMCFAM

References

1. Climate Central (2023) **2.** World Meteorological Organization (WMO) (2023) **3.** Hehre WJ, et al. (1972). J Chem Phys 56:2257–2261. **4.** Francl MM, Pietro WJ, Hehre WJ, et al (1982) J Chem Phys 77:3654–3665. **5.** McLean AD, Chandler GS (1980) J Chem Phys 72:5639–5648. **6.** Krishnan R, Binkley JS, Seeger R, Pople JA (1980) J. Chem. Phys. 72:650–654. **7.** Frisch, M. J.; et. al. DJ (2016) Gaussian 16, Revision C.01. **8**. Boys S, Bernardi F (1970) Mol Phys 19:553–566. **9.** Singh UC, Kollman PA (1984). J Comput Chem 04. **10**. Nibe M, Svanborg M, Lemos-silva R, et al (2021) Work function difference of naphthyl end-capped Org Electron 89:106060. **11**. Lemos Silva RA, et al (2022) . Sci. Rep. 12. **12.** Bader RFW (1991) Chem Rev 91:893–928. **13**. Bader RFW, Essén H (1984) J Chem Phys 80:1943. **14.** Bader RFW (1990) Oxford,UK. **15.** Contreras-García J, et al (2011) J Chem Theory Comput 7:625–632. **16.** Johnson ER, et al (2010) J Am Chem Soc 132:6498–6506. **17.** Lemos Silva RA, et al. Harnessing Molecules 27:2968. **18.** Vessally E, et al (2017) Talanta 162:505–510.

Theoretical and experimental study of a new antioxidant xanthone: the role of the solvent and intramolecular hydrogen bond effects

Rodrigo Gester [1.3], Neidy S.S. dos Santos [1], Mayra Pinheiro [1], Herbert Georg [2], Kaline Coutinho [3], Sylvio Canuto [3]

1) *Instituto de Ciências Exatas, Universidade Federal do Sul e Sudeste do Pará, 68507-590, Marabá-PA, Brazil.*
2) *Instituto de Física, Universidade Federal de Goiás, 74690-900, Goiânia-GO, Brazil.*
3) *Instituto de Física, Universidade de São Paulo, Rua do Matão 1371, 05588-090, São Paulo-SP, Brazil.*

Free radicals are harmful reactive species that cause various problems in the human body. Antioxidant compounds, such as xanthones found in natural products, can help prevent these effects. This study focuses on the antioxidant behavior of ravenelin (RVL) and ravenelin B (RVLB), two new xanthones extracted from the Exserohilum rostratum fungus. Experimental and *in silico* tests were conducted, comparing them to ascorbic acid, a standard antioxidant. The results showed that RVL has a lower bond dissociation energy than ascorbic acid, indicating comparable antioxidant performance. This difference is mild but agrees with the experiment that indicates RVL efficiency is equivalent to ascorbic acid at low concentrations. RVLB, however, demands higher dissociation energy and consequently it has a lower antioxidative efficiency. Thus, antioxidant capacity is found as RVL > ascorbic acid > RVLB. From experimental assays, the RVL performance was confirmed through experimental tests at different solute concentrations. The study also examines the effects of solvents and intramolecular hydrogen bonds.

Keywords: xanthones, antioxidant, DFT, solvent effects, hydrogen bonds

Theorical study of the stationary phase-analyte interaction on liquid chromatography

Thales André de Oliveira Paula[1], Valter Henrique Carvalho Silva[1] and Flávio Olímpio Sanches Neto[1,2]

[1]Laboratório de química teórica e estrutural de Anápolis, Universidade Estadual de Goiás, Anápolis- Goiás, Brasil.

[2] Instituto Federal de Goiás, IFG-Câmpus Valparaíso de Goiás – GO, 72876-601, Brazil
thales_andre@hotmail.com

Keywords: DFT, chromatographic column, interaction energy, QTAIM.

Abstract

Chromatography is a widely used technique in various industries, especially in the pharmaceutical sector, where it plays a crucial role in assessing product purity, determining impurity levels, and conducting other analyses. However, this technique can be costly, leading to expenses and time consumption that could be avoided if the testing processes were optimized. One way to reduce these costs is by performing a preliminary evaluation of the behavior of the substance to be analyzed in relation to the chromatographic column used in the method, using Density Functional Theory. This study assessed the interaction energy of five commercially significant molecules in the pharmaceutical industry with their stationary phases through calculations conducted using Gaussian and Quantum Theory Atoms in Molecule.

Introduction

Chromatography, a pivotal separation technique in the scientific community, has maintained its prominence over the years. At the core of this technique lies the chromatographic column, whose continual development has driven significant advancements in chromatographic methodologies. The performance and efficiency of these columns are intrinsically linked to the chemical structure of their ligands, the particle sizes, and the column dimensions including length and diameter (3).

The interaction between an analyte and the stationary and mobile phases in chromatography is based on the polarity affinity of the compound. These interactions determine retention time and separation efficiency. However, understanding the structural details of these interactions remains complex. Factors like molecular size, shape, and functional groups, along with the composition of the phases, contribute to the dynamics. Despite advancements, accurately predicting these interactions continues to be a challenge, with ongoing research employing techniques like molecular dynamics and DFT to improve chromatographic separations (1).

The Density Functional Theory (DFT) is one of the most prominent in electronic structure methods, calculating the system's energy through the electronic density expressed by Kohn-Sham spin orbitals (2).

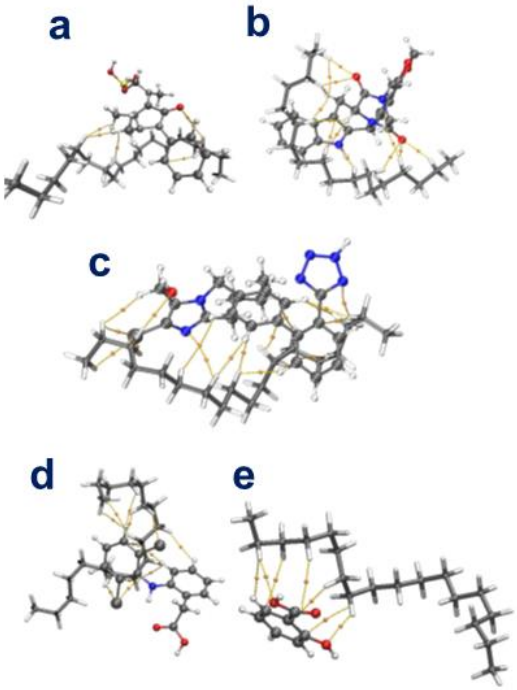
Methodology

The selected molecules are those widely commercialized by Brazilian pharmaceutical industries. The electronic structure calculations were carried out using Density Functional Theory (DFT) with the B3LYP hybrid exchange-correlation functional. The 3-21g and 6-31+g(d) basis set were employed to enhance the accuracy of the calculations. These computations were performed using the GAUSSIAN 09 software. An implicit solvent model was applied to more accurately simulate the reaction environment. This method provided a reliable prediction of the electronic properties and behaviors of the molecules. The interaction between the

stationary phase and the molecules was more effectively analyzed using the QTAIM software, where the visual representations were also generated (4).

Results and Discussion

Through QTAIM, it was possible to observe the behavior of molecules interacting with the stationary phase. Figure 1 illustrates the interaction between the chromatographic column and the molecule, where critical points reveal how the drug is adsorbed by the column, showing a strong polarity affinity with the stationary phase, which suggests slower elution in a chromatographic run. The molecules observated were Dipyrone (a), Tadalafil (b), Losartan (c), Diclofenac (d), and Salicylic Acid (e).



Using the results obtained from the drug-column complex formation through the Gaussian 16 software, it was possible to determine the interaction energy (IE), interaction enthalpy (IH), and Gibbs free energy of interaction (GI). These results, detailed in Table 1, were calculated by summing the energies of the drug and the column individually and subtracting the energy of the drug-column complex.

Molecules	IE	IH	GI
Dipyrone	-6.1	-8.4	13.0
Tadalafil	-0.9	-1.3	19.7
Losartan	-12.5	-11.9	3.9
Diclofenac	-2.5	-2.7	4.8
Salicyic Acid	-5.4	-4.7	6.5

These data are crucial as they confirm the validity of the calculations performed and provide insight into how these molecules are adsorbed by the column.

Conclusions

The tests conducted confirm that it is possible to gain prior knowledge of how an analyte will interact with the chromatographic column in the analyzed method through the approximations provided by computational chemistry. The preliminary results were satisfactory in determining a potential elution order for the analyzed compounds based on their interaction with the stationary phase. An analyte that exhibits higher interaction energy with the chromatographic column tends to have a slower elution compared to one with weaker interaction energy with the stationary phase. Therefore, it can be concluded that the development of an analytical method in the pharmaceutical industry can be streamlined by using theoretical predictions before conducting experimental analysis.

Acknowledgements

The State University of Goiás, CNPq, and the High-Performance Computing Center of the State University of Goiás.

References

1. GRITTI, F.; LEONARDIS, I.; ABIA, J.; GUIOCHON, G. Physical properties and structure of fine core–shell particles used as packing materials for chromatography Relationships between particle characteristics and column performance. Journal of Chromatography A. v.1217, p. 3819-3843, 2010.

2. KOHN, W.; SHAM, L. J. Self-Consistent Equations Including Exchange and Correlation Effects. **Physical Review**, v. 140, n. 4A, p. 1133–1138, 1965.

3. ZUVELA, P.; SKOCZYLAS, M.; JAY LIU, J.; BAZCEK, T.; KALISZAN, R.; WAH WONG, M.; BUSZEWSKI, B. Column Characterization and Selection Systems in Reversed-Phase High-Performance Liquid cromatography.Chemical Reviews, v. 119, n.6, p. 3674-3729, 2019.

4. THAMEL, R.; ŚWIĄTEK, M. M.; HEMMERICH, J.; MAURER, J. M.; ZHANG, K.; RUPPERT, T.; FUCHS, H.; PANKOWSKI, S.; WIEGAND, T.; SCHNEIDER, S. Enantioseparation of amino acids by high-performance liquid chromatography coupled with ion mobility spectrometry: A proof-of-principle study. *Analytica Chimica Acta*. v. 1235, p. 1-11, 2023

Stone-Wales defect lines in graphene: Mechanical properties and hydrogen storage capacity

Thales Machado F.[1], Pedro Alves da Silva Autreto[1].
[1]Centro de Ciências Naturais e Humanas, Universidade Federal do ABC (UFABC), Rua Santa Adélia 166, Bairro Bangu, 09210-170, Santo André-SP, Brazil.
thales.machado@aluno.ufabc.edu.br.
Keywords: Graphene; Hydrogen Storage; Mechanical properties

Abstract
Two-dimensional (2D) carbon-based structures have attracted considerable interest due to their unique mechanical and electronic properties, with potential applications in catalysis and hydrogen storage. This study proposes new 2D structures by introducing patterned Stone-Wales defect patterns into graphene's hexagonal lattice. The primary focus is on understanding how the distribution of these defects influences mechanical properties, such as Young's modulus, and hydrogen storage capacity. Using classical molecular dynamics simulations with the ReaxFF potential, it was found that increased defect line thickness or reduced spacing between defect lines decreases Young's modulus. Additionally, structures with closely spaced defect lines exhibited enhanced hydrogen storage capacity.

Introdução

As estruturas bidimensionais (2D) têm recebido imensa atenção da comunidade científica nos últimos anos por conta de suas propriedades mecânicas, térmicas e eletrônicas únicas. Em especial, as estruturas bidimensionais baseadas em carbono têm sido amplamente estudadas devido a sua alta área superficial, que proporciona um vasto potencial para aplicações em catálise e armazenamento de hidrogênio.

Das modificações estruturais na rede hexagonal do grafeno, podemos citar vacâncias, definidas pela ausência de um ou mais átomos na rede e *Stone-Wales*, caracterizado pela rotação de dois átomos por 90 graus no plano da estrutura ao redor do ponto médio entre os átomos [1].

No presente trabalho estamos propondo novas estruturas bidimensionais geradas por meio da formação de padrões de defeitos do tipo Stone-Wales na rede hexagonal do grafeno. O objetivo principal foi determinar como a formação de padrões desses defeitos afeta as propriedades mecânicas e a capacidade de armazenamento de hidrogênio.

Metodologia

As estruturas utilizadas neste estudo foram geradas a partir do grafeno, formando linhas de defeitos do tipo Stone-Wales. Cada estrutura possui uma determinada distância entre as linhas de defeitos e uma certa espessura de linha.

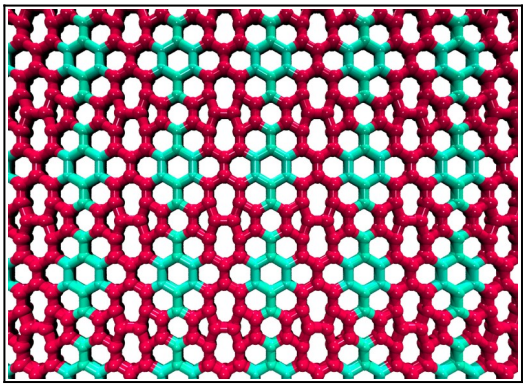


Figura 1: Linhas de defeitos do tipo Stone-Wales na rede hexagonal do grafeno. Em vermelho são os hexagonos modificados, e em ciano os hexagonos normais do grafeno.

A investigação das propriedades de estruturas compostas por muitos átomos, utilizando mecânica quântica, pode ser inviável por conta do alto custo computacional. Dessa forma, optou-se por métodos clássicos, utilizando potenciais interatômicos parametrizados para a descrição das interações de cada par de átomos.

Utilizamos o código computacional *Large-scale Atomic/Molecular Massively Parallel Simulator* (LAMMPS) e o campo de forças reativo ReaxFF para performar dinâmica molecular atomística de estruturas com milhares de átomos [2][3].

As propriedades mecânicas dos materiais estudados foram obtidas por meio de simulações com condições de contorno periódicas, utilizando três etapas. Primeiramente, a folha da estrutura tem sua energia total minimizada pelo algoritmo de gradiente conjugado. Após isso, a estrutura é mantida a 300 K por 20 ps no ensemble NPT. Por último, o tamanho da caixa em uma das direções é aumentado a uma taxa constante de 0.0000001 fs^{-1} até o rompimento das ligações metodologia. Essa aplicada com sucesso em outras simulações similares [4],

Para a investigação da capacidade de armazenamento de hidrogênio da estrutura, uma folha finita do material é exposta a atmosfera de hidrogênio. Em seguida, o sistema tem sua energia minimizada, e é mantido a 300 K por 300 ps. Ao fim da simulação, é calculado a porcentagem de carbonos ligados a hidrogênios em relação a quantidade total de carbonos dentro da região hidrogenada.

Resultados e Discussões

Foi realizado cálculos para obtenção da energia total, módulo de Young, estresse máximo e tensão máxima de 200 estruturas diferentes. Tais resultados indicam que o aumento da espessura ou a redução do espaçamento entre as linhas de defeitos reduzem o módulo de Young.

Nossos resultados demonstram que estruturas com grande espaçamento entre as linhas de defeito e linhas com pequena espessura possuem um módulo de young próximo do valor experimental do grafeno, 1+-0.1 TP. Esse resultado pode ser melhor compreendido na Figura 2 que apresenta o módulo de Young de centenas de estruturas calculadas em função da distância entre os defeitos e a largura dessas linhas (na Figura 2 representado respectivamente por “Distance” and “Thickness of Defects”)

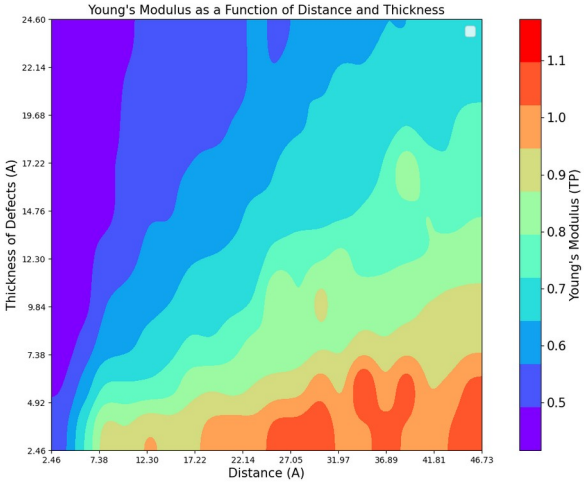


Figura 2: Módulo de Young por espessura de linha de defeito por distância entre as linhas.

Simulações de hidrogenação preliminares para cinco estruturas com diferentes distâncias e espessuras de defeitos indicam que correlação direta no densidade de defeitos, distância entre essas linhas e a taxa de hidrogenação.

Por fim nossos resultados demonstram que a formação de linhas de defeito com diferentes espessuras podem ajudar a construir estruturas com perfis ajustáveis de propriedades mecânicas e taxa de hidrogenação.

Agradecimentos

Agradeço ao PRH-ANP pelo financiamento da pesquisa, e a Central Computacional Multiusuário (CCM) da UFABC pela disponibilidade de clusters.

References

1. Tiwari, Santosh K., et al. "Stone–wales defect in graphene." *Small* 19.44 (2023): 2303340.

2. A. P. Thompson, H. M. Aktulga, R. Berger, D. S. Bolintineanu, W. M. Brown, P. S. Crozier, P. J. in 't Veld, A. Kohlmeyer, S. G. Moore, T. D. Nguyen, R. Shan, M. J. Stevens, J. Tranchida, C. Trott, S. J. Plimpton, “LAMMPS - a flexible simulation tool for particle-based materials modeling at the atomic, meso, and continuum scales”, Comp Phys Comm, 271 (2022) 10817.

3. A. C. Van Duin, S. Dasgupta, F. Lorant, and W. A. Goddard, “Reaxff: a reactive force field
for hydrocarbons,” The Journal of Physical Chemistry A, vol. 105, no. 41, pp. 9396–9409, 2001.

4. ensen, Benjamin D. and Wise, Kristopher E. and Odegard, Gregory M. “The effect of time step, thermostat, and strain rate on ReaxFF simulations of mechanical failure in diamond, graphene, and carbon nanotube”, Journal of Computational Chemistry, vol. 36, no. 21, pp. 1587-1596, 2015

Cluster size and structural distortion, a computational evaluation.

Thiago M. Mizumoto[1], Lenin J. D. Soto[1,2], Lucas G. Randolli[1], Leonardo J. Duarte[1,3], Ataualpa A. C. Braga[1].
[1]Instituto de Química da Universidade de São Paulo, São Paulo-SP / Brazil.
[2]Instituto de Química (UFRJ), Rio de Janeiro-RJ / Brazil.
[3]Universidade de Coimbra, Coimbra / Portugal.

tzumizumoto@usp.br
Keywords: DFT; Heterocatalysis; Zeolite; ZSM-5; Adsorption;.

Abstract
Various clusters were evaluated through composite DFT methodology in order to validate a model suitable for exploring the reaction mechanism of methanol conversion to dimethyl ether. The model's accuracy was verified by its congruence to experimental structural data and further evaluated by its thermochemistry.

Introduction

Zeolites are porous solids containing regular cages and channels. The restricted space within the framework allows the zeolite to discriminate molecules based on both size and shape, which is why they are often referred to as molecular sieves with extensive applications in gas separation, ion exchange, and catalytic processes. The confinement effect of zeolites is believed to enable reaction pathways by stabilizing highly energetic transition states or through shape selectivity[1]. In this study, we examine the influence of cluster size on the structural deformation of ZSM-5 and HZSM-5 zeolites.

Methodology

The crystallographic data for ZSM-5 was obtained from the International Zeolite Association (IZA) database. Three models—A, B and C—were investigated, as shown in Figure 1a-c, each with a distinct number of tetrahedral (T) sites and total atoms.

A homemade Python script was employed to generate model A (113 T sites and 376 atoms) and model B (83 T sites and 279 atoms). Model C (70 T and 239 atoms) was built from model B. Two methodological approaches: (i) the semiempirical GFN2-xTB[2] and (ii) the Density Functional Theory (DFT) composite method r2scan-3c[3] were employed. All the calculations were performed using ORCA 6.0.0 software. Calculations performed in parallel with nprocs 8 on AMD Opteron(tm) Processor 6376.

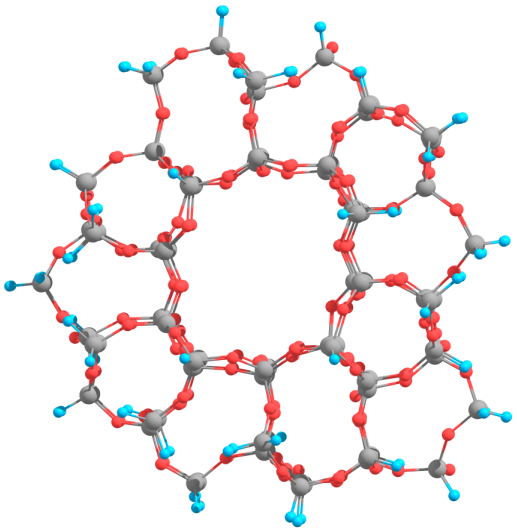


Figure 1a — Cluster model A containing 113 tetrahedra, 376 atoms. Si in gray; O, red; H, blue.

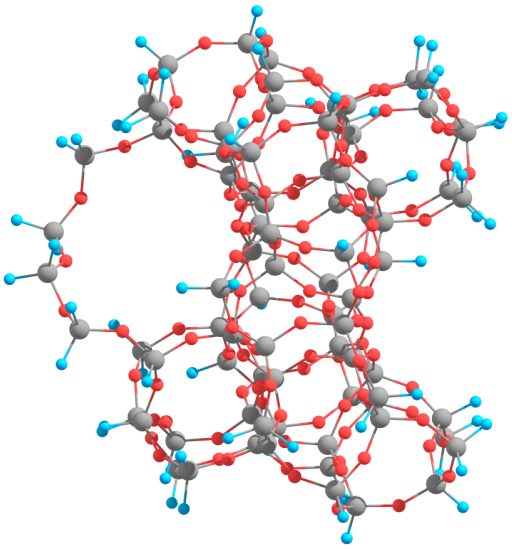


Figure 1b — Cluster model B containing 83 tetrahedra, 279 atoms. Si in gray; O, red; H, blue.

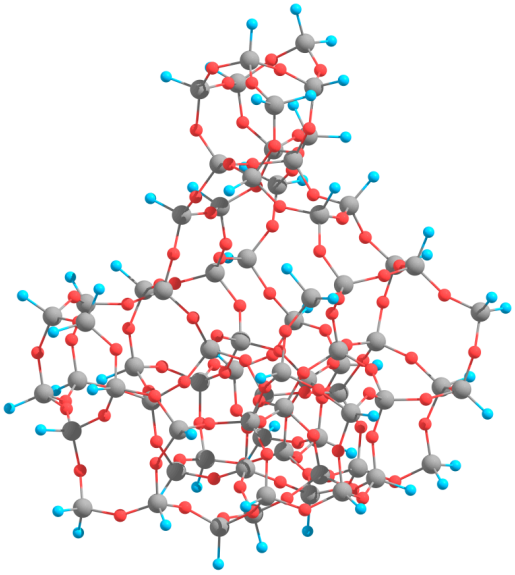


Figure 1c — Cluster model C containing 70 tetrahedras, 239 atoms. Si in gray; O, red; H, blue.

Results and discussion

The aforementioned methods resulted in structures that are satisfactorily congruent with same-site structures obtained from experimental crystallographic data available in the International Zeolite Association database.

Table 1 shows the Root Mean Square Error (RMSD) between the reference data from IZA and the calculations obtained using r2scan-3c and GFN2-xTB. For models A, B and C the RMSD value is 0.09, indicating that the models were only slightly distorted.

RMSD were evaluated by the displacement of Si and O positions. Values shown below:

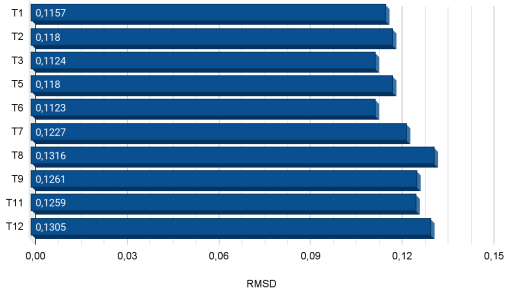
Table 1. RMSD of cluster models optimized with r2scan-3c and XTB

Model A (r2scan-3c)	0.0856
Model B (r2scan-3c)	0.0881
Model C (r2scan-3c)	0.0867
Model A (GFN2-xTB)	0.1665
Model B (GFN2-xTB)	0.1094
Model C (GFN2-xTB)	0.1095

Calculation time employed on these systems ranged from 15 to 60 hours, promising considering the system's size.

After replacing one Si by an Al and adding a H atom to a nearby oxygen, the acid form of the ZSM-5, H-ZSM-5 is obtained.Figure 2 displays the distortion, measured by the RMSD value, resulting from replacing the Si atom in each of the 12 crystallographically distinguishable positions of ZSM-5. The RMSD values, ranging from 0.1124 to 0.1305, indicate that the introduction of Al alters the pure Si structure. The highest RMSD value was observed at the T8 and T12 positions.

Figura 2. RMSD (r2scan-3c) of Cluster B substituted with Al to reference:



Acknowledgements
CAPES, CNPQ and FAPESP

References

1. Chai Y.; Dai W.; Wu G.; Guan N.; Li L. Accounts of Chemical Research 2021 *54* (13), 2894-2904
2. Bannwarth C.; Ehlert S.; Grimme S. Journal of Chemical Theory and Computation 2019 *15* (3), 1652-1671
3. Grimme S.; Hansen A.; Ehlert S.; Mewes J-M.; r^{2}SCAN-3c: A "Swiss army knife" composite electronic-structure method. *J. Chem. Phys.* 14 February 2021; 154 (6): 064103.

Variação da teoria de Weizmann com cálculos de Brueckner Doubles (W1BD) adaptada a pseudopotencial: teoria W1BDCEP

Thiago Soares Silva[1] e Douglas Henrique Pereira[2].
[1] Programa de Pós-Graduação em Química, Universidade Federal do Tocantins, Campus Gurupi - Badejós, Caixa Postal 66, Gurupi, Tocantins, 77 402-970, Brasil
[2] Departamento de Química, Instituto Tecnológico de Aeronáutica (ITA), São José dos Campos, SP 12228-900, Brasil.
thiago.soares1@mail.uft.edu.br
Keywords: Métodos compostos; Pseudopotencial; Teorias de Weizmann-n.

Abstract
Composite methods are the combination of *ab initio* calculations used to achieve high precision in the face of a computational reduction. Weizmann's n theories (n=1, 2, 3 and 4) stand out for presenting a high precision, and a version of the W1 theory, is the W1BD theory that uses *ab initio* Brueckner Doubles (BD) methods. One way to reduce the computational cost of composite methods and maintain accuracy is to use pseudopotentials in the calculation steps, in this context W1BDCEP composite method was developed from the respective W1BD all-electron version by considering the implementation of compact effective pseudopotential (CEP). The test set used to evaluate the theory were 8 proton affinities (PA_0), 46 electron affinities (EA_0), 54 ionization energies (IE_0), 80 enthalpies of formation (Δ_fH^0) and 10 bond dissociation energies (BDE). The mean absolute deviation values (MAD) for W1BD and for the version adapted to the pseudopotential, W1BDCEP, were similar, with values of 0.97 kcal mol^{-1} and 1.03 kcal mol^{-1}, respectively when the properties PA_0, EA_0, IE_0 and Δ_fH^0 were evaluated together. Comparing the versions of the theories that employs *ab initio* Brueckner doubles calculations with the W1 and W1CEP theories it is possible to observe that the W1BD and W1BDCEP theories are more accurate than the W1 theory (MAD_{W1} = 1.25 kcal mol^{-1}) and W1CEP (MAD_{W1CEP} = 1.44 kcal mol^{-1}), proving the accuracy of using the BD method. Pseudopotential reduces computational time by up to 30% and thus enables more accurate calculations with less computational time.

Introduction
Determinar as propriedades termoquímicas, energéticas e estruturais de átomos e moléculas com precisão e baixo custo computacional é um dos objetivos da química computacional [1,2]. Para alta precisão, são aplicados métodos *ab initio* altamente correlacionados, com grandes conjuntos de bases, que exigem um alto tempo de processamento e limitam o tamanho do sistema a ser estudado devido ao grande número de átomos [3]. Portanto, a necessidade de redução do tempo computacional levou ao desenvolvimento e uso de métodos ou teorias que visam reduzir o custo computacional e manter a precisão [4].

As teorias de Weizmann-n se destaca pela precisão dos cálculos, por utilizar sequências de extrapolações de cálculos *ab initio* e por não empregar parâmetros empíricos [4]. Para reduzir o custo computacional dos métodos compostos, aplicados a sistemas químicos maiores, e para manter a precisão, algumas teorias Gaussian e Weizmann foram adaptadas ao pseudopotencial [4,5]. A ideia central do uso do pseudopotencial é adaptar o conjunto de base para que os elétrons internos sejam substituídos pelo pseudopotencial. Assim o objetivo do trabalho foi aplicar o pseudopotencial efetivo compacto (CEP) e os conjuntos de bases adaptados utilizados no

desenvolvimento da teoria W1CEP [4] para avaliar a precisão do pseudopotencial adaptado à W1BD.

Metodologia

A teoria W1BDCEP foi desenvolvida usando as etapas realizadas por Heerdt et al. [4] para a teoria W1CEP e a energia final da teoria W1BDCEP pode ser escrita pela Eq. 1:

$$W1BDCEP(0K) = E_{BD(ref);INF,CEP} + E_{COR,BD,INF,CEP} + E_{COR,BD(T),INF,CEP} + E_{DKH,CEP} + E_{ZPE,CEP} + E_{SO} \quad \text{(Eq. 1)}$$

Os termos $E_{BD(ref);INF,CEP}$, $E_{COR,BD,INF,CEP}$, $E_{COR,BD(T),INF,CEP}$, $E_{DKH,CEP}$, e $E_{ZPE,CEP}$ são os mesmos que na teoria com todos os elétrons, mas com a substituição dos elétrons internos pelo pseudopotencial CEP e com o uso de conjuntos de base adaptados. As correções spin-órbita (E_{SO}) e o parâmetro β são os mesmos para a teoria com todos os elétrons.

A teoria W1BDCEP foi desenvolvida e validada usando 8 afinidades por prótons (PA_0), 46 afinidades de elétrons (EA_0), 54 energias de ionização (IE_0) e 80 entalpias de formação ($\Delta_f H^0$), conforme descrito no desenvolvimento da teoria W1CEP [4]. Também foi utilizado 10 energias de dissociação de ligação (BDE) que foram calculadas e comparados com os resultados de diferentes métodos [6,7,8].

Resultados e discussão

Analisando os resultados para PA_0 (Gráfico 01):

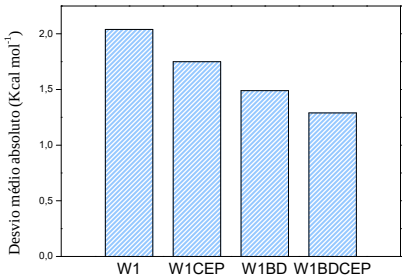


Gráfico 01. Afinidade por Próton (AP_0)

As teorias que aplicaram as correções de Brueckner foram as que apresentaram os menores desvio médio absoluto (MAD), com valores de 1,49 e 1,29 kcal mol^{-1} para as teorias W1BD e W1BDCEP, respectivamente. É possível inferir que o maior erro para todas as teorias foi apresentado pelo etino (C_2H_2), com valores acima de 2,0 kcal mol^{-1}.

Os valores dos desvios para as afinidades eletrônicas estão representados no Gráfico 02. Em contraste com PA_0, a EA_0 obteve resultados de desvios maiores para a teoria W1BDCEP quando comparada à teoria W1BD, com valores de MAD de 0,031 eV e 0,025 eV, respectivamente.

Os resultados para as teorias W1BD e W1BDCEP foram melhores que os das teorias W1 e W1CEP, comprovando que as correções de Brueckner melhoram os resultados de EA_0.

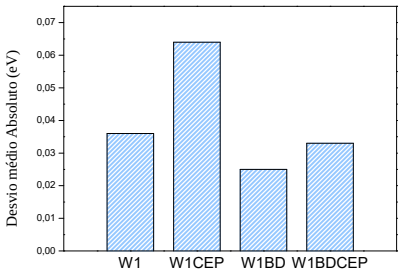


Gráfico 02. Afinidade Eletrônica (EA_0)

Os MADs das energias de ionização estão listados no Gráfico 03 e seguem a mesma tendência dos resultados da PA_0, em que a teoria W1BDCEP apresentou melhores resultados do que a da teoria original (W1BD), com um MAD de 0,037 eV para a teoria W1BDCEP e 0,040 eV para a teoria com todos os elétrons.

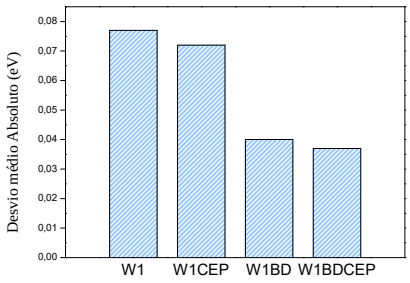


Gráfico 03. Energia de Ionização (IE_0)

Os resultados para entalpias de formação estão listados no Gráfico 04 e mostram que a implementação do CEP na teoria W1BD não alterou significativamente os desvios e segue a mesma tendência das teorias W1 e W1CEP. Algumas moléculas exibiram desvios superiores a 2,0 kcal mol^{-1}, com a

maioria delas contendo átomos de silício (Si_2H_6, SiH_2 ($^1A_1$), SiH_2 ($^3B_1$), SiH_3, SiH_4). Comparados a outras propriedades termodinâmicas, os valores de Δ_fH^0 foram ligeiramente maiores para as teorias W1BD e W1BDCEP quando comparados com as teorias W1 e W1CEP.

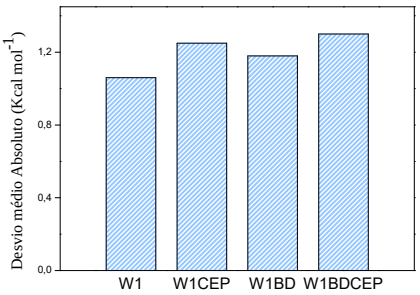


Gráfico 04. Entalpia de formação (Δ_fH^0)

A energia de dissociação de ligação (BDE) também foi avaliada (Gráfico 05). Os resultados foram comparados com os dados da literatura e mostram que os cálculos usando as teorias W1BD e W1BDCEP são melhores do que aqueles usando métodos DFT e semelhantes aos métodos CBS-Q e CBS-Q3.

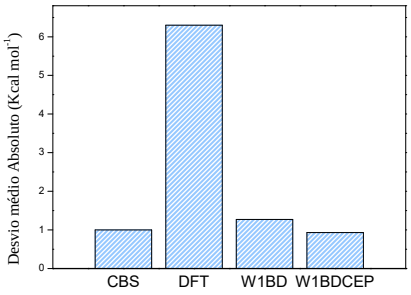


Gráfico 05. Energia de Dissociação de ligação (BDE)

Avaliando o MAD para as propriedades PA_0, EA_0, IE_0 e Δ_fH^0 em conjunto, pode-se observar que os métodos W1BD e W1BDCEP apresentam menor MAD, com valores de MAD_{W1BD} = 0,97 kcal mol^{-1} e $MAD_{W1BDCEP}$ = 1,03 kcal mol^{-1} quando comparados com as teorias W1 e W1CEP, que apresentam MAD_{W1} = 1,25 kcal mol^{-1} e MAD_{W1CEP} = 1,44 kcal mol^{-1}.

De acordo com Barnes et al. [3], os cálculos W1BD são ligeiramente mais caros computacionalmente do que os correspondentes W1U e W1 (RO). Em contraste, de acordo com Heerdt et al. [4], as modificações no conjunto de base adaptado ao CEP pseudopotencial podem ter uma redução de custo computacional de 13–30%, dependendo do sistema.

Conclusão

Neste trabalho, uma nova teoria composta adaptada ao pseudopotencial foi desenvolvida e nomeada de W1BDCEP. Considerando as propriedades analisadas juntas, as teorias W1BD e W1BDCEP apresentaram os melhores MADs, comprovando a precisão do uso do método BD. E a teoria desenvolvida apresenta uma alta precisão com um menor custo computacional.

Acknowledgements

Os autores agradecem o apoio da CAPES (Código 001), a Fundação de Amparo à Pesquisa do Estado de São Paulo #2023/17727-2, o Centro de Engenharia e Ciências Computacionais (apoio financeiro da FAPESP, #2013/08293–7 e #2017/11485–6) e do Centro Nacional de Processamento de Alto Desempenho em São Paulo (CENAPAD), pelos recursos computacionais.

References

1. Karton, A.; WIREs Comput Mol Sci. 2016, 6, 292–310.
2. Martin, J.M.L.; de Oliveira, G.; J Chem Phys. 1999, 111, 1843–1856.
3. Barnes, E.C.; Petersson, G.A.; Montgomery, J.A.; et al.; J Chem Theory Comput. 2009, 5, 2687–2693.
4. Heerdt, G.; Pereira, D.H.; Custodio, R.; Morgon, N.H.; Comput Theor Chem. 2015. 1067, 84–92.
5. Pereira, D.H.; Ramos, A.F.; Morgon, N.H.; Custodio, R.; J Chem Phys. 2011, 135, 034106.
6. Jursic, B.S.; J Mol Struct (Thoechem) 1998, 422, 253–257.
7. Wood, G.P.F.; Radom, L.; Petersson, G.A.; et al.; J Chem Phys. 2006, 125, 094106.
8. Li, X.H.; Tang, Z.X.; Jalbout, A.F.; et al.; J Mol Struct (Thoechem). 2008, 854, 76–80.

Referência do artigo publicado

Silva, T.S.; Cruz, A.B.; Rodrigues, K.G.O.; Pereira, D.H.; J Mol Model. 2022, 28, 284.
DOI: 10.1007/s00894-022-05281-x

10º SIMPÓSIO DE ESTRUTURA ELETRÔNICA & DINÂMICA MOLECULAR
SEEDMOL 4 a 8 novembro | 2024
Pirenópolis, Goiás

TDDFT Study of R- and S-Warfarin Enantiomers Complexed with Human Serum Albumin

Vanessa Regina Miranda[1,*], Isabela Cristina Alves Topan[1], Laís Pádua Dos Santos[1], Nelson Henrique Morgon[1]
[1]Institute of Chemistry, University of Campinas, 13083-970, Campinas, SP, Brazil.
* *miranda.vanessar@gmail.com*
Keywords: TDDFT; UV-Visible; Circular Dichroism; HSA; Warfarin.

Abstract
Human Serum Albumin (HSA) transports endogenous molecules and drugs like warfarin. However, due to low specificity in the complexation of R- and S-warfarin with HSA, we performed quantum studies on the electronic transitions at the binding site to better understand the interactions involved.

Introduction
Human Serum Albumin (HSA) is an important protein present in the blood, and its main characteristic is its ability to bind to molecules that are poorly soluble in blood plasma and transport them.[1] HSA is highly targeted for drug transport due to its ability to complex with a significant number of molecules (depending on their concentration), thus facilitating efficient transport.[2] In the case of the anticoagulant warfarin, the complexation is 99% at therapeutic doses.[3] The favored interaction of warfarin has been used as a probe in assays to identify binding sites and study competition with other ligands for the binding site.[4] Warfarin binds to drug site I (in subdomain IIA), considering both R- and S-warfarin enantiomers (Fig. 1).

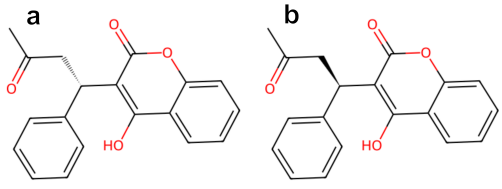


Figure 1. Structural formula (a) S-warfarin (CAS: 5543-57-7); (b) R-warfarin (CAS: 5543-58-8)

However, the two enantiomers of warfarin exhibit similar conformations when bound to HSA, showing a lack of stereospecificity in the protein-warfarin complex.[5] This indicates a still-limited understanding of the shape and reasons behind these interactions. In this context, the use of quantum mechanics to study the electronic transitions occurring between the warfarin enantiomers and the residues of the binding site enables a better understanding of these interactions. Studies of excited states in the ultraviolet and visible regions (UV-Vis) and electronic circular dichroism (ECD) can provide insights into these interactions. The goal of this work was to understand the interactions between the R- and S-enantiomers of warfarin and the residues of subdomain IIA of HSA, using Time-Dependent Density Functional Theory (TDDFT)[6]. Understanding the structural information and interactions between warfarin and the residues of the active site is crucial for elucidating binding site for other drugs, natural ligands or new therapeutic molecules.

Methodology
Computational studies were conducted on R-warfarin (CAS: 5543-58-8) and S-warfarin (CAS: 5543-57-7). Based on the

experimental data, the studies were conducted in ethanol (ε=24.852) and in the gas phase for both structures. The studies were conducted with explicit description, and using both the explicit solvent model SMD (Solvent Model Density) and D3 version of Grimme's dispersion with Becke-Johnson damping (Empirical Dispersion=GD3BJ).[7] Optimization and frequency calculations were performed in two stages: the first stage at a lower level, DFT-B3LYP/6-31G(d), and the second stage at DFT-B3LYP/6-311++G(2d,p). The optimized structures were subjected to excited state calculations using TD-PBE/6-311++G(3df,2p), with the first 30 electronic spectra in singlet states calculated for the structures shown in Fig. 1. The focus was on understanding electronic transitions through UV-Visible and ECD spectra. The methodology was validated using experimental data available in the literature. Thus, this methodology was applied to the bioactive conformations of R-warfarin and S-warfarin, obtained from PDB IDs 1H9Z[5] and 1HA2[5], respectively. The active site of each structure was defined within 6 Å (using Molden), and hydrogens were added at physiological pH. Their coordinates were then optimized using the semi-empirical PM7 method. The R-warfarin and S-warfarin structures were isolated from the binding sites, single-point calculations were performed, and electronic properties were studied using TD-DFT. Calculations were carried out with Gaussian 16.[8]

Results and Discussion

The results of the optimization and frequency calculations for R-warfarin and S-warfarin in ethanol and in the gas phase are shown in Table 1, which includes the corrected energy values resulting from the sum of electronic and thermal free energies. It is noteworthy that the optimized geometries showed no imaginary frequencies.

Table 1. Values of the energies (kcal.mol^{-1}) for the optimized structures and the calculated frequencies (DFT-B3LYP/6-311++G(2d,p))

Structure	$E_{ETHANOL}$	E_{GAS}
R-warfarin	-746608.3739	-649232.7789
S-warfarin	-746608.9135	-649232.7789

The optimized structures were subsequently subjected to electronic studies, revealing maximum absorption peaks in the UV-Vis spectrum, as shown in Table 2.

Table 2. Maximum absorption, λ_{max}, for each R- and S-warfarin structure obtained in different environments, calculated at the TD-PBE/6-311++G(3df,2p) level, considering thirty excited states

	R-warfarin (λ_{MAX} / nm)	S-warfarin (λ_{MAX} / nm)	Experim. (λ_{MAX} / nm)
Solvent: Ethanol	313.4	313.7	306
Gas phase	348.5	348.5	----
Bioactive form	310.3 (1H9Z)	317.6 (1HA2)	----

As shown in Table 2, the λ_{MAX} values from the UV-Vis absorption calculations are the same for both R- and S-warfarin structures in ethanol and in the gas phase, as expected. However, when analyzing the maximum absorption calculated for the same molecules with the bioactive conformations from the crystal structures 1H9Z and 1HA2, a shift of approximately 7 nm in λ_{MAX} was observed. It was observed that the benzyl and coumarin groups are nearly superimposable in the interaction of the R- and S-enantiomers of warfarin with the amino acids comprising binding site I (in subdomain IIA) of HSA, while the acetonyl group shows greater differences in conformations. This suggests that the acetonyl group is responsible for influencing the λ_{MAX} of the UV-Vis spectrum. The influence observed in the specific conformations in each case results from interactions with certain specific

residues of the binding site, in relation to the R- and S-structures, and This characterized a positive solvatochromism[9] of S-warfarin compared to R-warfarin, as it exhibited a bathochromic shift.

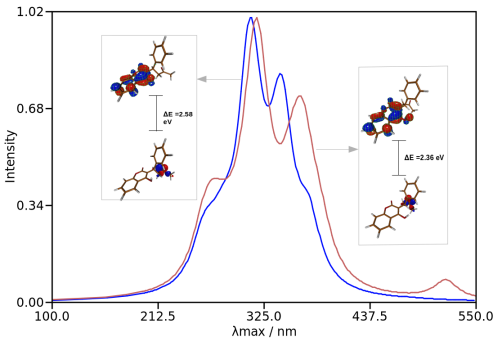


Figure 2. Theoretical absorption spectra and HOMO-LUMO transitions of R-warfarin (blue) and S-warfarin (brown) in the bioactive conformation obtained from PDB structures 1H9Z and 1HA2, respectively

The contributions of molecular orbitals describing electronic transitions predominantly come from the HOMO orbitals (Fig. 2), with the observed gaps showing very similar values. In this figure, it is also possible to observe the regions of the two molecules with the highest electron density. Figure 2 also shows the regions of highest electronic density in the two molecules. The electronic density related in both enantiomers to the HOMO is predominantly over the acetyl group, while the LUMO density is concentrated on the coumarin portions. ECD studies are being conducted, to complement this approach, based on the results obtained so far, aiming to better understand the structures with optical activity involved in this interaction.

Conclusions

The results obtained so far suggest that the changes in electronic transitions of R-warfarin and S-warfarin, as derived from their complexation with HSA, result from differences in their conformations, particularly concerning the acetyl group, influenced by interactions with residues in subdomain IIA of binding site I. To gain a deeper understanding of how chirality in warfarin impacts interactions with amino acid residues, studies on electronic transitions involving specific residues of binding site I (in subdomain IIA) are also being conducted.

Acknowledgements

The authors would like to thank CAPES, FAPESP – grants nº 2013/08293-7 and 2015/22338-9 (CCES/UNICAMP, Brazil) and CNPq – grant nº 303581/2018-2.

References

1. Roopenian, D. C. *et al.* Mabs, 2015, 7, 344-351.

2. Lee, P.; Wu, X. Curr Pharm Des. 2015, 21(14),1862-5.

3. Holford, N. H. G.; Benet, L.Z.; Katzung, B.G.; Basic and Clinical Pharmacology, 7th Ed. Appleton and Lange, Stamford CT, 1998, 34-49.

4. Huang, S. *et al.* Journal of Molecular Structure. 2023, 1291, 136017.5.

5. Petitpas, I., Bhattacharya, A. A., Twine, S., East, M., Curry, S. Journal of Biological Chemistry, 2001, 276(25), 22804-9.

6. Bauernschmitt, R. Ahlrichs, R. Chem. Phys. Lett. 1996, 256, 454-64

7. Grimme, S.; Ehrlich, S.; Goerigk, L. Journal of computational chemistry. 2011, 32(7), 1456-1465.

8. Frisch, M.J. *et al.* Gaussian 16, Revision A.03, Inc., Wallingford CT, 2016.

9. Buncel, E.; Rajagopal, S. . Accounts of Chemical Research. 1990, 23, 7, 226-31.

Predição Eficiente de Espectros de Absorção Usando o Método dos *Ensembles*: Uso de IA na Seleção de Geometrias.

Víctor de Souza Assumção Bonfim[1,2], Victor dos Reis Rodrigues[1], Victor Eduardo Ramos Camargo[1], Matheus de Oliveira Bispo[3], e Demetrio Antônio da Silva Filho[1].
[1]Instituto de Física, Universidade de Brasília, 70919-970, Brasília, Brasil.
[2]Centro Internacional de Física, Universidade de Brasília, 70919-970, Brasília, Brasil.
[3]*Institut de Chimie Radicalaire, Aix-Marseille Université*, 13013, *Marseille*, França.
dasf@unb.br
Keywords: Absorption Spectra; Machine Learning; Nuclear Ensemble Method.

Abstract
This work explores the use of Machine Learning (ML) to enhance the Nuclear Ensemble (NE) method efficiency in the prediction of absorption spectra of organic molecules. Traditional Time-dependent Density Functional Theory (TDDFT) often misses vibrational effects, and this study aims to address that gap. By integrating ML techniques, particularly clustering algorithms and embedding methods, the goal is to speed up and improve the accuracy of spectral calculations. Initial tests will use simple, well-known molecules, with plans to expand to more complex ones. The approach seeks to reduce computational costs and pave the way for future research in ML-driven molecular property prediction.

Introdução

A Inteligência Artificial (do inglês "Artificial Intelligence") e o Aprendizado de Máquina ("Machine Learning", em inglês) têm transformado a química quântica e a física molecular por serem técnicas estatísticas e computacionais capazes de acelerar cálculos, melhorar simulações moleculares e prever propriedades de novas moléculas. Trata-se de algoritmos que permitem previsões mais rápidas e precisas de propriedades moleculares e aprimoram a interpretação de dados. Contudo, o uso de técnicas de Machine Learning (ML) à predição de espectros teóricas de absorção UV-VIS de moléculas tem sido ainda pouco explorada, e o uso conjunto dela com o método do Nuclear Ensemble (NE) nunca tentado.

Dada a sua relevância multifacetada, numerosos trabalhos computacionais têm se concentrado no cálculo teórico de espectros de absorção UV-VIS de moléculas orgânicas. Investigações baseadas na teoria do funcional da densidade (DFT) são particularmente promissoras, oferecendo descrições confiáveis e escaláveis. O protocolo convencional TDDFT (de *Time-dependent Density Functional Theory*) avalia os espectros de absorção de geometrias otimizadas, sem considerar a influência das vibrações intramoleculares. No entanto, mecanismos de espalhamento podem ser fortemente influenciados por mudanças na geometria. Isso é especialmente verdadeiro para fenômenos foto-físicos.

Por essa razão, metodologias que incorporam efeitos vibracionais nas estimativas de espectros eletrônicos possuem relevância prática e teórica. O método do NE é uma abordagem atraente que pode ser facilmente integrada aos fluxos de trabalho em DFT. Atualmente, o formalismo é uma peça central na obtenção de espectros de absorção e fluorescência além da aproximação de Frank-Condon [1–2]. Com base no mesmo princípio, foi feita uma recente proposta para a generalização da energia de reorganização, que é crucial

para transferência de carga do tipo Marcus [3]. Adicionalmente, Barbatti et al. construíram um banco de dados para aprendizado de máquina de múltiplas moléculas através do NE, onde propriedades de ponto único, como gap, magnitude do dipolo e polarizabilidade isotrópica, foram avaliadas [4]. Apesar desses avanços, permanece uma questão em aberto como o método NE poderia ter seu desempenho aprimorado por algoritmos de IA.

Nesse cenário, uma oportunidade se abre quando passamos a considerar a capacidade de se analisar os modos normais de uma molécula para identificar suas contribuições para o cálculo de uma certa propriedade molecular. Dessa forma, qo focar-se a atenção nos modos normais de maior relevância, seria possível acelerar a obtenção de espectros de alta qualidade sem o oneroso custo associado com o cálculo explícito de 50.000 conformações. É, então, nessa tarefa de analisar e selecionar modos mais relevantes que se abre o espaço para a entrada dos algoritmos de Machine Learning.

Propomos, portanto, neste trabalho, uma nova abordagem que integra técnicas de Machine Learning para acelerar o cálculo do espectro que seria gerado pelo método do Nuclear Ensemble por meio da seleção e descarte de geometrias a serem consideradas, conforme sejam altas ou não suas respectivas contribuições para a determinação de uma propriedade de interesse, a qual, no presente estudo, se trata do espectro vibracional de absorção de uma molécula.

O objetivo do presente trabalho se centrará, portanto, em explorar o uso de diversos modelos de Machine Learning para analisar a viabilidade de implementação, assim como a performance e desempenho de diferentes modelos e abordagens.

Metodologia

Quanto ao banco de dados, começaremos as primeiras análises e treinamentos com moléculas já exaustivamente estudadas e documentadas, como o fulveno e o bifenilo. Caso os primeiros modelos se mostrem bem-sucedidos, proceder-se-á ao estudo de mais moléculas; se possível, mais complexas.

Pretendemos também testar e avaliar diversas abordagens e as performances de diferentes algoritmos de Machine learning na resolução deste problema.

Uma primeira proposta basear-se-á em algoritmos de agrupamento (*clustering algorithms* [5]) e terá o seguinte *workflow*:

1. Geração de um conjunto inicial pequeno de geometrias.
2. Tradução dessas geometrias em uma sequência vetorial por meio de algum descritor ou embedding.
3. Aplicação do algoritmo de agrupamento para categorizar as geometrias, de forma que, dentro de um grupo, os deslocamentos ao longo de um modo normal sejam mais uniformes do que quando considerada a distribuição tomada de todas as geometrias iniciais.
4. Cálculo dos espectros de absorção para cada grupo gerado na clusterização.
5. Análise e seleção dos grupos cujas geometrias mais contribuam para o os espectros, tendo por base algum critério de convergência.
6. Geração de um novo conjunto de geometrias, diferentes das iniciais, que serão classificadas em conformidade com os grupos criados no passo 3, após serem codificadas no passo 2.
7. Calcula-se os espectros das geometrias que caírem nos grupos selecionados na etapa 5.

Já nesta primeira abordagem, há uma certa riqueza a se explorar.

A primeira tarefa a ser superada será a criação de um embedding ou a seleção de algum descritor capaz de representar de forma eficiente as moléculas (suas geometrias de equilíbrio e deslocamentos ao longo de seus modos normais). Em uma futura abordagem, pode-se partir de um vetor inicial que será codificado em uma segunda representação mais eficiente a ser a

aprendida por uma rede neural transformer, por exemplo.

Outros problemas incluem: avaliar a performance de diferentes algoritmos de agrupamento; buscar os hiperparâmetros que otimizem a performance dos algoritmos, seja por buscas combinatórias (como o grid search) ou por meio de algoritmos evolutivos; testar o impacto do uso de diferentes critérios de convergência.

É importante mencionar que, caso esse primeiro método funcione, pretende-se estudar outras abordagens baseadas em outros métodos de Machine Learning, usando, por exemplo Redes Neurais Recorrentes (RNNs) [5], ou Redes Transformers, na tentativa de fazer o algoritimo aprender de forma contínua, conforme cada geometria vá sendo gerada, quais são as que devem ser escolhidas ou descartadas para o cálculo de DFT ou TD-DFT.

Resultados

Por meio deste trabalho pretendemos realizar de forma mais rápida, eficiente e precisa, o cálculo de espectros teóricos de moléculas. Também pretendemos encontrar boas abordagens diferentes de ML capazes de lidar com esse problema, dada a possibilidade de isso abrir áreas de exploração para futuros trabalhos. Esperamos sublinhar o enorme potencial que a Inteligência Artificial

Conclusões

O presente trabalho pretende contribuir de modo significativo à área de predição de propriedades moleculares. Caso funcione, a primeira vantagem de nosso trabalho será a possibilidade de facilmente adaptá-lo ao cálculo de outras propriedades além do espectro de absorção de moléculas.

Além disso, integrar técnicas de IA ao método NE permitirá acelerar o cálculo de certas propriedades, e isso a um custo computacional reduzido, já que esperamos que nosso método dependa de menos geometrias para o cálculo de DFT ou TD-DFT.

Vale mencionar que o presente trabalho apresenta inúmeras perspectivas de exploração futura. Pode-se estudar, por exemplo: a criação de *embeddings*, outros métodos de ML, expansão do banco de dados e estudo de cada vez mais moléculas (o que pode aumentar a capacidade preditiva de alguns modelos) e etc.

Agradecimentos

Os autores agradecem o apoio financeiro das agências de fomento brasileiras CNPq (Bolsas 307108/2023-6 e 306080/2022-2), CAPES, FAP-DF (00193-00001831/2023-47), Edital DPI/DPG N. 04/2024, Edital Interno IF/UnB 0004/2024, e INCT-CiMol (Bolsa CNPq 406804/2022). V.S.A.B. agradece a bolsa de pós-doutorado do Instituto Nacional de Ciência e Tecnologia em Ciências Moleculares (INCT-CiMol), Bolsa CNPq 406804/2022-2.

Referências

1. Sousa, L. E.; Ribeiro, L. A.; Fonseca, A. L. d. A.; da Silva Filho, D. A.; The Journal of Physical Chemistry A 120 (2016) 5380–5388. (doi: 10.1021/acs.jpca.6b02141).
2. Sousa, L. E.; Silva, P.; Journal of Chemical Theory and Computation 2021, 17 5816–5824. (doi:10.1021/acs.jctc.1c00476).
3. Cassiano, T. D. S. A., de Sousa, L. E., Gargano, R., & de Oliveira Neto, P. H. *Chemical Physics Letters*, 2023, *815*, 140384.
4. Pinheiro Jr, M., Zhang, S., Dral, P. O., & Barbatti, M.; *Scientific Data*, 2023, *10*(1), 95.
5. Hastie, T.; Tibshirani, R.; Friedman, J. The Elements of Statistical Learning: Data Mining, Inference, and Prediction, 2nd ed.; Springer: New York, 2009.

Assessing the impact of vibrational modes on the static polarizability of small molecules.

Tiago de Sousa Araújo Cassiano[1], Víctor de Souza Assumção Bonfim[1,2], Pedro Henrique de Oliveira Neto[1,2], and Demetrio Antônio da Silva Filho[1].
[1]Institute of Physics, University of Brasília, 70919-970, Brasília, Brazil.
[2]International Center of Physics, University of Brasília, 70919-970, Brasília, Brazil.
dasf@unb.br.
Keywords: Polarizability; ionization cross-section; CFC, HFC; Kerr-effect.

Abstract
The accuracy of electron impact ionization cross-section calculations is closely tied to the molecular polarizability. This study investigates the polarizability tensor, with particular emphasis on its isotropic and anisotropic components. Conventional theoretical approaches often limit their scope to optimized molecular geometries, overlooking the significant impact of vibrational motion on polarizability. We delve into the effects of intramolecular vibrations on the electrostatic properties of molecules frequently employed in gas-phase interactions. Our analysis demonstrates that nuclear vibrations can induce substantial variations in isotropic and anisotropic polarizabilities, with deviations reaching up to 6% and 50%, respectively. Furthermore, our normal mode analysis has identified specific vibrational modes that contribute to the enhancement of molecular polarizability. These findings highlight the importance of considering vibrational effects in the accurate determination of electron impact ionization cross-sections.

Introduction

The study of electron impact ionization cross sections is fundamental to various fields, including atomic and molecular physics, plasma physics, and astrophysics. These cross sections are particularly significant in understanding the behavior of molecules under electron impact. Accurate calculations of ionization cross sections require detailed knowledge of the molecular structure, particularly the vibrational modes that influence polarizability. Polarizability, a measure of the molecule's ability to distort its electron cloud in response to an electric field, plays a crucial role in determining the ionization cross section [1].
The vibrational modes of a molecule can significantly impact its polarizability, which in turn affects the accuracy of ionization cross section calculations. The Nuclear Ensemble method [2–5], combined with the ωB97X-D functional and the aug-cc-pVTZ basis set, provides a robust approach for calculating these properties. This method accounts for the distribution of nuclear geometries corresponding to different vibrational states, offering a more comprehensive picture of how vibrational modes influence polarizability and ionization cross sections. In this study, we evaluate both the isotropic and anisotropic polarizabilities for eight small molecules, including CF_3CH_2F and CF_2Cl_2, both well known as refrigerant gases.

Methodology

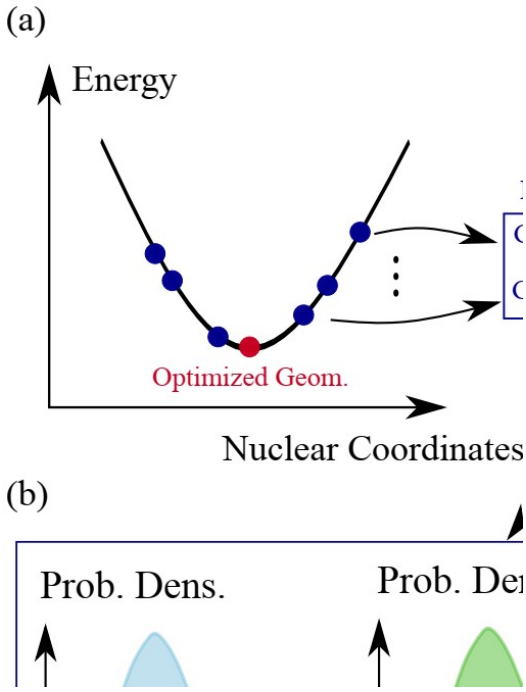


Fig. 1. Schematic representation of the Nuclear ensemble method: (a) Out-of-equilibrium geometries are generated from the equilibrium geometry; (b) each geometry of the ensemble has its isotropic and anisotropic polarizabilities sampled, producing probability distributions.

The polarizabilities were calculated using the Nuclear Ensemble method, which incorporates the effects of vibrational modes by sampling an ensemble of nuclear geometries. In the current work, the total number of geometries sampled N was set to $N = 500$ and the temperature set to $T = 300$ K. The calculation level for each geometry was the ωB97X-D density functional with the aug-cc-pVTZ basis set.

Results and Discussion

The results indicate that the calculated polarizabilities are consistent with experimental data, with standard deviations very specific to each molecule. For molecules with many normal modes like CF_2Cl_2, only certain vibrational modes had a pronounced effect on polarizability. The Nuclear Ensemble method proved effective in capturing these effects, highlighting the importance of considering vibrational contributions in such calculations. While the overall agreement with experimental ionization cross sections is satisfactory, the study underscores the need for further refinement, particularly in handling complex vibrational structures.

Conclusion

This study emphasizes the critical role of vibrational modes in determining molecular polarizability and, consequently, ionization cross sections. The use of the Nuclear Ensemble method, along with the ωB97X-D/aug-cc-pVTZ calculation level, offers a detailed approach to capturing these effects. However, further work is necessary to refine the methodology, especially for molecules with intricate vibrational dynamics. These findings contribute to the ongoing development of more accurate predictive models for electron impact

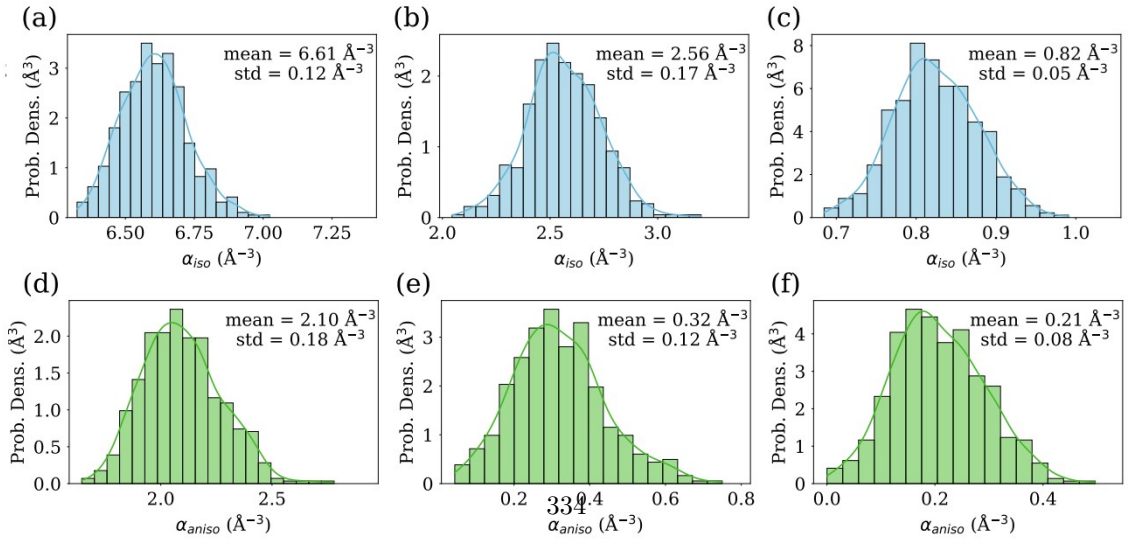


Fig. 2. Nuclear ensemble results for the polarizability distributions of CF2Cl2, CF4, and HF: (a), (b), and (c) show the respective isotropic polarizabilities, while (d), (e), and (f) show the anisotropic ones.

ionization processes.

Acknowledgements

The authors acknowledge the financial support by the brazilian funding agencies CNPq (Grants 307108/2023-6 and 306080/2022-2), CAPES, FAP-DF (00193-00001831/2023-47), Edital DPI/DPG N. 04/2024, Edital Interno IF/UnB 0004/2024. and INCT-CiMol (CNPq grant 406804/2022). V.S.A.B. acknowledges a post-doc scholarship from the National Institute of Science and Technology on Molecular Sciences (INCT-CiMol), Grant CNPq 406804/2022-2. T.S.A.C. acknowledges financial support from IF/UnB grant 0005/2024.

References

1. Bull, N. P.; Harland, W.; Vallance, C.; The Journal of Physical Chemistry A, 2012, 116, 767–777.
2. Sousa, L. E.; Ribeiro, L. A.; Fonseca, A. L. d. A.; da Silva Filho, D. A.; The Journal of Physical Chemistry A, 2016, 120, 5380–5388.
3. Sousa, L. E.; Silva, P.; Journal of Chemical Theory and Computation 2021, 17 5816–5824.
4. Cassiano, T. D. S. A., de Sousa, L. E., Gargano, R., & de Oliveira Neto, P. H. *Chemical Physics Letters*, 2023, *815*, 140384.
5. Pinheiro Jr, M., Zhang, S., Dral, P. O., & Barbatti, M.; *Scientific Data*, 2023, *10*(1), 95.

.

Using ML to predict device parameters of Organic Solar Cells

Victor dos Reis Rodrigues[1], Víctor de Souza Assunção Bonfim[1,2], Demétrio Antônio da Silva Filho[1,2].
[1]Institute of Physics, University of Brasília, 70919-970, Brasília, Brazil.
[2]International Center of Physics, University of Brasília, 70919-970, Brasília, Brazil.
vreis6327@gmail.com; ercamargo.victor@gmail.com ; *dasf@unb.br*.
Keywords: Organic Solar Cells; Machine Learning; Descriptors Selection; Bulk Heterojunction; Power Conversion Efficiency.

Abstract
Organic Photovoltaic (OPV) cells present a promising alternative to traditional solar technologies, yet the vast chemical space and complex material interactions pose significant challenges in optimizing their performance. This work explores the application of Machine Learning (ML) to accelerate the discovery and design of highly efficient OPV materials. By selecting relevant descriptors and implementing diverse ML algorithms, we aim to provide a framework to help to improve predictive accuracy and to streamline the selection of promising molecules for synthesis. We hope our findings demonstrate ML's potential to enhance material discovery, offering valuable insights to both experimental chemists and theoretical researchers in the pursuit of more efficient and stable OPV systems.

Introduction

Organic Photovoltaic Cells (OPV) represent a rapidly growing area of research within renewable energy, offering a potentially low-cost and flexible alternative to traditional inorganic-based solar cells. The efficiency and stability of OPVs have improved significantly over the past decade, driven by advances in material science and device engineering, pushing power conversion efficiency (PCE) up to 20% [1]. However, designing and optimizing OPV materials remains challenging due to the vast chemical space of organic molecules and the complex interplay of factors influencing their performance.

Unlike inorganic semiconductors, organic compounds can give rise to an immense variety of materials with diverse properties. While this vast chemical space allows for exploring many molecular combinations and arrangements that could result in novel materials for photovoltaic applications, it also introduces the challenge of selecting, among hundreds or thousands of molecules, those with potential for further investigation. Experimental trial-and-error methods, although valuable, become impractical in this context due to their labor-intensive nature and high demand of time and resources.

Theoretical approaches offer an alternative path to address material selection, since a deeper understanding of the physical phenomena involved in photoconversion processes can guide the design and synthesis of more efficient molecules. Nonetheless, this task remains challenging due to the extremely complex, non-linear relationships governing the underlying processes [2]. Even one of the most well-known theoretical models, the Scharber model [3], was quickly deemed unviable due to its poor performance, limited application domains, and the intensive computational power required to calculate predictors.

In this scenario, the urgent need for innovative methodologies has made Machine Learning (ML) a powerful tool to address these challenges, given its ability to uncover hidden patterns in large datasets and make accurate predictions [4]. In fact, recent advances in ML, combined with the growing availability of experimental and computational data is opening new avenues for the rational design of OPV materials,

allowing the prediction of molecular properties and optimization of device's architectures priorly to any laboratory effort [5].

This work intends to explores the application of ML in OPV research, discussing challenges and opportunities while presenting case studies that demonstrate ML's effectiveness in accelerating material discovery and optimization. Our goals include selecting key descriptors for ML models, comparing various ML algorithms, training models on diverse datasets, and trying to uncover new correlations between descriptors and device properties.

Our aim is to select models and descriptor that might assist chemists in selecting molecules and polymer candidates for synthesis and characterization and to highlight the transformative potential of ML in the quest for efficient and sustainable solar energy solutions.

Methodology

- **Dataset:** Several small databases have already been compiled, based on publications of devices that were fabricated and experimentally characterized, and made available by other works [5, 6, 7]. In this proposal, a mixed database of approximately 2000 molecules of fullerene and non-fullerene acceptors for bulk heterojunction (BHJ) devices will be used, given the small number of studies carried on mixed datasets. Other architectures (such as tandem or ternary systems) will be excluded. If possible, recently documented molecules will be included.
- **Descriptors:** The selection of descriptors is crucial for the performance of ML models, as demonstrated in several works [7]. In this work, we intend to analyze several descriptors, including electronic (e.g., energy of HOMO/LUMO, polarizability, fundamental gap), structural (Morgan fingerprint [8], CDK fingerprint [9]), and morphological descriptors (D/A weight ratio and surface roughness, since morphology can affect device performance [3]), as well as experimental conditions, aiming to select a smaller, computationally inexpensive subset for model development. Algorithms of sequential feature selection, regularization (Ridge and Lasso) and techniques like principal component analysis (PCA) will be employed. The relevance of each descriptor will be determined through calculation of feature relevance with tree-based methods [10], since it could offer a greater understanding of the phenomena affecting photoconversion processes, as well as new insight principles for designing more efficient molecules. Part of the molecules of our database have been submitted to geometry optimization calculations at L.S.S.C/UnB, in such a way that we soon expect to have a good dataset that includes descriptors calculated via DFT and TD-DFT.
- **ML Algorithms:** Several ML models have been successfully applied to PCE prediction. The work of Sahu et al. [11], for example, have trained treed-based models (GBRT and RF) to predict PCE with person correlation coefficients as high as 0.7~0.8. Other works have also used more sophisticated models like Convolutional Neural Networks (CNNs) [12] and Graph Neural Networks (GNNS) [13], reaching incredible prediction accuracy in computational datasets, but not comparable correlation in experimental datasets. In our work we will train some baseline models, like GBRT, RF, SVR, and compare their performance with that of more sophisticated ones (CNNs and GNNs).

Results and Discussion

We aim to demonstrate that ML models can accurately predict experimental properties with good accuracy, analyze feature relevance, and use statistical analysis to uncover correlations between descriptors and device parameters. Various models will be tested with data not seen in the training set (the data will be split into training, validation and test data) and metrics will be used to evaluate and compare their efficiency and accuracy. Some of the algorithms we intend to implement are: Neural Networks (ANN, CNN, GNN), k-NN, Support Vector Regression [14], Kernel Ridge Regression, tree-based models (BART, RF, GBRT) [10].

Conclusion

We hope this work will highlight ML's potential to guide experimental chemists and theoretical scientists in OPV research and open up new perspective for future studies that could explore, among other things, new ML algorithms, molecular representations and embeddings, and applications to more complex device architectures (like tandem and ternary systems).

One thing is noticed here: the lack of unified experimental databases greatly hinders the exploration of experimental data, since it forces researchers to carry careful reviews of various experimental articles or to analyze several smaller databases created by other works, all time-consuming tasks, in order to create their own databases. Therefore, we hope that future centralized datasets may foster more comprehensive and reproducible research, accelerating advancements in the field of OSC's engineering

Acknowledgements

We'd like to express a special acknowledgment to Tiago Cassiano, T.S.A.C and to professor Pedro, P.H.O.N, both from the Institute of Physics of the University of Brasilia for allowing us to use the computer equipment of the L.S.S.C/UnB.

References

(1) Liu, K.; Jiang, Y.; Ran, G.; Liu, F.; Zhang, W.; Zhu, X.; Joule 2024, 8 (3), 835–851.
(2) Ma, W.; Tumbleston, J. R.; Wang, M.; Gann, E.; Huang, F.; Ade, H.; Advanced Energy Materials 2013, 3 (7), 864–872.
(3) Padula, D.; Simpson, J. D.; Troisi, A.; Materials Horizons 2019, 6 (2), 343–349.
(4) Nasrabadi, N.; Journal of Electronic Imaging 2007, 16 (4), 049901.
(5) Sun, W.; Zheng, Y.; Yang, K.; Zhang, Q.; Shah, A. A.; Wu, Z.; Sun, Y.; Feng, L.; Chen, D.; Xiao, Z.; Lu, S.; Li, Y.; Sun, K.; Science Advances 2019, 5 (11).
(6) Nagasawa, S.; Eman Al-Naamani; Saeki, A.; Journal of Physical Chemistry Letters 2018, 9 (10), 2639–2646.
(7) Zhao, Z.; Geng, Y.; Troisi, A.; Ma, H.; Advanced Intelligent Systems 2022, 4 (6), 2100261.
(8) Morgan, H. L.; Journal of Chemical Documentation 1965, 5 (2), 107–113.
(9) Steinbeck, C.; Han, Y.; Kuhn, S.; Horlacher, O.; Luttmann, E.; Willighagen, E.; Journal of Chemical Information and Computer Sciences 2003, 43 (2), 493–500.
(10) Hastie, T.; Tibshirani, R.; Friedman, J. The Elements of Statistical Learning: Data Mining, Inference, and Prediction, 2nd ed.; Springer: New York, 2009.
(11) Sahu, H.; Ma, H.; The Journal of Physical Chemistry Letters 2019, 10 (22), 7277–7284.
(12) Sun, W.; Li, M.; Li, Y.; Wu, Z.; Sun, Y.; Lu, S.; Xiao, Z.; Zhao, B.; Sun, K.; Advanced Theory and Simulations 2018, 2 (1).
(13) Eibeck, A.; Nurkowski, D.; Menon, A.; Bai, J.; Wu, J.; Zhou, L.; Mosbach, S.; Akroyd, J.; Kraft, M.; ACS Omega 2021, 6 (37), 23764–23775.
(14) Smola, A. J.; Schölkopf, B.; 2004, 14 (3), 199–222.

Machine Learning Models for Predicting the Degradation Kinetics of Organic Compounds in Aquatic Environments

Vinícius Freire Gomes Ferreira (PG)[1]*, Valter Henrique Carvalho Silva (PQ)[1] e Flávio Olimpio Sanches Neto (PQ)[1,2]
[1]Theoretical and structural chemistry laboratory of Anápolis, State University of Goiás, Anápolis-Goiás, Brazil.
[2]Theoretical and Structural Chemistry Laboratory of Anápolis, State University of Goiás and Federal Institute of Goiás, Anápolis-Goiás, Brazil.
e-mail: viniciusfgomesferreira@gmail.com
Keywords: Acid Hydrolysis, Degradation, Artificial Intelligence, Kinetic Constant.

Abstract
The presence of organic compounds (OCs) in aquatic environments is a growing concern due to their negative impacts on the biosphere and human health. Current water treatment plants are not effective at removing emerging pollutants, including pharmaceuticals, which are ultimately released into the environment through wastewater treatment plant effluents. These contaminants, detected at concentrations ranging from ng/L to µg/L in various water matrices, represent a significant risk, particularly due to the development of antibiotic resistance. To address this challenge, the study proposes the use of advanced computational methods to predict the degradation of OCs, focusing on acid and base hydrolysis reactions. The methodology involves constructing a database with 880 OCs and their respective kinetic constants (kH^+), extracted from various scientific sources. Molecular representations were generated using the Morgan fingerprint, and four machine learning (ML) algorithms - Neural Network (NN), Random Forest (RF), LightGBM (LGB), and XGBoost (XGB) - were applied to predict the kinetic constants. The results showed that XGB, with a fingerprint length of 3072 bits, performed the best in predicting acid hydrolysis kinetic constants, followed by RF. The NN model performed better with a fingerprint length of 1024 bits, while LGB showed inferior performance, suffering from overfitting. The analysis of the results indicated that the XGB model was successful in predicting the experimental data, demonstrating robustness and accuracy. This study significantly contributes to the understanding of OC degradation reactions, offering a powerful predictive tool for application in real-world water treatment scenarios, aligned with international regulatory guidelines.

Introduction
The presence of OCs in aquatic environments is a significant concern due to their potential impacts on the biosphere and human health [1]. Water treatment plants are not equipped to handle emerging pollutants, including pharmaceuticals released into the environment through wastewater treatment plant effluents [2]. More than 61 active pharmaceutical ingredients have been detected in rivers worldwide, causing adverse effects on aquatic organisms and the development of antibiotic resistance in bacteria [3].

Organic contaminants are classified as pharmaceutical compounds, personal care products, microcystins, pesticides, veterinary products, surfactants, dyes, and endocrine disruptors [4]. Studies indicate that treated effluents still contain traces of these compounds in various water matrices, including drinking water, with concentrations ranging from ng/L to µg/L [5]. To address this issue, it is essential to develop effective degradation protocols,

such as advanced oxidative processes (AOPs) and acid and base hydrolysis, which accelerate the kinetic constant of OC transformation [6]. However, these methods are expensive and time-consuming. Therefore, the application of theoretical and computational protocols is crucial to understanding these phenomena. Electronic structure calculations and modern kinetic theories help predict OC degradation, providing parameters such as reaction rate constants and half-life times. Models like SPARC and QSAR/QSPR are used to predict chemical properties but require high computational costs and sophisticated physical-chemical knowledge. Recently, ML algorithms have shown accuracy in predictions, utilizing large datasets and advanced computational resources. Protocols like pySiRC, which combine molecular fingerprints (MF) with ML, have demonstrated effectiveness in predicting kinetic constants of OC degradation with hydronium radicals [7].

This work aims to extend the kinetic constant prediction protocol for OCs in oxidative environments to include acid and base hydrolysis reactions, adding temperature as a crucial parameter. The goal is to align with the principles of the OECD, EMA, RDC 53/2015 from ANVISA, ICH guidelines, and FDA, clearly defining the applicability domain and adopting measures of adequacy, robustness, and predictive capability.

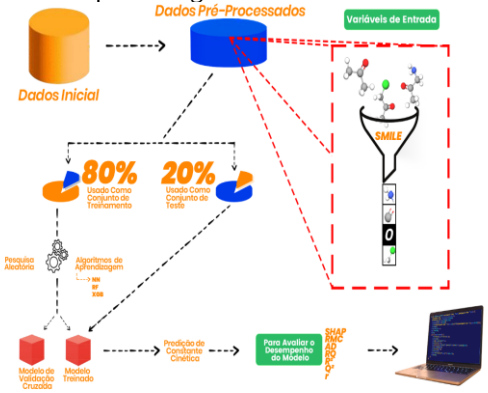
Methodology

Initially, a database was constructed encompassing 880 OCs with their respective kH^+ values. These data were extracted from various scientific sources and include kinetic constants for acid-catalyzed hydrolysis reactions under different temperature conditions in the aqueous phase. For building machine learning models, molecular representations were used, specifically the Morgan fingerprint, generated with the RDKit program. The Morgan fingerprints were created with different bit lengths (512, 1024, 2048, 3072, 4096, and 8192) [8].

Four machine learning algorithms were employed to predict the acid hydrolysis kinetic constants: NN, RF, LGB, and XGB. XGB was chosen for its robustness and ability to combine multiple decision trees. XGB, efficient and fast, constructs decision trees sequentially, correcting previous errors. NN was used for its capability to capture complex and non-linear relationships between variables. These models leverage the specific advantages of each approach in predicting the kH^+ kinetic constants [9].

To ensure the robustness and accuracy of the models, both internal and external validations were performed. The kH^+ constant data were divided into training (80%) and testing (20%) sets. Performance indices such as external validation (Q_{ext}) and the Correlation Coefficient were calculated. For training, a 10-fold cross-validation was used, where the data were divided into 10 subsets, with one subset being validated while the other nine were used for training. External validation tested the models on data not included in the training set. Statistical significance was assessed with a p-value (<0.05), and residual plots were analyzed to verify model adequacy [8].

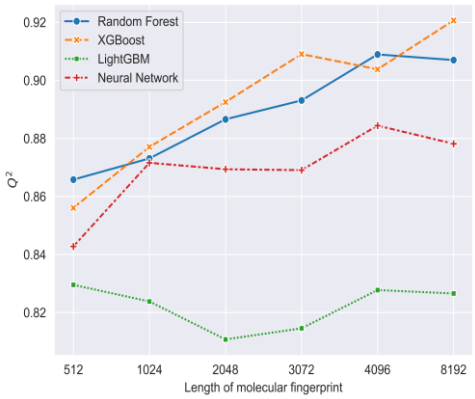
Figure 1: Operation of the machine learning model for predicting kinetic constants.



Results and Discussion

A database was created with kinetic constant information for 880 OCs for acid hydrolysis. The evaluation of the predictive power (Q^2) of the RF, XGB, LGB, and NN models across a range of fingerprint lengths between 512 and 8192 bits revealed distinct trends among the models, highlighting the importance of selecting the appropriate length to optimize performance, as shown in Figure 2.

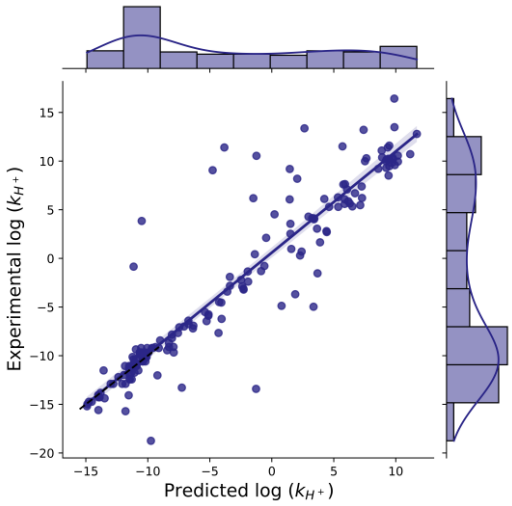
Figure 2: Effects of Morgan fingerprint length on Q^2 values for the RF, XGB, LGB, and NN models.



To select the optimal MF length for the Morgan type, a preliminary analysis was conducted. Figure 2 illustrates the effect that varying the MF length has on the Q^2 of the different models employed. For the kH$^+$ radical dataset, a length of 3072 bits showed the best performance for the XGB and RF models, while for the NN model, a length of 1024 bits was the most effective.

Models like LGB, which generally exhibited inferior performance, appeared to suffer from overfitting with longer fingerprints and were thus disregarded. Consequently, the length of 3072 bits was selected; lengths greater than 3072 bits led to an insignificant increase in Q^2 but made the calculations more demanding.

Figure 3: Predicted versus experimental values plot for datasets of the oxidative process mediated by -H$^+$ radicals in aqueous OCs.



The prediction plots of the XGB model with 3072-bit fingerprints versus experimental values for both datasets are shown in Figure 3. They cover a significant range of values from 5.85 x 10^{-13} a 14 x 10^7 $M^{-1}s^{-1}$ in the case of the kH$^+$ dataset. When the data tend to align with the reference line, they are considered well-predicted. The XGB model applied to the dataset achieved a successful representation (solid line) of the reference line, indicating the robustness of the models used to evaluate the external data.

Acknowledgements

Thanks to UEG for the financial support and to my advisors.

References

1. Wilkinson, J. L.; et al. "Pharmaceutical pollution of the world's rivers." Proc. Natl. Acad. Sci. USA 2022, 119, e2113947119.
2. Aus der Beek, T.; et al. "Pharmaceuticals of emerging concern in aquatic systems." Water Res. 2019, 151, 445–451.
3. Rodriguez-Narvaez, O. M.; et al. "Evaluation of emerging pollutants of concern in aquatic systems." Environ. Sci. Technol. 2016, 50, 7433–7450.
4. Zheng, S.-S.; et al. "Machine learning approaches to predict the apparent rate constants for aqueous organic compounds by ferrate." J. Environ. Manage. 2023, 329, 116904.
5. Benotti, M. J.; et al. "Pharmaceuticals and endocrine-disrupting compounds in U.S. drinking water." Environ. Sci. Technol. 2008, 43, 597–603.
6. Huang, M.; et al. "Mineralization of emerging contaminants by advanced oxidation processes." Chemosphere 2018, 206, 46–53.
7. Peng, Y.-S.; et al. "SHAP fingerprinting: predicting the reaction kinetics between chlorine and aqueous organic contaminants." Environ. Sci. Technol. 2023, 57, 5195–5204.
8. Sanches-Neto, F. O.; et al. "pySiRC: Machine Learning Combined with Molecular Fingerprints." *Environ. Sci. Technol.*
8. Sudhakaran, S.; et al. "QSAR models for oxidation of organic micropollutants in water." Water Res. 2013, 47, 1111–1122.

Advancing Understanding of CaO Nanocluster Adsorption Sites Through DFT/ML-DFTB Sequential Approach

Wallison dos S. Dias (PG)[1], Gabriela M. B. da Silva (IC)[1], Roberta Dias (PQ)[2], Maicon P. Lourenço (PQ)[3] and Julio C. S. da Silva (PQ)[1].

[1]Instituto de Química e Biotecnologia, Universidade Federal de Alagoas - UFAL.
[2]Núcleo Interdisciplinar de Ciências Exatas e da Natureza, Universidade Federal de Pernambuco - UFPE
[3]Departamento de Química e Física, CCENS, Universidade Federal do Espírito Santo – UFES

wallison.dias@iqb.ufal.br

Keywords: Machine Learning; DFT; Glycerol; Catalysis; Absorption.

Abstract

In this work, we applied a sequential approach based on the DFT/ML-DFTB scheme to map the PES concerning the adsorption of glycerol on the CaO oxide surface. Different binding sites were characterized, all thermodynamically favorable, where the most favorable one has adsorption energy ΔE_{ads}=-3.15 eV.

Introduction

Recent environmental and meteorological data underscore the increasing severity of global warming, exacerbated by society's heavy reliance on fossil fuels, which account for 80% of energy production [1,2]. Biodiesel is a significant renewable option due to its low toxicity, absence of aromatic compounds and sulfur, and emissions-reducing properties.

However, large-scale biodiesel production yields by-products such as crude glycerol, presenting disposal challenges due to its impurities and toxicity, rendering it unsuitable for direct use or combustion. Chemical catalysis reforming glycerol for hydrogen production shows promise, particularly with alkaline earth metal oxides that enhance stability and activity by reducing site basicity [3].

Computational approaches like density functional theory (DFT) and density functional-based tight binding (DFTB) assist in elucidating molecular interactions and accelerating catalyst development. Despite the computational demands of DFT, economical alternatives like DFTB are considered viable [4,5,6,7].

Methodology

The initial structure of the CaO nanocluster used in this study was proposed by Chen et al., 2017. For machine learning (ML) simulations based on active learning methods, the QML Material program [10] was employed. This AI-based program uses DFTB and ML regression to find near-global minimum structures on the energy surface, employing statistical models for property calculation selection.

A number of active learning steps (N=200, 400, 600, 800, 1000) was used to find low-energy glycerol adsorption structures on a fixed CaO nanocluster. Glycerol's translational and rotational flexibility pinpointed stable regions on the catalyst surface.

Ten ML-generated structures were selected according to energetic criteria and optimized via DFT with Gaussian 09 v.D01, applying the B3LYP-D3 functional and 6-31G basis set, including dispersion corrections per Grimme's D3 approach.

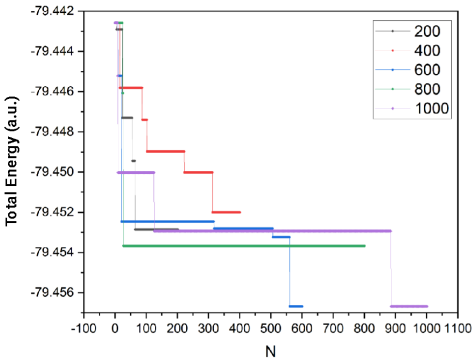
Adsorption energies (ΔE_{ads}) were calculated from DFT geometry optimization calculations started from structures generated from ML-DFTB simulations.

Results and Discussions

Gaussian process regressions were applied to create regression models for each data point analyzed during the active learning

steps. These models underwent initial validation testing. The training dataset's average root mean square error (Av. RMSE) was approximately 0.6, indicating satisfactory model performance. Figure 1 shows the total energy of each structure generated via ML calculated via DFTB.

Fig 1. Total energy (a.u.) calculated for different ML-DFTB simulations as a function of the number of active learning steps (N).



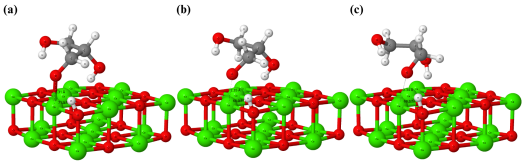
Testing across different numbers of steps and different simulations consistently achieved the minimum energy level from the initial structure. The lowest minimum was obtained for N=600 and 1000 simulations.

Figures 2-4 show the DFT-optimized structures of the ten selected initial structures from ML-DFTB simulations. Complexes 1-3 showed the shortest Ca-O bond lengths (2.31-2.35 Å) and coordination angles (68.0-71.5°), suggesting a strong interaction. In this case, a proton transfer of one of the OH glycerol groups was characterized. Table 1 shows the calculated adsorption energies for the then complexes.

Table 1. ΔE_{ads} values calculated at the B3LYP-D3/6-31G(d) from the ML-DFTB and DFT optimized structures started, respectively.

Complex	$\Delta E_{ads}^{DFT//ML-DFTB}(eV)$	$\Delta E_{ads}^{DFT}(eV)$
1	-0.64	-3.15
2	-0.62	-3.08
3	-0.61	-3.06
4	-0.54	-1.91
5	-0.46	-1.88
6	-0.45	-1.85
7	-0.37	-1.77
8	-0.35	-1.61
9	-0.29	-1.53
10	-0.21	-1.50

Fig 2. Optimized structures of the complexes 1-3.



Complexes 4-7 had ΔE_{ads} values of -1.70 to -1.95 eV, showing lower stability than complexes 1 to 3, where an effective proton transfer occurred (~ -3.0 eV). Complexes 8-10 displayed longer Ca-O bond lengths (2.57-2.63 Å), indicating less favorable adsorption configurations. On the other hand, complexes 8 and 10 showed a bidentate adsorption mode with glycerol's central OH group interacting with calcium atoms without proton transfer.

Fig 3. Optimized structures of the complexes 4-7.

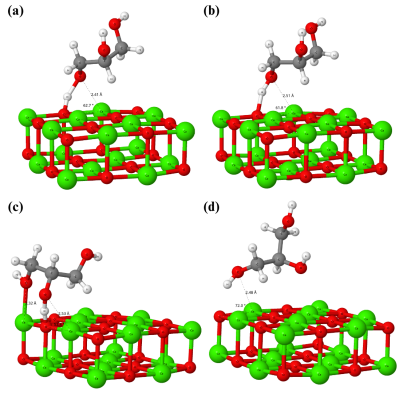
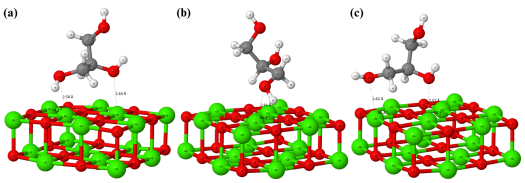


Fig 4. Optimized structures of the complexes 8-10



Single-point energy calculations on ML-DFTB generated structures were

compared with DFT-optimized ΔE_{ads} values. The DFT's results presented relatively superior stability. Despite ML/DFTB's potential to show an efficient approach for exploring potential energy surfaces (PES), the significantly larger stabilization calculated from DFT optimization calculations suggests that refinement of ML-DFTB structures using DFT calculations is essential to improve accuracy.

Conclusions

The findings suggest that sequential machine learning (or active learning) with quantum chemical methods effectively maps the potential energy surface during glycerol adsorption onto CaO nanoclusters. DFT calculations confirm that glycerol adsorption onto CaO is thermodynamically favorable. The preferred mode of interaction involves glycerol's terminal oxygens bonding with calcium atoms situated on the periphery of the catalyst's surface.

Acknowledgements

PPGQB-UFAL, CNPq, CAPES, and FAPEAL.

References

1. ESMAEIL, H. A critical review on the economic aspects and life cycle assessment of biodiesel production using heterogeneous nanocatalysts. Fuel Processing Technology. 2022, 230.

2. Saetiao, P. et al. Catalytic conversion of palm oil into sustainable biodiesel using rice straw ash supported-calcium oxide as a heterogeneous catalyst: Process simulation and techno-economic analysis. Case Studies in Chem. and Env. Eng. 2023, 8.

3. Lin, Y. Catalytic valorization of glycerol to hydrogen and syngas. Int. J. of Hydrogen Energy. 2013, 38.

4. CHEN, G. et al. Mechanism insights into Hg(II) adsorption on kaolinite(001) surface: A density functional study. Applied Surface Science. 2019, 488.

5. CUNY, J. et al. Density-functional tight-binding approach for metal clusters, nanoparticles, surfaces and bulk: application to silver and gold. Journal of Physics: Condensed Matter. 2018, 30.

6. SANTOS, E.; SCHMICKLER, W. Hydrogen adsorption on doped graphene investigated by a DFT-based tight-binding method. Journal of Physics: Condensed Matter. 2021, 33.

7. SELLI, D. et al. Water Multilayers on TiO_2 (101) Anatase Surface: Assessment of a DFTB-Based Method. Journal of Chemical Theory and Computation. 2017, 13.

8. YANG, Z.; GAO, W. Applications of Machine Learning in Alloy Catalysts: Rational Selection and Future Development of Descriptors. Advanced Science. 2022, 9, 2106043.

9. GOLDSMITH, B. R. et al. Machine learning for heterogeneous catalyst design and discovery. American Institute of Chemical Engineers. 2018, 64, 9.

10. Lourenço, M. P.; Herrera, L. B; Hostaš, J.; Calaminici, P.; Köster, A.; Tchagang, A.; Salahub, D. R.; QMLMaterial─A Quantum Machine Learning Software for Material Design and Discovery. J. Chem. Theory Comput. 2023, 19, 17.

10º SIMPÓSIO DE ESTRUTURA ELETRÔNICA E DINÂMICA MOLECULAR
SEEDMOL 4 a 8 novembro | 2024
Pirenópolis, Goiás

Investigando a dinâmica conformacional da diidroorotato desidrogenase (MtbDHODH) de *Mycobacterium tuberculosis* para descoberta de inibidores antituberculose.

Wemenes Jośe Lima Silva[1,2], Marina Sena Mendes[2], Maria Cristina Nonato[2], Melina Mottin[1,2] and Carolina Horta Andrade[1,2]*
[1] LabMol - Laboratory for Molecular Modeling and Drug Design, Faculdade de Farmácia, Universidade Federal de Goiás, Goiânia.
[2] CRAFT - Center for the Research and Advancement of Fragments and Molecular Targets, Faculdade de Ciências Farmacêuticas de Ribeirão Preto, USP, Ribeirão Preto, Brazil.
Email: *carolina@ufg.br*
Palavras-chave: Tuberculose; Inibidor; Dinâmica Molecular Acelerada Gaussiana; Diidroorotato desidrogenase.

Abstract
Tuberculosis (TB) is the most lethal bacterial infection, requiring prolonged treatment and highlighting the need for new therapies. The dihydroorotate dehydrogenase from *Mycobacterium tuberculosis* (MtbDHODH) has emerged as a promising drug target due to its essential role in pyrimidine biosynthesis. This study employed molecular dynamics and GaMD simulations to investigate MtbDHODH interactions with dihydroorotate, flavin mononucleotide, and the inhibitor QU22, which exhibits an IC_{50} of 5 µM. The analysis revealed that residue F10 is pivotal in binding QU22 to the enzyme's active site. These findings provide valuable insights for the design of new, potent, and selective MtbDHODH inhibitors.

Introdução

A tuberculose (TB) é uma doença bacteriana crônica e altamente contagiosa, causada principalmente por *Mycobacterium tuberculosis*[1]. Atualmente, existem apenas 12 fármacos aprovados pelo FDA para o tratamento da TB[2]. Devido à escassez de opções terapêuticas e ao tratamento prolongado, que pode durar até dois anos, é crucial buscar novas moléculas candidatas a fármacos contra TB.

Nesse contexto, a enzima diidroorotato desidrogenase de *M. tuberculosis* (MtbDHODH) surge como um alvo promissor para o desenvolvimento de novos fármacos anti-TB, devido ao seu papel essencial na biossíntese de pirimidinas, uma via metabólica conservada em todos os organismos[2]. A inibição seletiva da DHODH reduz as concentrações de pirimidinas, destacando-a como um alvo terapêutico de grande interesse[3,4].

O processo de pesquisa e desenvolvimento de novos fármacos é lento e dispendioso[5,6], mas metodologias computacionais como a dinâmica molecular (MD), têm contribuído para reduzir o tempo e os custos[7,8]. Neste contexto, a dinâmica molecular acelerada gaussiana (GaMD) se destaca como uma abordagem robusta para amostragem aprimorada e cálculos de energia livre de biomoléculas, permitindo simulações mais eficientes de processos biológicos complexos[9]. Este trabalho utilizou GaMD para investigar aspectos estruturais da enzima MtbDHODH, com o objetivo de auxiliar no planejamento de novos inibidores para o tratamento da tuberculose.

Metodologia

A estrutura da DHODH de classe 2 de *Mycobacterium tuberculosis* (cepa H37Rv) foi predita utilizando o *software* ColabFold[10]. Em seguida, foram realizados ensaios inibitórios de uma biblioteca *in-house* por meio da medição indireta da atividade enzimática da MtbDHODH,

monitorando a redução do 2,6-diclorofenolindofenol (DCIP), conforme protocolo previamente estabelecido[11].

Para avaliar os modos de ligação do composto com melhor atividade no ensaio enzimático (QU-22), foram realizados cálculos de docking molecular entre a enzima MtbDHODH e o composto QU-22, utilizando o software GLIDE[12], e campo de força OPLS4. O complexo MtbDHODH, cofator mononucleotídeo de flavina e o produto diidroorotato, juntamente com o composto QU-22A foi simulado através de GaMD no software AMBER22, utilizando campo de força ff14SB[13]. O sistema foi solvatado em uma caixa de água octaédrica TIP3P. Após a minimização de energia inicial e a termalização, foi aplicado a GaMD para simular o sistema[9]. A simulação incluiu uma etapa de equilíbrio de 50 ns, seguido de uma etapa de produção de 1 µs.

Resultados e Discussão

Após os ensaios de inibição *in vitro* da biblioteca *in-house* de fragmentos testada contra a MtbDHODH, o composto 2,6-dibromoquonaclorimida (QU-22) apresentou IC_{50} de 5 µM.

Os cálculos de docking molecular entre o inibidor QU-22 e a MtbDHODH sugerem que a interação ocorra através de duas ligações de hidrogênio com a R106 e interações hidrofóbicas com A17, V21 e I318, como demonstrado na Figura 1. Na enzima DHODH humana, o resíduo de arginina correspondente desempenha um papel crucial no reconhecimento de inibidores de DHODH[14].

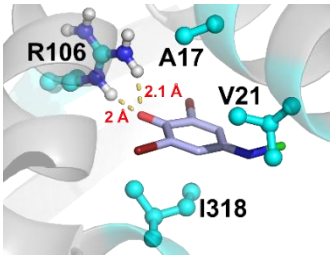


Figura 1. Docking molecular entre QU-22 (azul claro) e a enzima MtbDHODH modelada (resíduos de aminoácidos, em ciano).

Durante a GaMD, o *backbone* da MtbDHODH variou menos de 2 Å (Figura 2). Por sua vez, o inibidor QU-22 apresentou picos de variação no início e final da simulação (Figura 2).

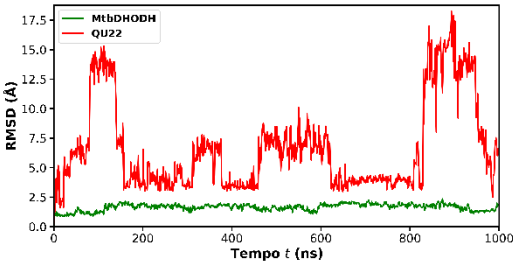


Figura 2. Raiz do desvio médio quadrático (RMSD) pelo tempo para os átomos do *backbone* da proteína (em verde) e dos átomos pesados do inibidor QU-22 (em vermelho).

Foi observado que o primeiro pico de variação do inibidor QU-22 foi causado pelo seu distanciamento dos resíduos de aminoácidos: R106, L9, I318 e V21 (Figura 3A, 3C, 3D, 3E); e sua aproximação com o resíduo F10 (Figura 3B). Por sua vez, o pico de variação ao final da simulação foi desencadeado pelo seu afastamento dos resíduos de aminoácidos R106, F10, I318, L9 e V21 (Figura 3A-E); e sua aproximação com os resíduos L38 e Y2 (Figura 3F-G).

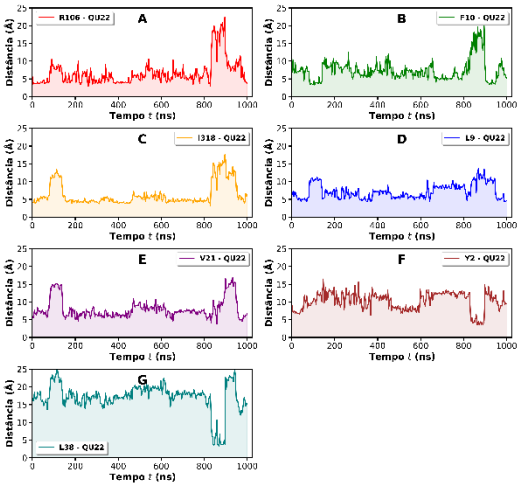


Figura 3. Séries temporais da distância entre o centroide dos resíduos de aminoácidos e o centroide do inibidor QU-22. A - R106; B - F10; C - I318; D - L9; E - V21; F - Y2; G - L38.

Além disso, foi observado que após o inibidor QU-22 fazer interações hidrofóbicas com os resíduos Y2 e L38, o inibidor QU-22 se dissocia do sítio de ligação e passa a interagir com o solvente. Em seguida, o QU-22 volta a interagir com

o resíduo de aminoácido F10, e entra novamente no sítio de ligação. Mostrando que o resíduo F10 é importante para a atividade inibitória do QU-22.

Conclusões

Os dados obtidos neste estudo fornecem insights valiosos para o planejamento de inibidores potentes e seletivos da MtbDHODH. Em particular, o resíduo de aminoácido F10 mostrou-se essencial para o reconhecimento do inibidor QU-22 no sítio de ligação, destacando a importância de considerar o papel de F10 no design de novos compostos terapêuticos destinados ao tratamento da tuberculose.

Agradecimentos

CAPES, CNPq, IPTSP, LabMol, CRAFT.

Referências

1. Quaglio, G.; Pizzol, D.; Isaakidis, P.; Bortolani, A.; Tognon, F.; Marotta, C.; Di Gennaro, F.; Putoto, G.; Olliaro, P. L.; *Am J Trop Med Hyg* **2019**, *101*, 12.
2. Jones, M. E.; *Annu Rev Biochem* **1980**, *49*, 253.
3. Reis, R. A. G.; Calil, F. A.; Feliciano, P. R.; Pinheiro, M. P.; Nonato, M. C.; *Arch Biochem Biophys* **2017**, *632*, 175.
4. Munier-Lehmann, H.; Vidalain, P.-O.; Tangy, F.; Janin, Y. L.; *J. Med. Chem.* **2013**, *56*, 3148.
5. Lombardino, J. G.; Lowe, J. A.; *Nat Rev Drug Discov* **2004**, *3*, 853.
6. Paul, S. M.; Mytelka, D. S.; Dunwiddie, C. T.; Persinger, C. C.; Munos, B. H.; Lindborg, S. R.; Schacht, A. L.; *Nat Rev Drug Discov* **2010**, *9*, 203.
7. Liao, C.; Sitzmann, M.; Pugliese, A.; Nicklaus, M. C.; *Future Med Chem* **2011**, *3*, 1057.
8. Braga, R. C.; Alves, V. M.; Silva, A. C.; Nascimento, M. N.; Silva, F. C.; Lião, L. M.; Andrade, C. H.; *Curr Top Med Chem* **2014**, *14*.
9. Wang, J.; Arantes, P. R.; Bhattarai, A.; Hsu, R. V.; Pawnikar, S.; Huang, Y. M.; Palermo, G.; Miao, Y.; *WIREs Computational Molecular Science* **2021**, *11*.
10. Mirdita, M.; Schütze, K.; Moriwaki, Y.; Heo, L.; Ovchinnikov, S.; Steinegger, M.; *Nat Methods* **2022**, *19*, 679.
11. Calil, F. A.; David, J. S.; Chiappetta, E. R. C.; Fumagalli, F.; Mello, R. B.; Leite, F. H. A.; Castilho, M. S.; Emery, F. S.; Nonato, M. C.; *Eur J Med Chem* **2019**, *167*, 357.
12. Friesner, R. A.; Murphy, R. B.; Repasky, M. P.; Frye, L. L.; Greenwood, J. R.; Halgren, T. A.; Sanschagrin, P. C.; Mainz, D. T.; *J Med Chem* **2006**, *49*, 6177.
13. Maier, J. A.; Martinez, C.; Kasavajhala, K.; Wickstrom, L.; Hauser, K. E.; Simmerling, C.; *J Chem Theory Comput* **2015**, *11*, 3696.
14. Liu, S.; Neidhardt, E. A.; Grossman, T. H.; Ocain, T.; Clardy, J.; *Structure* **2000**, *8*, 25.

10º SIMPÓSIO DE ESTRUTURA ELETRÔNICA E DINÂMICA MOLECULAR
SEEDMOL 4 a 8 novembro | 2024 Pirenópolis, Goiás

Virtual Screening de *minor cannabinoids* com alvo na inibição da agregação da β-amilóide

Wendel Souza da Luz[1], Letícia de Almeida Nascimento[1], Érica Cristina Moreno do Nascimento, João Batista Lopes Martins
[1]Laboratório de Química Computacional, Instituto de Química, Universidade de Brasília, CP 4478, Brasília-DF, Brasil.
Email: wendel.souza.daluz@gmail.com
Keywords: Alzheimer; β-amilóide; docking molecular; virtual screening; canabinoides; *in silico*

Abstract
This study aims to investigate the beta-amyloid aggregation inhibition potential of compounds derived from *Cannabis sativa*, the minor cannabinoids, by conducting in silico studies via docking molecular and non-covalent interactions (NCI), and using virtual screening techniques.

Introdução

A doença de Alzheimer (DA) disparou o alerta a saúde pública global, uma vez que, é a causa de mais de 70% de todos os casos de demência. É um distúrbio neurodegenerativo crônico caracterizado pelo declínio progressivo cognitivo e de habilidades funcionais como pensar, falar, incapacidade de exercer atividades do dia a dia entre outras.[1]

Como marcadores patológicos a DA apresenta supressão dos níveis colinérgicos de acetilcolina, hiperfosforilação da proteína Tau, formação de emaranhados neurofibrilares no meio sináptico e acúmulo de placas da proteína β-amilóide.[2]

A agregação dos protofilamentos de β-amilóide decorrem do desbalanço entre a produção e depuração das espécies Aβ associados a mutações na proteína precursora denominada APP[3], os quais podem se transformar estruturalmente de monômeros em múltiplos estados oligoméricos tóxicos.[4]

A Aβ é gerada a partir da proteína APP por meio da clivagem sequencial de β- e γ-secretase e a sua homeostase cerebral depende de diferentes vias, como degradação enzimática, cruzamento da barreira hematoencefálica, fluxo de massa do fluido intersticial e absorção do líquido cefalorraquidiano (LCR).[5] Sendo assim, formas de inibição da agregação dos protofilamentos Aβ têm sido a principal aposta como alvo para o desenvolvimento de terapias para a DA. [5]

Até o momento, os tratamentos para a DA disponíveis são eficazes apenas no estágio inicial da doença, logo outra abordagem explorada para o desenvolvimento de novas estratégias terapêuticas para a DA é o uso potencial de canabinoides frente aos sintomas neurodegenerativos. Isto possivelmente justifica-se pela alta expressão, no hipocampo e córtex, do sistema endocanabinoide (SEC). [6]

Boa parte desses estudos desenvolvidos concentram-se no canabidiol (CBD) e no tetrahidrocanabinol (THC), entretanto sabe-se que cerca de 120 tipos de fitocanabinoides também estão presentes em menor quantidade nas folhas da planta *Cannabis sativa*, os chamados canabinoides raros. [7]

Este estudo tem por objetivo avaliar *in silico*, a interação entre 130 moléculas pertecentes aos canabinoides raros e fármacos clássicos usados no tratamento da doença de Alzheimer e os protofilamentos β-amilóide 1-42, sob código PDB 2BEG.[8]

Metodologia

As estruturas dos canabinoides raros foram obtidas e extraídas após uma extensa busca de dados em diversas bases de dados.[9] Posteriormente foi preparado o sistema bioquímico utilizando como biorreceptor os

protofilamentos β-amilóide 1-42 (código PDB 2BEG) e as estruturas moleculares encontradas como ligantes, os quais foram submetidos a um estudo de docking molecular, por meio do software AutoDock Tools[10] e o algoritmo Vina, visando obter os resultados de energia de ligação (score) durante o processo de inibição Aβ dos compostos selecionados.

Em sequência, um estudo de Virtual Screening dos resultados de score obtidos pelo estudo anterior de docking molecular foi realizado com o propósito de selecionar o conjunto de fitocanabinoides com o maior potencial de inibição. As interações entre os candidatos e o alvo biológico foram analisadas minuciosamente em relação às suas conformações para os complexos de maior energia de ligação.

Resultados e Discussão

Foi observado que a maior parte das moléculas com a energia de ligação mais estável interagiram com os resíduos Ala21, Leu34 e Val34 das cadeias A, B e C dos protofilamentos Aβ. Foram observadas interações do pi-stacking, pi-alquila, pi-sigma e interações do tipo van der Waalls de longo alcance, que ocorreram majoritariamente com o resíduo Glu22.

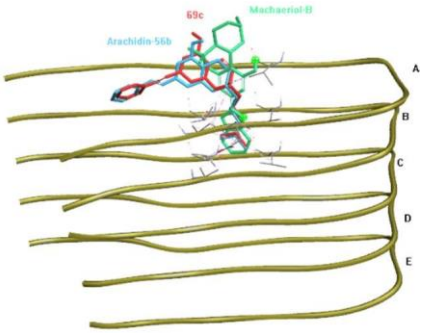


Figura 1: Complexos obtidos através do estudo de docking molecular.

As moléculas com maiores valores de score foram a Machaeriol-B (-8,00 kcal/mol), 69c (-8,10 kcal/mol) e Arachidin-56b (-8,50 kcal/mol). Estas moléculas conseguiram interagir com os resíduos das cadeias A, B e C dos protofilamentos Aβ.

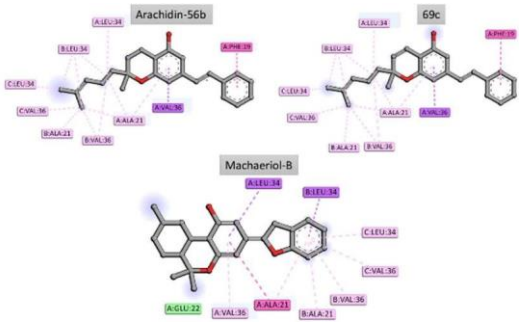


Figura 2: Interações formadas com os ligantes Arachidin-56b, 69c e Machaeriol-B.

Conclusão

Os canabinoides raros apresentaram interações favoráveis com os resíduos dos filamentos da β-amilóide, revelando ser uma classe de moléculas promissoras para o tratamento da DA.

Estudos posteriores deverão ser realizados para melhor investigação das interações entre estes compostos com os protofilamentos da proteína Aβ.

Agradecimentos
Unb, FAP-DF, CNPq e CAPES.

Referências

1. PERNECZKY, R; D, G; C, A; F, P; B, C. European Jour. of Neurology. 31, 2, 2024.
2. Twarowski, B.; H, M. Intern. Jour. of Mol. Scie., 24, 7, 1 abr. 2023.
3. MURPHY, M. P.; L., H. Jour. of Alzh. Dise. J., 19, 1, 311, 2010.
4. LEE, S. J. C. et al. Chem. Soc. reviews, 46, 2, 310–323, 2017.
5. ZHANG, Yun et al. Sig. Trans. and Tar. The., 8,1, 2023.
6. Abate, G.; U, D.; T, S. Biology, 10, 6, 1 jun. 2021.
7. KIM, Juyong et al. Inter. Jour. of Mol. Scie. 24, 7, 2023.
8. T. Lührs, C. Ritter, M. Adrian, D. Riek-Loher, B. Bohrmann, H. Döbeli, D. Schubert and R. Riek,

Proc. Natl. Acad. Sci. U.S.A., 2005, 102, 17342–17347.

9. Philip E.**Nuc. Acids Resea.**, 28, 1, 235–242, 2000.
10. Morris, G. M. et al. Jour. of Comp. Chem., 30, 16, 2785–2791, 27 dez. 2009.

10º SIMPÓSIO DE ESTRUTURA ELETRÔNICA & DINÂMICA MOLECULAR
SEED MOL 4 a 8 novembro | 2024 Pirenópolis, Goiás

Análise das reações de óxido de Formaldeído com gases poluentes atmosféricos usando a dinâmica de colisões moleculares AB initio e surface-hopping

[1]Weslley Nascimento de Lima, [2]Ademir João Camargo, [3]Solemar Silva Oliveira
[1]Universidade Estadual de Goiás, Laboratório de Química Teórica e Estrutural, Anápolis-GO, Brasil,
[2]Universidade Estadual de Goiás, Laboratório de Química Teórica e Estrutural, Anápolis-GO, Brasil
[3]Universidade Estadual de Goiás, Laboratório de Química Teórica e Estrutural, Anápolis-GO, Brasil

lima787b@gmail.com

Keywords: Óxido de Carbonila; Gases poluentes; Dinâmica molecular; Estado excitado; Intermediários Criegee

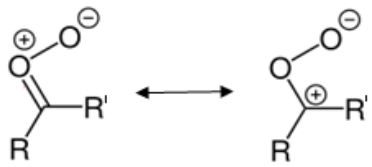
Abstract

Criegee intermediates, also known as carbonyl oxides, are unstable molecules capable of reacting with atmospheric pollutants such as CO, SO_2 and NO_x to form volatile organic compounds (VOCs). Although many of these reactions occur in excited states, the mechanisms are still not fully understood. This project aims to investigate the mechanisms of formaldehyde oxide reactions with these atmospheric gases both in the ground state and in excited states, using ab initio molecular collision dynamics. In addition, the photochemical stability will be analyzed using Surface-Hopping molecular dynamics. The potential energy curves generated by molecular collision dynamics will be used to calculate the rates of gas phase reactions.

Introdução

O Óxido de Carbonila é uma substância química dotada de duas cargas elétricas ressonantes, tal como ilustrado na Figura 1. Foi pela primeira vez postulado na década de 1950 por Rudolf Criegee, sendo conhecido por Intermediários Criegee, Zwitterions Criegee ou ainda Birradicais Criegee. (Welz et al., 2012).

Figura 1. Estrutura ressonânte dos óxidos de carbonila.



Os estudos pioneiros dos mecanismos de Crieege desencadearam investigações intensivas subsequente. Por volta de meados dos anos 70, o mecanismo de Criegee com a presença do óxido de carbonila haviam sido confirmados, entretanto, raramente foram detectadas em condições laboratoriais, devido à alta instabilidade química dos intermediários Criegee (IsC) que tem um período de vida muito curto.

A compreensão dos IsC a partir de evidências experimentais indiretas sobre a sua verdadeira natureza química, ou seja, se é um Zwitterion ou Birradical foi tema de debate por longo tempo.(Hassan et al., 2021)

Esses óxidos são extremamente reativos e podem reagir com SO_2 e NO_x presentes na atmosfera terrestre. Estes gases poluentes formam aerossóis e estão envolvidos no controle do clima global. O fato desses poluentes poderem ser transportados por grandes distâncias, está bem ilustrado pela poluição do ar no Ártico, a qual pode as vezes se tornar tão grave quanto a de áreas industriais. Tais episódios de poluição são conhecidos como *Arctic*

Haze. Os poluentes são originários da combustão de combustíveis fósseis, fundição e outros processos industriais no norte da Europa e Rússia. Os poluentes são transportados para o Ártico por fluxo de ar em escala sinótica padrão, principalmente entre dezembro e abril. Desde que a atmosfera ártica em geral seja estavelmente estratificada durante essa época do ano, a mistura vertical fica limitada. Além disso, as precipitações são raras de modo que a remoção úmida é enfraquecida e consequentemente, os poluentes podem ser transportados por grandes distâncias com relativamente pouca diluição. Um dos principais contribuintes para o Arctic haze é o SO_2 , que é convertido em partículas de sulfato ao longo das grandes distâncias de transporte. Registros glaciais indicam que a poluição do ar ártico aumentou consideravelmente desde a década de 1950, paralelamente aos aumentos de emissões de SO_2 e NO da Europa. Curiosamente a análise de séries cronológicas de amostras de gelo profundas da Groelândia revelaram concentrações de chumbo altas durante o período 500 A.C a 3000 D.C, isso é atribuído as atividades de mineração e fundição de chumbo e prata gregos e romanos que aparentemente poluíram grandes regiões do hemisfério Norte (Wallace & Hobbs, 2006).

Os óxidos de carbonila são importantes também no processo de produção dos radicais OH (Stone et al., 2012), os quais são reagentes importantes da atmosfera e ajudam a controlar a poluição (Finlayson-Pitts Barbara & Pitts James, 1999). Estudo de espectroscopia de infravermelho (IR) tem mostrado que os óxidos de carbonilas apresentam essencialmente um caráter zwitteriônico, ao contrário do caráter birradical proposto inicialmente (Su et al., 2013).

Os intermediários Criegee podem sofrer decaimento unimolecular logo após sua formação, produzindo radicais OH. No entanto, a interação do óxido de carbonila com outras moléculas gasosas podem levar a sua estabilização. Outra maneira de estabilizar os óxidos crieege é através das colisões com outras moléculas gasosa.

Metodologia

Neste projeto, o estudo da colisão das moléculas dos gases poluentes atmosféricos contra o óxido de formaldeído será realizado usando métodos de dinâmica molecular ab initio (dinâmica molecular de Born-Oppenheimer DMBO e/ou dinâmica molecular de Car-Parrinello- DMCP).

Todos os cálculos de dinâmica molecular serão realizados usando o software CPMD 4.3 (*CPMD. Car-Parrinello Molecular Dynamics Manual: An Ab Initio Electronic Structure and Molecular Dynamics Program*, 2015). Uma caixa cúbica de adequado será construída e dentro dela será colocado uma molécula de óxido de formaldeído e uma molécula de gás SO_2 ou NO_x. Essa caixa deve ser grande o bastante para posicionar a molécula do gás a uma distância de aproximadamente 6 Å da molécula do HCOO. A essa distância não existe interação significativa entre as duas moléculas. O core iônico será descrito usando as pseudopotenciais ultrasoft de Vanderbilt (Vanderbilt, 1990). As funções de onda dos elétrons de valência serão expandidas usando ondas planas como funções de base com uma energia de corte de 25 Ry, e 200 Ry serão usados na expansão da densidade de cargas. O funcional de troca e correlação que será usado nos cálculos de DFT será selecionado a partir de testes preliminares. As condições periódicas de fronteiras serão impostas nos cálculos e a temperatura não será controlada (ensemble NVE). As equações de movimento serão integras numericamente usando o algoritmo de *Velocity-Verlet* com passo de integração de 4 unidades atômicas de tempo.

Não existe uma maneira direta de estudar colisões moleculares usando o programa CPMD. Portanto, será necessário fazermos alguns procedimentos adicionais para simular as colisões. A ideia é, inicialmente, rodar um passo de dinâmica no CPMD. Dessa forma, obteremos os arquivos de saída GEOMETRY e GEOMETRY.xyz. Estes dois arquivos contém as posições e as velocidades atuais de todos os átomos do sistema. A partir do arquivo GEOMETRY.xyz, poderemos construir um novo arquivo GEOMETRY

que contém a orientação e as velocidades iniciais dos átomos da molécula de ataque. Em seguida, com o novo o arquivo GEOMETRY, reinicializamos o cálculo no CPMD. Desse modo, a molécula de ataque terá a energia cinética previamente estipulada para a colisão.

Os resultados dos cálculos serão armazenados no arquivo TRAJEC.xyz que pode ser visualizado usando o programa VMD 1.9. Várias trajetórias serão construídas com o objetivo de determinar, com a melhor precisão possível, a energia cinética da molécula de ataque necessária para que ocorra a reação.

Para o estudo da estabilidade fotoquímica do H_2COO faremos uso da dinâmica molecular de Surface-Hopping.

Resultados

Espera-se, ao final do projeto, entender as etapas da reação do H_2COO com os gases poluentes SO_2 e NO_x tanto em seu estado fundamental quanto excitado, quantificar as barreiras energéticas da complexação, identificar as interações formadas e avaliar a estabilidade fotoquímica do H_2COO, incluindo seus impactos no meio ambiente e saúde humana.

Conclusões

Ainda não foi iniciada a dinâmica de colisões, portanto o projeto ainda está em adamento.

Agradecimentos

Agradeço ao apoio da UEG para a realização desse projeto, bem como os docentes e colegas de laboratório, ao meu orientador e a todos da minha família.

Referências

1.Berendsen, H. J. C., Grigera, J. R., & Straatsma, T. P. (1987). The missing term in effective pair potentials. *The Journal of Physical Chemistry*, *91*(24), 6269–6271. https://doi.org/10.1021/j100308a038

2.Car, R., & Parrinello, M. (1985). Unified Approach for Molecular Dynamics and Density-Functional Theory. *Physical Review Letters*, *55*(22), 2471–2474. https://doi.org/10.1103/PhysRevLett.55.2471

3.Chetouani, L. (2005). *Path Integrals in Quantum Mechanics* (U. Oxford University Press, Ed.; Vol. 38). https://doi.org/10.1088/0305-4470/38/23/B03

4.CPMD. Car-Parrinello Molecular Dynamics Manual: An ab initio Electronic Structure and Molecular Dynamics Program (pp. 202–202). (2015).

5.Dykstra, C. E. (1993). Electrostatic interaction potentials in molecular force fields. *Chemical Reviews*, *93*(7), 2339–2353. https://doi.org/10.1021/cr00023a001

6.Finlayson-Pitts Barbara, & Pitts James. (1999). *Chemistry of the Upper and Lower Atmosphere Theory, Experiments, and Applications* (1st Edition). Academic Press.

7.Halgren, T. A., & Damm, W. (2001). Polarizable force fields. *Current Opinion in Structural Biology*, *11*(2), 236–242. https://doi.org/10.1016/S0959-440X(00)00196-2

8. Hassan, Z., Stahlberger, M., Rosenbaum, N., & Bräse, S. (2021). Criegee Intermediates Beyond Ozonolysis: Synthetic and Mechanistic Insights. *Angewandte Chemie International Edition*, *60*(28), 15138–15152. https://doi.org/10.1002/anie.202014974

9.Hobbs, P. v. (2000). *Introduction to Atmospheric Chemistry* (1st Edition). Cambridge University Press. https://doi.org/10.1017/CBO9780511808913

10.Kohn, W., & Sham, L. J. (1965). Self-Consistent Equations Including Exchange and Correlation Effects. *Physical Review*, *140*(4A), A1133–A1138. https://doi.org/10.1103/PhysRev.140.A1133

11.M. P. Allen, & D. J. Tildesley. (1987). *Computer Simulation of Liquids*. Clarendon Press.

12.Marx, D., & Hutter, J. (2000). *Ab initio molecular dynamics: Theory and Implementation* (J. Grotendorst, Ed.; 1st ed., Vol. 1). http://www.fz-juelich.de/nic-series/

13.Marx, D., & Hutter, J. (2009). *Ab Initio Molecular Dynamics*. Cambridge University Press.

https://doi.org/10.1017/CBO9780511609633

14. McCammon, J. A., Gelin, B. R., & Karplus, M. (1977). Dynamics of folded proteins. *Nature*, *267*(5612), 585–590. https://doi.org/10.1038/267585a0

boldface typing or capital letter except for section headings].

Aqueous Solvation of Pyridoxine (Vitamin B6) Using Car-Parrinello Molecular Dynamics

Wilson R. Lopes Filho[1], Lóide O. Sallum[2] and Ademir. J. Camargo[1]
[1]Grupo de Química Teórica e Estrutural de Anápolis, UEG, Anápolis, GO, Brazil.
[2]Laboratório de Ciências Farmacêuticas, Universidade Evangélica de Goiás, Anápolis, GO, Brazil.
wilsonrobertolopesfilho99@gmail.com; loide.sallum@gmail.com; ajc@ueg.br
Keywords: Hydrogen bonding, QTAIM, Ab Initio.

Abstract
Pyridoxine, one of the natural forms of vitamin B6, is an enzymatic cofactor involved in a multitude of biochemical transformations. It is used for the treatment of sideroblastic anemia, pyridoxine-dependent epilepsy, isoniazid-induced peripheral neuropathy, and vitamin B6 deficiency, which is directly related to an increased risk of cardiovascular disease, stroke, hypertension, diabetes, and some types of cancer. Despite its pharmacological importance, the underlying mechanisms of its effects are not fully understood. Given that its biological activities occur in an aqueous environment and that there is a scarcity of studies explicitly considering the interaction of pyridoxine with water, this study aims to understand the effects of an aqueous solvent on its geometric and electronic parameters using Car-Parrinello Molecular Dynamics (CPMD). CPMD results show that the aqueous environment primarily affects the bond lengths and angles of nitrogen and hydroxyl groups in pyridoxine due to the interaction between water molecules and these sites. Radial distribution function (RDF) and mean residence time (MRT) were used to characterize the solvation structure. Four stable hydrogen bonds between water molecules and the H22, H23, O3, and N4 sites were identified. Helmholtz free energy indicates that the formation of these interactions is thermodynamically favorable, and the topological analysis of electron density (QTAIM) shows that the strength of the H23-Ow, N4-Hw, and O2-Hw bonds ranges from weak to moderate after the bonds stabilize, while for the H22-Ow bond, it varies from weak to strong. The supramolecular arrangement of pyridoxine in the solid state was studied using Hirshfeld surface analysis. These findings enhance the understanding of pyridoxine chemistry in the human body and contribute to explaining its biological activities.

Introduction

Pyridoxine and its derivatives, pyridoxamine and pyridoxal, are the three natural forms of vitamin B6. In the body, they are converted into their active form, a coenzyme that participates in a multitude of biochemical transformations [1].

As such, pyridoxine, a water-soluble substance, is indispensable for human health, possessing various bioactivities. Among them, its role in regulating heart rate, immune system function, and neurotransmitter biosynthesis stands out [1]. In the pharmaceutical industry, it is used to treat sideroblastic anemia, pyridoxine-dependent epilepsy, isoniazid-induced peripheral neuropathy, and vitamin B6 deficiency [2]. A low level of vitamin B6 is associated with an increased risk of cardiovascular disease, stroke, inflammatory bowel disease, hypertension, diabetes, and some types of cancer [2], [3], [4].

Although pyridoxine is essential for body homeostasis, the mechanisms related to its effects are not yet fully understood. The structure and dynamics of the hydration shell significantly impact any chemical reaction in aqueous solvents. Therefore,

understanding the solvation structure of pyridoxine in the human body, an aqueous environment, is crucial to understanding its mechanisms of action.

Thus, pyridoxine has become the target of several theoretical studies aimed at investigating the influence of aqueous solvation on its effects [5], [6], [7], [8]. Most use density functional theory together with polarized continuum models to simulate the aqueous solvent, with few explicitly considering the interaction of pyridoxine with water. To the best of our knowledge, no studies have examined the effects of solvation using Ab Initio Molecular Dynamics. Recently, this technique has been used to study the aqueous solvation of biomolecules [9], [10].

Therefore, the present study aims to investigate the effects of aqueous solvation on the geometric and electronic parameters of pyridoxine using Car-Parrinello Molecular Dynamics. QTAIM will be used to characterize hydrogen bonding interactions. Additionally, a topological study was conducted using Hirshfeld surface analysis.

Methodology

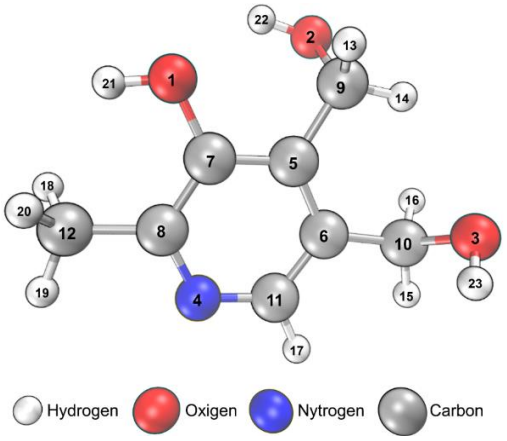
The CPMD simulations were conducted using the CPMD software package. To evaluate the effects of the aqueous solvent on pyridoxine, two systems were simulated: one containing a single pyridoxine molecule and another with 84 water molecules and one pyridoxine molecule. Both systems were built in a cubic periodic box of 16 Å. Geometric parameters and Helmholtz free energies for the bonds, as well as analyses of the RDF and MRT for the active sites, were calculated using the gqtea program.

Results and Discussion

Figure 1 contains the molecular structure of pyridoxine with its respective atomic numbering used in the calculations.

A comparison of bond lengths and angles between isolated pyridoxine and pyridoxine with water reveals that the most affected parameters directly involve the hydroxyls and nitrogen of pyridoxine. This study shows that these changes are due to the interaction between water molecules and these sites.

Figure 1: Geometric structure of pyridoxine and the respective atomic numbering used in the calculations.



RDF was employed to identify water molecules interacting with specific sites and to measure the limits of hydration layers. The results show well-defined distribution peaks for the H22, H23, O3, and N4 sites, indicating the presence of water molecules in the region of maximum distribution. For these sites, the first solvation layer of g(H(22)--O(w)), g(H(23)--O(w)), g(O(3)--H(w)), and g(N(4)--H(w)) has extremes of 1.40-2.45; 1.35-2.65; 1.50-2.45; and 1.40-2.45, respectively, with the maximum distribution at 1.55 Å, 1.55 Å, 1.75 Å, and 1.85 Å, respectively (The symbol w indicates that it is a water atom).

The integral of the RDF function indicates that only one oxygen atom from water molecules, on average, remained within the first hydration sphere for the H22 and H23 sites. For the O3 and N4 sites, the integral of the radial distribution function gave 1.519 and 1.317 hydrogen atoms, respectively. For O(2), the distribution peak corresponding to the first solvation layer showed a low value of the RDF function, lower than that of the second solvation layer. It is also observed that the integral of the RDF function was 0.673, indicating that, on average, less than one water molecule remains in the first layer. This may indicate that the hydrogen atoms of water molecules do not stay in the first layer for long, requiring further analysis to evaluate this site.

To confirm the validity of the bonds, MRT was performed for the O2, O3, H22, H23, and N4 sites, which estimates the average time a water molecule was coordinated to a specific solute site. For the H(22) and H(23) sites, it was found that one water molecule remained within the solvation layer for 98 and 99% of the simulation time. For the O2 site, up to four different water molecules enter and leave the first solvation sphere; however, only one remains for a considerable time (64% of the simulation time), exiting and re-entering multiple times. For the O(3) and N(4) sites, more than one water molecule is present within the first layer at the same time. However, for both, only one water molecule remains coordinated for a significant period, 87.14% and 80.56%, respectively.

To characterize the hydrogen bonds formed, the geometric and energetic parameters of each were analyzed. The shortest bond lengths and the most linear angles were observed for the H22-Ow (1.731, 162.87) and H23-Ow (1.7815, 164.08) bonds, also presenting the lowest formation energies. For the O2-Hw, O3-Hw, and N4-Hw bonds, the lengths were 2.515, 2.212, and 2.357, and the angles were 145.089, 125.055, and 135.468, respectively. Helmholtz free energy shows that the formation of these interactions is thermodynamically favorable.

To characterize the strength of the hydrogen bonds formed, QTAIM was used. For the largest bond distances, $\nabla^2 \rho(r)$ was less than 0.1 and V(r)/G(r) was less than 1.0, indicating that at the limit of oscillation, the interactions are weak, with hydrogen bond character. For the shortest distances, the H23-Ow, O3-Hw, and N4-Hw interactions showed $\nabla^2 \rho(r)$ less than 0.1 and V(r)/G(r) between 1 and 2, indicating moderate bond strength with partially covalent character. For the shortest distance of the H22-Ow interaction, $\nabla^2 \rho(r)$ was less than 1 and V(r)/G(r) greater than 2, showing that the interaction between pyridoxine and water molecules was strong and covalent. Therefore, for the H23-Ow, O3-Hw, and N4-Hw bonds, the interaction strength ranges from weak to moderate after the bond stabilizes, while for the H22-Ow bond, it varies from weak to strong.

The packing of vitamin B6 crystals, studied using Hirshfeld surface analysis, explains the relationship between intermolecular contacts and physicochemical properties in aqueous media. The supramolecular arrangement generates a zigzag sheet-like structure within the crystalline network, which contributes to the solubility of vitamin B6 in aqueous media.

Acknowledgements

I thank the UEG and my advisor, Ademir J. Camargo, for their support.

References

1. Parra, M.; Stahl, S.; Hellmann, H. Cells, v. 7, p. 84, 2018.
2. Bowling, F. G. Seminars in Cell & Develop. Bio, v. 22, n. 6, p. 611-618, 2011.
3. Shtyrlin, Y.G.; Petukhov, A.S.; Strelnik, A.D. et al. Russ Chem Bull, v. 68, p. 911–945, 2019.
4. Merigliano, C.; Mascolo, E.; Burla, R.; Saggio, I.; Vernì, F. Front. Genet., v. 9, p. 388, 2018.
5. Matxain, J. M.; Ristilä, M.; Strid, Å.; Eriksson, L. A. Chemistry–A European Journal, v. 13, n. 16, p. 4636-4642, 2007.
6. Abyar, F.; Farrokhpour, H. Journal of Photochemistry and Photobiology A: Chemistry, v. 336, p. 77-88, 2017.
7. Gamov, G. A.; Khokhlova, A. Yu.; Gushchina, A. S.; Grazhdan, K. V.; Sharnin, V. A. The Journal of Chemical Thermodynamics, v. 97, p. 322-330, 2016.
8. Škorňa, Peter; Rimarčík, Ján; Poliak, Peter; Lukeš, Vladimír; Klein, Erik. Computational and Theoretical Chemistry, v. 1077, p. 32-38, 2016.
9. Camargo, L. T. D. M.; Signini, R.; Rodrigues, A. C. C.; Lopes, Y. F.; Camargo, A. J. The Journal of Phys. Chem. B, v. 124, n. 32, p. 6986-6997, 2020.
10. Rodrigues, A. C. C.; Camargo, L. T. D. M.; Lopes, Y. F.; Sallum, L. O.; Napolitano, H. B.; Camargo, A. J. Journal of Molecular Liquids, v. 343, 117451, 2021.

Unveiling the effect of phosphorylation and pH conditions on the conformational dynamics TMEM176B with an approach based on hybrid methods

Marcello, Y. M. B.[1], Pantaleão, S. Q.[1], Gasparini P.[1], General I. J.[2], Magro, A. J.[3], Scott, A. L.[1]
[1]Computational Biology and Biophysics Laboratory, Universidade Federal do ABC (UFABC), Santo André, São Paulo, Brazil.
[2]School of Science and Technology, Universidad Nacional de San Martin, ICIFI and CONICET, Argentina.
[3]Department of Bioprocesses and Biotechnology, School of Agriculture (FCA), Universidade Estadual Paulista Júlio de Mesquita Filho (Unesp), Botucatu, São Paulo, Brazil.
ana.scott@ufabc.edu.br
Keywords: TMEM176B; Molecular Dynamics; Normal Modes Analysis.

Abstract
This study explores the structural dynamics and metastable states of the transmembrane protein TMEM176B, focusing on its function as a non-selective monovalent cation channel. Using Normal Mode Analysis (NMA) and Molecular Dynamics simulations(MD), the researchers investigated the protein's flexibility and conformational transitions under varying conditions, including pH levels and phosphorylation states. The study used VMOD, a method that combines NMA and MD, to sample the conformational heterogeneity space of TMEM176, generating intermediate structures to assess the protein's structural behavior. The distances between specific Cα atoms were analyzed to distinguish between closed and open conformations, with projections onto essential principal components for a detailed conformational analysis. Channel properties of TMEM176B were further analyzed using MOLE 2.5, focusing on radius, length, charge, and polarity, with findings suggesting an optimal channel configuration at pH 4 when phosphorylated. The study reveals that TMEM176B's structural flexibility is influenced by phosphorylation and pH, with key mutations (Q153A and A134T) exhibiting significant deviations in flexibility compared to the wild-type. Overall, this research provides insights into the mechanistic role of TMEM176B in immune responses and suggests avenues for further investigation, particularly in comparing phosphorylated and non-phosphorylated states.

Introduction

The transmembrane protein 176B (TMEM176B) is an acid-sensitive homo or heterodimeric protein that is localized intracellularly within various immunological cells and functions as a non-selective monovalent cation channel [4,6]. Research by Mercedes Segovia (2019) has associated TMEM176B with the negative regulation of the NLRP3 inflammasome, particularly in anti-tumor responses, where ion flux triggered by pathogen-associated molecular patterns and damage-associated molecular patterns serves as a primer for inflammasome activation. Moreover, by the same authors, high stromal expression of TMEM176B has been correlated with significantly reduced survival in patients with colon cancer and molecules that enhance the efficacy of immune checkpoint inhibitors by inhibiting TMEM176B-dependent ion flux were detected. In vitro assays using CHO-7 cells demonstrated that BayK8644, known for modulating Ca2+ channels, inhibited Na+

flux and increased IL-1β secretion and caspase-1 activation in wild-type bone marrow-derived dendritic cells, but not in Tmem176b knockout cells. Additionally, in both human and mouse dendritic cells, TMEM176B is found in the Golgi apparatus, endosomes, and phagosomes. Phylogenetic analyses suggest a relationship between TMEM176B and MSA4, though they diverged from a common evolutionary ancestor [5]. Furthermore, Tmem176b knockout bone marrow-derived dendritic cells displayed a transiently alkalinized phagosomal pH compared to wild-type cells, leading to speculation that TMEM176B may regulate endophagosomal pH similarly to MSA4 [4]. Recent studies by Marcelo Hill at the Pasteur Institute in Montevideo indicate an inverse correlation between TMEM176B expression and inflammasome activation in critically ill COVID-19 patients. The current study aims to investigate the structural dynamics and metastable states of TMEM176B in both its wild-type and mutant forms, identifying the collective movements responsible for the transition between metastable states, which may elucidate the mechanisms of channel function.

Methods

Normal Mode Analysis and Conformational Space Sampling

Normal Mode Analysis (NMA) is employed to simplify the potential energy of a system through harmonic approximation. This technique involves representing the potential energy as a matrix, where its Hessian is diagonalized to identify normal modes and their associated vibrational frequencies. Energy minimization is conducted in two steps: first, with gradually decreasing harmonic restraints, and second, using the Adopted Basis Newton-Raphson method without restraints. After minimization, NMA is applied using the Iterative Mixed-Basis Diagonalization method and CHARMM36 force field. Root Mean Square Fluctuation (RMSF) values for alpha carbon atoms are then calculated to identify flexible regions of the structure.

Conformational Space Sampling along Collective Normal Modes

The selected normal modes were used in VMOD simulations, a CHARMM facility that applies energy minimization along the normal modes by adding restraints to the potential energy, leading to more realistic energy calculations. Structures were displaced along the selected modes, generating 81 intermediate structures, with non-bonded interactions kept constant. The distance between specific Cα atoms was measured to differentiate between closed and open conformations. These structures were then analyzed under varying conditions, including different pH levels and phosphorylation states, by projecting their distributions onto a subspace defined by the first two principal components using ProDy [3].

Channel Analysis

Attempts were made to detect TMEM176B channels using the MOLE 2.5 server, evaluating physicochemical properties as channel radius and polarity through Delaunay triangulation calculations of atomic centers and Voronoi diagram [1].

Molecular Dynamics with Excited Normal Modes

MDeNM combines Molecular Dynamics with Normal Mode Analysis to efficiently explore protein motions on micro to millisecond timescales. It involves short MD simulations where low-frequency NMs are excited by adding velocities along NM vectors. This method enhances conformational sampling and provides better insights into free energy landscapes compared to longer standard MD simulations [2].

Results and discussion

The phosphorylated structures at pH 4 and pH 5 exhibited the highest flexibility and accessed only one or two specific points, as determined by PCA (Fig. 1 and 2).

Figure 1 - Normalized RMSF for TMEM176B heterodimer WT. Ranges and modes on x and on y axis, respectively.

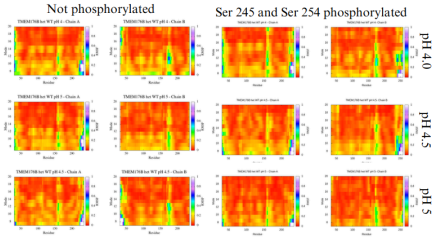
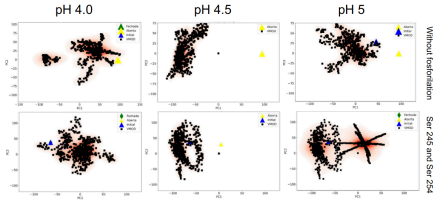
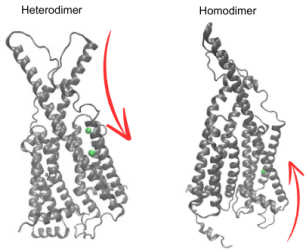


Figure 2 - Comparison of experimental and predicted space conformations for TMEM176B heterodimer WT. Brown points indicate values accessed by VMOD simulations, yellow and blue localize the open and initial, respectively, conformations on phase space of PC1 e 2.



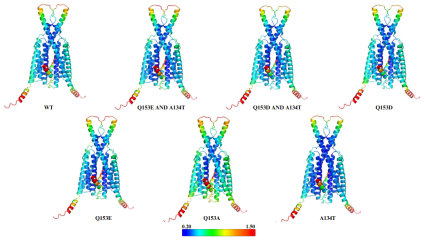
Channel analysis reveals that TMEM176B heterodimer, when phosphorylated at Ser 245 and Ser 254 at pH 4, exhibits the most promising channel potential, taking into account the significance of ionization. Channel analysis further elucidated that the most favorable channel between both is at pH 4 (Fig. 2).

Figure 3 - MDeNM performed with NAMD and CHARMM for heterodimeric state (left) and Molecular Dynamics performed with NAMD for homodimeric state (right).



The MD performed at pH 4 for homodimeric TMEM176B showed the expected channel mechanism. For phosphorylated heterodimeric case, the channel appears to be in the chain B, which is different from the expected by channel analysis (Fig 3).

Figure 4 - Average RMSF for TMEM176B homodimeric WT and mutants.



The Q153A and A134T mutations were significantly more and less flexible than the WT case, as has been experimentally predicted (Fig. 4).

Conclusion

TMEM176B plays crucial roles in various cellular processes and a substantial number of *in vitro* studies have examined its functionality. Otherwise, there is a notable lack of *in silico* studies that address TMEM176B conformational dynamics and the stability of its metastable states. In this study, we modeled the channel as a dimer, validated the model, and investigated the dynamic structure of this ionic channel, focusing on how phosphorylation and pH influence its intrinsic movements. Our findings clearly indicate that phosphorylation and pH significantly impact the channel's movement, either facilitating or hindering its opening. Further studies are required, such as comparing phosphorylated and non-phosphorylated states, as well as mutant cases using MDeNM and Steered Molecular Dynamics.

Acknowledgements

CAPES; FAPESP; CNPq; UFABC.

References

1. Berka, K. et al. Nucleic Acids Res. 2012, 40 (W1), W222-W227
2. Costa, M. G. S. et al J. Chem. Theory Comput. 2015, 11 (6), 2755-2767.
3. Floquet, N. et al. J. Mol. Biol. 2009, 385 (2), 653-664.
4. Hill, M. et al. Front. cell dev. biol. 2022, 10, 1038429.
5. Zuccolo, J. PLoS ONE. 2010, 5 (2), e9369.
6. Segovia, M. et al. Am. J. Transplant. 2014, 14 (5), 1021-103.
7. Segovia, M. et al. Cell Rep. 2019, 35, 767-781.e6.

Índice Remissivo

Alexandre A. Leitão, 5
Ana V. Cunha, 6
Andréia Luísa da Rosa, 7
Breno R. L. Galvão, 9
Celso Ricardo Caldeira Rêgo, 10
Diego Fernando da Silva Paschoal, 12, 27
Diego Guedes-Sobrinho, 11
Evangelos Miliordos , 13
Gerd Bruno Rocha, 28
Gregory S. Tschumper, 14
Guilherme D. R. Matos, 29
Isaac Martins Carvalho, 15
Kauê Santana, 30
Marco Antonio Chaer do Nascimento , 31
Munir Skaf, 16
Nailton Martins Rodrigues, 32
Pablo A. Denis, 17
Patricia R.P. Barreto, 20
Sérgio Emanuel Galembeck, 21
T. Daniel Crawford, 22
Valter Henrique Carvalho-Silva, 23
Werner Treptow, 24
Ángel Martín Pendás, 8
Airan Felipe Soares Brito , 35
Alessandra Ferreira Albernaz , 38
ALEX BISPO GAMA , 41
Ana Carolina Felisberto Araujo , 44
Ana Cristina Mora Tello , 47
Ana Paula de Oliveira , 50
ANDERSON PEDROSA DA SILVA , 53
André Corrêa Souza , 56, 59
André Luis de Oliveira Batista , 62
Anelisa Granato de Sousa , 66
Antonio Luiz de Almeida , 68
Antonio Rafael de Oliveira , 71
Arthur Alves Nascimento , 74
Asdrubal Lozada Blanco , 76, 79
AYSLLA CAMPOS MOURA , 82, 85
Bruno Bercini de Araújo , 88
Bruno Guilherme Araujo Pimenta , 91, 94
Caique Campos de Oliveira , 97
CARLOS ADOLFO VILCA HUAYHUA , 100
Carolina Manhães Santos , 103
Caroline Reis Santiago Paschoal , 106
Cristiane Alves da Fonseca do Espírito Santo , 109
Daniella Cintra Hilário de Paula , 112
Danilo Neves Silveira , 114
Diego Coelho Abreu , 117
Edna da Silva Machado Rodrigues , 120
Emanuel José Alexandrino dos Santos , 123
Erick dos Santos Morais , 127
Evangelos Miliordos , 130
Fabiani Fernanda Triches , 131
Felipe Ferreira de Araújo Braz , 134
Felipe Schoma Cardoso , 137
Fernando Teixeira Bueno , 140
Flávio Olimpio Sanches Neto , 142
Gabriel de Sousa Martins , 145
Gabriel Maia Tonin , 148
Gabriel Reynald da Silva , 149
Glauco Endrigo Moura de Lima , 152
Gustavo Gomes de Sousa , 154
Henrique de Araujo Chagas , 157
Hugo Xavier Rodrigues , 160
Isaac Martins Carvalho , 164, 165
Isaac Oliveira Miranda Magalhães , 166
Isabelle Alves Pereira , 169
Jailton Romão Viana , 171
Josenaide Pereira do Nascimento , 184
José Luiz Felix Santos , 181
João Felipe Camargo Pinheiro , 174
João Victor Ferreira da Costa , 177
Juan Rafael Gomez Quispe , 187
Julielson dos Santos Sousa , 190
Julio Cesar Verli Chagas , 193
Karinna mendanha Soares , 196

Kauê Santana da Costa , 199
Kelvyn Magalhães Lopes Rocha , 202
Larissa dos Santos Born , 205
Letícia Carolaine Silva Faria , 208
Letícia de Almeida Nascimento , 211, 214
Linara Tarusa Damascena Correa , 217
Luana Lemos Reis , 220, 222
Lucas Aires de Sousa , 225, 228
Lucas Bernardes Pena , 231
LUCAS DE SOUSA SILVA , 233
Lucas Gonçalves Randolli , 236
Lucca Moraes Gomes , 239
Luciano Ribeiro , 241
Luis Octavio de Araujo , 243
Luiz FMA Benicio , 246, 249
Maria Vitória Gerheim Rocha Dias , 252
Marina Heloysa Sanino da Silva , 255, 256
Matheus Rodrigues de Amorim Medina , 257
Murielly Fernanda Ribeiro Bihain , 259
Nalberth Batista Farias , 262, 266
Nícolas Ricardo de Melo Alves , 269
Patricia R P Barreto , 272
Paulo Henrique Silva Miranda , 275
Paulo Ricardo de Carvalho Magalhaes , 277
Pedro Henrique Ferreira Matias , 280
Pierre Carlos de Souza Junior , 282
Raabe Freitas dos Santos , 285
Rafael de Almeida Cordeiro , 287
Rafael do Couto Campos de Jesus , 290, 294
Rafael Ferreira Veríssimo , 297
Ramiro Marcelo dos Santos , 300
Renato Medeiros , 303
Roberto Luiz Andrade Haiduke , 306
Rodrigo Alves Costa , 309
Rodrigo Aparecido Lemos Silva , 311
Rodrigo do Monte Gester , 314
Thales André de Oliveira Paula , 315
Thales Machado Fernandes , 318
Thiago Mineo Mizumoto , 321
Thiago Soares Silva , 324
Vanessa Regina Miranda , 327
Victor de Souza Assumção Bonfim , 330
Vinícius Freire Gomes Ferreira , 339
Víctor de Souza Assumção Bonfim , 333
Víctor dos Reis Rodrigues , 336
Wallison dos Santos Dias , 342
Wemenes José Lima Silva , 345
Wendel Souza , 348
Weslley Nascimento de Lima , 351
Wilson Roberto Lopes Filho , 355
Yolanda Maria Barros Marcello , 358

APOIO:















www.seedmol.com.br